UNDERSTANDING THE DRIVERS OF TERROIR IN THE BAROSSA



FINAL REPORT TO WINE AUSTRALIA

Project Number: **UA1602**

Project Supervisors: **Cassandra Collins and Paul Petrie**

Understanding the drivers of terroir in the Barossa

Wine Australia Final Report

Project No. UA 1602

Project Supervisors: **A/Prof Cassandra Collins (UA)**
A/Prof Paul Petrie (SARDI)

Principal Researchers: **A/Prof Susan Bastian (UA)**
Dr Keren Bindon (AWRI)
Dr Marcos Bonada (SARDI)
Dr Paul Boss (CSIRO)
Dr Rob Bramley (CSIRO)
Prof Tim Cavagnaro (UA)
Dr Lukas Danner (UA)
Dr Leigh Francis (AWRI)
Dr Lira Souza Gonzaga (UA)
Prof Leigh Schmidtke (CSU)

University of Adelaide, Australia

September 2022

Disclaimer: The advice presented in this document is intended as a source of information only. The University of Adelaide (UA) and Wine Australia accept no responsibility for the results of any actions taken on the basis of the information contained within this publication, nor for the accuracy, currency or completeness of any material reported and therefore disclaim all liability for any error, loss or other consequence which may arise from relying on information in this publication.

Table of Contents

..... 1

1. Abstract..... 6

2. Executive Summary..... 7

3. Background 10

4. Project Aims 11

5. Methods..... 16

5.1 Experimental design and site establishment..... 16

5.1.1 Experimental design..... 16

5.1.2. Site establishment..... 17

5.1.3 Within-vineyard analysis..... 21

5.1.4 Regional scale analysis..... 22

5.1.5 Weather station installation..... 23

5.1.4 Soil moisture monitoring assembly and installation..... 24

5.2 Soil and vine measures 26

5.2.1 Soil measures..... 26

5.2.2 Vine measures..... 27

5.3 Grape chemistry..... 29

5.3.1 Amino acids, glutathione and vitamins B5 and B6..... 29

5.3.2 Fatty acids..... 29

5.3.3 Grape phenolics and skin tannins..... 31

5.3.4 Grape carotenoids..... 31

5.3.5 Grape volatile compounds..... 32

5.3.6 Grape 'Bound Volatile' Compounds..... 35

5.4 Small-lot winemaking..... 39

5.5 Wine chemistry 42

5.6 Sensory analysis 43

5.6.1 Samples..... 43

5.6.2 Methodology..... 43

5.6.3 Data analysis..... 44

5.7 Chemometric analysis of combined datasets..... 46

5.7.1 Data modelling..... 46

5.7.2 Consensus sensory spaces..... 47

5.7.3 Multiblock data sets..... 48

5.7.4 Sample selection for data modelling..... 62

6. Results/Discussion 64

6.1 Vineyard variability 64

6.2 Soil and vine measures 67

6.2.1 Soil Measures..... 67

6.2.1.1 Soil monitoring during the season..... 68

6.2.1.2 Plant available water capacity of soils at regional scale..... 69

6.2.2 Vine measures..... 70

6.2.2.1 Benchmarking water-limited yield potential and yield gaps of Shiraz..... 70

6.2.2.2 The relationship between terroir and the phenology of Barossa Shiraz..... 70

6.2.2.3 Carbon Isotope discrimination..... 71

6.3 Grape chemistry 77
6.3.1 Amino acids, glutathione and vitamins B5 and B6 77
6.3.2 Fatty acids 86
6.3.3. Tannin Composition 93
6.3.4. Carotenoids 98
6.3.5. Grape volatile compounds 102
6.3.6. Grape bound volatile compounds 110

6.4 Grape phenolics and wine non-volatiles and volatiles 118
6.4.1 Grape Phenolics 118
6.4.2 Wine non-volatiles and volatiles 118

6.5 Wine sensory 121
6.5.1 Vintage 2018 121
6.5.2 Vintage 2019 122
6.5.3 Vintage 2020 124
6.5.4 Vintage 2021 126

6.6 Chemometric analysis of combined datasets 129
6.6.1 AMOPLS Models of Region and site 129
6.6.2 Single vintage AMOPLS 129
6.6.3 All Vintage AMOPLS Models 130
6.6.4 Single Vintage AMOPLS Models – 2018 135
6.6.5 Single Vintage AMOPLS Models – 2019 137
6.6.6 Single Vintage AMOPLS Models – 2020 139
6.6.7 Single Vintage AMOPLS Models – 2021 141
6.6.8 Discussion of model performance 145
6.6.9 Unsupervised Cluster analysis of four vintage datasets – K-means 147
6.6.10 K-means variable importance Vintage 2018 149
6.6.11 K-means variable importance Vintage 2019 151
6.6.12 K-means variable importance Vintage 2020 152
6.6.13 K-means variable importance Vintage 2021 153
6.6.14 K-means variable importance All Vintages 154
6.6.15 Random Forests classification model 156
6.6.16 RF model visualisation 156
6.6.17 Global model 157
6.6.17.1 Sample classification accuracy and clustering 157
6.6.17.2 Predictor selection based on region 160
6.6.18 Binary classification models 167

7. Outcome/Conclusion 171

8. Recommendations 174

9. Appendix 1: Communication 175

1.1 Presentations 175

1.2 Publications 176
1.2.1 Published 176
1.2.2 In preparation 176

10. Appendix 2: Intellectual Property 177

11. Appendix 3: References 178

12. Appendix 4: Staff and Students 182

13. Appendix 5: Draft Manuscripts 183

5.1 Plant available water capacity of soils at regional scale: Analysis of fixed and dynamic field capacity 183

5.2 Benchmarking water-limited yield potential and yield gaps of Shiraz in the Barossa and Eden Valleys 204

5.3 The relationship between terroir and the phenology of Barossa Shiraz 227

14. Appendix 6: Models between sub-regions 255

6.1.1 Model between Central Grounds and Eastern Edge 255
6.1.2 Model between Central Grounds and Eden Valley 256
6.1.3 Model between Central Grounds and Northern Grounds 259
6.1.4 Model between Central Grounds and Southern Grounds 261
6.1.5 Model between Central Grounds and Western Ridge 263
6.1.6 Model between Eastern Edge and Eden Valley 264
6.1.7 Model between Eastern Edge and Northern Grounds 266
6.1.8 Model between Eastern Edge and Southern Grounds 267
6.1.9 Model between Eastern Edge and Western Ridge 269
6.1.10 Model between Northern Grounds and Eden Valley 270
6.1.11 Model between Southern Grounds and Eden Valley 271
6.1.12 Model between Western Ridge and Eden Valley 272
6.1.13 Model between Northern Grounds and Southern Grounds 274
6.1.14 Model between Northern Grounds and Western Ridge 276
6.1.15 Model between Southern Grounds and Western Ridge 278

1. Abstract

Despite being instrumental in selling a wine's story and commanding a price premium; terroir remains an enigmatic concept. This project aimed to scientifically investigate Barossa Shiraz terroir at regional, sub-regional and management scales using climatic, soil, vine, chemistry and sensory data. Binary models generally achieved good separation between Barossa Valley and Eden Valley within the Barossa Zone. Global models showed that samples from Northern Ground, Western Ridge and Eden Valley were relatively easy to classify compared to other sub-regions. This study improved our understanding of wine provenance and established novel approaches that can be applied to other wine growing regions.

2. Executive Summary

Despite being instrumental in selling a wine's story and commanding a price premium; terroir remains an enigmatic concept. This project aligned with the two main priorities areas in the Wine Australia 2015-2020 Strategic Plan, namely, 'Increasing demand and the premium paid for all Australian wine' and 'Increasing competitiveness'. This project aimed to understand how the vineyard drivers of wine uniqueness work, to determine the marker compounds or chemical profiles for regionality/unique Australian Barossa Shiraz wine and using this information to investigate strategies for manipulating wine quality in the vineyard to better express terroir. This included determining the key environmental drivers for fruit style/quality and how they can be better managed to best exhibit the typical style of the region in which they are grown.

This study would not have been possible without the huge support of producers and managers in the Barossa who allowed us access to vineyards, fruit and wine, Sentek and Green Brain. This support is gratefully acknowledged, with a special mention to Barossa Australia for helping us to make industry connections and being committed to the extension and delivery of outcomes for industry. The main findings from the study are outlined below.

Vineyard-only analysis provided a basis for considering sub-regionalisation of the Barossa GI. The analysis was confined to the land under vine and also made use of an updated climate data set. The vineyard-only analysis clearly separated the Eden and Barossa Valleys, but within the Barossa Valley, offers a basis for separation into three zones rather than a single one.

Yield and its components were measured in 24 Shiraz vineyards during three vintages in the Barossa zone. The frequency distribution of yield was L-shaped. The seasonal ratio of actual crop evapotranspiration and reference evapotranspiration was below 0.48 in most cases, highlighting the prevalence of a substantial water deficit in these vineyards. Yield gaps increased with increasing vine water deficit, quantified with carbon isotope composition in must. The yield gap was smaller with higher rainfall before budburst, favouring early-season vegetative growth and reproduction. Higher rainfall between flowering and veraison, favoured fruit set and early berry growth. The gap was larger with higher rainfall and lower radiation between budburst and flowering. The yield gap declined with altitude, however the Eden Valley departed from this trend, with a yield gap that was higher than expected from its elevation. The yield gap increased linearly with vine age.

Vine phenology was assessed in three zones of 24 vineyards over three vintages using the E-L scale before veraison, and total soluble sugars (TSS) in berries during ripening. The spatial structure of the timing of phenological events followed gradients in topography and soils across the landscape, and were maintained despite the effect of the season (vintage). Phenology responded mainly to temperature until flowering, and to temperature and canopy size from flowering to maturity. The spatial variation in development was maintained despite vintage effects and management practices. Variation in temperature due to topography and elevation were the major drivers of vine phenological development until flowering. During ripening, development was driven by temperature and carbon capture and partitioning.

Of the grape berry chemistry measures conducted, grape volatile profiles gave the best evidence of some compositional attributes being aligned to the sub-regions. It appears that

grape volatile compounds may be more affected variables at the geospatial scale rather than variables at the vineyard or intra-vineyard scale. Overlaying these data with the re-analysis of the geospatial clustering would be an interesting test of the hypothesis that this can drive the bound volatile compound profiles in Shiraz berries.

Analysis of the composition of grape anthocyanins, together with extractable measures of tannin and anthocyanin in grapes, statistical models were developed to attempt to distinguish the phenolic markers for each sub-region. Partial least squares-discriminant analysis (PLS-DA) models were only able to discriminate the Eden Valley samples from the other sub-regions over multiple seasons. Grape phenolics were found to be an important discriminating factor in the comprehensive multivariate analyses conducted using the entire data set for the project.

For each season of the study, the wines made from each site were analysed for anthocyanins, flavonols, tannin concentration and composition, polysaccharides, metals and multiple classes of volatile compounds. Phenolic compounds were important to all of the multivariate models developed, and it was of interest to note that for the Eden Valley, the key predictors were similar to the models developed for grapes on a seasonal basis. The preliminary PLS-DA results showed that wine composition could be used to discriminate the sub-regions on a seasonal basis, with greater consistency observed for the Eden Valley, and to a lesser extent, the Northern Grounds.

Sensory analysis of Shiraz wines from the six Barossa sub-regions showed several consistent sub-regional characteristics for both standardised small-lot wines and industry scale wine samples across the four investigated vintages. Across the four vintages, Eden Valley, irrespective of winemaking, was separated most consistently compared to the other sub-regions. Western Ridge samples were consistently described as more textural wines for the small-lot wines but this effect was not observed for the commercial samples. Additionally, wines from Northern Grounds were not associated with woody and intense fruit aroma and flavours in any of the vintages for the small-lot set but were positively associated with the commercially produced ones, indicating a consistent effect of the winemaking scale and practices on the sensory profiles.

Unsupervised clustering of samples was undertaken and the most consistent and stable k-means models were obtained with a two-cluster solution. The cluster solutions were consistent with cluster assignment and increasing vineyard elevation. A correlation to cluster assignment was also evident for soil cation exchange capacity, available water holding capacity, growing degree days, and mean January temperature.. The contributions of grape amino acids, grape volatiles, and wine volatiles to sample cluster assignments demonstrated the importance of grape and volatile composition to the two clusters in the data. Importantly, grape berry amino acid profiles can be modified through vineyard management such as nitrogen and water applications and these aspects of site management may account for some of the variance within the observed sample cluster assignment.

Interestingly, diethyl succinate, a volatile compound measured in grapes, was the only predictor ranked in the top 25% of importance in all regions as well as in the overall model. Other important predictors included plant area index, sodium and cobalt in wine, as well as ethyl octanoate measured in grapes.

This study improved our understanding of wine provenance, and established novel approaches to measures of quality that can be applied to other wine growing regions. Grapegrowers, winemakers and wine brands can use this information to further inform their understanding of the expression of terroir in wine to help secure a sustainable future for the Australian wine industry.

3. Background

Terroir is a combination of environmental factors (including climate, soil, topography and management) that give a wine its distinctive character (Laville 1990, van Leeuwen et al. 2004, Gladstones 2011). The ultimate influence of terroir means that wines from a particular region are discernibly unique, incapable of being reproduced outside that area, even if the grape variety and winemaking techniques are replicated. Currently there is no scientific explanation for what drives these unique characters, but it is clear that they are likely to be multifarious and complex.

Vine growth and development are the major drivers of wine (grape) style/quality. In premium vineyards, yields are generally managed to levels where they are unlikely to have a significant impact on fruit quality (Jackson and Lombard 1993) – beyond strategic thinning to remove under-ripe or sunburnt fruit. Canopy growth and development are primarily regulated by water availability (Matthews and Anderson 1988) which is in turn controlled by soil type, rainfall pattern and irrigation. This is at its most apparent when comparing adjacent blocks (or parts of blocks) with the same planting material and climate but markedly different vine growth and fruit quality (Bramley 2005). In an assessment of the terroir of Bordeaux (van Leeuwen et al. 2009), climate and soil had a significant effect on berry composition (e.g. anthocyanins) and many of the variables correlated with the intensity of water stress. This is likely to be due to direct and indirect effects e.g. the impact of water stress on shoot growth and resulting fruit exposure.

The importance of terroir is twofold. Firstly, combined with the cultural practices, it defines the style and quality of the wine. Secondly, it is a fundamental tool to position our wines in international markets. While management techniques can have a significant influence on vineyard performance, there is distinct variation in Shiraz wine style within and between Australian wine regions (and in some cases over very short distances within vineyards). Large amounts of data have been generated to assess terroir in Australia – for example http://www.barossa.com/wine/barossa-grounds. These can be further scrutinised with additional measures using new approaches and technologies.

This project was developed to focus on addressing Priority 1, Strategy 3: Building Australian grape and wine excellence - Wine provenance and measures of quality, in the Wine Australia Strategic Plan 2015-2020. The plan states that 'the general global perception of the quality and provenance of our wines is underestimated, and this translates into lower prices for our wine than are warranted'. One way to address this is to better understand Australia's unique terroirs and how they influence wine style and quality by providing tangible evidence to support our 'fine wine' messaging. By developing measures to assess grape and wine provenance and quality, it may be possible to optimise viticultural and winemaking practices so that the influences of terroir can be captured, enhanced and preserved.

In many cases, an iconic vineyard that may set the style/quality benchmarks for a region will grow adjacent to an average vineyard with few apparent differences between the two. This project aimed to develop a suite of metrics to quantify the differences between sites/regions and in doing so, to determine the impact of terroir on wine style and quality. The findings from this project may be used as a platform to help elevate the international perception of Australian Barossa wines.

4. Project Aims

- Understand how the vineyard drivers of wine uniqueness and hence terroir work
- Develop strategies for manipulating wine quality in the vineyard to better express terroir (i.e. to determine what 'levers' winegrowers can pull)
- Determine the marker compounds or chemical profiles for regionality/unique Australian Barossa Shiraz wines

4.1 Outputs and Activities

Outputs and Activities 2016–17

Year 1	Output	Target Date	Activities
a	Industry Reference Group.	31/03/2017	Recruit members for an Industry Reference Group (IRG), to provide input and guidance on project planning and execution.
b	A suite of replicated experimental sites and sub-regions, including the Barossa Grounds program.	30/06/2017	Select 100+ experimental sites for an initial benchmarking study. Select appropriate sites (20 - 25) to capture variability across sub-regions, for more detailed study (including chemistry and sensory analysis).
c	Decision on vineyard management practices to be trialled and the timing of their application.	30/06/2017	Determine the most effective management treatments to be applied to the trial sites: · Review the outcomes of previous 'vine balance' projects and other relevant reports. · Convene an IRG meeting to seek members' advice on potential viticultural treatments.
d	Finalised sampling strategy and measurement techniques at all scales.	30/06/2017	Develop standard operating procedures for major sampling/analysis activities across vineyards, grape and wine chemistry and sensory analysis.
e	Report on findings from the 2016 Barossa Grounds pilot study.	30/06/2017	Conduct additional RNASeq analyses on berry samples and relate the results to Barossa Grounds pilot study site measures.
f	A functional database and sample storage system.	30/06/2017	Develop a field site, sample tracking and analysis database, to facilitate the collation and sharing of samples and analytical results across the research team.

Outputs and Activities 2017–18

Year 2	Output	Target Date	Activities
a	A set of confirmed grape and wine sampling and analysis protocols. An agreed list of target compounds.	30/09/2017	Review vineyard, grape and wine sampling and analysis protocols to finalise strategies across regions and research institutions.
b	A portfolio of project briefing material on the drivers of terroir, suitable for broad dissemination.	31/12/2017	Develop project briefing material on understanding the drivers of terroir, suitable for a range of audiences. Present an overview of the project at industry events.
c	Vineyard environment data set for 2018 vintage. Knowledge on the differences and similarities within and between sub-regions and management practices.	30/06/2018	Collect and collate environment, vineyard and fruit maturity data across all trial sites.
d	Grape samples from vintage 2018, ready for analysis.	30/06/2018	Collect, catalogue and process grape samples and initiate analysis of grape chemistry parameters.
e	Vintage 2018 trial wines and unfinished commercial wines ready for bottling.	30/06/2018	Harvest fruit and complete small-lot winemaking. Collect samples of unfinished commercial wines.
f	Revised project plan reflecting the outcomes of the review with Wine Australia.	30/06/2018	Provide a report to Wine Australia, as part of a project 'stop/go' review. Amend the project plan, as necessary, following the review.

Outputs and Activities 2018–19

Year 3	Output	Target Date	Activities
a	Bottled wines in preparation for chemistry and sensory analysis.	30/09/2018	Bottle unfinished commercial and small-lot wines from the Barossa.
b	A set of unique and distinct descriptors associated with sub-regions of Barossa Shiraz.	31/12/2018	Train sensory panel to reliably identify descriptors of Barossa Shiraz.
c	Vineyard environment data set for 2019 vintage. Knowledge on the differences and similarities within and between sub-regions and management practices.	30/06/2019	Collect and collate environment, vineyard and fruit maturity data. Assess whether sub-regions can be separated on the basis of terroir parameters.
d	Data set of grape and wine chemistry analytical results for vintage 2018. Knowledge on the differences and similarities within and between sub-regions and management practices for 2018 vintage.	30/06/2019	Complete analysis of grape and wine chemistry for vintage 2018. Initiate grape analyses for vintage 2019.
e	Grape samples from vintage 2019, ready for analysis. Knowledge on the key sensory attributes of Barossa Shiraz. Vintage 2019 trial wines and unfinished commercial wines ready for bottling.	30/06/2019	Collect, catalogue and process grape samples and initiate analysis of grape chemistry parameters. Conduct sensory evaluations of selected Barossa Shiraz wines using a trained panel. Identify key sensory features to compare and contrast sub-regions, management interventions and commercial unfinished wines. Harvest fruit and complete small-lot winemaking. Collect samples of unfinished commercial wines.
f	A report summarising the key features of Barossa sub-regions.	30/06/2019	Analyse collation of 2018 vintage results demarcating sub-regions in the Barossa.

Outputs and Activities 2019–20

Year 4	Output	Target Date	Activities
a	Bottled wines in preparation for chemistry sensory analysis.	30/09/2019	Bottle unfinished commercial and small-lot wines from the Barossa.
b	Greater industry awareness of the drivers of terroir.	31/12/2019	Develop a project communication package suitable for a range of audiences, to improve industry understanding of the drivers of terroir. Present project results to date at relevant industry events.
c	Vineyard environment data set for 2020 vintage. Knowledge on the differences and similarities within and between sub-regions and management practices.	30/06/2020	Collect and collate environment, vineyard and fruit maturity data. Assess whether sub-regions can be separated on the basis of terroir parameters.
d	Data set of grape and wine chemistry analytical results for vintage 2019. Knowledge on the differences and similarities within and between sub-regions and management practices. Grape samples from vintage 2020, ready for analysis.	30/06/2020	Complete analysis of grape and wine chemistry for vintage 2019. Collect, catalogue and process grape samples and initiate grape analyses for vintage 2020.
e	Knowledge on the key sensory attributes of Barossa Shiraz.	30/06/2020	Conduct sensory evaluations of selected Barossa Shiraz wines using a trained panel. Integrate results across two vintages. Identify key sensory features to compare and contrast sub-regions and commercial unfinished wines.
f	Vintage 2020 trial wines and unfinished commercial wines ready for bottling.	30/06/2020	Harvest fruit and complete small-lot winemaking. Collect samples of unfinished commercial wines.

Outputs and Activities 2020–21

Year 5	Output	Target Date	Activities
a	Bottled wines in preparation for chemistry sensory analysis.	30/09/2020	Bottle unfinished commercial and small-lot wines from the Barossa
b	Greater industry awareness of the management options for terroir. Revised project plan reflecting the outcomes of the review with Wine Australia.	31/12/2020	Develop a project communication package suitable for a range of audiences, to improve industry understanding of practical management options for terroir. Present project results to date at relevant industry events. Provide a report to Wine Australia, as part of a project 'Stop/Go' review. Amend the project plan, as necessary, following the review.
c	Vineyard environment data set for 2021 vintage. Knowledge on the differences and similarities within and between sub-regions and management practices.	30/06/2021	Collect and collate environment, vineyard and fruit maturity data. Assess whether sub-regions can be separated on the basis of terroir parameters.
d	Data set on grape and wine chemistry results for vintage 2020. Knowledge on the differences and similarities within and between sub-regions and management practices. Grape samples from vintage 2021, ready for analysis.	30/06/2021	Complete analysis of grape and wine chemistry for vintage 2020. Collect, catalogue and process grape samples and initiate grape analyses for vintage 2021.
e	Knowledge on the key sensory attributes of Barossa Shiraz.	30/06/2021	Conduct sensory evaluations of selected Barossa Shiraz wines using a trained panel. Integrate results across three vintages. Identify key sensory features to compare and contrast sub-regions and commercial unfinished wines.
f	Vintage 2021 trial wines and unfinished commercial wines ready for bottling.	30/06/2021	Harvest fruit harvested and complete small-lot winemaking. Collect samples of unfinished commercial wines.

Outputs and Activities 2021–22

Year 6	Output	Target Date	Activities
a	Wines bottled in preparation for chemistry sensory analysis.	30/09/2021	Bottling of unfinished commercial and small-lot wines from the Barossa.
b	Data set on grape and wine chemistry analysis for vintage 2021. Knowledge on the differences and similarities within and between sub-regions.	30/06/2022	Complete analysis of grape and wine chemistry for vintage 2021.
c	Knowledge on the key sensory attributes of Barossa Shiraz.	30/06/2022	Conduct sensory evaluations of selected Barossa Shiraz wines using a trained panel. Integrate results across four vintages. Identify key sensory features to compare and contrast sub-regions, management interventions and commercial unfinished wines.
d	Integrated data set across all vintages. Knowledge on the relationships between environment (across all scales) and management practices and fruit and grape and wine chemistry and wine sensory.	30/06/2022	Apply chemometric and machine learning algorithms to data sets to identify environment and management components of terroir and integrity of chosen sub-regions.
e	Knowledge on vine physiological drivers of wine uniqueness and terroir. Strategies for manipulating wine quality in the vineyard to optimise the expression of terroir.	30/09/2022	Submit Final Report to Wine Australia, outlining key findings from the project, with a focus on: · vine physiological drivers of terroir · strategies to manipulate wine quality in the vineyard to optimise the expression of terroir.

5. Methods

5.1 Experimental design and site establishment

5.1.1 Experimental design

Barossa Shiraz terroir in this project was researched across a range of scales (Figure 5.1.1), using six potential sub-regions from the Barossa Grounds program. At a regional scale samples were taken from vineyards and wine from 100+ sites in the Barossa, including sites in the Barossa Grounds program. Vine, fruit and wine parameters that typify particular regions were identified and related to the environment using GIS (Yellow, Figure 5.1.1). At the sub-regional scale, 24 sites were selected and monitored in greater detail, including the weather, key soil physicochemical properties, soil moisture, phenology and canopy growth (Green, Figure 5.1.1). Fruit was sampled for maturity, yield and small-lot winemaking. Wine descriptive analysis has been performed on small-lot wines and compared to commercial wine. Fruit and wine was analysed for compounds relating to wine quality and style to relate them to the vine, environmental and sensory parameters. Management interventions have been imposed on up to six selected sites to determine the potential to optimise a site's terroir (Blue, Figure 5.1.1). These management practices aim to influence vine growth and development and to confirm a cause and effect for environmental impacts on fruit and wine style. Grapes and wine have been analysed as above.



Figure 5.1.1 Diagram of the relationship between the three scales of sites to investigate Australian Barossa Shiraz terroir.

5.1.2. Site establishment

Sub-region, benchmarking and trial sites were established during the 2018 and 2019 growing seasons. Selection of sites was undertaken through a series of phone calls and vineyard visits to determine their suitability for the project needs and to confirm that producers were agreeable and able to commit for the duration of the project.

Twenty-four sub-region sites were established, four from each of six sub-regions (Table 5.1.1 and Figure 5.1.2). Note that these sub-regions were identified through the Barossa Grounds program prior to this project. They were used here simply as a guide for differentiating areas of potential interest within the study region and to facilitate location of study sites throughout the Barossa Zone GI. Three sampling zones within each sub-region site were established to capture the variation across the site. In 2018, these zones were selected based on variations in PAI measures derived from VitiCanopy (see example Figure 5.1.3). In 2019, zones were selected based on a combination of EM38, PCD imagery and PAI measures (see section 5.1.3 for more details).

Table 5.1.1 Site numbers and corresponding sub-regions.

Site Number	Sub Region
1	Northern Grounds
2	Northern Grounds
3	Northern Grounds
4	Northern Grounds
5	Central Grounds
6	Central Grounds
7	Central Grounds
8	Central Grounds
9	Eastern Edge
10	Eastern Edge
11	Eastern Edge
12	Eastern Edge
13	Southern Grounds
14	Southern Grounds
15	Southern Grounds
16	Southern Grounds
17	Western Ridge
18	Western Ridge
19	Western Ridge
20	Western Ridge
21	Eden Valley
22	Eden Valley
23	Eden Valley
24	Eden Valley

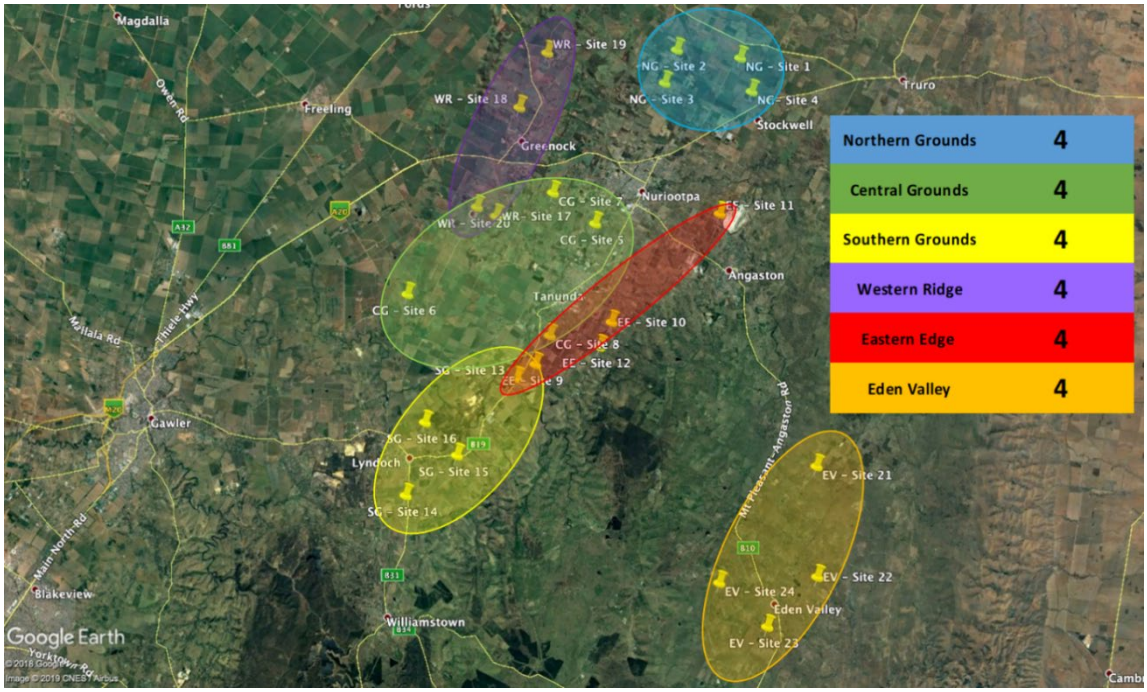


Figure 5.1.2 Location of sub-region sites in the Barossa.

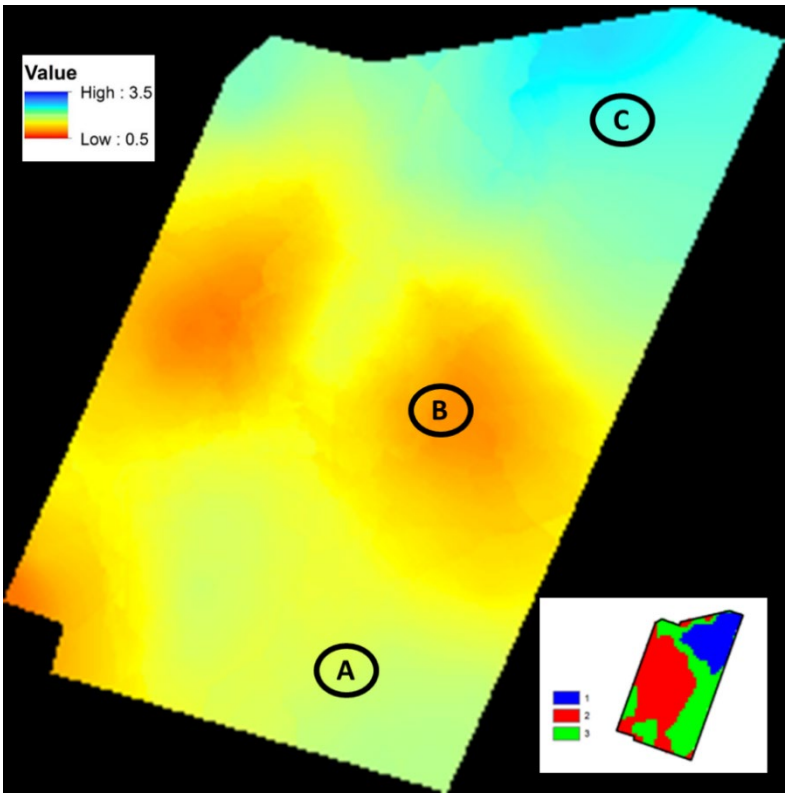


Figure 5.1.3 Example of PAI at a sub-region site measured using VitiCanopy and mapped using ArcGIS.

Approximately 75 benchmarking sites were established (Figure 5.1.4). This number changed each season due to changes in vineyard ownership, fruit being harvested before we could access it for samples, fruit being blended with other blocks before we could get a wine

sample and additional producers joining the project. The three trial sites were used to assess management intervention (see Figures 5.1.5-5.1.7). Another two sites were established in 2019 but due the frosts, no fruit was available at these sites and no measurements were taken.

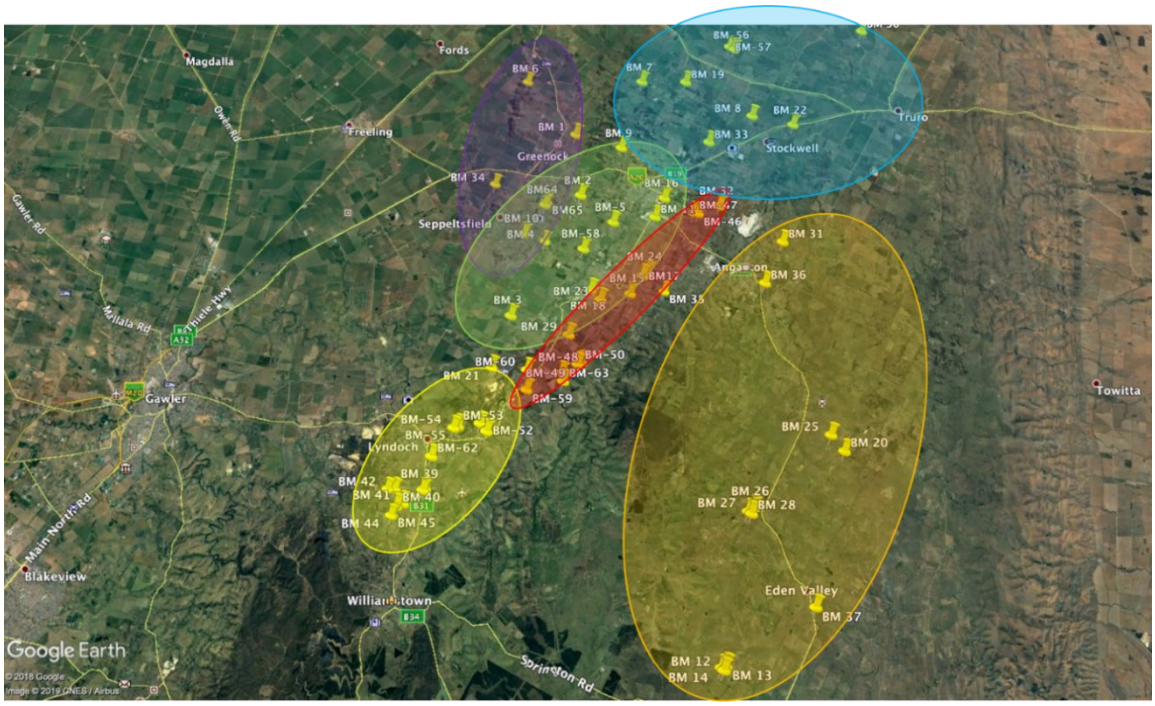


Figure 5.1.4 Location of benchmarking sites in the Barossa.

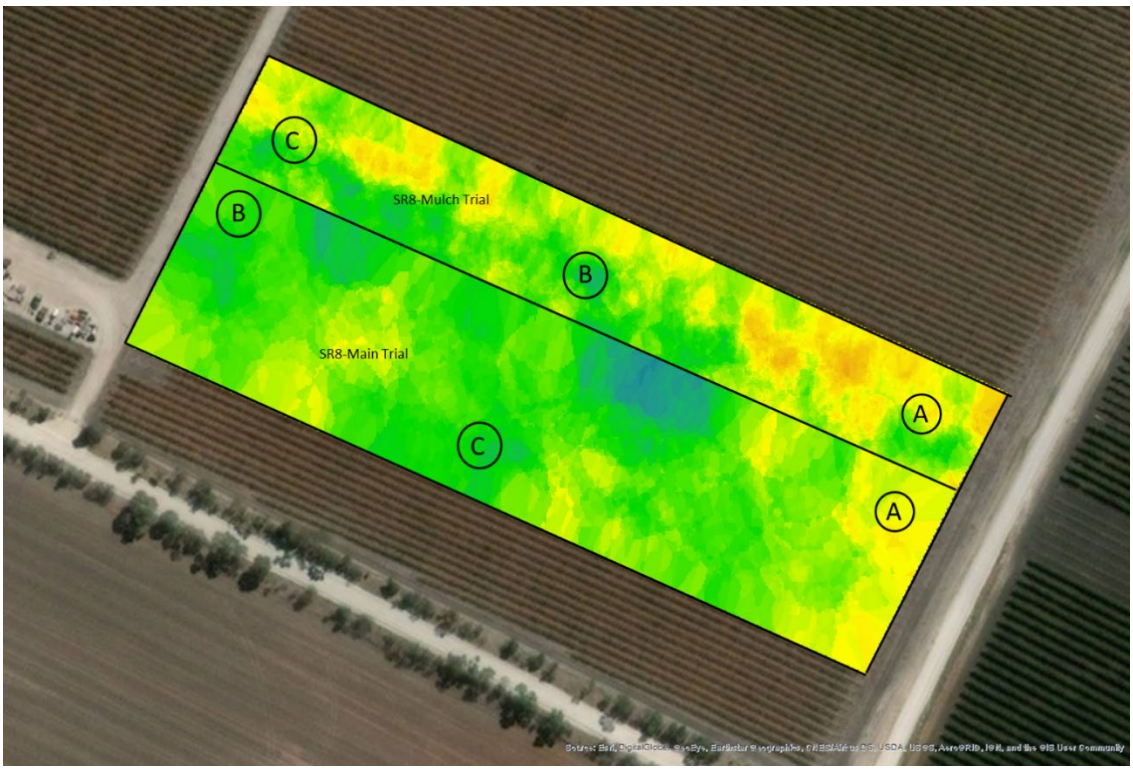


Figure 5.1.5 Location of replicates at Dorrien mulch trial site and sub-region site in the Barossa.

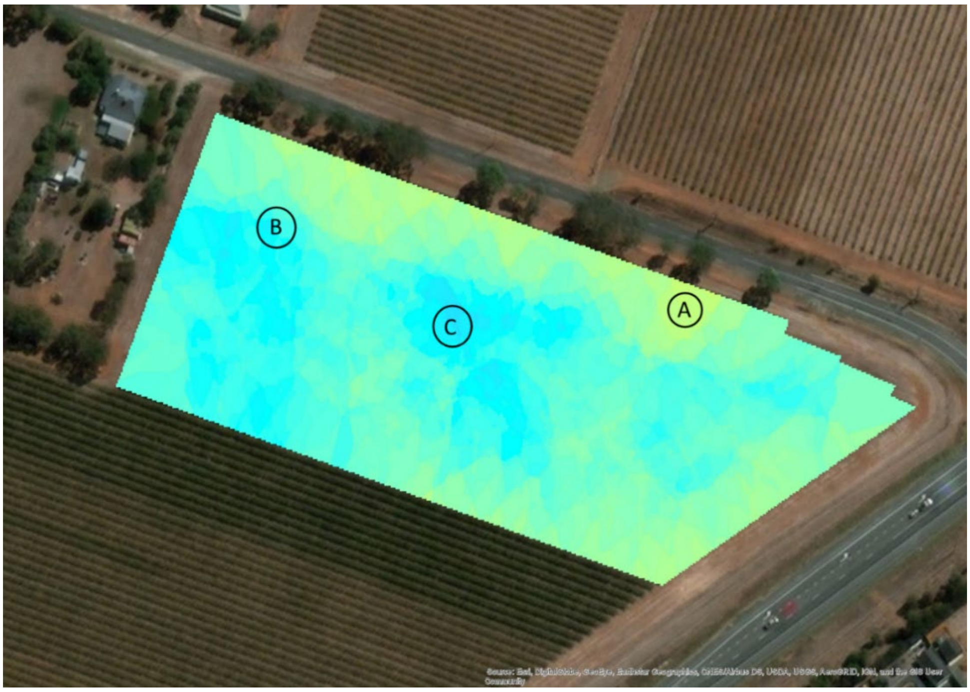


Figure 5.1.6 Location of replicates at Hahn irrigation trial site in the Barossa.

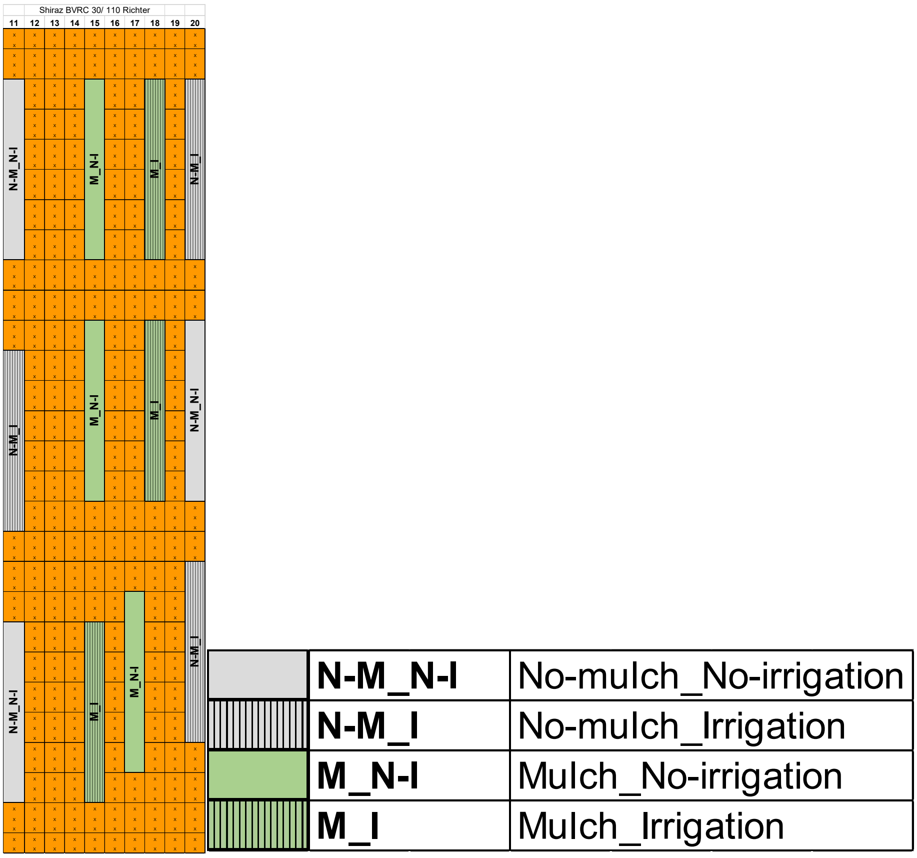


Figure 5.1.7 Experimental design for trial site established at Nuriootpa Research Station.

5.1.3 Within-vineyard analysis

A commercial provider was engaged to conduct a high resolution electromagnetic (EM38) soil survey of these blocks. Remotely sensed imagery of these blocks was also acquired at veraison (the majority in 2018; subsequently in 2019 for the added sites only) from a commercial provider supplying so-called 'PCD' imagery at 40 cm resolution. PCD, otherwise known as the simple ratio, is calculated as the ratio of infrared:red reflectance and has been shown to be closely related to vine vigour (Dobrowski et al., 2003) with veraison shown as the optimum time for acquisition of such imagery (Lamb et al., 2004). Following the training of project staff in block boundary survey, all sites had their block boundaries surveyed using a differentially corrected GPS (accurate to approximately +/- 50 cm in the x and y planes) and from the resultant boundaries, raster grids of 2 m pixels (i.e. 4 m^2) were derived onto which all subsequently produced maps were interpolated.

Maps of bulk electrical soil conductivity were interpolated using local block kriging. The PCD imagery had the non-vine signal removed using a proprietary algorithm (Specterra Services, Leederville, WA) and was smoothed to the same 2 m raster as used for map interpolation. These data were then clustered using *k*-means to identify vineyard zones based on the EM38 and PCD data (see example below Figure 5.1.8); note that *k*-means clustering identifies zones through minimisation of the within-cluster variance and maximisation of the difference between cluster means. All methods of spatial analysis used for this work were as described by Bramley et al. (2011) and Proffitt et al. (2006) and references therein.

Note that almost all of the blocks used in this study were small – approximately 1.5 ha or less. Experience in vineyard variability research over many years supports the view that commercial application of precision viticulture in blocks of < 2.5 ha is neither likely to be attractive to growers nor to have much commercial application. In the former case, maps with a resolution of 2 m often appear quite pixelated in such small blocks, whilst, depending on the size of tanks used for winemaking / availability of crushers, harvesting of small tonnage parcels may not be commercially viable. For example, a winery whose smallest tank size is 20 t and which aims to produce fruit at approximately 8 t ha^{-1} will likely also regard 2.5 ha as its smallest viable management unit. More importantly for this study, it is a fact that in small blocks, the range of variation in factors that impact on vineyard performance (soil, topography, etc) is likely to be much smaller than in larger blocks (> 5 ha). Accordingly, the classification of within-vineyard variation using quantiles (20^{th} percentiles) may lead to perceptions of more within-vineyard variation than is meaningful. Note therefore that for this work, these analyses were used as a guide only, for selection of sampling locations; in our opinion, studies of within-vineyard variation in terroir in such blocks is unlikely to be of much value – although between site comparisons of such blocks within the Barossa GI may well inform improved understanding of Barossa terroir.

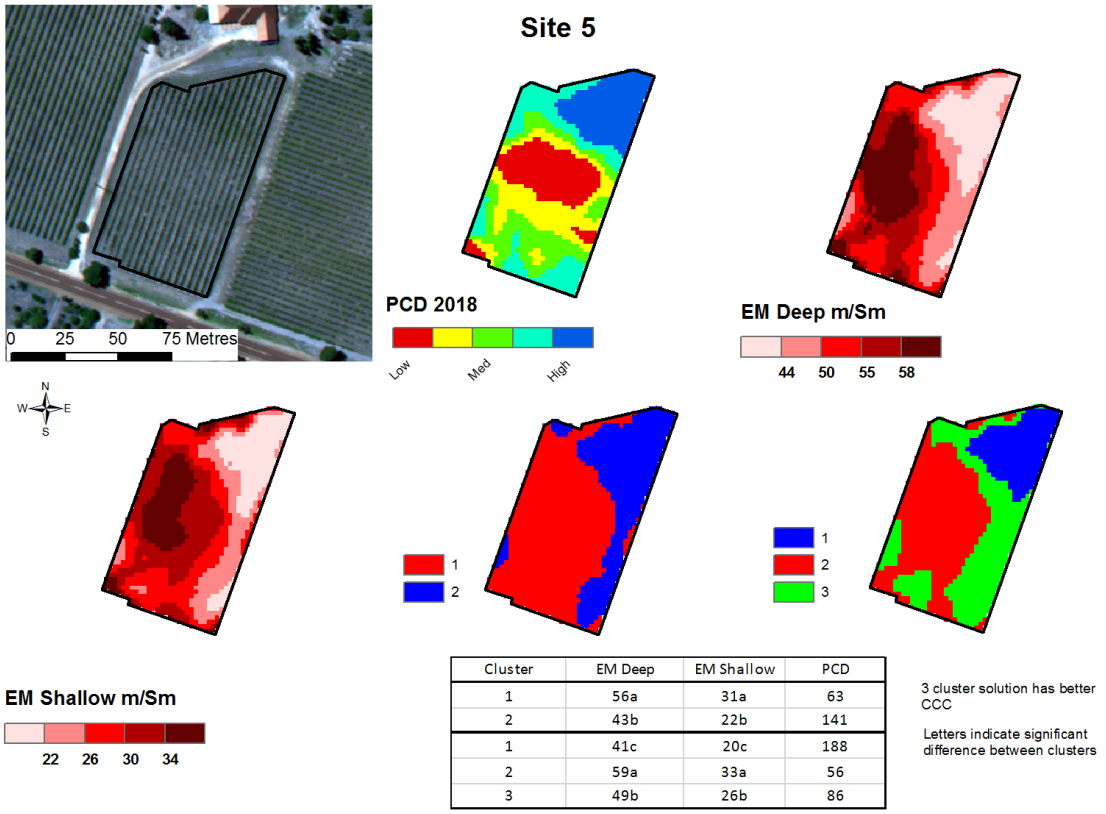


Figure 5.1.8 Example of clustering using *k*-means to identify vineyard zones based on the EM38 and PCD data.

5.1.4 Regional scale analysis

Like its counterpart associations in several other winegrowing regions in Australia, The Barossa Grape and Wine Association (BGWA) has been considering the merits of identifying sub-regions within its established geographical indications. This follows the idea that such a strategy might nuance the 'premiumisation' of Australian wine (Wine Australia, 2015) and promote an ability to enhance the marketing of wines using stories based on terroir.

The Barossa Grounds is a project through which the BGWA is seeking to better understand variation in wine style across the Barossa Zone geographical indication (GI), with a particular focus on Shiraz wines (www.barossawine.com/vineyards/barossa-grounds/). The Australian Geographical Indications define the official boundaries of the Barossa Zone and the regions within it, which are the Barossa Valley and Eden Valley (Figure 5.1.9). A sub-region of High

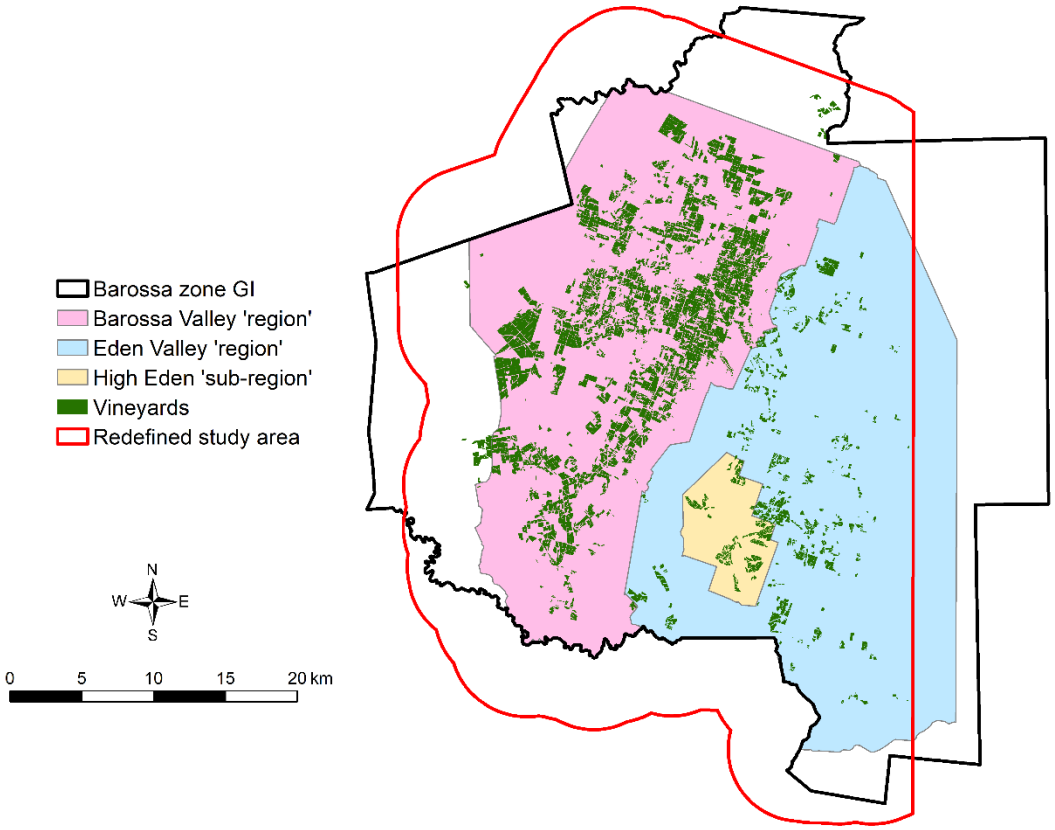


Figure 5.1.9 Geographical indications in the Barossa wine region of South Australia. The Barossa zone comprises the regions of Barossa Valley and Eden Valley and the High Eden sub-region. Also shown are the locations of vineyards (data kindly provided by Vinehealth Australia) and a redefined boundary used for the present study.

Eden is also recognised. In addition to understanding differences between these (sub) regions, there is also interest in exploring variation within the Barossa Valley itself. Thus, at the time of writing, three 'distinctive Grounds' have been identified (Northern Grounds, Central Grounds and Southern Grounds), with two smaller grounds (Eastern Edge and Western Ridge) also acknowledged. It was not the intention in the present project to 'critique' or 'referee' the Barossa Grounds project or the delineation of Grounds which arose from it. Rather, we wished to take an independent and data-driven approach to analysis of regional-scale biophysical variation as a means to identify a possible underpinning geographical basis for the analysis of wine chemical and sensory data collected during the project. Of particular interest was the question of which data should be brought to bear in such an analysis – data describing the region as a whole, or just that pertaining to the approximately 10% of the GI land area which is under vine (Figure 5.1.9).

5.1.5 Weather station installation

At each of the sub-region and trial sites, an MEA weather station was installed (with the exception of those that already had one in February - May 2018 and December 2018 (Figure 5.1.10). Weather stations were positioned at each site in a location that was not shaded by surrounding vegetation and not impacted by other vineyard activities. These decisions were made in consultation with producers. Once the location for a weather station was determined, North was located using a compass and a metal post erected so that the weather station could be positioned facing North. A trench of approximately 15 cm depth was dug approximately 2

m from the post. At the end of the trench a rain gauge mounted to a cement slab with screws was placed on a cleared and levelled area. The cable from the rain gauge was run along the trench to the post and then covered with dirt and compacted. The weather station was then attached to the post 1m above the ground using brackets and screws. The cable from the rain gauge was run up the post and held in place with cable ties and attached to the weather station. MEA was then contacted to ensure each weather station was working, to reset it and start recording. The weather station number and GPS co-ordinates were then recorded and sent to MEA so that data collected could be accessed in Green Brain.



Figure 5.1.10 MEA weather station.

Climatic data was continuously monitored during the project and was visualised by the project team and participating producers using the MEA Green Brain web app which holds and displays the data collected by the weather stations. Green Brain presents data in a summarised form on a dashboard to allow the user to quickly observe the critical parameters at each site. Where necessary, data can be analysed with graphs and tables. Measurement parameters included: temperature, wine speed, solar radiation, rainfall, degree days, chill units, frost hours, daylight and evapotranspiration.

5.1.4 Soil moisture monitoring assembly and installation

From November 2017 until January 2018 soil moisture probes were assembled. To start the assembly, probe rods were removed from the access tube and then the handle was loosely attached to the rod with two screws and the main board pressed onto the probe below the handle and secured with a cable tie. Each sensor was then placed at depths of 20 cm, 50 cm, 80 cm and 100 cm. The ribbon cable header from each sensor was then pressed into the connector located within the rod and the addressing pin on the cable header adjusted to the correct sensor position on the rod ready for calibration. Before calibration, the cable was connected to the probe cap by threading the cable with a ferrite bead and then feeding the cable through the expandable bung on the probe cap and siliconed into place. For each probe, the exposed wires were attached to the main board in a specific order, ready for calibration. To calibrate and ensure sensors were working correctly, each probe was connected to a logger head attached to a computer. Probes were then fed through an esky filled with water, stopping at each sensor to check that it was working using the program Probe Utility.

In the sub-regional sites, three soil moisture probes (Figure 5.1.11), one in each vineyard zone, were installed by a contractor during August 2018, making a total of 72 probes.

Moisture status was continuously monitored using an EnviroSCAN system (Sentek, Magill, SA). This system consists of four capacitance sensors located, when possible, at depths of 20, 50, 80 and 110 cm. The capacitance sensors measure the dielectric constant of the soil-air-water mixture surrounding the access tubes and return volumetric soil moisture. The length of the PVC access tube and depth of the sensors was modified if a layer of rock was encountered during installation, as this may otherwise cause poor contact between the soil and the access tube and lead to inaccurate readings. For consistency, the sensors were installed at similar depths across the three zones of each site. The PVC access tubes were installed directly below the irrigation lateral and between drippers. The installation of the sensors and operational procedures were carried out according to the manufacturer's recommendations. Data from the logger were retrieved monthly using a SOLOPorter (Sentek, Magill, SA) data logger and downloaded onto a computer for display using the Sentek IrriMax10 software.



Figure 5.1.11 Soil moisture probe connected via cable to the SOLO data logger.

At the trial sites, soil moisture monitoring systems were installed at the time of the establishment of the trials following the same installation and operational procedures as described for the sub-region sites.

5.2 Soil and vine measurements

5.2.1 Soil measurements

Soil samples for physical and chemical analyses were collected during winter 2019, from June to August, at each sub-region site and zone. For chemical analysis, two composite samples were collected at 5-15 and 30-45 cm depth. Samples were collected using a 4 cm internal diameter hydraulic hammer-driven probe (Figure 5.2.1) at four positions within each zone. Cores were collected 40 cm from the dripper line towards the inter-row space and between drippers. Core samples were divided into the depth classes, and thoroughly mixed in a plastic container before being bagged for transport to the laboratory. Samples were oven-dried for 7 days at 40 ºC and kept in sealed bags until processing. Two intact 5 cm long samples were taken at 5-15 and 30-45 cm from one of the cores in each zone for the determination of bulk density.



Figure 5.2.1 System used for soil sampling. (a) an RTV was used to tow the trailer with the soil sampler between the rows. (b) the hydraulic hammer-driven system is mounted in a trailer with a telescopic arm that allows for lateral adjustments. (c) composited samples were collected at 5-15 and 30-45 cm depth across four cores within each vineyard zone.

For physical determinations, two intact cores were taken from each vineyard zone up to 100 cm depth in PVC clear sleeves, using a Geoprobe Macro-Core® soil sampling system (Earthtech Drilling Products Pty. Ltd., Victoria, Australia) (Figure 5.2.2). Cores were maintained in the oven at 40 ºC until completely dry.

Soil chemical analysis was conducted around December 2019 and included organic carbon, N, C:N, P and phosphorus buffering index, K, exchangeable cations (Ca, Mg, K, Na), trace elements (Mn, Zn, Cu, Fe), Boron and Molybdenum. Similarly, physical characterisation of soil samples included particle size analysis, bulk density and saturated water content.

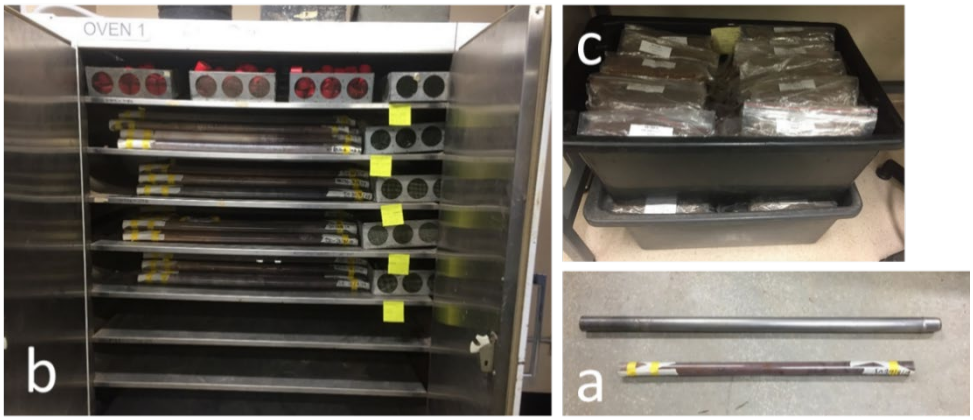


Figure 5.2.2 (a) intact 100 cm cores collected in PVC clear sleeves for soil physical analysis. (b) intact cores and (c) composited samples were oven-dried at 40^{o} C for microbial stabilisation until laboratory analysis.

5.2.2 Vine measurements

Weekly to fortnightly assessments of phenology and fortnightly to monthly assessments of canopy development were recorded during the 2018/19, 2019/20, 2020/21 seasons from each sub-region zone. Due to the delayed start of the project in 2017/18, leaf blades were collected for elemental analysis and petioles in 2018/19 from all sub-region sites.

Berry maturity was monitored weekly from EL 35 until harvest. Five bunches from each zone within each sub-region site were collected from these samples for the assessment of berry weight (g), pH, total acidity (TA), TSS, total anothocyanin, total tannin and total phenolics. A 100 berry sample was randomly collected from each sample and frozen for future phenolic analysis.

At harvest, the number of bunches and yield per metre of cordon were recorded from three sections within every zone of all sub-region sites. From yield and bunch number, the average bunch weight was determined. The harvested fruit from each zone of each sub-region site was combined into two-three, 20 kg vented crates to form one sample per zone, which was used for winemaking. At harvest, sub-samples of the following were collected from all zones from sub-region and benchmarking sites; 250 berries for berry chemistry (CSIRO) stored at -80°C until processing (not for benchmarking sites), 100 berries for phenolic assessments were stored at -20°C until processing, 50 g berry sample collected for wine-like assays and a juice sample for average berry weight (g), pH, total acidity (TA), TSS, elemental analysis (10 mL), and carbon isotope analysis (50 mL) (not in 2018).

The carbon isotope discrimination (d13C) measured on grape juice has been shown to be a robust physiological indicator of vine water status during ripening (Gaudillere, 2002; van Leeuwen, 2009; Spangenberg and Zuffrey, 2018). This test measures the relative concentration of ^{12}C and ^{13}C in berry sugars produced during the photosynthesis, and is primarily defined by the contribution of CO_2 from the atmosphere (mainly ^{12}C) and the intracellular CO_2 (^{13}C). When the stomata close due to water stress, there is an increase in the proportion of CO_2 cycled within the intracellular space inside the leaf, thereby increasing the relative proportion of ^{12}C contained in berry sugars. The carbon isotope discrimination provides a fingerprint of the berry sugars that allows the level of water stress experienced by the vine to be traced during the season. Similarly, d13C can integrate the effects of the

management practices (especially irrigation), the site (soil physico-chemical properties, topology and climate) and plant material (variety, clone and combination of rootstock/scion) that modulated soil water availability and vine water uptake during the season.

A water stress integral was used to confirm the relationship between vine water status during the growing season and d13C for irrigated Shiraz, as previous work from Europe largely focused on rain-fed systems and occurred in a more humid climate. The water stress integral was calculated using negative notation but expresses as absolute values, therefore larger S_Ψ relates to higher accumulated water stress (Myers, 1988).

Samples were processed for d13C analysis using the following method. Juice collected at the time of harvest was centrifuged for four minutes at 4500 RPM and 50 mL was sterilised the same day by autoclaving at 120 ºC for 20 minutes. Samples were stored at room temperature until isotopic analysis was performed at the Biogeochemistry and Stable Isotope Facility, University of Adelaide. Carbon isotope composition of the grape sugars was measured on 5 µL of berry juice using a continuous flow isotope ratio mass spectrometer.

5.3 Grape chemistry

5.3.1 Amino acids, glutathione and vitamins B5 and B6

Analysis of the 20 proteinogenic amino acids as well as β-alanine and γ-aminobutyric acid was conducted on ground whole berry samples using the method described in Boss et al. (2015). In brief, amino acids were quantified in grape juice using an AccQ Fluor Reagent Kit (Waters Corporation, Milford, MA) and a method based on that of Cohen and Michaud (1993). An SPE step was added prior to derivatisation to reduce chromatographic background (Chen et al. 2010). The grape juice was obtained from a 200 mg aliquot of frozen ground grape material that had been prepared from approximately 25 g of berries. Calibration curves covering the range of amino acid concentrations seen in the samples were prepared using at least five data points in duplicate.

Glutathione was quantified using a method based on that of Adams and Liyanage (1991). Two mL of 5% 5-sulfosalicylic acid (SSA) was added to 250 mg of frozen ground grape in a 5 mL Eppendorf tube and incubated for 5 min mixing by vortex twice during this time. The mixture was then centrifuged at 3,200 × g for 10 min at room temperature and the supernatant transferred to a 1.5 mL Eppendorf tube containing 30 mg PVPP. This was incubated at room temperature for 5 min and then spun at 20,000 × g for 5 min. A 10 µL aliquot of the supernatant was added to 150 µL of assay buffer (100 mM potassium phosphate pH 7, 1 mM EDTA, 40 µg/mL 5,5'-dithio-bis(2-nitrobenzoic acid), 0.15 units/mL glutathione reductase) in a Corning polystyrene flat bottom nine-well plate and incubated at room temperature for 5 min. The reaction was initiated by the addition of 50 µL of NADPH (0.16 mg/mL). Absorbance was then measured at 412 nm every min for 5 min and compared to blanks and a calibration curve in duplicate ranging from 25 - 200 µM of glutathione.

Vitamins B5 (pantothenic acid) and B6 (pyridoxine) were quantified using an LC-MS method. Samples were prepared by adding add 2 mL of 50 mM ammonium formate and 100 µL of 5 ng/µL d2-pyridoxine internal standard to 1 g of ground frozen whole berry tissue. The samples were then incubated overnight at 37 °C before centrifugation at 4,000 × g for 10 min. The supernatant was collected, and a 1 mL sub-sample transferred to a glass vial for injection into the LC-MS. Separation and detection were carried out using a 1200 series HPLC coupled to a 6410 triple quad mass spectrometer (Agilent, Santa Clara, CA). The injected samples (4 µL) were separated on a 2.1 x 100 mm x 2.7 µm InfinityLab Poroshell 120 SB-AQ column (Agilent) maintained at 25 °C during the analysis. Two eluents were used (A: water + 0.1% formic acid and B: acetonitrile + 0.1% formic acid) with a flow rate of 0.25 mL/min in the following gradient mode: 0-3 min 100 % A; 3–8.5 min 80 % A and 20 % B; 8.5–10 min: 5 % A and 95 % B; 10–15 min 100 % B 15-30 min 100% A to equilibrate the column. The effluent was introduced into the ESI ion source with a desolvation gas temperature of 350°C, the nebulizer pressure at 40 psi, a gas flow rate of 8.0 L/min and a capillary voltage of 1.0 kV. Detection was performed by multiple reaction monitoring in positive ion mode. Optimisation of fragmentation was done with commercially obtained d2-pyridoxine-d2 (CDN isotopes) and pyridoxine and calcium pantothenate standards using the Agilent MassHunter Optimizer software. The collision energy ranged between 12 and 21 eV. The following transitions were used for quantification; d2-pyridoxine m/z 172.0 – 154, pyridoxine m/z 170.1 – 152, pantothenic acid m/z 220.2 – 90.0.

5.3.2 Fatty acids

Fatty acids were extracted from ground, de-seeded berry samples using the method of Han and Yuan (2009). One gram of berry tissue and 1 mL of isopropanol were mixed and incubated at 75 °C for 15 min and then cooled to room temperature. The internal standard (50

µL of 1.2 mM d_{33}-heptadecanoic acid (C/D/N Isotopes Inc.)) was added, as was 1 mL of chloroform and 2 mL of methanol and the sample was mixed for 1 h on a flatbed stirrer. Separation of the fatty acids and their methylation was conducted according to Yunoki et al. (2004) with some modification. First, to partition the phases, 1 mL of both chloroform and water were added, the solutions mixed and then centrifuged at 200 × *g* for 2 min. The lower chloroform layer was collected, re-extracted with 3 mL of chloroform:methanol:water (3:48:47) twice then concentrated under N_2. To methylate the fatty acids, 2 mL methanol in 5% HCl was added and the samples incubated for 2 h at 95 °C. The samples were then cooled to room temperature and 1 mL water and 2 mL n-hexane added. After shaking, the upper layer was collected and the bottom layer extracted twice more with 2 mL n-hexane. The combined n-hexane extracts were concentrated under N_2. The extract was resuspended in 100 µL dichloromethane for injection into the GCMS. A 1:10 dilution was also made for quantification of the more abundant fatty acids.

Chromatographic separation of the fatty acids was conducted with an Agilent 6890 gas chromatograph and 5973 mass spectrometer. The inlet was in split mode (10:1) at a temperature of 230 °C, and 1 µL of each sample (undiluted and diluted) was injected onto a ZB-5 column (length 30 m, 0.25 mm i.d., film thickness 0.25 µm; Phenomenex). Helium was the carrier gas, and this was maintained at a constant flow of 1.5 mL/min. The oven temperature program was as follows: initial 40 °C, then ramped at 12 °C/min up to 200 °C, then increasing at 0.5 °C/min to 230 °C, followed by a ramp at 3 °C/min until a final temperature of 250 °C was reached and held for 15 min. The mass spectrometer was set with a transfer line temperature of 250 °C, source temperature of 240 °C, quadrupole temperature of 150 °C and ionising potential at 70 eV. Positive-ion electron impact spectra (70 eV) were recorded in scan mode (range: m/z 40-500, scan rate: 3.15 scans/s).

Table 5.3.1 lists the extracted ions used to quantify the fatty acid methyl esters relative to the internal standard (methyl ester of D_{33}-heptadecanoic acid). The identity of the fatty acid methyl esters was determined by comparing mass spectra with those of authentic standards and spectral libraries.

Table 5.3.1 List of methyl esters quantified in the grape fatty acid extracts, retention indices and the ions used for quantification.

COMPOUND	RETENTION INDICES[1]	QUANTIFICATION ION (*m/z*)
Methyl dodecanoate (12:0)	1810	66
Methyl tridecanoate (13:0)	1927	74
Methyl tetradecanoate (14:0)	2034	74
Methyl pentadecanoate (15:0)	2114	74
Methyl (*Z*)-9-hexadecenoate (16:1 n-7)	2230	55
Methyl heptadecanoate (17:0)	2303	74
Methyl (*Z*)-10-heptadecenoate (17:1 n-7)	2345	55
Methyl nonadecanoate (19:0)	2523	74
Methyl 2-hydroxyhexadecanoate (16:0 OH)	2611	97
Methyl eicosanoate (20:0)	2634	74
Methyl (*Z*)-13-eicosanoate (20:1 n-7)	2661	55
Methyl heneicosanoate (21:0)	2726	74

COMPOUND	RETENTION INDICES[1]	QUANTIFICATION ION (*m/z*)
Methyl (*Z*,*Z*,*Z*)-11,14,17-eicosatrienoate (20:3 n-3)	2752	79
Methyl docosanoate (22:0)	2834	74
Methyl (*Z*)-13-docosenoate (22:1 n-9)	2850	55
Methyl tricosanoate (23:0)	2926	74
Methyl tetracosanoate (24:0)	3000+	74
Methyl pentacosanoate (25:0)	3000+	74
Methyl hexacosanoate (26:0)	3000+	74
Methyl heptacosanoate (27:0)	3000+	74
Methyl octacosanoate (28:0)	3000+	74
Methyl 2-hydroxy-tetracosanoate (24:0 OH)	3000+	97
Methyl tricontanoate (30:0)	3000+	74
Quantified in 1:10 dilution		
Methyl hexadecanoate (16:0)	2239	74
Methyl octadecanoate (18:0)	2434	74
Methyl oleate (18:1 n-9)	2478	55
Methyl elaidate (tr18:1 n-9)	2486	264
Methyl linoleate (18:2 n-6)	2493	67
Methyl linolenate (18:3 n-3)	2594	79

[1] RI calculated from retention relative to the retention of a series of n-alkanes (C_8-C_{30}).

5.3.3 Grape phenolics and skin tannins

Grape total and extractable tannin and anthocyanin were analysed as described by Bindon et al. (2014). The anthocyanin profile of extracts was determined by HPLC according to Mercurio et al. (2007). A published HPLC method (Hanlin and Downey 2009), was used to profile the berry skin tannin composition with the various flavan-3-ol terminal and extension sub-units quantified along with an estimate of the degree of polymerisation.

5.3.4 Grape carotenoids

Carotenoids were analysed using a method adapted from Lashbrooke et al. (2010). A 500 mg sample of seedless ground grapes was transferred into a 2 mL amber microcentrifuge tube and placed on ice before the addition of 1 mL cold acetone, 0.1% N-ethyldiisopropylamine and 10 µL of 1 mg/mL β-apo-carotenal in chloroform. The mixture was then vortexed for 10 s and sonicated for 30 min on ice. Following a centrifugation at 21,000 × g at 4 °C for 5 min, 600 µL of the supernatant was added to 1 mL of cold extraction buffer (50 mM Tris-HCl (pH 7.5), 1 M NaCl) and kept on ice. After the addition of 200 µL cold ethyl acetate, the mixture was vortexed briefly and sonicated for 5 min on ice. After a 5 min centrifugation at 21,000 × g at 4 °C for 5 min, 50 µL of the upper ethyl acetate phase was sampled in low light conditions and placed in an amber high-recovery HPLC vial containing 200 µL of cold methanol and 0.125 % w/v butylhydroxytoluene.

Samples were run (20 µL injection) on an Agilent 1200 series HPLC fitted with an Acclaim C30 column (3 µm, 2.1 x 250 mm) and an Acclaim C30 guard column (5 µm, 2.1 mm x 10 mm) held at 25 °C. The column flow rate was 250 µL/min using two solvents: A, methanol, 3 % v/v H_2O, 0.2 % w/v NH_4OAc, 0.05 % triethylamine; B, Tert-butylmethylether, 0.05 %

triethylamine. The solvent gradient used was: 0-17 min 100% A; 17-29 ramp to 32 % A and 68 % B; 29-34 hold at 32 % A and 68 % B; 34-36 min ramp to 100 % A; 36-55 hold at 100% A to equilibrate the column. Diode array detector signals were captured at 420 nm, 450 nm and 470 nm at bandwidths of 16 nm, 4 nm and 4 nm respectively with the reference being 800 nm for each signal with a bandwidth of 100 nm. Spectra were also collected for each sample ranging from 250 – 850 nm with a 1 nm step.

5.3.5 Grape volatile compounds

The analysis of non-targeted grape volatile compounds was conducted using the method outlined in Kalua and Boss (2009) but with a different sample preparation and a greater number of internal standards. In short, the sample preparation was altered by the addition of 2.5 mL 4mM $ZnSO_4$, to inhibit lipoxygenase activity, to 2.5 g of powdered grape tissue and 2.5g NaCl in a 10 mL amber headspace vial. The internal standards added and ions used for quantification are listed in Table 5.3.2. The internal standard used for each compound was designated by using the one with the most similar functional group (Table 5.3.3). The spectra were recorded in scan mode (range: m/z 35-350, scan rate: 4.45 scans/s), but an extracted ion was used for quantification of each grape volatile compound as indicated in Table 5.3.3.

Table 5.3.2 List of internal standards used for quantification of grape volatile compounds by GCMS

COMPOUND	RETENTION INDICES[1]	CONCENTRATION IN VIAL (µg/L)	QUANTIFICATION ION
d8-Ethyl Acetate	870	1.97	66
d16-Octanal	1241	1.64	96
2-n-Hexyl furan	1295	0.27	152
d17-2-Ethyl-1-Hexanol	1433	1.33	94
(*Z*)-3-Hepten-1-ol	1443	34	81
d11-Hexanoic acid	1799	37.2	63
d7-Benzyl alcohol	1822	10.4	115

[1] RI calculated from retention relative to the retention of a series of n-alkanes (C_8-C_{26}).

Table 5.3.3 Compounds for which relative quantities were obtained in the headspace of crushed grape samples.

COMPOUND	RETENTION INDICES[1]	IDENTIFICATION[2]	QUANTIFICATION ION (*m/z*)	INTERNAL STANDARD[3]
Ethyl acetate	875	A	61	d8-EA
2-Butanone	895	B	72	d17-EH
2-Methyl butanal	906	B	57	d16-Oct
3-Methyl butanal	909	A	58	d16-Oct
1-Methoxy-hexane	938	B	56	d17-EH
2-Ethyl-furan	943	B	81	2-HF
2-Methyl-3,4-dihydro-2H-pyran	945	C	98	d17-EH
2,5-Dimethyloctane	953	B	57	d17-EH
2,6-Dimethyloctane	964	B	57	d17-EH

COMPOUND	RETENTION INDICES[1]	IDENTIFICATION[2]	QUANTIFICATION ION (*m/z*)	INTERNAL STANDARD[3]
Pentanal	969	A	58	d16-Oct
Methyl butanoate	976	B	74	d8-EA
Methyl glycolate	984	C	90	d8-EA
Decane	999	A	57	d17-EH
1-Methoxycyclohexene	1001	B	114	d17-EH
α-Pinene	1009	A	93	d17-EH
1-Penten-3-one	1012	A	55	d17-EH
4-Heptanone	1019	B	114	d17-EH
Methylbenzene	1027	A	91	d7-BA
2-Butenal	1029	B	70	d16-Oct
Hexanal	1075	A	56	d16-Oct
Ethylbenzene	1107	A	91	d7-BA
(*E*)-2-Pentenal	1114	A	83	d16-Oct
2-n-Butyl furan	1115	B	81	2-HF
p-Xylene	1121	B	91	d7-BA
(*E*)-3-Hexenal	1123	B	69	d16-Oct
1-Butanol	1129	A	56	d17-EH
1-Penten-3-ol	1144	A	57	Z3H
1,1-Dimethoxyhexane	1151	A	75	d17-EH
3-Ethylthiophene	1153	B	112	d17-EH
Heptanal	1169	B	70	d16-Oct
Methyl hexanoate	1172	B	74	d8-EA
Limonene	1176	A	93	d17-EH
Cyclohexene oxide	1183	A	83	d17-EH
Eucalyptol	1189	A	108	d17-EH
Isoamyl alcohol	1191	A	70	d17-EH
(*E*)-2-Hexenal	1207	A	83	d16-Oct
2-Pentyl-furan	1215	A	81	2-HF
1-Pentanol	1229	A	55	d17-EH
3-Octanone	1236	A	99	d17-EH
Styrene	1238	A	104	d7-BA
Hexyl acetate	1254	A	56	d8-EA
2-Octanone	1265	A	58	d17-EH
3-Hydroxy-2-butanone	1266	A	88	d17-EH
Octanal	1270	A	84	d16-Oct
1-Octen-3-one	1281	A	70	d17-EH
2,2,6-Trimethyl-cyclohexanone	1293	B	82	d17-EH
(*Z*)-3-Hexenyl acetate	1297	A	82	d8-EA

COMPOUND	RETENTION INDICES[1]	IDENTIFICATION[2]	QUANTIFICATION ION (*m/z*)	INTERNAL STANDARD[3]
(*Z*)-2-Penten-1-ol	1298	B	57	Z3H
(*E*)-2-Heptenal	1302	A	83	d16-Oct
Vinyl caproate	1305	C	99	d8-EA
3-Ethoxypentane	1307	C	87	d17-EH
6-Methyl-5-hepten-2-one	1316	A	108	d17-EH
1-Hexanol	1331	A	56	d17-EH
(*E*)-3-Hexen-1-ol	1340	A	67	Z3H
(*Z*)-3-Hexen-1-ol	1361	A	67	Z3H
Nonanal	1374	A	98	d16-Oct
2,4-Hexadienal	1381	A	81	d16-Oct
(*E*)-2-Hexen-1-ol	1383	A	57	Z3H
(Z)-2-Hexen-1-ol	1392	A	67	Z3H
2,2,6-Trimethyl-4-methylene-2H-pyran	1403	C	123	d17-EH
(*E*)-2-Octenal	1406	A	70	d16-Oct
Ethyl octanoate	1416	A	88	d8-EA
(*E*)-Linalool oxide	1420	A	111	d17-EH
1-Octen-3-ol	1429	A	57	Z3H
1-Heptanol	1432	A	55	d17-EH
(*E,Z*)-2,4-Heptadienal	1443	A	81	d16-Oct
Furfural	1444	A	95	2-HF
Acetic acid	1449	A	60	d11-HA
2-Ethyl-1-hexanol	1468	A	83	d17-EH
(*E,E*)-2,4-Heptadienal	1471	A	81	d16-Oct
Decanal	1480	A	112	d16-Oct
Theaspirane A	1480	B	138	d17-EH
Benzaldehyde	1501	A	106	d16-Oct
(*E*)-2-Nonenal	1513	A	70	d16-Oct
Theaspirane B	1518	B	138	d17-EH
2,5-Dihydro-thiophene	1522	C	85	d17-EH
Linalool	1527	A	93	d17-EH
1-Octanol	1535	A	83	d17-EH
5-Methyl-2-furfural	1552	B	110	2-HF
5,6-Dihydro-2H-pyran-2-carboxaldehyde	1577	C	83	d17-EH
(*E*)-2-Octen-1-ol	1593	A	57	Z3H
β-Cyclocitral	1597	B	152	d17-EH
γ-Butyrolactone	1608	A	86	d17-EH

COMPOUND	RETENTION INDICES[1]	IDENTIFICATION[2]	QUANTIFICATION ION (*m/z*)	INTERNAL STANDARD[3]
Phenylacetaldehyde	1623	A	91	d16-Oct
1-Hepten-3-one	1633	C	55	d17-EH
2-Furanmethanol	1638	A	98	2-HF
Humulene	1649	A	93	d17-EH
Diethyl succinate	1655	A	129	d8-EA
γ-Terpineol	1678	A	121	d17-EH
(*E,E*)-2,4-Nonadienal	1680	A	81	d17-EH
Dodecane-6,7-dione	1700	B	99	d17-EH
Pentanoic acid	1731	A	60	d11-HA
β-Cadinene	1736	B	161	d17-EH
5-Ethyl-2(5H)-furanone	1738	B	83	d17-EH
2-Phenylethyl acetate	1794	A	104	d8-EA
β-Damascenone	1799	A	121	d17-EH
Hexanoic acid	1836	A	60	d11-HA
Benzyl alcohol	1855	A	108	d7-BA
Phenylethyl Alcohol	1889	A	91	d7-BA
Methyl 2-oxo-hexanoate	1945	C	85	d17-EH
Phenol	1988	A	94	d7-BA

[1] RI calculated from retention relative to the retention of a series of n-alkanes (C_8-C_{26}). [2]A, identity confirmed by matching mass spectra and RI with that of authentic standards; B, tentative assignment based upon comparison with mass spectral libraries and published RI. C, compound not identified or named based on mass spectral match only. [3] d8-EA = d8-ethyl acetate, d16-Oct = d16-octanal, 2-HF = 2-n-hexyl furan, d17-EH = d17-2-ethyl-1-hexanol, Z3H = (*Z*)-3-hepten-1-ol, d11-HA = d11-hexanoic acid, d7-BA = d7-benzyl alcohol.

5.3.6 Grape 'Bound Volatile' Compounds

The extraction of 'bound' volatiles from the grape samples was achieved using a method adapted from that of Martin et al. (2012). Two grams of powdered grape was mixed with 8 mL of water, mixed every 2 min for 10 min and centrifuged at 3500 × *g* for 15 min at 4 °C. The supernatant was then passed through a Strata-X SPE column (60 mg/3 mL, Phenomenex) conditioned previously with 3 mL methanol and 3 mL water. The column was washed with 6 mL water and 6 mL pentane before the 'bound' volatiles were eluted with 6 mL methanol. The extracts were then dried using a vacuum evaporator without heat (Savant SpeedVac, ThermoFisher, MA, USA).

Hydrolysis of the 'bound' volatiles was conducted using citric acid and heat, and compounds released were extracted using diethyl ether and hexane (1:1), as outlined in Kotseridis et al. (1999). A 10 µL aliquot of 45 mg/L ethyl-4-acetyl benzoate in 50% ethanol was added as an internal standard. The extracted volatile compounds were analysed by GCMS (Agilent 6890N gas chromatograph and 5973 mass spectrometer). A 1 µL aliquot of each hydrolysate was injected into an inlet in pulsed splitless mode at a temperature of 220 °C and separated on a ZB-Wax column (length 30 m, 0.25 mm i.d., film thickness 0.25 µm; Phenomenex). The pressure pulse was 25.0 psi for 0.6 min at which time purging at 30 mL/min began. Helium was used as the carrier gas at a constant flow of 1.2 mL/min. The temperature program of the oven was as follows: 40 °C, held for 1 min; ramped at 10 °C/min up to 90 °C; ramped at 4 °C/min to 190 °C; ramped at 10 °C/min to 240 °C and held for 10 min. Positive-ion electron

impact spectra (70 eV) were recorded in scan mode (range: m/z 35-350, scan rate: 4.45 scans/s).

A laboratory generated library (377 compounds) as well as the US National Institute of Standards and Technology-11 (NIST-11) and the Wiley Registry 9th Edition mass spectral libraries was used to identity volatile compounds. Many of the compounds could only be tentatively identified or remain unknown (Table 5.3.4).

Table 5.3.4 Compounds for which relative quantities were obtained in the bound volatile fractions of the grape samples.

COMPOUND	RETENTION INDICES[1]	QUANTIFICATION ION (*m/z*)	REFERENCE NUMBER IN PCA
2-Ethenyltetrahydro-2,6,6-trimethyl-2H-pyran	1110	139	1
m-Xylene	1134	91	2
o-Xylene	1161	91	3
3-Hexanone	1165	57	4
3-Hexanol	1182	55	5
2-Hexanol	1201	45	6
(*E*)-2-Hexenal	1205	83	7
2-Pentyl furan	1231	81	8
cis-Rose oxide	1234	139	9
Styrene	1279	104	10
1,3-Dimethyl-1-cyclohexene	1289	95	11
4-Methoxy-1,3-benzenediamine	1397	123	12
(*Z*)-Linalool oxide	1425	94	13
α-Ionene	1431	159	14
3,4,5-Trimethylpyrazole	1444	109	15
(*E*)-Linalool oxide	1451	94	16
Benzaldehyde	1506	105	17
1-(2,4-Dimethyl-3-furyl)ethanone	1547	123	18
2-Methyl-2-butanol	1567	59	19
4-Methyl-2-pentanol	1591	69	20
Ocimenol	1638	93	21
α-Fenchene	1667	93	22
4-Oxoisophorone	1673	96	23
1,1,4,6,7-Pentamethyl-2,3-dihydroindene	1715	173	24
1,2-Dihydro-1,1,6-trimethylnaphthalene (TDN)	1722	157	25
β-Damascenone	1801	121	26
1(2,3,6-Trimethylphenyl)but-1,3-diene (TPB)	1807	157	27
Guaiacol	1835	124	28

COMPOUND	RETENTION INDICES[1]	QUANTIFICATION ION (*m/z*)	REFERENCE NUMBER IN PCA
Benzyl Alcohol	1864	108	29
1,1,6,8-Tetramethyl-1,2-dihydro-naphthalene	1890	171	30
α-Calacorene	1891	157	31
1-[4-(1-Hydroxy-1-methylethyl)phenyl]-ethanone	1910	163	32
3-(2,6,6-Triimethyl-1-cyclohexen-1-yl)-2-propenal	1921	163	33
2,2-Dimethyl-3,3-(1'2'-ethylidene)-5-methyl-1,2-dihydrobenzofuran	1943	173	34
1,2-Dihydro-2,5,8-trimethyl-naphthalene	1971	157	35
4-(2,6,6-Trimethylcyclohexa-1,3-dienyl)but-3-en-2-one	1985	175	36
Unknown 1	2003	163	37
1,2-Dihydro-1,4,6-trimethyl-naphthalene	2011	157	38
2-Methylenebornane	2031	107	39
1,2-Dihydro-3,5,8-trimethyl-naphthalene	2039	157	40
1-(2,3,6-Trimethylphenyl)-3-buten-2-one	2095	173	41
1,2-Dihydro-4,6,8-trimethyl-naphthalene	2187	157	42
2-Hydroxy-5-methylacetophenone	2191	135	43
4-(2,6,6-Trimethyl-2-cyclohexen-1-yl)-3-buten-2-ol	2201	95	44
1-(2,3,6-Trimethylphenyl)-2-butanone	2219	132	45
Megastigmatrienone	2285	175	46
2,3-Dihydro-3,3,4,5-tetramethyl-1H-Inden-1-one	2296	173	47
2,3-Dimethyl-4-amino-1,4-benzoquinone	2305	151	48
2,4-bis(1,1-Dimethylethyl)-phenol	2320	191	49
4-(2,4,6-Trimethylphenyl)-butan-2-ol(1)	2370	192	50
4-(2,3,6-Trimethylphenyl)-2-butanone	2377	157	51
4-Vinylphenol	2408	120	52
(Z)-5-Methyl-4-phenyl-3-hexen-2-ol	2443	157	53
2,3-Dihydro-2,4,7-trimethyl-1H-indene-2-methanol	2506	157	54
3-Hydroxy-β-damascone	2528	193	55
3-Oxo-α-ionol	2600+	108	56
Eucalyptol	1184	85	57
1-Hexanol	1334	56	58
(E)-3-Hexen-1-ol	1357	67	59
Cyclohexanol	1382	82	60
Vitispirane	1507	192	61

COMPOUND	RETENTION INDICES[1]	QUANTIFICATION ION (*m/z*)	REFERENCE NUMBER IN PCA
3-Methyl-4-heptanone	1552	100	62
2-Hexanone	1579	58	63
Unk monoterpene 1	1598	93	64
4-Methyl-benzaldehyde	1626	120	65
8-Methyl-tricyclo[3.3.0.0(2,8)]octan-3-one	1666	94	66
α -Terpineol	1677	93	67
Methyl salicylate	1757	120	68
Unknown 3	1790	190	69
Octa-2,4,6-triene	1811	108	70
2,5-Hexanediol	1830	85	71
p-Cymen-8-ol	1832	135	72
Hexanoic acid	1845	60	73
Unknown 4	1859	173	74
Unknown 5	1893	85	75
Benzothiazole	1934	135	76
2-Ethylhexanoic acid	1944	88	77
Heptanoic acid	1952	60	78
1-Nonadecene	2034	83	79
Octahydro-1,1-dimethyl-7H-benzocyclohepten-7-one	2067	177	80
Octanoic acid	2072	60	81
7-Methyl-1-naphthol	2103	177	82
Nonanoic acid	2161	60	83
Unknown 7	2244	193	84
1-Docosene	2250	83	85
Decanoic acid	2274	60	86
4-(2,4,6-Trimethylphenyl)-butan-2-ol(2)	2364	192	87
Dodecanoic acid	2430	60	88
Benzoic acid	2471	105	89
Methyl vanillate	2584	151	90
7,9-di-tert-butyl-1-oxaspiro[4,5]deca-6,9-diene-2,8-dione	2600+	205	91
Methyl 2-hydroxy-4-methylbenzoate	2600+	134	92
Vanillyl acetone	2600+	194	93
2,4-Hexanedione	1284	114	94
1,3-Dihydro-5-propyl-isobenzofuran	1781	162	95
4-Ethyl-benzaldehyde	1796	134	96
8-Hydroxycoumarin	1834	162	97

COMPOUND	RETENTION INDICES[1]	QUANTIFICATION ION (*m/z*)	REFERENCE NUMBER IN PCA
2-Isopentyl-1,3,5-trimethylbenzene	1927	190	98
Ethyl 4-ethoxybenzoate	2150	121	99
2-Methyl-2-decanol	2159	59	100
2-Methyl-2-dodecanol	2401	59	101
Butyl benzoate	2600+	105	102
Methyl syringate	2600+	212	103

[1] RI calculated from retention relative to the retention of a series of n-alkanes (C_8-C_{26}).

5.4 Small-lot winemaking

All sub-region and trial site fruit was harvested and delivered to the WIC winemaking service team for small-lot winemaking in 2018, 2019, 2020 and 2021. In 2018, 50 kg of fruit per site/zone (or treatment replicate) was harvested. Due to lower yields in 2019-21, 30 kg of fruit per site/zone was harvested.

A schematic of the small scale red winemaking protocol is shown in Figure 5.4.1. Vineyard replicates were weighed and then stored overnight in a 0°C cool room. This was to bring the core temperature of the fruit down to approximately 5°C prior to processing, which is a critical step to reduce the oxidation rate and fruit degradation in such small batch sizes. The following day, fruit was crushed through a small 1 t/hour crusher and destemmer, 50 ppm SO_2 as a 10% solution was added to the must once crushed and re-weighed based on an estimated 500 L/t extraction rate, and pectolytic maceration enzyme was added at the equivalent volume of 30 mL/t. The crushed must was then stored overnight in a 15°C cool room under dry ice coverage to allow the core temperature to rise to 15°C for yeast inoculation. Yeast addition of 250 ppm was made using AB Biotek PDM yeast strain and yeast preparation was conducted in accordance with the manufacturer's standard protocol. Temperature and Baume results were recorded daily, and the ferments received twice daily hand plunging using standardised plunging tools and a standardised technique to maintain consistency in the cap management process.

On the day following crushing, if the Baume result was in excess of 15 Baume, a water addition to the must was made using an estimated extraction of 600 L/t, and the amount of dilution determined using the AWRI water addition calculator. The timing of this addition and the accuracy of the reading of Baume at 24 hours post crush proved to be much more accurate in achieving the desired level of alcohol adjustment, a much more integrated addition and was less likely to result in sluggish or stuck primary or secondary ferments. Any water adjustment was made with slightly acidified water to account for the increase in volume. A 5 g/L addition of tartaric acid to the water was the standard rate. Any other acid adjustment was made as early in the ferment stage as possible to provide the best possible environment for the fermentation. 2019 was a difficult year for acidification as both pH and TA was high. In this instance, a target TA of 7 g/L, after accounting for TA reduction caused by MLF, would dictate the amount of acid added. This however meant that a number of wines still had a pH of 3.8-4.0 post acid addition.

At 48 hours post yeast inoculation, 10 ppm of MLF bacteria made up in a 5% solution was added to initiate ML fermentation. The ferments were conducted at 15°C until the Baume dropped below 3, where the replicates were then moved to the 20°C cool room until pressing and the completion of both sugar and ML fermentations. In all cases, these wines were

pressed on day 8, where yeast inoculation is day 0, and cap management commenced on day 1. A standardised press cycle was used for each replicate and generally yielded between 630-650 L/t extraction then wines are consolidated off ullage as best as possible after pressing and for the duration of MLF.

Upon completion of primary and secondary fermentation, the wines were dosed with 80 ppm SO_2, again modified from commercial winery additions due to the small volume sizes and the tendency for rapid wine degradation. The wines were then moved to the 0°C cool room for a minimum of four weeks for cold settling and natural cold stabilisation, prior to a series of racking to achieve cellar brightness prior to bottle. Due to the number of replicates in this trial, filtration was not performed as there would be significant time variation and ullage management between the first and last batches processed. Final pre-bottling additions were performed to achieve FSO_2 of 35-45 ppm and copper trials conducted to determine sulfide reduction as required. Each batch was then bottled and labelled in 750 mL punted claret bottles and closed using a standard Stelvin screw cap closure.

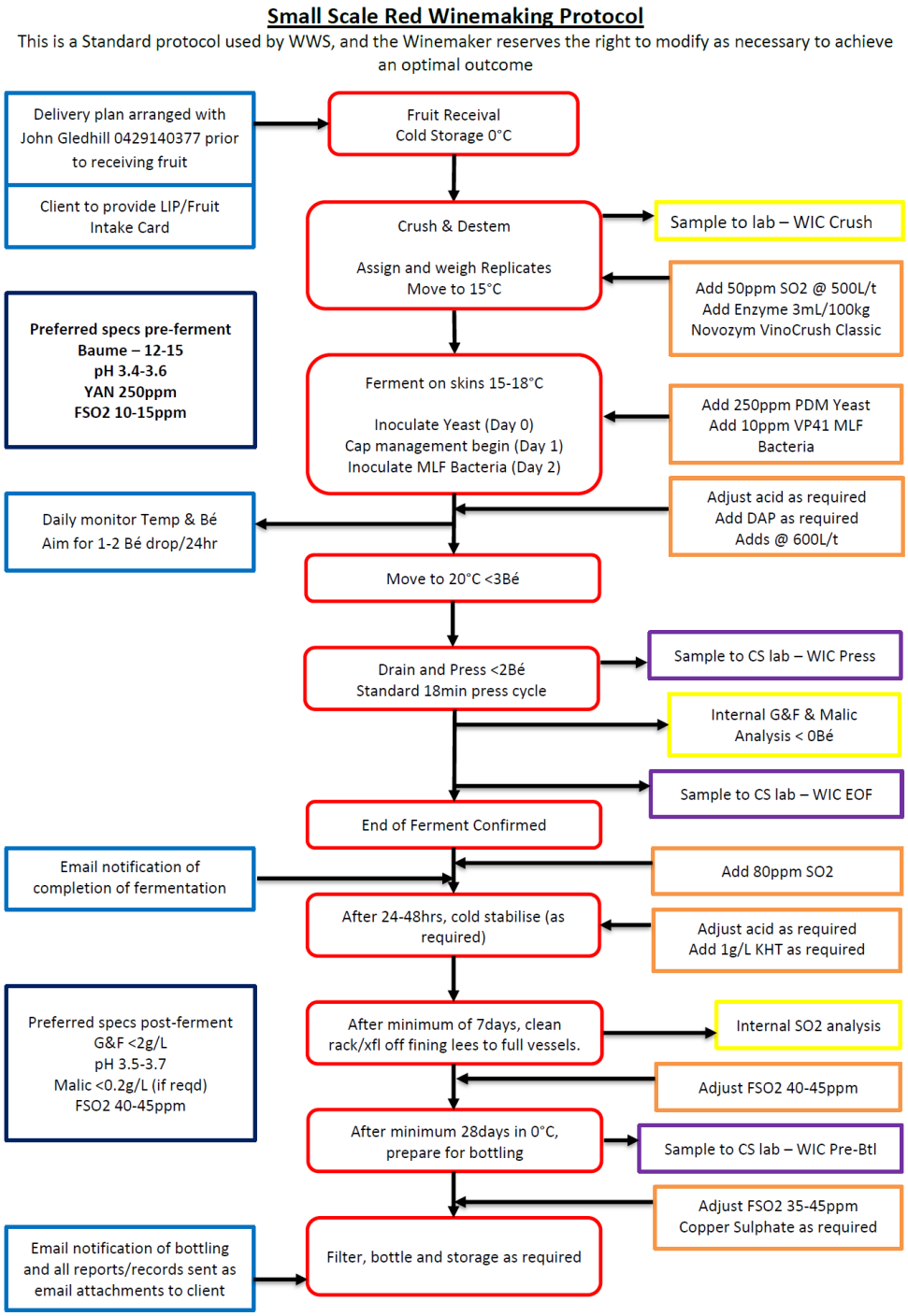


Figure 5.4.1 Small scale winemaking protocol courtesy of John Gledhill, WIC winemaking services, Adelaide.

5.5 Wine chemistry

Basic wine compositional analysis, including pH, titratable acidity (TA), specific gravity, alcohol concentration, residual sugar, free and total SO_2, volatile acidity, malic acid and wine metal composition was performed at the AWRI's commercial laboratory (Affinity Labs). Wine tannin concentration, colour composition and anthocyanin profile was determined using a published protocol (Mercurio et al., 2007) with flavonols identified and quantified as described by Jeffery et al. (2008). Wine tannin and polysaccharide composition was determined as described by Bindon et al. (2019). For wine volatile composition, C6 compounds were identified and quantified according to Capone et al. (2012). Low molecular weight thiols were quantified as described by Siebert et al. (2010), and polyfunctional thiols according to Capone et al. (2015) with the modifications of Cordente et al. (2022). Monoterpenes and C_{13}-norisoprenoids were analysed as described by Pisaniello et al. (2022). Wine fermentation and oxidation products were measures by the methods of Siebert et al. (2005) and Mayr et al. (2015) respectively.

5.6 Sensory analysis

5.6.1 Samples

Three sample sets from six Barossa sub-regions were analysed.

1. *Small-lot winemaking wines*
   Four vineyards were chosen from each of the six sub-regions. From each of the vineyards, three wines from grapes sourced from different locations in the vineyard were produced under standardised conditions by the University of Adelaide winery.
2. *Commercial scale wines from sub-regional sites*
   Wines produced on a commercial scale were sourced from the same vineyards as the small-lot winemaking samples just after completing malolactic fermentation.
3. *Commercial scale wines from benchmarking sites*
   Wines produced on a commercial scale from vineyards, different to the small-lot winemaking sites, but from the same six sub-regions were sourced. The wines were collected generally after completing malolactic fermentation (MLF), but for a small number of samples, MLF was completed in-bottle when batches were blended by the winery before MLF completion.

For reasons out of the control of the researchers (e.g. drought, frost, change in vineyard management, fruit blended at harvest), the number of samples varied between vintages (Figure 5.6.1)

Table 5.6.1 Number of wine samples undergoing sensory analysis.

	2018	**2019**	**2020**	**2021**
Small-lot wines	68	72	79	64
Commercial wines				
- Sub-regional sites	21	22	21	18
- Benchmarking sites	23	54	45	59

5.6.2 Methodology

To quantitatively profile the sensory characteristics of the wine samples, descriptive analysis (DA) (Lawless & Heymann, 2010) was used. A professional DA panel was created and panellists were recruited based on their sensorial abilities, availability across the four seasons and previous participation on wine DA panels. All panellists underwent screening in aroma and taste identification, and discrimination abilities as well as their teamwork abilities. The best 12 panellists, aged between 24-60, were selected for each analysis. For the consecutive vintages, panellists who had completed the DA for the previous vintage were prioritised. If any were unavailable, they were replaced with newly screened panellists.

Ten (2018 and 2019) and nine (2020, 2021) training sessions of two hours were held over four weeks. Initial training sessions consisted of basic taste discrimination, aroma identification and development of the attribute and reference list. For the vintages 2019, 2020 and 2021, the attribute list from 2018 was used as a starting point and only marginally modified. The remaining training sessions were dedicated to improving attribute understanding, scale usage, alignment of the assessors, and providing feedback on individual performance. The training sessions also included two practice evaluation sessions conducted in sensory booths, under the same conditions used during the formal assessment. Data were evaluated after each practice evaluation to assess panellist-by-sample interactions, and to

determine when formal assessment should commence, where a consensus was reached and minimal interactions were significant.

Formal evaluation:
Small-lot winemaking wines
Formal two hour assessment sessions were held three times a week, with 12 to 14 wines presented per session. All wines were assessed blind and in duplicate. Wine aliquots of 30 mL were presented in coded and covered, black 215 mL stemmed ISO wine tasting glasses, using a randomised presentation order. Panellists assessed each wine in an isolated tasting booth at 21-22 °C, rating the intensity of each sensory descriptor using a 15 cm line scale with anchor points of 'low' and 'high' placed at 1.5 cm and 13.5 cm on the scale, respectively. Sensory reference standards (Table 5.6.2) were developed during training sessions and provided to panellists at each formal assessment session in covered, black glasses (2018 and 2019) and in 50 mL centrifuge tubes in 2020 and 2021 to accommodate COVID-19 restrictions. Panellists were required to reacquaint themselves with the sensory reference standards and definitions of attributes before and several times during each evaluation. Deionised water, pectin solution (2 g/L) and crackers were provided as palate cleansers, and panellists were required to have a one minute break between samples and a five minute break after every 5-6 samples. Sample data were collected using Red Jade software (2016, Redwood City, USA).

Commercial winery wines
Following the assessment of the small-lot winemaking wines, the same panel assessed the commercially produced wines in a similarly structured two hour assessment session following the same procedure.

5.6.3 Data analysis

Panel performance was checked using Analysis of Variance (ANOVA) with regards to attribute ratings, considering panellist (random factor), samples and replicate (fixed factors), and including all their second-order interactions. Two-way ANOVAs with samples as fixed factors and panellists as random factors, including their interactions, were performed on all rated attributes to identify attributes significantly discriminating among samples.

Canonical variate analysis (CVA) was used to investigate and comprehend the sub-regional sensory differences. With this statistical methodology, it is clear to understand and identify the segregation and the similarities between the Barossa subdivisions, along with the sensory attributes mostly associated with each.

Table 6.5.2 List of sensory attributes scored in the descriptive analysis of fine Australian Shiraz wines with definitions and reference standards.

Attribute	Definition (reference standard, in 25 mL base wine)
Aroma	
Alcohol	The smell of ethanol 0.75 mL Ethanol (Tarac Technologies, Australia)
Dark fruits	Any combination of dark fruit, (2 frozen blueberries (Woolworths Frozen Mixed Berries, Australia) and 1 frozen blackberry (Woolworths Frozen Mixed Berries, Australia) both cut in half
Red fruits	Any combination of red fruit e.g. strawberry, raspberry, red cherry (half frozen strawberry (Woolworths Frozen Mixed Berries, Australia) and 2 frozen raspberries (Woolworths Frozen Mixed Berries, Australia)
Dried fruits	Prune, fig, raisin (half-dried prune (Sunsweet Prunes Pitted, Grocery Corporation Pty. Ltd, Australia), 3 raisins (Macro, Austalia)
Confectionery	Candy, lolly, fruit drops (quarter raspberry drop (Allen's Ripe Raspberries Lollies, Australia)
Jammy	Fruit jam, stewed fruits (1 tsp Fruit of the Forest Jam (Cottee's, Australia) and Plum jam (Cottee's, Australia))
Green	Leafy, herbaceous, green capsicum (5 cm of fresh cut grass and 1x1 cm fresh green capsicum)
Chemical/Medicinal	Band-aid, medicinal, barnyard (1 cm piece of band-aid (Leukoplast GMBH, Hamburg, Germany))
Mint/Eucalypt	Mint (1 x 1 cm of fresh mint leaf and 1 x 1 cm fresh eucalyptus leaf)
Earthy	Earthy, Mushrooms, forest floor (1 slice of fresh mushroom, pinch of potting soil)
Savoury	Savoury, meaty, soy sauce (0.2 g of beef stock powder (Continental, Unilever, Australia) and a pinch of Vegemite (Vegemite, Australia)
Pepper	Pepper (a pinch of freshly ground black (G-Fresh, Australia) and white pepper (McKenzie's, Australia)
Floral	Perfume, Violet, Rose (0.03 mL Natural Rosewater (Queen, Australia))
Smoky/toasty	Bushfire, charred wood (charred wood toothpick)
Spice	Sweet spice, allspice, liquorice (pinch fresh cinnamon (MasterFoods, Mars Food Australia) and pinch Allspice (Select, Woolworths Australia)
Cooked Vegetables	1 tablespoon of canned Sliced Green Bean juice plus 1 tablespoon of canned Mixed Vegetables (peas and carrots) (both Woolworths, Australia)
Wood	Raw wood, Pencil shaving (a pinch of un-toasted oak chips)
Taste	
Bitter	Basewine 10%, Base wine plus 0.8 g/L caffeine (Sigma-Aldrich, China) 60%
Sweet	Basewine 20%, 10 g/L Sucrose (Woolworths Homebrand, Australia) 90%
Sour	1 g/L Tartaric acid (Merc, Australia) 10%, 2 g/L Tartaric acid 90%,
Mouthfeel	
Astringency	10 % 0.3 g/L grape seed extract (Tarac Technologies, Australia) + 0.5 g/L tartaric acid, 90% 1.0 g/L grape seed extract + 0.5 g/L tartaric acid
Body	Base wine 20%, Base wine plus 0.1 g/L Xanthan gum (The Melbourne Food Ingredient Depot, Australia) 80%
Tanning quality	Smooth to rough
Heat	10% Base wine 13.5%, 90% Base wine plus 3% EtOH (16.5% in total)
Aftertaste	
Fruity aftertaste	Duration of any fruit aftertaste
Non-fruit	Duration of any non-fruit aftertaste (excluding astringency and basic tastes)

5.7 Chemometric analysis of combined data sets

5.7.1 Data modelling

Several approaches to data modelling have been used, which can broadly be defined as supervised discriminant analysis and unsupervised clustering. The various approaches have relative strengths and weaknesses and no single approach for data interrogation is suitable for all data sets. For the purposes of this report, the supervised discriminate analysis has focused on single vintage ANOVA Multiblock Orthogonal PLS (AMOPLS) models for 2018 to 2021 vintage data sets, and a four-year (All Vintage) AMOPLS model using as many variables as possible across each of the data blocks. AMOPLS methods partition data variance according to the explanatory factor (EF) levels within the experimental design before application of multivariate linear methods to discriminate samples. Removal of structured and orthogonal information makes interpretation of AMOPLS models easier, however, these models have limitations for discrimination of many EF levels. For the AMOPLS data decomposition each data block is equally weighted at the commencement of data modelling, thus the relative contributions of each data block indicate the weighting of that data to the extracted predictive component associated with the EF. Random forest methods are non-linear and employ an ensemble of decision trees for EF level discrimination and are therefore ideal for complex data sets. With origins in metabolomics of high-resolution mass spectrometry data sets, random forest methods are very good at dealing with highly colinear variates and multiple levels of EF (Enot, et al. 2008). Interpretation of random forest methods requires a different approach for determining variable importance than latent variable methods and therefore both approaches provide interesting perspectives and insights into the correlation of data set information and a sample class. In contrast to the strategy used in AMOPLS, variables were gradually removed from the model based on the degree of contribution to the classification accuracy, irrespective of the original data block structure. Eventually, an optimal model could be achieved with the highest classification accuracy using the least number of variables that showed the most variation among the sub-regions.

Non-supervised models were constructed using the identical sample sets and measured attributes for the AMOPLS models and used either k-means (linear) clustering. The inclusion of non-supervised clustering methods allows the data to speak for itself and avoids *a priori* assumptions of sample class. Prior to unsupervised clustering, vintage variation was effectively removed from the data set by normalising the total variance to 1 for each year. Equalisation of variance for each year ensures variations in the data used for sample clustering are more likely associated with regional influences without the confounding effects of vintage. This approach differs from the AMOPLS approach which seeks to partition variation in accordance with explanatory factor levels such as vintage in the all vintage model. As some measured attributes of composition were not measured for the full term of the project, we have used only those measurements that have been reported for the entire duration of the project. In summary the clustering models reported herein are:

- AMOPLS
    - All Vintage (Vintage & Region)
    - 2018 (Region & Site)
    - 2019 (Region & Site)
    - 2020 (Region & Site)
    - 2021 (Region & Site)
- K-means Cluster
    - All Vintage (Vintage & Region)
    - 2018 (Region & Site)

    - 2019 (Region & Site)
    - 2020 (Region & Site)
    - 2021 (Region & Site)
- Random Forest
    - All Vintage (Region)
    - Reduced variables RF
    - Binary comparison of models

5.7.2 Consensus sensory spaces

Sensory data are inherently variable and require a considered approach for modelling, especially across multiple vintages when sensory adjectives vary in importance from year to year. To avoid a 'regression to the mean with high variance' outcome and to accommodate the high dimensionality of sensory data sets, a consensus sensory space for each vintage was determined using STATIS (Abdi, et al. 2012). STATIS is a commonly applied multiblock analysis tool that seeks to create a multivariate dimension that represents the commonality of the sensory domains for each wine and assessor combination. From each of the consensus multivariate spaces created for each vintage sensory data set, five latent variables representing approximately 18-20% of total data variance for each sensory data sets for each vintage were used as a surrogate sensory data block for multiblock clustering and discriminant analysis. The projection of the sensory data into a consensus space for each vintage enables the four vintage models to be constructed with common sensory attributes being the latent variables representing the consensus. The consensus space for each vintage also enables the latent variables to be used within the framework for a four-vintage data modelling exercise. The percent data variance captured by each latent variable, and the cumulative variance in the STATIS consensus space for each vintage, is shown in Figure 5.7.1. As expected, the first two latent variables capture the most sensory data variance for each year (range 3.6 to 7.5%) with higher order latent variables capturing around 3% or less of total variance int eh sensory data. A decision to include the sample scores from the first five latent variables as surrogates for raw sensory data was considered prudent as this represented approximately 17-20% of variance in the sensory data for each year.

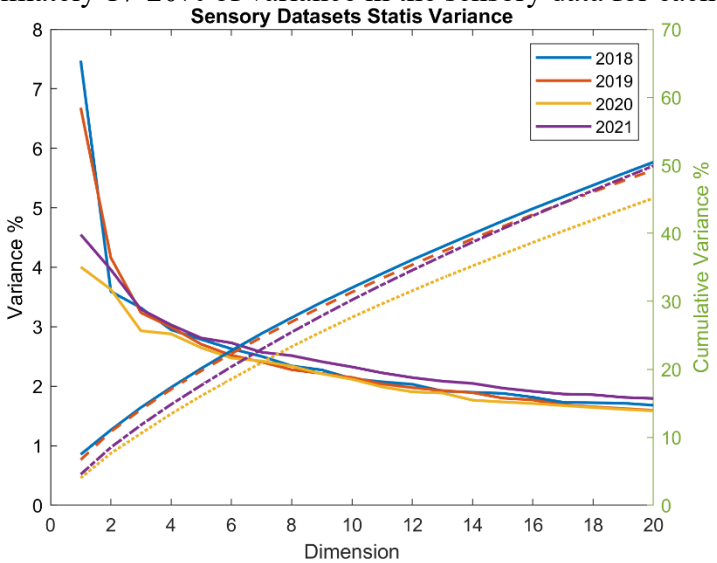


Figure 5.7.1 Variance and cumulative variance for each dimension for sensory data sets for vintages 2018 to 2021. Five latent variables were chosen to represent the consensus space for each vintage.

5.7.3 Multiblock data sets

Data were arranged as 15 discrete data blocks containing varying numbers of attributes which are summarised in Table 5.7.1 with each data block colour coded to assist in identifying trends associated with the data sets. The total number of variables for each data set block is provided in parenthesis, and a more in-depth description of each data block is presented in Table 5.7.2. Where possible, each multiblock chemometric method was constructed using the largest possible number of site sample replicates and measured attributes. The selection of attributes for each vintage and the combined vintage models is shown in Table 5.7.2.

Table 5.7.1. Data block attributes including colour code used in variable loadings plots, block order and number and the total number of measured attributes for each table are indicated in parentheses.

Block #	Description	Block #	Description
1	Vine Performance (7)	8	Grape Phenolics (19)
2	Crop Maturation (12)	9	Grape Tannin (16)
3	Grape Amino Acids (22)	10	Wine Basic Chemistry (10)
4	Grape Bound Volatiles (106)	11	Wine Metals (15)
5	Grape Carotenoids (14)	12	Wine Phenolics & Colour (51)
6	Grape Fatty Acids (29)	13	Wine Polysaccharides (11)
7	Grape Volatiles (101)	14	Wine Volatiles (63)
		15	Wine Sensory (5LV)

Table 5.7.2 Data block variables used in the vintage and four vintage supervised and non-supervised discriminant analysis and clustering models.

Data block description	Variable Number	Attribute	Use in AMOPLS, k-means and Random Forest Analysis				
			2018	2019	2020	2021	All Vintages
1. Vine Performance	1	Pruning Shoot Number	X	X	X	X	X
	2	Pruning Weight m/kg	X	X	X	X	X
	3	Yield m/kg	X	X	X	X	X
	4	Bunch Number	X	X	X	X	X
	5	Average Bunch Weight g	X	X	X	X	X
	6	Porosity	X	X	X	X	X
	7	Plant Area Index	X	X	X	X	X
2. Crop Maturation	8	Tannin	X	X			
	9	Tannin mg/L Epicatechin Eq	X	X		X	
	10	Tannin Homogenate	X	X		X	
	11	Phenolics mg/berry	X	X	X	X	X
	12	Phenolics mg/g	X	X	X	X	X
	13	Anthocyanin mg/berry	X	X	X	X	X
	14	Anthocyanin mg/g	X	X	X	X	X
	15	Berry Weight g	X	X	X	X	X
	16	pH (grape)	X	X	X	X	X
	17	Titratable Acidity	X	X	X	X	X
	18	Brix	X	X	X	X	X
	19	Baume					
3. Grape Amino Acids	20	Hydroxyproline	X	X	X	X	X
	21	Aspartic acid	X	X	X	X	X
	22	Asparagine	X	X	X	X	X
	23	Serine	X	X	X	X	X
	24	Glutamic acid	X	X	X	X	X
	25	Histidine	X	X	X	X	X
	26	Glutamine	X	X	X	X	X
	27	Glycine	X	X	X	X	X
	28	Arginine	X	X	X	X	X
	29	Threonine	X	X	X	X	X
	30	Beta-Alanine	X	X	X	X	X
	31	Alanine	X	X	X	X	X
	32	Proline	X	X	X	X	X
	33	gamma-Aminobutyric Acid	X	X	X	X	X
	34	Cysteine					
	35	Tyrosine	X	X	X	X	X
	36	Valine	X	X	X	X	X

Data block description	Variable Number	Attribute	Use in AMOPLS, k-means and Random Forest Analysis				
			2018	2019	2020	2021	All Vintages
	37	Methionine	X	X	X	X	X
	38	Lysine	X	X	X	X	X
	39	Isoleucine	X	X	X	X	X
	40	Leucine	X	X	X	X	X
	41	Phenylalanine	X	X	X	X	X
4. Grape	42	2-Ethenyltetrahydro-2,6,6-trimethyl-2H-pyran	X	X	X	X	X
Bound	43	p-Xylene	X				
Volatiles	44	4-Methyl-3-penten-2-one	X				
	45	m-Xylene	X				
	46	o-Xylene	X				
	47	3-Hexanone	X	X	X	X	X
	48	3-Hexanol	X	X	X		
	49	Eucalyptol	X	X	X		
	50	2-Hexanol	X	X	X	X	X
	51	(E)-2-Hexenal	X	X	X	X	X
	52	2-Pentyl furan	X	X	X	X	X
	53	cis-Rose oxide	X	X	X	X	X
	54	Ethenyl benzene	X	X			
	55	2,4-Hexanedione		X	X		
	56	1,3-Dimethyl-1-cyclohexene	X	X	X	X	X
	57	1-Hexanol	X	X	X	X	X
	58	(E)-3-Hexen-1-ol		X	X	X	
	59	Cyclohexanol		X	X	X	
	60	4-Methoxy-1,3-benzenediamine	X				
	61	Linalool Oxide 1	X	X	X	X	X
	62	Alpha-Ionene	X	X	X	X	X
	63	3,4,5-Trimethylpyrazole	X				
	64	Linalool Oxide 2	X	X	X	X	X
	65	Benzaldehyde	X	X	X	X	X
	66	Vitispirane	X	X	X	X	X
	67	1-(2,4-Dimethyl-3-furyl)ethanone	X	X			
	68	3-Hexanone		X			
	69	2-Methyl-2-butanol	X	X			
	70	2-Hexanone		X			
	71	4-Methyl-2-pentanol	X	X			
	72	Unk monoterpene 1		X	X	X	
	73	4-Methyl-benzaldehyde	X	X	X	X	X
	74	Ocimenol	X	X	X	X	X
	75	alpha-Fenchene	X	X	X	X	X

Data block description	Variable Number	Attribute	Use in AMOPLS, k-means and Random Forest Analysis				
			2018	2019	2020	2021	All Vintages
	76	8-Methyl-tricyclo[3.3.0.0(2,8)]octan-3-one		X	X	X	
	77	4-Oxoisophorone	X	X	X	X	X
	78	Alpha-Terpineol	X	X	X	X	X
	79	1,1,4,6,7-Pentamethyl-2,3-dihydroindene	X	X	X	X	X
	80	1,2-Dihydro-1,1,6-trimethyl-naphthalene	X	X	X	X	X
	81	Methyl salicylate		X	X	X	
	82	1,3-Dihydro-5-propyl-isobenzofuran	X	X	X	X	X
	83	Unknown 3		X	X	X	
	84	4-Ethyl-benzaldehyde	X	X	X	X	X
	85	Damascenone	X	X	X	X	X
	86	1-(2,4,6-Trimethylphenyl)buta-1,3-diene	X	X	X	X	X
	87	Octa-2,4,6-triene		X	X	X	
	88	2,5-Hexanediol		X	X	X	
	89	Para-cymen-8-ol		X	X	X	
	90	8-Hydroxycoumarin	X	X	X	X	X
	91	Guaiacol	X	X	X	X	X
	92	Hexanoic Acid		X	X	X	
	93	Benzyl alcohol	X	X	X	X	X
	94	1,1,6,8-Tetramethyl-1,2-dihydro-naphthalene	X	X			
	95	Unknown 4		X			
	96	alpha-Calacorene	X	X	X	X	X
	97	Unknown 5		X	X		
	98	1-[4-(1-Hydroxy-1-methylethyl)phenyl]-ethanone	X	X	X	X	X
	99	3-(2,6,6-Triimethyl-1-cyclohexen-1-yl)-2-propenal	X	X	X	X	X
	100	2-Isopentyl-1,3,5-trimethylbenzene	X	X	X	X	X
	101	Benzothiazole		X	X	X	
	102	2,2-Dimethyl-3,3-(1'2'-ethylidene)-5-methyl-1,2-dihydrobenzofuran	X	X	X	X	X
	103	2-Ethylhexanoic acid		X	X	X	
	104	Heptanoic acid		X	X	X	
	105	1,2-Dihydro-2,5,8-trimethyl-naphthalene	X	X	X	X	X

Data block description	Variable Number	Attribute	Use in AMOPLS, k-means and Random Forest Analysis				
			2018	2019	2020	2021	All Vintages
	106	Unknown 6		X			
	107	4-(2,6,6-Trimethylcyclohexa-1,3-dienyl)but-3-en-2-one	X	X	X	X	X
	108	Unknown 1	X	X	X	X	X
	109	1,2-Dihydro-1,4,6-trimethyl-naphthalene	X	X	X	X	X
	110	2-Methylenebornane	X	X	X	X	X
	111	1,2-Dihydro-3,5,8-trimethyl-naphthalene,	X	X	X	X	X
	112	1-Nonadecene		X	X		
	113	Octahydro-1,1-dimethyl-7H-benzocyclohepten-7-one		X	X	X	
	114	Octanoic acid		X	X	X	
	115	1-(2,3,6-Trimethylphenyl)-3-buten-2-one	X	X	X	X	X
	116	7-Methyl-1-naphthol	X	X	X	X	X
	117	Ethyl 4-ethoxybenzoate	X	X	X	X	X
	118	2-Methyl-2-decanol	X	X	X	X	X
	119	Nonanoic acid		X	X	X	
	120	1,2-Dihydro-4,6,8-trimethyl-naphthalene,	X	X			
	121	2-Hydroxy-5-methylacetophenone	X	X		X	
	122	4-(2,6,6-Trimethyl-2-cyclohexen-1-yl)-3-buten-2-ol	X	X	X	X	X
	123	1-(2,3,6-Trimethylphenyl)-2--butanone	X	X	X	X	X
	124	Unknown 7		X	X	X	
	125	1-Docosene		X	X	X	
	126	Megastigmatrienone	X	X	X	X	X
	127	2,3-Dihydro-3,3,4,5-tetramethyl-1H-Inden-1-one	X	X	X	X	X
	128	Decanoic acid		X	X	X	
	129	2,3-Dimethyl-4-amino-1,4-benzoquinone	X	X	X	X	X
	130	2,4-bis(1,1-Dimethylethyl)-phenol	X	X	X	X	X
	131	4-(2,4,6-Trimethylphenyl)-butan-2-ol(1)	X	X	X	X	X
	132	4-(2,3,6-Trimethylphenyl)-2--butanone	X	X	X	X	X
	133	2-Methyl-2-dodecanol		X	X	X	
	134	4-Vinylphenol	X	X	X	X	X

Data block description	Variable Number	Attribute	Use in AMOPLS, k-means and Random Forest Analysis				
			2018	2019	2020	2021	All Vintages
	135	4-(2,4,6-Trimethylphenyl)-butan-2-ol(2)		X	X	X	
	136	(Z)-5-Methyl-4-phenyl-3-hexen-2-ol	X	X	X	X	X
	137	Dodecanoic acid		X	X	X	
	138	2,3-Dihydro-2,4,7-trimethyl-1H-indene-2-methanol	X	X	X	X	X
	139	Benzoic acid		X		X	
	140	3-Hydroxy-beta-damascone	X	X		X	
	141	Methyl vanillate	X	X	X	X	X
	142	3-Oxo-alpha-ionol	X	X	X	X	X
	143	Butyl benzoate	X	X	X	X	X
	144	7,9-di-tert-butyl-1-oxaspiro[4,5]deca-6,9-diene-2,8-dione		X			
	145	Methyl 2-hydroxy-4-methylbenzoate	X	X	X	X	X
	146	Vanillyl acetone		X	X		
	147	Methyl syringate	X	X	X	X	X
5. Grape Carotenoids	148	Neoxanthin	X	X	X	X	X
	149	Lutein	X	X	X	X	X
	150	Zeaxanthin	X	X	X	X	X
	151	Chlorophyll B	X	X	X	X	X
	152	Chlorophyll A	X	X	X	X	X
	153	Beta-Carotene	X	X	X	X	X
	154	Unk1	X	X	X	X	X
	155	Unk2	X	X	X	X	X
	156	Pheophytin B	X	X	X	X	X
	157	Pheophytin A	X	X	X	X	X
	158	Total Carotenoids	X	X	X	X	X
	159	Glutathione µg/g	X	X	X	X	X
	160	Pantothenate ng/g	X	X	X	X	X
	161	Pyridoxine ng/g	X	X	X	X	X
6. Grape Fatty Acids	162	Methyl dodecanoate	X	X	X	X	X
	163	Methyl tridecanoate	X	X	X	X	X
	164	Methyl tetradecanoate	X	X	X	X	X
	165	Methyl pentadecanoate	X	X	X	X	X
	166	Methyl (*Z*)-9-hexadecenoate	X	X	X	X	X
	167	Methyl heptadecanoate	X	X	X	X	X
	168	Methyl (Z)-10-	X	X	X	X	X

Data block description	Variable Number	Attribute	Use in AMOPLS, k-means and Random Forest Analysis				
			2018	2019	2020	2021	All Vintages
		heptadecenoate					
	169	Methyl nonadecanoate	X	X	X	X	X
	170	Methyl 2-hydroxyhexadecanoate	X	X	X	X	X
	171	Methyl eicosanoate	X	X	X	X	X
	172	Methyl (*Z*)-13-eicosanoate	X	X	X	X	X
	173	Methyl heneicosanoate	X	X	X	X	X
	174	Methyl (*Z*,*Z*,*Z*)-11,14,17-eicosatrienoate	X	X	X	X	X
	175	Methyl docosanoate	X	X	X	X	X
	176	Methyl (Z)-13-docosenoate	X	X	X	X	X
	177	Methyl tricosanoate	X	X	X	X	X
	178	Methyl tetracosanoate	X	X	X	X	X
	179	Methyl pentacosanoate	X	X	X	X	X
	180	Methyl hexacosanoate	X	X	X	X	X
	181	Methyl heptacosanoate	X	X	X	X	X
	182	Methyl octacosanoate	X	X	X	X	X
	183	Methyl 2-hydroxy-tetracosanoate	X	X	X	X	X
	184	Methyl triacontanoate	X	X	X	X	X
	185	Methyl hexadecanoate	X	X	X	X	X
	186	Methyl octadecanoate	X	X	X	X	X
	187	Methyl (Z)-9-octadecenoate	X	X	X	X	X
	188	Methyl (E)-9-octadecenoate	X	X	X	X	X
	189	Methyl (Z,Z)-9,12-octadecenoate	X	X	X	X	X
	190	Methyl (Z,Z,Z)-9,12,15-octadecenoate	X	X	X	X	X
7. Grape Volatiles	191	Ethyl acetate	X	X	X	X	X
	192	2-Butanone	X	X	X	X	X
	193	2-Methyl butanal	X	X	X	X	X
	194	3-Methyl butanal	X	X	X	X	X
	195	1-Methoxy-hexane	X	X	X	X	X
	196	2-Ethyl-furan	X	X	X	X	X
	197	2-Methyl-3,4-dihydro-2H-pyran	X	X	X	X	X
	198	2,5-Dimethyloctane	X	X		X	
	199	2,6-Dimethyloctane	X	X	X	X	X
	200	Pentanal	X	X	X	X	X
	201	Methyl butanoate	X	X	X	X	X
	202	Methyl glycolate	X	X	X	X	X

Data block description	Variable Number	Attribute	Use in AMOPLS, k-means and Random Forest Analysis				
			2018	2019	2020	2021	All Vintages
	203	Decane	X	X	X	X	X
	204	1-Methoxycyclohexane	X	X	X	X	X
	205	alpha-Pinene	X	X	X	X	X
	206	1-Penten-3-one	X	X	X	X	X
	207	4-Heptanone	X	X	X	X	X
	208	Methylbenzene	X	X	X	X	X
	209	2-Butenal	X	X	X	X	X
	210	Hexanal	X	X	X	X	X
	211	Ethylbenzene	X	X	X	X	X
	212	2-Pentenal	X	X	X	X	X
	213	2-n-Butyl furan	X	X	X	X	X
	214	p-Xylene	X	X	X	X	X
	215	3-Hexenal	X	X	X	X	X
	216	1-Butanol	X	X	X	X	X
	217	1-Penten-3-ol	X	X	X	X	X
	218	Dimethoxyhexane	X	X			
	219	3-Ethylthiophene	X	X	X	X	X
	220	Heptanal	X	X	X	X	X
	221	Methyl hexanoate	X	X	X	X	X
	222	Limonene	X	X	X	X	X
	223	Cyclohexene oxide	X	X	X	X	X
	224	Eucalyptol	X	X	X	X	X
	225	IsoamylAlcohol	X	X	X		
	226	(E)-2-Hexenal	X	X	X	X	X
	227	Pentylfuran	X	X	X	X	X
	228	1-Pentanol	X	X	X	X	X
	229	3-Octanone	X	X	X	X	X
	230	Styrene	X	X	X	X	X
	231	Hexyl acetate	X	X	X	X	X
	232	1-Octen-3-one	X	X			
	233	Hydroxy2butanone	X	X			
	234	Octanal	X	X	X	X	X
	235	Octen3one	X	X	X	X	X
	236	2,2,6-Trimethyl-cyclohexanone	X	X	X	X	X
	237	(Z)-Hexenyl acetate	X	X	X	X	X
	238	(Z)-2-Penten-1-ol	X	X		X	
	239	(E)-2-Heptenal	X	X	X	X	X
	240	Vinyl caproate	X	X	X	X	X
	241	3-Ethoxypentane	X	X	X	X	X
	242	6-Methyl-5-hepten-2-one	X	X	X	X	X
	243	1-Hexanol	X	X	X	X	X
	244	(E)-3-Hexen-1-ol	X	X	X	X	X

Data block description	Variable Number	Attribute	Use in AMOPLS, k-means and Random Forest Analysis				
			2018	2019	2020	2021	All Vintages
	245	(Z)-3-Hexen-1-ol	X	X	X	X	X
	246	Nonanal	X	X	X	X	X
	247	2,4-Hexadienal	X	X	X	X	X
	248	(E)-2-Hexen-1-ol	X	X	X	X	X
	249	(Z)-2-Hexen-1-ol	X	X	X	X	X
	250	2,2,6-Trimethyl-4-methylene-2H-pyran	X	X	X	X	X
	251	(E)-2-Octenal	X	X	X	X	X
	252	Ethyl octanoate	X	X	X	X	X
	253	(E)-Linalool oxide	X	X	X	X	X
	254	1-Octen-3-ol	X	X	X	X	X
	255	1-Heptanol	X	X	X	X	X
	256	(E,Z)-2,4-Heptadienal	X	X	X	X	X
	257	Furfural	X		X	X	
	258	Acetic acid	X	X	X	X	X
	259	2-Ethyl-1-hexanol	X	X	X	X	X
	260	(E,E)-2,4-Heptadienal	X	X	X	X	X
	261	Decanal	X	X	X	X	X
	262	Theaspirane A	X	X	X	X	X
	263	Benzaldehyde	X	X	X	X	X
	264	(E)-2-Nonenal	X	X	X	X	X
	265	Theaspirane B	X	X	X	X	X
	266	2,5-Dihydro-thiophene	X	X	X	X	X
	267	Linalool	X	X	X	X	X
	268	1-Octanol	X	X	X	X	X
	269	5-Methyl-2-furfural	X	X	X	X	X
	270	5,6-Dihydro-2H-pyran-2-carboxaldehyde	X	X	X	X	X
	271	(E)-2-Octen-1-ol	X	X	X	X	X
	272	beta-Cyclocitral	X	X	X	X	X
	273	gamma-Butyrolactone	X	X	X	X	X
	274	Phenylacetaldehyde	X	X	X	X	X
	275	1-Hepten-3-one	X	X	X	X	X
	276	2-Furanmethanol	X		X	X	
	277	Humulene	X	X	X	X	X
	278	Diethyl succinate	X	X	X	X	X
	279	gamma-Terpineol	X	X	X	X	X
	280	(E,E)-2,4-Nonadienal	X	X	X	X	X
	281	Dodecane-6,7-dione	X	X	X	X	X
	282	Pentanoic Acid	X		X		
	283	beta-Cadinene	X	X	X	X	X
	284	5-Ethyl-2(5H)-furanone	X	X	X	X	X
	285	2-Phenylethyl acetate	X		X	X	

Data block description	Variable Number	Attribute	Use in AMOPLS, k-means and Random Forest Analysis				
			2018	2019	2020	2021	All Vintages
	286	beta-Damascenone	X	X	X	X	X
	287	Hexanoic acid	X	X	X	X	X
	288	Benzyl alcohol	X	X	X	X	X
	289	Phenylethyl Alcohol	X	X	X	X	X
	290	Methyl 2-oxo-hexanoate	X	X	X	X	X
	291	Phenol	X	X	X	X	X
8. Grape Phenolics	292	Delphinidin-3-glucoside (grape)	X	X	X	X	X
	293	Cyanidin-3-glucoside (grape)	X	X	X	X	X
	294	Petunidin-3-glucoside (grape)	X	X	X	X	X
	295	Peonidin-3-glucoside (grape)	X	X	X	X	X
	296	Malvidin-3-glucoside (grape)	X	X	X	X	X
	297	Delphinidin-3-acetyl-glucoside (grape)	X	X	X	X	X
	298	Cyanidin-3-acetyl-glucoside (grape)	X	X	X	X	X
	299	Petunidin-3-acetyl-glucoside (grape)	X	X	X	X	X
	300	Peonidin-3-acetyl-glucoside (grape)	X	X	X	X	X
	301	Malvidin-3-acetyl-glucoside (grape)	X	X	X	X	X
	302	Delphinidin-3-coumaroyl-glucoside (grape)	X	X	X	X	X
	303	Petunidin-3-caffeoyl-glucoside (grape)	X	X	X	X	X
	304	Cyanidin-3-coumaroyl-glucoside + malvidin-3-caffeoyl-glucoside (grape)	X	X	X	X	X
	305	Petunidin-3-coumaroyl-glucoside (grape)	X	X	X	X	X
	306	Peonidin-3-coumaroyl-glucoside (grape)	X	X	X	X	X
	307	Malvidin-3-coumaroyl-glucoside (grape)	X	X	X	X	X
	308	Total anthocyanin (by HPLC (grape))	X	X	X	X	X
	309	Extractable tannin (as mg/g berry weight (grape))	X	X	X	X	X
	310	Extractable anthocyanin (as mg/g berry weight (grape))	X	X	X	X	X
9. Grape	311	Epigallocatechin extension	X	X	X	X	X

Data block description	Variable Number	Attribute	Use in AMOPLS, k-means and Random Forest Analysis				
			2018	2019	2020	2021	All Vintages
Tannin	312	Catechin extension	X	X	X	X	X
	313	Eepicatechin extension	X	X	X	X	X
	314	Epicatechin gallate extension	X	X	X	X	X
	315	Catechin terminal	X	X	X	X	X
	316	Epicatechin terminal	X	X	X	X	X
	317	Epicatechin gallate terminal	X	X	X	X	X
	318	Total tannins mg	X	X	X	X	X
	319	Degree of polymerisation	X	X	X	X	X
	320	Epigallocatechin extension %	X	X	X	X	X
	321	Catechin extension %	X	X	X	X	X
	322	Epicatechin extension %	X	X	X	X	X
	323	Epicatechin gallate extension %	X	X	X	X	X
	324	Catechin terminal %	X	X	X	X	X
	325	Epicatechin terminal %	X	X	X	X	X
	326	Epicatechin gallate terminal %	X	X	X	X	X
10. Wine Basic Chemistry	327	Alcohol	X	X	X	X	X
	328	Glucose + Fructose	X	X	X	X	X
	329	Specific Gravity	X	X	X	X	X
	330	pH (wine)	X	X	X	X	X
	331	Titratable Acidity (pH8.2)	X	X	X	X	X
	332	Volatile Acidity	X	X	X	X	X
	333	Free Sulfur dioxide	X	X	X	X	X
	334	Total Sulfur dioxide	X	X	X	X	X
	335	Titratable Acidity (pH7.0)		X	X	X	
	336	Malic Acid		X	X	X	
11. Wine Metals	337	Calcium	X	X	X	X	X
	338	Chromium	X	X	X	X	X
	339	Cobalt	X	X	X	X	X
	340	Copper	X				
	341	Iron	X	X	X	X	X
	342	Lead	X	X	X	X	X
	343	Lithium	X	X	X	X	X
	344	Magnesium	X	X	X	X	X
	345	Manganese	X	X	X	X	X
	346	Nickel	X	X	X	X	X
	347	Potassium	X	X	X	X	X
	348	Sodium	X	X	X	X	X

Data block description	Variable Number	Attribute	Use in AMOPLS, k-means and Random Forest Analysis				
			2018	2019	2020	2021	All Vintages
	349	Strontium	X	X	X	X	X
	350	Zinc	X	X	X	X	X
	351	Selenium				X	
12. Wine Phenolics & Colour	352	Delphinidin-3-glucoside (wine)	X	X	X	X	X
	353	Cyanidin-3-glucoside (wine)	X	X			
	354	Petunidin-3-glucoside (wine)	X	X	X	X	X
	355	Peonidin-3-glucoside (wine)	X	X	X	X	X
	356	Malvidin-3-glucoside (wine)	X	X	X	X	X
	357	Vitisin A	X	X		X	
	358	Delphinidin-3-acetyl-glucoside (wine)	X	X	X	X	X
	359	Cyanidin-3-acetyl-glucoside (wine)	X	X			
	360	Petunidin-3-acetyl-glucoside (wine)	X	X	X	X	X
	361	Peonidin-3-acetyl-glucoside (wine)	X	X	X	X	X
	362	Malvidin-3-acetyl-glucoside (wine)	X	X	X	X	X
	363	Delphinidin-3-coumaroyl-glucoside (wine)	X		X	X	
	364	Peounidin-3-caffeoyl-glucoside (wine)	X	X			
	365	Cyanidin-3-coumaroyl-glucoside + malvidin-3-caffeoyl-glucoside (wine)	X	X	X	X	X
	366	Petunidin-3-coumaroyl-glucoside (wine)	X	X	X	X	X
	367	Peonidin-3-coumaroyl-glucoside (wine)	X	X	X	X	X
	368	Malvidin-3-coumaroyl-glucoside (wine)	X	X	X	X	X
	369	Polymeric Pigments	X	X	X	X	X
	370	Total anthocyanins (wine)	X	X	X	X	X
	371	Quercetin-3-glucuronide	X	X	X	X	X
	372	Syringetin-3-glucoside	X	X	X	X	X
	373	Myricetin	X	X	X	X	X
	374	Quercetin	X		X	X	
	375	Laricitrin	X	X			
	376	Kaempferol	X	X	X	X	X
	377	Isorhamnetin	X	X	X	X	X
	378	Chemical Age-1	X	X	X	X	X

Data block description	Variable Number	Attribute	Use in AMOPLS, k-means and Random Forest Analysis				
			2018	2019	2020	2021	All Vintages
	379	Chemical Age-2	X	X	X	X	X
	380	Wine Colour Density	X	X	X	X	X
	381	Wine Colour Density - sulfur dioxide corrected	X	X	X	X	X
	382	Hue - Wine Colour Hue	X	X	X	X	X
	383	Ion % - Anthocyanins in ionised form %	X	X	X	X	X
	384	Total phenolics	X	X	X	X	X
	385	Non-bleachable pigments	X	X	X	X	X
	386	Total tannin	X	X	X	X	X
	387	Tannin molecular mass by sub-unit composition	X	X	X	X	X
	388	Mean Degree of Polymerisation	X	X	X	X	X
	389	Trihydroxylation %	X	X	X	X	X
	390	Galloylation %	X	X	X	X	X
	391	Mass Conversion %	X	X	X	X	X
	392	Epigallocatechin-phloroglucinol %	X	X	X	X	X
	393	Catechin-phloroglucinol %	X	X	X	X	X
	394	Epicatechin-phloroglucinol %	X	X	X	X	X
	395	Catechin %	X	X	X	X	X
	396	Eepicatechin gallate - phloroglucinol %	X	X	X	X	X
	397	Epicatechin %	X	X	X	X	X
	398	Epicatechin gallate %	X	X	X	X	X
	399	Tannin molecular mass (50% elution)	X		X	X	
	400	CIELab - L*	X	X	X	X	X
	401	CIELab - a*	X	X	X	X	X
	402	CIELab - b*	X	X	X	X	X
13. Wine Polysaccharides	403	Mannose	X	X	X	X	X
	404	Rhamnose	X	X	X	X	X
	405	Glucuronic Acid	X	X	X	X	X
	406	Galacturonic Acid	X	X	X	X	X
	407	Glucose	X	X	X	X	X
	408	Galactose	X	X	X	X	X
	409	Xylose	X	X	X	X	X
	410	Arabinose	X	X	X	X	X
	411	Fucose	X	X	X	X	X
	412	Total Polysaccharides	X	X	X	X	X
	413	Proline mg/L	X		X	X	

Data block description	Variable Number	Attribute	Use in AMOPLS, k-means and Random Forest Analysis				
			2018	2019	2020	2021	All Vintages
14. Wine Volatiles	414	2-methyl propyl acetate	X	X	X	X	X
	415	2-methyl butyl acetate	X	X	X	X	X
	416	3-methyl butyl acetate	X	X	X	X	X
	417	Hexyl acetate	X	X	X	X	X
	418	2-methyl propanol	X	X	X	X	X
	419	Butanol	X	X	X	X	X
	420	2-methyl butanol	X	X	X	X	X
	421	3-methyl butanol	X	X	X	X	X
	422	Ethyl acetate	X	X	X	X	X
	423	Ethyl propanoate	X	X	X	X	X
	424	Ethyl-2-methyl propanoate	X	X	X	X	X
	425	Ethyl butanoate	X	X	X	X	X
	426	Ethyl-2-methyl butanoate	X	X	X	X	X
	427	Ethyl-3-methyl butanoate	X	X	X	X	X
	428	Ethyl hexanoate	X	X	X	X	X
	429	Ethyl octanoate	X	X	X	X	X
	430	Ethyl decanoate	X	X	X	X	X
	431	2-phenylethyl acetate	X	X	X	X	X
	432	2-phenylethanol	X	X	X	X	X
	433	Propanoic acid	X		X	X	
	434	2-methyl propanoic acid	X		X	X	
	435	Butanoic acid	X	X	X	X	X
	436	2-methyl butanoic acid	X	X	X	X	X
	437	3-methyl butanoic acid	X	X	X	X	X
	438	Hexanoic acid	X	X	X	X	X
	439	Octanoic acid	X	X	X	X	X
	440	Decanoic acid	X	X	X	X	X
	441	E2-Hexenol	X	X	X	X	X
	442	Z3-Hexenol	X	X	X	X	X
	443	Limonene	X				
	444	1,8-Cineole	X	X	X	X	X
	445	Linalool	X		X	X	
	446	(-)-cis-Rose oxide	X	X	X	X	X
	447	(-)-trans-Rose oxide	X	X		X	
	448	α-Terpineol	X	X	X	X	X
	449	β-Citronellol	X	X	X	X	X
	450	Nerol	X				
	451	Geraniol	X		X	X	
	452	β-Damascenone	X	X	X	X	X
	453	β-Ionone	X	X	X	X	X
	454	Carbon disulfide	X	X	X	X	X

Data block description	Variable Number	Attribute	Use in AMOPLS, k-means and Random Forest Analysis				
			2018	2019	2020	2021	All Vintages
	455	Dimethyl sulfide	X	X	X	X	X
	456	Hydrogen sulfide	X			X	
	457	Methanethiol	X	X	X	X	X
	458	Methyl thioacetate	X	X	X	X	X
	459	4-methyl-4-mercaptopentan-2-one	X				
	460	3-Mercaptohexan-1-ol	X	X	X	X	X
	461	3-mercaptohexylacetate	X	X	X	X	X
	462	2-Methylpropanal	X	X		X	
	463	3-Methylbutanal	X	X			
	464	E-2-Hexenal	X	X	X	X	X
	465	Methional	X	X		X	
	466	Phenylacetaldehyde	X	X		X	
	467	E-2-Nonenal	X				
	468	Maltol	X	X	X		
	469	Eugenol	X		X	X	
	470	Benzaldehyde	X	X	X	X	X
	471	Acetic Acid		X	X	X	
	472	Hexanol		X	X	X	
	473	Unknown		X	X	X	
	474	1,1,6,-trimethyl-1,2-dihydronapthalene		X	X	X	
	475	Furfural Thiol		X			
	476	Furfural		X	X	X	
15. Wine Sensory	477	LV1	X	X	X	X	X
	478	LV2	X	X	X	X	X
	479	LV3	X	X	X	X	X
	480	LV4	X	X	X	X	X
	481	LV5	X	X	X	X	X
		n =	420	435	419	422	364

5.7.4 Sample selection for data modelling

Samples for individual vintage and combined vintage chemometric models were selected based on the availability of full data sets for each sample site replicate across each of the 15 data blocks. Site and replicate sample selection for each vintage is presented in Table 5.7.3 noting that the all vintage model comprised a concatenation of each of the vintage sample data sets. Where data for a measured attribute were missing for a specific sample replicate, median substitution for a value was used based upon the regional sample set with a maximum of 0.05 percent of data substitution for any vintage data set.

Table 5.7.3 Sample site replicate selection for models for each vintage. Shaded cells indicate a complete set of data in all data tables for that specific sample enabling selection for modelling for single and combined vintage models. Numbers in each cell indicate a unique sample index for each site and vintage combination for the duration of the investigation.

Region	Site	2018			2019			2020			2021		
		R 1	R2	R 3	R1	R2	R3	R1	R2	R3	R1	R2	R3
Northern Grounds	SR1	1	2	3	76	77	78	151	152	153	226	227	228
Northern Grounds	SR2	4	5	6	79	80	81	154	155	156	229	230	231
Northern Grounds	SR3	7	8	9	82	83	84	157	158	159	232	233	234
Northern Grounds	SR4	10	11	12	85	86	87	160	161	162	235	236	237
Central Grounds	SR5	13	14	15	88	89	90	163	164	165	238	239	240
Central Grounds	SR6	16	17	18	91	92	93	166	167	168	241	242	243
Central Grounds	SR7	19	20	21	94	95	96	169	170	171	244	245	246
Central Grounds	SR8	22	23	24	97	98	99	172	173	174	247	248	249
Eastern Edge	SR9	25	26	27	100	101	102	175	176	177	250	251	252
Eastern Edge	SR10	28	29	30	103	104	105	178	179	180	253	254	255
Eastern Edge	SR11	31	32	33	106	107	108	181	182	183	256	257	258
Eastern Edge	SR12	34	35	36	109	110	111	184	185	186	259	260	261
Southern Grounds	SR13	37	38	39	112	113	114	187	188	189	262	263	264
Southern Grounds	SR14	40	41	42	115	116	117	190	191	192	265	266	267
Southern Grounds	SR15	43	44	45	118	119	120	193	194	195	268	269	270
Southern Grounds	SR16	46	47	48	121	122	123	196	197	198	271	272	273
Western Ridge	SR17	49	50	51	124	125	126	199	200	201	274	275	276
Western Ridge	SR18	52	53	54	127	128	129	202	203	204	277	278	279
Western Ridge	SR19	55	56	57	130	131	132	205	206	207	280	281	282
Western Ridge	SR20	58	59	60	133	134	135	208	209	210	283	284	285
Eden Valley	SR21	61	62	63	136	137	138	211	212	213	286	287	288
Eden Valley	SR22	64	65	66	139	140	141	214	215	216	289	290	291
Eden Valley	SR23	67	68	69	142	143	144	217	218	219	292	293	294
Eden Valley	SR24	70	71	72	145	146	147	220	221	222	295	296	297
Eastern Edge	SR25	73	74	75	148	149	150	223	224	225	298	299	300
	n =	59			65			56			58		

6. Results/Discussion

6.1 Vineyard variability

Rob Bramley and Jackie Ouzman, CSIRO

CSIRO input to this project was focussed on work at two scales. At the within-vineyard scale, our role has been to provide a precision viticulture-based input to data analysis to support field activities undertaken by other project team members. At regional scale, we are focussed on better understanding the basis (if any) for sub-regionalisation within the Barossa GI.

As this work has been fully published already (Bramley 2022, Bramley et al. 2020, Bramley and Ouzman 2022, Bramley et al. 2022a,b,c) readers are referred to these papers for full details; here, we provide a brief summary.

Conventional approaches to terroir zoning have traditionally relied on a mix of land classification based on thematic mapping, expert opinion and heuristics (Bramley et al. 2020, Bramley and Gardiner 2021, Bramley and Ouzman 2022, Brillante et al. 2020a). The Barossa work of Robinson and Sandercock (2014) provides a good example of the former. This noted that 33 of the 61 soil types found in a 1:50,000 scale reconnaissance soil survey of South Australia (Hall et al. 2009) exist in the Barossa Zone GI, thus highlighting the complexity of the GI. When a mix of heuristics and expert opinion are mixed with this, leading to classification of the soil available water capacity, elevation, rainfall and growing degree days into categories of assumed viticultural importance, 147 of the 600 possible class combinations were seen to exist in the Barossa GI. Simplifying things just on the basis of elevation and AWC still retained 21 classes (Robinson and Sandercock 2014) – arguably far too many for a sensible sub-regionalisation of the GI in relation to its terroir, and no doubt the reason why the Barossa Grounds were essentially identified on the basis of the sensory evaluation subsequently conducted by local winemakers.

As described in detail in Bramley et al. (2020), who provide the relevant references and data descriptions, we assembled a base data set from publicly-available sources comprised of elevation (derived from the 1 second Shuttle Radar Mission conducted in the early 2000s), annual (AnnR) and seasonal (GSR) rainfall, season growing degree days (GDD), mean growing season (GST) and January temperature (MJT – all obtained from the SILO database maintained by the Queensland Government in partnership with the Bureau of Meteorology), and soil available water capacity (AWC) and cation exchange capacity (CEC – obtained from the Soil and Landscape Grid of Australia). These data were projected to a base raster of 100 m (i.e. 1 ha) pixels and then clustered using *k*-means to explore similarities in regional scale patterns of variation. Note that the climate data used in this initial analysis were the same as those used by Robinson and Sandercock (2014).

The results of clustering these data on a whole of region basis (Figure 6.1.1) identified the distinction between the Barossa and Eden Valleys but did not otherwise promote a basis for sub-regionalisation of the GI more broadly. Accordingly, and given that terroir is about wine expression, we repeated the analysis but this time with input to the clustering confined to just that land which supports wine production – i.e. the land under vineyard (Figure 5.1.9).

As discussed in detail by Bramley and Ouzman (2022), this vineyard-only analysis (Figure 6.1.2) provides a more robust basis for considering sub-regionalisation of the Barossa GI. Note that, in addition to being confined to the land under vine, the result shown in Figure 6.1.2 also made use of an updated climate data set (Bramley and Ouzman 2022) compared to that used in the earlier work (Robinson and Sandercock 2014, Bramley et al. 2020); the spatial variability of the two climate data sets was nonetheless very similar. As can be seen, the vineyard-only analysis shown in Figure 6.1.2 again clearly separates the Eden and Barossa Valleys, but within the Barossa Valley offers a basis for separation into three zones rather than the single one seen in Figure 6.1.1. Clearly, this result also differs somewhat from the maps of 'Barossa Grounds' produced by BGWA.

It is not suggested here that the result shown in Figure 6.1.2 is 'right' and that the Barossa Grounds are 'wrong', but it is suggested that Figure 6.1.2 provides a more robust data-driven basis for examining terroir through integration of this analysis with wine chemical and sensory data (see elsewhere in this report) to better understand the Barossa terroir. The opportunity also exists to integrate such analysis with data describing vineyard performance as suggested by Bramley (2022), Bramley et al. (2020, 2022a,b,c) and Brillante et al. (2020a).

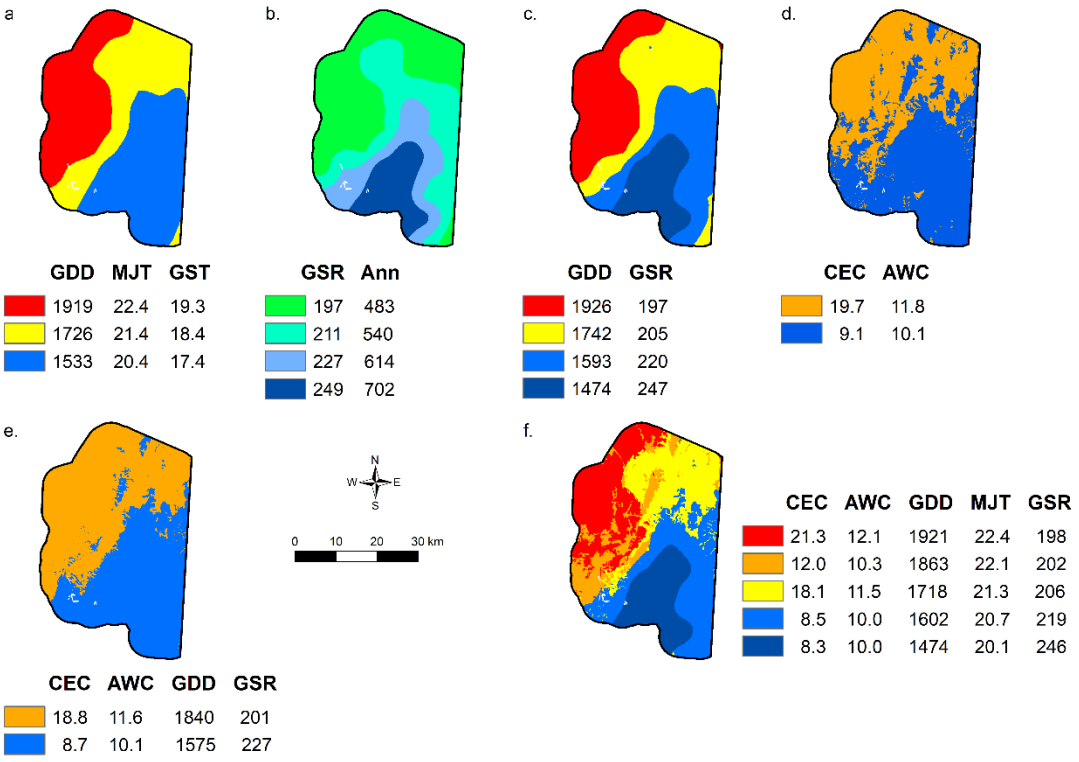


Figure 6.1.1 Results of clustering map layers of various biophysical attributes using *k*-means. For each combination of input data, the result shown here is that selected as optimal based on the Cublic Clustering Criterion (SAS, 1983). GDD, growing degree days; MJT, mean January temperature; GST, growing season temperature; GSR, growing season rainfall; Ann, Annual Rainfall, CEC, soil cation exchange capacity; AWC soil available water capacity.

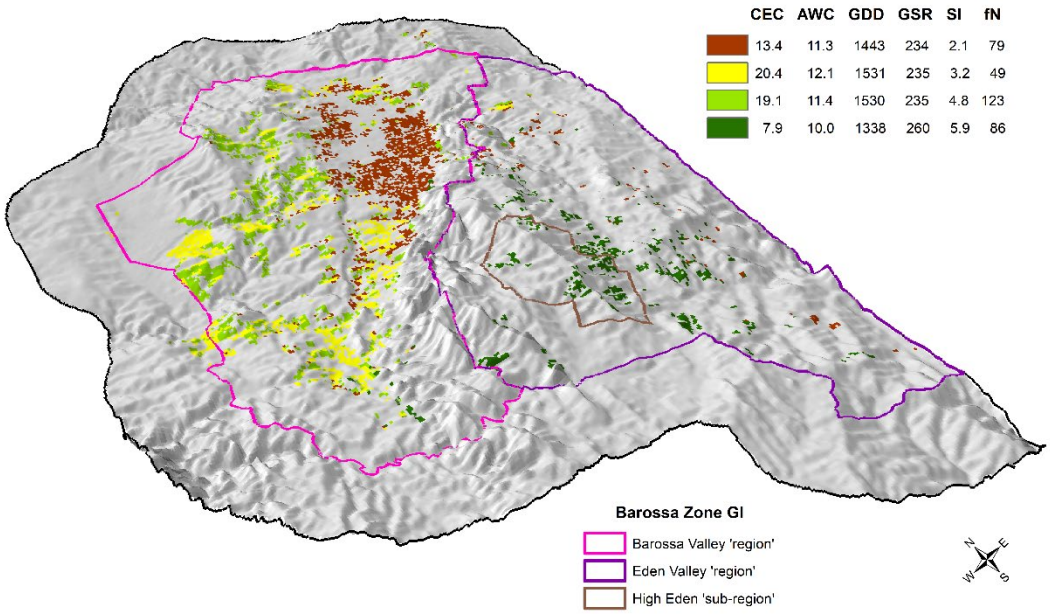


Figure 6.1.2 Results of clustering selected soil properties (CEC, soil cation exchange capacity; AWC, soil available water capacity), climate indices (GDD, season growing degree days; GSR, growing season rainfall) and topographic attributes (Sl, slope; fN, aspect, expressed as degrees from north) for land under vineyard in the Barossa using *k*-means. The data have been draped over a digital elevation model from which the hillshade was derived. Note that in this map, elevation has been exaggerated by a factor of eight relative to the horizontal, and that the position of the north arrow is approximate only. Numbers in the legend are cluster means. Data of Bramley and Ouzman (2022).

6.2 Soil and vine measurements

Marcos Bonada, Paul Petrie, Cassandra Collins, SARDI and the University of Adelaide

6.2.1 Soil Measurements

Volumetric water content, as obtained from capacitance sensors used in this project, indicates the content of water present in the soil at a particular time and depth, but does not reflect differences in plant water availability between zones of the vineyard or regions with different soil composition. There is a unique relationship between water content and soil water potential for a particular soil that determine plant water availability, and it is defined for soil physical-chemical properties (Figure 6.2.1). For a given soil water content, the finer the particle size, the harder is for the roots to extract that water, as water is more strongly adsorbed by the larger surface area of the particles. Therefore, even though a clay soil is able to hold more water than a sandy soil, water is not necessarily available for the plant. To better reflect differences on plant water availability across sites, regions and seasons that are likely to be modulating vine growth, yield and, ultimately, grape and wine style, volumetric soil moisture content was transformed into soil water potential. A pedotransfer function as describe in Grant et al., (2010) was used to convert volumetric water content into soil water potential using soil physical properties such as particle size composition and saturated water content.

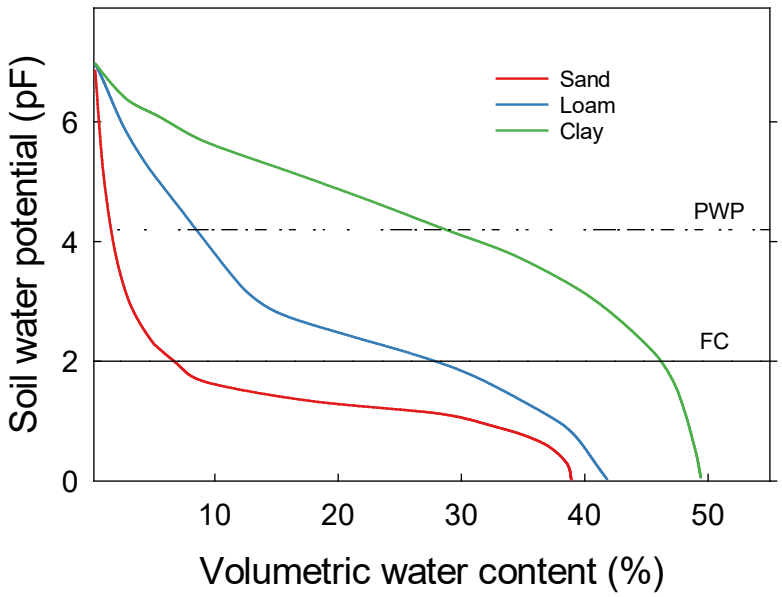


Figure 6.2.1 Relationship between soil water content and soil water potential for different soil textures. Plant water availability for each soil is defined for the amount of water that the soils can hold between field capacity (FC) and permanent wilting point (PWP).

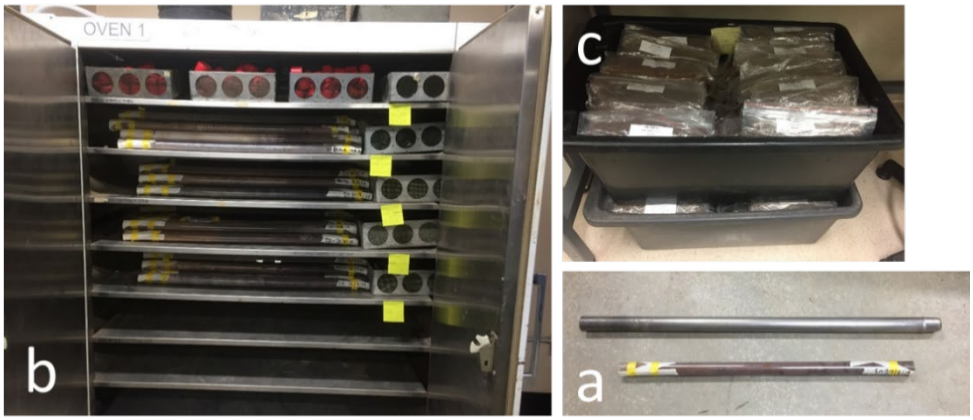


Figure 6.2.2 (a) intact 100 cm cores collected in PVC clear sleeves for soil physical analysis. (b) intact cores and (c) composited samples were oven-dried at 40° C for microbial stabilisation until laboratory analysis.

6.2.1.1 Soil monitoring during the season

Volumetric soil moisture was monitored and logged at one-hourly intervals. Data were processed using the Irrimax software, which allows the distribution and activity of the roots in the profile to be identified by monitoring changes in soil moisture at different depths (Figure 6.2.3a), and the water content to be calculated by integrating readings at different depths across the profile (Figure 6.2.3b). Data from the weather stations or management practices, i.e. irrigation, can also be integrated with the soil moisture data as part of the post-processing. This allows looking at the effectiveness of irrigation or rainfall events on the depths of infiltration by monitoring changes in soil moisture across sensors. For example, a wet period around 21 November 2018 (Figure 6.2.3c) was effective in wetting the soil up to 80 cm depth, as reflected by the positive signal of the sensors located at 20, 50 and 80 cm (Figure 6.2.3a and b). Similarly, it allows the assessment of water uptake and evaporation in the context of weather conditions during the growing season.

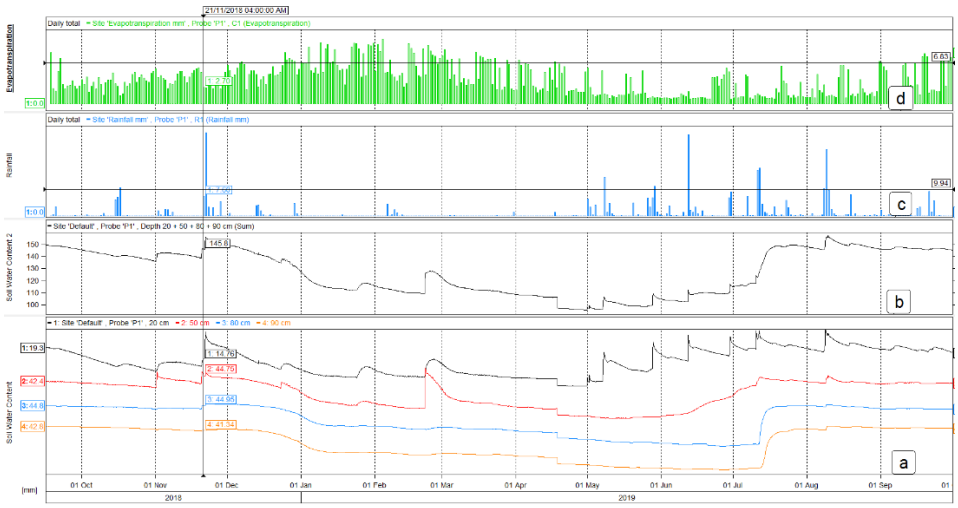


Figure 6.2.3 (a) dynamics of volumetric water content during season 2018/2019 at four depths. (b) accumulated moisture in the soil profile up to 90 cm depth. (c) Rainfall and (d) evapotranspiration records from the weather station installed at each sub-region site. The vertical line across figure indicate the onset of a wet period around 21 November 2018.

A wide range of soil moisture was recorded, which can be seen for season 2018/19 across sub-regional sites (Figure 6.2.4). Accumulated soil moisture at 80 cm depth ranged from approximately 73 to 144 mm across sites and sub-regions. Intra-site variations in soil moisture during the season were sometimes as high as the differences between sites in contrasting sub-regions.

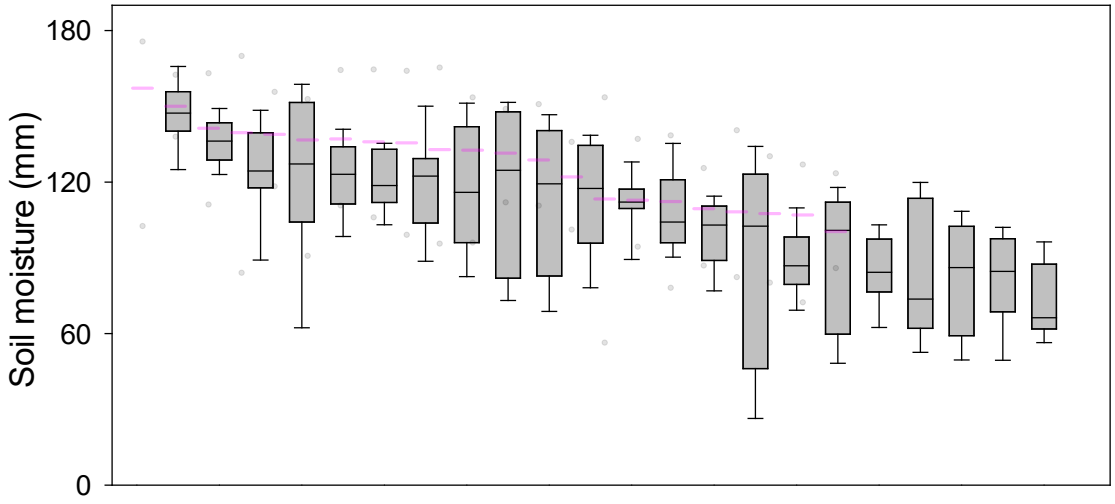


Figure 6.2.4 Box-plot diagram showing the soil moisture content up to 80 cm depth from 22 sub-region sites during season 2018/19. Data in each box plot correspond to weekly soil moisture readings from mid-September to mid-February from three zones of the vineyard (n = 66). In the boxes, the boundary of the box closest to zero indicates the 25th percentile, the pink line indicates the mean, the black line the median and the boundary farthest from zero indicates the 75th percentile. Whiskers above and below the box indicate the 5th and 95th percentiles and points above and below the whiskers indicate outliers.

6.2.1.2 Plant available water capacity of soils at regional scale

Estimation of the plant available water capacity (PAWC) of soils at a regional scale helps in adopting better land use planning, developing suitable irrigation schedules for crops, and optimising the use of scarce water resources. In the current study, 72 soil profiles were sampled from the Barossa Region of South Australia to estimate pedo-transfer functions deduced from easily estimated soil properties. These functions were then used to estimate the fixed (10, 33 kPa) and dynamic pressure head (hfc) water content at field capacity (FC) for minimum drainage flux (q = 0.01 and 0.001 cm/day), which serves as the upper boundary for plant-available water in the soils. The estimated crop lower limit (CLL, θwp) was corrected for subsoil constraints, especially the exchangeable sodium percentage (ESP). The data showed that the mean values of hfc in sand-dominated light and medium textures (i.e. sand, loamy sand, sandy loam, and loam) varied in a narrow range (15.8–18.2 kPa), while in the clay-dominated heavy textured soils (i.e. clay loam) showed the widest range of hfc (11.3–49.3 kPa). The data showed wide variability in the PAWC for dynamic FC (PAWCfc) and fixed FC at 10 kPa (PAWC10), 33 kPa (PAWC33), and a mix of 10 and 33 kPa (PAWC10,33) pressure heads depending on soil texture. Normally, the difference between PAWC at hfc and 10 kPa (ΔPAWC10) was positive, whereas the corresponding difference between PAWC at 33 kPa and hfc (ΔPAWC33) was negative across all sites. Nevertheless, the estimation of PAWC assuming a fixed FC at 10 and 33 kPa pressures (PAWC10,33) for

sandy, clay, and silty soils reduced the deviation between dynamic and fixed pressure PAWC < 10% across the region. The estimation of PAWC was improved by incorporating the impact of subsoil constraints, such as high ESP in the soil, which was more pronounced for clay and silty texture soils occurring at lower depths. These findings demonstrate the inherent inconsistencies between static pressure and flux-based dynamic field-capacity estimations in soils. Soil heterogeneity, intra-texture variability, subsoil constraints, and swell–shrink clays can have great impacts on the water retention capacity in response to dynamic and fixed pressure FC values (see Appendix 5.1 for further details).

6.2.2 Vine measurements

6.2.2.1 Benchmarking water-limited yield potential and yield gaps of Shiraz

Management of water in vineyards needs an update to account for direct (i.e., shifts in amount and seasonality of rainfall, reduced availability of water for irrigation, and higher temperature and vapour pressure deficit) and indirect effects of climate change including the use of irrigation to manage heat stress. In this context, we benchmarked water-limited yield potential (Yw), calculated yield gaps as the difference between Yw and actual yield (Ya), and explored the underlying environmental and management causes of these gaps.

Yield and its components were measured in two sections of 24 Shiraz vineyards during three vintages in the Barossa zone. The frequency distribution of yield was L-shaped, with half the vineyards below 5.2 t/ha, and an extended tail of the distribution that reached 24.9 t/ha. The seasonal ratio of actual crop evapotranspiration and reference evapotranspiration was below 0.48 in 85% of cases, with a maximum of 0.65, highlighting the prevalence of a substantial water deficit in these vineyards. A boundary function relating actual yield and seasonal rainfall was fitted to quantify Yw. Yield gaps increased with increasing vine water deficit, quantified with carbon isotope composition in must. The yield gap was smaller with higher rainfall before budburst, putatively favouring early-season vegetative growth and allocation to reproduction, and with higher rainfall between flowering and veraison, putatively favouring fruit and seed set and early berry growth. The gap was larger with higher rainfall and lower radiation between budburst and flowering. The yield gap declined with altitude at 0.038 t/ha/m in the range from 186 to 326 m.a.s.l.; the Eden Valley departed from this trend, with a yield gap that was higher than expected from its elevation. The yield gap increased linearly with vine age between six and 33 yr at a rate of 0.3 t/ha/yr. The correlation between yield gap and yield components ranked bunch weight ≈ berries per bunch > bunch number > berry weight; the minimum to close the yield gap was 185,000 bunches/ha, 105 g/bunch, 108 berries/bunch and 1.1 g/berry.

Water deficit and vine age were major causes of yield gaps. Winter irrigation needs attention in the context of climate change and drier winters. The cost of dealing with older, less productive vines (vine removal, new planting, and delay of productivity of young vines) needs to be weighed against the rate of increase in yield gap with vine age.

A boundary function to estimate water-limited yield potential returned viticulturally meaningful yield gaps (see Appendix 5.2 for further details).

6.2.2.2 The relationship between terroir and the phenology of Barossa Shiraz

Vine phenology results from the interaction between the genotype, environment and management, with implications for fruit, and wine composition. The impact of weather, site

and management practices, underlying elements of terroir, impacting the timing of key phenological stages were explored across the Barossa Zone (GI).

Vine phenology was assessed in three zones of 24 vineyards over three vintages using the E-L scale before veraison, and total soluble sugars (TSS) in berries during ripening. We explored the associations between weather, plant traits and viticultural variables, and development in four periods: pre-budburst, budburst-flowering, flowering-veraison and veraison-maturity. The spatial structure of the timing of phenological events suggested three main groups of vineyards. This structure followed gradients in topography and soils across the landscape, and was maintained despite the effect of the season (vintage). On average, differences between early and late groups of vineyards were 13 days at budburst, 20 days at flowering and 24 days at TSS = 24 ºBrix. Phenology responded mainly to temperature until flowering, and to temperature and canopy size from flowering to maturity. The strength of the relationship between the duration of the period and temperature ranked pre-budburst (r^2 = 0.94) > budburst-flowering (r^2 = 0.40) > veraison-maturity (r^2 = 0.17). Duration of pre-budburst and budburst-flowering periods was shortened at 6 d/ºC, compared to 2 d/ºC for veraison-maturity. The duration from veraison to maturity increased with yield (r^2 = 0.29, P_a < 0.0001).

The spatial variation in development was maintained despite vintage effects and management practices. Variation in temperature due to topography and elevation were the major drivers of vine phenological development until flowering. During ripening, development was driven by temperature and carbon capture and partitioning.

This is the first attempt to show spatial variability on phenology across the Barossa Valley GI. The observed switch of phenological drivers during development from temperature-driven processes before flowering, to resource-dominated processes during ripening, has implications for modelling and vineyard management (see Appendix 5.3 for further details).

6.2.2.3 Carbon Isotope discrimination

To benchmark d13C analysis all the samples from the sub-region sites and a set of extra samples from ancillary experiments in the 2018/19 season were sent to the laboratory in June 2019 for carbon isotopes analysis. The ability of the d13C analysis to integrate differences in vine water status during the growing season was assessed. For this purpose an existing experiment was used where vines were subjected to different irrigation treatments early in spring, and where vine water status dynamics are well characterised (Figure 6.2.1b).

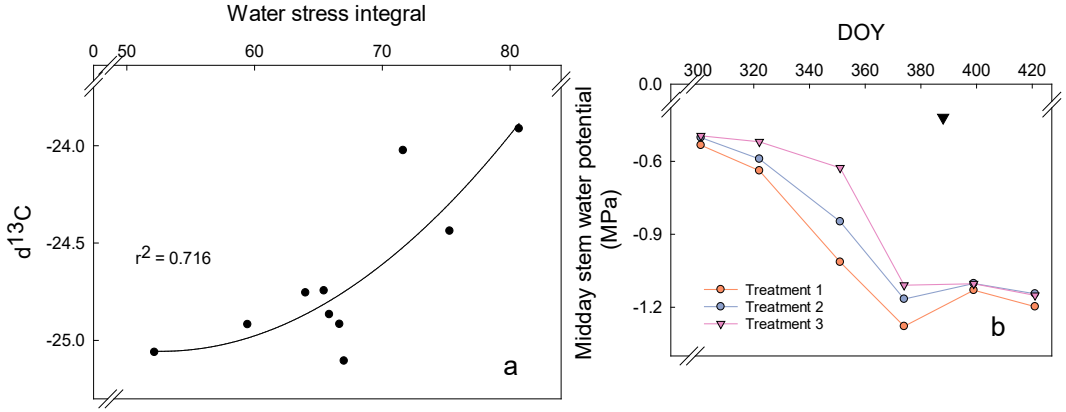


Figure 6.2.1 (a) the relation between water stress integral and carbon isotopic discrimination in the berry juice at harvest. Water stress integral was estimated from (b) the evolution of

stem water potential on vines subjected to different irrigation treatments during winter. Triangle indicates the timing of veraison.

There was a significant high relationship between d13C and the integral of water stress during the season, defined by the parameters of a second-order polynomic function (Figure 6.2.1a). High levels of water stress during the season, as reflected by the high water stress integral, related to low d13C values. This reveals that the sugars produced by photosynthesis under water stress have a higher proportion of the ^{13}C isotope. We also tested the effect of changes in sugar concentration during ripening on the carbon isotopic composition of the juice. We collected samples at two points during berry development, early in ripening and around commercial harvest, from vines that were exposed to different levels of transient water deficit before veraison (Figure 6.2.1b). There was a clear scatter at each sampling time that is caused by the differences in d13C between irrigation treatments. However, there was no significant linear relationship between the concentrations of sugars and the d13C (Figure 6.2.2). Likewise, the repeated measures ANOVA did not show significant effects for the time of sampling or for the interaction between the time of sampling x irrigation treatment, that may reflect that d13C increases as the fruit ripens. These preliminary analyses suggest that the level of maturity of the grape is unlikely to drive differences in d13C. However, we do not know how early in ripening the d13C analysis can reflect differences in water stress, especially when the vines are subject to water deficit late in ripening (as is common in the Barossa) and further experiments are required to clarify this point.

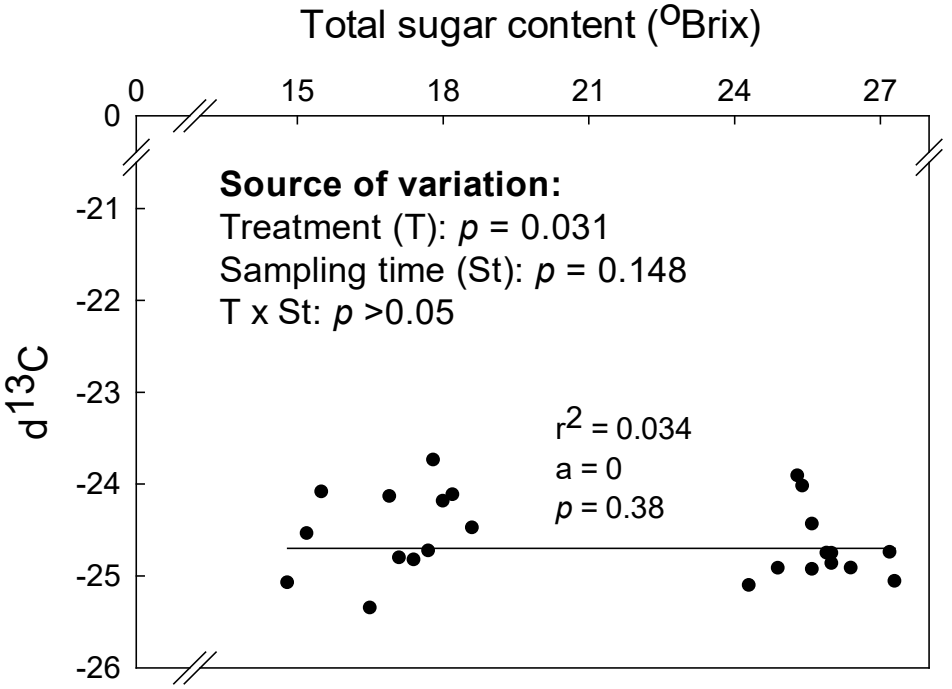


Figure 6.2.2 Relationship between the concentration of sugars in the berry at different maturity and the relative concentration of ^{12}C and ^{13}C on the sugars. Data are from an irrigation trial where vines are exposed to different irrigation regimes before veraison (Figure 6.2.1b).

We found a significant and unsurprisingly weak negative relationship between soil moisture content during the season and d13C (Figure 6.2.3). As described before, volumetric soil moisture indicates the amount of water present in the soil, but this moisture is not necessarily available for the vines; therefore, explaining the weak relationship between soil moisture

content and water stress. We expect to be able to better characterise vine water uptake during the season using soil water tension (as calculated from the relationship between volumetric water content and water potential) and d13C.

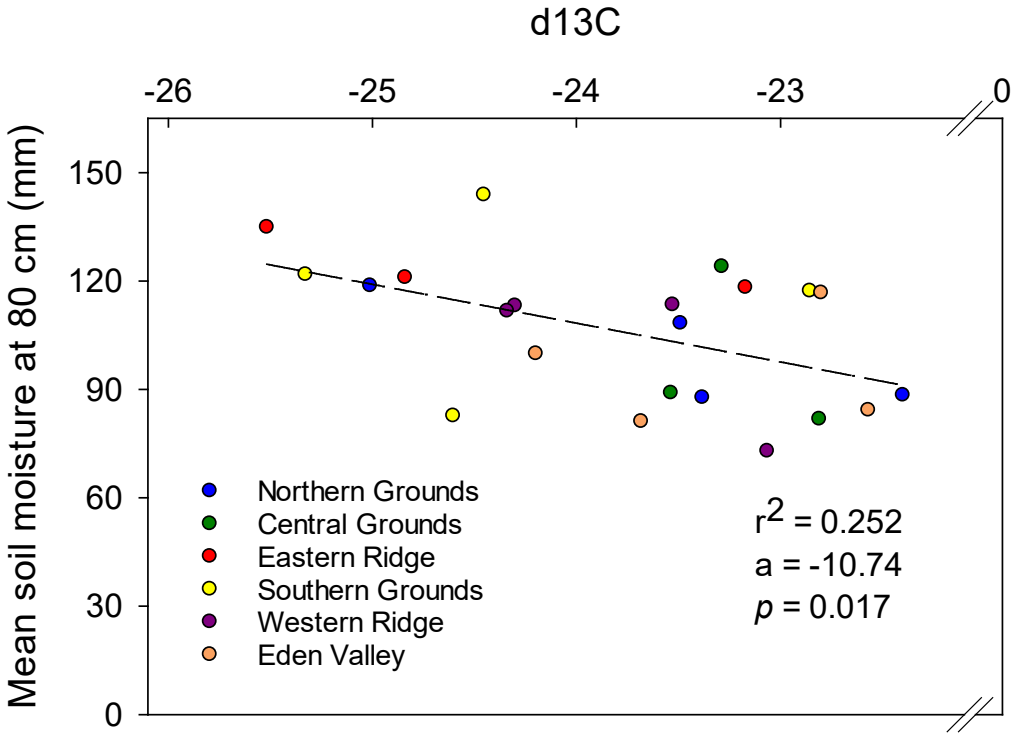


Figure 6.2.3 Relation between soil moisture content and carbon isotopic discrimination on berry sugar at harvest 2019. Each point is the mean from three zones of the vineyard. The colour of the point indicates the location of the vineyard in the Barossa Valley.

When the d13C data were pooled across seasons and zones within each vineyard, there was a large range in the d13C readings. Average values across two seasons and 24 vineyards ranged from -21.8 to -26.2 (Figure 6.2.4), which is within the range observed in vineyards of irrigated (Brillante et al. 2020b) and rain-fed regions (Spangenberg and Zuffrey 2018). The three-ways ANOVA between seasons, vineyards and zones, showed a significant effect of the season ($P = 0.033$), the vineyard ($P < 0.001$) and the zone ($P = 0.011$), as well as the interactions between season x vineyard ($P < 0.001$) on d13C readings at harvest. Differences in d13C between season 2018/19 and 2019/20 mirrored records of precipitation during the vine growing period and the preceding winter (June to March). During the drier season 2018/19 (296 mm) d13C was higher (-23.82) than during the wetter season 2019/20 (361 mm, -24.02), suggesting that the vines suffered more water stress during the season 2018/19 than during the season 2019/20. Most of the vineyards showed consistent d13C readings between seasons (Figure 6.2.4), which indicated the repeatability of d13C analysis in multi-year studies and across multiple sites, and even in conditions were supplementary irrigation is applied during the season. However, as indicated by the season x vineyard interaction, a few of vineyards showed different d13C readings between years, more likely, due to adjustments to the irrigation program between years and vineyards. Notwithstanding differences between vineyards, differences between zones of the vineyard were consistent across seasons; zones with high capacity, as indicated by the high PCD, were consistently lower in d13C than zones with medium and high capacity.

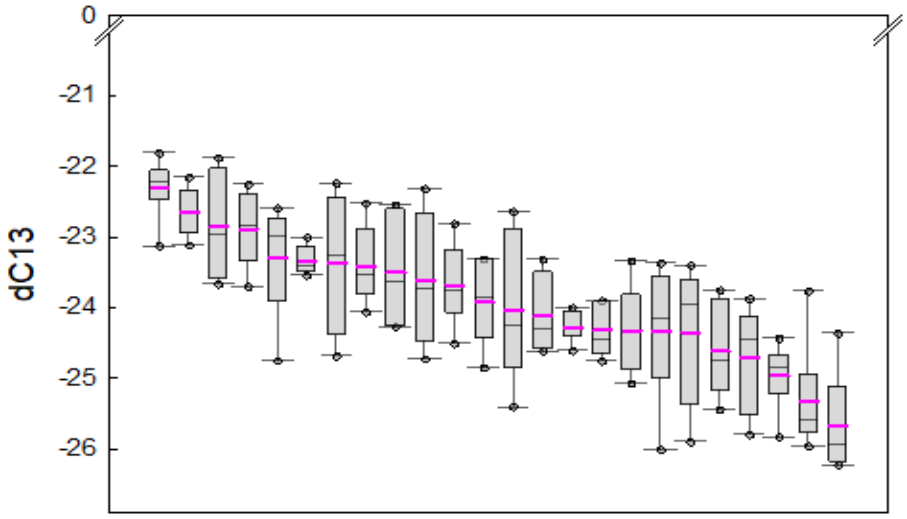


Figure 6.2.4 Carbon isotopic discrimination on berry sugar at harvest. Each box plot corresponds to a vineyard; data in each box are d13C readings across seasons 2019 and 2020, and three zones of the vineyard (n = 6). In the boxes, the boundary of the box closest to zero indicates the 25th percentile, the pink line indicates the mean, the black line the median and the boundary farthest from zero indicates the 75th percentile. Whiskers above and below the box indicate the 5th and 95th percentiles and points above and below the whiskers indicate outliers.

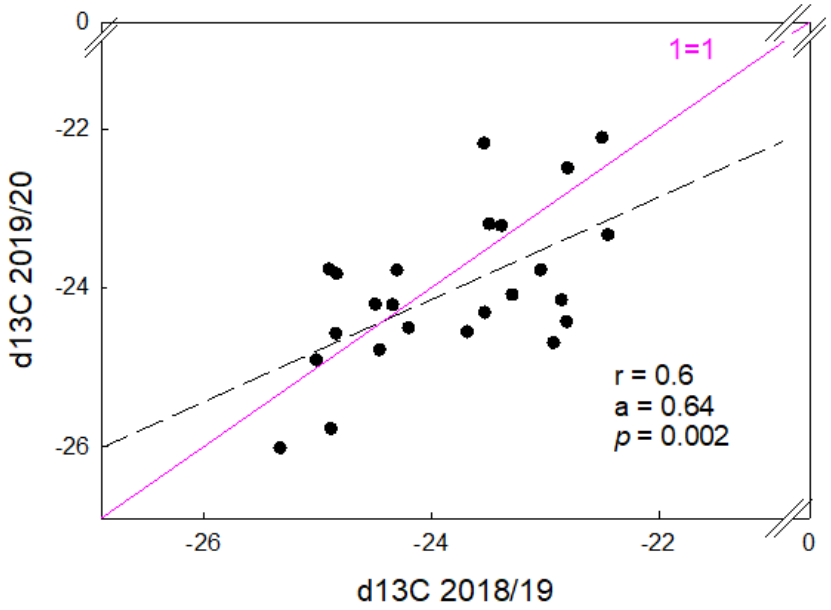


Figure 6.2.5 Relationship between d13C in seasons 2018/19 and 2019/20. Each point is the mean of three readings. The dashed line is the fitted regression and the solid (pink) reference line is the x = y. Scatter from the reference line indicates discrepancies on d13C readings for the same site across seasons.

When d13C data from the vineyards were pooled together based on their location (sub-regions), the ANOVA revealed some consistent differences between sub-regions and across

years (Figure 6.2.10). The two-way ANOVA between seasons and location showed no interaction between these factors but a significant effect of the location ($P < 0.001$). Southern Ground (SG) vineyards segregated from the remaining vineyards due to the significantly lower d13C. There were no differences between Eastern Edge (EE) and Western Ridge (WR) vineyards, and between Central Grounds (CG) and Northern Ground (NG) vineyards; however, ER vineyards were significantly lower in d13C than CG and NG vineyards. Similarly, there were no differences in d13C between Eden Valley (EV) with NG and CG, but EV was significantly higher in d13C than WR, EE and SG. Overall, these preliminary findings suggest that besides different management practices across sites (e.g. irrigation, use of mulch, cover crops) and seasons (i.e. rainfall) that may be affecting soil water availability, there are underlying factors, such as soil texture, that have a higher impact on vine water status. d13C readings have been previously used for zoning at a vineyard scale on irrigated and rain-fed vineyards. However, these preliminary findings are the first indication that d13C is a powerful measurement to integrate and distinguish components of terroir affecting vine water status at a much bigger regional scale. Likewise, d13C is a reliable proxy of vine water availability, which remains sound even when the vines receive supplementary irrigation.

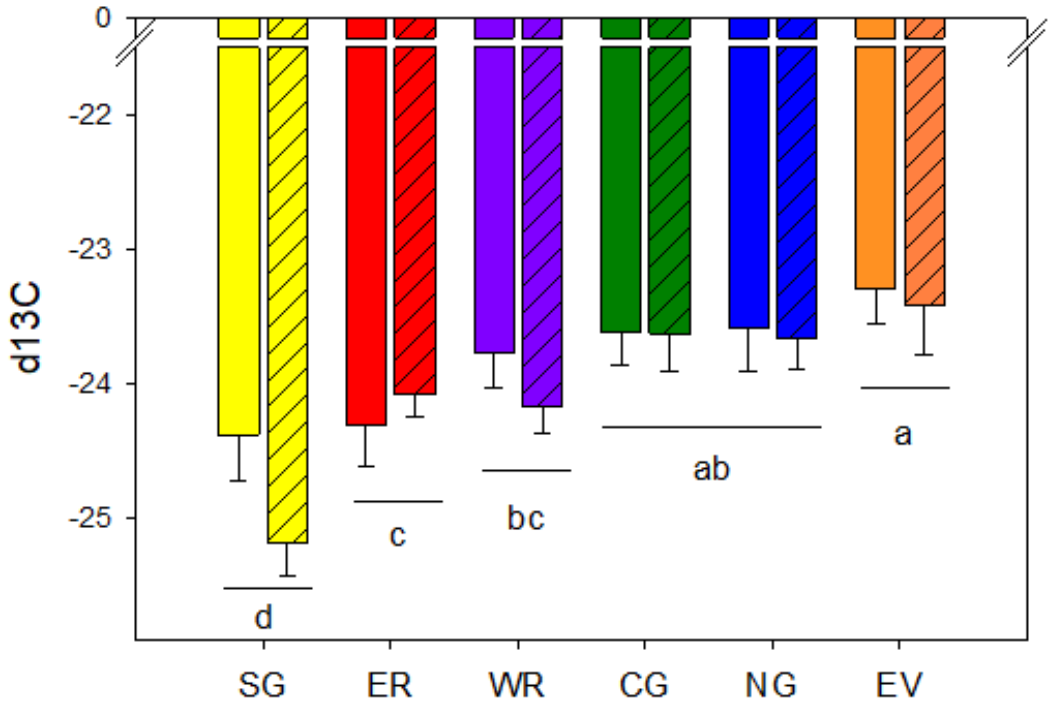


Figure 6.2.6 Carbon isotopic discrimination on berry sugar at harvest during seasons 2019 and (crossed) 2020. Bars represent the mean ± one standard error from four vineyards and three zones within each vineyard (n = 12). Different letters indicate significant differences at P = NG = Northern Grounds (blue), CG = Central Grounds (green), EE = Eastern Edge (red), SG = Southern Grounds (yellow), WR = Western Ridge (purple), EV = Eden Valley (orange).

Yield formation is defined by the availability of resources during the season, chiefly water and nutrients. To investigate the regulation of yield by water availability, we compared yield against d13C readings at harvest (Figure 6.2.7). The boundary function fitted on the data across two years indicates that yield was potentially limited by water stress during the season, at some sites. The maximum potential yield was defined by the soil water availability and

water stress during the season; for example, the SG and EE vineyards that experienced lower water stress (more negative d13C) yielded higher than vineyards from the other sub-regions, and were able to sustain relatively higher yield irrespective of the season. Other regions such as CG, EV and WR, exhibited consistently lower yields irrespective of the level of water stress. This may be due to the impact of other climate variables or management practices, such as extreme temperatures that have not been captured as part of this analysis.

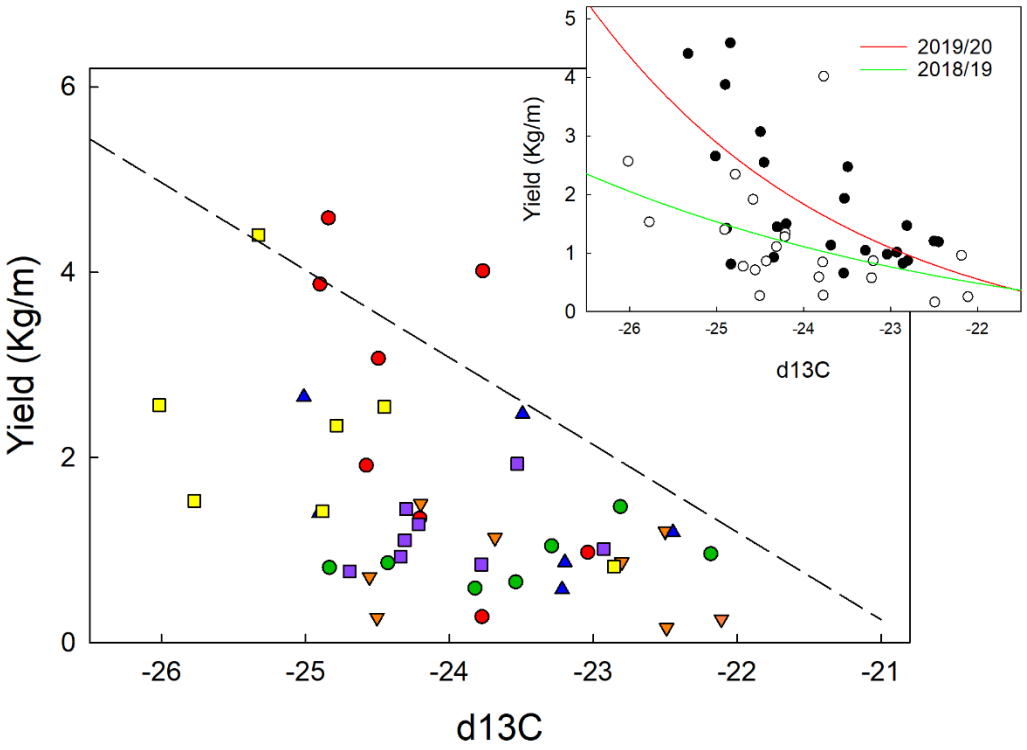


Figure 6.2.7 Relationship between yield and the integral of water stress during the growing season, measured as d13C. Each point is the mean of three measurements across the same vineyard. 24 vineyards were followed during two years from different sub-regions of the Barossa Valley. Different symbols and colours indicate the location of the vineyard: NG = Northern Grounds (blue), CG = Central Grounds (green), EE = Eastern Edge (red), SG = Southern Grounds (yellow), WR = Western Ridge (purple) and EV = Eden Valley (orange). The crossed line is the boundary function calculated from the 95th percentile of the relation between yield and d13C in 0.5 % intervals. Solid lines in the inset are fitted regressions between yield and d13C in the season 2018/19 (green) and 2019/20 (red).

6.3 Grape chemistry

Paul Boss, CSIRO

6.3.1 Amino acids, glutathione and vitamins B5 and B6

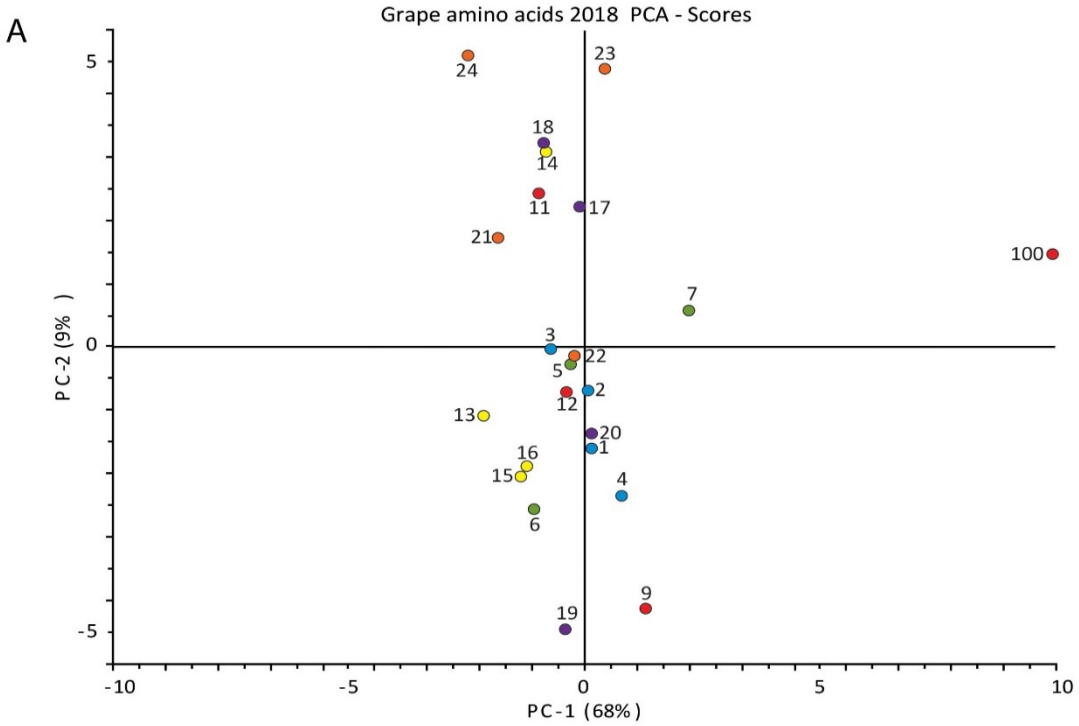
2018 Vintage
Nineteen of the 20 proteogenic amino acids (all except tryptophan) were analysed in the grape samples, although cysteine was below the limit of detection for the method. Hydroxyproline, β-alanine and γ-aminobutyric acid are non-proteogenic amino acids were also analysed using the same method.

Proline and arginine were the most abundant amino acids in the samples, being present at a mean concentration of 1.4 mg/mL and 1.1 mg/mL (of juice) respectively. Glutamine, glutamic acid, threonine, alanine and γ-aminobutyric acid were all present in the samples at concentrations between 100-200 µg/mL. Aspartic acid, asparagine, serine, histidine, tyrosine, lysine, isoleucine, leucine and phenylalanine concentrations in the samples fell between 10-100 µg/mL of juice and hydroxyproline, glycine, β-alanine and methionine concentrations were all below 10 µg/mL in the grape juice. Total amino acids ranged from 1.9 mg/mL in Sample 24 to 13.4 mg/mL in Sample 100. Sample 100 was very much an outlier, as the total amino acids concentrations ranged from 1.9-4.8 mg/mL when this sample was removed from the data set.

Glutathione and two nitrogenous vitamins, pantothenate (B5) and pyridoxine (B6) were included in the subsequent multivariate analysis of the amino acids and so their concentrations are also discussed in this section. There was not great variation in glutathione concentrations across the sites, with a maximum concentration measured in Sample 100 (258 µg/g) and the minimum observed in Sample 13 which contained 111 µg/g. Similarly, there was a lack of variation of pyridoxine concentration across the sites ranging from 118 ng/g in Sample 23 to 198 ng/g in Sample 16. Pantothenate varied by approximately two-fold across the samples with the lowest (Sample 23) containing 373 ng/g and the highest 711 ng/g (Sample 100).

The easiest way to visualise the similarities and differences in the amino acid and vitamin composition of the samples is by principal component analysis (PCA). An initial PCA included all samples and showed that Sample 100 was an obvious outlier (Figure 6.3.1). Most of the variation (68%) was described on the first PC, with only 9% described by PC2. Sample 100 was found on the extreme right of the plot indicating a strong separation on PC1, which was mainly driven by total amino acids and most of the amino acids were co-located on this side of the loadings plot. The separation on PC2 was separating the abundance of the two B vitamins measured from the concentration of aspartic acid (Figure 6.3.1). Given the issue of Sample 100 being an outlier, the PCA was repeated without this sample to allow a better visualisation of the relationship between the other samples (Figure 6.3.2). The separation of PC1 described less of the variation (48 %) but was still driven by the difference in concentration of a lot of the amino acids as well as total amino acids. PC2 described 15 % of the variation and separated samples with higher concentrations of aspartic acid and phenylalanine towards the top of the plot with those that contain more hydroxyproline, pantothenate and γ-aminobutyric acid. Grouping of samples from the same sub-regions was not apparent in the PCA score plot (Figure 6.3.2A), although samples from Western Ridge

were found in a tight band in the middle of the horizontal axis with those from Southern Grounds found just to the left of these on PC1. However, the samples from both of these sub-regions were then well separated on PC2. Eden Valley samples were all located in the upper half of the plot but they were well discriminated on PC1. The Northern Grounds, Central Grounds and Eastern Edge samples did not tend to group based on the abundance of these compounds in the grapes.



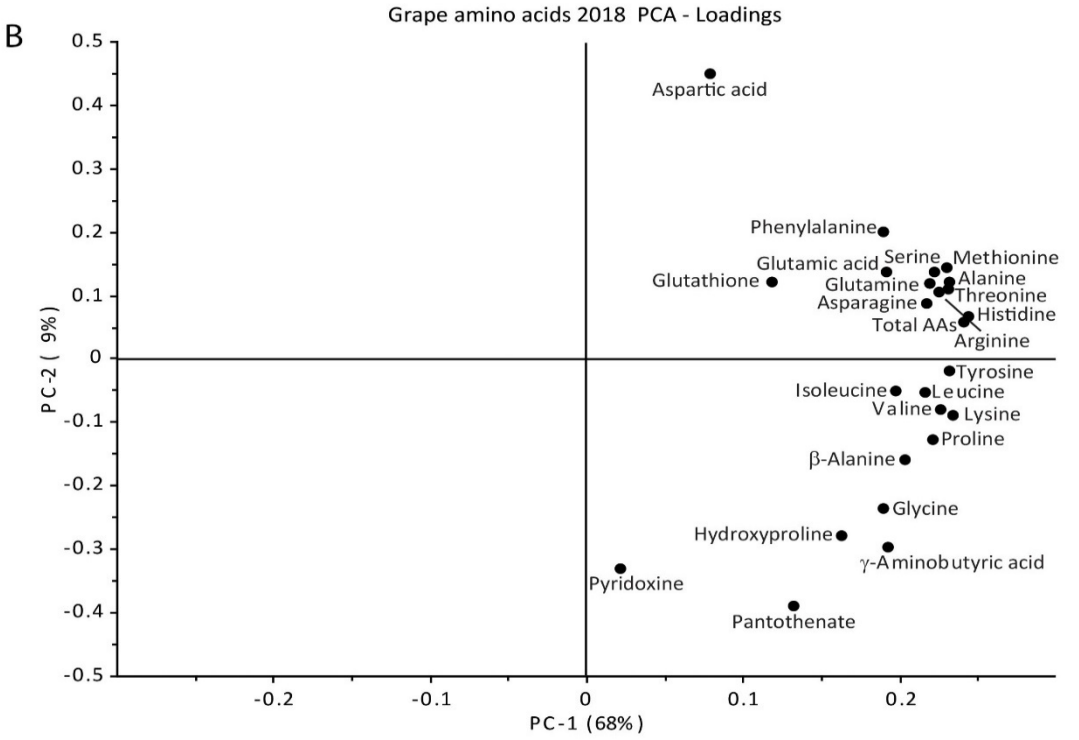


Figure 6.3.1 PCA scores (A) and loadings (B) plots of 23 different 2018 Shiraz grape samples from six sub-regions across the Barossa Valley, South Australia and the amino acids, glutathione and B vitamins measured in these samples.

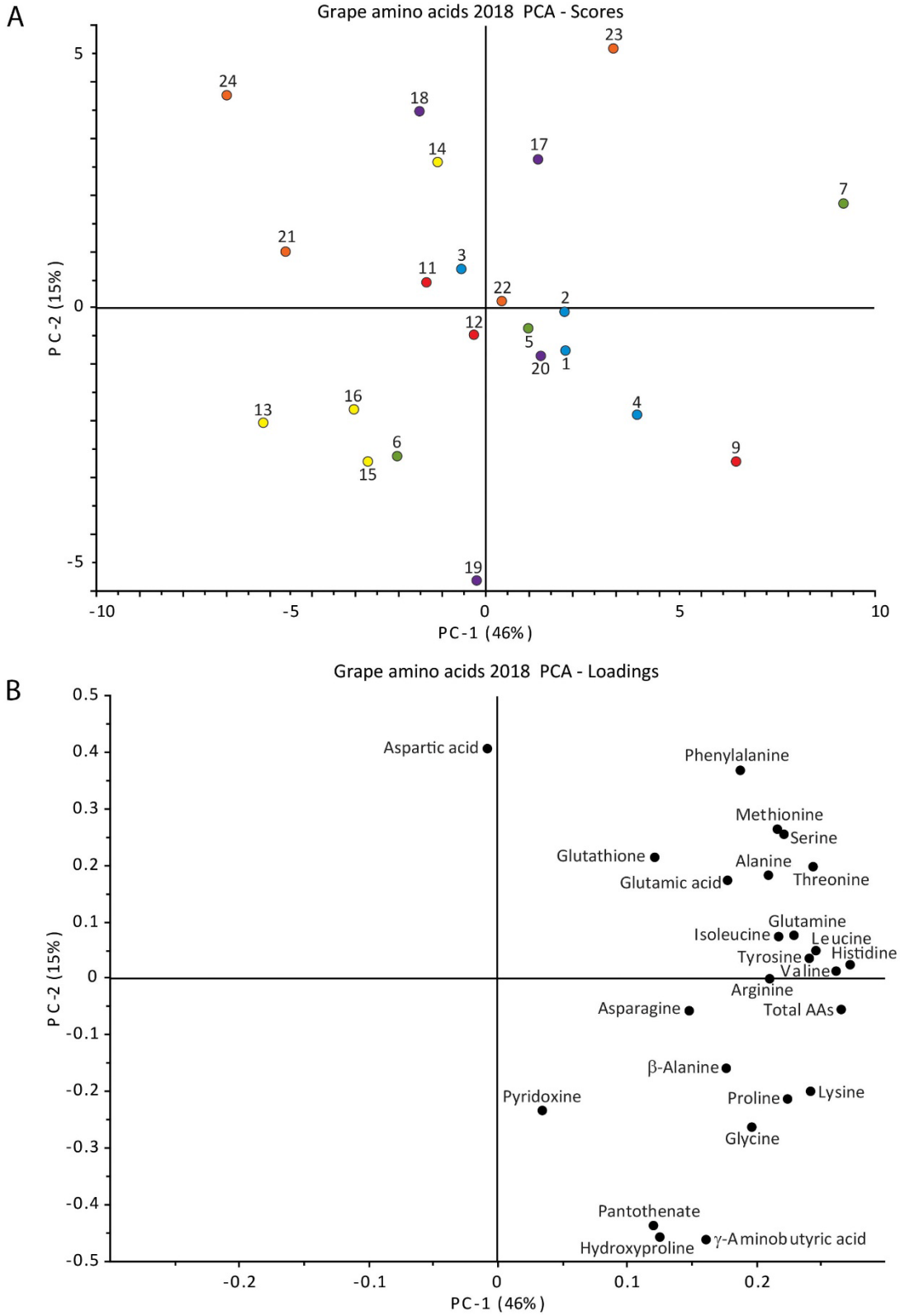


Figure 6.3.2 PCA scores (A) and loadings (B) plots of 22 (Sample #100 eliminated) different

2018 Shiraz grape samples from six sub-regions across the Barossa Valley, South Australia and the amino acids, glutathione and B vitamins measured in these samples.

2019 Vintage

The same amino acids were measured in the fruit from the 2019 vintage and again cysteine was below the detection limit. In general, amino acid concentrations were lower in 2019 than in the samples from the 2018 vintage. For example, the mean concentrations of the two most abundant amino acids, proline and arginine, were 1.2 and 0.7 mg/mL of juice respectively compared to 1.4 and 1.1 mg/mL. The range of concentrations of the individual amino acids was also broader than that seen in 2018. Glutamine, glutamic acid, threonine, alanine and γ-aminobutyric acid were present in the samples at concentrations between 20-450 µg/mL. Aspartic acid, asparagine, serine, histidine, tyrosine, lysine, isoleucine, leucine and phenylalanine concentrations in the samples fell between 3-230 µg/mL of juice and hydroxyproline, glycine, β-alanine and methionine concentrations were all below 20 µg/mL in the grape juice. Total amino acids ranged from 0.8 mg/mL in Sample 18 to 5.9 mg/mL in Sample 10.

The variation in glutathione concentrations across the sites was greater in 2019 than it was in 2018, with a maximum concentration measured in Sample 23 (302 µg/g) and the minimum observed in Sample 18 which contained 36 µg/g. There was a lack of variation of pyridoxine concentration across the sites ranging from 137 ng/g in Sample 24 to 210 ng/g in Sample 4, similar to the range observed in 2018. Pantothenate varied by just under two-fold across the samples with the lowest (Sample 24) containing 381 ng/g and the highest 653 ng/g (Sample 4).

The relationship between the samples and the amino acid, glutathione and vitamin composition was visualised again using PCA (Figure 6.3.3). A total of 79 % of the variation was described by the first two PCs, with 61 % represented by the separation on PC1. This variation was driven by the total amino acids, with those samples on the right of the plot being associated with higher concentrations of most amino acids (Figure 6.3.3). There was no clear separation according to sub-region on PC1. However, there was some grouping of samples from the same regions on PC2, which represented 18 % of the total variation. The samples from Eden Valley were all found in the top half of the plot as they generally had higher concentrations of aspartic acid, compared with most of the other samples, and low concentrations of the B vitamins, γ-aminobutyric acid, hydroxyproline, lysine and arginine (Figure 6.3.3). In contrast, the samples from Eastern Edge and Northern Grounds were located in the bottom half of the plot and hence were associated with higher amounts of the compounds co-located in the lower sections of the plot. The samples obtained from Southern Grounds were not well described by this PCA as indicated by their localisation in the centre of the plot. Finally, the grape parcels obtained from the Central Grounds and Western Ridge tended to be more similar to those from Eden Valley with regards to their amino acid composition, but one sample from each area was also found in the lower half of the score plot (Figure 6.3.3). When comparing the 2018 and 2019 vintages, the main similarity between the two data sets is the tendency for the samples from Eden Valley to have higher concentrations of aspartic acid and lower B vitamins than samples from the other regions (Figure 6.3.2 & 6.3.3).

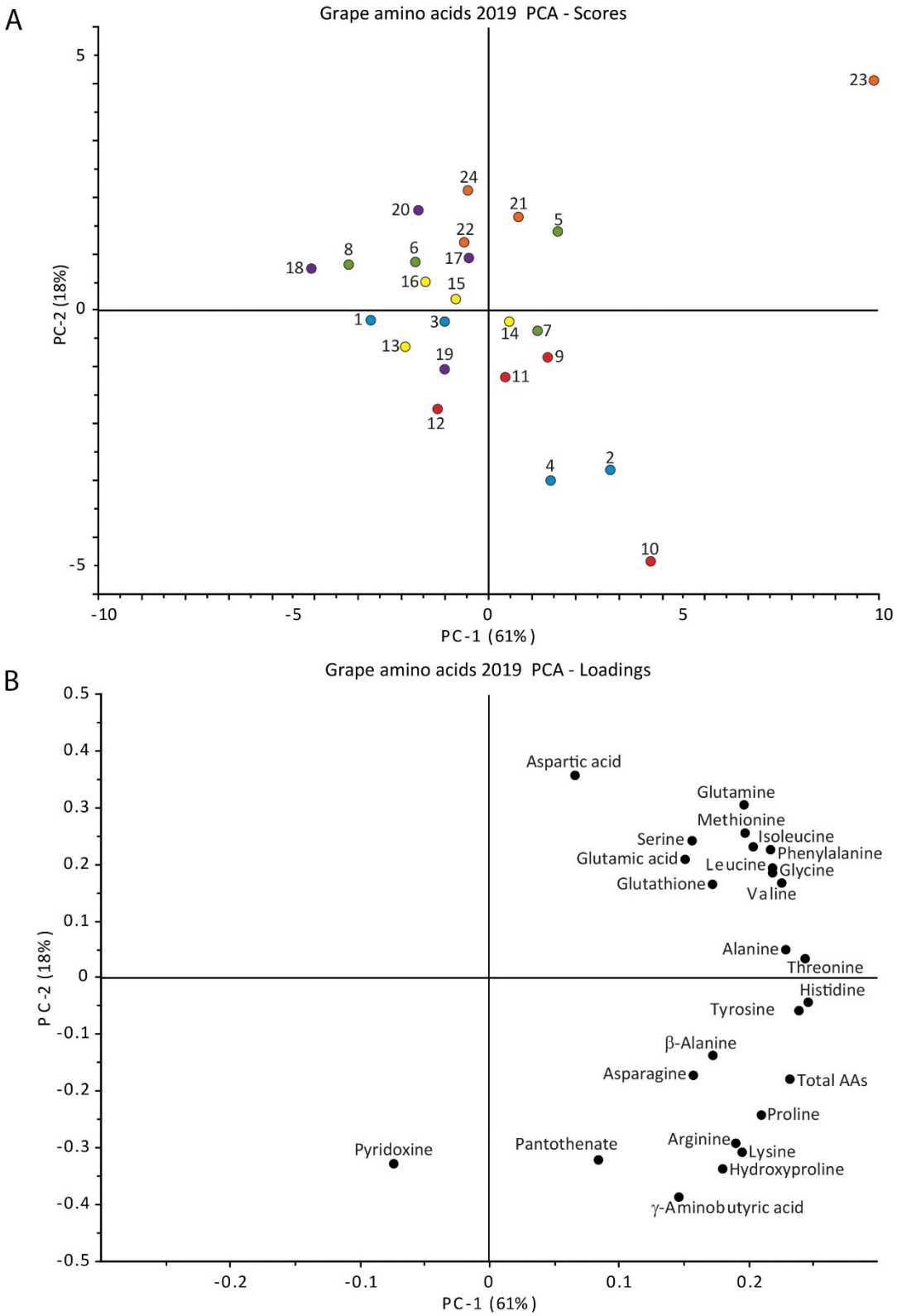


Figure 6.3.3 PCA scores (A) and loadings (B) plots of 24 2019 Shiraz grape samples from six sub-regions across the Barossa Valley, South Australia and the amino acids, glutathione and B vitamins measured in these samples.

2020 Vintage

The samples from the 2020 vintage had a slightly higher variation in total amino acids compared to the previous vintages, ranging from 0.7 mg/mL (Sample 12) of juice to 6.3 mg/mL (Sample 23), and the overall average was 2.7 mg/mL. The mean concentrations of the two most abundant amino acids, proline and arginine were 0.9 mg/mL and 0.8 mg/mL respectively which was the lowest observed for proline in the first three years. The range in concentration of the other amino acids was similar to previous years, with hydroxyproline, glycine, β-alanine and methionine, having low concentrations between 0-11 µg/mL, and the rest falling between 3-318 µg/mL. Arginine had the broadest range of all the amino acids, being quantified at 121 µg/mL in Sample 12 and 2814 µg/mL in Sample 23. More often than not, these samples contained the lowest and highest concentrations respectively of each amino acid across the range of samples.

The highest glutathione concentration was measured in Sample 19 at 342 µg/g and the lowest in Sample 12 (90 µg/g) representing a smaller range than observed in 2019. Pyridoxine was again not greatly variable with concentrations ranging from 120 ng/g (Sample 6) to 151 ng/g (Sample 4). Pantothenate concentrations were similar to 2018 and 2019 with a ~1.5-fold difference between the highest in Sample 23 (620 ng/g) and the lowest in the Sample 13 (396 ng/g).

Principal component analysis of the data set resulted in a similar loadings plot to that seen in previous vintages with separation of samples driven by the total and most of the individual amino acid concentrations on the right side of the plot (Figure 6.3.4). The separation on PC1 represented 69 % of the total variation in the data. PC2 only represents 11 % of the variation and this separation is associated with higher proline, hydroxyproline and aspartic acid concentrations in samples near the top of the plot and those with higher isoleucine, asparagine, methionine and leucine towards to bottom of the plot. Sample 23 is an outlier in the 2020 vintage, which was also observed in 2019 (Figure 6.3.3) and it contained the highest concentration of most amino acids. The separation of the other samples is not great and no patterns of separation were observed among sub-regions. In fact, no sub-region has all of the samples on either the left or right or the top or bottom half of the score plot (Figure 6.3.4).

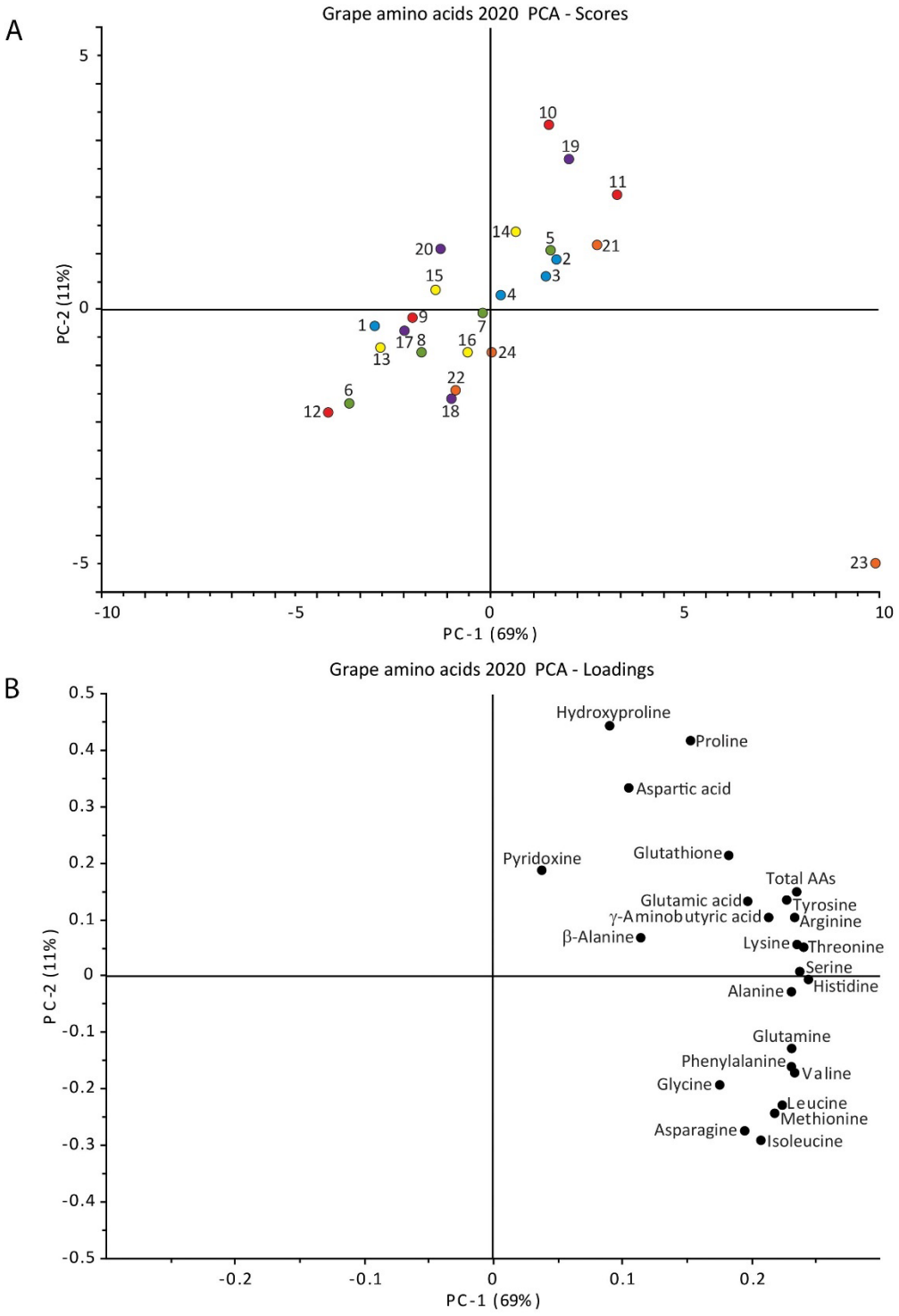


Figure 6.3.4 PCA scores (A) and loadings (B) plots of 24 2020 Shiraz grape samples from six sub-regions across the Barossa Valley, South Australia and the amino acids, glutathione and B vitamins measured in these samples.

2021 Vintage

The amino acid results from the 2021 vintage were most similar to 2018, with the total concentrations ranging from 1.3 mg/mL in Sample 12 to 5.2 mg/mL in Sample 22. Proline and arginine were again the most abundant amino acids, averaging 1.2 mg/mL and 0.8 mg/mL of juice respectively. The amino acids with the lowest concentrations in most samples were hydroxyproline, asparagine, glycine, β-alanine, methionine and lysine with concentrations ranging from 0-20 µg/mL and with averages below 12 µg/mL. The rest of the amino acids all averaged over 20 µg/mL in the samples with a range of values from 8-296 µg/mL. The broadest range of concentrations was seen for arginine which varied from 139 µg/mL in Sample 12 to 2040 µg/mL in Sample 22.

Glutathione concentrations were less variable than those seen in 2020, with the lowest concentration measured in Sample 7 (122 µg/g) and the highest in Sample 22 (268 µg/g). Pyridoxine was slightly more varied in 2021 than in previous vintages, ranging from 146 ng/g in Sample 23 to 238 ng/g in Sample 14. The average concentration of pantothenic acid in the 2021 samples was 665 ng/g and was the highest across all the years of the study. The lowest concentration was measured in Sample 12 (533 ng/g) and the highest in Sample 19 (793 ng/g).

PCA of the 2021 data was consistent with the other years of the study with regards to the loadings plot showing that the main separation on PC1 is driven by the total concentration of amino acids in the samples (Figure 6.3.5). PC1 explains 56 % of the variation among the samples and 17% is explained by PC2. The separation on PC2 is associated with higher concentrations of pyridoxine, γ-aminobutyric acid, glycine and lysine towards the top of the plot and isoleucine, glutamine and aspartic acid towards the bottom. Unlike 2020, there was some separation of the samples according to sub-region in 2021 (Figure 6.3.5). All of the Eden Valley samples are located in the lower half of the plot, although Sample 21 is near the origin and likewise the Northern Grounds juice samples were found in the bottom half of the scores plot. Discrimination between the sub-regions did not occur on PC1, with all regions except Central Grounds having samples on both sides of the plot. The Central Grounds samples were found on the left of the plot indicating that they tended to have lower amino acid concentrations compared to samples from other sub-regions.

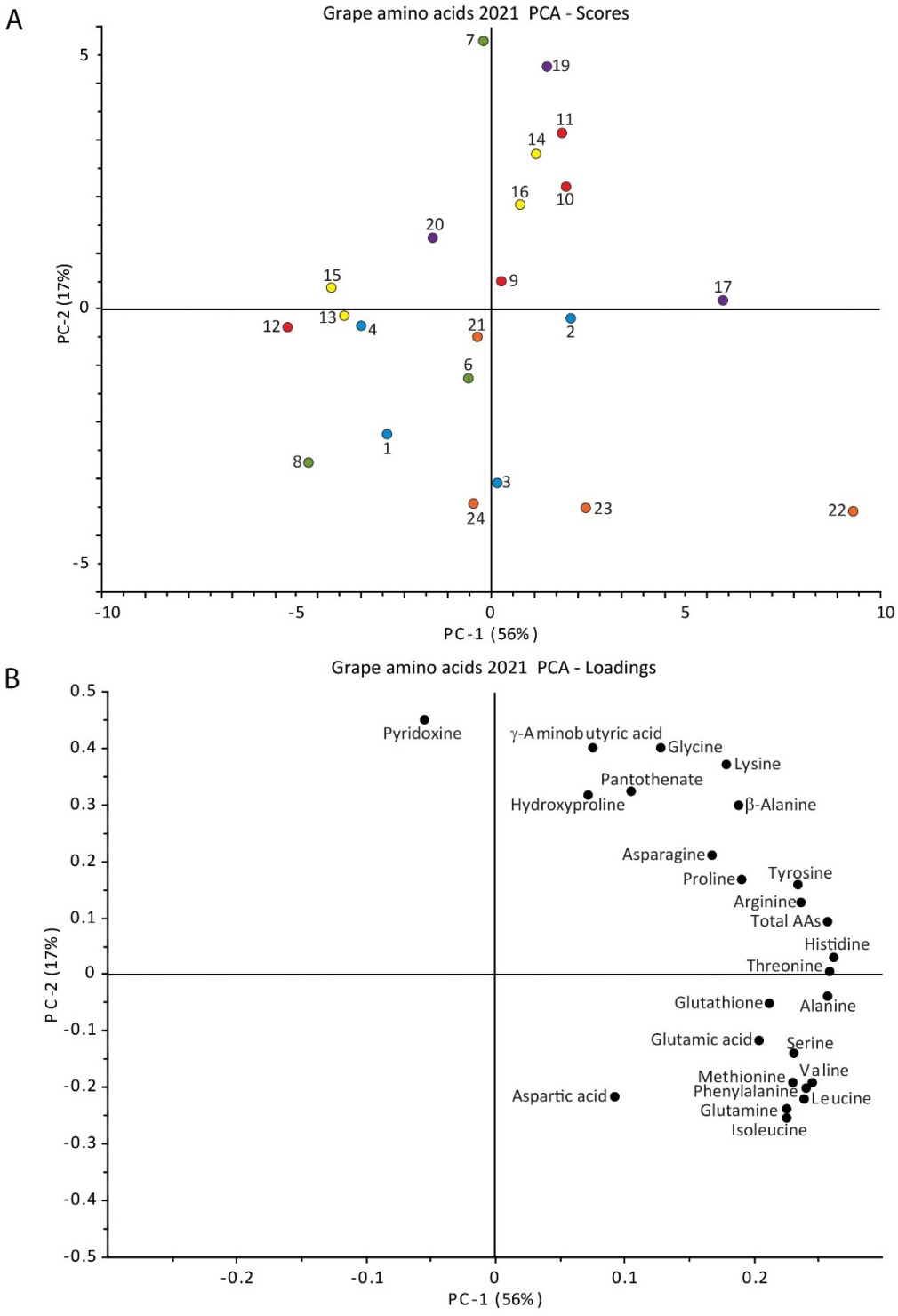


Figure 6.3.5 PCA scores (A) and loadings (B) plots of 22 2021 Shiraz grape samples from six sub-regions across the Barossa Valley, South Australia and the amino acids, glutathione and B vitamins measured in these samples.

6.3.2 Fatty acids

2018 Vintage
Fatty acids have been shown to alter yeast metabolism and, therefore, alter the volatile composition of wines. Lipids are also of interest as they may all be targets for singlet and triplet oxygen, and free lipids, which will be available for enzymatic degradation by the lipoxygenase pathway are also important. The compounds resulting from these degradation pathways can also be further metabolised into various alcohols and esters that contribute to the volatile profiles of wines. The method used to quantify the individual fatty acid moieties of the lipids incorporates a simple solvent extraction of all the lipids in de-seeded berries followed by methylation to enable detection of the methyl esters by GS-MS. Twenty-nine fatty acids were quantified using this method and 21 of these were significantly different ($p<0.05$) among the samples. The data were summarised using PCA.

Like the amino acid analysis, the major variation driving separation on the first PC was associated with overall concentration of fatty acids in the samples (Figure 6.3.6). The samples on the right of the plot had higher concentrations of many fatty acids compared to those on the left of the plot. The second PC only described 18 % of the variation, compared with 62 % for PC1, and separated samples with higher concentrations of unsaturated fatty acids near the top of the plot, with those samples that had more saturated fatty acids at the bottom of the plot (Figure 6.3.6).

There was some grouping of sites from the same sub-region according to fatty acid composition (Figure 6.3.6A). The Northern Grounds and Central Grounds vineyards clustered on the right of the plot, due to higher concentrations of a number of fatty acids. The Eden Valley sites were all located on the left of the plot, suggesting they have lower abundance of many fatty acids compared to the other sub-regions. Three of the four Western Ridge samples were located near the top of the plot indicating they have a higher amount of unsaturated fatty acid than the other samples. Three of the Eastern Edge and Southern Grounds samples clustered near the origin, suggesting they were not well differentiated by the variation described in these two PCs. Interestingly, the outlier samples for Western Ridge (19), Southern Grounds (14) and Eastern Edge (9) in the fatty acid PCA (Figure 6.3.6), also appeared to be outliers from their respective groups in the amino acid analysis (Figure 6.3.2).

2019 Vintage
The same 29 fatty acids quantified in the 2018 vintage were also quantified from the grape samples obtained in 2019. However, only 13 were significantly different ($p<0.05$) among the grape parcels in 2019 and these were predominantly saturated fatty acids.

Similar to 2018, the relative concentration of a number of saturated fatty acids was the main driver of the separation on PC1, which described 52 % of the total variation (Figure 6.3.7). PC2 accounted for 22% of the variation and the separation was due to differences in the concentration of two unsaturated fatty acids and the relatively short-chain tetradecanoic acid.

The only clear grouping of samples from a sub-region are those from Eden Valley which are found on the left of the plot as they have lower concentrations of a number of the saturated fatty acids compared to the grapes from the other sub-regions (Figure 6.3.7). This was also observed in 2018 (Figure 6.3.6). There was no clear grouping of the samples from the other sites with samples from the other sub-regions being found in three of the four quartiles of the PCA score plot (Figure 6.3.7).

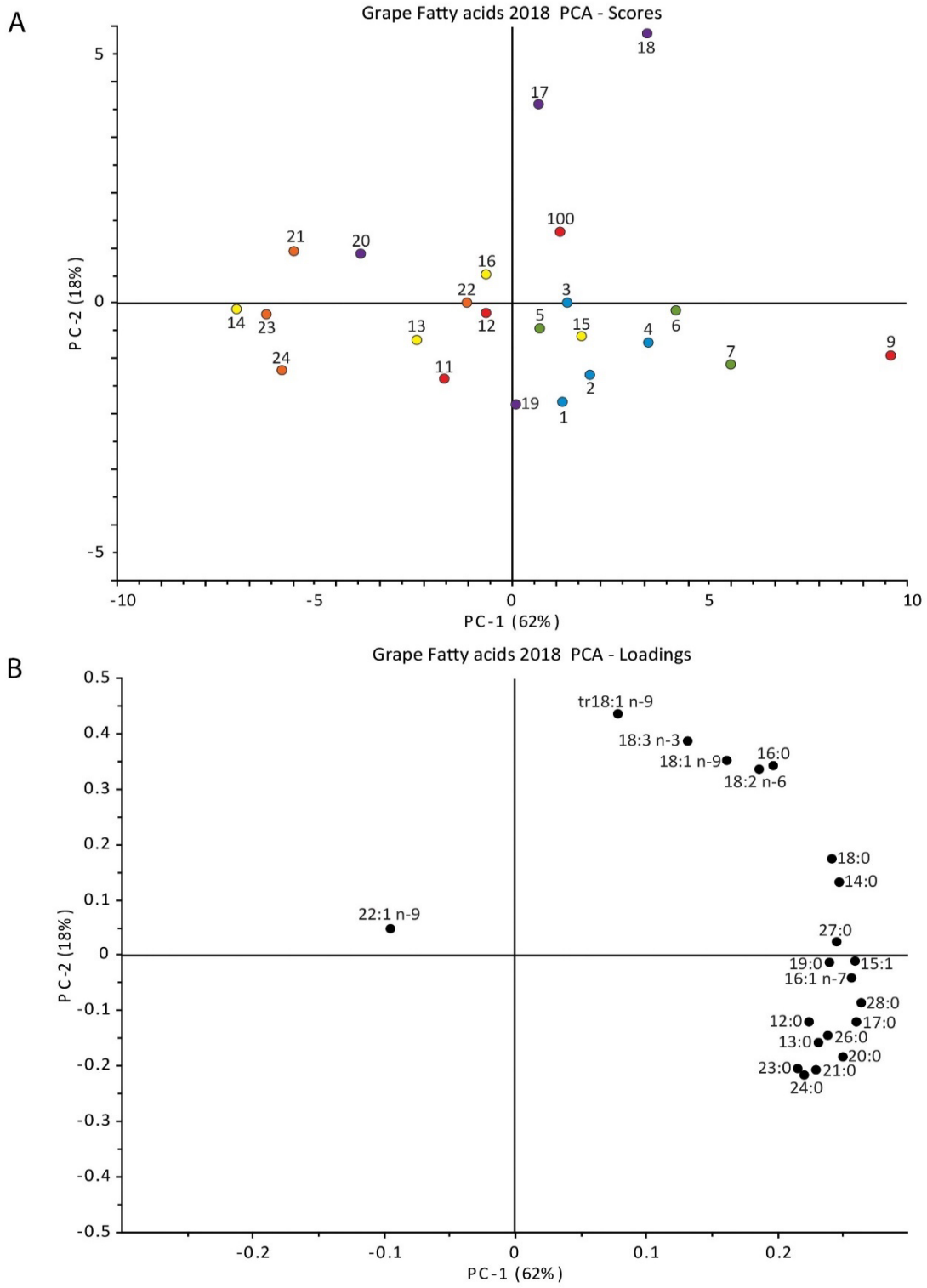


Figure 6.3.6 PCA scores (A) and loadings (B) plots of 23 different 2018 Shiraz grape samples from six sub-regions across the Barossa Valley, South Australia and the significantly different fatty acids measured in these samples. In the fatty acid nomenclature X:Y n-Z, a compound has X carbon atoms, Y double bonds and Z carbon atoms from the last double bond to the terminal methyl group.

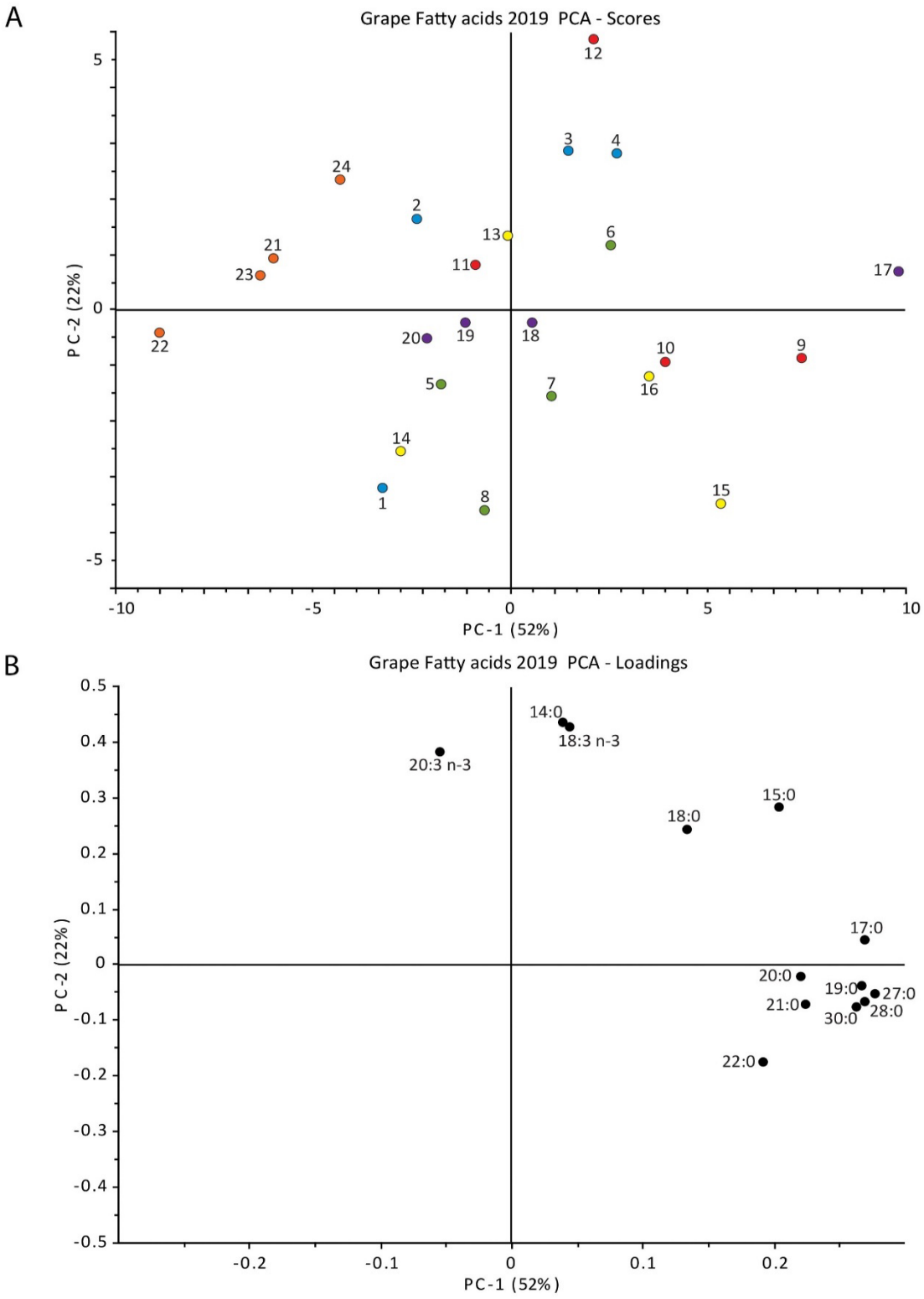


Figure 6.3.7 PCA scores (A) and loadings (B) plots of 24 different 2019 Shiraz grape samples from six sub-regions across the Barossa Valley, South Australia and the significantly different fatty acids measured in these samples. In the fatty acid nomenclature X:Y n-Z, a compound has X carbon atoms, Y double bonds and Z carbon atoms from the last double bond to the terminal methyl group.

2020 Vintage

Twelve of the lipids measured in the samples from the 2020 vintage were significantly different ($p<0.05$). These were a blend of saturated and unsaturated fatty acids including six saturated fatty acids ranging in length from 14 to 20 carbons and a mixture of 18 to 22 carbon length unsaturated fatty acids with one to three double bonds.

As observed for the previous two years, the main separation on PC1, which described 51% of the variation, is driven by high or low concentrations of the unsaturated fatty acid on the right of the plot (Figure 6.3.8). Similar to the 2018 vintage, the samples on the left of the plot are associated with higher concentrations of (*Z*)-13-docosenoic acid (22:1 n-9). PC2 described 19 % of the variation, and distinguished samples with higher concentrations of unsaturated fatty acids towards the top of the plot compared to those with lower unsaturated fatty acids towards the bottom (Figure 6.3.8). This was driven most strongly by linoleic acid (18:2 n-6) and eicosatrienoic acid (20:3 n-3).

The localisation of the Eden Valley samples on the left of the plot (Figure 6.3.8) was consistent with the 2018 and 2019 vintages (Figures 6.3.6 & 6.3.7). Again, this was due to these samples have lower concentrations of the saturated fatty acids, and their localisation in the top left of the PCA is because they have higher concentrations of (*Z*)-13-docosenoic acid and (*Z*)-13-eicosnaoate than the other samples. The samples from Central Grounds are all located on the right of the plot, although some are very close to the origin, and three of the four Western Ridge samples are also on the right of the scores plot. Three of the four Western Ridge samples are in the top half of the plot and are associated with higher concentrations of unsaturated fatty acids than the samples towards to bottom. In this half of the scores plot were three of four samples from the Central Grounds, Eastern Edge and Southern Grounds sub-regions (Figure 6.3.8).

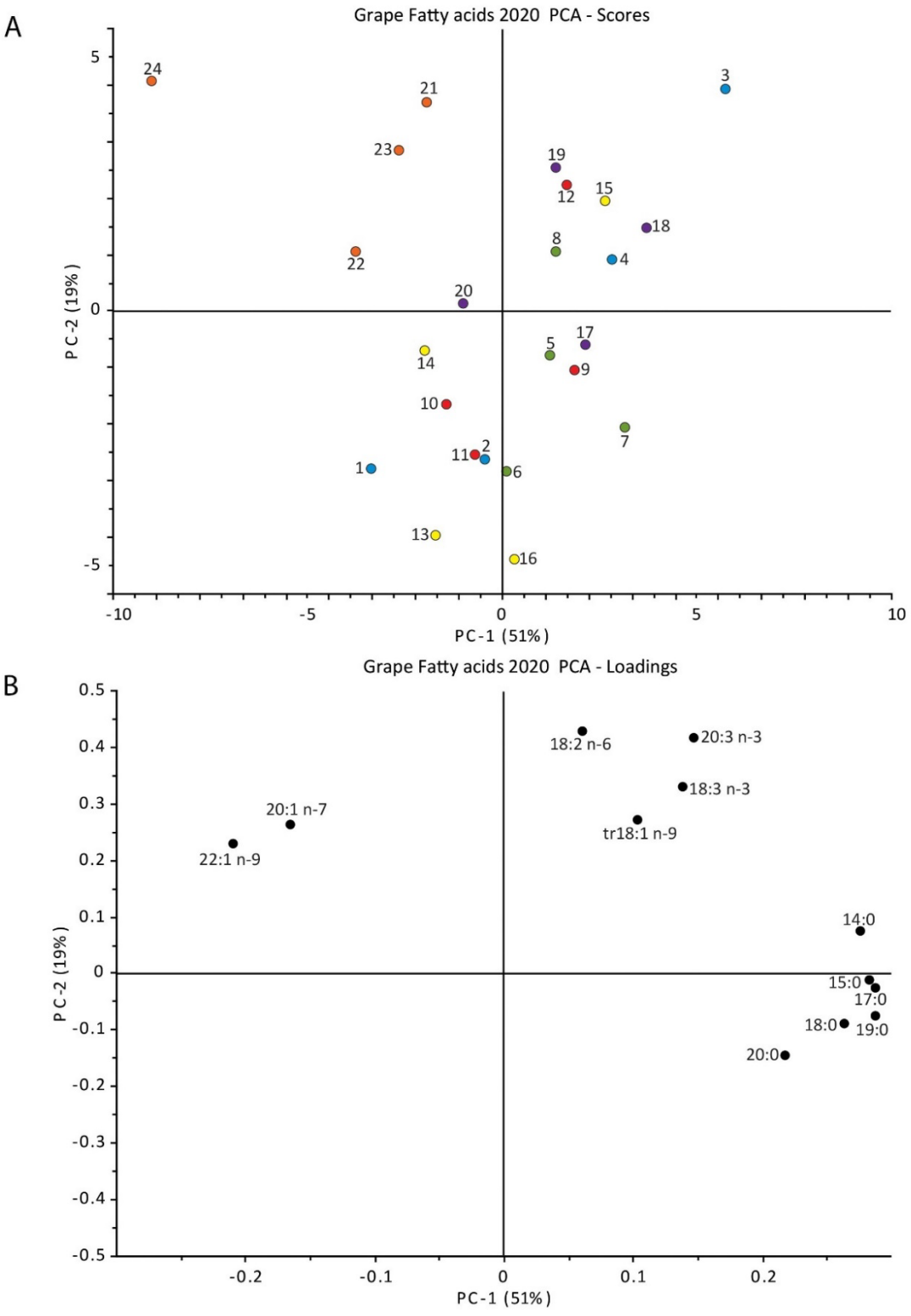


Figure 6.3.8 PCA scores (A) and loadings (B) plots of 24 different 2020 Shiraz grape samples from six sub-regions across the Barossa Valley, South Australia and the significantly different fatty acids measured in these samples. In the fatty acid nomenclature X:Y n-Z, a compound has X carbon atoms, Y double bonds and Z carbon atoms from the last double bond to the terminal methyl group.

2021 Vintage

Compared to other years the greatest number of fatty acids was significantly different (p<0.05) among the samples in the 2021 vintage (28). All of the straight-chain unsaturated fatty acids measured from 12 to 30 carbons long were significantly different as were all of the unsaturated compounds; the only fatty acid measured that was not significantly different was hydroxy-substituted compound 2-hydroxyhexadecanoic acid.

The compounds driving the separation on the horizontal axis (PC1 – 52 % of total variation) were slightly different in 2021 compared to the other vintages. While most of the unsaturated fatty acids are located on this side of the loadings plot, linoleic (18:2 n-6) and linolenic acid (18:3 n-3) as well as a couple of other unsaturated fatty acids are also influencing separation on the positive end of PC1 (Figure 6.3.9). As was observed in 2018 and 2020, higher concentrations of (*Z*)-13-docosenoic acid (22:1 n-9) were associated with samples on the right side of the PCA plot. The separation on PC2 represented 13% of the variation. In past vintages, this PC has been driven by differences in the concentrations of unsaturated fatty acids, but it is more subtle in the 2021 vintage. The samples found towards the top of the scores plot have higher concentrations of oleic (18:1 n-9) and elaidic acids (tr18:1 n-9), whereas those near the bottom of the plot have higher concentrations of long chain saturated fatty acids 24 to 30 carbons long.

The one consistent finding with the fatty acids across all of the vintages is that the samples from Eden Valley were always associated with lower concentrations of saturated fatty acids, as they were again on the left side of the scores plot (Figure 6.3.9). The three Western Ridge samples taken in 2021 were located on the right of the plot with two in the lower right quadrant associated with high concentrations of long chain unsaturated fatty acids. While not as consistent as the Eden Valley findings, there was a trend for the Western Ridge samples over the years to be high in unsaturated fatty acids. While all four Eastern Edge samples were associated with the unsaturated fatty acids which were located towards the top of the plot in 2021, this was not a consistent finding across the vintages. Samples from the other three sub-regions were spread across the PCA with no obvious grouping or association with specific types of fatty acids (Figure 6.3.9).

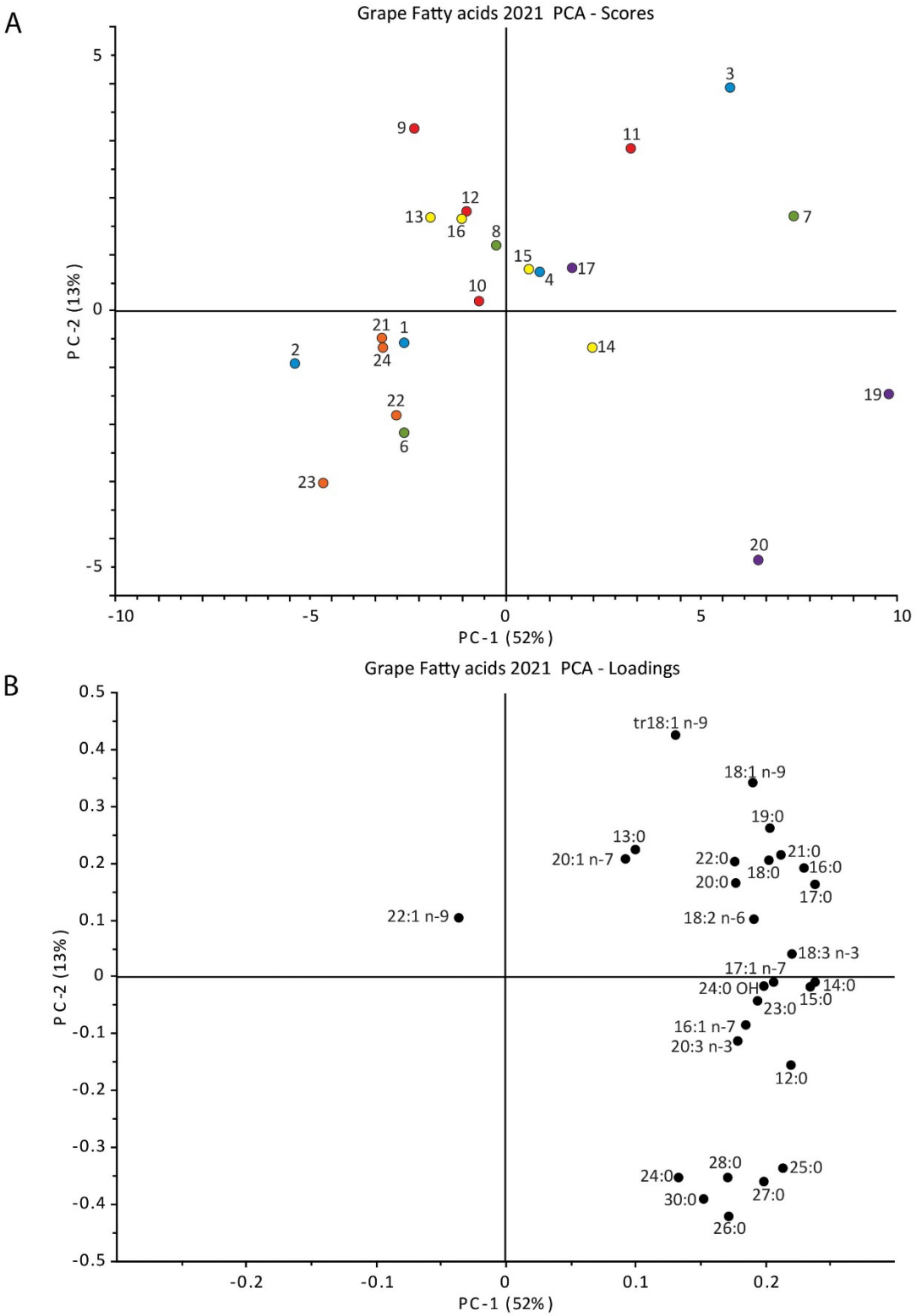


Figure 6.3.9 PCA scores (A) and loadings (B) plots of 22 different 2021 Shiraz grape samples from six sub-regions across the Barossa Valley, South Australia and the significantly different fatty acids measured in these samples. In the fatty acid nomenclature X:Y n-Z, a compound has X carbon atoms, Y double bonds and Z carbon atoms from the last double bond to the terminal methyl group.

6.3.3. Tannin Composition

2018 Vintage

The composition of the tannin in the skin of the grape samples was determined following chemical extraction, hydrolysis of the tannin polymers and analysis by HPLC. Seven sub-unit concentrations were determined along with total tannin and an estimate of the degree of polymerisation, and percentage composition was also determined for the seven types of sub-units identified. Only four of the various measures were shown to be significantly different among the samples and these were subject to PCA (Figure 6.3.10). Separation on PC1 described 61% of the variation and discriminated samples that had a higher percentage of epicatechin and epicatechin gallate extension sub-units on the right of the plot with those that had more catechin extension sub-units on the left. PC2 described 26% of the variation and separated samples with high percentages of all of these extension sub-units near the top of the plot from those with lower percentages at the bottom (Figure 6.3.10). Samples from within each region tended to be separated across PC1, with only the three Central Grounds samples being located on the same side of the plot. There was some sub-region grouping on PC2 with the Eden Valley associated with higher percentages of the three extension sub-units in the top half of the biplot, whereas the Eastern Edge samples were all located in the lower half of the plot (Figure 6.3.10).

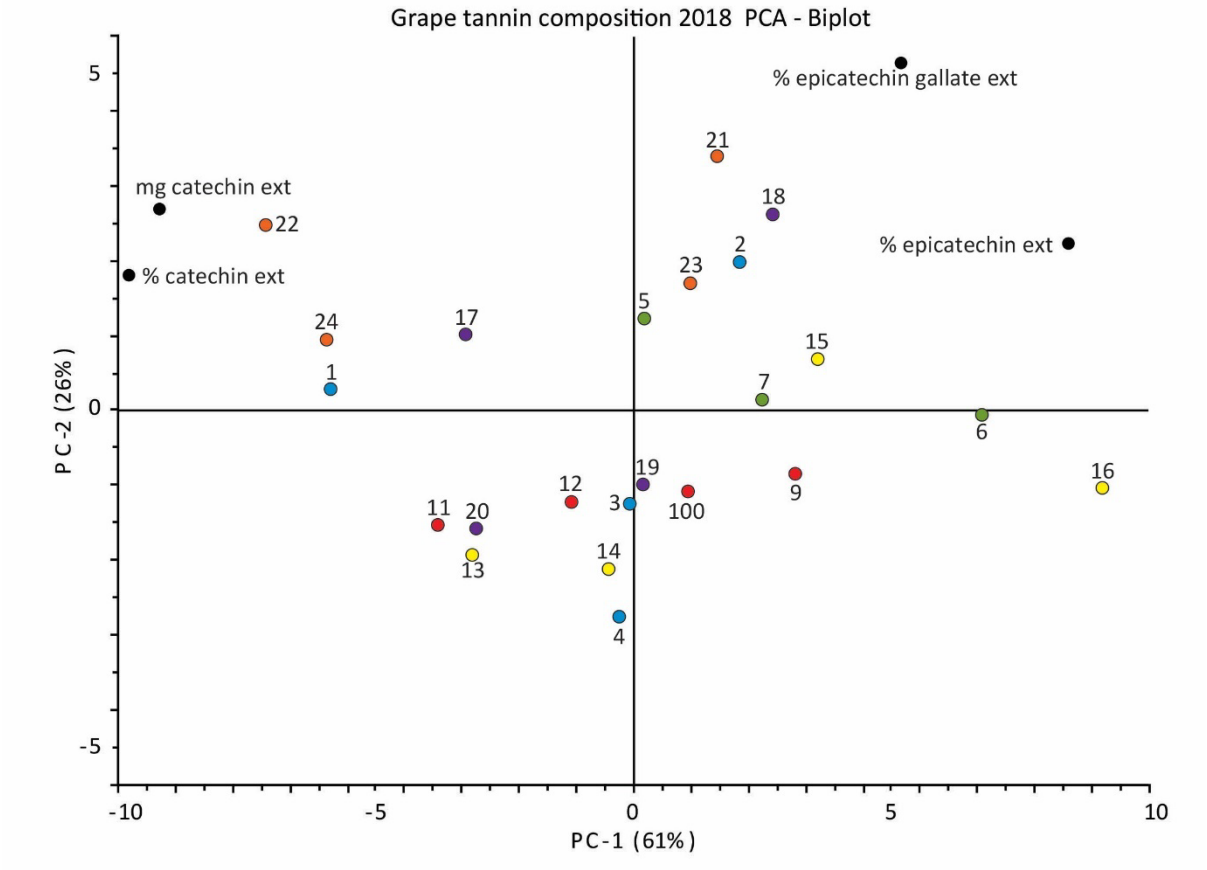


Figure 6.3.10 PCA biplot showing the scores of the 23 different 2018 Barossa Valley Shiraz grape samples from five sub-regions (coloured) and the associated tannin profile parameter loadings in black.

2019 Vintage

The analysis of the tannin composition of the 2019 samples showed that many more parameters were significantly different (p<0.05) among the samples than was observed in 2018 (12 compared to four). PC1 described 45 % of the variation and discriminated samples based on the total amount and percentage of several tannin sub-units (Figure 6.3.11). Total tannins had an influence on the separation on both PC1 and PC2, with those samples in the top right quadrant having the highest concentrations of tannins. PC2 described 29 % of the variation and was influenced by the degree of polymerisation of the tannins and the concentration of epigallocatechin extension units.

When comparing the localisation of the samples from the various sub-regions, the Eden Valley samples are all located on the right of the plot, although they are very well separated on PC2 (Figure 6.3.11). They are associated with higher concentrations and percentages of a number of the tannin sub-units measured, which was also seen in 2018. The grapes from the other sub-regions tend to be well spread across the plot, although three of the four samples from Eastern Edge and Central Grounds were found on the left of the plot, associated with lower concentrations and percentages of a number of tannin sub-units (Figure 6.3.11).

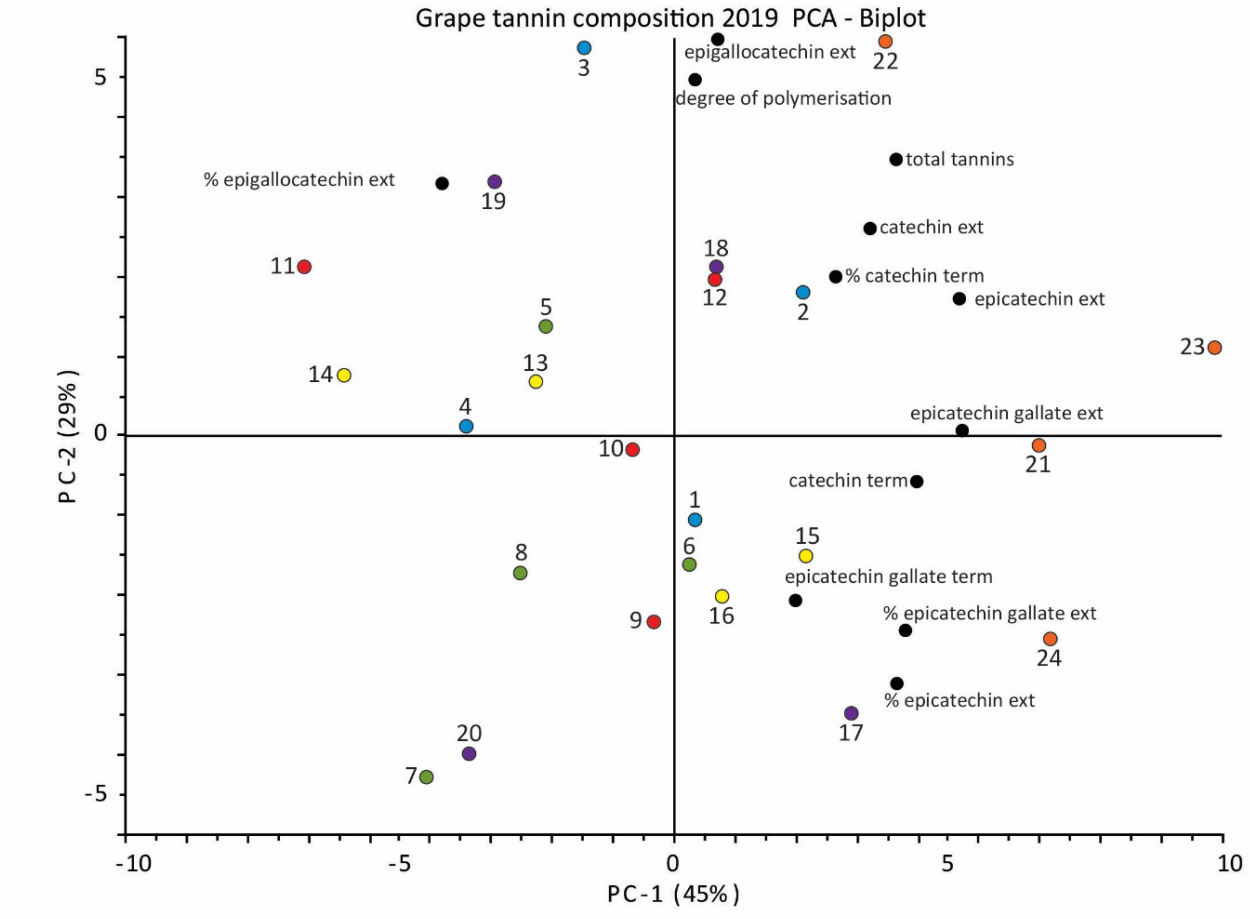


Figure 6.3.11 PCA biplot showing the scores of the 24 different 2019 Barossa Valley Shiraz grape samples from five sub-regions (coloured) and the associated tannin profile parameter loadings in black.

2020 Vintage

Only four of the various tannin measures were significantly different between the samples in the 2020 vintage. When examined by PCA, the first principal component explained 68 % of the total variation and was driven by higher measures of % epigallocatechin extension sub-units on the right of the plot and high % epicatechin extension and % epicatechin gallate extension sub-units on the left (Figure 6.3.12). PC2 distinguished the samples with a high percentage of catechin terminal sub-units towards the top of the plot.

Like the previous vintages, the samples from the Eden Valley sub-region do group together, this time on the left of the plot and are associated with high percentages of epicatechin and epicatechin gallate extension sub-units, but low % epigallocatechin extension sub-units (Figure 6.3.12). The opposite was true for the samples taken from the Eastern Edge and Southern Grounds sub-regions which were all located on the right of the PCA biplot (Figure 6.3.12). The Northern Grounds samples fell into the lower left quadrant of the biplot due to the presence of a high percentage of epicatechin gallate extension sub-units and a low percentage of catechin terminal sub-units. The Central Grounds samples had a low percentage of catechin terminal sub-units and hence were found in the lower half of the PCA plot (Figure 6.3.12).

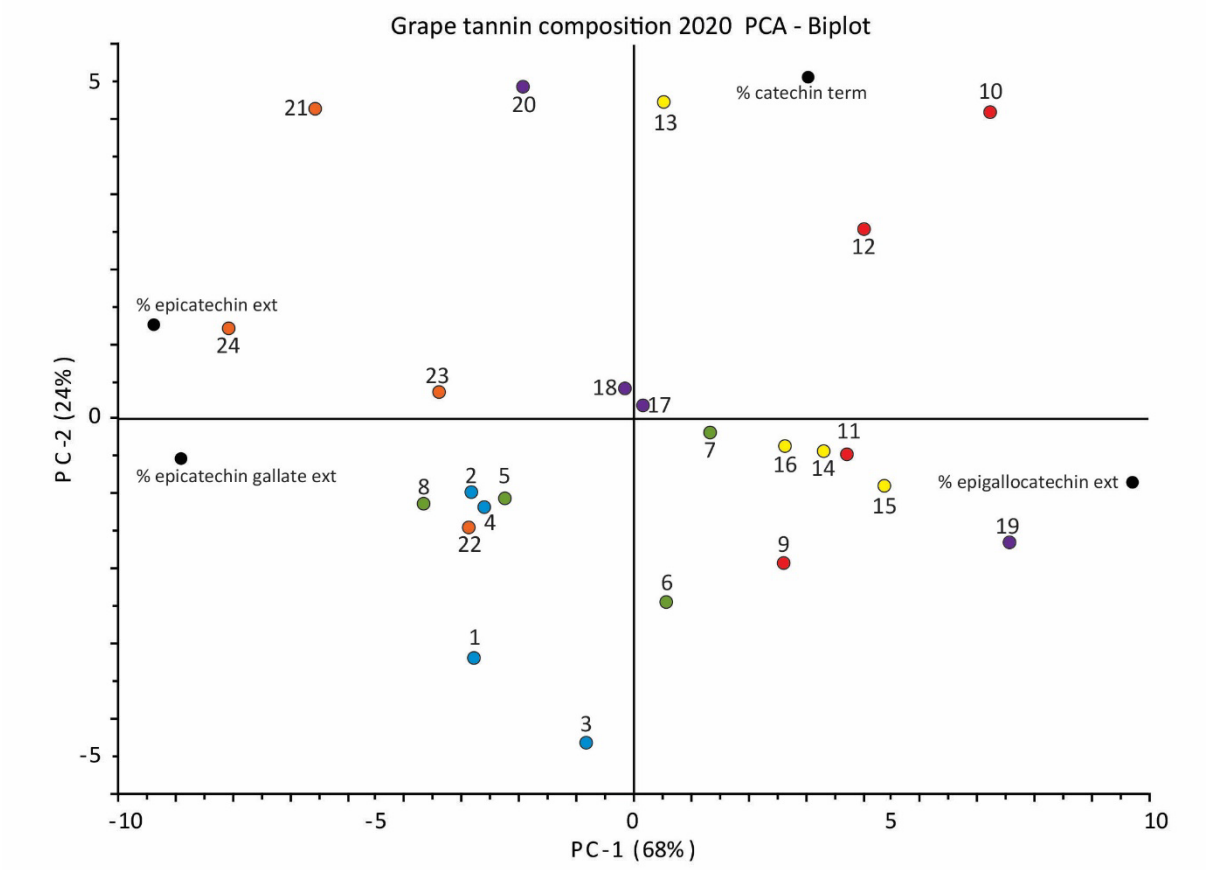


Figure 6.3.12 PCA biplot showing the scores of the 24 different 2020 Barossa Valley Shiraz grape samples from five sub-regions (coloured) and the associated tannin profile parameter loadings in black.

2021 Vintage

In the 2021 vintage, six of the tannins measured were significantly different and these were subjected to a PCA. PC1 described 58 % of the variation and is separating samples based on total tannins, and the concentration of epicatechin, epicatechin gallate and epigallocatechin extension sub-units (Figure 6.3.13). Those samples with higher concentration of these measures were located on the right of the plot. The second PC described 37 % of the variation and was driven by the percentage of epicatechin extension sub-units towards the top of the plot and the amount and percentage of epigallocatechin extension sub-units towards the bottom of the plot (Figure 6.3.13).

The three samples collected from the Western Ridge sub-region grouped on the right side of the plot due to high measures of total tannins and the extension sub-units with loadings on this side of the PCA biplot (Figure 6.3.13). This was the first vintage in which samples from this sub-region grouped in the first two PCs. In contrast, the Eden Valley samples had similar trends in their composition in all vintages and in 2021 were all located in the bottom half of the plot, indicating they had high concentrations and percentage of epigallocatechin (Figure 6.3.13). This was the only vintage in which they were not associated with higher epicatechin gallate extension unit concentrations and/or percentages compared with samples from other sub-regions. Three of the Eastern Edge samples were found on the extreme left of the biplot, driven by lower total tannins.

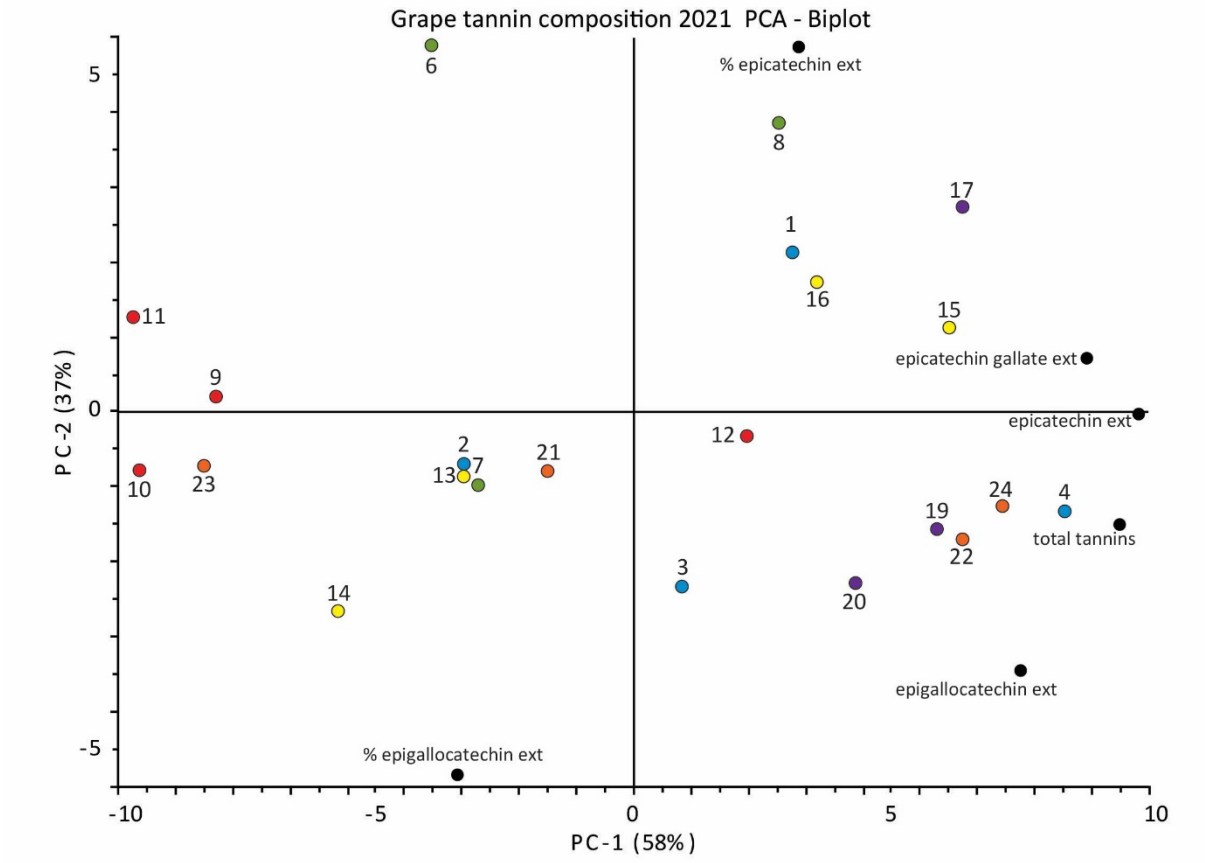


Figure 6.3.13 PCA biplot showing the scores of the 22 different 2020 Barossa Valley Shiraz grape samples from five sub-regions (coloured) and the associated tannin profile parameter loadings in black.

6.3.4. Carotenoids

2018 Vintage

As precursors to norisoprenoids, carotenoids have potential to influence wine volatile composition and sensory properties. The four main carotenoids found in grape berries were quantified in the samples along with two chlorophylls and two pheophytins. All of these compounds were found to vary significantly ($p<0.05$) in the grape samples. Total carotenoids ranged from 3.3 µg/g in Sample 4 to 7.5 µg/g in Sample 12. Lutein was normally found in the highest concentration with β-carotene the second most abundant carotenoid in the grape samples.

Principal component analysis of the carotenoid/chlorophyll profiles was conducted to explore the association and grouping of samples based on these measures (Figure 14). The biplot showed that the main driver on PC1, which explains 63% of the variation, was total carotenoids. This was associated with higher concentrations of all four of the carotenoids measured. The chlorophyll concentrations were also higher in those samples with higher carotenoid concentrations. The Eastern Edge samples had a greater abundance of carotenoids and chlorophylls, as seen by their location on the right of the biplot. In contrast, the Northern Grounds samples were found on the left of the plot, indicating that they had less carotenoids and chlorophylls than the other samples (Figure 6.3.14). The other sub-regions had samples discriminated by both PC1 and PC2 with no obvious grouping.

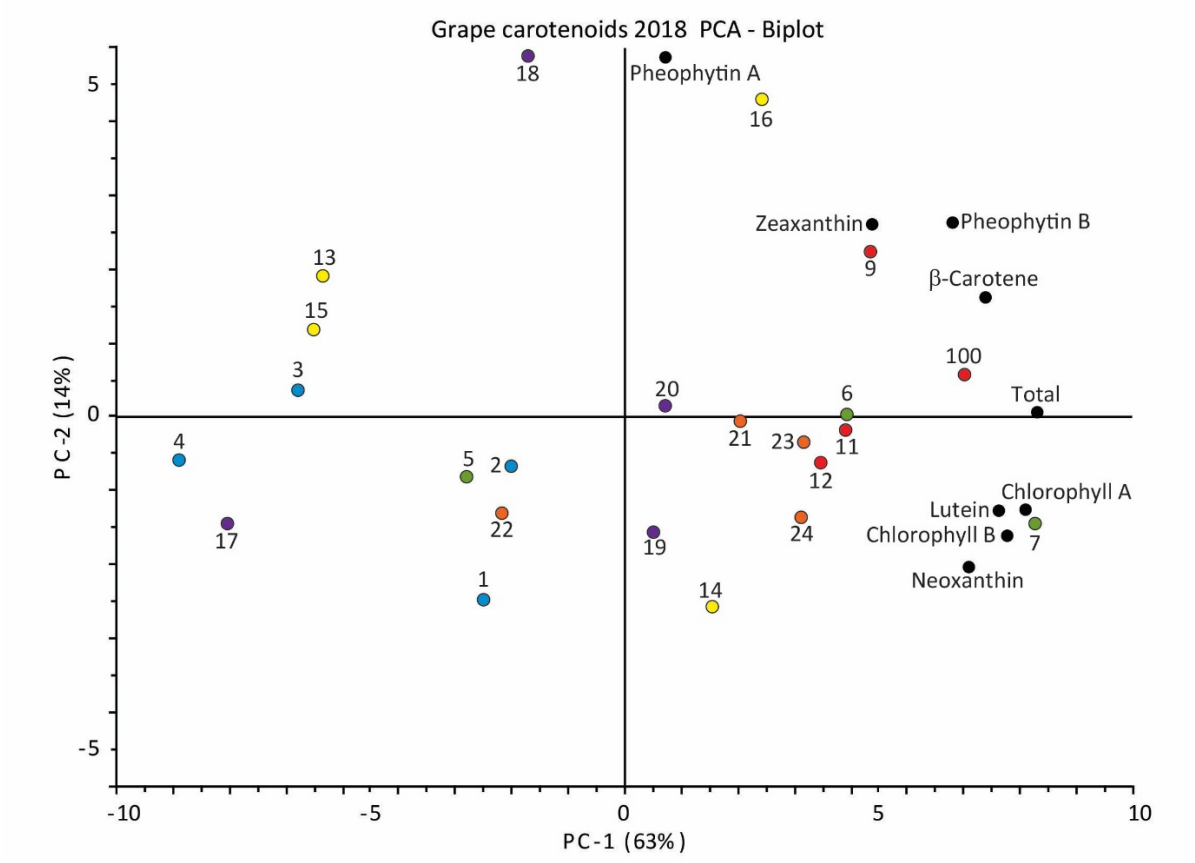


Figure 6.3.14 PCA biplot showing the scores of the 23 different 2018 Barossa Valley Shiraz grape samples from five sub-regions (coloured) and the associated carotenoid profile parameter loadings in black.

2019 Vintage

The PCA of the carotenoid/chlorophyll profiles in the 2019 vintage grapes showed similar trends to those seen in 2018. The main separation on PC1 was driven by the concentration of the total carotenoids, chlorophylls and pheophytins and described 65 % of the total variation. PC2 represented 22% of the variation and was discriminating samples based on the concentration of a couple of unknown carotenoids detected on the chromatograms and the pheophytins (Figure 6.3.15). The Eastern Edge samples were found on the right of the biplot as they had relatively high carotenoid concentrations. The Eden Valley samples were also located on the right of the plot, as was the case for three of the four sites in 2018. Interestingly, the Northern Grounds samples, which were associated with lower carotenoid concentrations in 2018, had more carotenoids and chlorophylls in 2019 compared to the samples from Central Grounds, Southern Grounds and Western Ridge, which were found on the left of the plot (Figure 6.3.15). PC2 discriminated most of the Eden Valley samples from those obtained from the Eastern Edge, with the Eden Valley samples being associated with higher concentrations of the two unknown carotenoids detected in the samples.

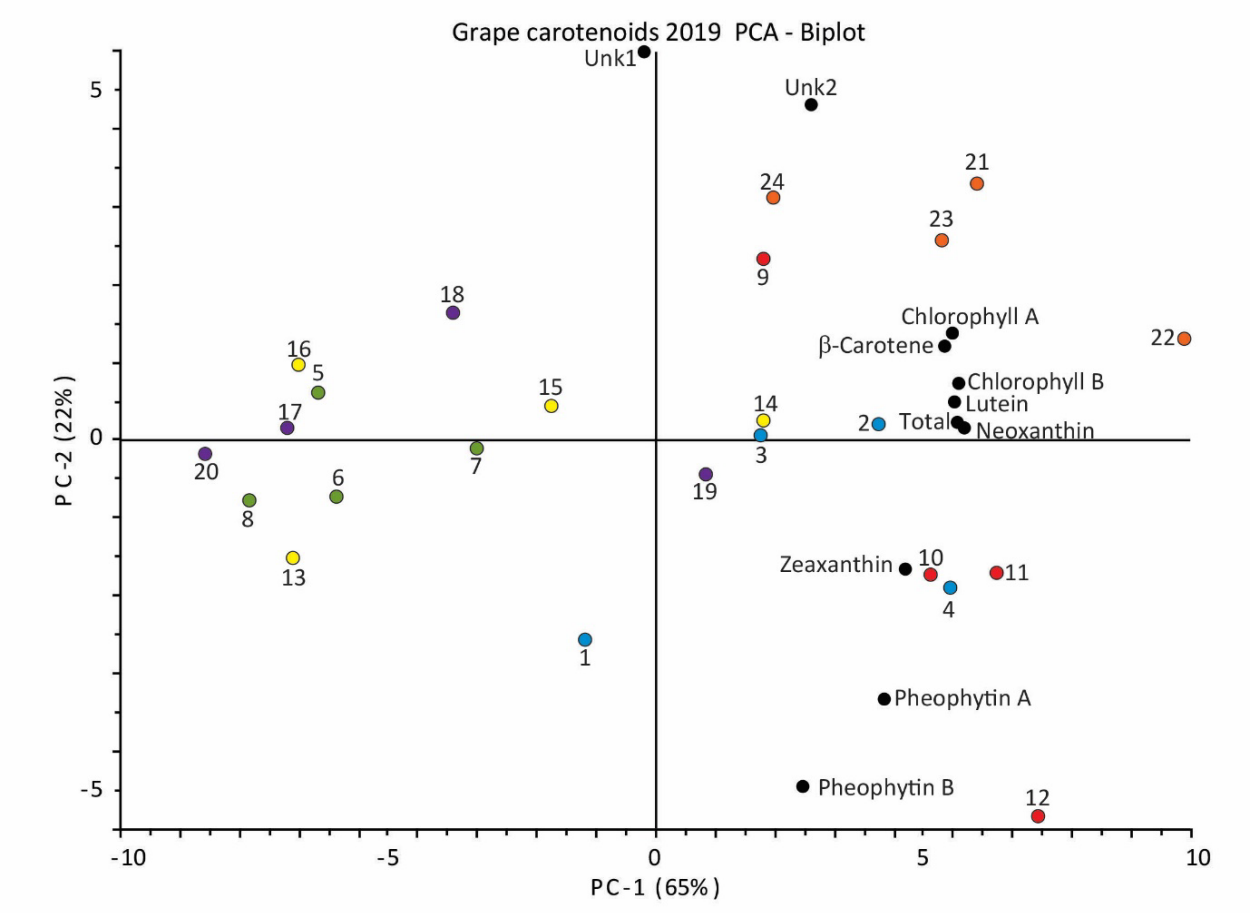


Figure 6.3.15 PCA biplot showing the scores of the 24 different 2019 Barossa Valley Shiraz grape samples from five sub-regions (coloured) and the associated carotenoid profile parameter loadings in black.

2020 Vintage

All of the compounds measured using the carotenoid analysis were significantly different in the 2020 vintage. The results of the PCA showed that the majority of the total variation was described by the first PC (71%) and PC2 added another 16% (Figure 6.3.16). Discrimination of the samples on PC1 was due to higher total carotenoids and chlorophylls, whereas the separation on PC2 was driven by the concentration of two unknown compounds towards the top of the plot and the pheophytins near the bottom. The sub-regions did not group as well as they did in the previous two vintages. The main finding of the PCA was that Sample 24 was an outlier with much higher concentrations of chlorophylls, pheophytins, β-carotene and lutein than the other samples (Figure 6.3.16). Grouping of sub-regional samples was not as apparent in the carotenoid measures in 2020 compared to the previous two vintages. More often than not, two or three of each set of four sub-regional samples were found on different sides or top and bottom halves of the biplot to the other samples from that sub-region. This makes it difficult to make generalisations about carotenoid composition and sub-region for this vintage.

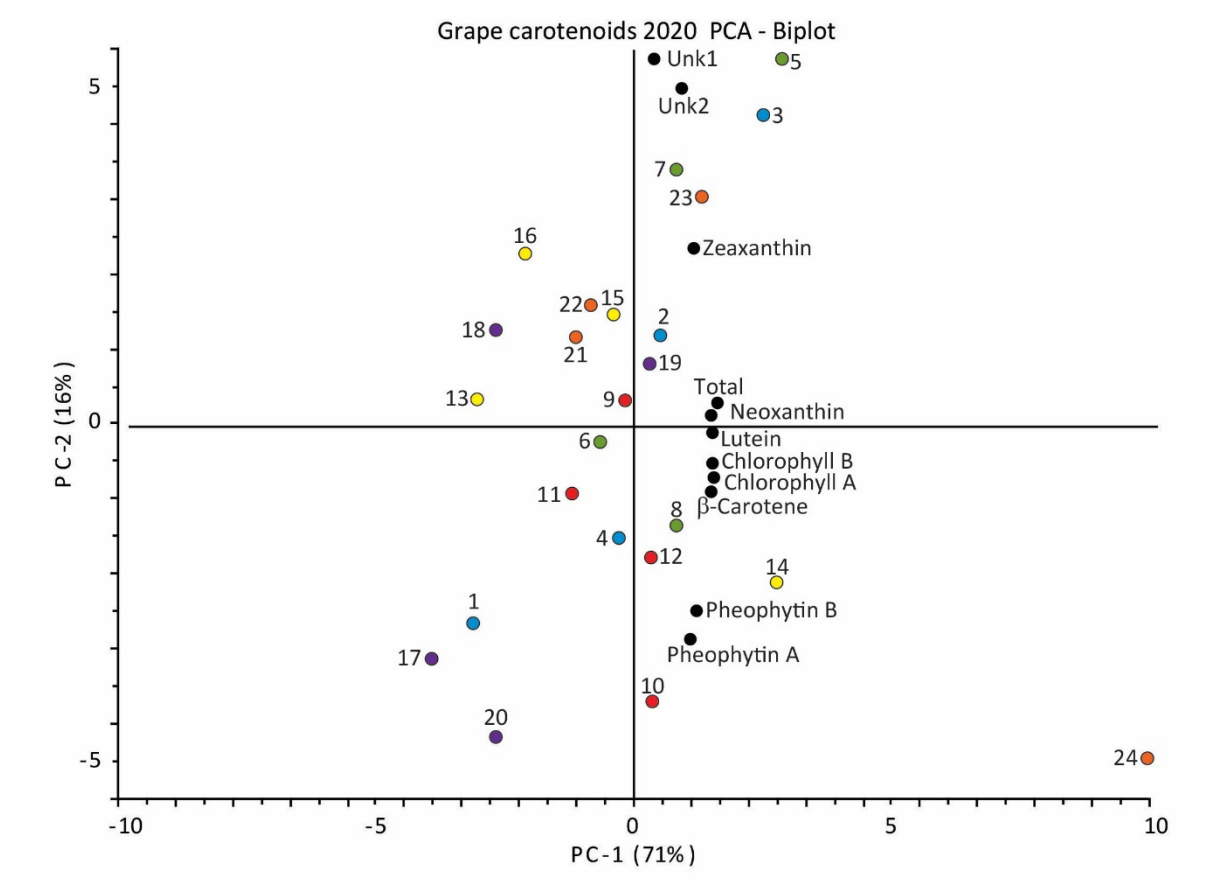


Figure 6.3.16 PCA biplot showing the scores of the 24 different 2020 Barossa Valley Shiraz grape samples from five sub-regions (coloured) and the associated carotenoid profile parameter loadings in black.

2021 Vintage

Again, the carotenoids, chlorophylls and pheophytins were all significantly different between the grape samples collected in the 2021 vintage. PCA revealed a similar pattern to previous vintages with regards to the loadings; PC1 (66%) discriminated samples based on total

carotenoids and chlorophylls to the right and PC2 (19%) separated samples with high concentrations of the two unknown compounds towards the top of the plot and the pheophytins towards the bottom (Figure 6.3.17). There was an outlier in 2021, with Sample 7 located at the lower right of the plot as it contained high concentrations of pheophytins. The Eden Valley and Western Ridge samples were found in the top half of the biplot because they contained relatively high concentrations of the two unknown compounds measured in the samples (Figure 6.3.17). However, none of the other sub-regional samples all grouped in similar area of the biplot. The inconsistency across vintages and lack of sub-regional trends in the carotenoid data suggest that micro-climatic or vineyard management effects dominate the plasticity of this phenotype, meaning that any sub-regional factors influencing the production of carotenoids were not observed. It is most likely that light interception by the berries influences this phenotype the most, which is probably driven by vineyard factors more than regional differences.

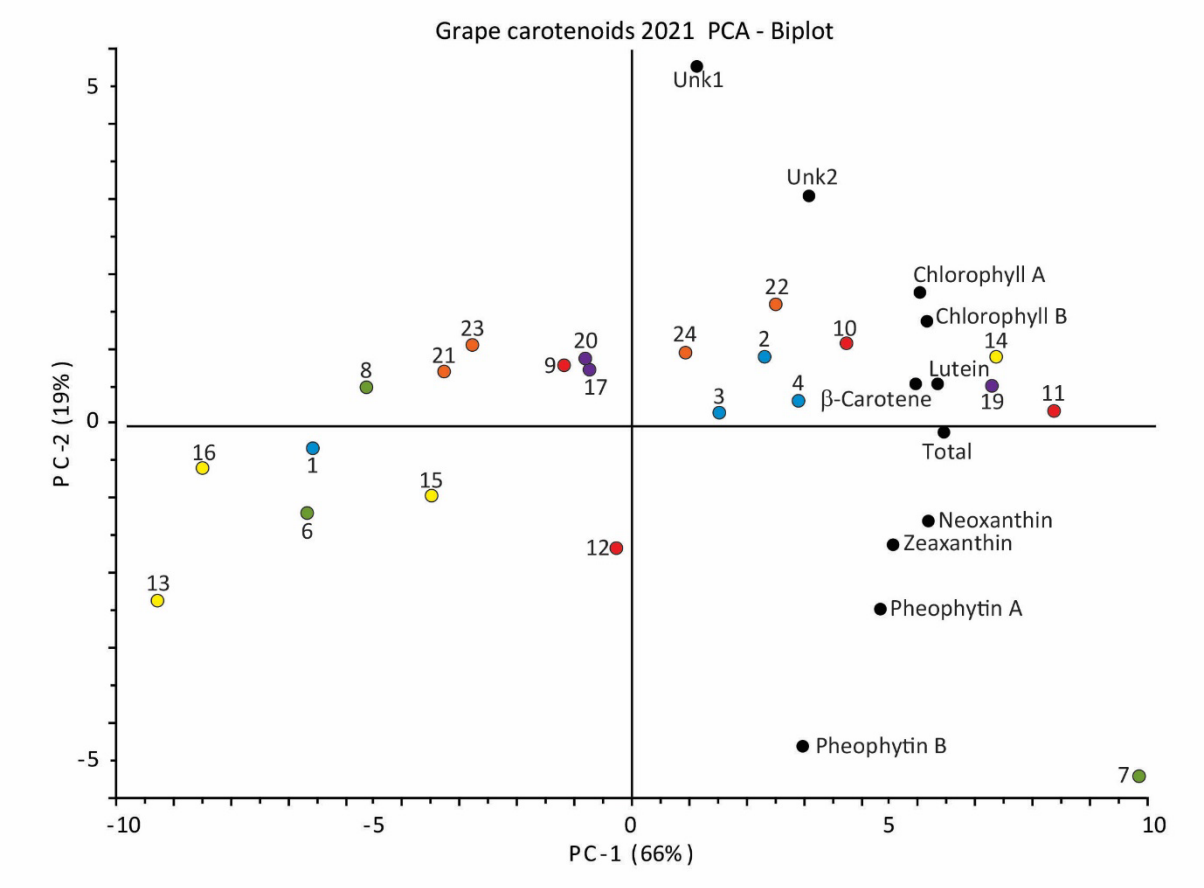


Figure 6.3.17 PCA biplot showing the scores of the 22 different 2021 Barossa Valley Shiraz grape samples from five sub-regions (coloured) and the associated carotenoid profile parameter loadings in black.

6.3.5. Grape volatile compounds

2018 Vintage

The major volatile compounds extracted from the headspace above crushed berries were also measured in the grape samples. In general, a profile of the volatile compounds from crushed grapes is much simpler than the profile of volatiles from a wine and this is due to the complexity added by the yeast during fermentation. Nevertheless, the volatile composition of the fruit should reflect the changes in metabolism in the berries as influenced by factors such as climate, soil properties, management, harvest timing and rootstock. This in turn will influence wine style by altering the source of nutrients or precursors of the yeast or by altering yeast metabolism.

A total of 101 volatile compounds were quantified in the grapes and 68 of these were significantly different among the samples ($p<0.05$). The significantly different compounds were used in a PCA to visualise associations between samples and volatile composition (Figure 6.3.18). The first two PCs only described 33% of the total variation (PC1 = 18% and PC2 = 15%). Some of the sub-regions were discriminated on the first two PCs. The Northern Grounds samples were clustered in the bottom right quandrant of the plot and they were associated with higher concentrations of some esters, hexanal and 2-ethyl hexanol and negatively associated with benzaldehyde and some sesquiterpenes and norisoprenoids (Figure 6.3.18). The Eden Valley samples were located on the left of the plot where the loadings for cyclohexane oxide, 3-ethylthiophene and β-cyclocitral were located. The Central Grounds grapes somewhat overlapped those from Northern Grounds but were found more towards the centre of PC1 and were driven mainly by separation on PC2. These samples had higher concentrations of styrene and phenol. The Southern Grounds and Western Ridge samples were mostly found in the upper half of the plot, associated with high concentrations of 2-butanone, 2-methyl-3,4-dihydro-2H-pyran, 1-pentanol and two sesquiterpenes (Figure 6.3.18). The Eastern Edge grape parcels were found mainly on the left of the plot on PC1, but Sample 9 was an outlier, being located in the top right. In general, the grape volatile analysis showed the tightest grouping of the sub-regions in comparison to the other grape measures.

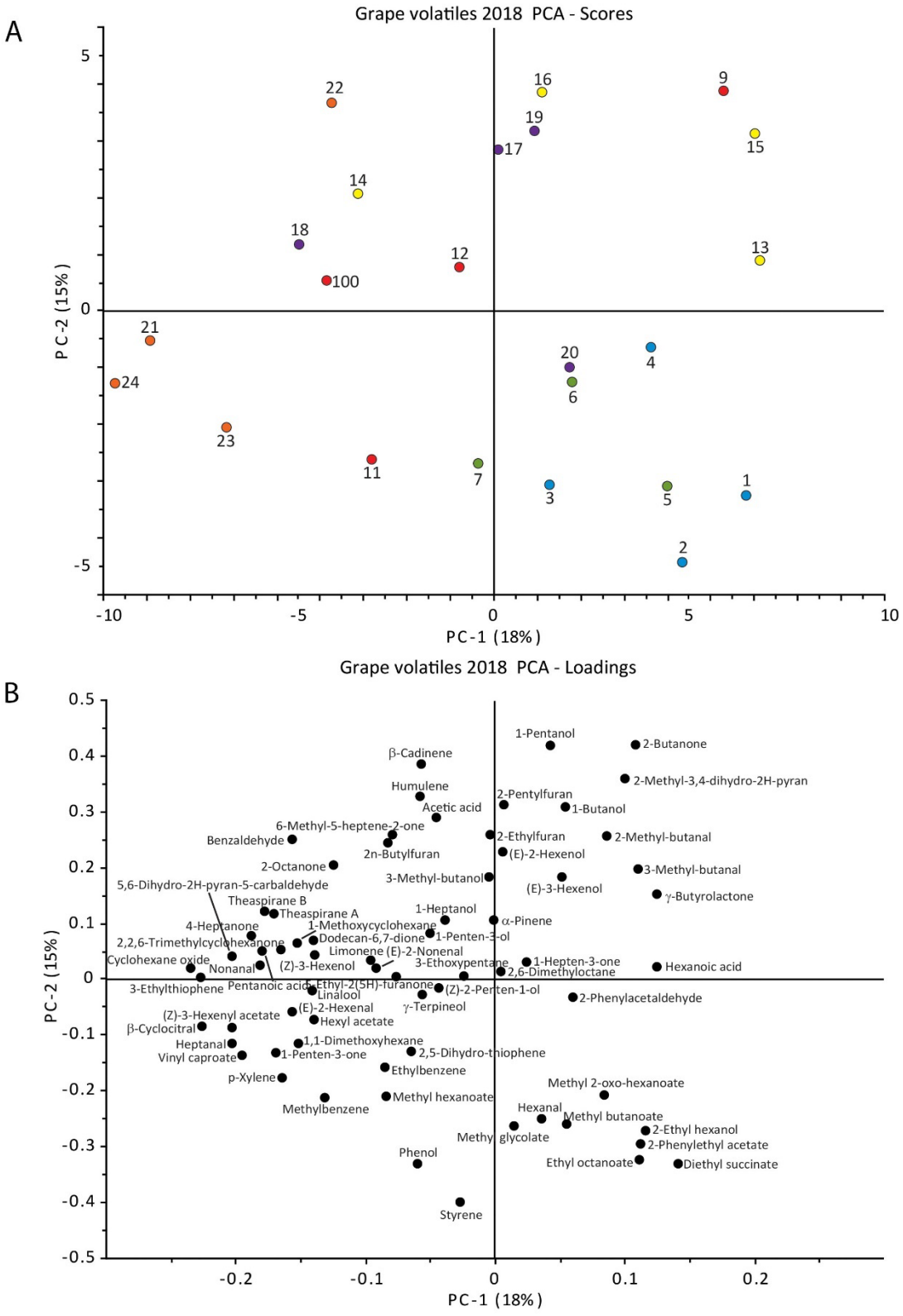


Figure 6.3.18 PCA scores (A) and loadings (B) plots of 23 different 2018 Shiraz grape samples from six sub-regions across the Barossa Valley, South Australia and the significantly different grape volatile compounds measured in these samples.

2019 Vintage

The same volatile compounds were targeted for quantification in the 2019 grape samples, and 97 of the 101 were above the level of detection in these samples. Of the 97 compounds detected, 73 volatile compounds were significantly different ($p<0.05$) among the grape samples.

Similar to 2018, the PCA resulted in a model that only described 38 % of the variation on the first two PCs. Nevertheless, some clear grouping of samples from sub-regions was observed (Figure 6.3.19). PC1, representing 25 % of the variation, discriminated the samples from the Central Grounds and Western Ridge from those in the Northern Grounds based on their volatile profiles. The Northern Grounds samples were located on the lower left quadrant of the plot and these were associated with higher concentrations of diethyl succinate, styrene, ethyl octanoate and 5-methyl-2-furfural (Figure 19). While those from the Western Ridge and Central Grounds were found on the right of the plot and had higher concentrations of a range of volatile compounds including 1-octen-3-one and cyclohexane oxide. PC2 (14 % of the variation), separated the samples from Eden Valley at the top of the plot from the parcels obtained from the Northern Grounds and Eastern Edge at the bottom of the plot (Figure 6.3.19). The Eden Valley samples are characterised as having higher concentrations of theaspiranes, (E)-2-nonenal and hexyl acetate, and lower concentrations of a number of compounds including the sesquiterpenes humulene and β-cadinene. Consistent with 2018, the volatile compound analysis provided the grape composition data set with the best discriminating power among the different sub-regions.

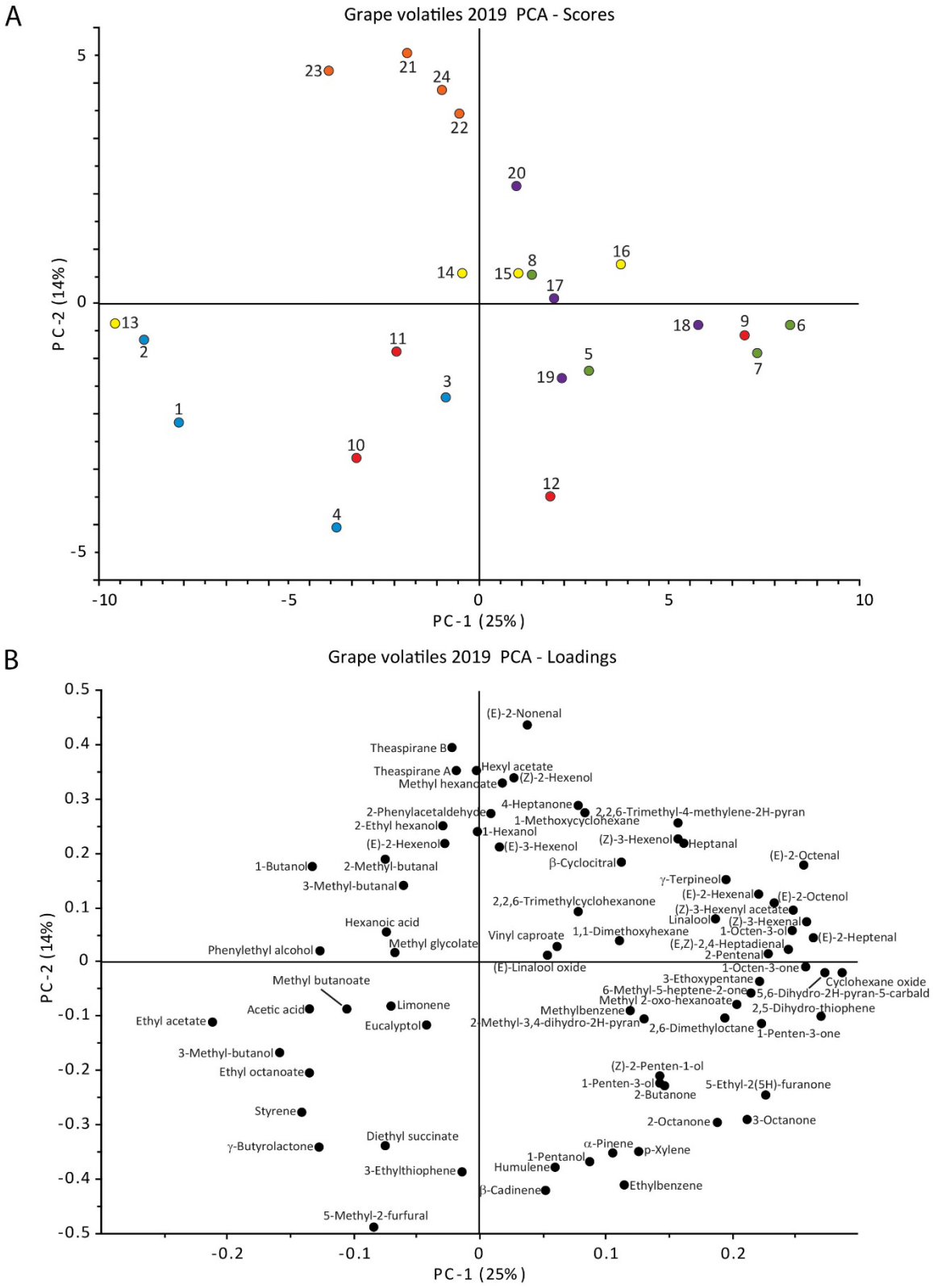


Figure 6.3.19 PCA scores (A) and loadings (B) plots of 24 different 2019 Shiraz grape samples from six sub-regions across the Barossa Valley, South Australia and the significantly different grape volatile compounds measured in these samples.

2020 Vintage

There were slightly fewer volatile compounds significantly different among the sub-regional samples in 2020 compared to 2019 with 71 falling into this category. When this data set was subjected to PCA, the first two PCs described more of the variation in 2020 than in the previous two vintages, with PC1 describing 30 % of the variation and PC2 accounting for 13 % of the variation (Figure 6.3.20). Again, sub-regions were generally discriminated well with the grape volatile profiles with clear groupings of the samples from Northern Grounds, Central Grounds, Western Ridge and Eden Valley. With regards to the Eastern Edge and Southern Grounds samples, in both cases three of the four samples form a distinct cluster, although the Eastern Edge samples are very much located around the origin.

The separation on PC1 is driven mainly by samples with higher concentrations of aliphatic alcohols and aldehydes (especially with 8 carbons) as well as (*E*)-linalool oxide on the right of the plot. The left of the plot is associated with higher concentrations of theaspiranes, 4-heptanone and 1-methoxycyclohexane. The samples from the Northern Grounds, Central Grounds and Western Ridge were all located on the right of the PCA plot, whereas Sample 16 from Southern Grounds was an outlier on the extreme left of the plot (Figure 6.3.20). Some of the sub-regions were also discriminated on PC2 with the Northern Grounds samples found in the upper half and the Eden Valley samples in the lower half of the PCA plot. The volatile compounds associated with the samples towards the top of the plot do not have a common functional group and include 2,4,-hexadienal, 5,6-dihydro-2H-pyran-5-carbaldehyde, phenol and pentanoic acid (Figure 6.3.20). The compounds found in higher concentrations in the samples in the lower half of the plot include the esters hexyl acetate, methyl butanoate, ethyl acetate and (*Z*)-3-hexenyl acetate, as well as benzyl alcohol. This was the second vintage in which high hexyl acetate concentrations have been associated with the Eden Valley samples.

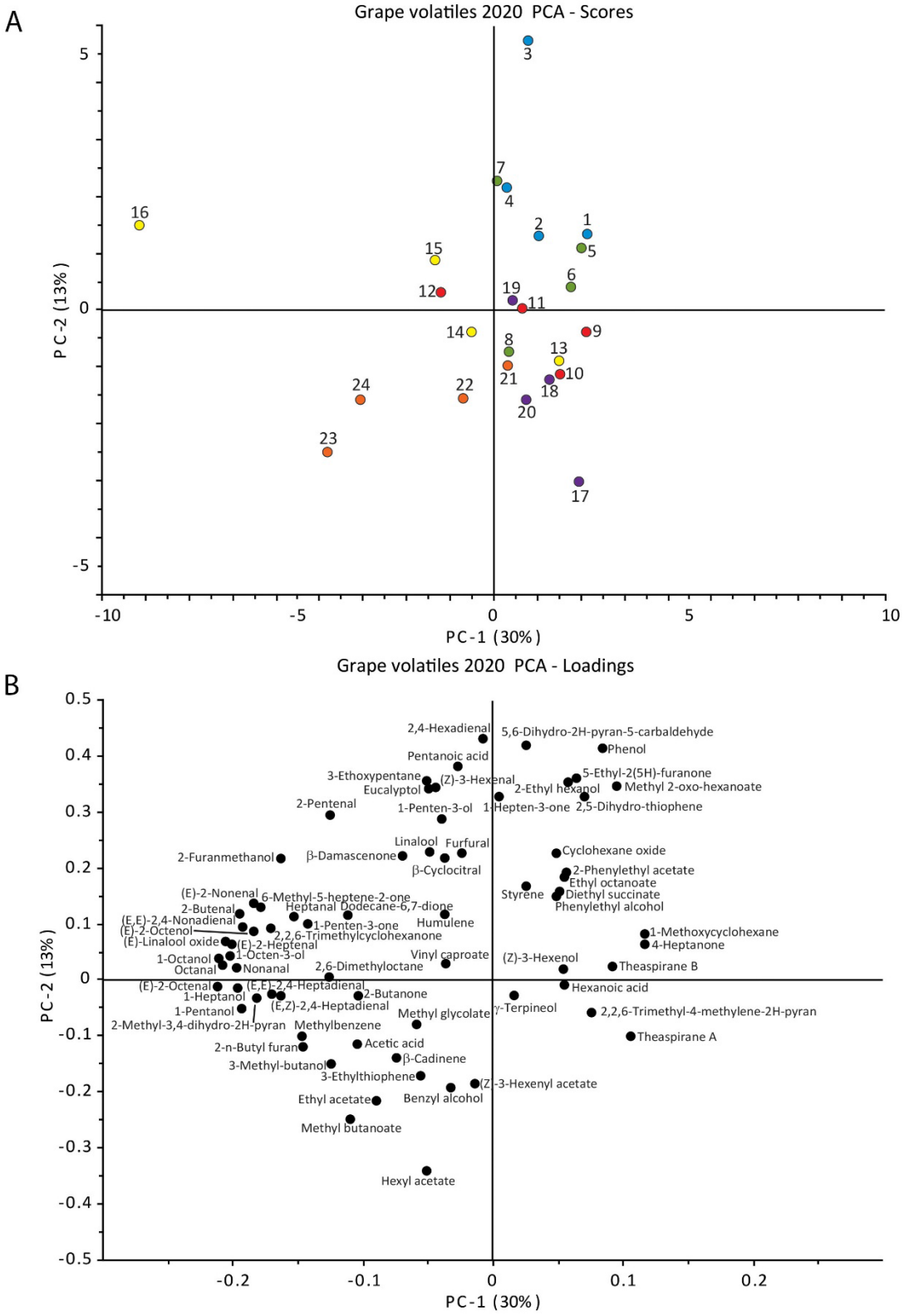


Figure 6.3.20 PCA scores (A) and loadings (B) plots of 24 different 2020 Shiraz grape samples from six sub-regions across the Barossa Valley, South Australia and the significantly different grape volatile compounds measured in these samples.

2021 Vintage

Ninety-three grape volatile compounds were significantly different between the samples from the various sub-regions in 2021. For the fourth year the grape volatile profiles were able to discriminate some of the sub-regional sites when subjected to PCA (Figure 6.3.21). PC1 described 29% of the total variation and separated the Northern Grounds samples on the right of the plot from the Eastern Edge samples on the left. PC2 described 18% of the variation and was able to discriminate the Eden Valley samples towards the top of the plot from the Northern Grounds samples towards the bottom. Interestingly, there may be an interaction between the first two PCs with the sub-regions falling into diagonal groupings from Northern Grounds in the bottom right quadrant to the Southern Grounds samples located more towards the upper left of the plot (Figure 6.3.21).

Separation on PC1 is driven by a number of saturated and unsaturated aliphatic aldehydes located on the extreme right of the plot (Figure 6.3.21). So, the samples located in this region, especially Sample 4, had higher concentrations of these compounds. In contrast, the samples on the left of the plot had lower concentrations of these aldehydes and higher amounts of methylbenzene, α-pinene and some aliphatic alcohols. Sub-regional samples located towards the top of the PCA plot had a greater abundance of the aromatic compounds p-xylene and ethylbenzene as well as the cyclic compound 1-methoxycyclohexane (Figure 6.3.21). Those samples near the bottom of the plot had higher concentrations of longer chain and branch-chained aldehydes as well as 2-butanone, 2,6-dimethyloctane and methyl butanoate.

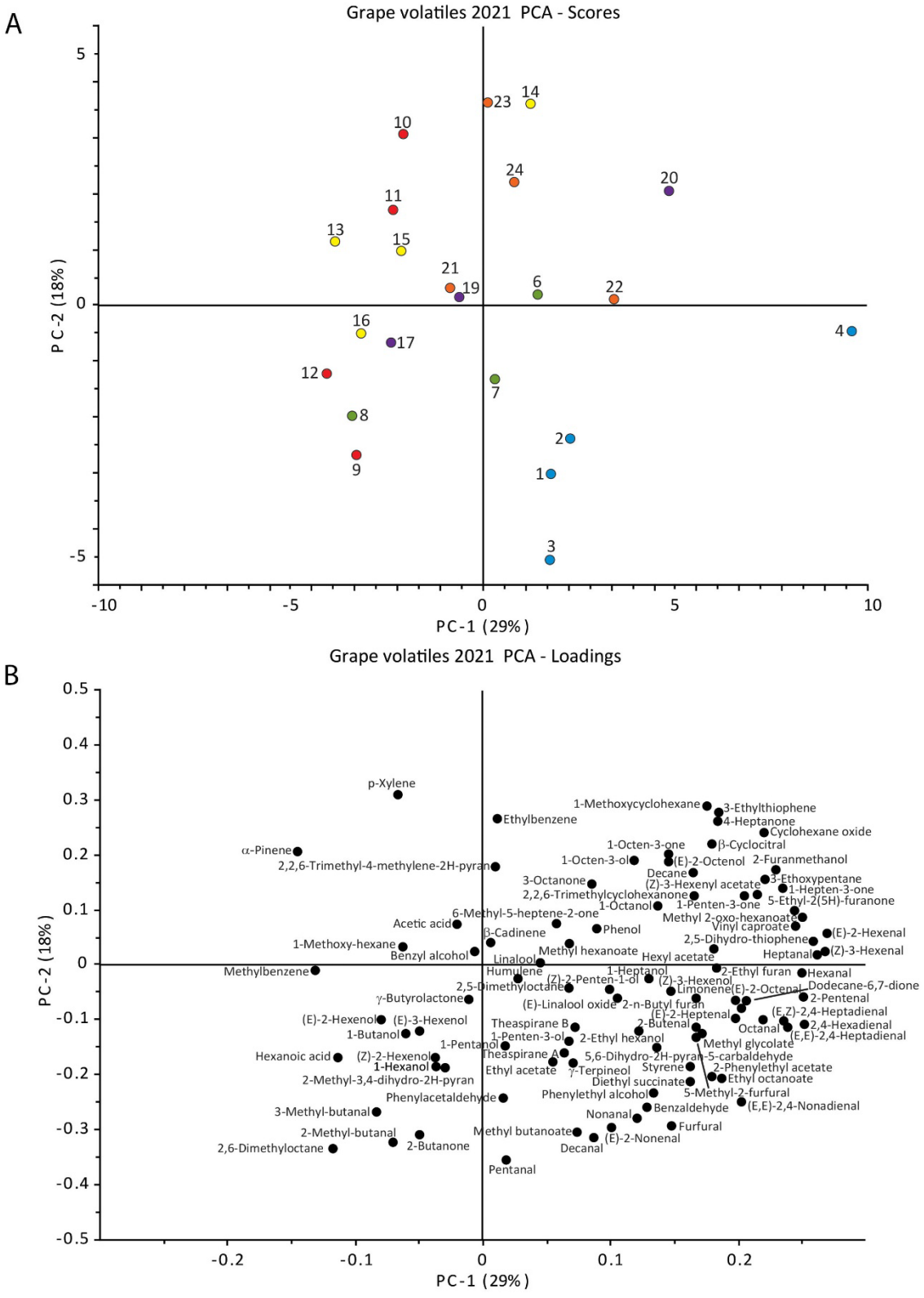


Figure 6.3.21 PCA scores (A) and loadings (B) plots of 22 different 2021 Shiraz grape samples from six sub-regions across the Barossa Valley, South Australia and the significantly different grape volatile compounds measured in these samples.

6.3.6. Grape bound volatile compounds

2018 Vintage
Some wine volatile compounds can have a pool of precursors that exist as non-volatile compounds in the grapes. To assess this aroma potential in the grapes, individual bound volatiles were quantified using solid phase extraction and acid hydrolysis of the bound forms and a liquid extraction before GC-MS analysis. The method allowed the detection of volatile compounds released from the bound volatile fraction and 75 of these compounds were quantified in the extracts. A subset of 56 compounds were found in significantly different ($p<0.05$) concentrations among the samples and the data set was subject to PCA (Figure 6.3.22). Because of the difficulty in placing the names of the compounds in the loadings plot in Figure 6.3.7B, the names of the numbered compounds are listed in Table 6.3.1.

The first two PCs described 59% of the variation. PC1 (37%) separated the samples based on the abundance of many of the bound volatiles as can been seen by the large number of compounds clustered on the right of the plot (Figure 6.3.22). However, there was also a subset of compounds that group at the bottom of the plot that were responsible for driving the separation on PC2 (22%). There was no general similarity in the functional groups and/or putative origin of these clustered compounds. There were some trends seen in the co-location of the sub-regional samples in the PCA plot. Three of the four Eastern Edge samples were located on the extreme right of the plot, indicating that they had a greater abundance of many of the bound volatiles than the other grape parcels (Figure 6.3.22). All the Western Ridge samples were also on this side of the PCA, indicating they tended to have more of these compounds than those samples located on the left of the plot. The Central Grounds samples grouped around the origin of PC1 with most of the Eden Valley, Southern Grounds and Northern Grounds samples located to the left of the plot, indicating they had lower concentrations of bound volatiles than those on the right. PC2 discriminated a few specific samples (Figure 6.3.22). It discriminated Samples 9 and 12 from the Eastern Edge and Samples 4, 6 and 15 from the other samples in their sub-regions.

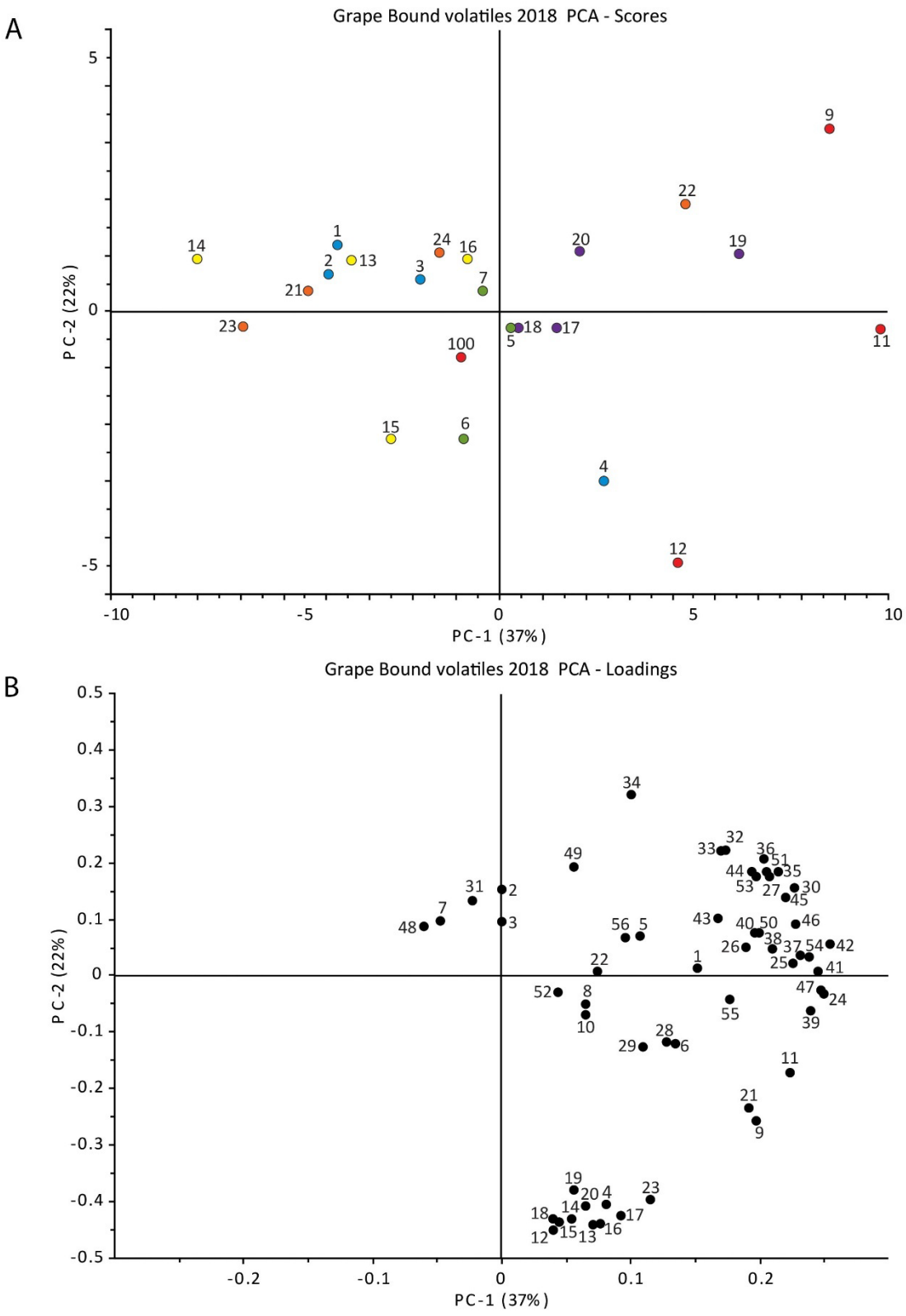


Figure 6.3.22 PCA scores (A) and loadings (B) plots of 23 different 2018 Shiraz grape samples from six sub-regions across the Barossa Valley, South Australia and the significantly different grape bound volatile compounds measured in these samples.

2019 Vintage

The bound volatile analyses in 2019 increased the number of compounds in the profiles to 100, with 31 new compounds detected, but six quantified in 2018 were not above the limits of detection in 2019. Statistical analysis of the 100 compounds showed that 88 of the 100 were significantly different among the sub-regional grape samples, and these were subject to PCA.

PC1 represented 31% of the variation and was discriminating the samples based on the concentration of most of the bound volatiles as can be seen by the localisation of most of the compounds on the left of the plot (Figure 6.3.23). PC2 described 20 % of the variation and the separation on this PC was driven by two subsets of compounds located on the top left or bottom left of the plot. There tended to be more monoterpenes in the cluster located top left, and more norisoprenoids in the bottom half of the plot (Figure 6.3.23). Similar to 2018, there was little indication of any sub-region-based grouping of the grape samples. The only incidence where all the samples from one area were found on one side of either of the first two PCs was the localisation of the samples from Western Ridge in the lower half of the plot, although they were well separated on PC1 (Figure 6.3.23). The data from 2018 and 2019 suggest that bound volatile profiles are the measures less likely to discriminate samples based on their sub-regional location.

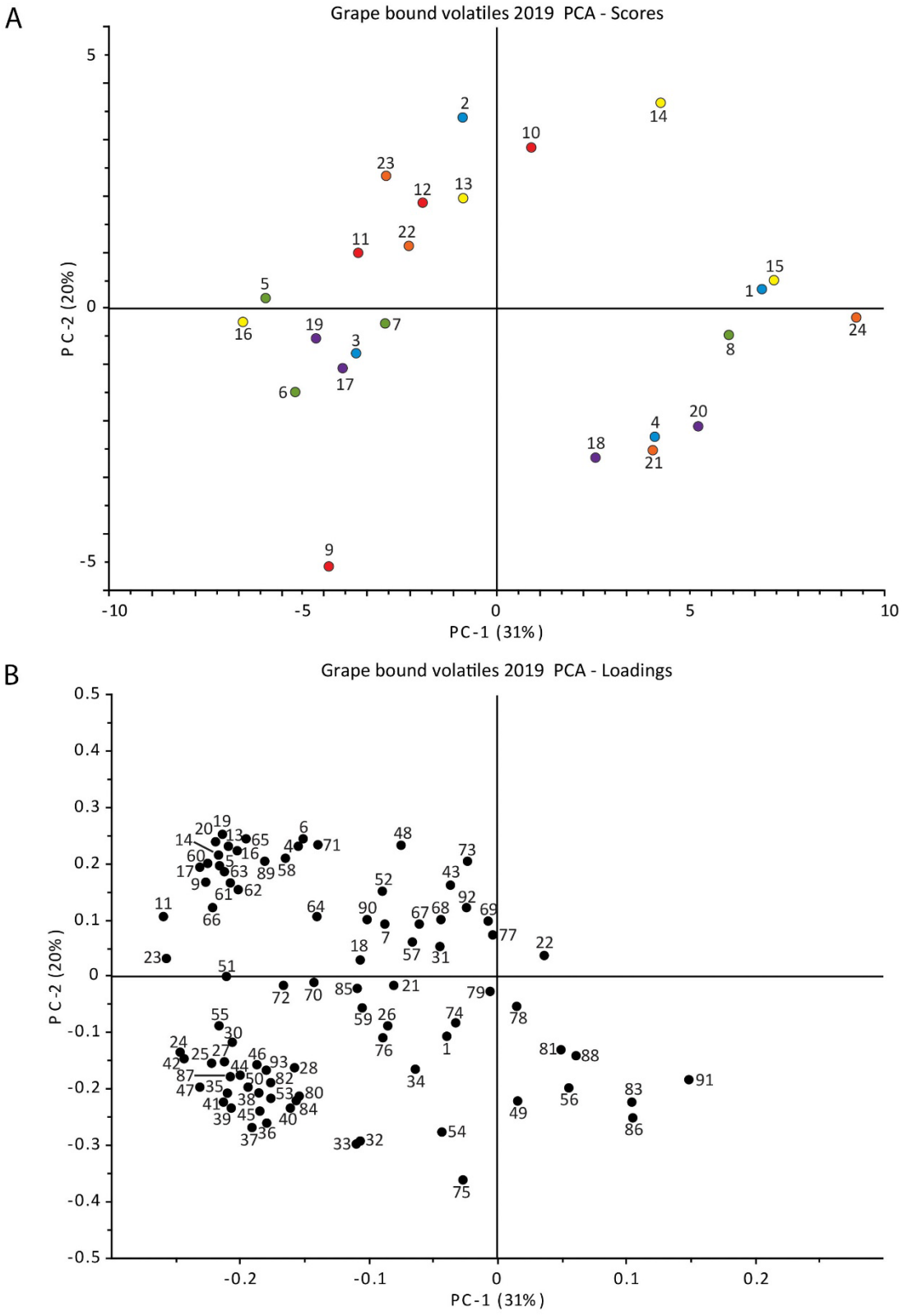


Figure 6.3.23 PCA scores (A) and loadings (B) plots of 24 different 2019 Shiraz grape samples from six sub-regions across the Barossa Valley, South Australia and the significantly different grape bound volatile compounds measured in these samples.

Vintage 2020

In the 2020 samples, 106 bound volatile compounds were targeted for quantification, and 19 of these were below the limits of detection. The 87 compounds quantified were tested to see if they were significantly different among the samples and 84 were significant at the $p<0.05$ level.

Principal component analysis showed that the bound volatile compound profiles have the potential to group the samples based on sub-region, which was not obvious from the first two vintages examined (Figure 6.3.24). PC1 described 32 % of the variation and PC2 explained 24 % of total variation. The discrimination of samples on PC1 was driven by the abundance of some monoterpenes, including two linalool oxides, aromatic compounds (4-methyl benzaldehyde, 4-ethyl benzaldehyde and methyl salicylate) and norisoprenoids on the right of the plot. Samples on the left are associated with higher concentrations of 2-ethenyltetrahydro-2,6,6-trimethyl-2H-pyran, 2-isopentyl-1,3,5-trimethylbenzene and ethyl 4-ethoxybenzoate. On PC2, samples near the top of the plot had higher concentrations of a number of norisoprenoids and medium chain fatty acids, whereas those at the bottom of the plot had more 1,3-dihydro-5-propyl-isobenzofuran, (*E*)-2-hexenal, 3-oxo-α-ionol and 8-hydroxycoumarin. Interestingly, two of the sub-regions showed grouping of samples on the left of the PCA plot, namely Central Grounds and Western Ridge (Figure 6.3.24). The Eden Valley samples also clustered together in the lower left of the plot (Figure 6.3.24). Three of the Southern Grounds samples were on the far right of the plot, being associated with higher concentrations of monoterpenes and aromatic compounds, but the other sample was located distantly on the left of the plot. Three of the four Northern Grounds and Eastern Edge samples were found on the right or top of the plot respectively (Figure 6.3.24), indicating a degree of similarity of the bound volatile compound profiles between these samples. Why the 2020 vintage should result in closer chemical composition among the samples within a sub-region is unknown, but it suggests these measures may be indicators of geospatial differences in some cases.

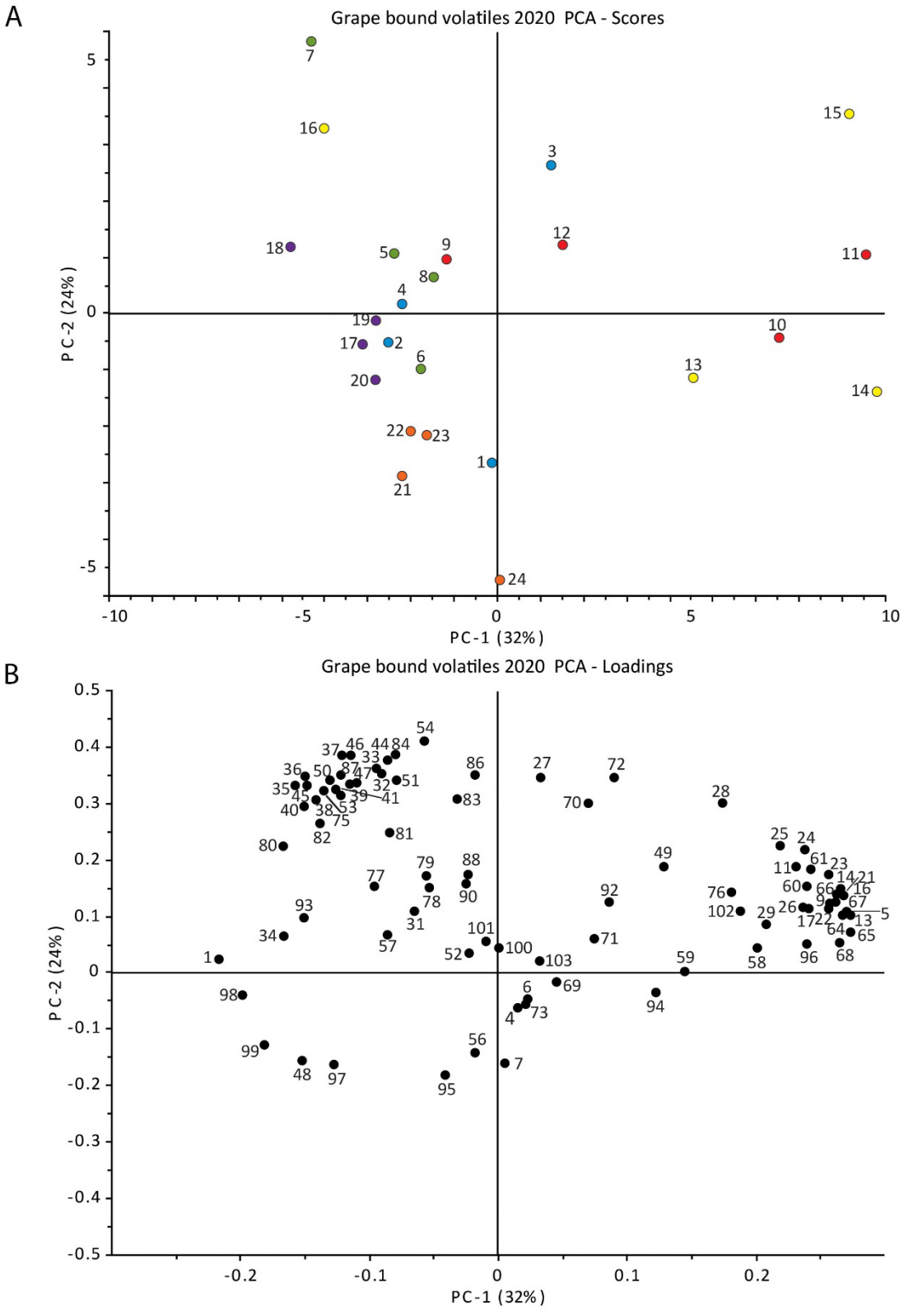


Figure 6.3.24 PCA scores (A) and loadings (B) plots of 24 different 2020 Shiraz grape samples from six sub-regions across the Barossa Valley, South Australia and the significantly different grape bound volatile compounds measured in these samples.

Vintage 2021

The same 106 bound volatile compounds targeted in 2020 were also analysed in 2021 and 83 were above the detection threshold. Statistical analysis found that 79 were significantly different among the samples at the $p<0.05$ level.

The clustering of the sub-regional samples was the best seen for any of the vintages. The separation was most apparent on PC2, which explained 22 % of the data, but a couple of the sub-regions were also discriminated on PC1, which accounted for 27 % of the total variation (Figure 6.3.25). The separation on PC1 was driven by the concentration of norisoprenoids on the right of the plot and aromatic compounds such as benzoic acid, methyl 2-hydroxy-4-methylbenzoate and 4-vinylphenol. This PC discriminated the Eden Valley samples from the Western Ridge samples (Figure 6.3.25). PC2 separates samples with high concentrations of monoterpenes and aromatic compounds at the top of the plot from those with higher concentrations of benzothiazole, 2-hexanol, 3-hexanone, 3-hydroxy-β-damascone, 3-oxo-α-ionol and 2-pentyl furan at the bottom of the plot. The samples from Northern Grounds and Central Grounds were located on the bottom of the plot and were discriminated from the Eastern Edge, Southern Grounds and Western Ridge samples on the upper half of the plot (Figure 6.3.25). Like the 2020 vintage, the ability of the bound volatile compound profiles from 2021 to cluster samples from the same sub-region is encouraging, suggesting that there are underlying variables among the sub-regions that can influence this aspect of berry composition. Overlaying these data with the re-analysis of the geospatial clustering would be an interesting test of the hypothesis that this can drive the bound volatile compound profiles in Shiraz berries.

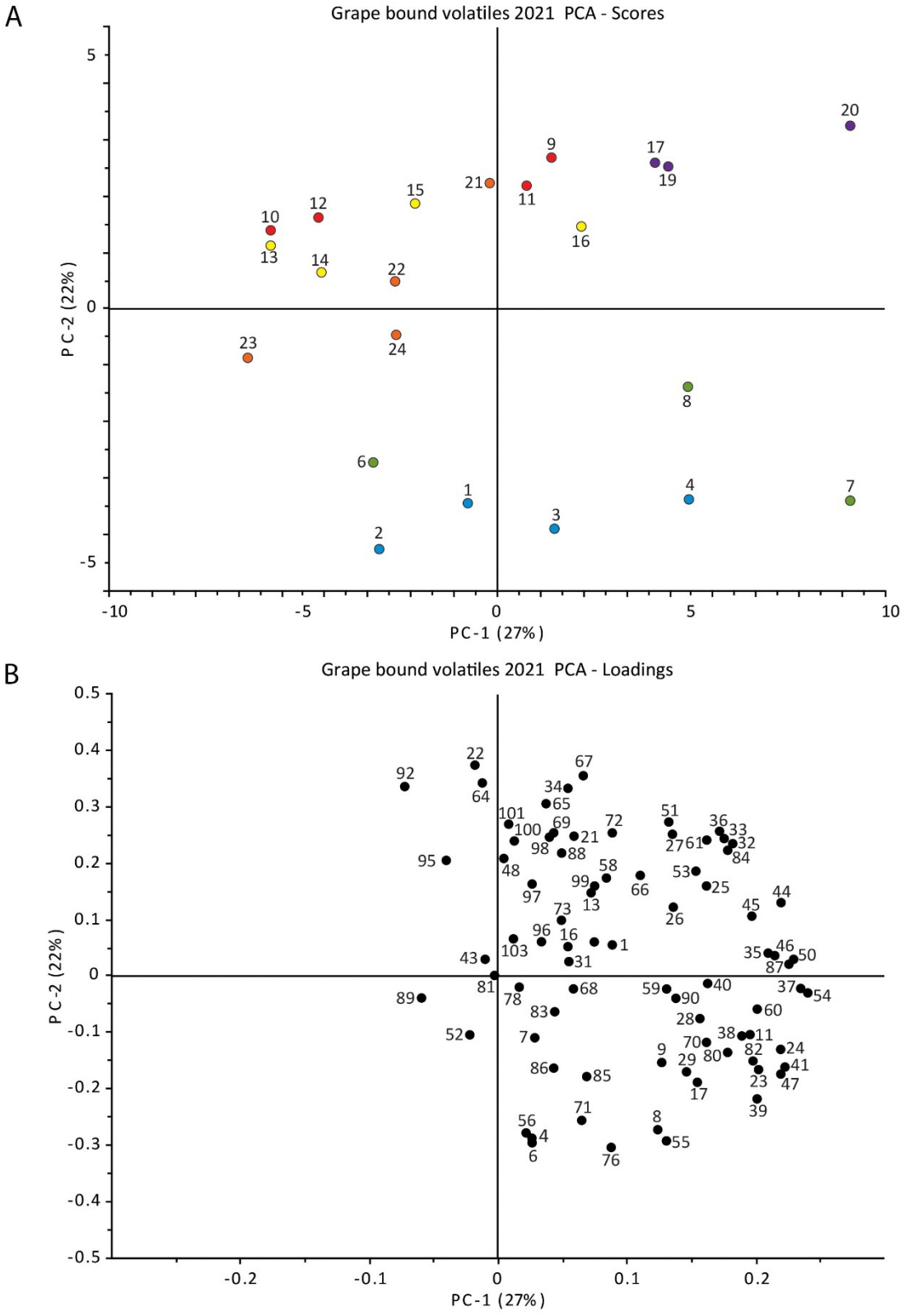


Figure 6.3.25 PCA scores (A) and loadings (B) plots of 22 different 2021 Shiraz grape samples from six sub-regions across the Barossa Valley, South Australia and the significantly different grape bound volatile compounds measured in these samples.

6.4 Grape phenolics and wine non-volatiles and volatiles

Keren Bindon, AWRI

6.4.1 Grape Phenolics

Based on analysis of the composition of grape anthocyanins, together with extractable measures of tannin and anthocyanin in grapes, statistical models were developed to attempt to distinguish the phenolic markers for each sub-region. Preliminary assessment of normality within the data sets showed that most of the phenolics analysed generally followed a classical normal distribution. Partial least squares-discriminant analysis (PLS-DA) models were developed in each season, and these were only able to discriminate the Eden Valley samples from the other sub-regions over multiple seasons. In 2018, the PLS-DA model for Eden Valley was the strongest (R^2calibration = 0.78, R^2validation = 0.72, RSME = 0.2) while in 2019 to 2020 (R^2calibration = 0.60 to 0.64, R^2validation = 0.48 to 0.52, and RSME = 0.26 to 0.28). In each model, variation in the concentration and composition of grape anthocyanins was able to discriminate the Eden Valley samples, however, clear seasonal consistency in the pattern of anthocyanin variability could not be defined for the four vintages studied. In 2018 and 2019, an interesting observation was that the anthocyanin in Eden Valley grapes was more extractable, but this was not observed in 2020 or 2021. The 2020 and 2021 seasons were also cooler than the first two seasons studied. It was interesting to note that some key variables relevant to Eden Valley fruit were similar between the 2018, 2019 and 2020 seasons, and demonstrated proportionally higher levels of non-malvidin mono-glucosides, while malvidin-3-glucoside was lower. In 2021, total anthocyanin, as reflected primarily by malvidin-3-O-glucoside was slightly higher in Eden Valley grape samples, and in particular, higher levels of all coumaroylated anthocyanins were observed. Grape phenolics were found to be an important discriminating factor in the comprehensive multivariate analyses conducted using the entire data set for the project, and this is discussed further in Section 6.6.

6.4.2 Wine non-volatiles and volatiles

For each season of the study, the wines made from each site were analysed for anthocyanins, flavonols, tannin concentration and composition, polysaccharides, metals and multiple classes of volatile compounds. Preliminary multivariate models, including PLS-DA, were built using the compiled chemical data. Of the six sub-regions defined, the PLS-DA models were capable of discriminating only two of the sub-regions successfully for multiple seasons (Table 6.4.1), which was also found for the global data set reported in Section 6.6. Each of the other sub-regions could be separated using the PLS-DA modelling in at least one season. Only the Eden Valley wines could be consistently discriminated from the other sub-regions in all four seasons of the study using PLS-DA.

Phenolic compounds were important to all of the multivariate models developed, and it was of interest to note that for the Eden Valley, the key predictors were similar to the models developed for grapes on a seasonal basis. In 2018 and 2019, Eden Valley wines had proportionally more of the non-malvidin anthocyanins, with lower malvidin-3-glucoside. In 2020 and 2021, the Eden Valley wines had lower levels of all anthocyanins, with reduced overall colour and non–bleachable pigment (Figure 6.4.1A). For 2020 and 2021, where PLS-DA models developed for the Northern Grounds wines were stronger, these were found to

have higher anthocyanin (Figure 6.4.1B), and in 2020 this was associated with increased wine colour density. For flavonols, these compounds varied in composition in the Eden Valley wines depending upon the season, for example, being higher in wines from this sub-region in the warmer 2018 season, and lower in the cooler 2020 and 2021 seasons. Wines from the Northern Grounds generally contained higher concentrations of the more abundant flavonol quercetin-3-glucuronide, but showed variability in the responses of other flavonols depending upon the season. Tannin composition was found to be important in the PLS-DA models, but the compositional aspects which discriminated wines from the different sub-regions varied substantially by season, and no clear patterns were observed.

In terms of volatile composition, a clear relationship was shown whereby the C6 compound Z-3-hexenol was consistently elevated in the Eden Valley wines for all four seasons (Figure 6.4.1A). On a seasonal basis, other C6 compounds and their derivatives were also important in defining Eden Valley wines, with E-2-hexenol and/or an associated ester hexyl acetate being observed to be elevated. In certain seasons, Eden Valley wines also had a higher contribution of multiple fermentation esters, however, this pattern was not found to be consistent. In the cooler, 2020 and 2021 seasons, Eden Valley wines having somewhat lower overall polysaccharide, with lower proportions of grape-derived monosaccharide residues. The Northern Grounds wine samples, on the other hand, were not found to be clearly defined by differences in their volatile or polysaccharide composition. The results of the preliminary PLS-DA results have shown that wine composition could be used to discriminate the sub-regions on a seasonal basis, with greater consistency observed for the Eden Valley, and a lesser extent, the Northern Grounds. More detailed statistical analysis was performed using the global data set, and is presented in Section 6.6.

Table 6.4.1 Partial Least Squares Discriminant analysis (PLS-DA) calibration and validation results for models developed from wine non-volatile and volatile data for four seasons (RMSE, root mean square error of validation).

Sub-region	PLS-DA Model	2018	2019	2020	2021
Eden Valley	R^2 calibration	0.77	0.78	0.85	0.85
	R^2 validation	0.65	0.70	0.71	0.77
	RMSE	0.23	0.20	0.20	0.19
Northern Grounds	R^2 calibration	0.56	-	0.72	0.83
	R^2 validation	0.40	-	0.51	0.75
	RMSE	0.30	-	0.24	0.20

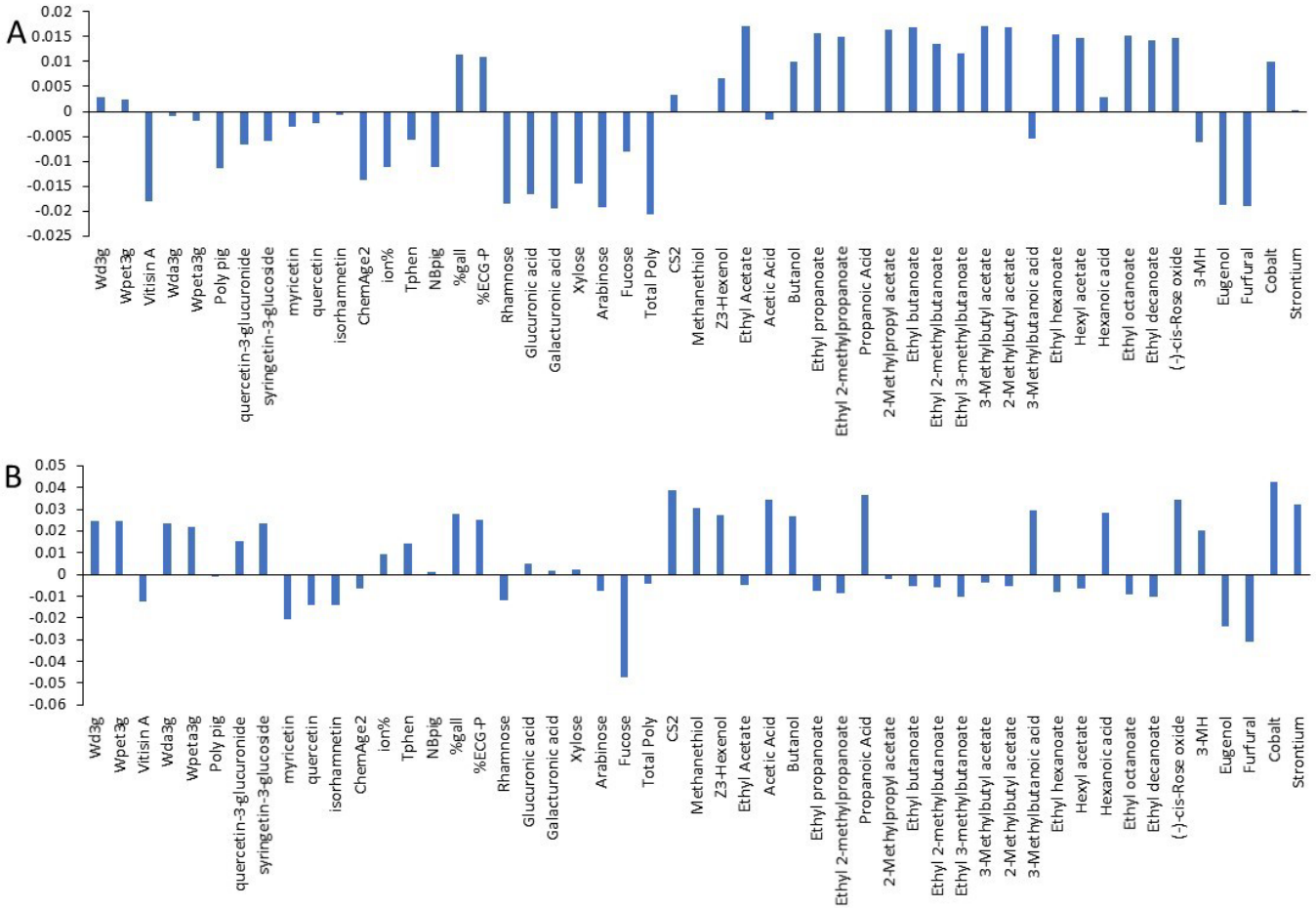


Figure 6.4.1 Weighted regression coefficients for significant wine volatile and non-volatile compounds in wines from A. the Eden Valley and B. Northern Grounds sub-regions using partial least squares-discriminant analysis for the 2021 season only (key to abbreviations; anthocyanins: d3g, delphinidin-3-glucoside, pet3g, petunidin-3-glucoside; da3g, delphinidin-3-acetyl-glucoside; peta3g, petunidin-3-acetyl-glucoside; Poly pig, polymeric pigment; ChemAge2, chemical age; ion%, degree of anthocyanin ionisation; Tphen, total phenolics; NBpig, non-bleachable pigments; %gall, tannin galloylation; %ECG-P, % epicatechin gallate extension sub-unit; monosaccharide constituent of polysaccharide (rhamnose, glucuronic acid, galacturonic acid, xylose, arabinose, fucose); Total poly, total polysaccharide; CS2, carbon disulfide; 3-MH, 3-mercaptohexan-1-ol.

6.5 Wine sensory

Lira Souza Gonzaga, Lukas Danner and Susan Bastian, University of Adelaide

In order to reveal sensory properties and distinctive profiles of wines that come from the Barossa grounds a set of sensory analysis was performed on the samples across four different vintages. As a gold standard methodology for understanding and identifying different sensory profiles of wine, the chosen methodology was a descriptive sensory analysis (DA). Wines from the six Barossa sub-regions were profiled using descriptive sensory analysis (DA) (see methodology above in section 5.7). In order to interpret the results, ANOVA was used to define significant attributes and canonical variate analysis (CVA) was used to identify and understand differences in the sub-regional profile of the Barossa.

6.5.1 Vintage 2018

Small-lot wines

An initial investigation of the CVA identified three samples, all from site 10, as outliers. A more detailed investigation showed that those samples were perceived as being substantially greener and more intense in cooked vegetables-like aroma and flavour. Relating these results with vineyard data, potential overuse of fertiliser might have caused these huge differences in sensory characteristics. To prevent bias in consecutive analyses and interpretations, these samples were removed and the data re-analysed.

CVA on the six sub-regions, excluding site 10, separated three sub-regions from each other, based on the first two dimensions. Wines from Eden Valley were more associated with mint/eucalypt, green, savoury and floral flavour and aroma. Samples from Western Ridge were more textural wines (higher in astringency and rougher mouthfeel) with higher perceived acidity. Wines from the Central Grounds were more intense in fruit characters such as overall-fruit aroma and dark fruit. Wines from the Northern Grounds, Eastern Ridge and Southern Grounds are all found close to the centre of the plot, close to Central Grounds wines and were not well discriminated from each other.

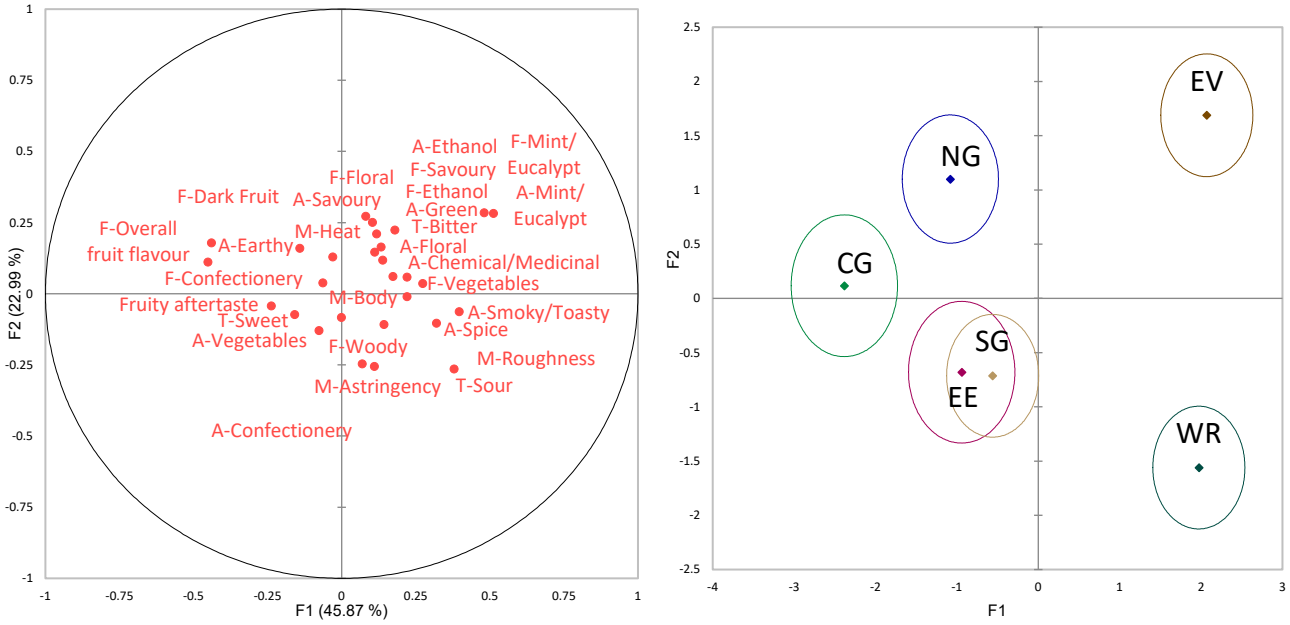


Figure 6.5.1 CVA biplot (factor 1 and factor 2) for small-lot wine reps by sub-region using only significant attributes ($p<0.05$) for the 2018 vintage. A) attribute loadings B) Sub-region centroids, circles indicate pooled confidence intervals for centroids.

Commercial scale wines
Wines from the sub-regional and benchmarking sites were analysed together to investigate sensory differences where winemaking had not been standardised on a commercial scale.

The results for the commercial samples (Figure 6.5.2) confirmed the separation between wines from the Eden Valley and Central Grounds, with Eden Valley wines being more intense in savoury and green aromas. These wines were additionally described as being more intense in medicinal and vegetable aromas and flavours. Wines from the Central Grounds were more related to overall fruit intensity (including red, dark and dried fruit) as well as confectionery. The other four sub-regions were grouped relatively close together with minimal separation.

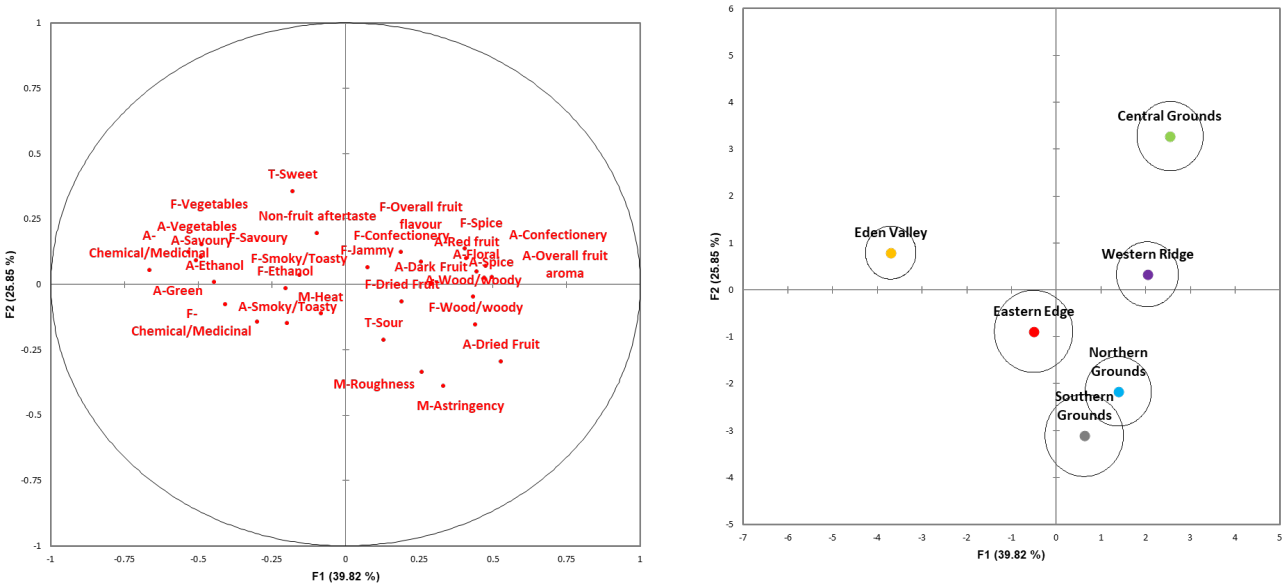


Figure 6.5.2 CVA biplot (factor 1 and factor 2) for commercial winemaking samples by sub-region using only significant attributes ($p<0.01$) for the 2018 vintage. A) attribute loadings B) Sub-region centroids, circles indicate pooled confidence intervals for centroids.

6.5.2 Vintage 2019

Small-lot wines
ANOVA identified 13 aroma, nine flavour, three taste, four mouthfeel and one aftertaste attribute significantly differentiating between samples.

Similar to the 2018 vintage Eden Valley and Western Ridge wines were separated from the other samples, with Eden Valley wines described as being more intense in savoury, vegetable and eucalypt aromas and flavours and Western Ridge samples again described as more textural (astringent and rough), slightly more intense spice and also chemical aromas and flavours. Central Grounds and Eden Valley samples were described as more fruit-forward wines.

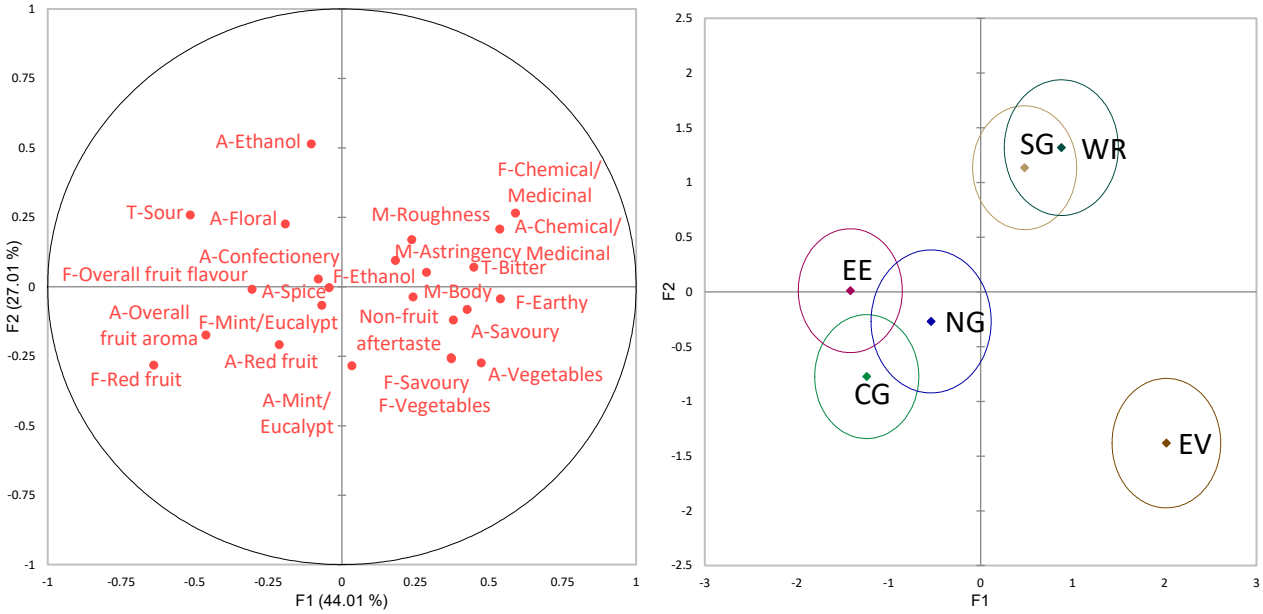


Figure 6.5.3 CVA biplot (factor 1 and factor 2) for small-lot wine reps by sub-region using only significant attributes ($p<0.05$) for the 2019 vintage. A) attribute loadings B) Sub-region centroids, circles indicate pooled confidence intervals for centroids.

Commercial scale wines

Wines from the sub-regional and benchmarking sites were analysed together to investigate sensory differences where winemaking had not been standardised on a commercial scale. Significant differences between samples were observed for 15 aroma, 13 flavour, three taste, four mouthfeel and two aftertaste attributes.

The results of the CVA for the commercial samples (Figure 6.5.4) confirmed the separation between wines from the Eden Valley and Eastern Edge, with Eden Valley wines being more intense in savoury, earthy and vegetable aromas and flavour. Wines from the Eastern edge were more related to overall fruit intensity and particularly red fruit and confectionary in contrast Western Ridge wines were more associated with dark fruit and interestingly in contrast to the small-lot wines with low astringency (opposite of astringency and roughness on the plot).

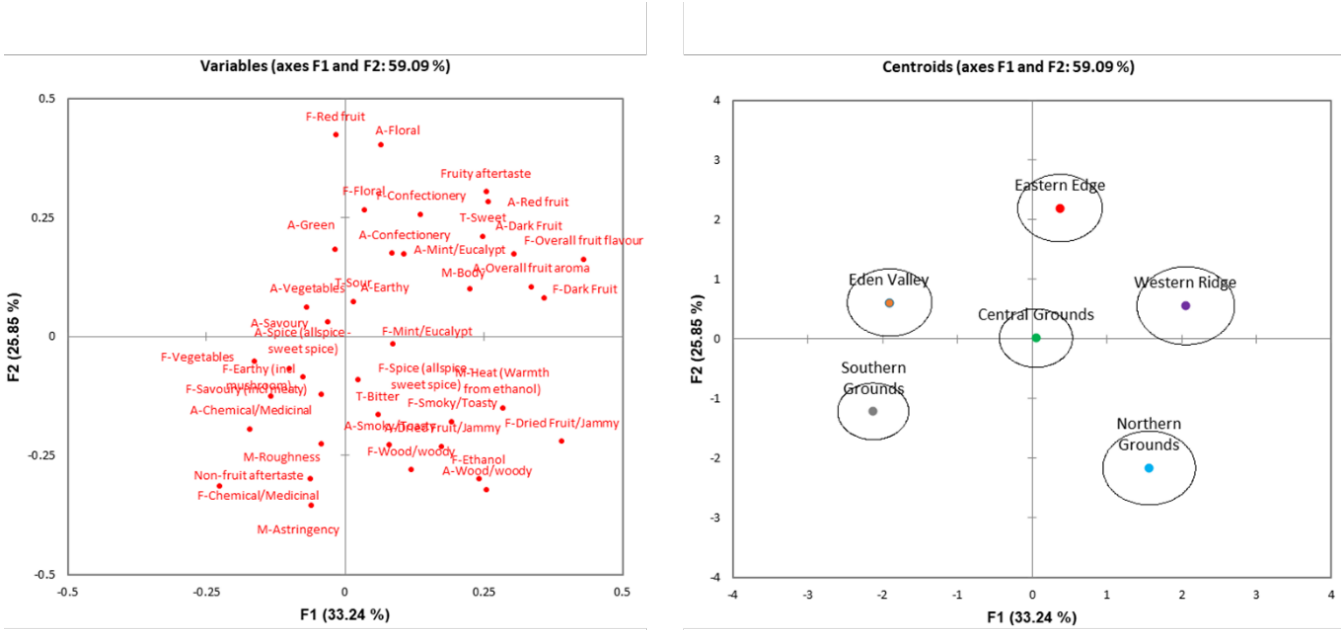


Figure 6.5.4 CVA biplot (factor 1 and factor 2) for commercial winemaking samples by sub-region using only significant attributes ($p<0.05$) for the 2019 vintage. A) attribute loadings B) Sub-region centroids, circles indicate pooled confidence intervals for centroids.

6.5.3 Vintage 2020

Small-lot wines
ANOVA identified seven aroma, eight flavour, one taste, four mouthfeel and one aftertaste attribute significantly differentiating between samples.

The results of the CVA (Figure 6.5.5) show a reasonable separation between Eden Valley, Western Ridge and Southern Grounds, with the other three sub-regions grouped closely together. Similar to the two previous vintages, Eden Valley samples were described as having more intense eucalypt/mint and savoury character (meaty, broth, cooked vegetables) compared to the other sub-regions. Also consistent with the previous vintage, Western Ridge wines were described as more textural higher in astringency and rougher in comparison to the other sub-regions. Southern Grounds wines were associated with pepper favour and woody aromas, as well as being astringent and rough.

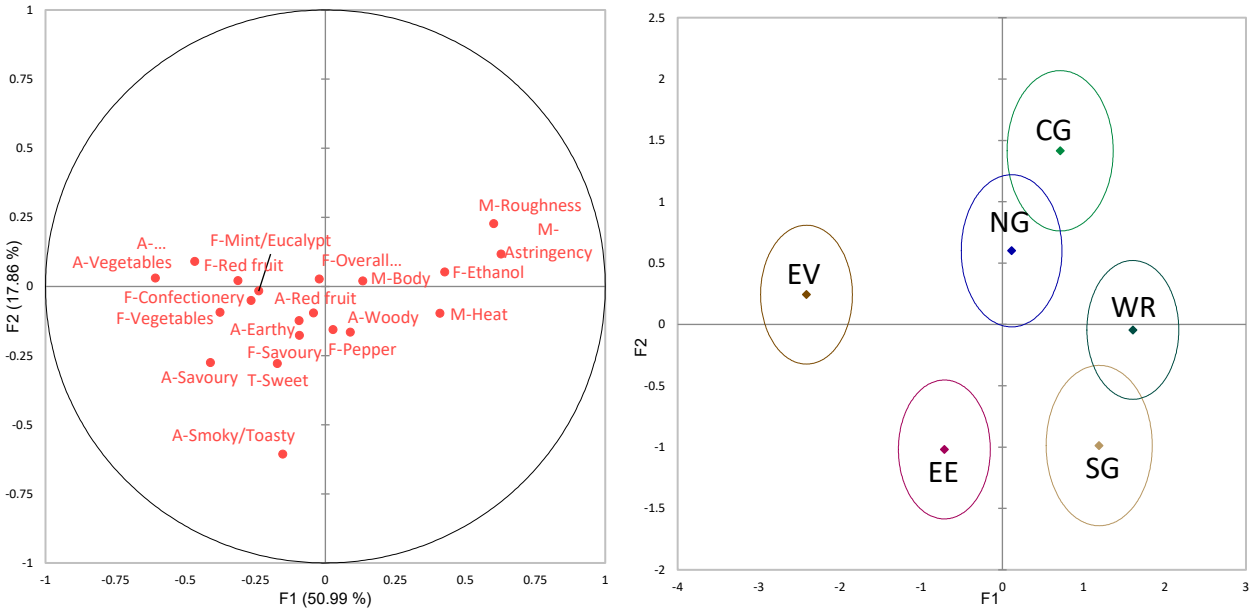


Figure 6.5.5 CVA biplot (factor 1 and factor 2) for small-lot wine reps by sub-region using only significant attributes ($p<0.05$) for the 2020 vintage. A) attribute loadings B) Sub-region centroids, circles indicate pooled confidence intervals for centroids.

Commercial scale wines

Wines from the sub-regional and benchmarking sites were analysed together to investigate sensory differences where winemaking had not been standardised on a commercial scale. Significant differences between samples were observed for 15 aroma, 15 flavour, three taste, four mouthfeel and one aftertaste attribute.

The results of the CVA for the commercial samples are shown in Figure 6.5.6. Confirming the results of the small-lot wines, Eden Valley wines were described as most intense in eucalypt/mint but also having some savoury green notes.

Interestingly, Northern Grounds samples, which were not well separated for the small-lot wines, stood out as being the most fruit-forward samples and additionally being high in spice and woody characteristics.

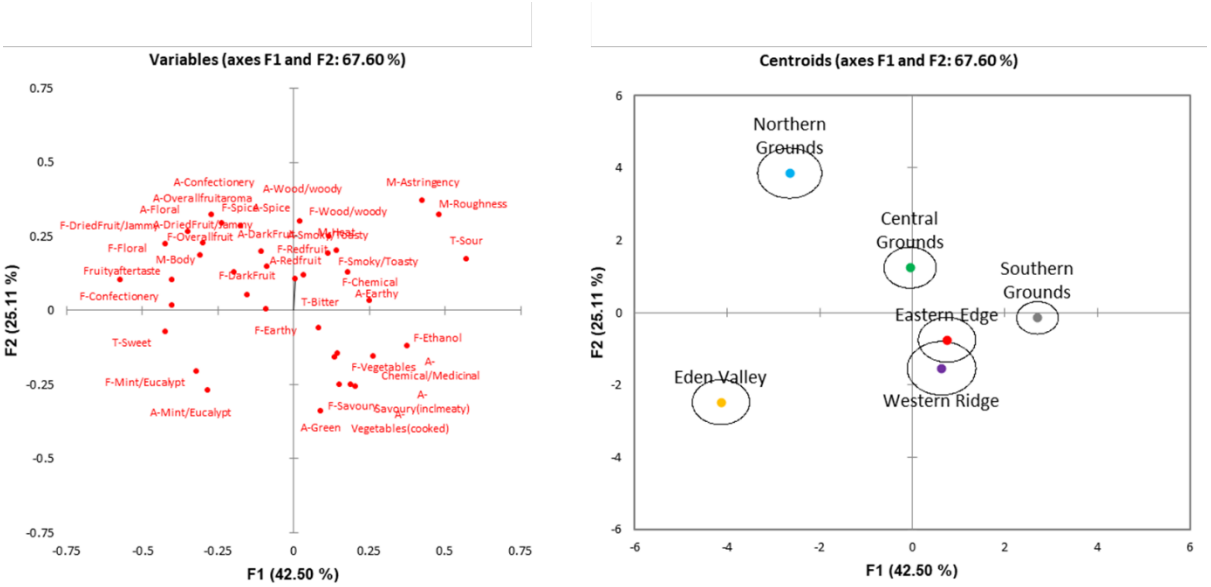


Figure 6.5.6 CVA biplot (factor 1 and factor 2) for commercial winemaking samples by sub-region using only significant attributes ($p<0.05$) for the 2020 vintage. A) attribute loadings B) Sub-region centroids, circles indicate pooled confidence intervals for centroids.

6.5.4 Vintage 2021

Small-lot wines
ANOVA identified six aroma, eight flavour, one taste, five mouthfeel and one aftertaste attribute significantly differentiating between samples.

The results of the CVA (Figure 6.5.7) show a reasonable separation between Eastern Edge and the other five sub-regions grouped closely together. Looking closer at the other other sub-regions, Eden Valley and Southern Grounds seemed to have a similar profile while Central Grounds and Western Ridge had another similar profile. Eastern Edge samples were described as having more intense vegetables and savoury character (meaty, broth, cooked vegetables) compared to the other sub-regions. Eden Valley and Southern Grounds wines were described as having a minty/eucalypt and fruity flavour while Northern Grounds had a green, spicy and floral profile. Central Grounds and Western Ridge displayed a more textural higher in astringency and rougher profile in comparison to the other sub-regions.

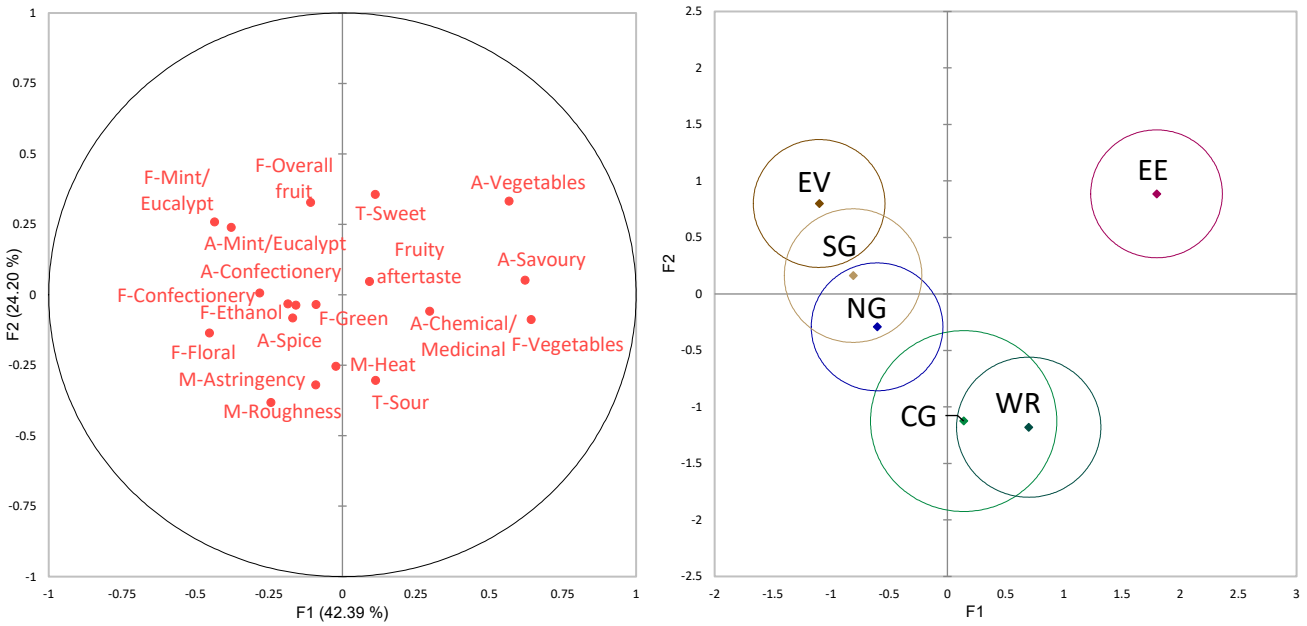


Figure 6.5.7 CVA biplot (factor 1 and factor 2) for small-lot wine reps by sub-region using only significant attributes ($p<0.05$) for the 2021 vintage. A) attribute loadings B) Sub-region centroids, circles indicate pooled confidence intervals for centroids.

Commercial scale wines

Wines from the sub-regional and benchmarking sites were analysed together to investigate sensory differences where winemaking had not been standardised on a commercial scale. Significant differences between samples were observed for 12 aroma, 13 flavour, two taste, four mouthfeel and one aftertaste attribute.

The results of the CVA for the commercial samples are shown in Figure 6.5.8. Confirming the results of the small-lot wines, Eden Valley wines were described as most intense in eucalypt/mint but also having some savoury notes. However, it showed a more distinct profile to the Southern Grounds that displayed spicy, woody and confectionery notes. Central Grounds were also segregated from the other sub-regions showing green, floral and red fruit aspects. Interestingly, the last three regions had an overlapping sensory profile characterised by textural aspects and a lack of fruit-forward notes.

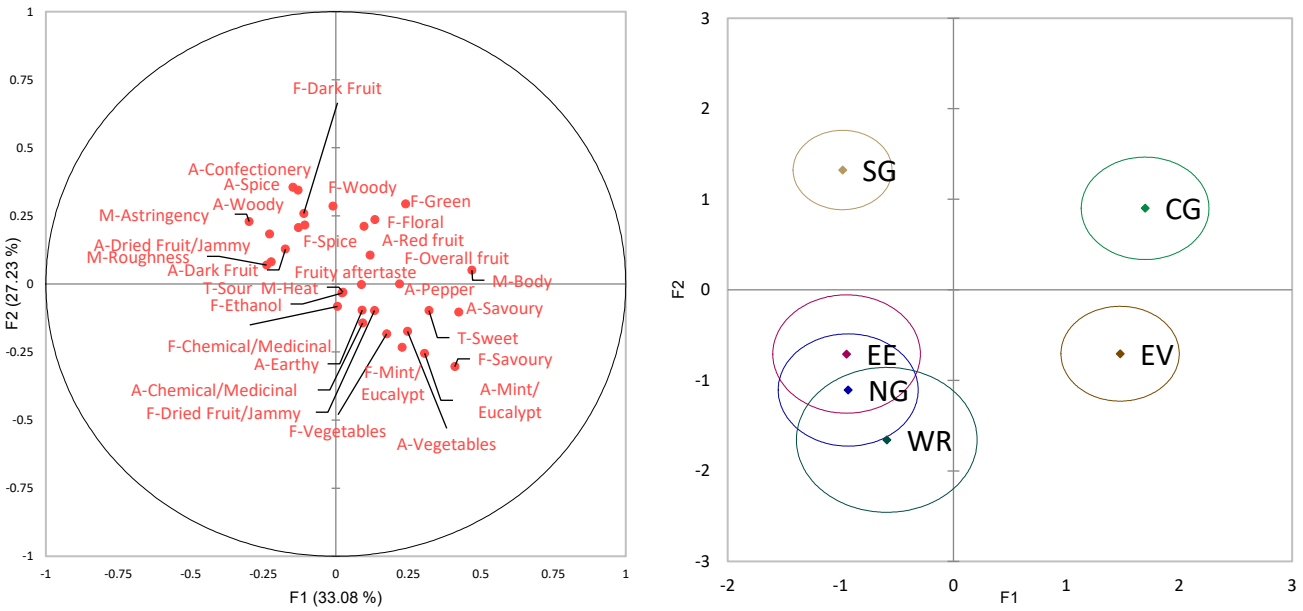


Figure 6.5.8 CVA biplot (factor 1 and factor 2) for commercial winemaking samples by sub-region using only significant attributes ($p<0.01$) for the 2021 vintage. A) attribute loadings B) Sub-region centroids, circles indicate pooled confidence intervals for centroids.

6.6 Chemometric analysis of combined data sets

Sijing Li and Leigh Schmidtke, Gulbali Institute, Charles Sturt University

The role of Charles Sturt University in the project has been to assimilate the data sets of vineyard characteristics, grape and wine compositions and sensory evaluation as measured by collaborators and use chemometric models to ascertain commonality of expression across the four years of data collection that has relevance to vintage and region.

6.6.1 AMOPLS Models of Region and site

The AMOPLS framework with its origins in metabolomics (Boccard and Rudaz 2016) has been successfully used to determine the underlying contribution of grape production site, harvest timing and cultivar with complex data sets (Schmidtke, et al. 2020). A significant advantage of the AMPLOS method is the sequential extraction of information from multiple data sets using explanatory factors (EF) within the overall experimental design, after extraction of unwanted structured information that is orthogonal to the overall interesting features. Extraction and subtraction of the orthogonal information thereby simplifies model interpretation and when combined with robust hypothesis testing of the EF design, significance of the factor contributions can be interpreted in a way similar to classic ANOVA reports. Orthogonal variance in these models was tested using 10000 permutations of the samples within each explanatory factor to determine appropriate numbers of extracted components for each model. The remaining variance and residuals were then modelled in accordance with described methods to elucidate environmental influence upon the environmental factors associated with terroir (Schmidtke, et al. 2020). For the purposes of these data sets, a single vintage and a combined 'All vintage' AMOPLS models were created. The contribution of specific variables to each model explanatory factor is presented as VIP plots (González-Ruiz, et al. 2017).

Overall model performance and significance of explanatory factors based upon permutation testing within the ANOVA experimental design are presented in Table 6.6.1. Performance metrics of the AMOPLS models indicate that significance variance can be attributed to explanatory factors Vintage (All Vintage model, RSR 2.70, EF p-value 0.0001); Region (All & single vintage models, RSR 1.16-2.20, EF p-value 0.0001) and Site (Single Vintage Models RSR 2.11-2.35, EF p-value 0.0001). The RSR values indicate a ratio of residual variance to the main effects for each predictive component and is therefore a multivariate measure of the level of significance for a specific EF. The relative sums of squares for each EF indicates the total variance captured within that EF for the ANOVA model. The levels for EFs – Vintage and Region are easily identified in scores plots associated with each model (Figures 6.6.1-6.6.3) however, levels for EF Site are not well discriminated. For the basis of this report, and in alignment with the goals of this project to explore influences of terroir at sub-regional (not site) levels within the Barossa Region, results for the EF site will not be presented.

6.6.2 Single vintage AMOPLS

The ANOVA model requires a consistent framework of variables across the sample sets, therefore measured attributes were selected that span the data and sample range for each vintage (2018 to 2020) which means that some variables were not modelled in each year. For single vintage AMOPLS the EF were sub-region and site and model summaries for each vintage are presented in Table 6.6.1. Due to limitations in ensuring balanced experimental designs for each level of the EF, interactions for the EF were not modelled.

Table 6.6.1 AMOPLS model relative sums of squares for explanatory factors, RSR indices and p-values for each effect.

Vintage	Explanatory Factor (EF)	EF p-value	Relative Sum of Squares	RSR
All Vintages 2018-2021	Vintage	p=0.0001	0.4051	2.7047
	Region	p=0.0001	0.0640	1.1620
	Residuals		0.5309	1.0000
2018	Region	p=0.0001	0.2115	1.7863
	Site	p=0.0001	0.4199	2.1125
	Residuals		0.3686	1.0000
2019	Region	p=0.0001	0.2504	2.2019
	Site	p=0.0001	0.4269	2.3458
	Residuals		0.3226	1.0000
2020	Region	p=0.0001	0.2045	2.0829
	Site	p=0.0001	0.4353	2.4831
	Residuals		0.3197	1.0000
2021	Region	p=0.0001	0.2636	2.0829
	Site	p=0.0001	0.4253	2.3292
	Residuals		0.3111	1.0000

6.6.3 All Vintage AMOPLS Models

The first AMOPLS model of consideration is the combined data sets spanning all four vintages. Explanatory factors for this model were ‘Vintage’ and ‘Region’ with extracted latent variables associated with each EF presented below. Levels within the Vintage EF have a significant influence upon the model which is not unexpected. Discrimination of ‘Region’ levels in the four vintage model however is less clear. Interesting extracted latent variables with obvious correlation to the explanatory factors are presented in Figure 6.6.1, the relative contribution of each data block to the discrimination of the EF are presented in Figure 6.6.2 and the contribution of important variables is presented in Figure 6.6.3.

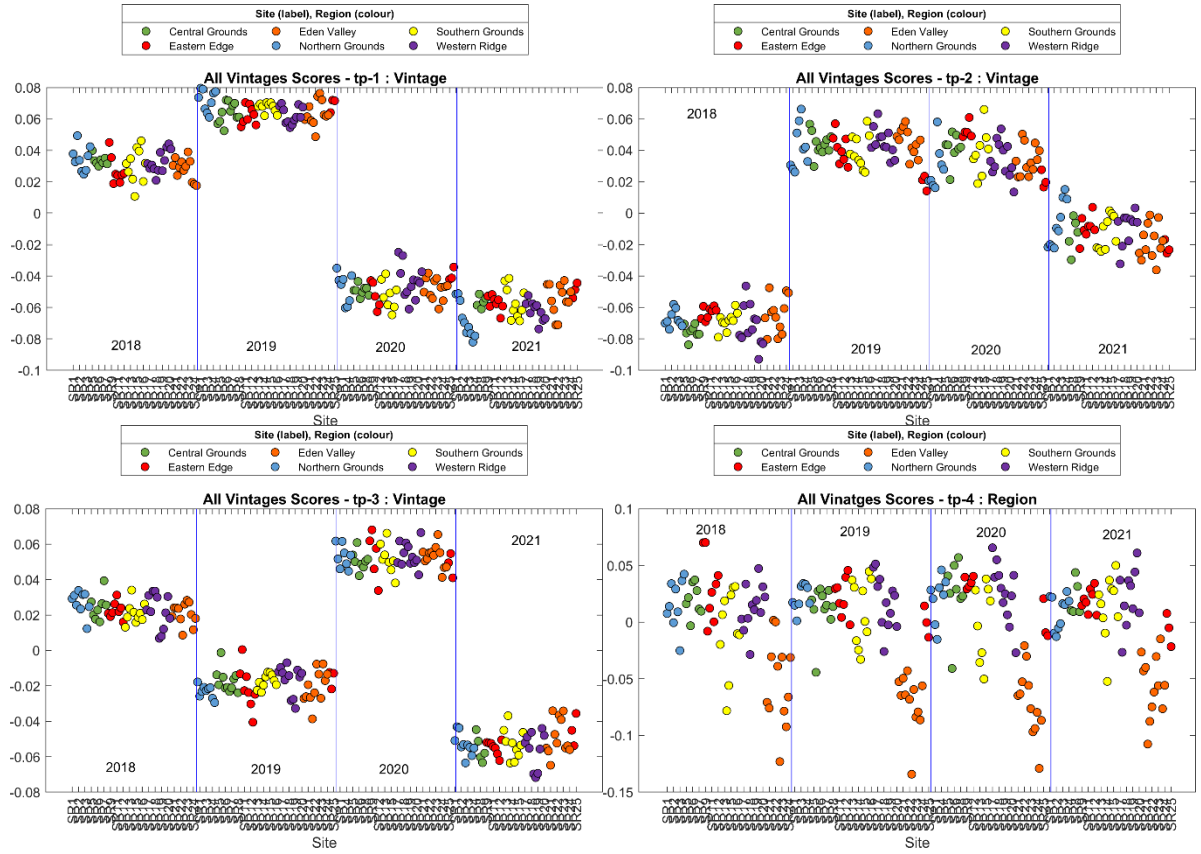


Figure 6.6.1 Predictive scores for samples in vintage (2018-2021) and site (SR1-25) order from the AMOPLS All Vintage Model for Explanatory Factor levels 'Vintage' and 'Region'. Higher level latent variables for sub-region did not show clear sub-region discrimination and are therefore omitted from the report.

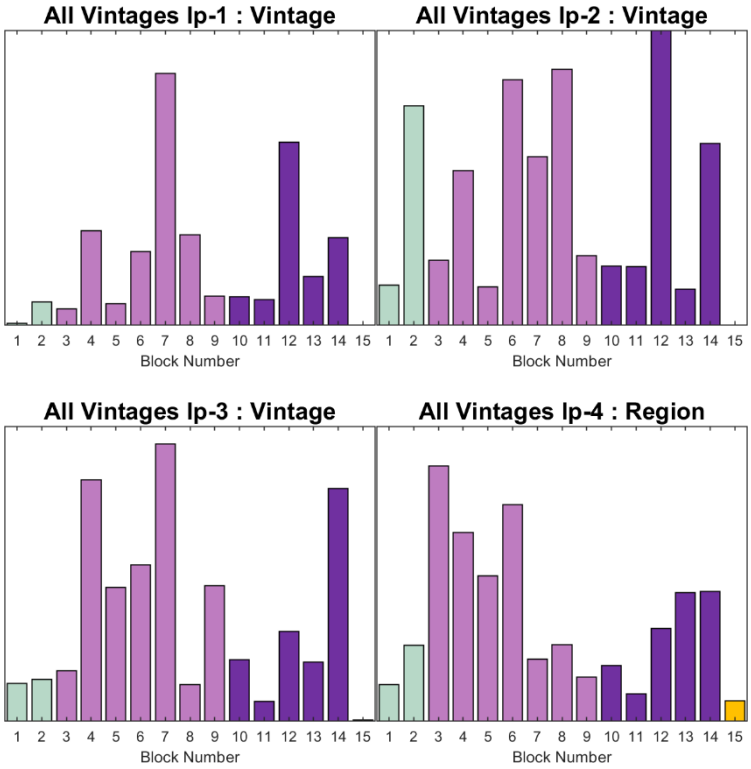


Figure 6.6.2 Data block contributions to the extracted predictive scores for the All Vintage AMOPLS model.

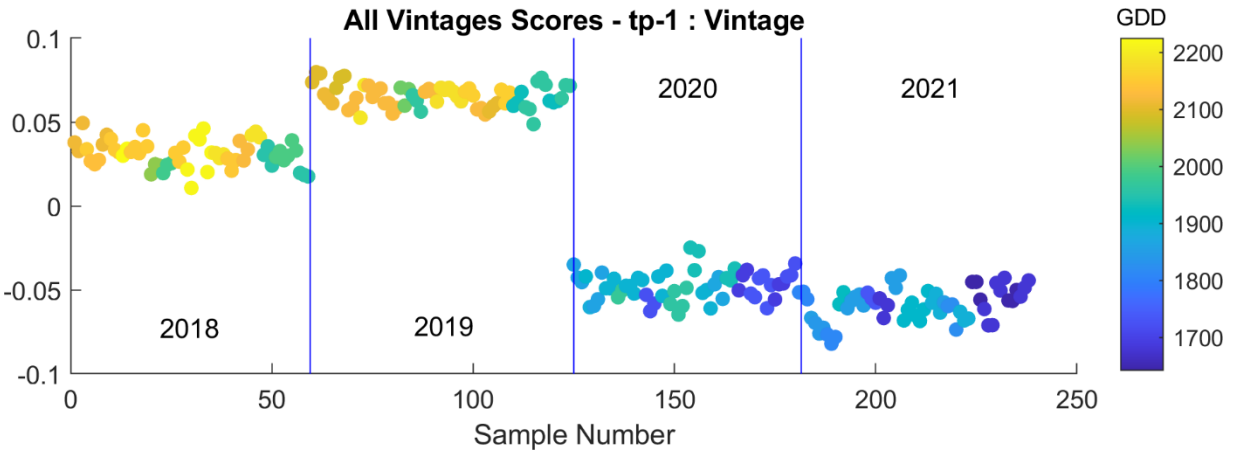


Figure 6.6.3 First predictive score for vintage extracted from the All Vintage AMOPLS model with samples colour coded for vineyard site growing degree days. No influence on this predictive score is evident from the GDD values.

The first three predictive latent variables (tp-1-3) are associated with vintage, evident in the scores plots for samples arranged in vintage and site order (top left) and data block contributions to the samples scores are shown in the top right figure. When sample scores are colour coded for heat accumulation (Growing Degree Days) a pattern is observed that is somewhat consistent with temperature, with the last two vintages being substantially cooler that the first two vintages. Thus a common vintage influence for cooler years (2020-2021) is evident in the position of samples for tp1 (Figure 6.6.3). Of interest is the relative contribution of data blocks for grape volatiles and wine phenolics and colour 7 and 12 to the dominant 'Vintage' sample scores in this latent variable. Such observations are well supported in literature that demonstrates a higher level of expression of grape phenolics and volatile components in cooler vintages (Antalick, et al. 2021, Schmidtke, et al. 2020). Scores for latent variable 1 (tp-1) appear to be associated with the discrimination of warm to cool vintage conditions but is inconsistent across sites, as some sites from Eden Valley in the first two vintages have GDD similar to the third vintage Southern Grounds sub-region, as shown in Table 6.6.2. GDD was not evidently correlated with any of the extracted latent variables associated with either the explanatory factors 'Vintage' or 'Region' for the four vintage data sets. Therefore, no further scores plots colour coded for GDD are presented in this report.

Common vintage variation for 2019 and 2020 is evident in scores plots for tp2 however, the source of this variation is not easily identified and is not related to heat accumulation during the growing season. This latent variable is strongly influenced by grape composition including maturation, grape volatiles, fatty acids and phenolics (blocks 2, 4, 6, 7, 8) which also translate into influential wine composition of phenolics and wine volatiles (blocks 12, 14).

Unique vintage variation is evident for tp-3 with grape compositional data (blocks 4, 5, 6, 7, 9) and wine phenolics and colour and wine volatiles data largely contributing.

Regional discrimination for samples in the 'All Vintage' sample selection is not clearly evident although the Eden Valley samples emerge as being largely different to all other samples used in this model. Higher order latent variables were not clearly associated with specific sub-regions and are therefore not shown in this report. A clearer indication of regionality from year to year is evident in the single vintage AMOPLS models and this observation is consistent with the highly variable and inconsistent contribution of vintage from year to year across the sample set.

Interestingly there is no apparent significant contribution of the sensory data sets to the extracted scores plots associated with vintage, and sensory data only makes a minor contribution to the sample scores for the first latent variable associated with sub-region (lp-4) suggesting a minor sensory difference is apparent for wines from the sub-region with the largest difference in compositional measures being the Eden Valley. The relative contribution of data blocks to the scores plot for region, is heavily skewed to grape composition and wine volatiles.

Table 6.6.2 Mean Growing Degree Days for sites in Barossa Grounds regions for each vintage of the investigation.

Region	2018	2019	2020	2021
Central Grounds	2169	2140	1916	1871
Eastern Edge	2056	2033	1799	1754
Eden Valley	1973	1946	1711	1662
Northern Grounds	2128	2109	1878	1829
Southern Grounds	2200	2167	1946	1896
Western Ridge	2161	2137	1909	1863

The top twenty measured attributes contributing to each EF (vintage and region) in the four vintage AMOPLS model are presented in the Figure 6.6.4. Measured attribute contributions to the projection are considered important when the VIP score is greater than 1. Notable is a lack of high VIP scores any attributes and a very steady and gentle decline in VIP scores in each of the EF is evident, inferring that no group or single attribute dominates the contribution of sample clusters for EF in the multivariate models. The top twenty traits associated with the 'Vintage' EF are mostly associated with grape phenolics and anthocyanins and these probably reflect the differing climatic influence from vintage to vintage, combined with individual vineyard management approaches during the project. Variation for these attributes from vintage to vintage is well supported in literature (Schmidtke, et al. 2020). For EF 'Region', interesting attributes are mostly associated with vine performance, grape maturation and composition including amino acids, volatiles and metals. The preponderance of grape compositional attributes associated with the EF 'Region' suggests that a level of regionality is evident in the data set but does not overtly manifest in the wine sensory scores and consensus space of the sensory data set.

To further explore the individual regional influence on terroir, single vintage (2018-2021) AMOPLS models were created, and results are presented below in Figures 6.6.5-6.6.16.

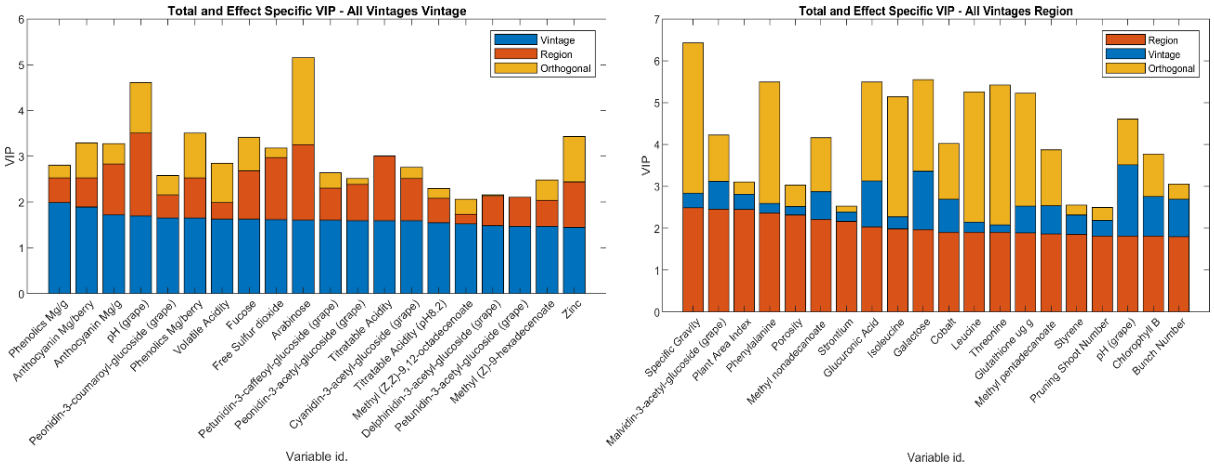


Figure 6.6.4 Variable importance to projection (VIP) scores for explanatory factors 'Vintage' (left) and 'Region' (right) for the four vintage AMOPLS model. Contributions of each variable to either 'Vintage', 'Region' or the extracted orthogonal components are illustrated. Influential variables typically have VIP scores greater than one for any EF.

6.6.4 Single Vintage AMOPLS Models – 2018

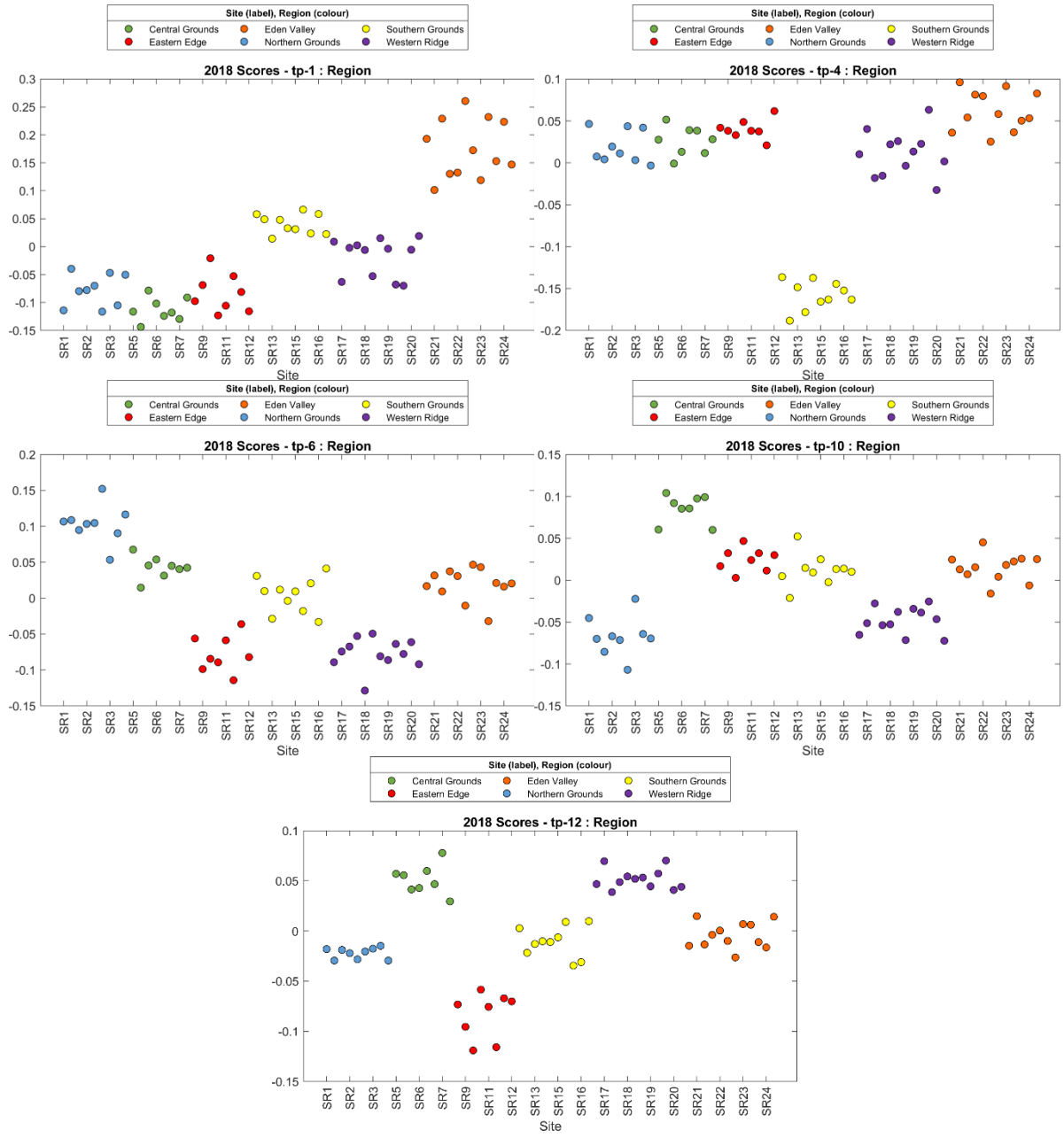


Figure 6.6.5 Predictive scores for samples in site (SR1-24) order from the AMOPLS 2018 model for Explanatory Factor levels 'Region'. Two sub-regions, Eden Valley and Southern Grounds can be easily discriminated whilst other sub-regions demonstrate a level of discrimination with overlapping boundaries.

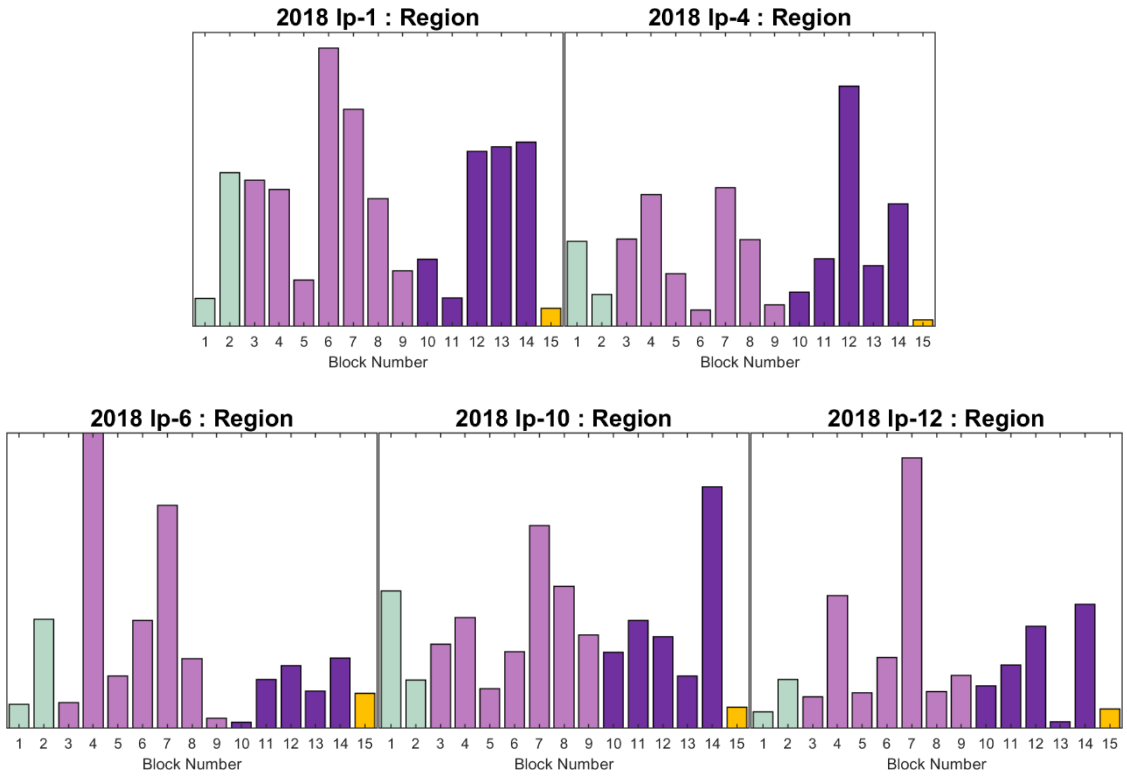


Figure 6.6.6 Block contributions to predictive latent variables for the 2018 AMOPLS model for explanatory factor 'Region'.

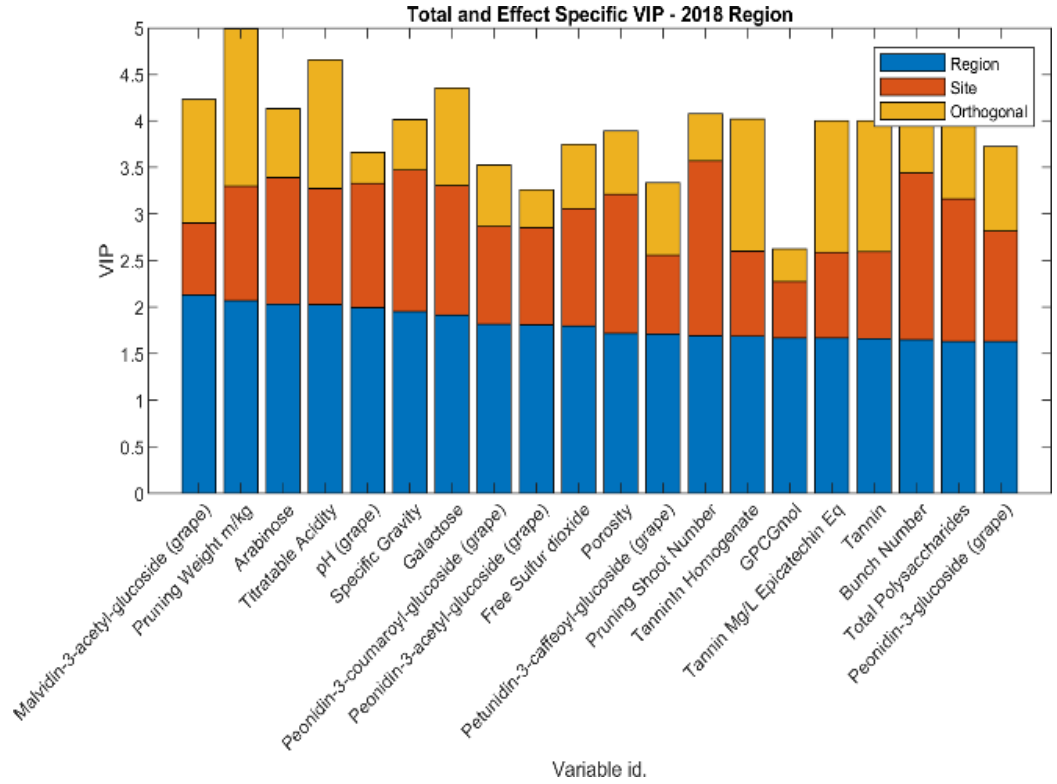


Figure 6.6.7 Variable importance to projection (VIP) scores for the explanatory factors 'Region' for the 2018 vintage AMOPLS model. Contributions of each variable to either 'Region', 'Site' or the extracted orthogonal components are illustrated. Influential variables typically have VIP scores greater than one for any EF.

6.6.5 Single Vintage AMOPLS Models – 2019

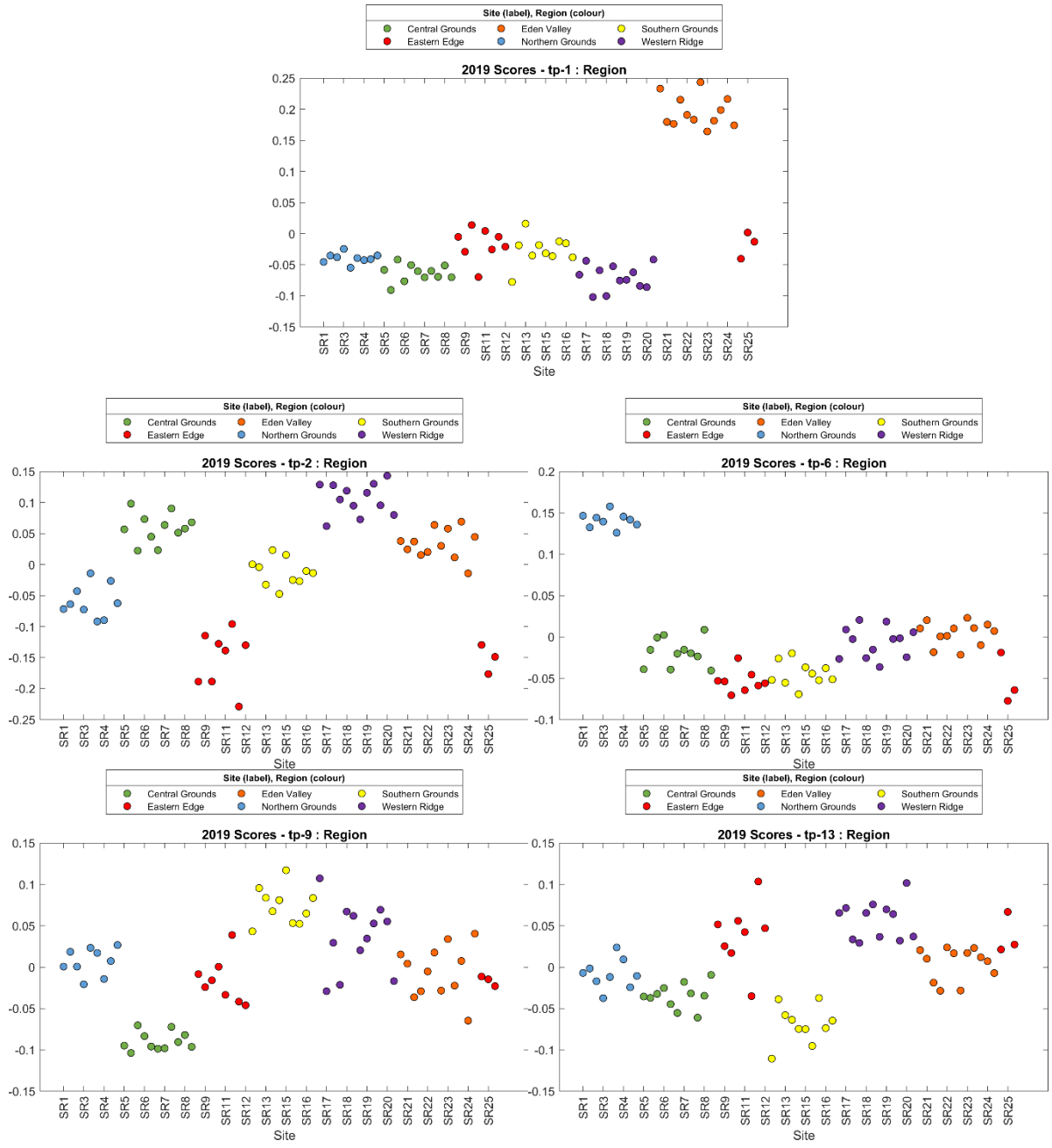


Figure 6.6.8 Predictive scores for samples in site (SR1-25) order from the AMOPLS 2019 model for Explanatory Factor levels 'Region'. Four regions, Eden Valley, Eastern Edge, Northern Grounds and Central Grounds can be easily discriminated whilst other regions share a similarity that does not enable clear discrimination for region.

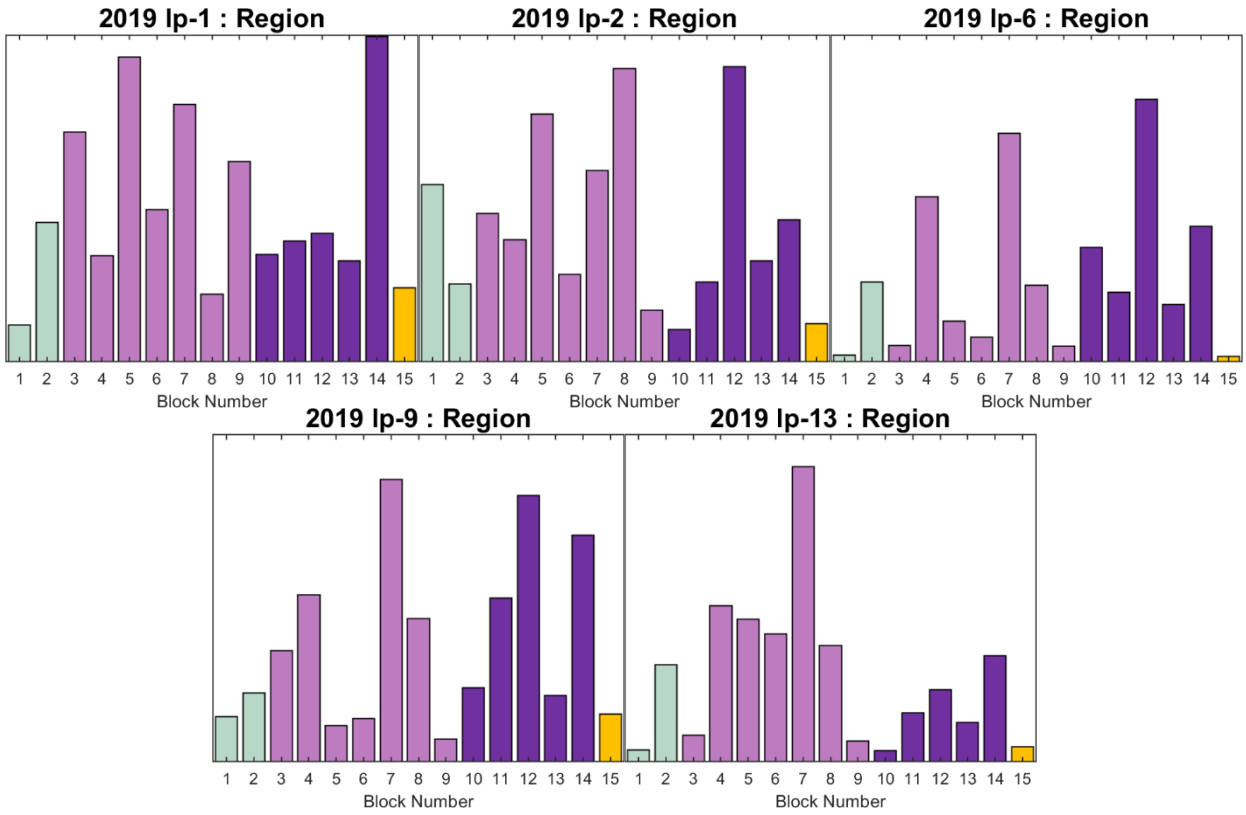


Figure 6.6.9 Block contributions to predictive latent variables for the 2019 AMOPLS model for explanatory factor 'Region'.

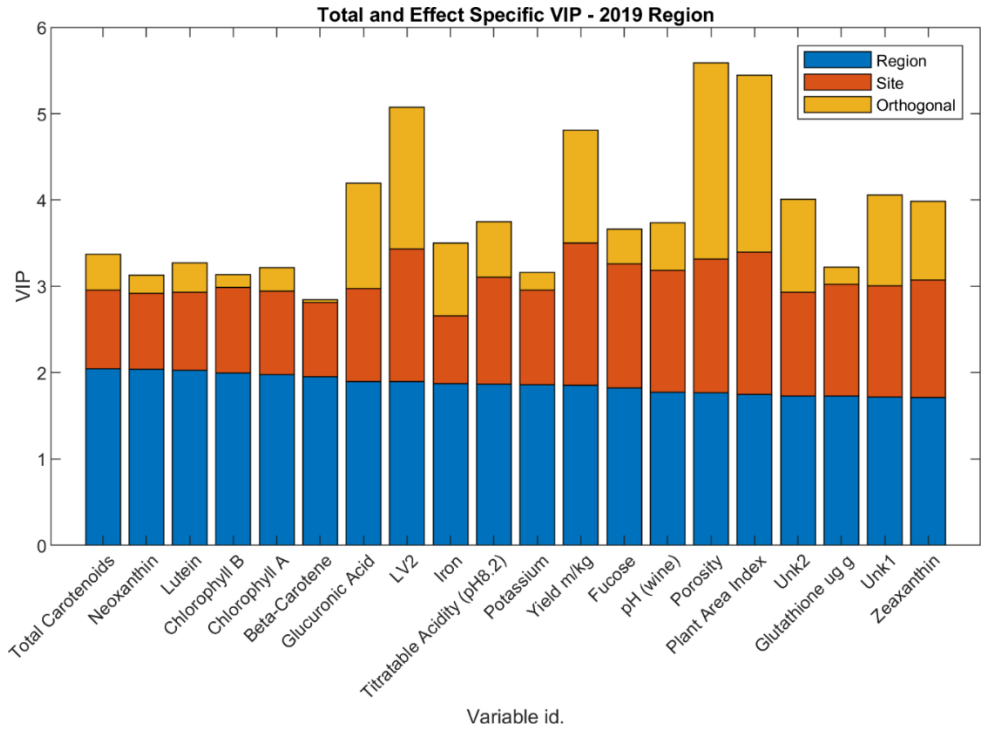


Figure 6.6.10 Variable importance to projection (VIP) scores for the explanatory factors 'Region' for the 2019 vintage AMOPLS model. Contributions of each variable to either 'Region', 'Site' or the extracted orthogonal components are illustrated. Influential variables typically have VIP scores greater than one for any EF.

6.6.6 Single Vintage AMOPLS Models – 2020

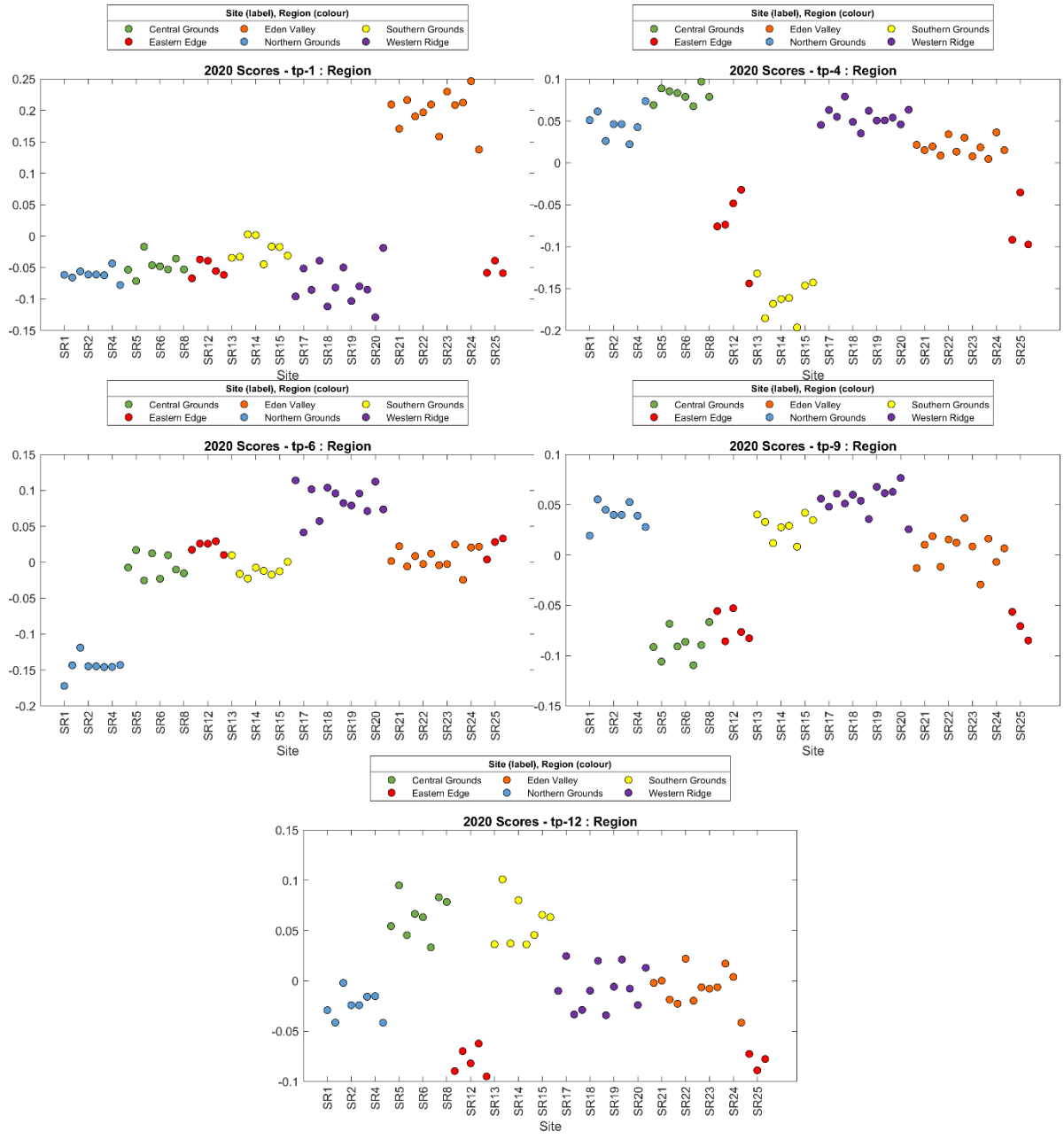


Figure 6.6.11 Predictive scores for samples in site (SR1-25) order from the AMOPLS 2020 model for Explanatory Factor levels 'Region'. Two regions, Eden Valley and Northern Grounds can be easily discriminated whilst other regions share a similarity that does not enable clear discrimination for region.

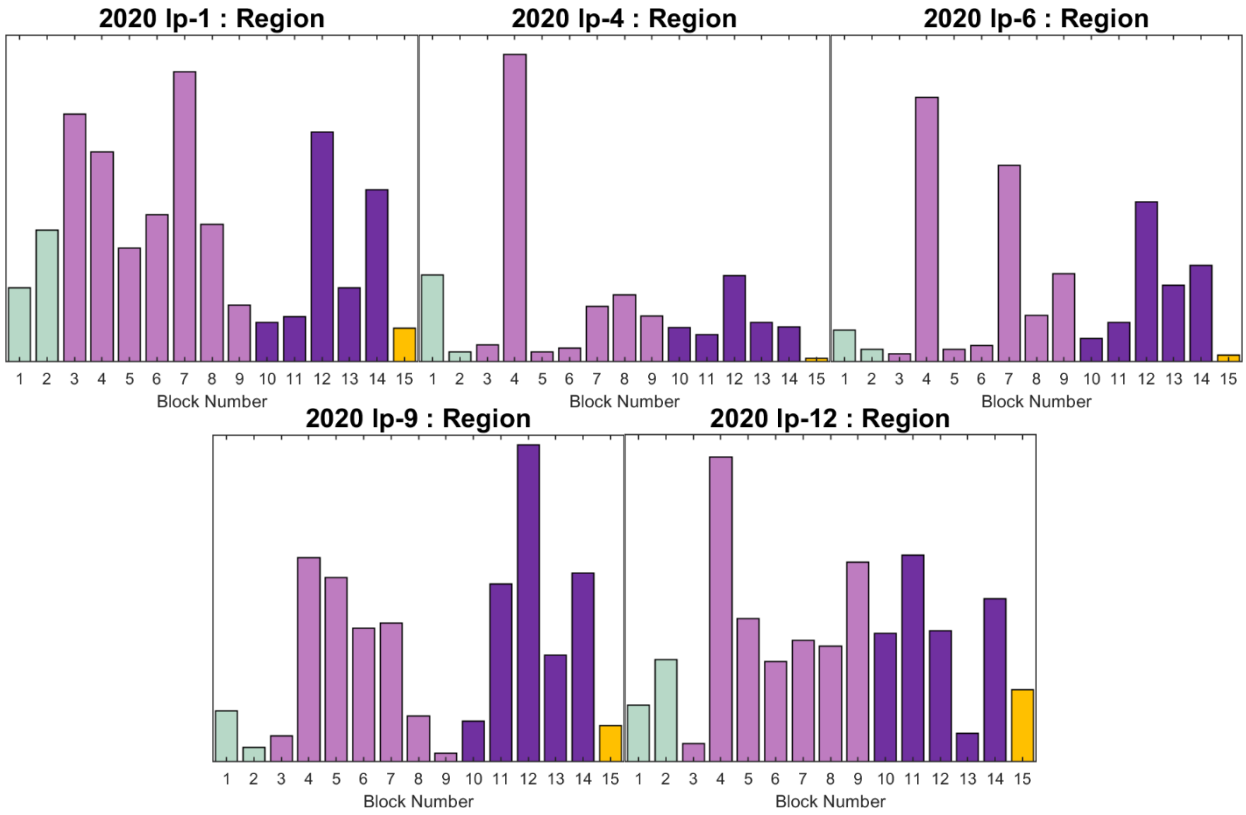


Figure 6.6.12 Block contributions to predictive latent variables for the 2020 AMOPLS model for explanatory factor 'Region'.

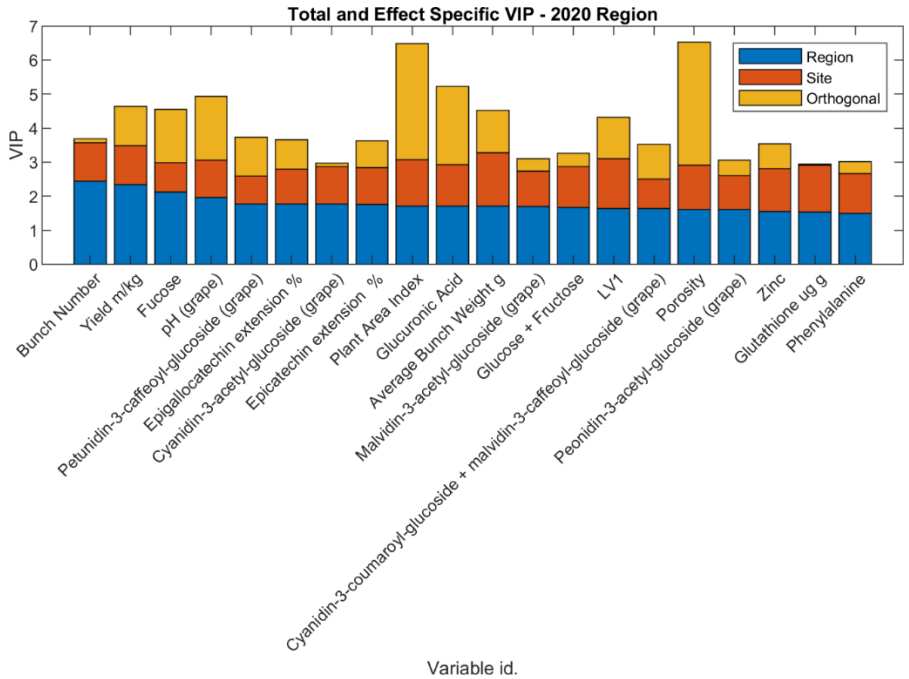


Figure 6.6.13 Variable importance to projection (VIP) scores for the explanatory factors 'Region' for the 2020 vintage AMOPLS model. Contributions of each variable to either 'Region', 'Site' or the extracted orthogonal components are illustrated. Influential variables typically have VIP scores greater than one for any EF.

6.6.7 Single Vintage AMOPLS Models – 2021

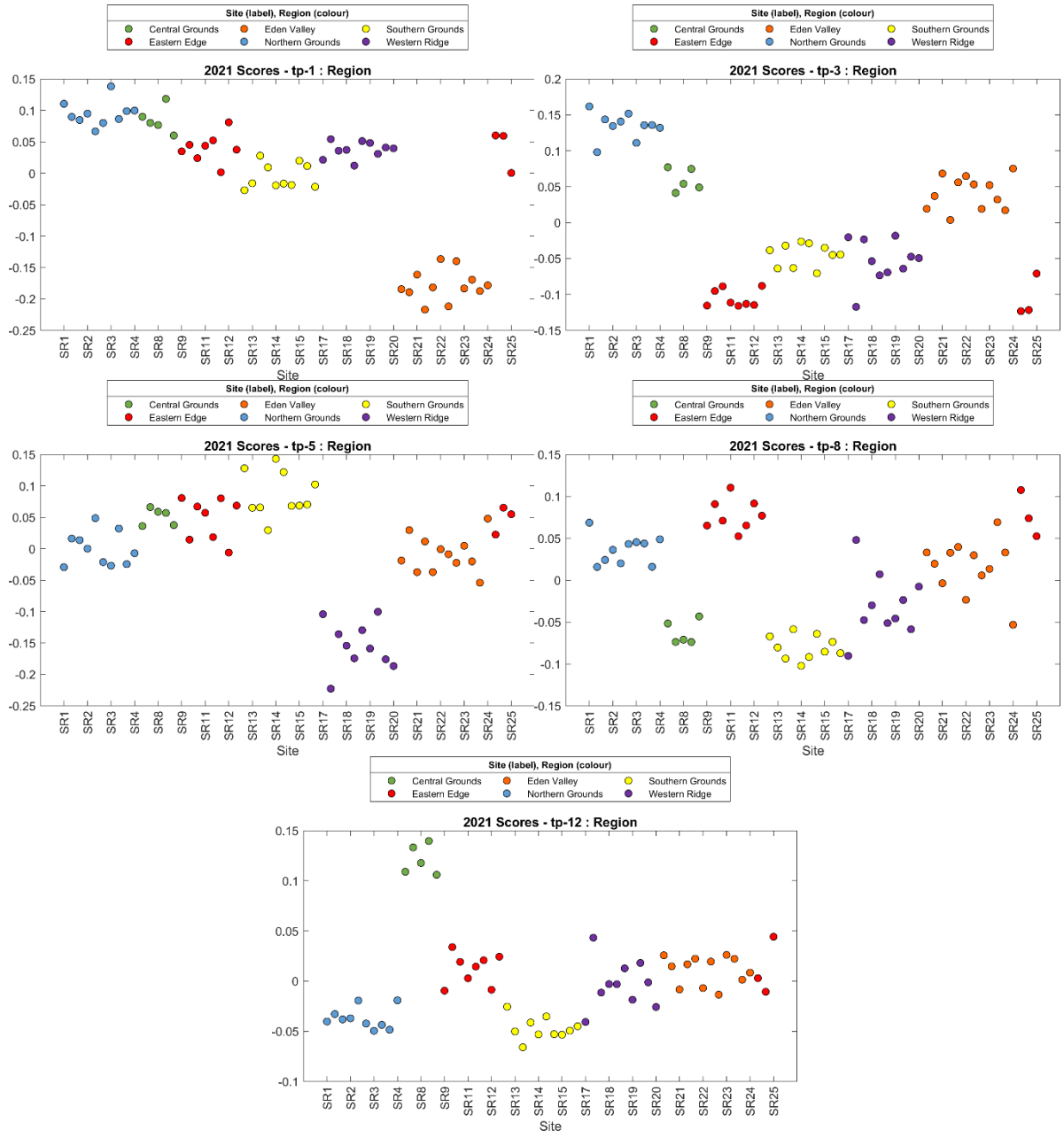


Figure 6.6.14 Predictive scores for samples in site (SR1-25) order from the AMOPLS 2021 model for Explanatory Factor levels 'Region'. Four regions, Eden Valley, Northern Grounds, Western Ridge and Central Grounds can be easily discriminated.

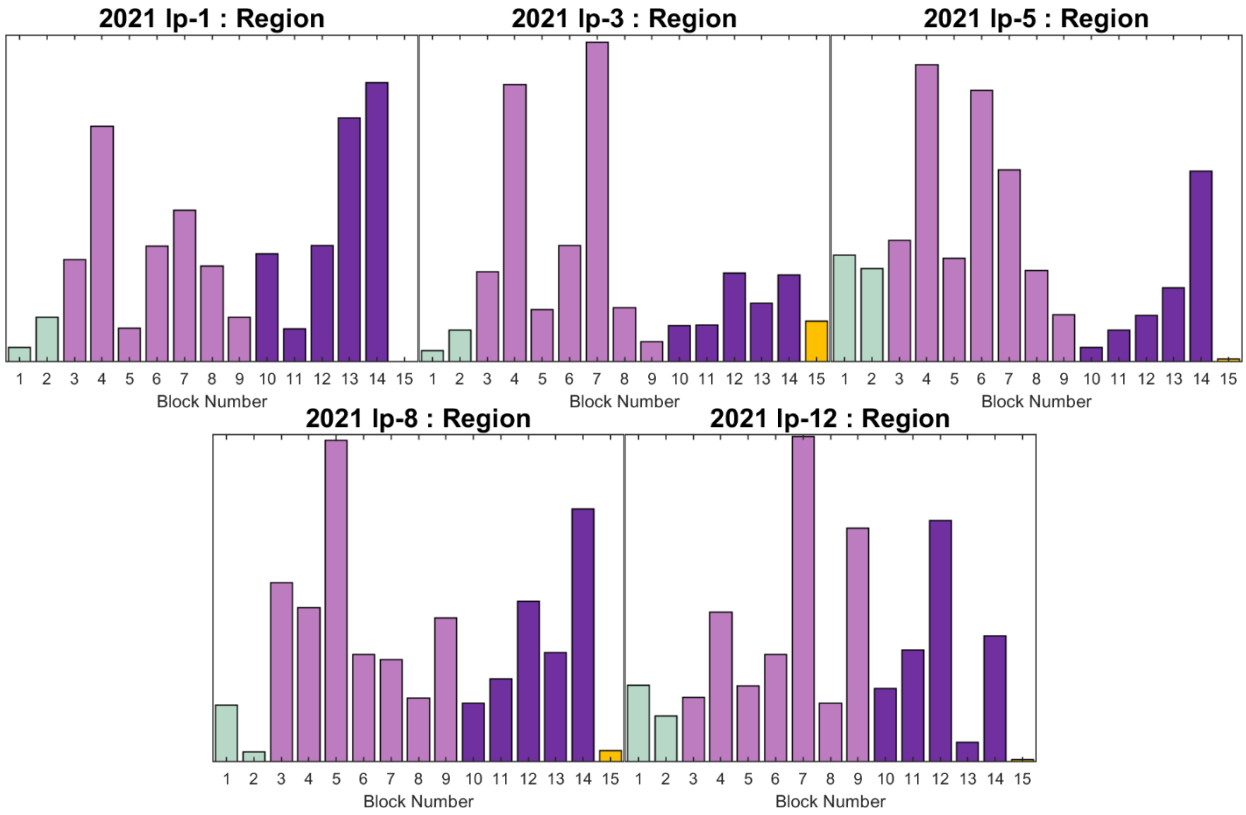


Figure 6.6.15 Block contributions to predictive latent variables for the 2021 AMOPLS model for explanatory factor 'Region'.

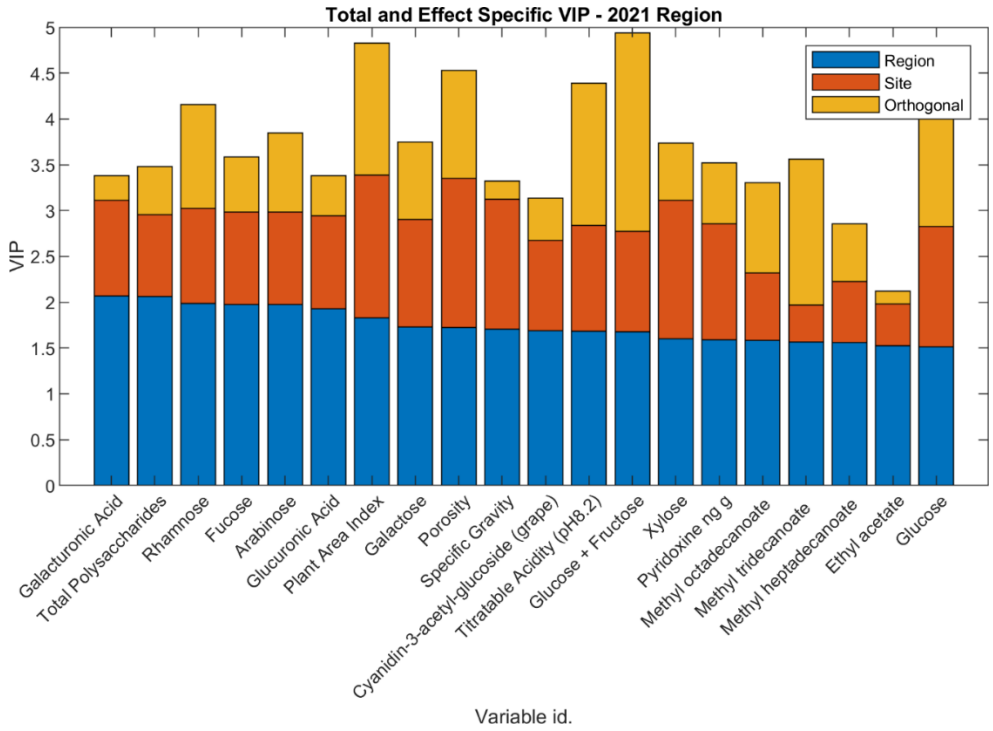


Figure 6.6.16 Variable importance to projection (VIP) scores for the explanatory factors 'Region' for the 2021 vintage AMOPLS model. Contributions of each variable to either 'Region', 'Site' or the extracted orthogonal components are illustrated. Influential variables typically have VIP scores greater than one for any EF.

Table 6.6.3 Summary of the substantial data block contributions to regional discrimination in the single vintage AMOPLS models.

Region	2018	2019	2020	2021
Eden Valley	tp-1 Crop maturation (B2) Grape amino acids (B3) Grape Bound Volatiles (B4) Grape Fatty Acids (B6) Grape volatiles (B7) Grape Phenolics (B8) Wine Phenolics & Colour (B12) Wine Polysaccharides (B13) Wine Volatiles (B12)	tp-1 Crop maturation (B2) Grape amino acids (B3) Grape carotenoids (B5) Grape Fatty Acids (B6) Grape volatiles (B7) Grape tannin (B9) Wine volatiles (B14) Wine Sensory (B15)	tp-1 Crop Maturation (B2) Grape amino acids (B3) Grape bound volatiles (B4) Grape carotenoids (B5) Grape Fatty Acids (B6) Grape volatiles (B7) Grape Phenolics (B8) Wine phenolics & colour (B12) Wine Volatiles (B14)	tp-1 Grape amino acids (B3) Grape bound volatiles (B4) Grape fatty acids (B6) Grape volatiles (B7) Grape phenolics (B8) Wine basic chemistry (B10) Wine phenolics & colour (B12) Wine polysaccharides (B11) Wine volatiles (B14)
Southern Grounds	tp-4 Grape bound volatiles (B4) Grape volatiles (B7) Wine phenolics & colour (B12) Wine volatiles (B14)	tp-13 Crop Maturation (B2) Grape bound volatiles (B4) Grape carotenoids (B5) Grape fatty acids (B6) Grape volatiles (B7) Grape phenolics (B8) Wine volatiles (B14)	tp-4 Grape bound volatiles (B4) Grape volatiles (B7) Wine phenolics and colour (B12)	
Northern Grounds	tp-6 Crop maturation (B2) Grape bound volatiles (B4) Grape fatty acids (B6) Grape volatiles (B7)	tp-6 Grape bound volatiles (B4) Grape volatiles (B7) Wine phenolics and colour (B12) Wine volatiles (B14)	tp-6 Grape bound volatiles (B4) Grape volatiles (B7) Wine phenolics and colour (B12)	tp-3 Grape amino acids (B3) Grape bound volatiles (B4) Grape fatty acids (B6) Grape volatiles (B7) Wine phenolics & colour (B12) Wine volatiles (B14)
Central Grounds	tp-10 Vine performance (B1) Grape volatiles (B7) Grape phenolics (B8) Wine volatiles (B14)	tp-9 Grape amino acids (B3) Grape bound volatiles (B4) Grape volatiles (B7) Grape phenolics (B8) Wine metals (B11) Wine phenolics and colour (B12) Wine volatiles (B14)	tp-9 Grape bound volatiles (B4) Grape carotenoids (B5) Grape fatty acids (B6) Grape volatiles (B7) Wine metals (B11) Wine phenolics and colour (B12) Wine polysaccharides (B13)	tp-12 Grape bound volatiles (B4) Grape fatty acids (B6) Grape volatiles (B7) Grape tannin (B9) Wine metals (B11) Wine phenolics & colour (B12) Wine volatiles (B14)

Region	2018	2019	2020	2021
			Wine volatiles (B14)	
Eastern Edge	tp-12 Grape bound volatiles (B4) Grape volatiles (B7)	tp-2 Vine performance (B1) Grape amino acids (B3) Grape carotenoids (B5) Grape volatiles (B7) Grape phenolics (B8) Wine phenolics and colour (B12) Wine volatiles (B14)	tp-12 Crop maturation (B2) Grape bound volatiles (B4) Grape carotenoids (B5) Grape fatty acids (B6) Grape volatiles (B7) Grape phenolics (B8) Grape tannin (B9) Wine basic chemistry (B10) Wine metals (B11) Wine phenolics and colour (B12) Wine volatiles (B14)	tp-8 Grape amino acids (B3) Grape bond volatiles (B4) Grape carotenoids (B5) Grape fatty acids (B6) Grape volatiles (B7) Grape tannins (B9) Wine phenolics & colour (B12) Wine polysaccharides (B13) Wine volatiles (B14)
Western Ridge				tp-5 Vine performance (B1) Crop maturation (B2) Grape amino acids (B3) Grape bound volatiles (B4) Grape carotenoids (B5) Grape fatty acids (B6) Grape volatiles (B7) Grape phenolics (B8) Wine volatiles (B14)

6.6.8 Discussion of model performance

As with all supervised discrimination methods, the ability of the AMOPLS approach to discriminate six sub-regions of the Barossa Valley consistently and accurately across four consecutive vintages must be considered in terms of how the borders for each of the sub-regions were first derived. An important observation from the AMOPLS models is the lack of substantial contribution of the sensory data block to regional identity. This observation would seem to contrast with a substantial part of the methodology used to initially define the Barossa Grounds sub-regions. Nonetheless, there are some evident differences of sub-regionality within the data set. Furthermore, the order in which predictive scores in each AMOPLS model are sequentially extracted from the data set provides some indication of the magnitude of differences for a level within the explanatory factors used in the ANOVA model. The first predictive scores describe the data set in the most robust manner, with higher order latent variables having diminished predictive acuity. Not all EF levels for sub-region (or site) have an associated latent variable. The absence of a predictive latent variable in orthogonal multivariate discriminant models for an EF level arises as extraction of n-1 predictive latent variables for n-EF levels allows an inferential prediction of class for the nth level. Therefore a sub-region in each model may lack a predictive latent variable and associated loadings of measured attributes.

Of note is the strong discriminatory power for samples from the Eden Valley sub-region based upon the results of all the single vintage AMOPLS models. The Eden Valley sample predictive scores are always associated with the first latent variable in all the models, indicating samples from this sub-region are clearly the most different to samples from all other sub-regions. The important data blocks contributions that differentiate the Eden Valley samples from samples from other regions are extensive, with between nine and 10 data blocks pertaining to grape and wine composition used to discriminate these samples (Table 6.6.3). These data blocks are consistently related to crop maturation, grape and wine composition for amino acids, bound and free volatiles, carotenoids, phenolics, colour and polysaccharides.

In contrast to the Eden Valley, samples from the Western Ridge sub-region are only associated with a single vintage predictive latent variable from the 2021 model. The absence of a predictive latent variable in vintages 2018, 2019 and 2020 AMOPLS models for the Western Ridge samples infers a level of distinctiveness compared to samples from the Southern, Northern and Central Grounds and Eastern Edge sub-regions with the challenge of an inferential prediction of class that arises with latent variable models. The samples from sub-regions Southern Grounds, Northern Grounds and Eastern Edge are the most challenging to discriminate.

An interesting aspect to the association of predictive latent variables to an EF level is overlapping boundaries of class. Overlapping class boundaries are clearly evident in the vintage 2020 AMOPLS model with the predictive latent variable (tp-9) for Central Grounds sub-region being unable to discriminate samples from the Eastern Edge sub-region (Figure 6.6.11), suggesting that these sub-regions are very similar in grape and wine expression for some vintages. Less obvious overlapping class boundaries for levels in EF ‘Region’ are present in the 2018 model tp-6 (Northern and Central Grounds); tp-10 (Central Grounds and Eastern Edge, Southern Grounds and Eden Valley); in the 2019 model tp-2 (Eastern Edge and

Northern Grounds); tp-9 (Central Grounds and Eden Valley) and tp-13 (Southern, Central and Northern Grounds); in the 2020 model tp-4 (Southern Grounds and Eastern Edge), and in the 2021 models tp-3 (Northern and Central Grounds) and tp-8 (Eastern Edge, Northern Grounds, Eden Valley and Western Ridge). The frequency of overlapping class boundaries for Central Grounds, Northern Grounds and Southern Grounds infers these sub-regions have some similarities in expression of regionality for grape and wine components in most vintages. Distinctiveness may be apparent in wines made from these sub-regions, however, an overall degree of similarity may also be present, thereby making a clear discrimination of wines from these sub-regions based on the measured attributes, difficult from year to year.

Total and specific contributions of attributes to the EF 'Region' for each vintage AMOPLS model are illustrated in Figures 6.6.7, 6.6.10, 6.6.13 and 6.6.16 for vintage models 2018, 2019, 2020 and 2021 respectively. For each model the twenty most influential attributes based upon VIP value for 'Region' are shown with VIP for region, site and orthogonal components illustrated to show explanatory factor and total contribution to explained discrimination. A summary table of data block influence as a count of measured attributes in the top twenty VIP scores for each of the four single vintage models is presented in Table 6.6.4. Of interest is the consistent contribution of data blocks 1- Vine performance, 10 – Wine basic chemistry and 13 – Wine polysaccharides which have highly important attributes for sub-regional discrimination in every vintage model. Data blocks 5 – Grape carotenoids, 8 – Grape phenolics and 13 – Wine polysaccharides also have influential attributes for sub-regional discrimination for most vintages. It is important to note that whilst the data blocks have influence across multiple years, the specific attributes vary from year to year which is evident in comparing the figures for variable influence to projection for region. Vintage-to-vintage variation in expression of grape or wine compositional attributes is inconsistent, however the expression of a broad range of similar attributes, i.e. those within assigned data blocks appears to have some basis for sub-regional discrimination.

Table 6.6.4 Count of data block attributes with the 20 highest VIP scores for EF 'Region' in single vintage AMOPLS models.

Block #	Description	2018	2019	2020	2021	Total
1	Vine Performance	4	3	5	2	14
2	Crop Maturation	5		1		6
3	Grape Amino Acids			1		1
4	Grape Bound Volatiles					
5	Grape Carotenoids		10	1	1	12
6	Grape Fatty Acids				3	3
7	Grape Volatiles					
8	Grape Phenolics	5		5	1	11
9	Grape Tannin	1		2		3
10	Wine Basic Chemistry	2	2	1	3	8
11	Wine Metals		2	1		3
12	Wine Phenolics & Colour					
13	Wine Polysaccharides	3	2	2	9	16
14	Wine Volatiles				1	1
15	Wine Sensory		1	1		2

6.6.9 Unsupervised Cluster analysis of four vintage data sets – K-means

Unsupervised clustering of samples was undertaken using the k-means clustering and random forest algorithm of the same measured attributes used for AMOPLS discriminant analysis. Prior to k-means clustering, each data block for each vintage model was mean-centred and variance scaled to unity before concatenation to create a data superblock which was passed to the k-means algorithm. Each variable in all data blocks, therefore, contributed equal variance. To overcome vintage influences for the four vintage k-means cluster, and random forest models, a combined vintage data superblock was constructed by concatenation of the mean-centred and variance scaled attributes in each data block for each vintage. Each vintage of data, therefore, contributed the same variance to the data superblock and each measured variable had equal variance for each year. K-means clustering was undertaken using the data superblocks with distance measures between samples using the 'cityblock' approach and five replicates for each iteration. The number of clusters for each model was based upon the inspection of silhouette profiles for cluster solutions with two to six clusters.

Correlation to vineyard site parameters (elevation, cation exchange capacity, average water holding capacity, 30 year mean (to 2018) growing degree days, mean January temperature, mean growing season temperature, growing season rainfall and annual rainfall with the k-means solutions was done based upon the range of observed values and assigning each site to one of three bands (low, medium or high) with boundaries based upon the 33rd and 66th percentiles of observations. Results for the sample site and replicate clustering using the k-means approach are shown in figure 18 for each vintage cluster solution and the four vintage models along with correlations to measures of the viticulture site characteristics.

K-means cluster solutions were not consistent with either two or three clusters being the optimised solution depending on vintage. When all vintages were modelled together, a two-cluster solution was deemed appropriate based on silhouette profiles, although it is interesting to note the three-cluster solution for vintage 2021 samples assigns samples from the Western Ridge sub-region assignment to a cluster, along with sub-region Eastern Edge SR11 and SR25 sample replicates and one sample from the sub-region Southern Grounds (SR14) (Figure 6.6.17). The most consistent and stable k-means models were obtained with a two-cluster solution. In comparing the cluster solutions for sample site replicates and vineyard characterisation a general trend consistent with cluster assignment and increasing vineyard elevation is apparent (Figure 6.6.17). A correlation to cluster assignment is also evident for soil cation exchange capacity, available water holding capacity, growing degree days, and mean January temperature with these measures of vineyard decreasing. However, correlation does not infer causation, and the trend observations between vineyard characters and sample cluster assignment are noted without attribution.

The influence of each variable to cluster groupings in each optimised cluster model was determined by inspection of the ratio of the measured attribute sum of squares for grouped samples to the total sum of squares for all samples. The twenty most important measured attributes to each cluster for each vintage model and the 'All vintages' model are in figures 19 to 23 and corresponding data block origins identified.

For the 12 assigned clusters in the five k-means models (V2018: 2; V2019: 3; V2020: 2; V2021: 3; All Vintage: 2) representing individual vintage and a combined vintage model, a total of 152 unique measured attributes were represented. Of the 152 measured attributes, 57 were included between two and five times each, leaving 95 attributes with a single

observation of the most important attributes for sample cluster assignment. A count of data block representations was compiled from the 57 measured attributes that were present at least twice, and the proportion of data block representation to sample cluster assignment determined. As each measured attribute used in the k-means models has equal weighting, the proportion of representation of a data block for the sample cluster assignment relative to the total data set enables a measure of importance of each data block to the cluster solutions when the data blocks for each attribute are identified. Representation proportion of data blocks were calculated from the mean number of measured attributes used for each vintage data set and the combined 'All vintage' data set (Table 2; $\bar{x}$ = 412: V2018: n = 420; V2019: n = 435; V2020: n =419; V2021: n = 422; All Vintage: n = 364). Over and under representation of data blocks to the k-means cluster solutions in shown in figure 24. Of note is the absences of attributes from data blocks 1. Vine performance, 6. Grape fatty acids, 8. Grape phenolics, 13. Wine polysaccharides and 15. Wine sensory. A demonstrative under representation of data blocks is evident for 4. Grape bound volatiles and 12. Wine phenolics and colour. Significant over representation for sample assignment to clusters is evident for attributes from data sets 3. Grape amino acids, 7. Grape volatiles and 14. Wine volatiles, with other data blocks contributions to the k-means solutions being close to their overall proportion of representation.

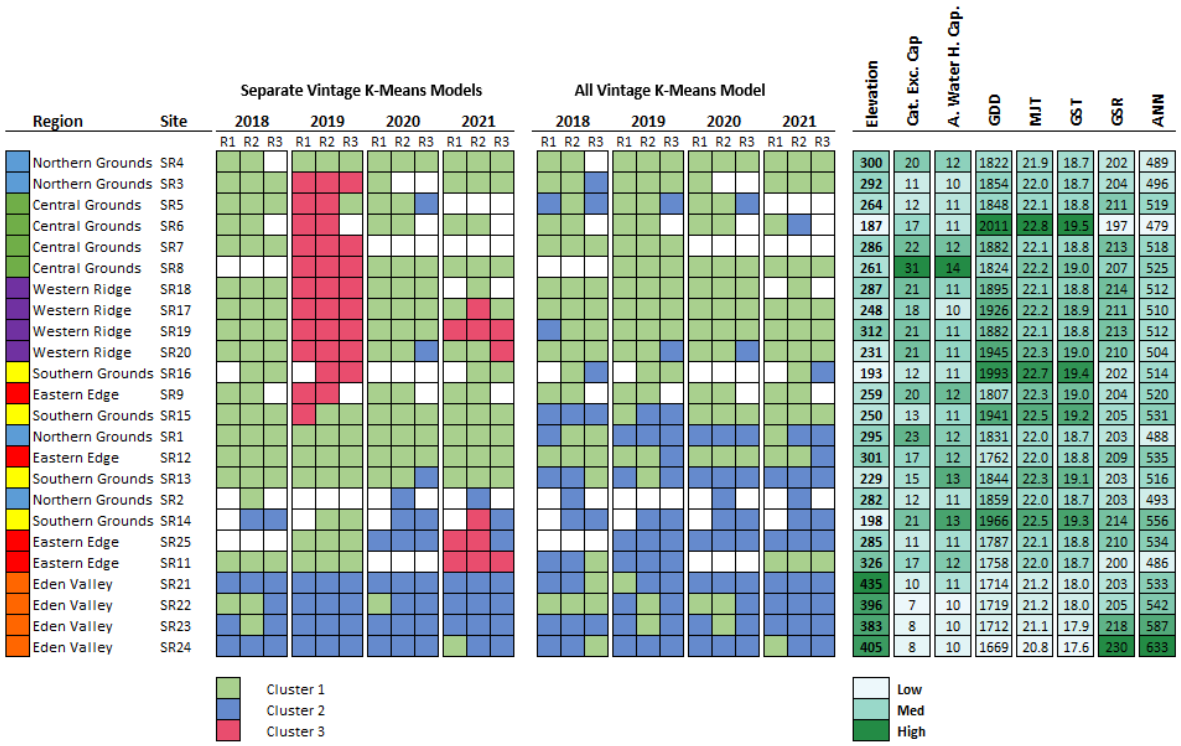


Figure 6.6.17 K-means cluster solutions for sites and replicates for each vintage model and comparison to the four vintage model. Each site replicate in each vintage is presented as a cluster identified by colour code for either cluster 1, 2 or 3. Separate vintage k-means solutions are shown for each replicate and compared with the cluster assignment for the all vintage model. Elevation = site m Australian height datum, Cat. Exc. Cap = profile weighted (5-60 cm) mean value for soil cation exchange capacity (cmol+/kg); A. Water H. Cap = profile weighted (5-60 cm) mean value for soil available water holding capacity (%); GDD = Season growing degree days (°C; base of 10 with no upper cap); MJT = Mean January Temperature (°C); GST = Mean growing season temperature (°C); GSR = Growing season rainfall (mm); ANN = Annual rainfall (mm).

6.6.10 K-means variable importance Vintage 2018

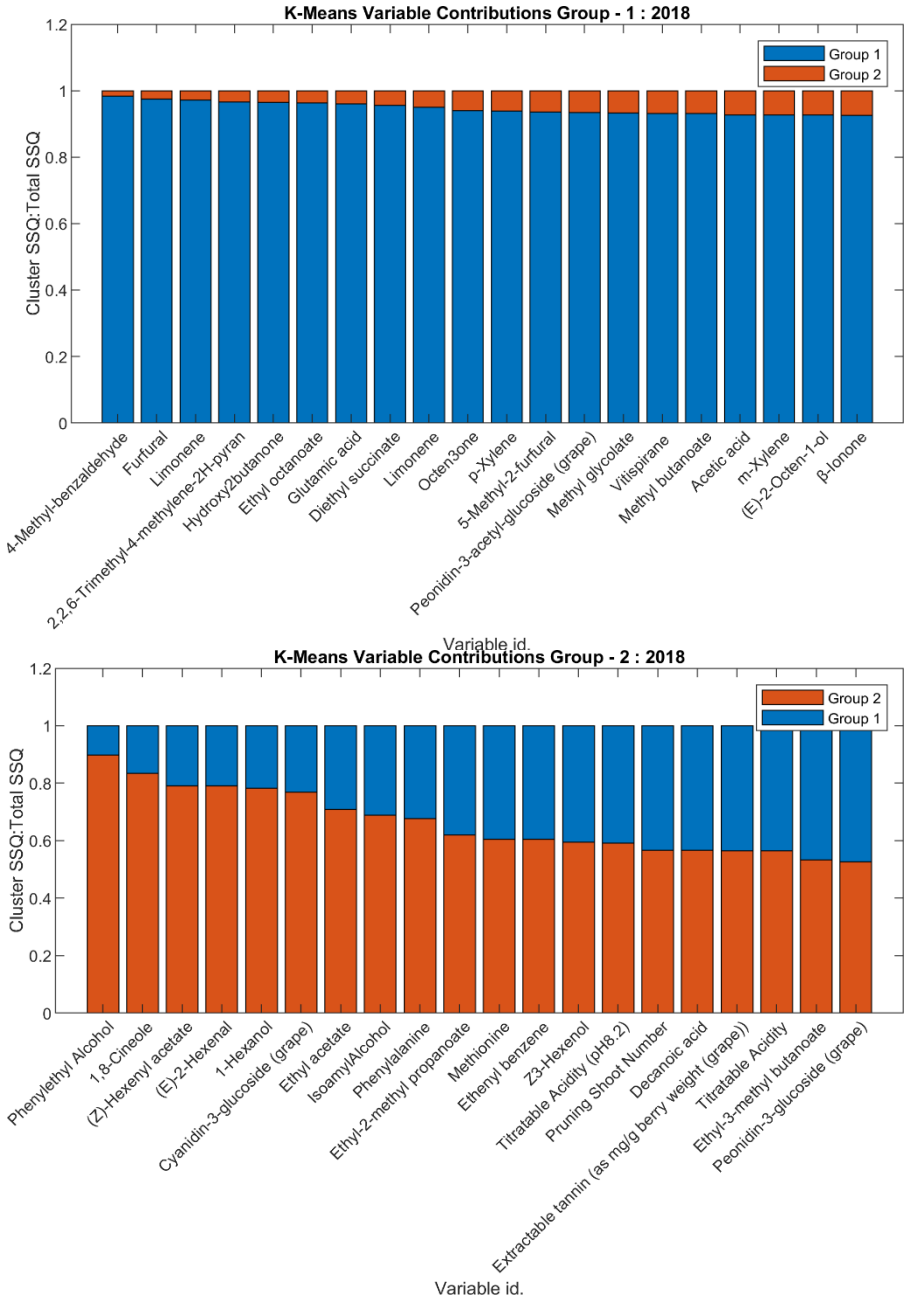


Figure 6.6.18 Variable importance of the twenty most influential attributes for k-means clusters for vintage 2018 model. Variable importance to group 1 and 2 is shown as a ratio of the sum of squares for samples in each cluster to the sum of squares of all samples for the measured attribute.

6.6.11 K-means variable importance Vintage 2019

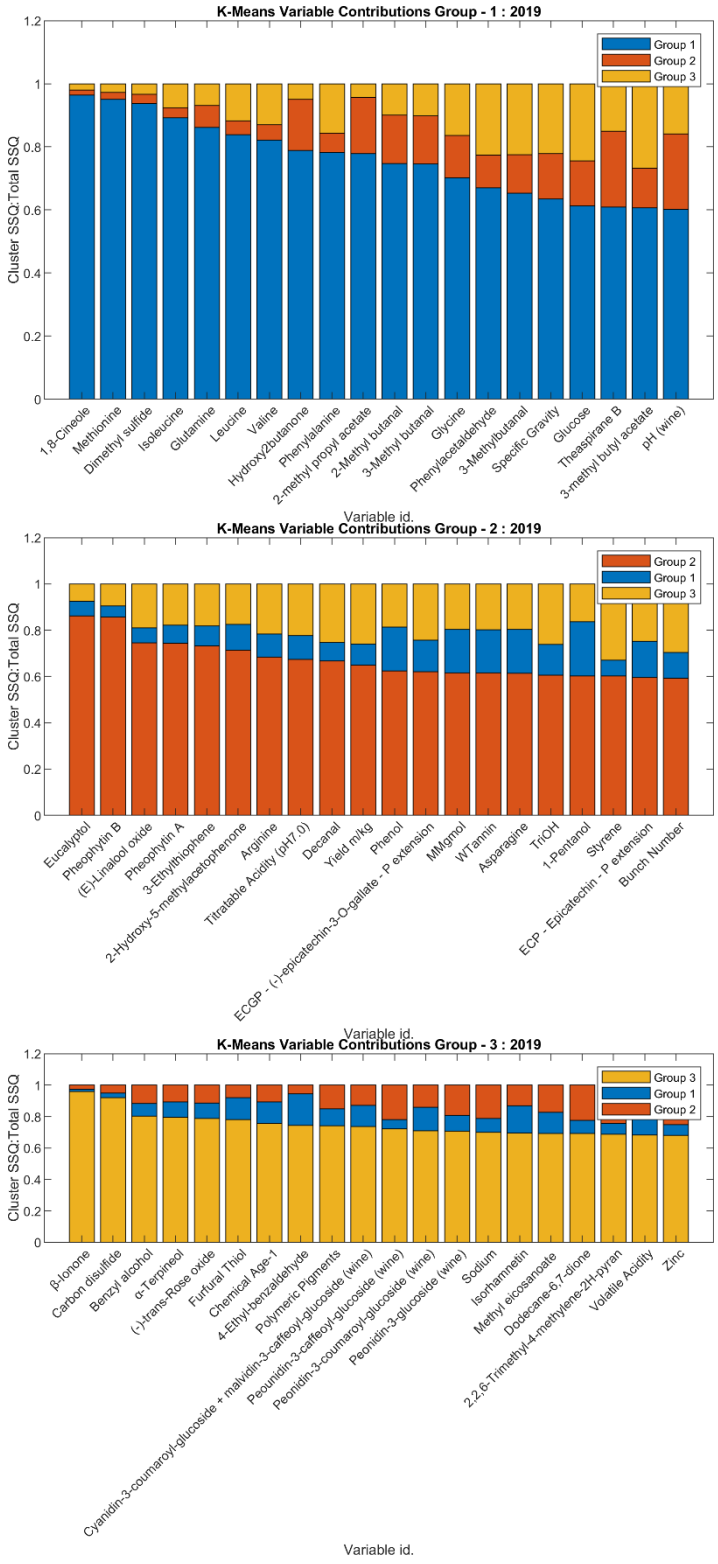


Figure 6.6.19 Variable importance of the twenty most influential attributes for k-means clusters for vintage 2019 model. Variable importance to group 1, 2 and 3 is shown as a ratio of the sum of squares for samples in each cluster to the sum of squares of all samples for the measured attribute.

6.6.12 K-means variable importance Vintage 2020

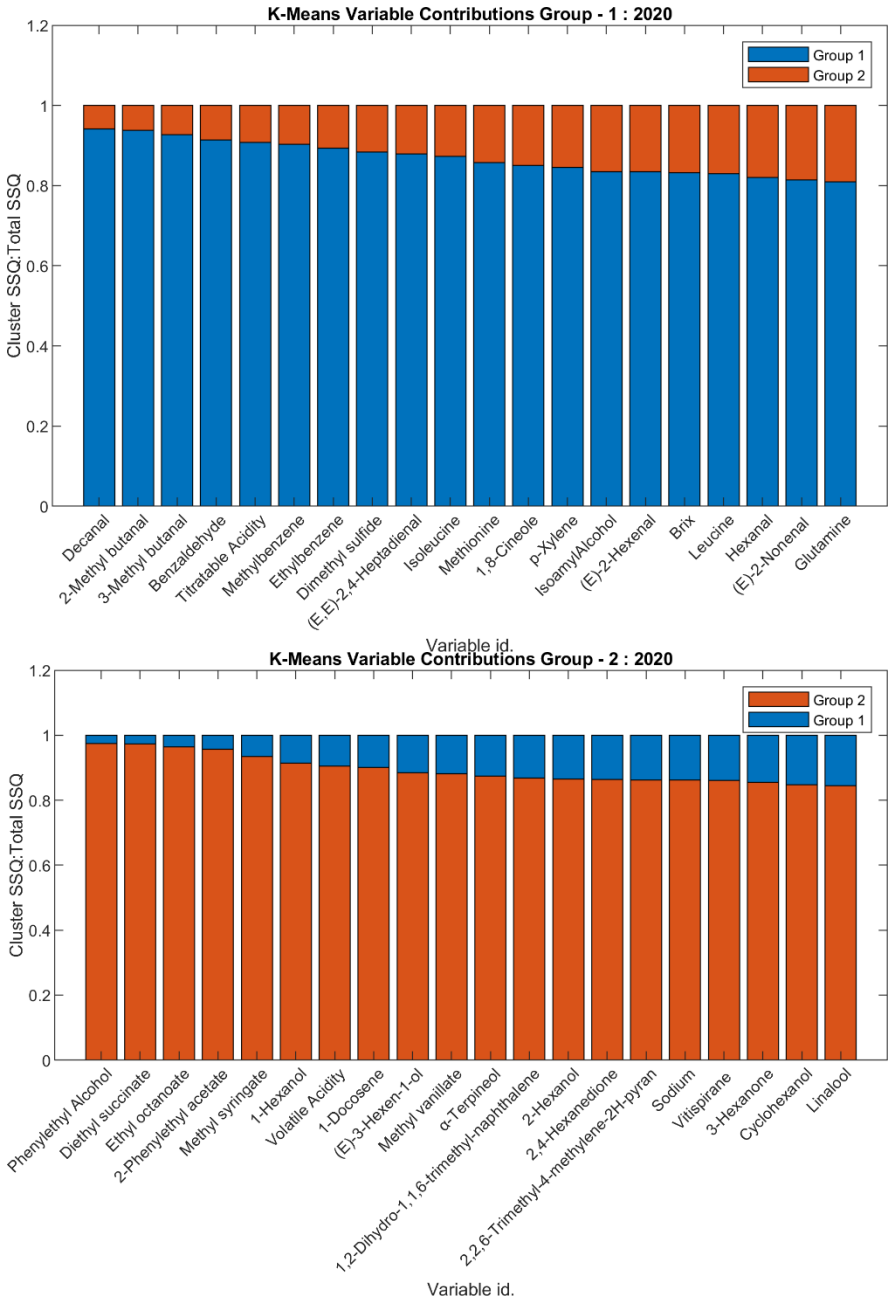


Figure 6.6.20 Variable importance of the twenty most influential attributes for k-means clusters for vintage 2020 model. Variable importance to group 1 and 2 is shown as a ratio of the sum of squares for samples in each cluster to the sum of squares of all samples for the measured attribute.

6.6.13 K-means variable importance Vintage 2021

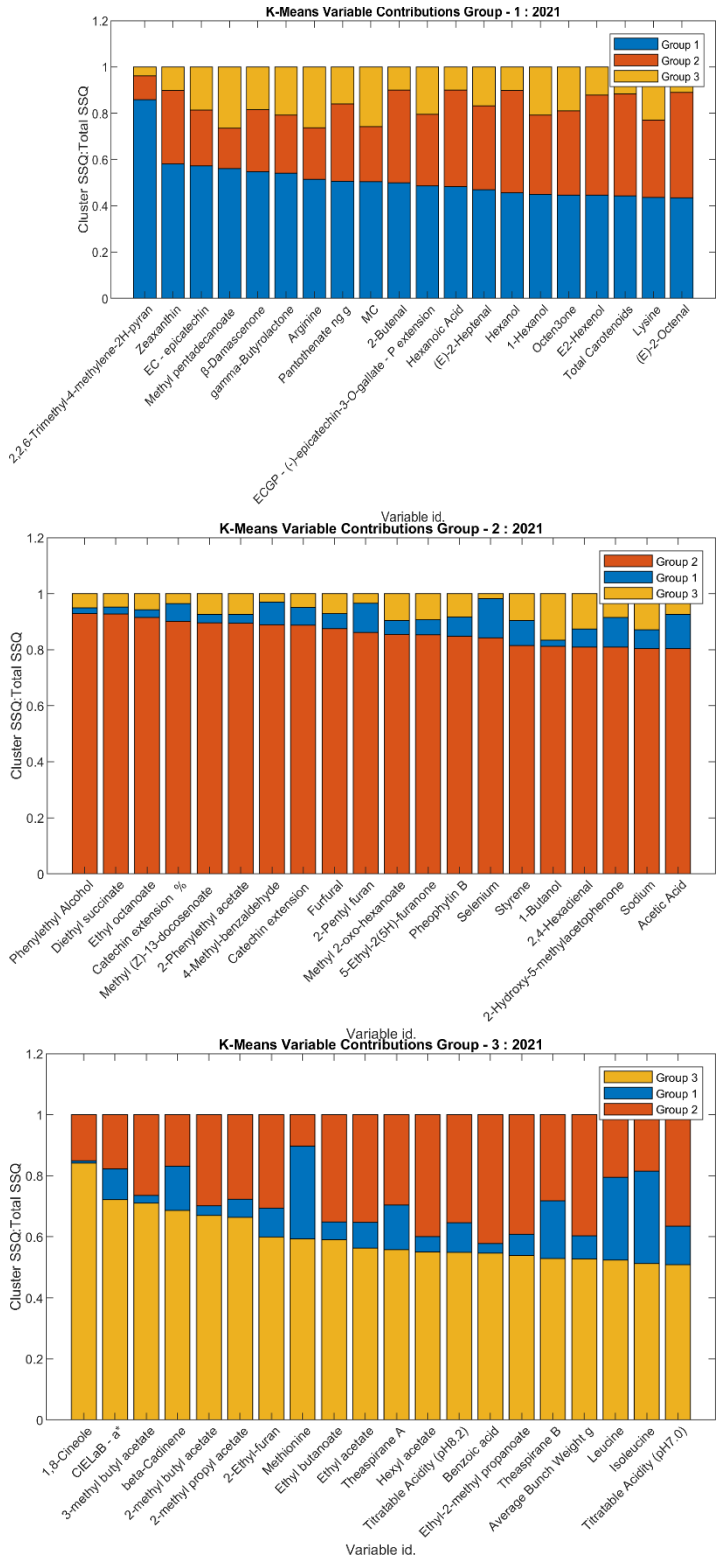


Figure 6.6.21 Variable importance of the twenty most influential attributes for k-means clusters for vintage 2021 model. Variable importance to group 1, 2 and 3 is shown as a ratio of the sum of squares for samples in each cluster to the sum of squares of all samples for the measured attribute.

6.6.14 K-means variable importance All Vintages

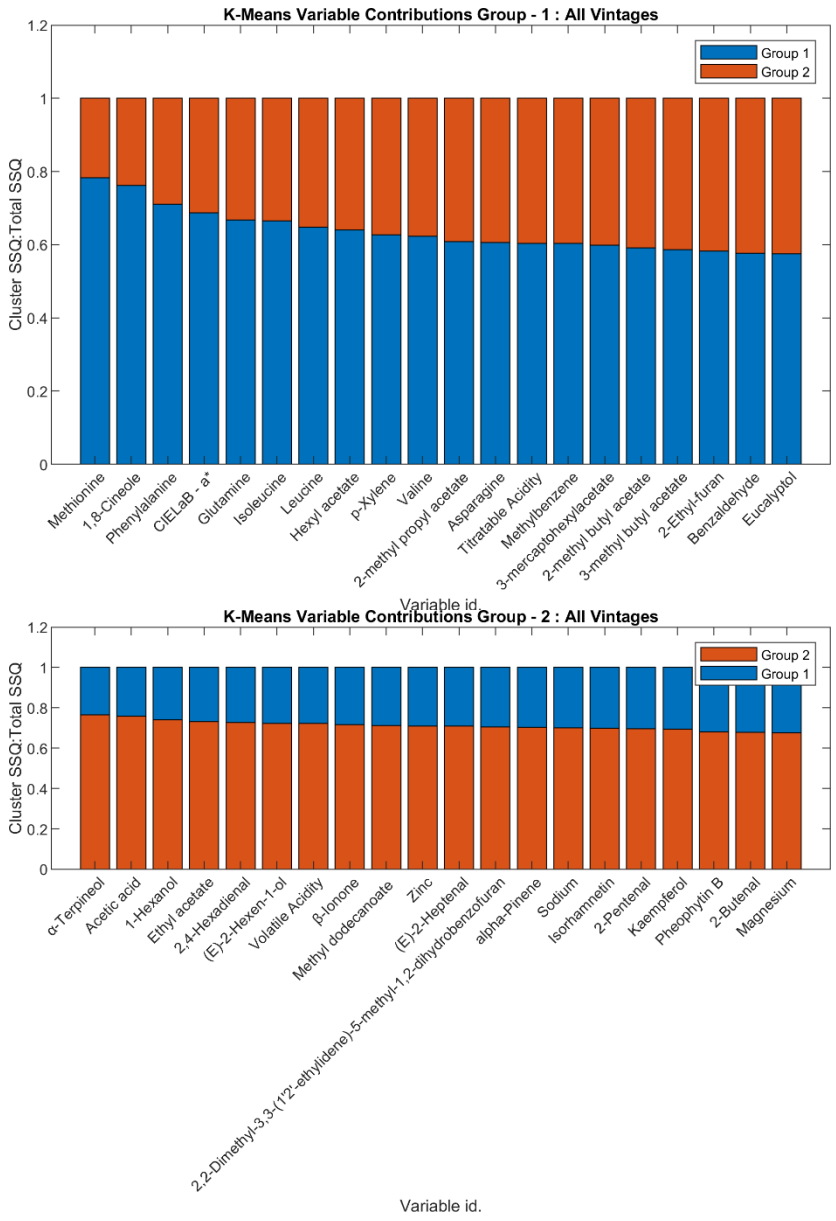


Figure 6.6.22 Variable importance of the twenty most influential attributes for k-means clusters for the 'All vintages' model. Variable importance to group 1 and 2 is shown as a ratio of the sum of squares for samples in each cluster to the sum of squares of all samples for the measured attribute.

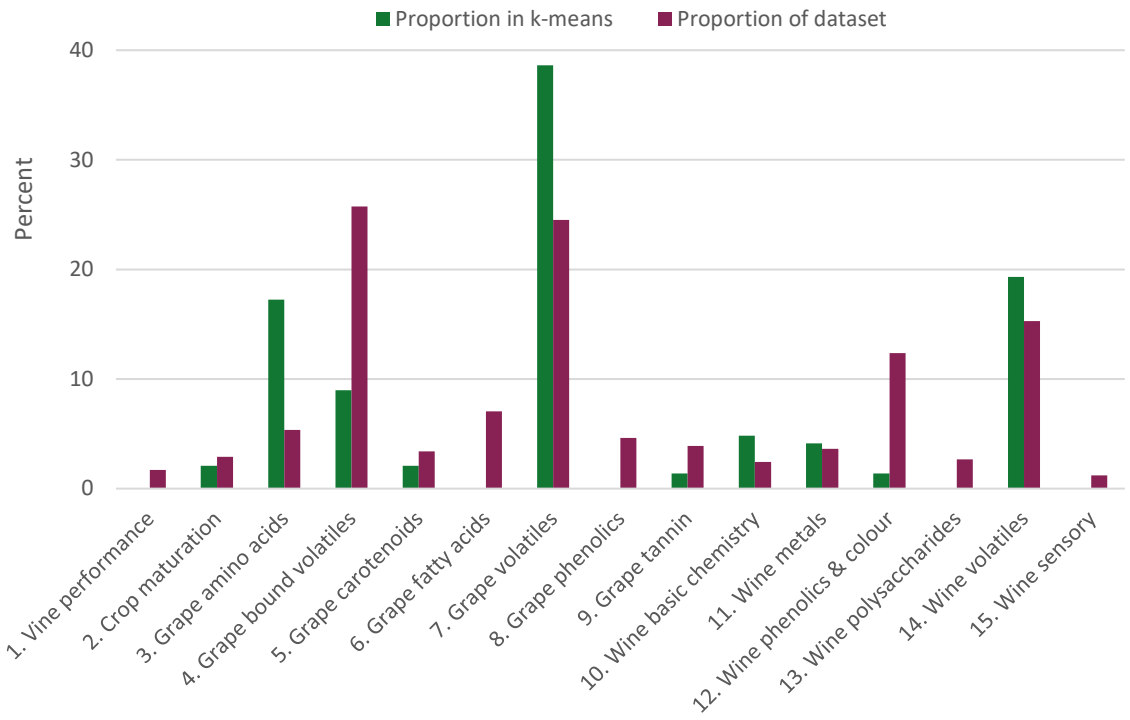


Figure 6.6.23 Under and over representation of data block attributes relative to the total data block size for the most influential attributes for assignment of sample to clusters in the k-means models.

6.6.15 Random Forests classification model

The Random forests (RF) algorithm (Breiman 2001) was used to build a classification modelto investigate the variables that may be responsible for the distinctiveness of Barossa sub-regions. The R package 'randomForest' (version 4.7 – 1.1) (Liaw and Wiener 2002) was used to fit and optimise models.

An initial RF model was built with 383 predictors to classify 238 samples, and subsequent optimisation steps were performed to find a final model that had the lowest classification error while using the fewest predictors. Out-of-bag (OOB) error, defined as the percentage of samples wrongly classified by the RF model, was the metric used to evaluate model performance. OOB error could be lowered by eliminating predictors that did not contribute to distinguish sample classes. Mean decrease in accuracy (MDA) and mean decrease in Gini index (MDG) are two metrics computed by the RF to indicate a predictor's contribution to classification accuracy of the model. A popular predictor selection strategy based on OOB, MDA and MDG, previously proposed by (Han, et al. 2016) was adapted to optimise the current model.

From the initial RF model, the MDA and MDG for each predictor were individually ranked in descending order (decreasing in importance to the model), and predictors were ordered according to the sum of the two ranks. The predictors among the bottom 10% of importance ranking were eliminated, and the reduced data set was used to fit a subsequent RF model. This process was carried out iteratively until there were less than 10 predictors left in the model. The model with the lowest OOB error was considered to be optimal. The true sub-region labels were permuted 200 times and fitted with a RF model with each permutation. The empirical *p*-value for each selected predictor was determined from the proportion of instances where the permuted MDA exceeded the MDA value in the initial RF model. The cut-off for *p*-value was set at 0.05 for validating predictor importance.

The current model contains six sample classes (sub-regions), which requires the RF algorithm to construct complex decision boundaries using a relatively large number of predictors. Some predictors may be included in the model because they were important for distinguishing a subset of classes, despite they may provide no predicting power for the rest of the classes. Decomposing a multiclass problem into a series of pairwise (binary) classification problems has been shown to be a viable strategy to render the results of predictor selection and sample grouping of a multiclass problem more interpretable (Enot, et al. 2008). As opposed to a global model considering all classes, a model discriminating two classes may only require a relatively small number of predictors with high variance between the two classes. This would also make it easier to interpret associations between selected predictors and class groupings. Thus, the six sub-region was decomposed into 15 two-sub-region pairs, and an RF model was fitted and optimised for each pair using the procedure performed for the global model. For all iterations of a binary model series, if multiple models reached the same lowest OOB error, the most parsimonious model with the fewest predictors was chosen.

6.6.16 RF model visualisation

RF model generates a proximity value between every pair of samples, where if they end up on the same terminal node of a decision tree, the proximity value is increased by one. The proximity value is normalised by dividing the number of trees in the forest, giving a final value between 0 and 1 (Breiman 2001). A Euclidean distance matrix was calculated from the

proximity matrix and decomposed with classic multidimensional scaling (MDS) using the smacof package (version 2.1-5) (Mair, et al. 2022). The predictors of the RF model were then regressed on the MDS configuration to obtain the coordinates in the same vector space as the samples. Biplots of both sample scores and predictor loadings were then generated to visualise class groupings as well as their associations with the predictors.

6.6.17 Global model

6.6.17.1 Sample classification accuracy and clustering

The 383 predictors included in the current data set were eliminated based on their importance ranking in 33 iterations, where within each iteration, 10% of the least important predictors were removed and the RF model was re-fitted (Figure 6.6.23). The classification error decreased at first probably due to elimination of 'noisy' predictors that did not show any clear pattern of variation among regions. The model built in the 14th iteration showed the lowest classification error at 11.3%, which equated to 27 wrongly classified samples out of all 238 samples. After the 14th iteration, the classification error gradually increased as more predictors were eliminated, indicating that predictors that showed regional variation were being eliminated. As such, model 14 was selected as the optimal global model. This model included 93 predictors. A confusion matrix that shows the overall performance of the global model for correct and misclassified samples is presented in Table 6.6.5. The rows in the table represented the true class of samples, while the first six columns represented the predicted classes. For example, the first row of the table showed that out of all samples collected in Central Grounds, 28 of them were correctly classified as Central Grounds, while two were wrongly classified as Eden Valley and another two as Northern Grounds. The classification error rate for Central Grounds was thus 12.5% (4/32). Table 6.6.5 showed that Eden Valley and Northern Grounds samples were predicted relatively well, with classification errors lower than 3%. In comparison, Eastern Edge samples had the lowest classification accuracy, with 26.3% of samples wrongly classified. The average margin of prediction value is a metric to indicate the model's confidence in predicting a class. A higher margin value indicates higher robustness of prediction for a class, with a value of 1 demonstrating that all decision trees within a forest unanimously predicted a class correctly. The current model found that Eden Valley samples were the easiest to classify, followed by Northern Grounds and Western Ridge samples.

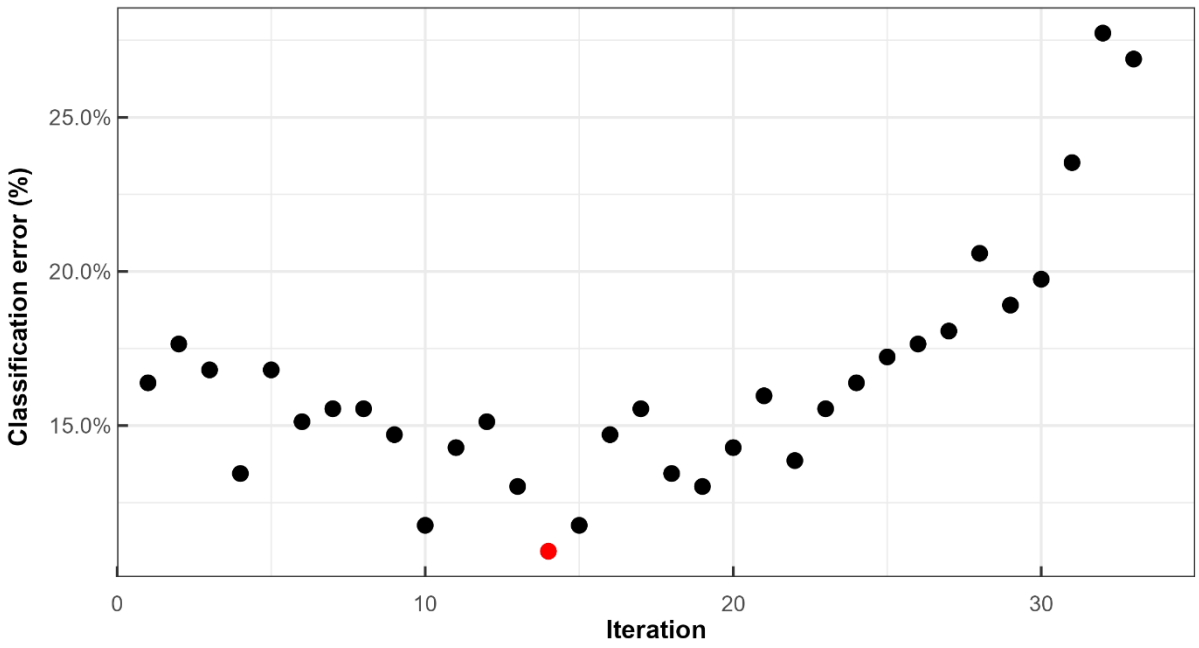


Figure 6.6.23 Classification error in a serious of predictor elimination iterations. In each iteration, 10% of predictors of the lowest importance ranking were eliminated. The model with lowest classification error is marked in red. This model has a classification error of 11.3%.

Table 6.6.5 Confusion matrix, class prediction error (%) and average margin of prediction for each region

	CG	EE	EV	NG	SG	WR	Class error (%)	Margin of prediction
CG	28	0	2	2	0	0	12.5	0.14
EE	4	28	0	1	1	4	26.3	0.15
EV	0	0	47	0	0	1	2.1	0.38
NG	0	0	1	35	0	0	2.8	0.27
SG	0	0	2	0	31	5	18.4	0.13
WR	0	1	2	0	0	43	6.5	0.21

Sample clustering based on multidimensional scaling analysis of the proximity matrix presented in Figure 6.6.24. The first two dimensions accounted for only 16% of the total data set variation, indicating the complexity of this data set. Some trends in clustering based on sub-region can be observed, despite overall separation among sub-regions being unclear. The Eden Valley sub-region was clearly separated from the rest of the sub-regions on the first dimension, while Western Ridge and Northern Grounds sub-regions can be separated on the second dimension. These three sub-regions also had the best classification accuracies and robustness (Table 5.8.1). The misclassified samples mostly existed in the space where multiple sub-regions intersected, except for sample no. 122, 123 and 272, which are site 16 from vintage 2019 and 2021. These samples appear to have a higher commonality to the Western Ridge sub-region samples rather than other Southern Grounds samples. Other than site 16, there were other sites that were consistently wrongly classified for multiple vintages (Table 6.6.6). Site 12 from Eastern Edge had two replicates misclassified as Western Ridge in 2018 and one replicate in 2020. Two replicates from Site 9 in were wrongly classified as

Central Grounds in 2019 and 2020 respectively but were wrongly classified as Northern Grounds and Western Ridge in 2021.

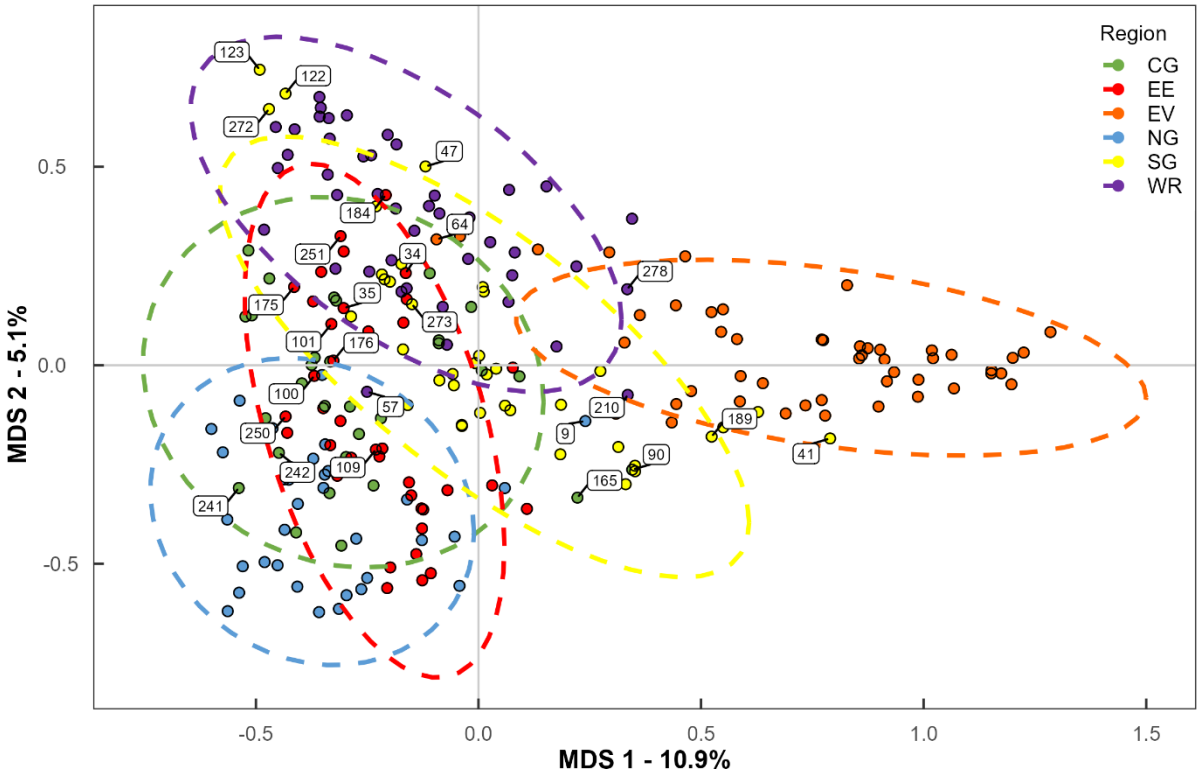


Figure 6.6.23 Multidimensional scaling plot based on the proximity matrix generated by the global RF model. Colour corresponds to region. The dotted lines represent the 95% confidence intervals based on multivariate *t*-distribution. The misclassified samples were labelled with their sample index.

Table 6.6.6 Misclassified samples in the global model.

Sample index (Table 3)	True region	Site	Vintage	Replicate	Predicted region
90	CG	SR5	2019	R3	EV
165	CG	SR5	2020	R3	EV
241	CG	SR6	2021	R1	NG
242	CG	SR6	2021	R2	NG
34	EE	SR12	2018	R1	WR
35	EE	SR12	2018	R2	WR
109	EE	SR12	2019	R1	SG
184	EE	SR12	2020	R1	WR
100	EE	SR9	2019	R1	CG
101	EE	SR9	2019	R2	CG
175	EE	SR9	2020	R1	CG
176	EE	SR9	2020	R2	CG
250	EE	SR9	2021	R1	NG
251	EE	SR9	2021	R2	WR
64	EV	SR22	2018	R1	WR
9	NG	SR3	2018	R3	EV
189	SG	SR13	2020	R3	EV
41	SG	SR14	2018	R2	EV
47	SG	SR16	2018	R2	WR
122	SG	SR16	2019	R2	WR
123	SG	SR16	2019	R3	WR
272	SG	SR16	2021	R2	WR
273	SG	SR16	2021	R3	WR
278	WR	SR18	2021	R2	EV
57	WR	SR19	2018	R3	EE
210	WR	SR20	2020	R3	EV

6.6.17.2 Predictor selection based on region

To explore associations between predictors and regions, the predictors were projected by linear regression onto the first two dimensions of the sample distribution (Figure 26). A few clusters could be identified where predictors from the same data block were correlated. In terms of phenolics and colour measurements in grapes, the first dimension is also highly correlated with degree of lightness in CIELab-L* measurement [400], while negatively associated with Wine Colour Density [380], total phenolics [384], chemical age2 [379] and malvidin-3-coumaroyl-glucoside in wine [368]. The first dimension was also positively correlated with grape titratable acidity (17) and negatively correlated with grape pH (16). The first dimension was positively associated with a range of fatty acid ethyl esters and acetates (hexyl acetate [417], ethyl butanoate [425], ethyl octanoate [429] and ethyl decanoate [430]). On the other hand, the first dimension was negatively associated with a cluster of fatty acids measured in grapes (methyl pentadecanoate [165], methyl heptadecanoate [167], methyl nonadecanoate [169], and methyl octadecenoate [186]); and a cluster of wine polysaccharide sub-units (glucuronic acid [405], galacturonic acid [406], galactose [408] and arabinose [410]). Other predictors that are highly negatively associated with the first dimension

included two grape anthocyanins (cyanidin-3-acetyl-glucoside [298] and malvidin-3-acetyl-glucoside [301]); three grape bound volatiles (2-methylenebornane [110], 1-(2,3,6-trimethylphenyl)-3-buten-2-one [115] and 2,3-dihydro-3,3,4,5-tetramethyl-1H-inden-1-one [127]); and specific gravity [10] in wine.

The second dimension was positively correlated with a cluster of wine phenolics and colour measurements (total phenolics [384], chemical age 2 [379], wine tannin mean degree of polymerisation [388] and wine tannin molecular mass (g/mol) [387]); sodium in wine [348]; 2-butanone in grape volatile [192]; fucose sub-unit in wine polysaccharide [411]; and canopy porosity [6]. On the other hand, the second dimension was negatively correlated with a cluster of grape volatile compounds (diethyl succinate [278], ethyl octanoate [252], and styrene [230]); a cluster of carotenoids in grapes (chlorophyll B [218], chlorophyll A[219] and beta-carotene [153]); a cluster of wine volatiles (beta-damascenone [452], 3-mercaptohexanol [119], and methanethiol [117]); and plant area index of grapevine [7].

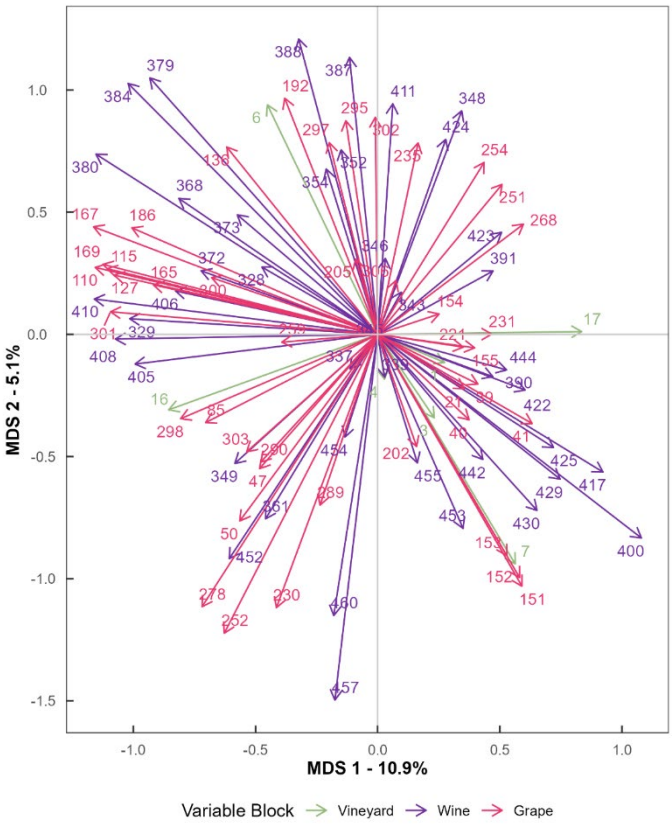


Figure 6.6.25 Loadings plot of predictors regressed onto the first two dimensions of multidimensional scaling. The predictors were coloured based on data block and labelled with their sequential number in Table 5.8.2.

To further explore the contribution of each predictor to classifying each region, a permutation test was performed. The true MDA score for each predictor was compared to a null distribution of MDA scores from 200 permutated RF models. A significant *p*-value ($p < 0.05$) indicates that the predictor contributed to the model's accuracy in predicting each region. Although all predictors significantly contributed to the global model, not all predictor significantly contributed to each sub-region (Figure 6.6.26). Notably, a few predictors

marginally negatively impacted prediction accuracies of samples from Eden Valley, Northern Grounds and Southern Grounds.

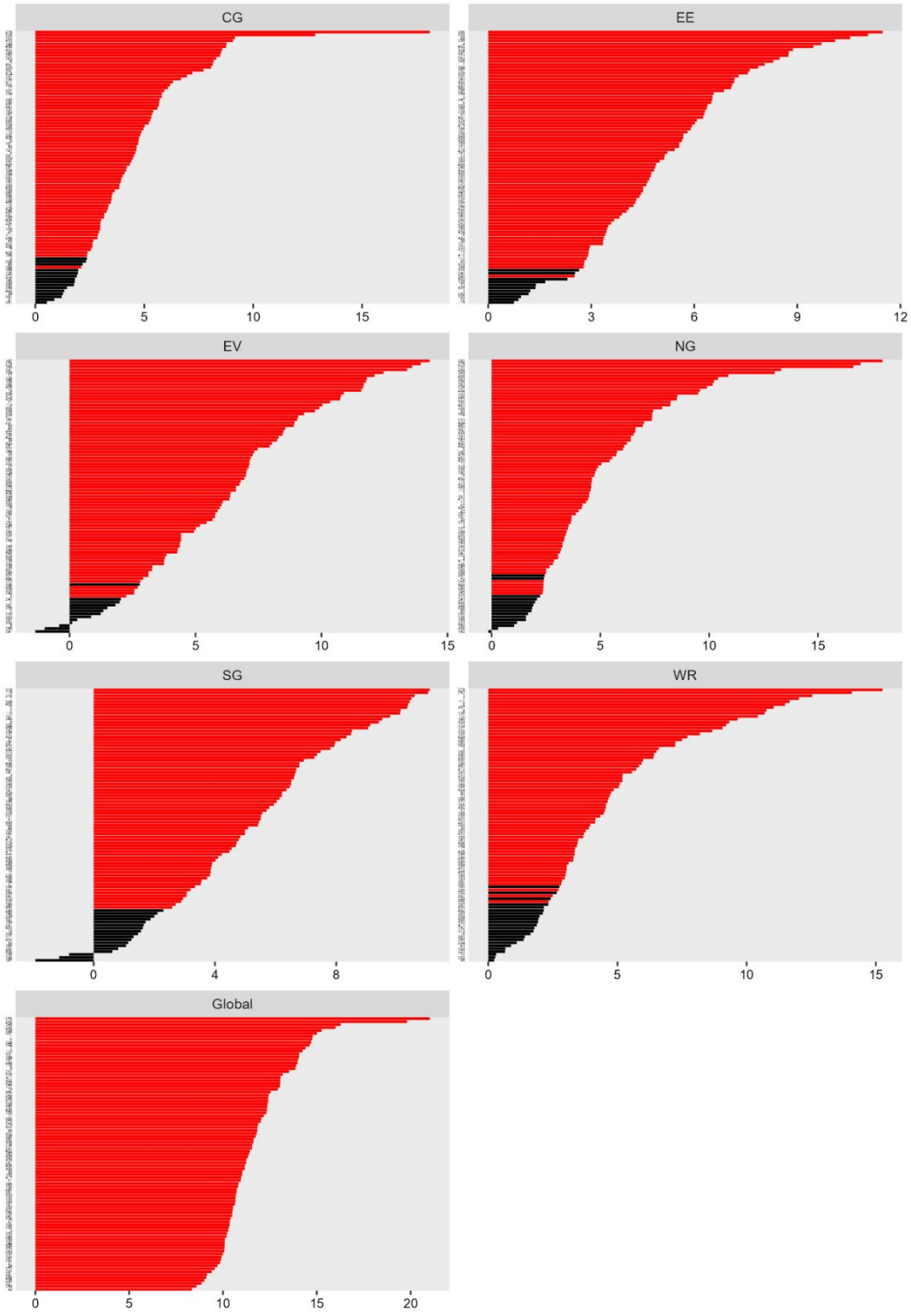


Figure 6.6.26 Mean decrease in accuracy (MDA) of predictors (x-axis) in each sub-region for the 93 attributes in the global model. The red colour showed that the MDA value was significant ($p < 0.05$) by a permutation test and black colouration infers an insignificant contribution of that attributes for class prediction. CG: Central Grounds; EE: Eastern Edge; EV: Eden Valley; NG: Northern Grounds; SG: Southern Grounds; WR: Western Ridge.

The top 25% of predictors contributing to the overall classification accuracy (Figure 6.6.27) and to each sub-region (Figure 6.6.28) are presented. Out of 93 predictors included in the model, 83 were ranked among the top 25% in at least one of the six sub-regions. However, 42 of them appeared to be important in only one region, and a further 14 were important in only two regions.

Diethyl succinate, a volatile compound measured in grapes, was the only predictor that was ranked in the top 25% of importance in all regions as well as in the overall model. It had the highest MDA in the global model (Figure 6.6.27), as well as in Central Grounds and Western Ridge (Figure 6.6.28). A further four predictors were among the top 25% in the global model, as well as five out of six regions, namely, plant area index [7], sodium [348] and cobalt [339] in wine, as well as ethyl octanoate measured in grapes [339].

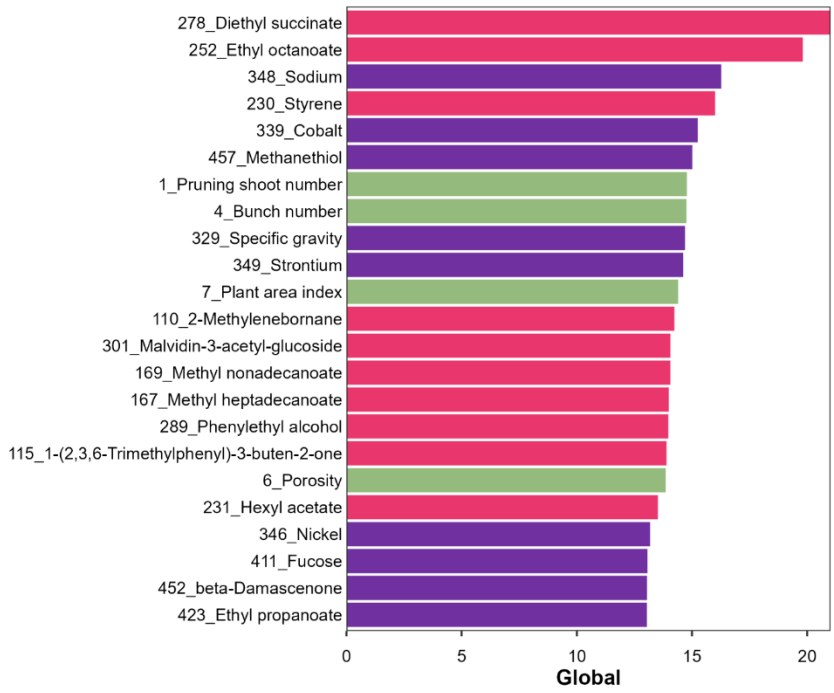


Figure 6.6.27 Top 25% predictors that contributed to the classification accuracy of the global model. X-axis showed the mean decrease in accuracy. The bars were coloured based on the type of measurement: vineyard measurements (green), grape measurements (magenta) and wine measurements (purple). Bars were labelled with predictor index and name (Table 5.8.2).

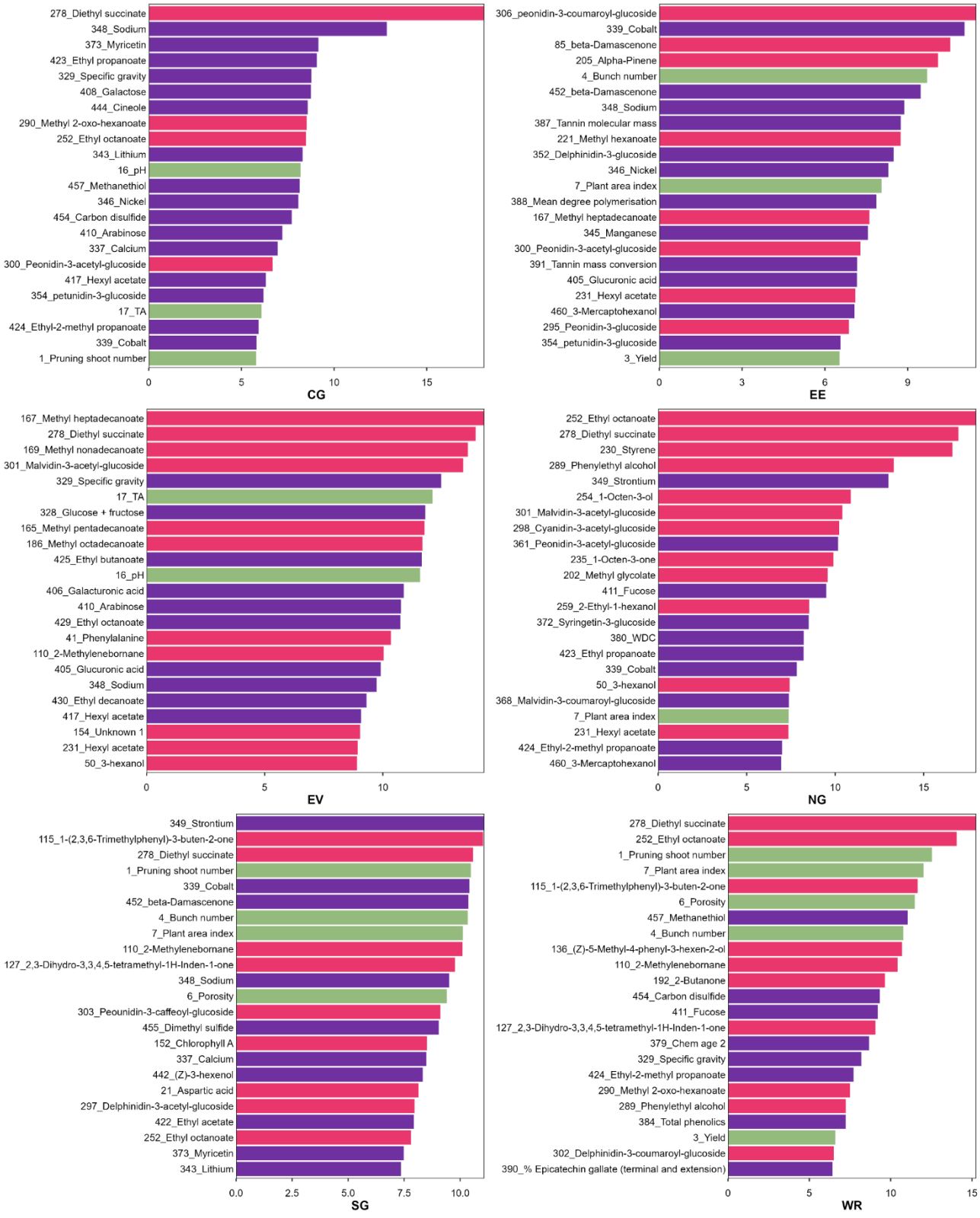


Figure 6.6.28 Top 25% predictors that contributed to the classification accuracy of each region. For each sub-plot, x-axis showed MDA score. The bars were coloured based on the type of measurement: vineyard measurements (green), grape measurements (magenta) and wine measurements (purple). Bars were labelled with predictor index and name (Table 5.8.2). CG: Central Grounds; EE: Eastern Edge; EV: Eden Valley; NG: Northern Grounds; SG: Southern Grounds; WR: Western Ridge.

The standardised concentration of the predictor with the highest MDA in each sub-region was plotted for each vintage (Figure 6.6.29). Diethyl succinate had the highest MDA in Central Grounds and Western Ridge, as well as the second highest MDA in Northern Grounds (Figure 6.6.28). This compound had relatively higher concentration in Central Grounds samples and lower in Western Ridge samples throughout the four-season data (Figure 6.6.29A). Although the median value of diethyl succinate was higher in Northern Grounds compared to all other regions, the variation in the Northern Grounds samples was also considerably higher, which may lead to confusion when used for classification. An anthocyanin measured in grapes, peonidin-3-coumaroyl-glucoside, had the highest MDA in classifying Eastern Edge, possibly because its concentration was lower in samples from this sub-region in vintage 2019, 2020 and 2021, although this trend was not clear for vintage 2018. Grape fatty acid methyl heptadecanoate had the highest MDA in predicting Eden Valley samples, and its concentration was lowest in grape samples from Eden Vally throughout the four vintages. Similarly, ethyl octanoate measured in grapes had the highest MDA for predicting Northern Grounds samples and was observed to be of highest concentrations in grape samples from this region. Lastly, Sortium had the highest MDA for predicting Southern Grounds samples, probably because wine samples from this sub-region consistently had the lowest concentration of Sortium throughout the four vintages.

In conclusion, the global RF model achieved partial separation of samples based on region. Eden Valley, Northern Grounds and Western Ridge samples seemed to have more distinctive features that allowed better separation from other regions. By using MDA values computed by the RF model, predictors that made significant contributions for predicting each region could be identified, which aided in investigation and interpretation of variables that drive regional differences in the Barossa Grounds.

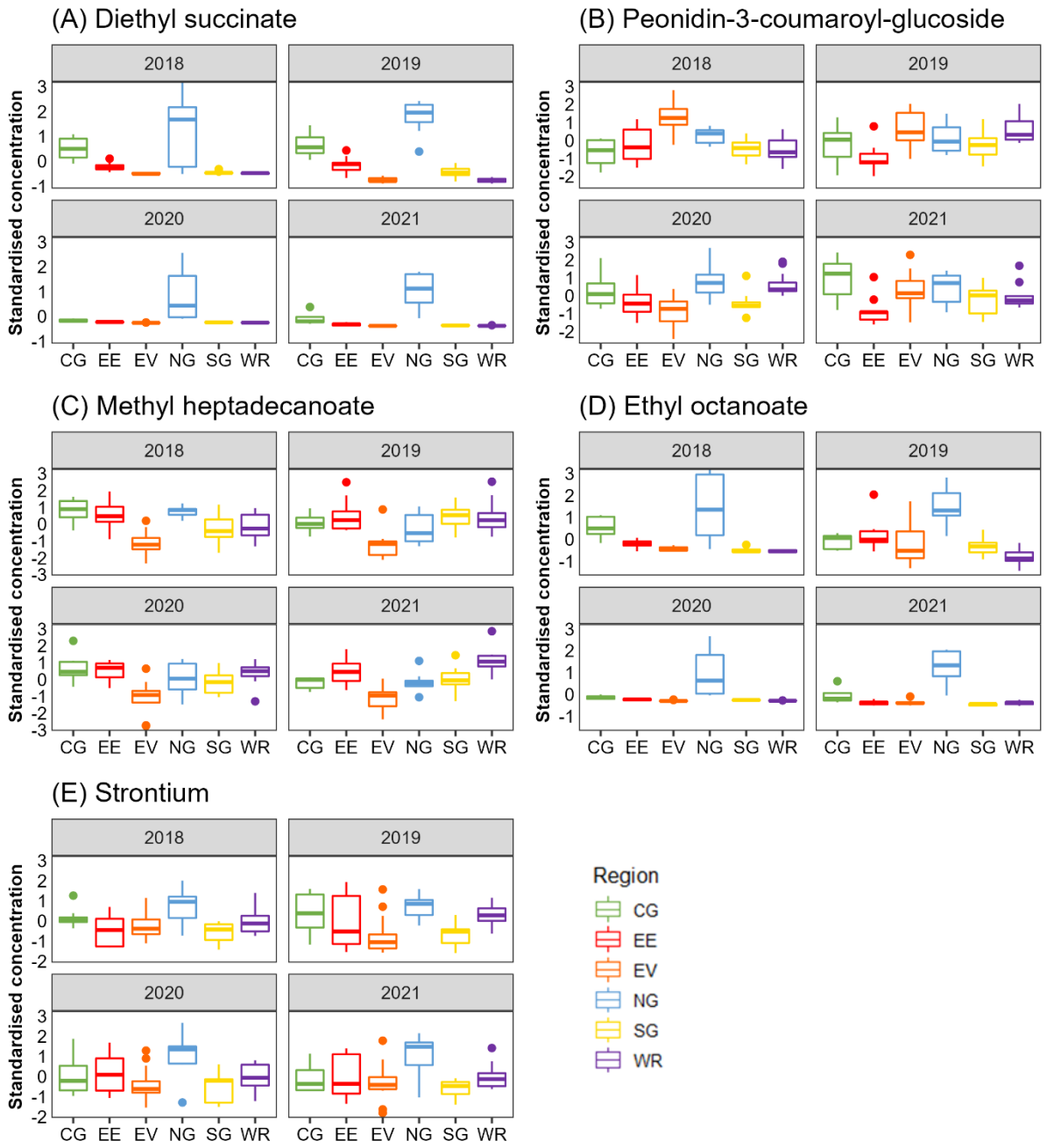


Figure 6.6.29 Box plots of standardised concentration of predictors that had the highest MDA score in predicting each of the six regions in the global RF model. Each vintage was plotted separately. The y-axis was limited to three standard deviations from the mean (mean = 0). Outliers outside this range were not shown in these plots. CG: Central Grounds; EE: Eastern Edge; EV: Eden Valley; NG: Northern Grounds; SG: Southern Grounds; WR: Western Ridge.

6.6.18 Binary classification models

Although the global model seemed to have relatively good classification power for samples from Eden Valley, Northern Grounds and Western Ridge, ambiguity remains for classification of samples from Central Grounds, Southern Grounds and Eastern Edge. Multi-class classification problems force complex algorithmic decisions and compromises to achieve the best overall accuracy. However, this might obscure some distinctive features for each individual class. Furthermore, the overall model contained 93 predictors, which was cumbersome to interpret. Thus, a series of 15 binary RF models were fitted. Compared to multi-class models, binary models usually could be achieved with fewer predictors and higher classification accuracy. Predictor elimination based on importance ranking was also performed for the binary models in order to find the least number of predictors to achieve the best separation between regions.

Figure 6.6.30 shows classification error (%) for each iteration of predictor elimination for each binary model. Out of 15 binary models, seven achieved 100% classification accuracy. For most binary models, few predictors were needed to achieve the best classification accuracy. Three models had higher classification error, i.e. between Central Grounds and Eastern Edge (binary model 1), between Southern Grounds and Eastern Edge (binary model 8), and between Southern Grounds and Western Ridge (binary model 15). For all three cases, most cases of misclassification came from samples from the same site, Site 9 in Eastern Edge, Site 12 in Eastern Edge, and Site 16 in Southern Grounds. These three sites were consistently misclassified in the global model as well. It is possible that these sites showed some dissimilarity with other sites within the same region. The 15 binary models included a total of 142 predictors, 61 of which were not included in the global model. However, most of these predictors were only included in one or two binary models, which means that none of them consistently distinguished a sub-region from all other five sub-regions. In comparison, a few important variables from the global model were also chosen by many binary models. In particular, diethyl succinate and ethyl octanoate, two volatile compounds measured in grapes, were chosen in 12 and 10 binary models respectively. Methanethiol measured in wines was chosen by seven binary models. Detailed information of binary models is given in Appendix 6.

Another interesting feature of binary models is that they could elucidate important predictors in a region, which may not seem clear from the global model. For example, two bound volatiles in grapes, 2-methylenebornane and 2,3-dihydro-3,3,4,5-tetramethyl-1H-inden-1-one, were selected in all binary models that included Southern Grounds. They were not ranked the highest in importance for classifying Southern Grounds samples in the global model. Box plot of these two compounds showed that they were generally lower in Southern Grounds than in other regions for all four vintages (Figure 6.6.31). Another example was four fatty acids measured in grapes. They were chosen by three out of five binary models that included Eden Valley. Box plots showed that they were generally lower in Eden Valley samples than those from other regions (Figure 6.6.32).

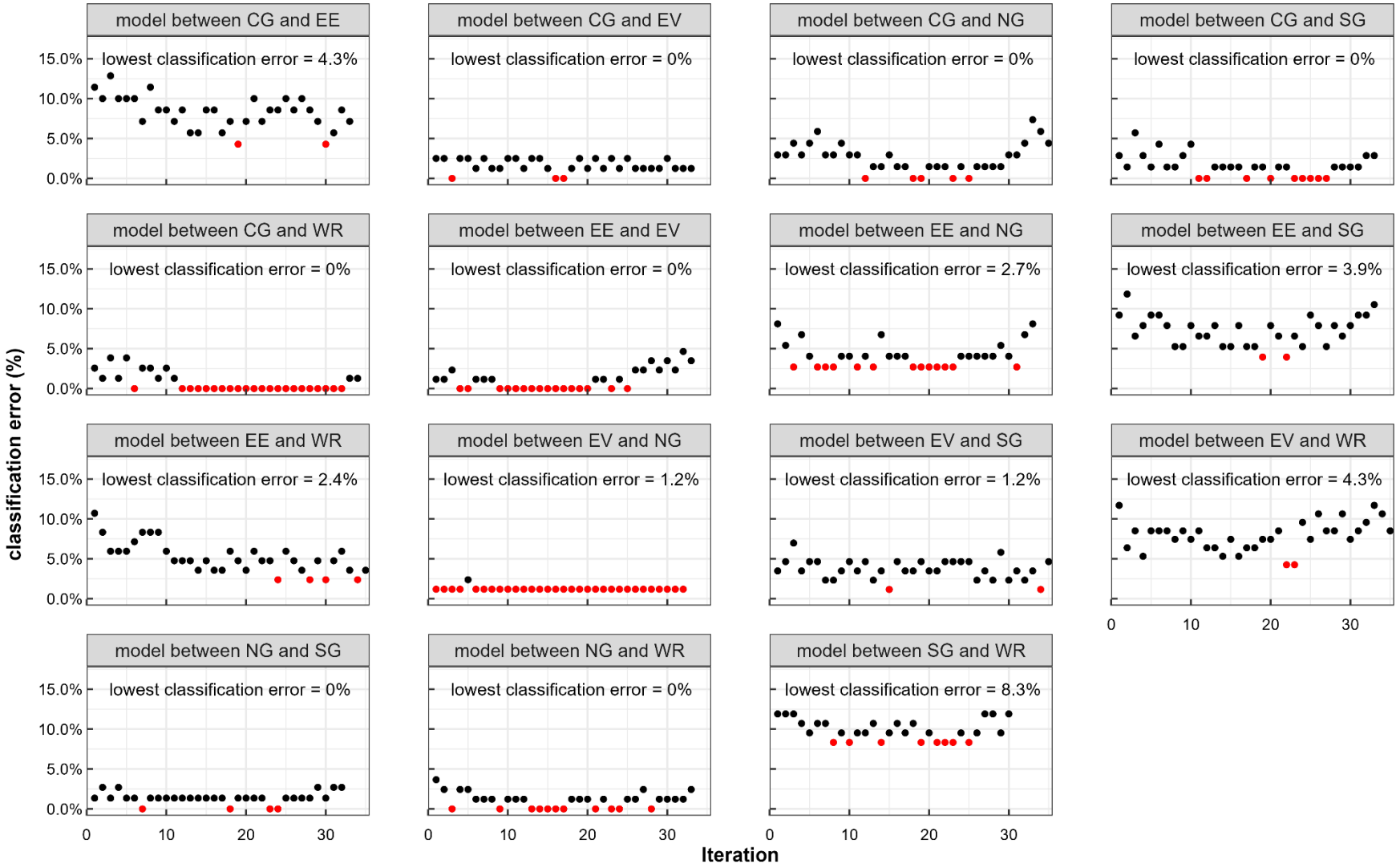


Figure 6.6.30 Percentage of sample misclassification in binary models after a serious of predictor elimination based on importance. The model with lowest classification error is marked in red, and the lowest classification error is shown in each subplot. CG: Central Grounds; EE: Eastern Edge; EV: Eden Valley; NG: Northern Grounds; SG: Southern Grounds; WR: Western Ridge.

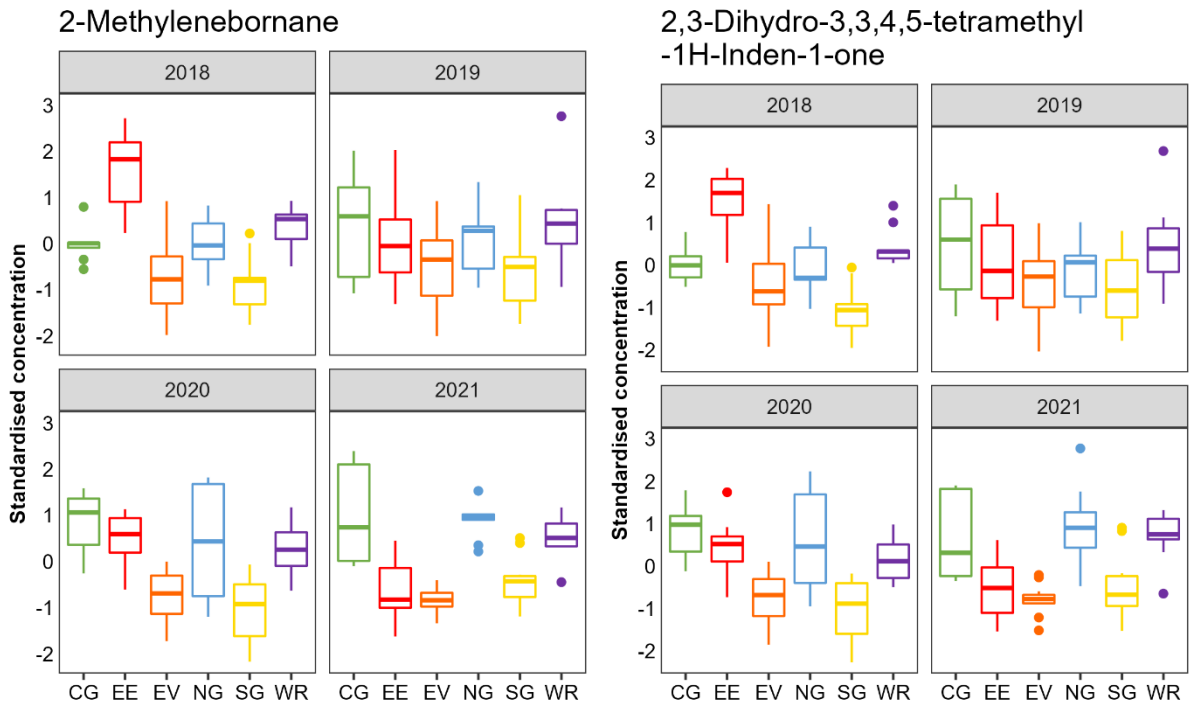


Figure 6.6.31 Box plots of standardised concentration of 2-methylenebornane and 2,3-dihydro-3,3,4,5-tetramethyl-1H-inden-1-one. Each vintage was plotted separately. The y-axis was limited to three standard deviations from the mean (mean = 0). CG: Central Grounds; EE: Eastern Edge; EV: Eden Valley; NG: Northern Grounds; SG: Southern Grounds; WR: Western Ridge.

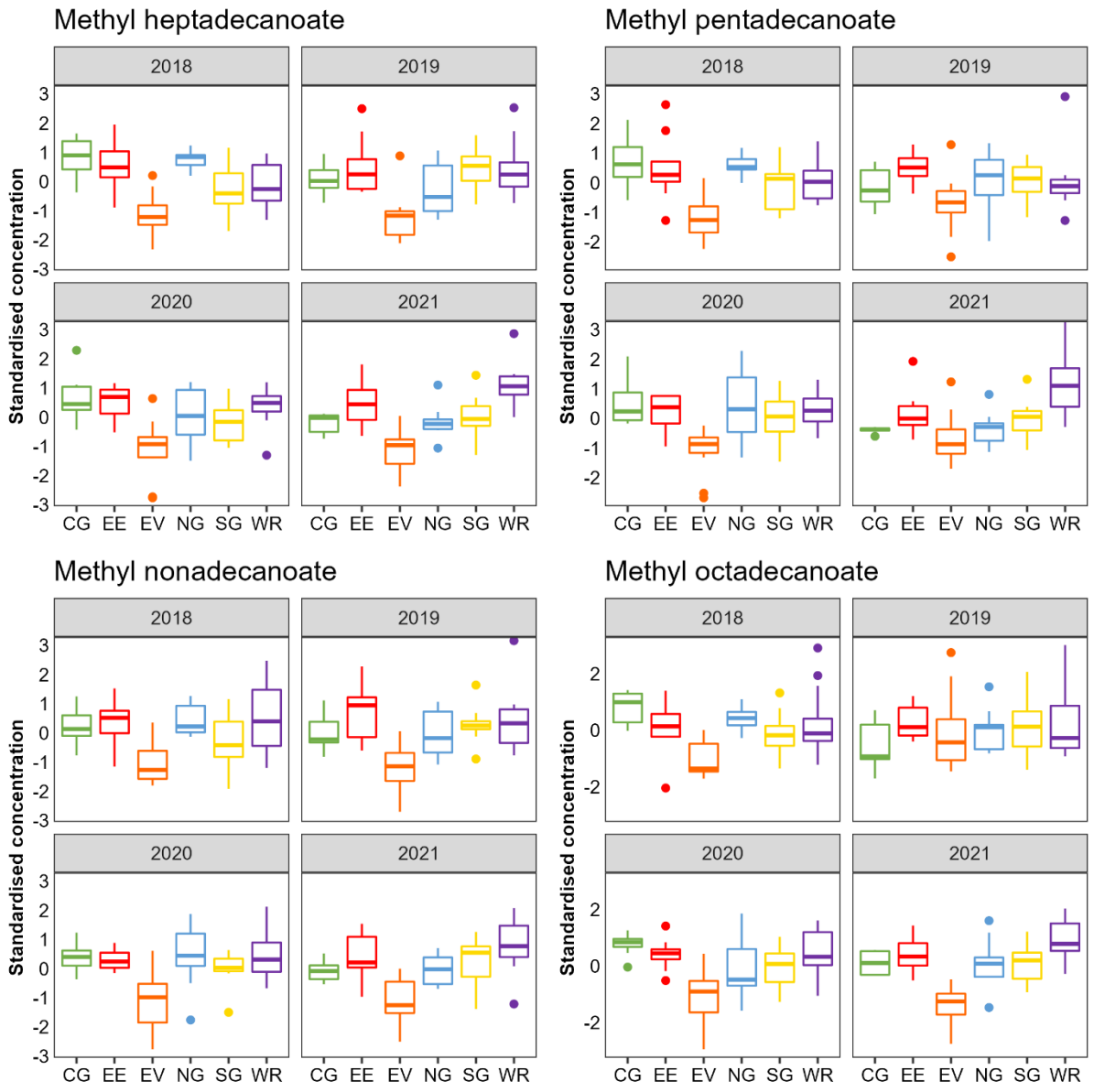


Figure 6.6.32 Box plots of standardised concentration of four fatty acids measured in grapes. Each vintage was plotted separately. The y-axis was limited to three standard deviations from the mean (mean = 0). CG: Central Grounds; EE: Eastern Edge; EV: Eden Valley; NG: Northern Grounds; SG: Southern Grounds; WR: Western Ridge.

7. Outcome/Conclusion

Vineyard-only analysis provided a basis for considering sub-regionalisation of the Barossa GI. The analysis was confined to the land under vine and also made use of an updated climate data set. The vineyard-only analysis clearly separated the Eden and Barossa Valleys, but within the Barossa Valley offers a basis for separation into three zones rather than a single one seen in Figure 6.1.1.

Yield and its components were measured in 24 Shiraz vineyards during three vintages in the Barossa zone. The frequency distribution of yield was L-shaped, with half the vineyards below 5.2 t/ha, and an extended tail of the distribution that reached 24.9 t/ha. The seasonal ratio of actual crop evapotranspiration and reference evapotranspiration was below 0.48 in 85% of cases, with a maximum of 0.65, highlighting the prevalence of a substantial water deficit in these vineyards. Yield gaps increased with increasing vine water deficit, quantified with carbon isotope composition in must. The yield gap was smaller with higher rainfall before budburst, putatively favouring early-season vegetative growth and allocation to reproduction, and with higher rainfall between flowering and veraison, putatively favouring fruit and seed set and early berry growth. The gap was larger with higher rainfall and lower radiation between budburst and flowering. The yield gap declined with altitude however the Eden Valley departed from this trend, with a yield gap that was higher than expected from its elevation. The yield gap increased linearly with vine age.

The impact of weather, site and management practices, underlying elements of terroir, impacting the timing of key phenological stages were explored across the Barossa Zone (GI). Vine phenology was assessed in three zones of 24 vineyards over three vintages using the E-L scale before veraison, and total soluble sugars (TSS) in berries during ripening. The associations between weather, plant traits and viticultural variables, and development in four periods were explored: pre-budburst, budburst-flowering, flowering-veraison and veraison-maturity. The spatial structure of the timing of phenological events suggested three main groups of vineyards. This structure followed gradients in topography and soils across the landscape, and were maintained despite the effect of the season (vintage). Phenology responded mainly to temperature until flowering, and to temperature and canopy size from flowering to maturity. The spatial variation in development was maintained despite vintage effects and management practices. Variation in temperature due to topography and elevation were the major drivers of vine phenological development until flowering. During ripening, development was driven by temperature and carbon capture and partitioning.

Of the grape berry chemistry measures conducted, grape volatile profiles gave the best evidence of some compositional attributes being aligned to the sub-regions. Having said that, while the samples from a sub-region often group together, these groups were not usually discrete and overlap with one or more of the other sub-regional groups. Nevertheless, it would appear that grape volatile compounds may be more affected variables at the geospatial scale rather than variables at the vineyard or intra-vineyard scale. Overlaying these data with the re-analysis of the geospatial clustering would be an interesting test of the hypothesis that this can drive the bound volatile compound profiles in Shiraz berries.

From analysis of the composition of grape anthocyanins, together with extractable measures of tannin and anthocyanin in grapes, statistical models were developed to attempt to

distinguish the phenolic markers for each sub-region. Partial least squares-discriminant analysis (PLS-DA) models were developed in each season, and these were only able to discriminate the Eden Valley samples from the other sub-regions over multiple seasons. In 2018 and 2019, an interesting observation was that the anthocyanin in Eden Valley grapes was more extractable, but this was not observed in 2020 or 2021. The 2020 and 2021 seasons were also cooler than the first two seasons studied. It was interesting to note that some key variables relevant to Eden Valley fruit were similar between the 2018, 2019 and 2020 seasons, and demonstrated proportionally higher levels of non-malvidin mono-glucosides, while malvidin-3-glucoside was lower. In 2021, total anthocyanin, as reflected primarily by malvidin-3-O-glucoside was slightly higher in Eden Valley grape samples, and in particular, higher levels of all coumaroylated anthocyanins were observed. Grape phenolics were found to be an important discriminating factor in the comprehensive multivariate analyses conducted using the entire data set for the project.

For each season of the study, the wines made from each site were analysed for anthocyanins, flavonols, tannin concentration and composition, polysaccharides, metals and multiple classes of volatile compounds. Phenolic compounds were important to all of the multivariate models developed, and it was of interest to note that for the Eden Valley, the key predictors were similar to the models developed for grapes on a seasonal basis. The results of the preliminary PLS-DA results have shown that wine composition could be used to discriminate the sub-regions on a seasonal basis, with greater consistency observed for the Eden Valley, and a lesser extent, the Northern Grounds.

Sensory analysis revealed that sensory profiles of Shiraz wines from the six Barossa sub-regions show several consistent sub-regional characteristics for both standardised small-lot wines and industry scale wine samples across the four investigated vintages (2018, 2019, 2020, and 2021). Across the four vintages, Eden Valley, irrespective of winemaking, has been separated most consistently and described as more savoury and having more green characteristics (eucalypt/mint) compared to the other sub-regions. A possible explanation could be that Eden Valley is the most geographically distinct sub-region with the highest average altitude (approximately 100 m higher than the other sub-regions) (Robinson & Sandercock, 2014). However, significant disparities between vintages and winemaking scales, highlight the importance of i) incorporating multiple vintages and ii) considering the influence of winemaking practices when characterising the expression of terroir. Western Ridge samples were consistently described as more textural wines (i.e. more astringent, rougher) for the small-lot wines but this effect was not observed for the commercial samples. Additionally, wines from Northern Grounds were not associated with woody and intense fruit aroma and flavours in any of the vintages for the small-lot set but were positively associated with the commercially produced ones. This demonstrated a consistent effect of the winemaking scale and practices on the sensory profiles.

Unsupervised clustering of samples was undertaken using the k-means clustering and random forest algorithm of the same measured attributes used for AMOPLS discriminant analysis. The most consistent and stable k-means models were obtained with a two-cluster solution. In comparing the cluster solutions for sample site replicates and vineyard characterisation, a general trend consistent with cluster assignment and increasing vineyard elevation is apparent (Figure 6.6.17). A correlation to cluster assignment is also evident for soil cation exchange capacity, available water holding capacity, growing degree days, and mean January temperature with these measures of vineyard decreasing. However, correlation does not infer

causation, and the trend observations between vineyard characters and sample cluster assignment are noted without attribution.

The contributions of grape amino acids, grape volatiles and wine volatiles to sample cluster assignments by k-means demonstrated the importance of grape and volatile composition to the two clusters in the data. While vine performance and crop maturation measures are not seemingly represented as contributors to the k-means solutions, these are still important contributors through their impact on grape composition. It is well understood that grape berry amino acids are utilised as yeast assimilable nitrogen during fermentation and are important precursors to wine volatiles especially ethyl esters (Antalick, et al. 2015). Importantly, grape berry amino acid profiles can be modified through vineyard management such as nitrogen and water applications and these aspects of site management may account for some of the variance within the observed sample cluster assignment.

The top 25% of predictors contributing to the overall classification accuracy (Figure 6.6.27) and to each sub-region (Figure 6.6.28) are presented above. Out of 93 predictors included in the model, 83 were ranked among the top 25% in at least one of the six sub-regions. However, 42 of them appeared to be important in only one region, and a further 14 were important in only two regions. Interestingly, diethyl succinate, a volatile compound measured in grapes, was the only predictor that was ranked in the top 25% of importance in all regions as well as in the overall model. A further four predictors were among the top 25% in the global model, as well as five out of six regions, namely, plant area index, sodium and cobalt in wine, as well as ethyl octanoate measured in grapes.

The global classification model showed that samples from Northern Grounds, Western Ridge and Eden Valley were relatively easy to classify compared to other regions. Binary models generally achieved good separation between the two regions concerned. Predictor selection strategies, in both the global model and the binary models, helped to identify variables that showed distinctiveness in each sub-region from a very large data set.

This study improved our understanding of wine provenance, and established novel approaches to measures of quality that can be applied to other wine growing regions. Grapegrowers, winemakers and wine brands can use this information to further inform their understanding of the expression of terroir in wine to help secure a sustainable future for the Australian wine industry.

8. Recommendations

Modelling of this very large data set revealed variables that showed distinctiveness in each sub-region. These variables, particularly grape amino acids, grape volatiles, and wine volatiles were identified as being able to discriminate between sub-regions studied and contribute to unsupervised clustering of samples. Further work is needed to determine how this new scientifically based information can be incorporated into the marketing and branding of Barossa Shiraz wine.

There was evidence of some compositional attributes being aligned to the geospatial scale rather than variables at the vineyard or intra-vineyard scale. Overlaying these data with the re-analysis of the geospatial clustering would be an interesting test of the hypothesis that this can drive the chemical profiles and hence quality in Shiraz berries.

Chemical markers identified in this research can be modified through vineyard management, such as the manipulation of nitrogen and water applications both directly and indirectly. Experiments were initiated in this area during the project but due to climatic events such as drought and frost and a loss of sites, detailed experimentation was not possible. Further studies could be undertaken to investigate how best to manipulate these levers to better express terroir.

Large amounts of data and resources (ie. grape and wine samples) have been generated from this project and could be used for other types of analysis. For example, a molecular understanding of differences in Barossa Shiraz was not possible to explore within this project. Grape berry samples collected from sub-region sites over four seasons could be utilised to explore this further.

The multi-disciplinary and -organisational approach used in this project could be extended to other wine growing regions in Australia to better understand wine provenance. However when designing future work in this area careful consideration to the level of funding, resources and the delivery team should be made. This project required a large amount of funding and resources to generate these very large data sets. Hopefully the insights gained from this study could be used to modify the approach of similar studies to find more cost-effective and strategic methods to investigate wine provenance/terroir in other wine regions. To gain the most from these studies a harmonious and committed research and industry team is essential.

9. Appendix 1: Communication

1.1 Presentations

An overview of the project was presented to the following groups and/or events;

- Vine balance workshop, Barossa (November 2017)
- Barossa Grape and Wine Association, Barossa (May 2018)
- Barossa Grounds Team, Barossa (May 2018)
- Wine Innovation Cluster Group, Urrbrae (June 2018)
- First Families of Wine (October 2018).
- School of Agriculture, Food and Wine Research Day, Hahndorf (November 2018)

Industry Reference Group (IRG) meeting 17 October 2018.

A summary of progress to date was presented to the group. Discussion and feedback from the group was provided on the types of treatments that could be applied to manipulate terroir. Irrigation, cover crops and canopy manipulation were discussed as possible management options for low and high capacity sites. The IRG also wanted to see industry tastings organised as part of the project and to work closely with the Barossa Grape and Wine Association to collaborate with the Barossa Grounds project to disseminate findings from the project.

Lukas Danner presented a summary of the sensory findings from the project in the Waite Seminar series in July 2019.

Barossa Terroir Industry Event 8 November 2019.

This event was held to provide all participants in the project with an overview of the project as well as findings from the first and second seasons where available. Research wines were available for tasting as well as soil cores from all sub-regional sites. The event was well attended by approximately 70 people. Discipline leaders from most project team institutes presented findings. Additional benchmarking sites were established from contacts made at this event.

Rob Bramley presented the regional scale part of the work described in section 6.2, either in full or in part, to:

- Winegrowing Research staff at E&J Gallo Winery, 12 December 2019, Modesto, California
- the XIIIth International Terroir Congress, 17-18 November 2020, Adelaide / virtual.
- the XIVth International Terroir Congress and 2nd ClimWine Symposium, 3-8, 2022 July Bordeaux, France.
- The Wine Tasmania Field Day, 12 October 2021
- the 'Fresh Science' session of the 18th Australian Wine Industry Technical Conference, 26-29 June 2022, Adelaide.
- the 25th Symposium of Precision Agriculture in Australasia. 6-7 September Adelaide. SPAA / University of Sydney.

A workshop on terroir was held as part of the 18th Australian Wine Industry Technical Conference, 26-29 June 2022, Adelaide.

This event was held to provide an overview of the project findings where available. Research wines were available for tasting. The event was attended by approximately 26 people.

1.2 Publications

1.2.1 Published

Bramley R. 2022. Underpinning terroir with data. Wine and Viticulture Journal, 37 (3), 54-62.

Bramley R.G.V. and Ouzman J. (2022). Underpinning terroir with data: On what grounds might sub-regionalisation of the Barossa Zone geographical indication be justified? Australian Journal of Grape and Wine Research, 28, 196-207. https://doi.org/10.1111/ajgw.12513.

Bramley RGV, Ouzman J, Trought MCT. 2020. Making sense of a sense of place – Precision Viticulture approaches to the analysis of terroir at different scales. Proceedings of the XIIIth International Terroir Congress, 17-18 November Adelaide / Oeno One, 54, 903-917. https://doi.org/10.20870/oeno-one.2020.54.4.3858.

Bramley R., Ouzman J. and Trought M. (2022a). If NZ can do it, why can't Australia ? Proceedings of the 18th Australian Wine Industry Technical Conference, 26-29 June, Adelaide. https://awitc.com.au/wp-content/uploads/2022/07/2_Bramley.pdf.

Bramley R., Ouzman J. and Trought M. (2022b). Precision Viticulture at regional scale: rethinking the terroir zoning paradigm. Proceedings of the 25th Symposium of Precision Agriculture in Australasia. 6-7 September, Adelaide. SPAA / University of Sydney.

Bramley R., Ouzman J., Sams B. and Trought M. (2022c). Underpinning terroir with data: rethinking the zoning paradigm. Proceedings of terclim – XIVth International Terroir Congress and 2nd ClimWine Symposium, 3-8 July, Bordeaux, France. https://ives-openscience.eu/12781/.

1.2.2 In preparation

Phogat, V., Petrie, P., Collins, C. and Bonada, M. (2022) Plant available water capacity of soils at regional scale: Analysis of fixed and dynamic field capacity (see Appendix 5.1)

Bonada, M., Phogat, V., Collins, C., Petrie, P. and Sadras, V. (2022). Benchmarking water-limited yield potential and yield gaps of Shiraz in the Barossa and Eden Valleys (see Appendix 5.2).

Bonada, M., Sadras, V., Thomas, D., Collins, C. Schmidtke, L., Phogat, V. and Petrie, P. (2022). The relationship between terroir and the phenology of Barossa Shiraz (See Appendix 5.3).

10. Appendix 2: Intellectual Property

All intellectual property developed by the project has been made publicly available and is not regarded as commercialisable at present. Nonetheless, the findings and new analytical methods used in the project are regarded as project-generated IP and position the team for further study of terroir whether in the Barossa or in other geographical indications.

11. Appendix 3: References

- Abdi, H., Williams, L.J., Valentin, D. and Bennani-Dosse, M. (2012). STATIS and DISTATIS: optimum multitable principal component analysis and three way metric multidimensional scaling. Wiley Interdisciplinary Reviews: Computational Statistics 4, 124-167. doi: 10.1002/wics.198.
- Adams, D.O. and Liyanage, C. (1991). Modification of an enzymatic glutathione assay for determination of total glutathione in grapevine tissues. American Journal of Enology and Viticulture, 42, 137-140.
- Antalick, G., Šuklje, K., Blackman, J.W., Meeks, C., Deloire, A. and Schmidtke, L.M. (2015). Influence of grape composition on red wine ester profile: Comparison between Cabernet Sauvignon and Shiraz cultivars from Australian warm climate. Journal of Agricultural and Food Chemistry, 63, 4664-4672. doi: 10.1021/acs.jafc.5b00966.
- Antalick, G., Šuklje, K., Blackman, J.W., Schmidtke, L.M. and Deloire, A. (2021). Performing sequential harvests based on berry sugar accumulation (mg/berry) to obtain specific wine sensory profiles. OENO One, 55, 131-146.
- Bindon, K.A., Kassara, S., Cynkar, W.U., Robinson, E.M., Scrimgeour, N. and Smith, P.A. (2014). Comparison of extraction protocols to determine differences in wine-extractable tannin and anthocyanin in Vitis vinifera L. cv. Shiraz and Cabernet Sauvignon grapes. Journal of Agricultural and Food Chemistry, 62(20), 4558-4570.
- Bindon, K.A., Kassara, S., Solomon, M., Bartel, C., Smith, P.A., Barker, A. and Curtin, C. (2019). Commercial Saccharomyces cerevisiae yeast strains significantly impact Shiraz tannin and polysaccharide composition with implications for wine colour and astringency. Biomolecules, 9(9), 466.
- Boccard, J. and Rudaz S. (2016) Exploring Omics data from designed experiments using analysis of variance multiblock Orthogonal Partial Least Squares. Analytica Chimica Acta 920, 18-28. doi: http://dx.doi.org/10.1016/j.aca.2016.03.042.
- Boss P.K., Pearce A.D., Zhao Y., Nicholson E.L., Dennis E.G. and Jeffery D.W. (2015). Potential grape-derived contributions to volatile ester concentrations in wine. Molecules, 20, 7845-7873.
- Bramley, R.G.V. (2005). Understanding variability in winegrape production systems. 2. Within vineyard variation in quality over several vintages. Australian Journal of Grape and Wine Research, 11, 33-42.
- Bramley, R. (2022). Underpinning terroir with data. Wine and Viticulture Journal, 37 (3), 54-62.
- Bramley, R. and Gardiner, P. (2021). Underpinning terroir with data: A quantitative analysis of biophysical variation in the Margaret River region. Australian Journal of Grape and Wine Research, 27, 11. https://doi.org/10.1111/ajgw.12491
- Bramley, R.G.V. and Ouzman, J. (2022). Underpinning terroir with data: On what grounds might sub-regionalisation of the Barossa Zone geographical indication be justified ? Australian Journal of Grape and Wine Research, 28, 196-207. https://doi.org/10.1111/ajgw.12513.
- Bramley, R.G.V., Ouzman, J. and Boss, P.K. (2011). Variation in vine vigour, grape yield and vineyard soils and topography as indicators of variation in the chemical composition of grapes, wine and wine sensory attributes. Australian Journal of Grape and Wine Research 17, 217–229.
- Bramley, R.G.V., Ouzman, J., Trought, M.C.T. (2020). Making sense of a sense of place – Precision Viticulture approaches to the analysis of terroir at different scales. Proceedings of the XIIIth International Terroir Congress, November 17-18, Adelaide / Oeno One, 54, 903-917. https://doi.org/10.20870/oeno-one.2020.54.4.3858.
- Bramley, R., Ouzman, J. and Trought, M. (2022a). If NZ can do it, why can't Australia ? Proceedings of the 18th Australian Wine Industry Technical Conference, 26-29 June, Adelaide. https://awitc.com.au/wp-content/uploads/2022/07/2_Bramley.pdf.
- Bramley, R., Ouzman, J. and Trought, M. (2022b). Precision Viticulture at regional scale: rethinking the terroir zoning paradigm. Proceedings of the 25th Symposium of Precision Agriculture in Australasia. 6-7 September, Adelaide. SPAA / University of Sydney.

- Bramley, R., Ouzman, J., Sams, B. and Trought, M. (2022c). Underpinning terroir with data: rethinking the zoning paradigm. Proceedings of TerClim – XIVth International Terroir Congress and 2nd ClimWine Symposium, July 3-8, Bordeaux, France. https://ives-openscience.eu/12781/.
- Breiman, L. (2001). Random Forests. Machine Learning, 45, 5-32.
- Brillante, L., Bonfante, A., Bramley, R.G.V., Tardaguila, J., Priori, S. (2020a). Unbiased scientific approaches to the study of terroir are needed! Frontiers in Earth Science, 8, 539377. doi: 10.3389/feart.2020.539377
- Brillante, L., Martínez-L., Yu, R. and Kurtural, S.K. (2020b). Carbon isotope discrimination ($\delta^{13}C$) of grape musts is a reliable tool for zoning and the physiological ground-truthing of sensor maps in precision viticulture. Frontiers in Environmental Science, 8. https://www.frontiersin.org/articles/10.3389/fenvs.2020.561477
- Capone, D.L., Black, C.A. and Jeffery, D.W. (2012). Effects on 3-mercaptohexan-1-ol precursor concentrations from prolonged storage of Sauvignon blanc grapes prior to crushing and pressing. Journal of Agricultural and Food Chemistry, 60(13), 3515-3523.
- Capone, D.L., Ristic, R., Pardon, K.H. and Jeffery, D.W. (2015). Simple quantitative determination of potent thiols at ultratrace levels in wine by derivatization and high-performance liquid chromatography–tandem mass spectrometry (HPLC-MS/MS) analysis. Analytical chemistry, 87(2), 1226-1231.
- Chen, W.-P., Yang, X.-Y., Hegeman, A.D., Gray, W.M. and Cohen, J.D. (2010). Microscale analysis of amino acids using gas chromatography-mass spectrometry after methyl chloroformate derivatization. Journal of Chromatography B: Analytical Technologies in the Biomedical and Life Sciences, 878, 2199-2208.
- Cohen, S.A. and Michaud, D.P. (1993). Synthesis of a fluorescent derivatizing reagent, 6-aminoquinolyl-N-hydroxysuccinimidyl carbamate, and its application for the analysis of hydrolysate amino-acids via high-performance liquid-chromatography. Analytical Biochemistry, 211, 279-287.
- Cordente, A.G., Curtin, C.D., Solomon, M., Kulcsar, A.C., Watson, F., Pisaniello, L., Schmidt, S.A. and Espinase Nandorfy, D. (2022). Modulation of Volatile Thiol Release during Fermentation of Red Musts by Wine Yeast. Processes, 10(3), 502.
- Dobrowski, S.Z., Ustin, S.L. and Wolpert, J.A. (2003). Grapevine dormant pruning weight prediction using remotely sensed data. Australian Journal of Grape and Wine Research 9, 177–182.
- Enot, D.P., Lin, W., Beckmann, M., Parker, D., Overy, D.P. and Draper, J. (2008). Preprocessing, classification modeling and feature selection using flow injection electrospray mass spectrometry metabolite fingerprint data. Nature Protocols, 3, 446-470. doi: 10.1038/nprot.2007.511.
- Gladstones, J. (2011). Wine, Terroir and Climate Change (Wakefield Press: Adelaide, SA, Australia).
- González-Ruiz, V., Pezzatti, J., Roux, A. Stoppini, L. Boccard, J. and Rudaz, S. (2017). Unravelling the effects of multiple experimental factors in metabolomics, analysis of human neural cells with hydrophilic interaction liquid chromatography hyphenated to high resolution mass spectrometry. Journal of Chromatography A, 1527, 53-60. doi: https://doi.org/10.1016/j.chroma.2017.10.055.
- Grant, C.D., Groenevelt, P.H. and Robinson, N.I. (2010). Application of the Groenevelt-Grant soil water retention model to predict the hydraulic conductivity. Soil Research, 48(5), 447-458.
- Hall, J.A.S., Maschmedt, D.J. and Billing, N.B. (2009). The soils of Southern South Australia. The South Australian Land and Soil Book Series, Volume 1; Geological Survey of South Australia, Bulletin 56, Volume 1. Department of Water, Land and Biodiversity Conservation, Government of South Australia: Adelaide, SA: pp. 188.
- Han P.P. and Yuan Y.J. (2009). Lipidomic analysis reveals activation of phospholipid signalling in mechanotransduction of *Taxus cuspidata* cells in response to shear stress. FASEB Journal, 23, 623-30.
- Han, H., Guo, X. and Yu, H. (2016). Variable selection using mean decrease accuracy and mean decrease Gini based on random Forest. Proceedings of the IEEE 7th International conference on

software engineering and service science (ICSESS), Beijing (Institute of Electrical and Electronics Engineers: Piscataway, NJ, USA) pp. 219-224.
- Hanlin, R.L. and Downey, M.O. (2009). Condensed tannin accumulation and composition in skin of Shiraz and Cabernet Sauvignon grapes during berry development. American Journal of Enology and Viticulture, 60, 13-23.
- Jackson, D.I. and Lombard, P.B. (1993). Environmental and management practices affecting grape composition and wine quality—A review. American Journal of Enology and Viticulture, 44, 409-430.
- Jeffery, D.W., Parker, M. and Smith, P.A. (2008). Flavonol composition of Australian red and white wines determined by high-performance liquid chromatography. Australian Journal of Grape and Wine Research, 14(3), 153-161.
- Kalua, C.M. and Boss, P.K. (2009). Evolution of volatile compounds during the development of Cabernet Sauvignon grapes (*Vitis vinifera* L.). Journal of Agricultural and Food Chemistry, 57,3818-3830.
- Kotseridis, Y., Baumes, R.L. and Skouroumounis, G.K. (1999). Quantitative determination of free and hydrolytically liberated β-damascenone in red grapes and wines using a stable isotope dilution assay. Journal of Chromatography A, 849, 245-54.
- Lamb, D.W., Weedon, M.M. and Bramley, R.G.V. (2004). Using remote sensing to predict grape phenolics and colour at harvest in a Cabernet Sauvignon vineyard: timing observations against vine phenology and optimising image resolution. Australian Journal of Grape and Wine Research, 10, 46–54.
- Lashbrooke, J.G., Young, P.R., Strever, A.E., Stander, C., Vivier, M.A. (2010). The development of a method for the extraction of carotenoids and chlorophylls from grapevine leaves and berries for HPLC profiling. Australian Journal of Grape and Wine Research, 16, 349-60.
- Laville P. (1990). Le terroir, un concept indispensable à l'élaboration et à la protection des appellations d'origine comme à la gestion des vignobles: le cas de la France. Bull. O.I.V. 709-710, 217-241.
- Liaw, A. and Wiener, M. (2002). Classification and refression by randomForest. R News 2/3, 18-22.
- Mair, P., Groenen, P.J.F. and de Leeuw, J. (2022). More on Multidimensional Scaling and Unfolding in R: smacof Version 2. Journal of Statistical Software 102, 1 - 47. doi: 10.18637/jss.v102.i10.
- Martin, D.M., Chiang, A., Lund, S.T. and Bohlmann, J. (2012). Biosynthesis of wine aroma: transcript profiles of hydroxymethylbutenyl diphosphate reductase, geranyl diphosphate synthase, and linalool/nerolidol synthase parallel monoterpenol glycoside accumulation in Gewürztraminer grapes. Planta, 236, 919-29.
- Matthews M. and Anderson, M. (1988). Fruit ripening in *Vitis vinifera* L.: responses to seasonal water deficits. American Journal of Enology and Viticulture, 39, 313-320
- Mayr, C.M., Capone, D.L., Pardon, K.H., Black, C.A., Pomeroy, D. and Francis, I.L. (2015). Quantitative analysis by GC-MS/MS of 18 aroma compounds related to oxidative off-flavor in wines. Journal of Agricultural and Food Chemistry, 63(13), 3394-3401.
- Mercurio, M.D., Dambergs, R.G., Herderich, M.J. and Smith, P.A. (2007). High throughput analysis of red wine and grape phenolics adaptation and validation of methyl cellulose precipitable tannin assay and modified Somers color assay to a rapid 96 well plate format. Journal of agricultural and food chemistry, 55(12), 4651-4657.
- Minasny, B., McBratney, A.B. (2003). Integral energy as a measure of soil-water availability. Plant and Soil, 249, 253-262.
- Myers, B.J. (1988). Water stress integral - a link between short-term stress and long-term growth. Tree Physiology, 4, 315-323.
- Pisaniello, L., Watson, F., Siebert, T., Francis, L. and Hixson, J.L. (2022). The varietal influence of flavour precursors from grape marc on monoterpene and C13-norisoprenoid profiles in wine as determined by membrane-assisted solvent extraction (MASE) GC-MS. Molecules, 27(7), 2046.

- Proffitt, T., Bramley, R., Lamb, D. and Winter, E. (2006). Precision viticulture—a new era in vineyard management and wine production (Winetitles: Adelaide, SA, Australia).
- Robinson, S. and Sandercock, N. (2014). An analysis of climate, soil and topographic information to aid the understanding of Barossa terroir. A report prepared for the Barossa Grape and Wine Association by PIRSA Spatial Information Services. PIRSA, Adelaide, SA.
- SAS Institute Inc. (1983). Cubic Clustering Criterion. SAS Technical Report A-108. SAS Institute Inc., Cary, NC, USA. 56 pp.
- Schmidtke, L.M., Antalick, G., Šuklje, K., Blackman, J.W., Boccard, J. and Deloire, A. (2020). Cultivar, site or harvest date: the gordian knot of wine terroir. Metabolomics 16, 52. doi: 10.1007/s11306-020-01673-3.
- Siebert, T.E., Smyth, H.E., Capone, D.L., Neuwöhner, C., Pardon, K.H., Skouroumounis, G.K., Herderich, M.J., Sefton, M.A. and Pollnitz, A.P. (2005). Stable isotope dilution analysis of wine fermentation products by HS-SPME-GC-MS. Analytical and bioanalytical chemistry, 381(4), 937-947.
- Siebert, T.E., Solomon, M.R., Pollnitz, A.P. and Jeffery, D.W. (2010). Selective determination of volatile sulfur compounds in wine by gas chromatography with sulfur chemiluminescence detection. Journal of Agricultural and Food Chemistry, 58(17), 9454-9462.
- Spangenberg, J.E. and Zufferey, V. (2018). Changes in soil water availability in vineyards can be traced by the carbon and nitrogen isotope composition of dried wines. Science of The Total Environment, 635, 178-187. https://doi.org/10.1016/j.scitotenv.2018.04.078.
- van Leeuwen C., Friant P., Choné X., Tregoat O., Koundouras S. and Dubourdieu D. (2004). Influence of climate, soil and cultivar on terroir. American Journal of Enology and Viticulture, 55, 207-217.
- van Leeuwen C., Trégoat, O., Choné, X., Bois, B., Pernet, D. and Gaudillère, J.-P. (2009). Vine water status is a key factor in grape ripening and vintage quality for red Bordeaux wine. How can it be assessed for vineyard management purposes? Journal International des Sciences de la Vigne et du Vin, 43(3), 121-134.
- Wine Australia Strategic Plan (2015-2020) https://www.wineaustralia.com/getmedia/cf1b4573-7576-46ca-95ae-a02473d0ea14/Wine-Australia-Strategic-Plan-2015-2020-Dec-2017.pdf
- Yunoki, K., Tanji, M., Murakami, Y., Yasui, Y., Hirose, S. and Ohnishi, M. (2004). Fatty acid compositions of commercial red wines. Bioscience, Biotechnology, and Biochemistry, 68, 2623-2626.

12. Appendix 4: Staff and Students

Project Supervisors:	A/Prof Cassandra Collins (UA)
	A/Prof Paul Petrie (SARDI)
Principal Researchers:	A/Prof Susan Bastian (UA)
	Prof Tim Cavagnaro (UA)
	Dr Lukas Danner (UA)
	Dr Rob Bramley (CSIRO)
	Dr Paul Boss (CSIRO)
	Dr Keren Bindon (AWRI)
	Dr Leigh Francis (AWRI)
	Dr Marcos Bonada (SARDI)
	Prof Leigh Schmidtke (CSU)
	Dr Lira Gonzaga (UA)
Technical Staff:	Mrs Annette James (UA)
	Mr Gaston Sepulveda (SARDI)
	Ms Jackie Ouzman (CSIRO)
	Ms Sue Maffei (CSIRO)
	Ms Emily Nicholson (CSIRO)
	Mr Luke Qi (AWRI)
	Mr Luke Ragless (SARDI)
Casual Staff:	Mr Lukas Papagiannis (UA)
	Mr Lucas De Simoni (UA/SARDI)
	Dr Alice Betteridge (UA)
	Mr Jingyun Ouyang (UA/SARDI)
	Mr Han Chao (SARDI)
	Mr Jose (SARDI)
Students:	Ms Masumi Ogita (UA)
	Ms Merek Kesser (UA)
Collaborators:	Dr Roberta De Bei (UA)
	Dr Cameron Grant (UA)

13. Appendix 5: Draft Manuscripts

5.1 Plant available water capacity of soils at regional scale: Analysis of fixed and dynamic field capacity

PLANT AVAILABLE WATER CAPACITY OF SOILS AT REGIONAL SCALE: ANALYSIS OF FIXED AND DYNAMIC FIELD CAPACITY

VINOD. PHOGAT[1,2,3,*], PAUL. R. PETRIE[1,2,3,4], CASSANDRA COLLINS[2,5] AND MARCOS BONADA[1,3]

[1]*South Australian Research and Development Institute, GPO Box 397, Adelaide, SA 5001 (Australia)*
[2]*School of Agriculture, Food and Wine, Waite Research Institute, University of Adelaide, Waite Campus, PMB1 Glen Osmond, SA, 5064 (Australia)*
[3]*College of Science and Engineering, Flinders University, Bedford Park SA 5042 (Australia)*
[4]*The University of New South Wales, Sydney, NSW 2052 (Australia)*
[5]*ARC Training Centre for Innovative Wine Production, University of Adelaide, PMB1 Glen Osmond, SA, 5064 (Australia)*

ABSTRACT

Estimation of the plant available water capacity (PAWC) of soils at a regional scale helps in adopting better land use planning, developing suitable irrigation schedules for crops, and optimising the use of scarce water resources. In the current study, 72 soil profiles were sampled from the Barossa Region of South Australia to estimate pedo-transfer functions deduced from easily estimated soil properties. These functions were then used to estimate the fixed (10, 33 kPa) and dynamic pressure head (h_{fc}) water content at field capacity (FC) for minimum drainage flux (q = 0.01 and 0.001 cm/day), which serves as the upper boundary for plant-available water in the soils. The estimated crop lower limit (CLL, θ_{wp}) was corrected for subsoil constraints, especially the exchangeable sodium percentage (ESP). The data showed that the mean values of h_{fc} in sand-dominated light and medium textures (i.e. sand, loamy sand, sandy loam, and loam) varied in a narrow range (15.8–18.2 kPa), while in the clay-dominated heavy textured soils (i.e. clay loam) showed the widest range of h_{fc} (11.3–49.3 kPa). The data showed wide variability in the PAWC for dynamic FC ($PAWC_{fc}$) and fixed FC at 10 kPa ($PAWC_{10}$), 33 kPa ($PAWC_{33}$), and a mix of 10 and 33 kPa ($PAWC_{10,33}$) pressure heads depending on soil texture. Normally, the difference between PAWC at h_{fc} and 10 kPa ($\Delta PAWC_{10}$) was positive, whereas the corresponding difference between PAWC at 33 kPa and h_{fc} ($\Delta PAWC_{33}$) was negative across all sites. Nevertheless, the estimation of PAWC assuming a fixed FC at 10 and 33 kPa pressures ($PAWC_{10,33}$) for sandy, clay, and silty soils reduced the deviation between dynamic and fixed pressure PAWC < 10% across the region. The estimation of PAWC was improved by incorporating the impact of subsoil constraints, such as high ESP in the soil, which was more pronounced for clay and silty texture soils occurring at lower depths. These findings demonstrate the inherent inconsistencies between static pressure and flux-based dynamic field-capacity estimations in soils. Soil heterogeneity, intra-texture variability, subsoil constraints, and swell–shrink clays can have great impacts on the water retention capacity in response to dynamic and fixed pressure FC values.

*Corresponding author. E-mail: vinod.phogat@sa.gov.au; vinod.phogat@adelaide.edu.au.

Key Words: plant available water capacity, field capacity, crop lower limit, soil hydraulic parameters

INTRODUCTION

The plant available water capacity (PAWC) of soils plays a crucial role in land use planning, devising irrigation scheduling for crops, drought risk assessment, modelling ecological and hydrological processes, and climate change impact assessments on agricultural systems and the environment. The PAWC has a great impact on water retention and hydraulic movement in the soil and regulates solute movement. Therefore, the assessment of PAWC of soils is key for enhancing the productive potential of crops and increasing food grain production from finite water resources. This information serves as an essential input for agrohydrological and environmental models and accurate estimation of the PAWC and related hydraulic functions are crucial for managing water- and climate-related risks and achieving sustainable crop production.

Conventionally, the PAWC in soils is quantified as the amount of water held between the field capacity (FC or θ_{fc}), drained upper limit (DUL), and wilting point (θ_{wp}) (Veihmeyer and Hendrickson, 1927; Veihmeyer and Hendrickson, 1931) or crop lower limit (CLL). The FC is defined as the amount of water content held in soils after excess water has drained away and the rate of downward movement of water has reached a minimum or negligible level (Veihmeyer and Hendrickson, 1931). Numerous methods which measure soil water content at the FC, such as measuring the water content at static matric potential, at an elapsed time since irrigation or rainfall, or the dynamic minimum drainage flux equivalent. However, there is no universally accepted fixed matric suction (h) for soils corresponding to FC (Asgarzadeh *et al*., 2010; Groenevelt *et al*., 2001; Minasny and McBratney, 2003). The water content is commonly measured at a h of 10 (Silva *et al*., 1994) and 33 kPa (Veihmeyer and Hendrickson, 1931). Similarly, an h of 1500 kPa has been used for θ_{wp} or CLL, irrespective of soil type (Asgarzadeh *et al*., 2014).

The conventional pressure-based approximation of FC at 10 or 33 kPa is inconsistent with the definition of FC, as it does not ensure the completion of drainage from the soil (Hillel, 1998; Meyer and Gee, 1999). Meaning that a fixed limit for FC in different soil textures may not accurately estimate the volume of water available for plants. Field measurements of FC can apply a fixed number of days (three days for coarse-textured soils or six or more days for medium- and fine-textured soils) until the drainage ceases (Burk and Dalgliesh, 2008). Thus, a time-based definition of FC fixes the pressure relative to time; however, the critical minimum drainage flux threshold may not occur within this predefined period. Spatial variation in soil water content may also deviate from the uniform arrival of (minimum drainage flux) threshold across the soil profile.

Several other approaches, such as the non-limiting water range (NLWR), least limiting water range (LLWR), and integral water capacity of the soil (IWC) (Letey, 1985; Silva *et al*., 1994; Groenevelt *et al*., 2001) also use static pressure-based approximations for FC (10 or 33 kPa). However, the occurrence of FC in different soils is highly dynamic (Ahuja *et al*., 2008; Hillel, 1980). These approaches also propose numerous improvements, such as introducing air-filled porosity (0.1 cm^3/cm^3), mechanical resistance (2.5 MPa), and salinity-induced osmotic pressure, in evaluating plant-available water in the soil. This makes the the definition of FC with a fixed pressure head “assuming the correspondence to the minimum/negligible drainage flow” implausible.

Several techniques have been developed for estimating FC using dynamic approaches (Assouline and Or, 2014; Campbell, 1985; Hillel, 1998; Meyer and Gee, 1999; Nasta and Romano, 2016; Twarakavi *et al*., 2009; Zacharias and Bohne, 2008). Meyer and Gee (1999) showed that the analytical approach to estimate field capacity, including the consideration of its dynamic nature, performed better

than the benchmark pressure heads. Nachabe (1998) proposed that the FC should correspond to the soil water content when the drainage flux from the soil is equal to the daily evapotranspiration rate, whereas Hillel (1998) recommended estimating the FC as the water content when the drainage flux from the soil reaches a value of 0.05 cm/day. Dirksen and Matula (1994) observed that the smallest amount of rainfall measured in meteorological stations (0.01 cm/day) could be used as a guide for negligible drainage flux for the FC determination. Twarakavi *et al*. (2009) compared the drainage fluxes of 0.001, 0.01, 0.1 cm/day using the van Genuchten Model (VAM) (van Genuchten, 1980) in HYDRUS-1D (Šimůnek *et al*., 2008) and found that the value of 0.01 cm/day can be considered as a convenient negligible drainage flux for FC estimation. Their model does not define the depth of the soil layer and assumes a free drainage boundary at the lower surface of the modelled domain, which presumably induces variations in the hydraulic gradient between the upper and lower surfaces of the modelled domain. This deviates from the assumption that there is a constant drainage flux threshold or a uniform water content across the domain. Similarly, Sun and Yang (2013) suggested a drainage flux of 0.01 cm/day while Cong *et al*. (2014) suggested a value of 0.005 cm/day for a relative drainage of 3% per day as a threshold. These studies suggest that the estimation of hydraulic properties of soils can help determine the flux-based estimation of the FC and PAWC of soils. Similarly, de Alencar *et al*. (2019) compared the static and dynamic approaches to FC estimation and hypothesised that the estimation of the characteristic pore diameter at FC can be used as a criterion for its estimation. However, this hypothesis was not confirmed by the field measurements.

The soil water content in relation to dynamic matric suction (θ-h) and the corresponding hydraulic conductivity–matric suction (K-h) are important functions for estimating the dynamic FC and PAWC in the soil; however, they are time-consuming, expensive, and require complex measurement devices, which makes them impractical to survey at the district scale to aid irrigation management (Sinowski *et al*., 1997). Alternative estimations, such as analytical functions or predictive models, can provide a viable option for characterising the hydraulic properties of various soil textures (Nasta and Romano, 2016; Twarakavi *et al*., 2009; Wösten *et al*., 2001). Numerous approaches and analytical functions relate soil hydraulic properties to more easily measurable soil properties (e.g. Brooks and Corey, 1964; Campbell, 1974; Hutson and Cass, 1987; van Genuchten, 1980). Among these approaches, the van Genuchten-Muleum (VGM) function (van Genuchten, 1980) is the best approximation of the hydraulic behaviour of many soils (Schaap and Leij, 2000) and is widely used (Twarakavi *et al*., 2009) and described as pedo-transfer functions (PTF) (e.g. Mallants *et al*., 2019; Vereecken *et al*., 2010). Schaap *et al*. (2001) proposed a neural network analysis to estimate VGM following an iterative calibration procedure (ROSETTA). This method requires a minimum particle size (% sand, % silt, and % clay) and bulk density data to estimate the hydraulic properties of the soil. However, these estimations require the integration of site-specific parameters or verification of the water content retained in soils, irrespective of the approach followed.

Studies comparing flux-based estimations of FC and PAWC with the static approach are limited, especially for Australian soils. Such comparisons require a comprehensive analysis at the regional scale to test the applicability of different approaches to a wide range of soils. The objectives of this study were to: i) determine the soil properties and textural distribution across the Barossa Valley of South Australia; ii) estimate the soil hydraulic properties from the measured data and other available soil information of the region; iii) determine the FC using a fixed pressure (10 and 33 kPa) and flux-based dynamic approaches and estimate PAWC for a large soil profile-based dataset; and iv) compare the deviation in the estimation of PAWC using the static and dynamic approach of water content at the upper threshold (FC). The information generated from this analysis aimed to characterise the soils of the Barossa Valley according to their PAWC and improve the understanding of the irrigation requirements for wine grapes in this region.

METHODS AND MATERIALS

Study sites

The study area lies in the Barossa region, recognised as a leading wine grape-producing area in Australia. The region experiences a Mediterranean climate characterised by hot, dry summers and cool-to-cold winters. The local long-term (124 years) average rainfall is 467 mm (station 023343; http://www.bom.gov.au/jsp/ncc/cdio/cvg/av), and annual evapotranspiration is 1300 mm, resulting in the need for irrigation to maintain crop production. Most rainfall occurs during the winter months, coinciding with grapevine dormancy. This means the water retention capacity of soils plays a crucial role in maintaining a water supply to the vineyards during the summer months; but, crop production still requires supplemental irrigation to sustain plant needs.

Soil sampling and measurements

Soil profile samples were collected from various areas (northern grounds, NG; central grounds, CG; eastern edge, EE; southern grounds, SG; western ridge, WR; and Eden Valley, EV) as described in the Barossa Grounds Project (Robinson and Sandercock, 2014) to represent the entire Barossa wine grape growing region (Fig. 1). This study focused on understanding the variability in the soil properties and PAWC in the region and was not intended to infer any relationship on the sub-regional distinctiveness of wine quality. A total of 24 sites were identified for sampling, and triplicate soil samples were collected between June and August 2019. Samples were collected using a hydraulic hammer-driven probe with a 4 cm diameter. Cores were collected from vineyards (0.4 m from the drip irrigation line towards the inter-row space and between the emitters. Two intact cores were collected up to a depth of 90 cm from each vineyard using a PVC clear sleeve for the Geoprobe Macro-Core® soil sampling system (Earthtech Drilling Products Pty. Ltd., Victoria, Australia). Sampling was restricted to shallower depths depending on the presence of rocks. The cores were detached from the assembly and capped immediately before being transferred to the laboratory. Core samples were oven-dried at 40 ^{o}C, capped, and stored at room temperature until processing.

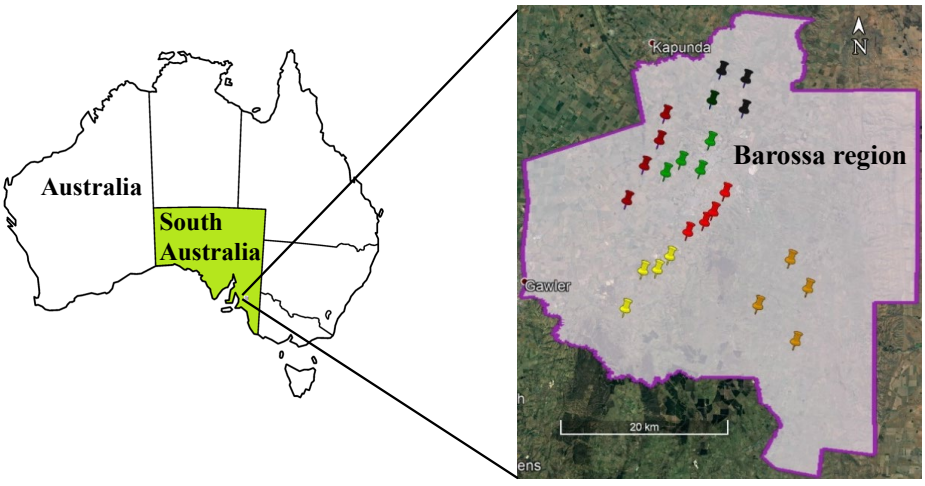


Fig. 1 Schematic map showing study sites in the Barossa region. Study sites are colour coded according to the sub-regions: northern grounds (grey), central grounds (green), eastern edge (red), southern grounds (yellow), western ridge (purple) and Eden Valley (orange). Source: Google Earth V 7.3.3.7721 (accessed on April 17, 2022).

Soil subsamples were drawn from the cores based on visual variations in texture and distinct horizons. Particle size analysis was performed for each soil sample, following mid infrared spectroscopy and least-squares analyses (Janik *et al*., 2016). For the bulk density determination, clods from each soil horizon were separated in duplicate from the cores and stored in plastic containers until analysis using

the clod method (Cresswell and Hamilton, 2002). Other soil properties, including organic C (OC), cation exchange capacity (CEC), exchangeable Na, Ca, Mg, and K, exchangeable sodium percentage (ESP), and B were estimated following the standard procedures outlined by Rayment *et al*. (2011).

Estimation of soil hydraulic properties

Soil hydraulic properties were initially estimated using a pedo-transfer function (PDF) approach (Schaap *et al*., 2001) based on measured values of particle size and bulk density. This approach is widely used in modelling studies to estimate soil hydraulic parameters, including residual water content (θ_r), saturated water content (θ_s), saturated hydraulic conductivity of soils (*Ks*), and fitting parameters (α, η, l). Site-specific values of θ_s and θ_r were separately estimated from the measured soil data to be used for the estimation of the water content- and hydraulic conductivity-pressure head ((θ-*h* and *K*-*h*, respectively) relations for each soil type. The saturated water content (θ_s) is the most sensitive parameter for the calculation of PDF in all soil types (Picciafuoco *et al*., 2019; Vereecken *et al*., 1989); which was deduced from the bulk density data and particle density (2.65 g/cm^3) for all collected soil samples and corrected for pore volume deviation (Burk and Dalgliesh, 2008). It compared well with the saturated water content (θs) of the soil estimated from the ROSETTA (Schaap *et al*., 2001).

The estimated air-dry water content (θ_r), normally assumed as the crop lower limit CLL), denotes the water content at 1500 kPa suction in the soil. The CLL shows a strong and significant linear relationship (r^2 values > 0.91) with average clay content at matric potentials in the plant-available range for soils from Barossa and the adjacent Riverland (Kew *et al*., 2004) and Northern Adelaide Plains (NAP) regions (Mallants *et al*., 2019). These relationships were used to improve the estimated CLL values from the clay fraction in the particle-size analysis. The CLL values were further improved for the impact of ESP on the lower limit of plant available water content (CLL) in different soils, following Hochman *et al*. (2007). They found that the ESP of the soil was the best indicator for evaluating the influence of sub-soil constraints, and this approximation was essential because significant ESP values were encountered in the measured exchange properties of the soil in this region. The values of θ_s and CLL (θ_r) were then incorporated into the soil hydraulic parameters that were used to develop the water content- and hydraulic conductivity–pressure head (θ-*h* and *K*-*h*, respectively) relations for each of the textural layers in the soil profiles collected from the 72 locations. The van Genuchten–Mualem approach was used (Mualem, 1976; van Genuchten, 1980) and is given as:

$$\theta(h) = \theta_r + \frac{\theta_s - \theta_r}{\left[1 + (\alpha h)^n\right]^m} \qquad h<0 \qquad (1)$$

$$\theta(h) = \theta_s \qquad h\geq 0 \qquad (2)$$

$$K(h) = K_s S_e^{\,l}\left[1 - \left(1 - S_e^{\,1/m}\right)^m\right]^2 \qquad (3)$$

$$S_e = \frac{\theta - \theta_r}{\theta_s - \theta_r} \qquad (4)$$

where S_e is the effective saturation (dimensionless); $K(h)$ is the unsaturated hydraulic conductivity function [L T^{-1}]; K_s is the saturated hydraulic conductivity [L T^{-1}]; h is the pressure head [L]; α [L^{-1}], n, and m (both dimensionless) are empirical shape parameters; and l is the pore connectivity parameter.

Determination of the static and dynamic field capacity

The static (fixed) FC of the soil was estimated from the θ-*h* relation drawn for each of the soil textural layers in the soil profiles at the study sites, as described in the previous section. The water content held against 10 and 33 kPa of pressure was considered as the field capacity water content in the soil. The water content in the soil at fixed and dynamic pressure head values for similar soil textures

were different between the study sites. Dynamic FC can be estimated assuming unidirectional (vertical) water flow in unsaturated soils according to Darcy's law:

$$q = -K(\theta)\frac{\partial H}{\partial z} \quad (5)$$

where q is the drainage flux from the soil [L T^{-1}], K is the hydraulic conductivity [L T^{-1}], θ is the volumetric water content [L^3 L^{-3}], H is the hydraulic head [L], z is the vertical coordinate [L], which is positive above the reference datum, and $\partial H/\partial z$ is the hydraulic gradient, which is usually negative in the vertical downward direction. For one-dimensional unit gradient water movement, the drainage flux, as per Darcy's law, becomes equal to the hydraulic conductivity of the soil. Other flux-based studies (e.g. Cong *et al*., 2014; Meyer and Gee, 1999; Twarakavi *et al*., 2009) have applied a uniform flux with a unit gradient assumption. Therefore, the *K-h* relation estimated from the VAM model can be used as the basis for estimating the field capacity suction head (h_{fc}) for an assumed negligible flow (0.01 or 0.001 cm/day). The water content at h_{fc} was then estimated from the *θ-h* function, making it a simple estimation following VAM and avoiding complex numerical analysis by simulating variable gradient flows at different boundaries (Twarakavi *et al*., 2009). The variability in the hydraulic gradient in the soil at different depths along with complex heterogeneous soil formation makes it difficult to model a uniform FC for a textural layer.

Estimation of the plant available water capacity of soils

The PAWC of the soils was estimated for each textural layer from the water content (θ_{fc}) at a fixed pressure of 10 and 33 kPa (h_{10} and h_{33}, respectively), and dynamic (h_{fc}) pressure head values (DUL/field capacity) and the respective water content at CLL (θ_{CLL}) as given below:

$$PAWCt_{10} = 10 \times \left(\theta_{fc\,10} - \theta_{CLL}\right) \times d \quad (6)$$

$$PAWCt_{33} = 10 \times \left(\theta_{fc\,33} - \theta_{CLL}\right) \times d \quad (7)$$

$$PAWCt_{fc} = 10 \times \left(\theta_{fc} - \theta_{CLL}\right) \times d \quad (8)$$

where $PAWCt_{10}$, $PAWCt_{33}$, and $PAWCt_{fc}$ are the estimated PAWC of a textural layer for a fixed FC at 10 and 33 kPa and at dynamic h_{fc} pressure heads, respectively; $\theta_{fc\,10}$ and $\theta_{fc\,33}$ are the water content at 10 and 33 kPa (cm^3/cm^3), respectively; θ_{fc} is the water content at h_{fc} (cm^3/cm^3) pressure heads; and d is the depth of the textural layer (cm).

The PAWC for 10 ($PAWC_{10}$), 33 ($PAWC_{33}$), and dynamic FC ($PAWC_{fc}$) was estimated by summing the PAWC of the respective soil texture in the soil profile at the different study sites.

RESULTS AND DISCUSSION

Physico-chemical properties of the soils

Soil textures were categorised using the particle size (% sand, % silt, and % clay) in the surface (0–65 cm), mid- (8–80 cm), and deep (50–95 cm) horizons (Fig. 2). The soils have a wide range of physical and chemical characteristics. The surface is dominated by loamy sand (38.5%) followed by loam (28.2%) soils, while sand-dominated light and medium textures (sand S, loamy sand LS, sandy loam SL, and loam L) account for 88.5% of the surface soil textures across the Barossa (Fig. 2a). The clay content increases in the middle layers (8–80 cm) of the soil (Fig. 2b). This is commonly related to clay eluviation from the surface layer (Chittleborough and Oades, 1980a; Chittleborough and Oades, 1980b) and represents the contrast subsurface layer (B horizon), which resembles the duplex red-brown earth (Hall *et al*., 2009). Among the different textural classes in the mid layer, clay loam (CL) forms the largest group (27.2%), followed by clay (C) (22.2%). The clay group represents 79.3% of the texture, with 33.8% CL, followed by 32.5% clay (Fig. 2c). Soils with medium to heavy clay, typically known as cracking clays, are also common in Barossa. Silt-dominated textures account for 10.4%, with half having a clay loam texture.

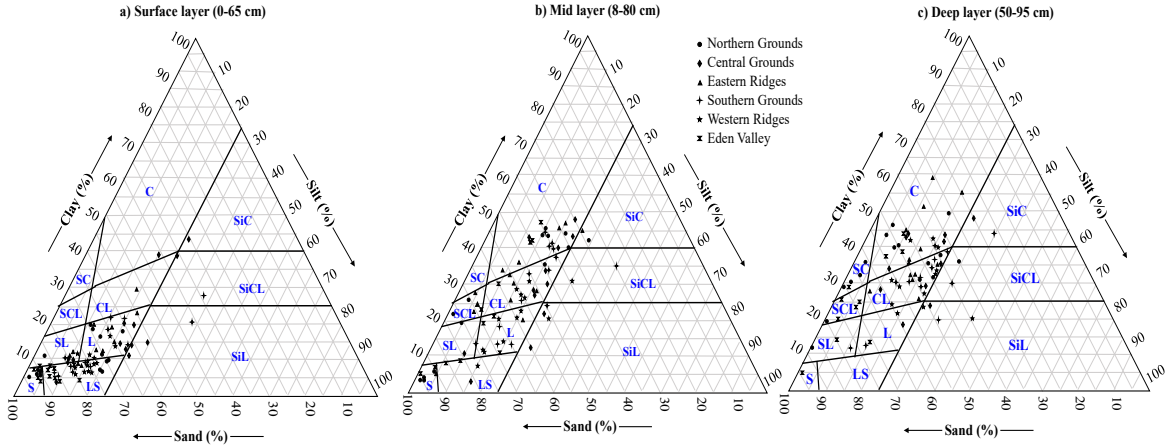


Fig. 2 Distribution of soil textures (S- sand, LS- loamy sand, SL- sandy loam, L- loam, SCL- sandy clay loam, SC- sandy clay, CL- clay loam, C- clay, SiL- silty loam, SiCL- silty clay loam, SiC- silty clay) in the a) surface (0–65 cm), b) mid (8–80 cm) and deep (50–95 cm) layers of the Barossa valley.

The OC content (%) varies between sub-regions and with depth (Table I). The SG show higher average OC values at the surface (1.46%) and subsurface depths (0.82%). In contrast, the lowest OC values are observed in the NG, followed by EV soil profiles at both depths. In other sub-regions (CG, EE, WR), similar OC distributions are recorded in surface (0.99–1.06%) and subsurface (0.52–0.55%) soils. The average bulk density values in the surface soil was from 1.5 to 1.6 g/cm^3 across the Barossa region. The bulk density in the middle (8–80 cm) and deeper soil depths (50–95 cm) increase slightly, except in the EV sites where higher average bulk density values are recorded at mid (1.71 g/cm^3) and deeper depths (1.8 g/cm^3). Relatively sandier textures at lower depths in the EV sub-region result in an increased occurrence of high bulk density values.

Table I

Soil properties in different sub-regions of the Barossa

Property	Depth	Sub-regions					
	(cm)	*NG	*CG	*ER	*SG	*WR	*EV
OC (%)	5-15	0.63 ±0.20	1.06 ±0.31	1.00 ±0.31	1.46 ±1.05	0.99 ±0.43	0.84 ±0.17
	30-45	0.25 ±0.12	0.55 ±0.21	0.52 ±0.13	0.82 ±0.56	0.54 ±0.15	0.30 ±0.07
Bulk	0-65	1.58 ±0.07	1.58 ±0.15	1.56 ±0.13	1.50 ±0.14	1.59 ±0.10	1.56 ±0.11
density	8-80	1.54 ±0.08	1.57 ±0.17	1.56 ±0.14	1.64 ±0.15	1.63 ±0.12	1.71 ±0.09
(g/cm3)	50-95	1.65 ±0.12	1.56 ±0.15	1.53 ±0.10	1.56 ±0.19	1.62 ±0.16	1.80 ±0.06
CEC	0-65	12.61 ±8.12	26.08 ±16.41	19.47 ±9.97	17.02 ±9.65	12.91 ±7.09	4.27 ±1.59
(Cmol/kg)	8-80	17.02 ±11.88	31.68 ±15.03	27.63 ±12.00	24.57 ±10.85	20.59 ±11.84	8.20 ±4.54
	50-95	23.95 ±12.63	30.87 ±14.22	34.29 ±9.00	30.65 ±12.02	25.00 ±7.95	9.52 ±3.39
ESP (%)	0-65	2.37 ±2.17	2.87 ±1.94	3.99 ±3.55	2.40 ±1.99	2.77 ±1.56	4.30 ±2.56
	8-80	6.11 ±5.29	5.05 ±3.95	6.65 ±3.78	5.09 ±4.52	6.46 ±4.78	10.21 ±5.05
	50-95	7.02 ±4.85	11.86 ±9.62	6.78 ±3.95	7.41 ±3.88	6.91 ±4.52	11.65 ±3.84
Boron	5-15	1.14 ±0.37	1.46 ±0.69	1.32 ±0.34	1.22 ±0.54	1.26 ±0.87	0.44 ±0.15
(mg/kg)	30-45	2.83 ±2.35	1.50 ±0.75	1.76 ±0.74	1.24 ±0.67	1.97 ±1.29	0.35 ±0.26

*NG = Northern grounds, CG = Central grounds, ER = Eastern ridges, SG = Southern grounds, WR = Western ridges, EV = Eden Valley

The values of CEC in the surface soils across the Barossa vary from 4.3 to 34.3 Cmol/kg, and increase with depth (Table I). Williams (1981) reported similar trends in the CEC of surface soils in

South Australia, including in the Barossa region. The ESP in the surface soils remained below the 6% threshold (Northcote and Skene, 1972) in all soil profiles. The ESP values typically increase beyond the threshold at mid- and deep depths. A high ESP coupled with cracking clays can create a perched water table at shallow depths and waterlog on the soil surface. Sub-soil constraints, including high ESP, can impact soil water-holding capacity by increasing the lower limit (CLL), thus decreasing the PAWC of the soil (Hochman et al., 2007).

Water retention and hydraulic functions

The water content–pressure head (*θ-h*) and hydraulic conductivity–pressure head (*K-h*) functions are important relations for unravelling the intricacies of soil PAWC, water balance, and solute movement processes in the soil. Therefore, these relationships were developed following the van Genuchten (1980) model for all textural groups at all sites (72) in Barossa. For example, the *θ-h* and *K-h* relations at the SR-3B location in the NG sub-region for sandy loam (SL), sand (S), sandy clay loam (SCL), and sandy clay (SC) at 0–25 (1), 25–50 (2), 50–70 (3) and 70–91(4) cm in the soil profile are shown in Fig. 3. The surface soil textures at depths of 1 and 2 exhibit a steep S-shaped curve, whereas at deeper depths (3 and 4), the steepness gradually decreases owing to an increase in the clay content at lower depths in the soils. Sharp decreases in the water content between 1 and 10 kPa indicate rapid water movement (deep drainage) in the soil, leading to small amounts of water being retained beyond the 10 kPa suction. The water content decreases gradually with depth, suggesting a lower drainage flux and higher moisture retention compared to surface soils. This shows that the presence of high clay content in the deeper layers of soils possibly controls the water movement from the surface, with restricted drainage flow from the bottom of the profile to deeper depths.

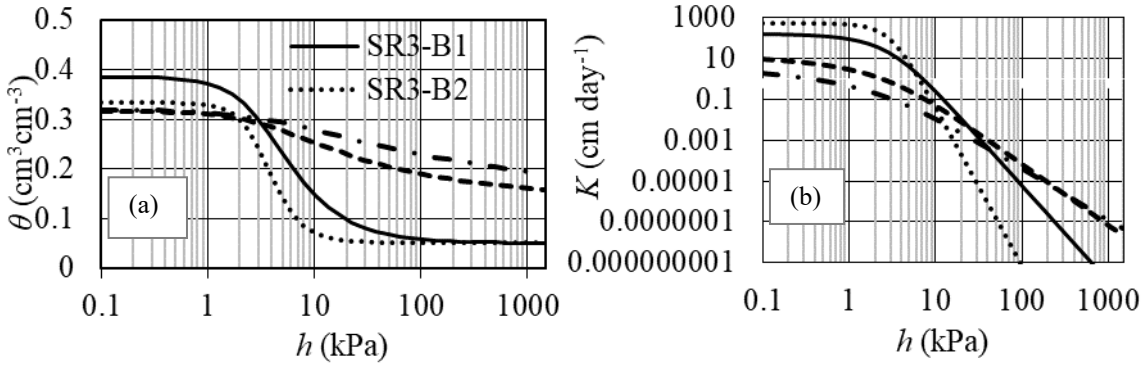


Fig. 3 Predicted (a) moisture content (*θ*) and (b) hydraulic conductivity (*K*) at different soil matric suctions (*h*) for sandy loam (SR3-B1, 0-25 cm), sand (SR3-B2, 25-50 cm), sandy clay loam (SR3-B3, 50-70 cm), and sandy clay (SR3-B4, 70-91) in the Barossa valley.

Similar water content relationships were developed for all other sites (72), which are sumarised in Fig. 4 for all the layers and sub-regions. In the NG sub-region, there is a sharp drop in the water content (*θ*) in the soil in the surface layer when the pressure increased from 1 to 8 kPa (Fig. 4a). In contrast, there is a gradual decrease in water content with increasing pressure in the deeper layer, indicating the prevalence of heavy-texture soil. Numerous outliners at different pressures, especially at the lower end, indicate the existence of light-textured soils at some sites. The mid layer in the NG sub-region represents a transitional zone between the surface and deeper layers, with wide variability in the water retention characteristics. It shows the occurrence of wide variability in the soil physical characteristics, including texture, structure, aggregate formation, and bulk density in the mid layer. The median values of *θ* held at 0.1, 10, and 1500 kPa were 0.37, 0.2, and 0.07; 0.42, 0.35, and 0.23; and 0.37, 0.36, and 0.28 cm^3/cm^3 in the surface, mid, and deeper layers, respectively, in the NG region. High values of θ at 1500 kPa (CLL) in the mid and deep layers not only reduced the plant available

water capacity of the soil but also indicated the presence of adverse hydraulic conditions or the existence of subsoil constraints such as soil compaction and high ESP in the soil (Rengasamy and Olsson, 1993).

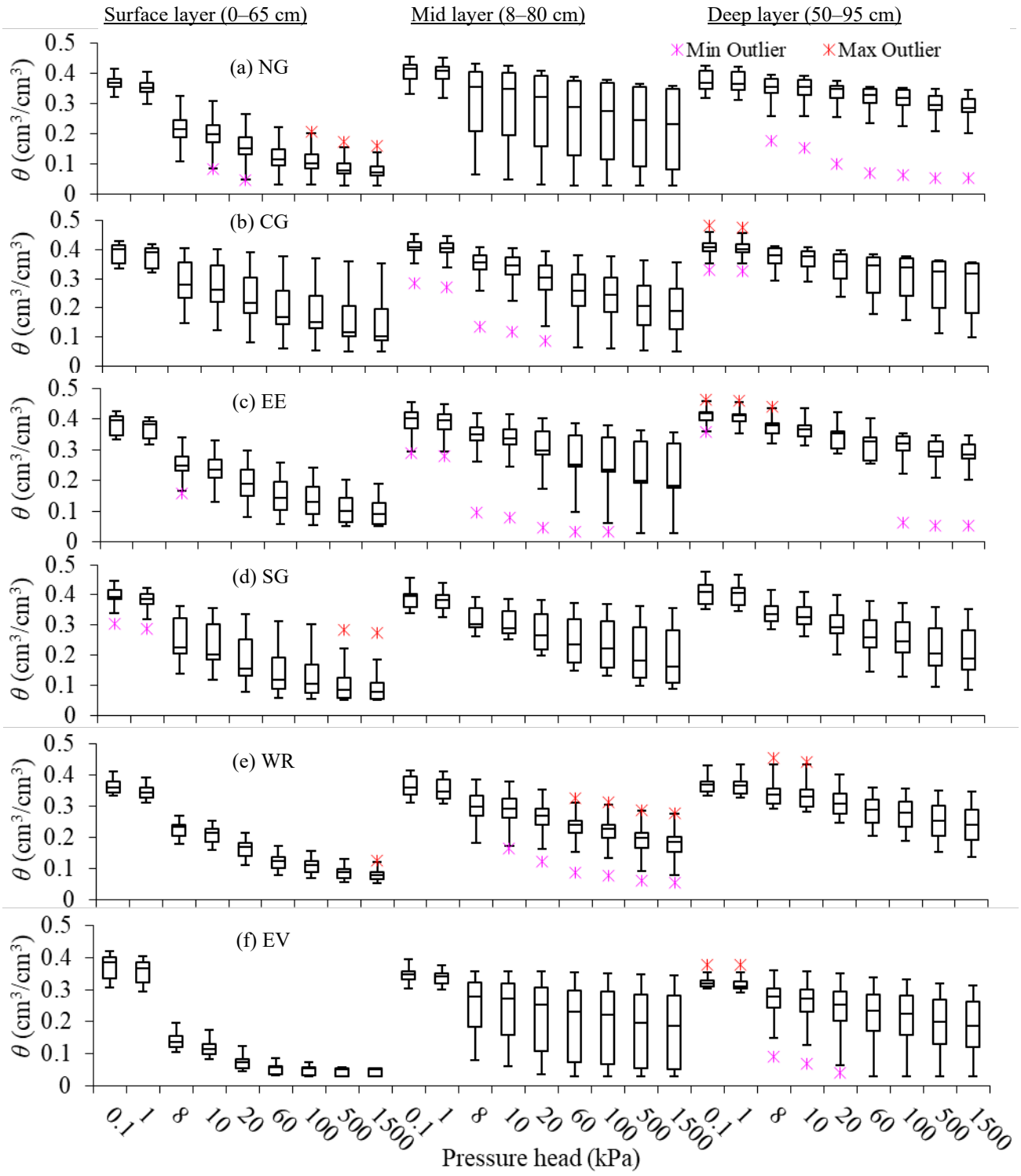


Fig. 4 Estimated water content (θ)- pressure head (h) relations in the soil surface (0–65 cm), mid (8–80 cm), and deep (50–95 cm) layers of (a) northern grounds (NG), central grounds (CG), eastern edge

(EE), southern grounds (SG), western ridge (WR), and Eden Valley (EV) sub-regions in the Barossa Region.

The water content-pressure head (θ-h) dynamics in the CG, EE, and SG regions show similar water retention behaviour of the soils (Fig. 4b, c, d). There is wide variability in the water content of the surface layer in the CG sub-region, especially in the upper half quartile, which suggests the occurrence of medium to heavy textured soils. Similarly, in the mid layer of the EE sub-region, increased scattering of θ-h values in the lower half quartile, including outliers with low water content, indicate the presence of light-textured soils. The small variability in the θ–h curve in the deeper layer in the EE sub-region may indicate the presence of heavy textured soil across this zone. The water content held at 10 and 1500 kPa ranged from 0.20–0.26 and 0.08–0.10; 0.29–0.35 and 0.16–0.19; and 0.33–0.38 and 0.19–0.32 cm^3/cm^3 in the surface, mid, and deep layers, respectively, of these sub-regions, with higher values for CG but median PAWC remained almost the same (113–117 mm). Despite the similarities in the median PAWC in these regions, there exists wide site-specific variability in the PAWC.

In the WR and EV sub-regions, there is a similar reduction in the θ values in response to an increase in pressure (Fig. 4e, f). A sharp drop in the water content between 1 and 8 kPa indicates the occurrence of light-textured soil in the surface layers of these sub-regions with low water retention capacity. The median value of water content at 10 kPa in the WR is almost two-fold (0.21 cm^3/cm^3) that of the EV sub-region (0.11 cm^3/cm^3) with similar θ values at 1500 kPa (0.05 and 0.08 cm^3/cm^3 in the WR and EV region, respectively). A more stable value of θ-h in the mid-and deeper layers of the WR region confirms the presence of similar and uniform textural formations across the sub-region. While there is wide variability in the water content values across the pressure range in the mid and deeper layers in the EV sub-region, the higher values in the lower half quartile in the mid layer indicate a greater proportion of light texture soils. Median θ values at 10 and 1500 kPa were 0.29 and 0.19, and 0.27 and 0.19 cm^3/cm^3 in the mid layer and 0.33 and 0.24, and 0.27 and 0.14 cm^3/cm^3 in the deep layer of the WR and EV sub-regions, respectively. Thus, the difference in θ at 10 and 1500 kPa is minimal in the mid- and deep layers, resulting in similar median PAWC values. A large difference in the minimum and maximum values of PAWC in the EV sub-region indicates the presence of varied extents of textural heterogeneity in the soil profiles, which suggests a wide range of PAWC in the soils.

The predicted hydraulic conductivity–suction head (K-h) relations for soils in different sub-regions, as obtained from the van Genuchten function (van Genuchten, 1980) (Fig. 5). Values below the respective minimum drainage (0.01 and 0.001 cm/day) line represent the soils yet to attain the FC threshold. Assuming a minimum drainage (q_{fc}) of 0.01 cm/day, in the NG region, 2.8, 8.3, 13.9, 25, 33.3, and 13.9% of the samples achieve the threshold DUL at 8, 10, 13, 17, 22, and 33 kPa, respectively, which means that 89% of the samples had a DUL level higher than the fixed pressure limit (10 kPa). If the minimum threshold limit is lowered to 0.001 cm/day, only 25% of the samples achieve at or higher than the 33 kPa threshold, most of which comprise sand to loamy sand textures. A q_{fc} limit of 0.001 cm/day imposes a more severe limit, which reduces water retention in the soils. The time required for *a* q_{fc} of 0.001 cm/day could increase by several orders of magnitude, which deviates from the traditionally accepted values of field capacity for different textures (Meyer and Gee, 1999; Twarakavi *et al*., 2009). Greater estimates of h_{fc} can deviate from the normal range making a drainage threshold of 0.01 cm/day more appropriate t (Dirksen and Matula, 1994; Twarakavi *et al*., 2009).

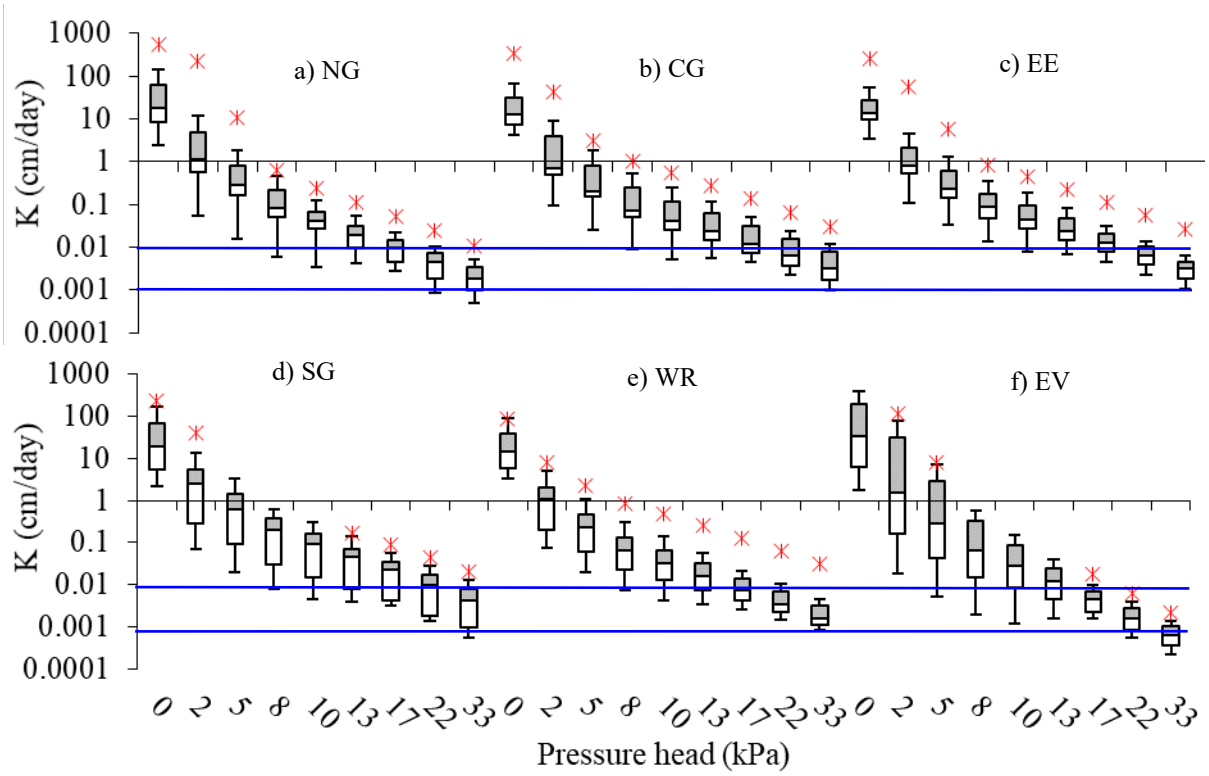


Fig. 5 Distribution of predicted average unit gradient drainage flux at different suctions (*h*) in the soils of the different sub-regions [NG, CG, EE, SG, WR, and EV] in the Barossa Region. Blue lines indicate the *K* (0.01 and 0.001 cm/day) for the field capacity (FC) threshold. The data in each box (n = 216) represent a textural class. The lower value of the box indicates the 25th percentile, the black line is the median, and the higher bar value of the box indicates the 75th percentile. Whiskers indicate the 5th and 95th percentiles.

In the CG sub-region, 2.9, 0, 11.8, 20.6, 35.3, and 11.8% of soils attain the threshold hydraulic limit at 8, 10, 13, 17, 22, and 33 kPa, respectively. In this region, 17.6% of the samples have a DUL hydraulic limit higher than 33 kPa indicating reduced hydraulic movement in these soils. This usually occurs in swelling-type subsoil clays coupled with a high ESP. In this region, 97% of the soil textures have a DUL higher than the fixed pressure threshold (10 kPa). Only 12.5% of the samples attained the DUL when the minimum hydraulic threshold is reduced to 0.001 cm/day. In the EE region, 91% of the soil profiles have DUL limits higher than 10 kPa, and only 2.8% of the samples show a hydraulic limit higher than 33kPa, indicating a low presence of typical heavy-textured clays. If the drainage limit is lowered to 0.001 cm/day, only 11% of the samples achieve DUL at 33 kPa and the rest may require a higher pressure. In contrast, the SG region with 16.7% textures fell in this category, where the hydraulic limit is higher than 33 kPa, which indicates a strong presence of swell–shrink heavy clay soils, especially at lower depths.

In the WR sub-region, most samples (42%) show a critical limit between 13 and 17 kPa, and only 16% had DUL attained at < 10 kPa. Samples with a pressure of >33 kPa are negligible. In contrast, in the EV sub-region, 23% of the samples have a DUL limit of <8 kPa, indicating a strong presence of sandy soils. Maximum samples (40%) have a DUL between 13 and 17 kPa, and 20% fall between the 17 and 22 kPa range. The rest of the samples have a DUL between 8 and 13 kPa, and none of the samples show a DUL pressure > 33 kPa. Therefore, owing to the predominance of sandy texture, more samples (69.4%) can achieve a drainage flux of 0.001 cm/day at or below 33 kPa suction. The variation in water retention at 0.01 and 0.001 cm/day dynamic FC threshold limits, especially for sandy and loamy sand soils, is very low; similar to other reports (Twarakavi *et al*., 2009) there are varied deviations in water content at these thresholds (0.01 and 0.001 cm/day) for clay-textured soils..

Therefore, the 0.01 cm/day drainage flux (Dirksen and Matula, 1994) seems to be a more appropriate threshold for negligible drainage flux in the Barossa soils.

Dynamic field capacity pressure head and water content in the soil

It is important to recognise how the estimated water content at field capacity (θ_{fc}) and the corresponding pressure head (h_{fc}) are related to the soil textures in the Barossa region. The water content values obtained at θ_{fc} in different soil textures at a drainage flux of 0.01 cm/day are presented in the boxplot in Fig. 6. In sandy soils, θ_{fc} values vary from 0.04 to 0.09 cm^3/cm^3 with a narrow inter-quartile range (IQR) value 0.015 cm^3/cm^3 representing low variability in θ_{fc} values. Similar narrow IQR values are also observed in SCL, SC, silty clay loam (SiCL), and silty clay (SiC) textures because of the small number of samples in these classes. The widest IQR value (0.065 cm^3/cm^3) is found in loamy sand (LS), followed by loam (L) soil. . Mean θ_{fc} values in LS, SL, L, CL and C textures correspond to 0.14, 0.17, 0.24, 0.31, and 0.37 cm^3/cm^3, respectively (Table II) and the mean θ_{fc} values increase as the clay content in the soil increase. There are few samples with silty textures, especially for the SiCL and SiC classes; therefore, they show θ_{fc} closer to or higher than clay soils. The water content for SiL was matched with that of SCL but lower than that of CL, which seems to be a normal outcome for silt-dominated soils, as silty soils retain less water than similar clay soils.

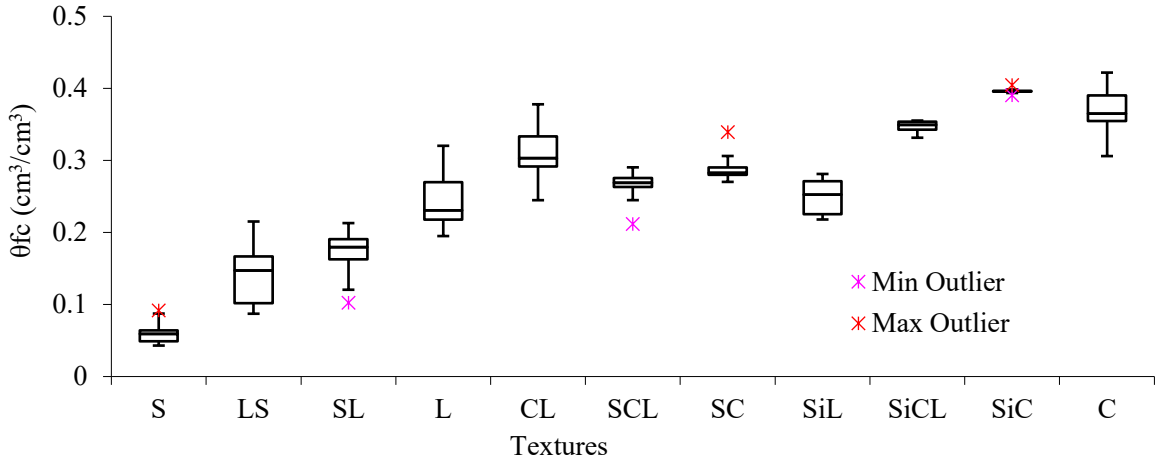


Fig. 6 Extent of water content values at field capacity (θ_{fc}) in different soil textures in the Barossa Region. Textures are: sandy (S), loamy sand (LS), sandy loam (SL), loam (L), clay loam (CL), sandy clay loam (SCL), sandy clay (SC), silty loam (SiL), silty clay loam (SiCL), silty clay (SiC) and clay (C). The lower value of the box indicates the 25th percentile, the black line is the median, and the higher bar value indicates the 75th percentile. Whiskers indicate the 5th and 95th percentiles.

Table II

Mean (m) and the standard deviation (sd) values for field capacity pressure head (h_{fc}), field capacity water content (θ_{fc}), crop lower limit (CLL), water content at 10 kPa (θ_{10}), water content at 33 kPa (θ_{33}) and change in the plant available water capacity at 10 ($\Delta PAWC_{10}$) and 33 kPa ($\Delta PAWC_{33}$) of soil estimated for different soil textures [sandy (S), loamy sand (LS), sandy loam (SL), loam (L), clay loam (CL), sandy clay loam (SCL), sandy clay (SC), silty loam (SiL), silty clay loam (SiCL), silty clay (SiC) and clay ©] occurring in the Barossa valley

Property	S	LS	SL	L	CL	SCL	SC	SiL	SiCL	SiC	C
h_{fc}_m (kPa)	15.77	15.09	17.21	18.18	16.93	21.48	13.72	23.38	26.82	25.42	18.28
h_{fc}_sd (kPa)	0.97	2.50	3.53	5.70	4.39	7.28	1.68	8.25	2.73	2.20	3.82
θ_{fc}_m (cm^3/cm^3)	0.06	0.14	0.17	0.24	0.31	0.26	0.29	0.25	0.35	0.40	0.37
θ_{fc}_sd (cm^3/cm^3)	0.01	0.04	0.03	0.03	0.03	0.02	0.02	0.02	0.01	0.00	0.03

CLL_m (cm^3/cm^3)	0.03	0.05	0.06	0.09	0.18	0.14	0.17	0.10	0.28	0.33	0.31
CLL_sd (cm^3/cm^3)	0.01	0.01	0.01	0.04	0.06	0.02	0.05	0.03	0.00	0.00	0.05
θ_{10}_m (cm^3/cm^3)	0.09	0.20	0.23	0.25	0.32	0.27	0.29	0.28	0.43	0.42	0.40
θ_{10}_sd (cm^3/cm^3)	0.03	0.04	0.02	0.01	0.07	0.01	0.03	0.02	0.00	0.00	0.04
θ_{33}_m (cm^3/cm^3)	0.04	0.11	0.14	0.21	0.24	0.3	0.28	0.23	0.34	0.39	0.36
θ_{33}_sd (cm^3/cm^3)	0.01	0.03	0.03	0.04	0.02	0.03	0.03	0.03	0.01	0.01	0.03
$\Delta PAWC_{10}$_m (mm)	7.90	7.09	10.02	7.03	5.52	8.17	1.14	13.47	9.52	6.08	2.57
$\Delta PAWC_{10}$_sd (mm)	5.42	4.63	6.74	6.33	5.12	7.67	0.65	10.50	3.05	1.96	2.71
$\Delta PAWC_{33}$_m (mm)	-5.30	-8.84	-9.38	-6.10	-3.83	-5.57	-2.86	-4.24	-1.98	-1.83	-1.76
$\Delta PAWC_{33}$_sd (mm)	3.41	3.06	3.96	3.80	2.82	1.50	0.74	3.66	0.72	0.93	1.12

Mean values of h_{fc} in sand-dominated textures (S, LS, SL, and L) vary in a narrow range of 15.8–18.2 kPa (Table II). The h_{fc} values increase as the clay content in the soil increase, and the maximum IQR (7.3 kPa) among the sand-dominated textures was recorded in L soil, which was twice the IQR observed in SL (Fig. 7). In the clay-dominated soils, CL soils show the widest range of h_{fc} (11.3–49.3 kPa), indicating the occurrence of field capacity at various pressures. Higher values for the CL texture usually represent the increased presence of cracking clays that swell in moist conditions, constricting the size of conducting pores and restricting normal drainage across the soil profile. The mean values of h_{fc} estimated for SCL, CL, SC, and C are 16.9, 21.5, 13.7, and 18.3 kPa, respectively (Table II). The mean h_{fc} for silty textures (SiL, SiCL, and SiC) vary within a narrow range (23.4– 26.8 kPa), but the SiL soil has the largest IQR (13.22 kPa), showing wide variability in 50% of the samples (Fig. 7). Similarly, the widest range of h_{fc} values are observed in SiL soils (11.1–37.1 kPa), corresponding to the variability in particle size within this textural class (Fig. 2). The C texture showed lower h_{fc} values than the SCL and silty textures, and h_{fc} ranged from 11.4 to 23.5 kPa. The obstruction of water movement by silt particles in the latter soils may require increased suction to achieve the minimum drainage threshold ($q_{fc\ 0.01}$). In C soils, the proportion of fine sand and silt particles and the fraction of macropores (conducting pores) are small, which may result in minimum drainage flux at low suctions. Understanding the role played by the swelling and shrinking behaviour of clay to encourage minimum drainage achieved at lower suction warrants attention.

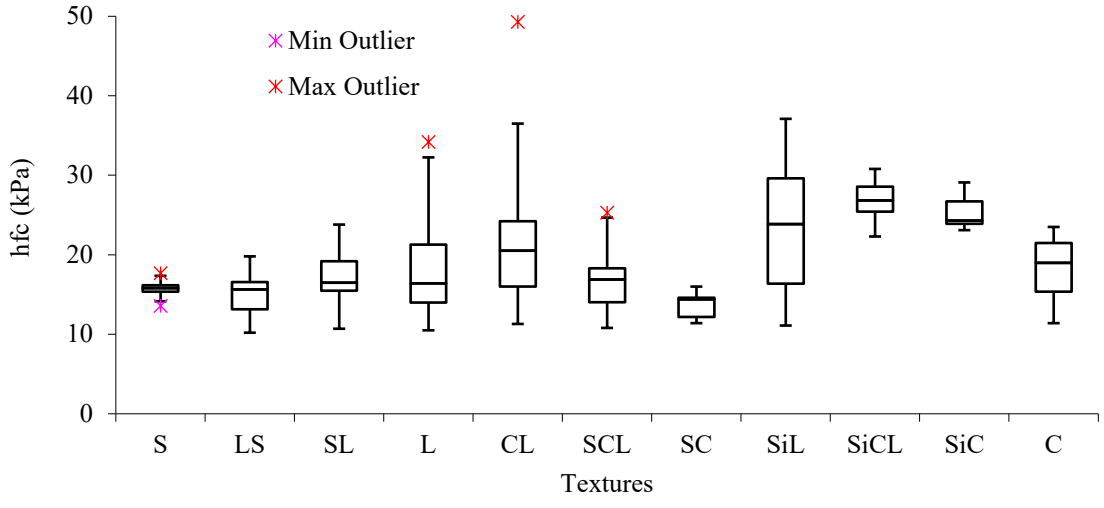


Fig. 7 Average field capacity (FC) pressure head (h_{fc}) in different soil profiles (72) textures (S- sand, LS- loamy sand, SL- sandy loam, L- loam, SCL- sandy clay loam, CL- clay loam, SiL- silty loam, SiCL- silty clay loam, SiC- silty clay) in the Barossa Region. The lower value of the box indicates the 25th percentile, the black line is the median, and the higher bar value indicates the 75th percentile. Whiskers indicate the 5th and 95th percentiles.

The dynamic pressure heads at field capacity (h_{fc}) relative to the minimum drainage flux (q_{fc}) obtained in this study represent the water retention capacity for various textures more realistically than the fixed pressure methods in the Barossa region. The flux-based method is consistent with the dynamic nature of soil moisture, and is based on the continuous soil drainage from saturation to FC (Jabro *et al*., 2009; Meyer and Gee, 1999; Twarakavi *et al*., 2009; Zacharias and Bohne, 2008). The dynamic approach can also perform better than other methods and can be estimated by numerical models (Twarakavi *et al*., 2009) or field measurements (Jabro *et al*., 2009).

Plant available water capacity of soils

The extent of plant available water capacities of soil profiles (50–94 cm) estimated by dynamic field capacity ($PAWC_{fc}$) pressure heads (h_{fc}) at minimum drainage of 0.01 cm/day ($q_{fc\ 0.01}$) in different sub-regions (see colours) in the Barossa are shown in Fig. 8. In the NG region, $PAWC_{fc}$ varies from 71.4 to 131.9 mm with a mean of 100.7 mm depending on the soil textural heterogeneity at different locations and depths. The mean values of PAWC in the CG, EE, SG, WR, and EV sub-regions are 121.5, 123.3, 130.0, 126.1, and 80.4 mm, respectively. Typically, the increased presence of medium-textured soils (SL, L, and CL) in the SG and WR sub-regions allow higher water retention and relatively higher $PAWC_{fc}$ compared to other sub-regions, although some heavily textured soils (e.g. SR9B and SR16A and B) at lower depths showed low $PAWC_{fc}$ due to the occurrence of higher CLL values (Table II). The presence of subsoil constraints, such as high ESP and compaction (high bulk density), further reduces the $PAWC_{fc}$ of clay and silty texture soils (Poulton *et al*., 2018). These conditions occurred across all the sub-regions, for example, in some repetitions at sites SR4 in NG, SR5, and SR8 in CG, SR9 and SR10 in EE, SR16 in SG, and SR22 and SR24 in EV sub-regions (Fig. 8). Meanwhile, minimum values of $PAWC_{fc}$ are observed in the EV sub-region because of the greater extent of sandy textures at the surface coupled with subsoil clays with high ESP and bulk density, which increase the CLL by >30%. The occurrence of low estimates of $PAWC_{fc}$ across the Barossa region is essentially associated with multiple factors, including texture, structure, clay mineralogy, subsoil compaction, extent and type of clay, and high ESP. These factors have a significant impact on the extent of water available to plants (Gaiser *et al*., 2000; Greacen and Williams, 1983; Hochman *et al*., 2001). The overestimation of bulk density by the clod method may result in lower porosity for water retention in soils, inducing errors in the estimation of PTF and the PAWC of soils (Hirmas and Furquim, 2006).

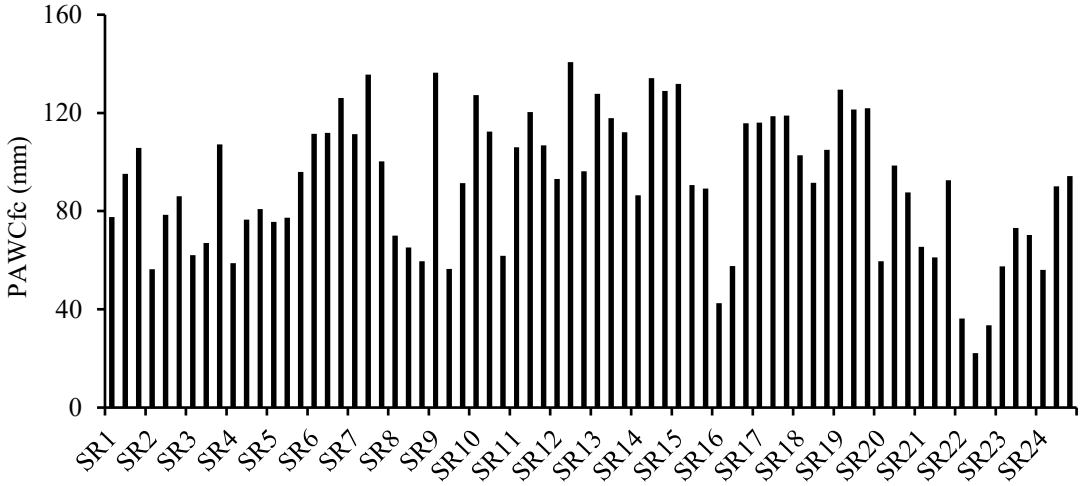


Fig. 8 Estimated plant available water by dynamic field capacity (PAWC*fc*) in the soil profiles collected at different sites (SR1 to SR24) in triplicates in the Barossa Valley, South Australia.

The inherent heterogeneity in soil texture, clay content, organic matter content, pore size distribution, soil aggregation, and clay type within the profile poses a challenge in achieving uniform and minimum levels of field capacity drainage (q_{fc}), similar to the values estimated in the current study. Assouline and Or (2014) summarised the challenges associated with reliable estimates of dynamic or time-dependent criteria for FC. This limits slowly permeable, restrictedly drained clay soils at the lower end of the crop root zone because the presence of heavy or cracking clays (swell–shrink) is a normal feature in the Barossa region, coupled with the occurrence of subsoil constraints such as soil compaction and high sodicity. The presence of high sodium content alters the water retention capacity due to the hydration of unstable aggregates and expansion and/or dispersion of clay particles, leading to a reduction in the pore diameter (Crescimanno *et al*., 1995). Apart from the reduction in PAWC of soils, subsoil constraints physically restrict downward root growth, reduce root biomass, and increase the inability of roots to extract water from the reduced rhizosphere (e.g. Poulton *et al*., 2018). A complex interaction of dynamic water movement processes, such as evaporation, transpiration, capillary rise, and leaching, may also have a significant influence on the hydraulic movement within the soil.

Comparison of fixed and dynamic plant available water capacity

The deviation in the PAWC estimated by the dynamic head (h_{fc}) and fixed pressure heads of 10 kPa for all textures ($\Delta PAWC_{10}$), 33 kPa for all textures ($\Delta PAWC_{33}$), and 10 kPa for sandy and 33 kPa for silty and clay soils ($\Delta PAWC_{10,33}$) are shown in Fig. 9. The average increase in PAWC in the soil in the NG, CG, EE, SG, WR, and EV sub-regions at 10 kPa ($\Delta PAWC_{10}$) are 19, 26.4, 24.3, 28.9, 20.9, and 16.1 mm, respectively. In some profiles the increase is as high as 63 mm (SR7), 57.9 mm (SR13C), and 53.5 mm (SR14), depicting the increased amount of water availability to plants if a fix pressure (10 kPa) is adopted. The soils at these sites are medium textured where the dynamic field capacity pressure head values are higher than 10 kPa, and at the same time, these soils had higher water retention capacity, meaning the corresponding change was much larger than that in other soils. The deviation in PAWC at 33 kPa ($\Delta PAWC_{33}$) at the profile scale is negative across all the sites, and the average reduction varies from -12 to -19.2% in different regions, which means that the dynamic h_{fc} values for the different soils fell between 10 and 33 kPa (Fig. 7). The estimation of fixed PAWC assuming FC at 10 and 33 kPa pressure for sandy, clay, and silty soils reduces the deviation ($\Delta PAWC_{10,33}$) between dynamic and fixed PAWC, and the average deviation across all the sites is only 5.3 mm. The deviation for individual soils ranges between -14.2 to 57.8 mm (Fig. 9C), and the percentage deviation for average values for different sub-regions remains below 10%. Therefore, assuming different texture-based fixed pressure values (10 and 33 kPa), the water content reduces the deviation between the dynamic and fixed approaches.

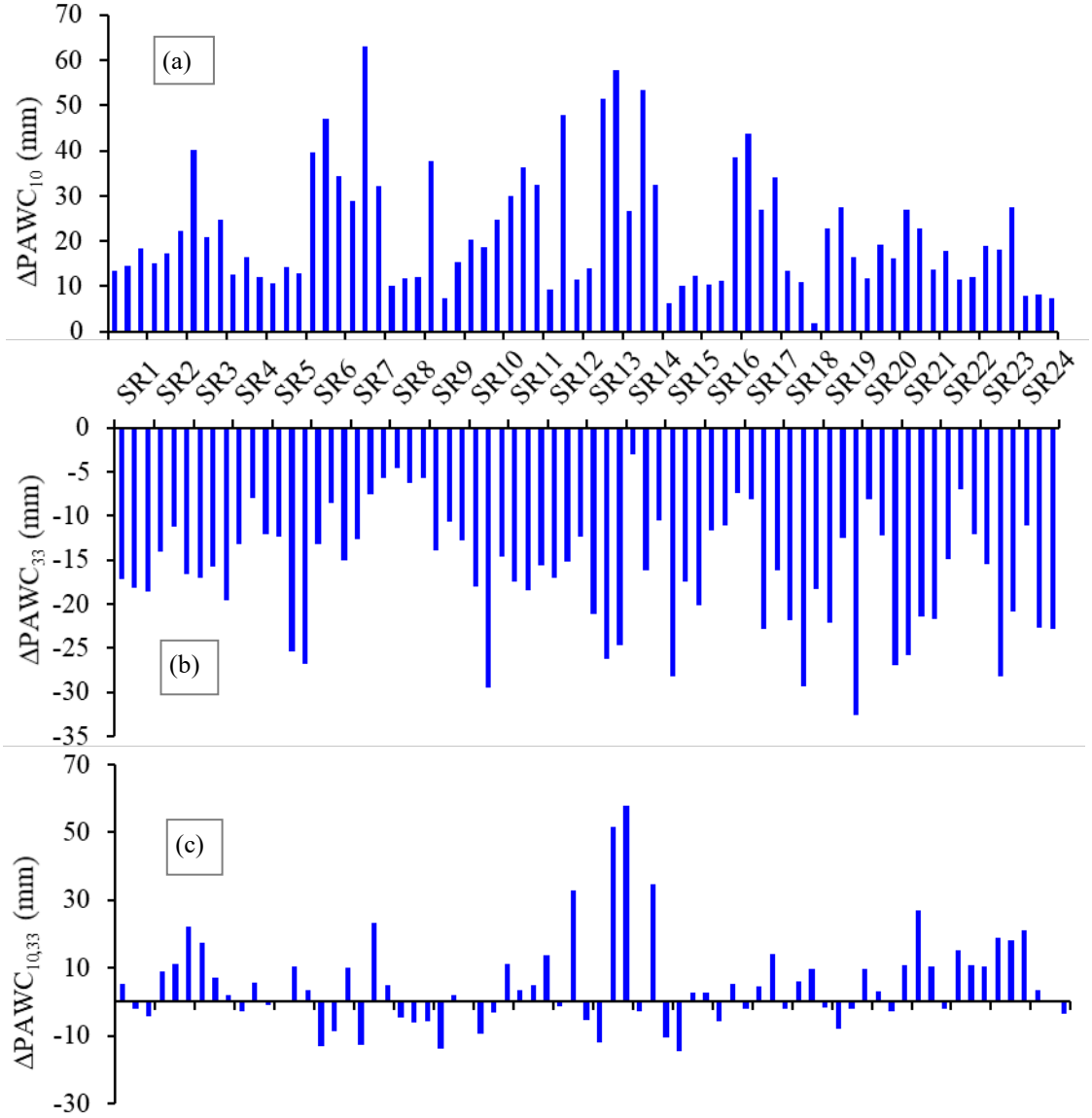


Fig. 9 Differences in the plant available water capacity between dynamic (h_{fc}) and static suctions at (a) 10 kPa ($\Delta PAWC_{10}$), (b) 33 kPa ($\Delta PAWC_{33}$), and (c) 10 and 33 kPa ($\Delta PAWC_{10,33}$) in the soils at different sites (SR1 to SR24) in the Barossa Region, South Australia. For the estimation of $\Delta PAWC_{10,33}$ a varied fix field capacity at 10 and 33 kPa for sandy, and clay, and silty soils was considered.

Among soil types, the deviation in PAWC for S at 10 kPa (ΔPAWC_10) varies from 2.08 to 22.3 mm with a mean value of 7.9 mm (Fig. 10a). The widest range is obtained in SiL (0.36–40.09 mm), with a mean of 13.5 mm. However, ΔPAWC_10 ranges between 0.3 and 18.8, 1.82 and 6.6, 0.32 and 7.1, 1.23 and 3.6, and 0.03 and 13.7 mm in LS, SL, L, CL, and C textures, respectively, which is common across the sub-regions. The average values of ΔPAWC_10 in these soils vary between 2.6 and 10 mm depending on the spatial dimensions and occurrence of the respective textures in the soil profile. At 33 kPa, the extent of deviation in $PAWC_{33}$ (ΔPAWC_33) from $PAWC_{fc}$ is largest for sand-dominated textures. The negative values indicate that the values of the dynamic field capacity pressure heads are lower than 33 kPa.

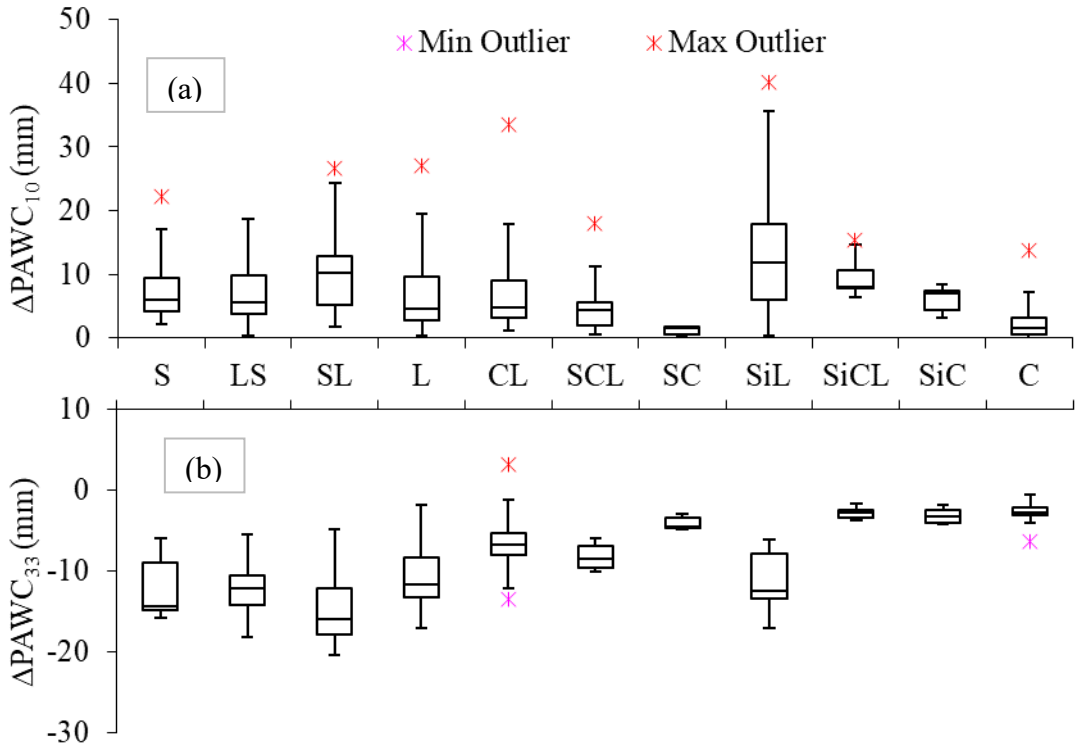


Fig. 10 Differences in the plant available water capacity (PAWC) between dynamic field capacity pressure heads (h_{fc}) and static heads of 10 kPa (ΔPAWC_10) and 33 kPa (ΔPAWC_33) in different (72) soil profile textures (S- sand, LS- loamy sand, SL- sandy loam, L- loam, SCL- sandy clay loam, CL- clay loam, SiL- silty loam, SiCL- silty clay loam, SiC- silty clay) in the Barossa Region. The data in each box vary (n = 5 to 48) depending on the number of observed textures in the study. The lower value of the box indicates the 25th percentile, the black line is the median, and the higher bar value indicates the 75th percentile. Whiskers indicate the 5th and 95th percentiles

The average values of ΔPAWC_33 in S, LS, SL, L, CL, SCL, SC, SiL, SiCL, SiC, and C textures are -5.30, -8.84, -9.38, -6.10, -3.83, -5.57, -2.86, -4.24, -1.98, -1.83, and -1.76 mm, respectively. Low values of ΔPAWC_33 in the latter five textures indicate that a fixed pressure head (33 kPa) and dynamic head values at field capacity occur within a close range. The assumption of FC at 33 kPa for these soils is unlikely to have a significant impact compared with a more complex and time-consuming dynamic head field capacity estimation. For sand-dominated textures, higher values of ΔPAWC_33 signify that these soils have dynamically variable field capacity pressure heads that are lower than 33 kPa, and the assumption of fixed pressure at 10 or 33 kPa is likely to have a greater impact and lead to large deviations in the estimation of the PAWC of soils.

These findings demonstrate the many inconsistencies between static pressure, time, and flux-based dynamic field-capacity estimations in soils. Soil heterogeneity, intra-texture variability, subsoil constraints, hysteresis, and swell–shrink clays have a significant impact on the water retention capacity of soils in response to dynamic and fixed-pressure FC (Gaiser *et al*., 2000; Greacen and Williams, 1983; Hillel, 1980; Hochman *et al*., 2001). The presence of different soil layers, such as sand, gravel, and clay, inhibits water redistribution, thereby increasing the FC. Hillel (1971) also noted how evapotranspiration affects the FC, where the rate of water extraction from the soil by plant roots affects water flow direction and redistribution. Even the proximity of the water table level results in varying FC owing to the capillarity rise in the root zone. Very low flow conditions for sodic swelling clay significantly delay the occurrence of FC, which may increase the PAWC, which has not been addressed by fixed or dynamic pressure heads.

CONCLUSIONS

Accurate estimation of the plant available water capacity (PAWC) of soils is one of the key components for devising appropriate irrigation schedules, sustainable crop production, and enhancing the water productivity of crops. The estimation of PAWC from dynamic head field capacity (FC) at the regional scale is complex, time-consuming, and expensive. In this study, we adopted a pedo-transfer function (PTF) approach to estimate PAWC using easily estimated soil properties. We estimated the dynamic FC (drained upper limit) water content for 236 soil textures from 72 locations at the minimum drainage flux (0.01 cm/day) assuming a unit hydraulic gradient. The crop lower limit (CLL, θ_{wp}) was corrected from site-specific estimated soil constraints such as compaction and high exchangeable sodium percentage (ESP). The PAWC values, estimated from fixed (10 and 33 kPa) and dynamic head FC values for different soil textures and soil profiles, were compared to understand the variability in PAWC occurring in the Barossa Region.

The values of the dynamic FC pressure heads (h_{fc}) for sand-dominated soil textures (sand, loamy sand, sandy loam, loam) ranged from 10.2–34.2 kPa and the mean values across these textures ranged between 15.8–18.2 kPa. For clay- and silt-dominated soils, the h_{fc} ranged between 10.8 and 49.2 kPa and average values across textures concentrated within 13.4–26.8 kPa. The estimated PAWC for individual texture and soil profile for the corresponding dynamic h_{fc} values showed large variability and inconsistency compared to the PAWC from fixed pressure (10 and 33 kPa) FC values. Normally, $PAWC_{fc}$ remains lower than $PAWC_{10}$ but higher than $PAWC_{33}$. However, PAWC estimation from a varied fixed FC value (i.e. 10 kPa for sand-dominated textures and 33 kPa for silt- and clay-dominated textures) narrowed the mean variation (<10%) among the dynamic and fixed-pressure FC methods. This suggests that when the water content at these pressures (10 and 33 kPa) is available, the PAWC of soils comparable to dynamic FC methods can be obtained.

These findings demonstrate that despite numerous inconsistencies between static pressure and flux-based dynamic FC estimation in soils, regional scale estimates of PAWC can be obtained from easily measured data. More ground truthing is essential to establish a better evaluation of the PAWC of soils using PTFs. Nevertheless, assuming a large level of uncertainty and heterogeneity in soil texture, subsoil constraints, hysteresis, and clay content, this estimation may serve as an effective pathway for developing reliable and robust estimates of water retention parameters and PAWC. The information generated in this study could serve as inputs for agro-hydrological, ecological, environmental, and climate change modelling studies.

ACKNOWLEDGEMENTS

The authors gratefully acknowledge Mr. Gaston Sepulveda, Mr. Lucas De Simoni, and Mrs. Annette James for their support in the collection of soil cores and the broader research team for their support. We are grateful to the growers of the Barossa Region for providing access to their vineyards. This research received financial support from Wine Australia. Wine Australia invests in and manages research, development, and extension on behalf of its grape growers, winemakers, and the Australian Government. The South Australian Research and Development Institute and the University of Adelaide are members of the Wine Innovation Cluster in Adelaide.

REFERENCES

Ahuja L R, Nachabe M H, Rockiki R. 2008. Soils field capacity. *In* Trimble B A S S W, Howell T A (eds.) Encyclopedia of Water Science. CRC Press, Boca Raton, Florida, USA. pp. 1128-1131.

Asgarzadeh H, Mosaddeghi M R, Dexter A R, Mahboubi A A, Neyshabouri M R. 2014. Determination of soil available water for plants: Consistency between laboratory and field measurements. *Geoderma*. **226-227:** 8-20.

Asgarzadeh H, Mosaddeghi M R, Mahboubi A A, Nosrati A, Dexter A R. 2010. Soil water availability for plants as quantified by conventional available water, least limiting water range and integral water capacity. *Plant Soil.* **335:** 229-244.

Assouline S, Or D. 2014. The concept of field capacity revisited: Defining intrinsic static and dynamic criteria for soil internal drainage dynamics. *Water Resour Res.* **50(6):** 4787-4802.

Brooks R H, Corey A T. 1964. Hydraulic Properties of Porous Media. Hydrology Paper No. 3. Colorado State University, Fort Collins, Colorado, USA.

Burk L, Dalgliesh N. 2008. Estimating Plant Available Water Capacity- A Methodology. Grain Research and Development Corporation, CSIRO Sustainable Systems, Canberra, Australia. pp. 40.

Campbell G S. 1974. A simple method for determining unsaturated conductivity from moisture retention data. *Soil Sci.* **117:** 311-314.

Campbell G S. 1985. Soil physics with BASIC: Transport models for soil-plant systems. Elsevier.

Chittleborough D J, Oades J M. 1980a. The development of a red-brown earth. II. Uniformity of the parent material. *Aust J Soil Res.* **18:** 375-382.

Chittleborough D J, Oades J M. 1980b. The development of a red-brown earth III. The degree of weathering and translocation of clay. *Aust J Soil Res.* **18:** 383-393.

Cong Z T, Lü H F, Ni G H. 2014. A simplified dynamic method for field capacity estimation and its parameter analysis. *Water Sci. Eng.* **7(4):** 351-362.

Crescimanno G, Iovino M, Provenzano G. 1995. Influence of salinity and sodicity on soil structural and hydraulic characteristics. *Soil Sci Soc Am J.* **59:** 1701-1708.

Cresswell H P, Hamilton G J. 2002. Bulk density and pore space relations. *In*McKenzie N, Coughlan K, Hamish H (Eds.) Soil Physical Measurement and Interpretation for Land Evaluation. CSIRO Publishing, Collingwood, Victoria, Australia. pp. 43-47.

de Alencar T L, Chaves A L, Freire A G, do Nascimento F V, Queiroz A S, Mota J C A. 2019. Field capacity: Methodological approach by static and dynamic criteria. *Geoderma*. **353:** 81-88.

Dirksen C, Matula S. 1994. Automatic atomized water spray system for soil hydraulic conductivity measurements. *Soil Sci Soc Am J*. **58:** 319-325.

Gaiser T, Graef F, Cordeiro J C. 2000. Water retention characteristics of soils with contrasting clay mineral composition in semi-arid tropical regions. *Aust J soil Res*. **38:** 523-536.

Greacen E L, Williams J. 1983. Physical Properties and Water Relations in Soils: An Australian Viewpoint. CSIRO Academic Press, Melbourne, Australia.

Groenevelt P H, Grant C D, Semetsa S. 2001. A new procedure to determine soil water availability. Aust J Soil Res. **39:** 577-598.

Hall J A S, Maschmedt D J, Billing N B. 2009. The soils of Southern South Australia: The South Australian Land and Soil Book Series1. Geological Survey of South Australia, Bulletin 56, Department of Water, Land and Biodiversity Conservation, Government of South Australia, Adelaide, SA, Auatralia, 188 pp.

Hillel D. 1971. Soil and Water: Physical Principles and Processes. Academic Press, New York, USA.

Hillel D. 1980. Fundamentals of Soil Physics. Academic Press, New York, USA.

Hillel D. 1998. Redistribution of water in soil. *In* Hillel D (Ed.) Environmental Soil Physics. Academic Press, San Diego, California, USA. pp. 449-470.

Hirmas D R, Furquim S A C. 2006. Simple modification of the clod method for determining bulk density of very gravelly soils. *Commun Soil Sci Plant Anal.* **37:** 899-906.

Hochman Z, Dalgliesh N P, Bell K L. 2001. Contributions of soil and crop factors to plant available soil water capacity of annual crops on Black and Grey Vertosols. *Aust J Agric Res.* **52:** 955-961.
Hochman Z, Dang Y P, Schwenke G D, Dalgliesh N P, Routley R, McDonald M, Daniells I G, Manning W, Poulton P L. 2007. Simulating the effects of saline and sodic subsoils on wheat crops growing on Vertosols. *Aust J Agric Res.* **58:** 802-810.
Hutson J L, Cass A. 1987. A retentivity function for use in soil–water simulation models. *J Soil Sci.* **38:** 105-113.
Jabro J D, Evans R G, Kim Y, Iversen W M. 2009. Estimating in situ soil–water retention and field water capacity in two contrasting soil textures. *Irrig Sci.* **27:** 223-229.
Janik L J, Soriano-Disla J M, Forrester S T, McLaughlin M J. 2016. Effects of soil composition and preparation on the prediction of particle size distribution using mid-infrared spectroscopy and partial least-squares regression. *Soil Res.* **54:** 889-904.
Kew G, Wetherby K, Zimmermann T, Meissner T. 2004. Estimation of readily available water holding capacity using field hand texture. 3rd Australian New Zealand Soils Conference, University of Sydney, Australia.
Letey J. 1985. Relationship between Soil Physical Properties and Crop Production. Advances in Soil Science. Springer New York, New York, NY. pp. 277-294.
Mallants D, Phogat V, Oliver D, Ouzman J, Beirgadhar Y, Cox J W. 2019. Sustainable Expansion of irrigated Agriculture and Horticulture in Northern Adelaide Corridor, Adelaide, South Australia.
Meyer P D, Gee G W. 1999. Flux-based estimation of field capacity. *J Geotech Geoenviron Eng.* **125:** 595-599.
Minasny B, McBratney A B. 2003. Integral energy as a measure of soil-water availability. *Plant Soil.* **249:** 253-262.
Mualem Y. 1976. A new model for predicting the hydraulic conductivity of unsaturated porous media. *Water Resour Res.* **12:** 513-522.
Nachabe M H, 1998. Refining the definition of field capacity in the literature. *J Irrig Drain Eng.* **124(4):** 230-232.
Nasta P, Romano N. 2016. Use of a flux-based field capacity criterion to identify effective hydraulic parameters of layered soil profiles subjected to synthetic drainage experiments. *Water Resour Res.* **52:** 566-584.
Northcote K H, Skene J K M. 1972. Australian Soils with Saline and Sodic Properties. Soil publication No. 27, CSIRO, Melbourne.
Picciafuoco T, Morbidelli R, Flamini A, Saltalippi C, Corradini C, Strauss P, Bloschi G. 2019. A pedotransfer function for field-scale saturated hydraulic conductivity of a small watershed. *Vadose Zone J.* **18:** 190018.
Poulton P, Verburg K, Verrall S. 2018. Scoping study reviewing the potential and feasibility to predict plant available water capacity for different crops. CSIRO, Brisbane, Australia.
Rayment G E, Lyons D J, Shelley B. 2011. Soil Chemical Methods - Australasia. Australian Soil and Land Survey Handbooks Series. CSIRO Publishing, Victoria.
Rengasamy P, Olsson K A. 1993. Irrigation and sodicity. *Aust J Soil Res.* **31:** 821-837.
Robinson S, Sandercock N. 2014. An analysis of climate, soil and topographic information to aid the understanding of Barossa terroir – A Barossa Grounds project, Adelaide, Australia.
Schaap M G, Leij F J. 2000. Improved prediction of unsaturated hydraulic conductivity with the Mualem-van Genuchten Model. *Soil Sci Soc Am J.* **64:** 843-851.
Schaap M G, Leij F J, van Genuchten M Th. 2001. rosetta: a computer program for estimating soil hydraulic parameters with hierarchical pedotransfer functions. *J Hydrol.* **251:** 163-176.
Silva A P D, Kay B D, Perfect E. 1994. Characterization of the least limiting water range of soils. *Soil Sci Soc Am J.* **58:** 1775-1781.
Šimůnek J, van Genuchten M Th, Sejna M. 2008. Development and applications of the HYDRUS and STANMOD software packages and related codes. *Vadose zone J.* **7(2):** 587-600.

Sinowski W, Scheinost A C, Auerswald K. 1997. Regionalization of soil water retention curves in a highly variable soilscape. 2. Comparison of regionalization procedures using a pedotransfer function. *Geoderma.* **78:** 145-159.

Sun H, Yang J. 2013. Modified numerical approach to estimate field capacity. *J Hydrol Eng.* **18:** 431-438.

Twarakavi N K C, Šimůnek J, Schaap M G. 2009. Development of pedotransfer functions for estimation of soil hydraulic parameters using support vector machines. *Soil Sci Soc Am J.* **73:** 1443-1452.

van Genuchten M Th. 1980. A Closed-form equation for predicting the hydraulic conductivity of unsaturated soils. *Soil Sci Soc Am J.* **44:** 892-898.

Veihmeyer F J, Hendrickson A H. 1927. Soil-moisture conditions in relation to plant growth. *Plant Physiol (Bethesda).* **2(1):** 71-82.

Veihmeyer F J, Hendrickson A H. 1931. The moisture equivalent as a measure of the field capacity of soils. *Soil Sci.* **32:** 181-193.

Vereecken H, Maes J, Feyen J, Darius P. 1989. Estimating the soil moisture retention characteristic from texture, bulk density, and carbon content. *Soil Sci.* **148:** 389-403.

Vereecken H, Weynants M, Javaux M. Pachepsky Y, Schaap M G, van Genuchten M. Th. 2010. Using pedotransfer functions to estimate the van Genuchten–Mualem soil hydraulic properties: A review. *Vadose Zone J.* **9:** 795-820.

Williams C H. 1981. Chemical Properties of Red-Brown Earth of Australia. University of Adelaide and CSIRO Division of Soils, Waite Research Institute, Adeliade, Australia. pp. 47-62.

Wösten J H M, Pachepsky Y A, Rawls W J. 2001. Pedotransfer functions: bridging the gap between available basic soil data and missing soil hydraulic characteristics. *J Hydrol.* **251:** 123-150.

Zacharias S, Bohne K. 2008. Attempt of a flux-based evaluation of field capacity. *J Plant Nutr Soil Sci.* **171:** 399-408.

Zhou J, Konate M, Cavagnaro T R, Bei R, Nelson D, Stephen J R, Metcalfe A, Gilliham M, Breen J, Collins C, Lopez C M R. 21. Wine terroir and the soil bacteria: An amplicon sequencing based assessment of the Barossa Valley and its sub-regions. *Front. Microbiol.* **11:** 597944. doi: 10.3389/fmicb.2020.597944.

5.2 Benchmarking water-limited yield potential and yield gaps of Shiraz in the Barossa and Eden Valleys

BENCHMARKING WATER-LIMITED YIELD POTENTIAL AND YIELD GAPS OF SHIRAZ IN THE BAROSSA AND EDEN VALLEYS

MARCOS BONADA[1], VINOD PHOGAT[1,2,3], CASSANDRA COLLINS[2], PAUL PETRIE[1,4,5], VICTOR SADRAS[1,2]

[1]South Australia Research and Development Institute, Waite Campus, Adelaide, Australia
[2]School of Agriculture, Food and Wine, University of Adelaide, Waite Campus, Adelaide, Australia.
[3]College of Agriculture, Chaudhary Charan Singh Haryana Agricultural University, India
[4]Faculty of Engineering, University of New South Wales, Sydney, Australia
[5]College of Science and Engineering, Flinders University, Adelaide, Australia

***Keywords**: carbon isotope composition, drought, evapotranspiration, rainfall, temperature, water*

Abstract

Background and Aims: Management of water in vineyards needs an update to account for direct (i.e., shifts in amount and seasonality of rainfall, reduced availability of water for irrigation, and higher temperature and vapour pressure deficit), and indirect effects of climate change including the use of irrigation to manage heat stress. In this context, we benchmarked water-limited yield potential (Yw), calculated yield gaps as the difference between Yw and actual yield (Ya), and explored the underlying environmental and management causes of these gaps.

Methods and Results: We measured yield and its components in two sections of 24 Shiraz vineyards during three vintages in the Barossa zone. The frequency distribution of yield was L-shaped, with half the vineyards below 5.2 t ha^{-1}, and an extended tail of the distribution that reached 24.9 t ha^{-1}. The seasonal ratio of actual crop evapotranspiration and reference evapotranspiration was below 0.48 in 85% of cases, with a maximum of 0.65, highlighting the prevalence of a substantial water deficit in these vineyards. A boundary function relating actual yield and seasonal rainfall was fitted to quantify Yw. Yield gaps increased with increasing vine water deficit, quantified with carbon isotope composition in must. The yield gap was smaller with higher rainfall before budburst, putatively favouring early-season vegetative growth and allocation to reproduction, and with higher rainfall between flowering and veraison, putatively favouring fruit and seed set and early berry growth. The gap was larger with higher rainfall and lower radiation between budburst and flowering. The yield gap declined with altitude at 0.038 t ha^{-1} m^{-1} in the range from 186 to 326 m.a.s.l.; the Eden Valley departed from this trend, with a yield gap that was higher than expected from its elevation. The yield gap increased linearly with vine age between 6 and 33 yr at a rate of 0.3 t ha^{-1} yr^{-1}. The correlation between yield gap and yield components ranked bunch weight ≈ berries per bunch > bunch number > berry weight; the minimum to close the yield gap was 185,000 bunches ha^{-1}, 105 g $bunch^{-1}$, 108 berries $bunch^{-1}$ and 1.1 g $berry^{-1}$.

Conclusions

Water deficit and vine age were major causes of yield gaps. Winter irrigation needs attention in the context of climate change and drier winters. The cost of dealing with older, less productive vines (vine removal, new planting, and delay of productivity of young vines) needs to be weighed against the rate of increase in yield gap with vine age.

Significance of the Study

A boundary function to estimate water-limited yield potential returned viticulturally meaningful yield gaps.

Introduction

Mediterranean regions feature at least 60% of annual rainfall in the winter half-year (di Castri and Mooney 1973). The Barossa and Eden Valle regions, the focus of this study, have a Mediterranean-type climate where vine growth and yield rely on three sources of water: soil-stored winter rainfall, variable amounts of summer rainfall from the tails of tropical storms, and supplementary irrigation (Dry, et al. 2005). Owing to climate change, management of water needs an update. First and most important, winter rainfall is diminishing in South-eastern Australia (Cai and Cowan 2013), and irrigation approaches are required to account for drier soil in spring (Bonada, et al. 2021, Bonada, et al. 2020). Second, irrigation to promote evaporative cooling is central to the management of heat stress, which is increasing in frequency and intensity (Sadras and Schultz 2012, Webb, et al. 2010). Third, pruning after budburst is being used to displace critical developmental stages onto cooler conditions, and requires further adjustments in irrigation to account for shifts in the dynamics of canopy cover (Moran, et al. 2019, Moran, et al. 2018, Moran, et al. 2021, Petrie, et al. 2017). For example, the evapotranspiration of Malbec in Mendoza was 5% lower in vines pruned at 2-3 separated leaves, and 10% lower in vines pruned at 8 separated leaves than in winter-pruned controls (Morgani, et al. 2022).
Production functions relating crop yield and water use (or irrigation water) are critical for irrigation management (Steduto, et al. 2012). These functions are usually tight, i.e., high r^2, because yield and water use are measured in experiments where water supply is the main source of variation and other factors are largely controlled (Steduto, et al. 2012). In contrast, the association between yield and water use is scattered where multiple, agronomically relevant sources of variation influence crop traits; for rainfed wheat in Australia, for example, the relationship between yield and water use has a typical r^2 ~ 0.3 (Sadras 2020). Dealing with a highly scattered yield-water use relation, French and Schultz (1984) insightfully fitted a boundary function with biophysically meaningful parameters, rather than a regression. Their boundary function is

$$\mathrm{Yw} = \mathrm{TE_Y} \cdot (\mathrm{ETc} - \mathrm{Es}) \qquad \text{eq. 1}$$

where Yw is water-limited yield potential, ETc is actual crop evapotranspiration, the slope TE_Y is the maximum transpiration efficiency for yield, and the x-intercept Es is an approximate measure of non-productive water loss, primarily soil evaporation. This model has many simplifications, including a constant soil evaporation and lack of consideration of the effect of timing of water supply on yield (French and Schultz 1984, Rockström 2003, Sadras, et al. 2015).

In a similarly simple, one equation model, Rockström (2003) relates ETc per unit yield and yield, hence accounting for the decline in Es:ETc with increasing crop vigour and yield:

$$\mathrm{ETc{:}\,yield} = \frac{a}{[1-e^{(b \cdot yield)}]} \qquad \text{eq. 2}$$

where *a* is the transpiration-to-yield ratio and *b* is the rate of decline in soil evaporation (Es) with increased canopy size, and therefore also the yield at which Es:ETc reaches its minimum. However, his model has an element of circularity because yield is common to *x* and *y* (Brett 2004). In grapevine, both these models (eq. 1 and eq. 2) further overlook yield response to water supply in the previous season, but so do the typical production functions that consider water use in the current season only (Steduto, et al. 2012) and more refined models of grapevine growth and yield (Yang, et al. 2022 and references cited therein).

Owing to its transparency and frugal data requirement, eq. (1) has been widely adopted in the industry where cereal farmers relate their actual yield (Ya) to the water-limited yield potential, calculate a yield gap, i.e., Yw – Ya, identify its causes, and modify their practices to close the gap (Sadras 2020). The yield gap, its causes, and remedies have motivated a global yield gap initiative that accounts for data-

rich and data-poor cropping systems (https://www.yieldgap.org/). Daily time-step models accounting for crop, soil, climate, and management are favoured to estimate the water-limited yield potential, hence overcoming the limitations of simpler approaches (van Ittersum, et al. 2013). Owing to carry over effects across seasons affecting processes such as bud fertility driving bunch number and the dynamics of carbohydrate reserves buffering berry growth (Dunn, et al. 2004, Iland, et al. 2011, Vasconcelos, et al. 2009), reliable models to predict yield are lagging and yield gap analysis is incipient in grapevine. For example, Yang et al. (2022) modelled a single yield component, bunch weight, to calculate yield gaps in European wine regions under the explicit assumption of no variation in both plant population density and number of bunches per ha.

In this study, we benchmark the water-limited yield potential, and calculate yield gaps of Shiraz in the Barossa region using a data set of actual yield that captures viticulturally relevant sources of variation including weather, soil, vineyard age, and management.

Methods

Study area and experimental sites

This study was conducted in the Barossa Zone GI, which includes the Barossa Valley and Eden Valley. The zone is internationally known for its full-bodied Shiraz wines. The complex system of valleys and twisting hills results in a variety of slopes, aspects and sites (Bramley and Ouzman 2021). The soils vary widely due to the complex geology of the region, but they primarily fall in a family of duplex soils, characterised by an abrupt texture change between the topsoil and subsoil (Dry, et al. 2005).

We measured yield and its components, and calculated actual crop evapotranspiration in 144 samples that resulted from the full combination of six sub-regions, four vineyards per sub-region, two sections per vineyard, and three consecutive vintages since 2019. The sub-regions are Northern Grounds (NG), Central Grounds (CG), Eastern Edge (EE), Southern Grounds (SG), Western Ridge (WR) and Eden Valley (EV) (Robinson and Sandercock 2014). Two vine vigour sections (high, low) were identified based on soil survey and vine vigour maps of each block, as explained in Bonada et al. (2022). Vineyard age, clone, rootstock, row orientation, pruning method, and trellising system were recorded (Table S1).

Vine traits

At harvest, the number of bunches and yield per metre of cordon were recorded from three sections within each sample. We calculated average bunch weight from yield and bunch number, and the number of berries per bunch from bunch weight and average berry weigh from a 100 berry sample. In winter, we counted the number of shoots and measured pruning weight in three one-meter canopy sections. Yield, bunch number, shoot number and pruning weight per ha were calculated based on the planting layout (Table S1).
To quantify crop water status, we measured carbon isotope composition ($\delta^{13}C$) in must. This trait integrates crop water status over the growing period until sampling time and is robust in relation to environmental conditions—radiation, wind speed, temperature, vapour pressure deficit (Condon, et al. 2002) – unlike traits such as stomatal conductance, leaf water potential, or canopy temperature that vary with conditions at sampling time. We measured $\delta^{13}C$ in 216 samples of must. Fruit juice collected at harvest was centrifuged for 4 minutes at 4500 RPM and 50 ml were sterilised the same day by autoclaving at 120 ^{o}C for 20 minutes (Ollat, et al. 2002). Carbon isotope composition was measured on approximately 10 µl of berry juice, freeze dried in tin capsules (3 mg dried weight) using a continuous flow isotope ratio mass spectrometer (Nu Horizon IRMS with EuroVector EA).

Weather, soil moisture and water balance

Bonada et al. (2022) describe the measurements of weather and components of the soil water balance in detail. Briefly, 24 weather stations (MEA Junior WS, Magill, South Australia), one at each site, were installed at the beginning of the experiment to log temperature, relative humidity, wind speed and direction, solar radiation, and rainfall at 15-minutes intervals; daily reference evapotranspiration (ETo) was calculated with the method of Penman–Monteith {Allen, 1998 #4188}. Soil moisture was continually monitored at four depths using capacitance probes (EnviroSCAN system, Sentek, Magill, South Australia). The PVC access tubes were installed directly below the irrigation lateral and between drippers. Data were logged every 15 minutes and retrieved from the logger at least monthly for processing using the IrriMax10 software (Sentek, Magill, South Australia). Details of probe calibration and calculations of plant available water are in Bonada et al. (2022).

Statistical analyses

The analysis was constrained to 127 out of 144 paired yield-ET points due to missing samples of yield or ET components. We used ANOVA to test the effect of main sources of variation on yield and its components, and other related traits. To explore associations between variables, we fitted least squares regression (LS, Model I) when error in *x* was negligible in comparison to error in *y* and reduced maximum axis regression (RMA, Model II) to account for error in both x and y (Niklas, 1994). Pearson's correlation coefficients (r) were calculated, with *p* derived from Fisher z-transformation that transforms the sampling distribution of r for it to become normally distributed. For both ANOVA and regressions, we follow updated statistical recommendations and avoid the wording "statistically significant", "non-significant", or the variations thereof, thus avoiding dichotomisation based on an arbitrary discrete *p*-value (Wasserstein et al., 2019). Instead, we report *p* as a continuous quantity, and Shannon information transform [$s = -\log_2(p)$] as a measure of the information against the tested hypothesis (Greenland, 2019). Although *s* is a function of *p*, the additional information is not redundant. With the base-2 log, the units for measuring this information are bits (binary digits). For example, the chance of seeing all heads in 4 tosses of a fair coin is 1/24 = 0.0625. Thus, $p = 0.05$ conveys only $s = -\log_2(0.05) = 4.3$ bits of information, "which is hardly more surprising than seeing all heads in 4 fair tosses" (Greenland, 2019).

Boundary functions were fitted using percentile regression to define water-limited yield potential, and yield gaps were calculated as the difference between water-limited yield potential and actual yield as outlined in Sadras et al. (2015). To explore the associations of yield gap and weather, location, vineyard features, and management we used ANOVA for discrete variables (e.g., trellising system), and regression for continuous variables (e.g., vine age).

Results

Growing conditions

Weather during the growing season varied with location, vintage, and intra-seasonally from budburst in spring to maturity in autumn (Figure 1). Minimum temperature varied 4.9-fold, vapour pressure deficit varied 4.3-fold, and maximum temperature and solar radiation varied 2.1-fold.

Plant available water in the soil at budburst ranged from 27 to 144 mm and averaged 91 mm with a coefficient of variation of 0.26. Rainfall was below reference evapotranspiration, particularly between flowering and veraison (Figure 1 d,e). Seasonal irrigation varied from 0 to 335 mm, and averaged 161 mm, with a coefficient of variation of 0.38. The seasonal ratio of actual crop evapotranspiration

(accounting for plant available water in the soil at budburst, rainfall, and irrigation), and reference evapotranspiration was below 0.48 in 85% of cases, with a maximum of 0.65 (Figure 1f), highlighting the prevalence of a substantial water deficit in these vineyards. Carbon isotope composition, a trait that relates to plant water status, varied from -26.74 to -21.70‰ (Figure 1g).

Yield and its components

Yield averaged 3.7 ± 0.37 t ha^{-1} in 2020, 5.9 ± 0.50 t ha^{-1} in 2019, and 10.1 ± 0.37 t ha^{-1} in 2021. For the pooled data, the frequency distribution of yield was L-shaped (Figure 2a), with skewness and kurtosis departing from the normal distribution's zero and three, respectively (Bradley 1982). Half the vineyards were below 5.2 t ha^{-1}, and the extended tail of the distribution reached 24.9 t ha^{-1} (Figure 2). Yield correlated with all its components (Table 1); the strength of the correlation declined in the order bunch number per ha, bunch weight, berries per bunch, berry weight. Yield correlated with vegetative traits including pruning weight and shoot number (Table 1). Yield, its components, and vegetative traits all declined with lower carbon isotope composition indicative of more severe water stress (Figure 2b, Table 1).

Table 1. Correlation matrix of yield, its components, vegetative traits and carbon isotope composition in must ($\delta^{13}C$) for Shiraz in the Barossa region. Sources of variation are 25 vineyard locations, two sites per vineyard, and three vintages. Numbers in italics are Pearson's correlation coefficients and numbers with coloured background are *p* from Fisher's r to z test.

p scale

0.0001	0.001	0.01	0.05	0.1	0.2	0.3	0.4	0.5	0.6	1

	Bunch no/ha	Bunch weight (g)	Berries/bunch	Berry weight (g)	Shoot no/m	Pruning wt (t/ha)	$\delta^{13}C$(‰)
Yield (t/ha)	*0.75*	*0.70*	*0.64*	*0.42*	*0.37*	*0.61*	*-0.36*
Bunch no/ha		*0.13*	*0.14*	*0.09*	*0.65*	*0.42*	*-0.30*
Bunch weight (g)			*0.91*	*0.55*	*-0.14*	*0.50*	*-0.28*
Berries/bunch				*0.20*	*-0.15*	*0.45*	*-0.19*
Berry weight (g)					*0.02*	*0.38*	*-0.26*
Shoot no/m						*0.43*	*-0.26*
							-0.18

Yield (t/ha)	0.0001	0.0001	0.0001	0.0001	0.0001	0.0001	0.0001
Bunch no/ha		0.0698	0.0542	0.2296	0.0001	0.0001	0.0001
Bunch weight (g)			0.0001	0.0001	0.0516	0.0001	0.0001
Berries/bunch				0.0054	0.032	0.0001	0.0079
Berry weight (g)					0.7929	0.0001	0.0002
Shoot no/m						0.0001	0.0116
Pruning wt (t/ha)							0.0002

Relationship between ETc:yield ratio and yield

Rockström (2003) described the relation between the ratio ETc:yield and yield with eq. 2. He interpreted the declining ETc:yield ratio with increasing yield in terms of shifts in the evapotranspiration components: with increasing yield and crop vigour, the Es:ETc ratio declines, and a higher proportion of ETc is used in plant transpiration. The actual relation between ETc:yield and yield conformed to the expected model (Figure 3a, r = 0.98, $p < 0.0001$, $s > 13.3$). However, this association involves a shared factor in *y* and *x*, with the potential for spurious correlations (Brett 2004). We tested the legitimacy of the association in Figure 3a with two complementary approaches. Statistically, a large spurious correlation emerges when the coefficient of variation of the shared factor is more than 1.5 times larger than the coefficient of variation of the non-shared factor (Brett 2004). In our data set, the coefficient of variation of the shared factor, yield, was 73.8%, and the coefficient of variation of the non-shared factor, seasonal ETc, was 22.5%; the ratio is 3.3, indicating the spurious nature of the correlation from a

statistical viewpoint. Biophysically, the association between Es:ETc and yield was weak and had a flat slope of 0.018 ± 0.002 (t ha^{-1})$^{-1}$ (Figure 3b). This analysis therefore supports the assumption of a conserved Es for the range of yield in our data and justifies a single relationship between yield and ETc (or rainfall) as summarised in eq. 1.

Benchmarking water-limited yield potential

The RMA regression between yield and seasonal ETc returned a slope representing yield per unit transpiration of 0.065 t ha^{-1} mm^{-1} and an x-intercept representing soil evaporation of 216 mm (Figure 4a, Table 2). The strength of the relationship improved with ETc corrected by VPD, but not with ETc normalised with ETo (Figure 4abc, Table 2). The RMA regression between yield and seasonal rainfall returned a slope of 0.117 t ha^{-1} mm^{-1} and an x-intercept of 74 mm (Figure 4d, Table 2); this association ($r = 0.62$, $F_{1,124} = 76.5$) did not improve with corrections by VPD or ETo (Table 2), or with the inclusion of winter rainfall ($r = 0.34$, $F_{1,124} = 16.7$).

Table 2. Statistics of reduced maximum axis regressions between yield and ETc, ETc · VPD^{-1}, ETc · ETo^{-1}, rain, rain · VPD^{-1} , rain · ETo^{-1} . Scatterplots and fitted regressions are in Figure 4.

Variable	r	$F_{1,124}$	*p*	*s*	slope	x-intercept
ETc (mm)	0.32	13.99	0.0003	11.7	0.065 t ha^{-1} mm^{-1}	216 mm
ETc · VPD^{-1} (mm kPa^{-1})	0.38	21.5	0.0001	13.3	0.160 t ha^{-1} mm^{-1} kPa^{-1}	72 mm kPa^{-1}
ETc · ETo^{-1}	0.30	12.6	0.0005	11.0	51.7 t ha^{-1}	0.265
Rain (mm)	0.62	76.45	0.0001	13.3	0.117 t ha^{-1} mm^{-1}	74 mm
Rain · VPD^{-1} (mm kPa^{-1})	0.59	64.87	0.0001	13.3	0.26 t ha^{-1} mm^{-1} kPa^{-1}	22 mm kPa^{-1}
Rain · ETo^{-1}	0.56	56.01	0.0001	13.3	88.1 t ha^{-1}	0.087

We fitted a boundary function relating yield and seasonal rainfall for benchmarking vine yield (Figure 4d, green line). Although seasonal rainfall is only one component of the total water input, we used rainfall instead of ETc for four reasons. First, seasonal rainfall returned the strongest correlation with yield (Table 2). Second, the spatial variation of seasonal rainfall in the Barossa region correlates with the spatial variation in annual rainfall (Bramley and Ouzman 2021). Third, there were more data available to fit a boundary function with rainfall than for ETc; the association between yield and seasonal rainfall for the larger data set returned $r = 0.59$, $F_{1,188} = 102.14$, $p < 0.0001$, $s > 13.3$. Fourth, rainfall is more readily available than ETc for industry applications.

Yield gap

The average yield gap was twice as large in 2021, the highest-yielding season, compared with 2019 and 2020 (Fig 5a). The average yield gap varied from 9.9 t ha^{-1} in the Central Grounds to 16.8 t ha^{-1} in the Southern Grounds (Figure 5b). Part of this variation was related to elevation, with yield gap declining at 0.038 ± 0.01 t ha^{-1} m^{-1} in the range from 186 to 326 m.a.s.l. (Figure 5c); the Eden Valley departed from this trend, with a yield gap that was higher than expected from its elevation (solid symbols in Figure 5c).

The yield gap did not vary with trellising system, pruning method, or row orientation (Figure 5def). The yield gap increased slightly with distance between vines at 3.0 ± 1.5 t ha^{-1} m^{-1} ($r = 0.14$, $p = 0.051$, $s = 4.3$), and did not vary with distance between rows ($p = 0.208$, $s = 2.3$) or rectangularity ($p = 0.251$, $s = 2.0$). The yield gap increased linearly with vine age between 6 and 33 yr at a rate of 0.3 ± 0.06 t ha^{-1} yr^{-1} (Figure 5g). The yield gap in vines reworked on 98-year-old Shiraz rootstock averaged 8.3 ± 0.70 t

ha^{-1} (solid symbols in Figure 5g); this compares with a projected gap from the fitted regression of 31 t ha^{-1}.

The yield gap correlated with all four yield components; the strength of the correlation ranked bunch weight ≈ berries per bunch > bunch number > berry weight (Figure 6a-d). The minimum to close the yield gap was 185,000 bunches ha^{-1}, 105 g $bunch^{-1}$, 108 berries $bunch^{-1}$ and 1.1 g $berry^{-1}$ (arrow heads in Figure 6a-d). The yield gap declined with increasing pruning weight, and the minimum pruning weight to close the gap was 3.2 t ha^{-1}.

Figure 7 shows Pearson's correlation coefficients between yield gap and weather factors in four periods, from late August to budburst, budburst to flowering, flowering to veraison, and veraison to maturity, and Table S1 shows the correlation matrix for all factors. The association between yield gap and both maximum and minimum temperature shifted from positive before budburst to negative after flowering. The association between yield gap and radiation was negative from budburst to flowering and from veraison to maturity, and positive in the intervening period from flowering to veraison. Larger yield gaps were associated with smaller VPD between budburst and maturity, and the association was stronger at earlier stages. The association between yield gap and rainfall was negative before budburst and between flowering and veraison, and positive between budburst and flowering. The larger yield gap with higher rainfall between budburst and flowering was partially associated with the strong negative correlation between rainfall and VPD (Table S1). The yield gap increased with increasing vine water stress quantified with carbon isotope composition of must (Figure 2c).

Discussion

Management of water in vineyards needs an update to account for direct (i.e., shifts in amount and seasonality of rainfall, reduced availability of water for irrigation, and higher temperature and vapour pressure deficit), and indirect effects of climate change including the use of irrigation to manage heat stress. In this context, we benchmarked the relation between yield and water use, calculated yield gaps, and explored their underlying environmental and management causes.

The reduced-maximum axis regression between yield and ETc returned a slope of 0.065 t ha^{-1} mm^{-1} and x-intercept of 216 mm (Table 2). This compares with slopes from 0.061 to 0.123 t ha^{-1} mm^{-1} and x-intercepts from 136 to 175 mm in a sample of vineyards in Spain, the US and China (Table S2). Parameters from least squares regressions, the default in most software packages, are included in Table S2 to highlight the flatter slopes and lower x-intercepts from this approach that assumes error in *x* is negligible in relation to error in *y* (Ludbrook 2012, Niklas 1994); the assumption is unjustified because error in ETc is not negligible. Indeed, yield correlated more strongly with seasonal rainfall than with ETc (Figure 4; Table 2). This was related to the uncertainty in the quantification of both soil water content and irrigation used in the calculation of ETc (Vinod et al. 2022 pre-print). We thus favoured a rainfall-based benchmark for water-limited yield potential and yield gap analysis. This model has several assumptions, including a single x-intercept representing soil evaporation. Rockström (2003) model explicitly accounts for the reduction in soil evaporation associated with larger canopies and higher yield (eq. 2). Our data conformed to Rockström's model, but statistical and biophysical criteria supported the conclusion that it is unsuitable for our analysis: the relationship ETc:yield vs yield is spurious (Brett 2004), and inconsistent with the small variation in Es:ET with increasing yield (Figure 3).

In contrast to annual crops where canopy size is a large source of variation in energy partitioning, the wide-row structure dampens the variation in Es:ETc of vineyards, particularly in low-rainfall environments and under drip irrigation that wets a limited soil area (Jiao, et al. 2018, Yunusa, et al. 1997, Yunusa, et al. 2004, Zhang, et al. 2010). In a furrow-irrigated Sultana vineyard in the dry Victorian Mallee, Australia, Es:ETc was 0.46-0.51 for a yield range between 7 and 22 t ha^{-1} (Yunusa, et al. 1997). In a drip-irrigated Sultana vineyard with a yield range from 6 to 20 t ha^{-1} in the same region, the RMA rate of decline in Es:ETc with increasing yield was 0.011 ± 0.003 $(t\ ha^{-1})^{-1}$ (Yunusa, et al. 1997) compared with the rate of 0.018 ± 0.002 $(t\ ha^{-1})^{-1}$ in our data set (Figure 3b). These two studies (Yunusa, et al. 1997, Yunusa, et al. 1997) are thus consistent with both the flat relation between Es:ETc

and yield in vineyards, and the lower Es:ETc at high yield under drip irrigation compared to furrow irrigation.

The spatial coherence of seasonal and annual rainfall in the Barossa region (Bramley and Ouzman 2021) and the biophysical and viticultural meaningful yield gaps derived from a rainfall-based benchmark reinforce the robustness of our approach. The yield gap was larger in the season with highest yield and varied with location (Figure 5ab). Elevation, a major factor in the clustering of locations in the Barossa region (Bramley and Ouzman 2021), accounted for part of the variation with smaller gaps with increasing elevation (Figure 5c). The Eden Valley locations departed from this trend, with larger yield gaps than expected from their elevation (Figure 5c). This larger-than-expected yield gaps can be related management shallow soil and limited access to irrigation water (Bramley and Ouzman 2021, Water 2022). Unlike the Barossa Valley that relies on irrigation water from the River Murray, the Eden Valley is heavily reliant on native sources, i.e., groundwater and surface water (Water 2022). Historically, the name Barossa Valley was used to describe the area below 400 masl, and the name Eden Valley, rather than Barossa Ranges, has been favoured since the 1950s (Fuller and Walsh 1999).

The yield gap did not vary with row orientation, trellis system or pruning method (Figure 5). Water use of vertically trained, potted vines was approximately 18% lower in east-west orientated vines compared to north-south vines in the northern hemisphere (Buesa, et al. 2020). Row orientation did not affect carbon assimilation; hence, the water use efficiency (based on both carbon assimilation and yield) was higher for the east-west vines was higher than the vines orientated north-south (Buesa et al 2020). Modelled intercepted radiation was higher in north-south than east-west orientated rows (Palmer 1989). However, the impact of row orientation is complicated by its interactions with and between canopy configuration, time of year, and row spacing (Jackson and Palmer 1972) as well as vine water status, crop load and the other practices discussed above. Shiraz vines in the Barossa and Eden Valleys are traditionally managed using spur pruning and a single cordon, with some vineyards maintaining a second cordon approximately 0.4 m above the first (Dry, et al. 2005). More recently, occasional vineyards have been changed to Guyot, locally described as rod or cane pruning, often to improve trunk disease management (Henderson, et al. 2021). Multiple cordons increase the number of buds retained on the vine and canes favour bud fertility, hence both systems have the potential to increase bunch number and yield relative to the single cordon spur pruned system (Jackson 2001).

The yield gap increased linearly with vine age, and this can be related to at least four factors: time to peak production, technological change, disease progression and vine management. Crop evapotranspiration and yield increase with vine age from establishment until the canopy and root system reach their full capacity to capture radiation and water, around 6 to 10 years after planting depending on management, variety and growing conditions (Evans, et al. 1993, Munkvold, et al. 1994, Sadras and Schultz 2012). Hence, age-related variation in vine capacity to capture water and radiation was a minor factor for the range from 6- to 33-year-old vines in which yield gap related to vine age. Eutypa dieback, caused by the fungus *Eutypa lata*, is a severe, widespread trunk disease of grapevines (Koussa, et al. 2006, Munkvold, et al. 1994, Sosnowski, et al. 2008). The fungus grows slowly in the plant and the onset of foliar symptoms occurs 3-8 years after infection. In south-eastern Australian vineyards, the incidence of trunk disease increased with vine age (Sosnowski, et al. 2016). The yield of Chenin blanc vineyards in California varied non-linearly with age, increasing up to a peak over 20 t ha^{-1} in 12-year-old vines, and declined dramatically after this peak in association with the period of rapid increase in Eutypa dieback (Munkvold, et al. 1994). The putative effects of disease can be partially confounded with mangement; arm wrapping into the cordon wire is a practice commonly used during the establishment of a new vineyard, which may bring a de-vigorating effect and potential drop in production as cordon strangulate over the years (O'Brien, et al. 2021). Irrespective of the causes, the costs of dealing with older, less productive vines (vine redevelopment, new planting, and delay of productivity of young vines) need to be weighed against the rate of increase in yield gap of 0.3 ± 0.06 t ha^{-1} yr^{-1} (Figure 5g).

Plant water deficit was neutral or slightly improved the tolerance of grapevine to infection and colonisation by *E. lata* (Sosnowski, et al. 2021). Once established in the plant, Eutypa dieback fungi invade bark tissues and xylem, resulting in the death of a portion of vascular cambium whereby infected structures are no longer able to produce newly functional xylem and phloem, and cankers develop (Pouzoulet, et al. 2014). Eutypa dieback reduced the water content and disrupted the dynamics of free abscisic acid (ABA) and its glucose esters (ABA-GE) in diseased organs of Cabernet sauvignon (Koussa, et al. 2006). Consistent with the disruption in the vascular system and altered water relations, the yield gap increased with water stress, as quantified with carbon isotope composition (Figure 2c). Other factors that contribute to water stress and yield gap include soil plant available water, primarily related to soil depth (Bramley and Ouzman 2021, Coipel, et al. 2006).

Yield correlated with all four yield components, particularly with bunch number (Table 1); bunch number is usually the largest source of variation in grapevine yield (Dunn, et al. 2004). The yield gap correlated with all four yield components, particularly bunch weight and berries per bunch, highlighting the incidence of berry set. The causes for the shift from bunch number as the main source of variation in yield to bunch size as the main source of variation in yield gap are unclear. Irrespective of the causes, the minimum bunch size (105 g bunch^{-1}, 108 berries bunch^{-1}) to close yield gaps maybe used as a rule-of-thumb to benchmark vineyard performance, but requires independent testing (Figure 6). The yield gap was smaller with higher rainfall before budburst, putatively favouring early-season vegetative growth and allocation to reproduction, and with higher rainfall between flowering and veraison, putatively favouring fruit set and early berry growth and seed set (Friend, et al. 2009, Ristic and Iland 2005). Consistent with our correlative findings, experimental evidence led to the conclusion that winter irrigation is required to maintain yield in the context of drier winters with climate change (Bonada, et al. 2020). The gap was larger with high rainfall, and associated low radiation, between budburst and flowering (Figure 7). For Godello in the Ribero Designation of Origin, the production of pollen spanned 2-3 weeks in May and June, and yield correlated negatively with rainfall in May (González-Fernández, et al. 2020). Three successive rainy days in late May (53 mm), just after the seasonal pollen peak, promoted a fast decrease in the airborne pollen concentration (González-Fernández, et al. 2020). The association between yield gap and temperature shifted from positive early in the season, to negative at later stages, particularly between flowering and veraison. This agrees with empirical evidence that indicates differential sensitivity to temperature between phenological stages. Consistent with the positive correlation between yield gap and temperature early in the season observed here, artificially elevated temperature two weeks before budburst decreased the number of flowers at a rate of –7.3 flowers per ºC for the lower inflorescence and – 5.5 flowers per ºC for the upper inflorescence, with no impact of temperature two weeks after budburst (Petrie and Clingeleffer 2005). Temperature sensitivity increases again during anthesis; the damage, however, depends on the threshold of temperature. Temperature over 35 ^{o}C at flowering reduced fruit set and the number of berries per bunch (Kliewer 1977), whereas temperature around 28 ^{o}C favour pollen germination and ovule fertilization (Staudt 1982). Therefore, we hypothesise that higher temperature from flowering to veraison during the mild seasons of this experiment may have contributed to reduce cold damage during flowering, contributing to increase fruit setting and closing the yield gap.

Acknowledgements

We thank Gaston Sepulveda, Annette James, and Han Chow for vineyard and laboratory work, Wine Australia for funding project UA1602, and our project partners. Wine Australia invests in and manages research, development and extension on behalf of Australia's grapegrowers and winemakers and the Australian Government. The South Australian Research and Development Institute is a member of the Wine Innovation Cluster in Adelaide.

Captions to figures

Figure1. Frequency distribution of (a) minimum (blue) and maximum (red) temperature, (b) vapour pressure deficit, (c) solar radiation, (d) rainfall (black) and reference evapotranspiration (red), and (e) rain-to-reference evapotranspiration ratio during the periods from 29 August to budburst to budburst (pre-BB), from budburst to flowering (BB-F), from flowering to veraison (F-V), and from veraison to maturity (V-M). Frequency distribution of (f) the seasonal ratio between actual and reference evapotranspiration ($ETc \cdot ETo^{-1}$) and (g) carbon isotope composition in must, a trait related to vine water status.

Figure 2. (a) Frequency distribution of yield of Shiraz in the Barossa region. (b) Relation between yield and carbon isotope composition. (c) Relation between yield gap and carbon isotope composition. In (b, c) lines are reduced maximum axis regressions.

Figure 3. (a) Comparison of the actual relation between the ratio of crop evapotranspiration and yield and the model in eq. (2). The parameters for eq. (2) are a = 80 mm/t ha^{-1}, b = -0.3 (Rockström 2003). In the inset, the line is the least-squares regression. (b) Relation between the ratio of soil evaporation and crop evapotranspiration and yield; the line is the reduced maximum axis regression. ETc: crop evapotranspiration, Es: soil evaporation.

Figure 4. Relationship between vine yield and seasonal (a) crop evapotranspiration, ETc; (b) ETc corrected by vapour pressure deficit; (c) ETc corrected by reference evapotranspiration, ETo; (d) rainfall; (e) rainfall corrected by vapour pressure deficit; (f) rainfall corrected by ETo. Black lines are reduced maximum axis regressions fitted to a common data set (open black circles), with statistics summarised in Table 2. In (d), green symbols are additional data, and the green line is the 95th percentile boundary derived from all data: $y = -1.92 + 0.124\ x$.

Figure 5. Variation in the yield gap of Shiraz in the Barossa region with (a) vintage, (b) sub-region, (c) elevation, (d) row orientation, (e) trellising system, (f) pruning method, and (g) vine age. In (a,b, d, e, f), error bars are two standard errors of the mean, and p and s from ANOVA. Sub-regions are Southern Grounds, shown as SG in (b) and open black symbols in (c), Eastern Edge (EE, blue symbols), Western Ridge (WR, red symbols), Northern Grounds (NG, gray), Central Grounds (CG, cyan), and Eden Valley (EV, closed black symbols). In (c), the line is the least squares regression fitted to all sub-regions but Eden Valley. In(f), the line is the least squares regression fitted to age between 6 and 33 years (open symbols); solid symbols (not included in the regression) are the yield gap of reworked vines on 98-year old rootstock.

Figure 6. Relations between yield gap of Shiraz in the Barossa region and (a) bunch number, (b) bunch weight, (c) berries per bunch, (d) berry weight, (e) shoot number, and (f) pruning weight. Lines are reduced maximum axis regressions. Arrowheads show the trait value for yield gap = 0.

Figure 7. Correlation coefficient for the association between yield gap and meteorological variables from 29 August to budburst to budburst (pre-BB), from budburst to flowering (BB-F), from flowering to veraison (F-V), and from veraison to maturity (V-M).

Table S1: Detail of 24 Shiraz vineyards (sites) selected from the existing sub-regionalization of the Barossa Zone GI (www.barossawine.com/vineyards/barossa-grounds/). Aspect (as degree from north) and slope are from a digital elevation model calculated in Bramley and Ouzman (2020). Elevation obtained as described in Bramley and Ouzman (2020). Coordinates are defined according to the GDA94 system.

Site	Location	Vineyard age	Clone	Rootstook	Pruning method	Trellising system	Density (vines ha^{-1})	Row orientation	Elevation (m.a.s.l.)	Longitude (m)	Slope (%)	Aspect (°)
1	Northern Grounds_NG	16	1654	Own root	Spur	Bilateral cordon	1515	E-W	295	319708.40	1.7	125.7
2	Northern Grounds_NG	26	Unknown	Own root	Spur	Bilateral cordon	1010	N-S	282	316561.61	1.1	86.5
3	Northern Grounds_NG	12	R6WV28	Own root	Spur	Bilateral cordon	1852	E-W	292	316124.42	0.8	77.8
4	Northern Grounds_NG	23	1654	Own root	Spur	Bilateral cordon	1852	E-W	300	320307.03	1.9	108.3
5	Central Grounds_CG	13	1654	Own root	Cane	Guyot	1515	N-S	264	313845.37	2.9	163.9
6	Central Grounds_CG	17	1654	Own root	Spur	Bilateral cordon	1667	N-S	187	305168.20	8.4	84.2
7	Central Grounds_CG	20	1654	Unknown	Spur	Bilateral cordon	1443	E-W	286	311546.54	2.0	86.8
8	Central Grounds_CG	Unknown	Unknown	Unknown	Spur	Double bilateral cordon	1852	N-S	261	312556.58	2.8	138.9
9	Eastern Edge_EE	23	1654	Own root	Spur	Bilateral cordon	1515	N-S	259	312119.36	3.8	67.4
10	Eastern Edge_EE	7	BVOVS10	Paulsen	Spur	Bilateral cordon	1429	E-W	285	315393.98	4.4	71.2
11	Eastern Edge_EE	6	R6WV28	Ruggeri 140	Spur	Bilateral cordon	2058	E-W	326	319812.37	4.7	72.4
12	Eastern Edge_EE	31	1654	Own root	Spur	Bilateral cordon	2304	E-W	301	314973.78	13.9	20.8
13	Southern Grounds_SG	98	Unknown	Own root	Cane	Guyot	1351	E-W	229	311179.18	1.8	0.1
14	Southern Grounds_SG	23	1654	Own root	Spur	Bilateral cordon	1196	N-S	198	306618.47	1.0	17.5
15	Southern Grounds_SG	24	1654	Unknown	Spur	Double bilateral cordon	1852	N-S	250	308809.91	19.2	57.1
16	Southern Grounds_SG	33	1654	Own root	Spur	Bilateral cordon	1389	N-S	193	306989.39	2.7	69.0
17	Western Ridge_WR	18	1654	Own root	Spur	Bilateral cordon	1792	E-W	248	308984.62	5.6	163.8
18	Western Ridge_WR	20	1654	Own root	Spur	Bilateral cordon	1515	N-S	287	309275.81	4.3	98.9
19	Western Ridge_WR	17	1654	Own root	Spur	Bilateral cordon	1389	E-W	312	310252.57	4.5	139.9
20	Western Ridge_WR	22	1654	Own root	Spur	Bilateral cordon	1786	N-S	231	307930.94	8.3	123.1
21	Eden Valley_EV	27	BVRC30	Own root	Cane	Guyot	1667	NE-SW	435	326454.21	3.6	12.9
22	Eden Valley_EV	24	BVRC12	Own root	Spur	Bilateral cordon	1563	E-W	396	327278.26	5.9	70.5
23	Eden Valley_EV	Unknown	Unknown	Unknown	Spur	Bilateral cordon	1667	E-W	383	325233.53	3.2	89.7
24	Eden Valley_EV	23	1654	Own root	Spur	Bilateral cordon	1563	E-W	405	322585.64	5.9	129.6

Table S2. Range of crop evapotranspiration (ETc) and yield, and slopes and x-intercepts from regressions between yield and ETc in a sample of vineyards from the literature. Regression methods are reduced-maximum axis (RMA, Model II) and least squares (LS, Model I) for comparison. Calculated from data reported by Intrigliolo and Castel (2008) (Spain), Williams (2010) (US) and Du et al. (2008) (China).

Variety	Location	ETc range (mm)	Yield range (t ha^{-1})	RMA		LS	
				slope (t ha^{-1} mm^{-1})	x-int (mm)	slope (t ha^{-1} mm^{-1})	x-int (mm)
Tempranillo	Requena, Spain	225-482	2.3-18.3	0.061	175	0.044	124
Cab. sauvignon	California, US	307-432	8.6-19.2	0.068	170	0.042	46
Rizamat	Shiyang, China	157-305	2.7-17.3	0.123	136	0.102	118

Figure 1:

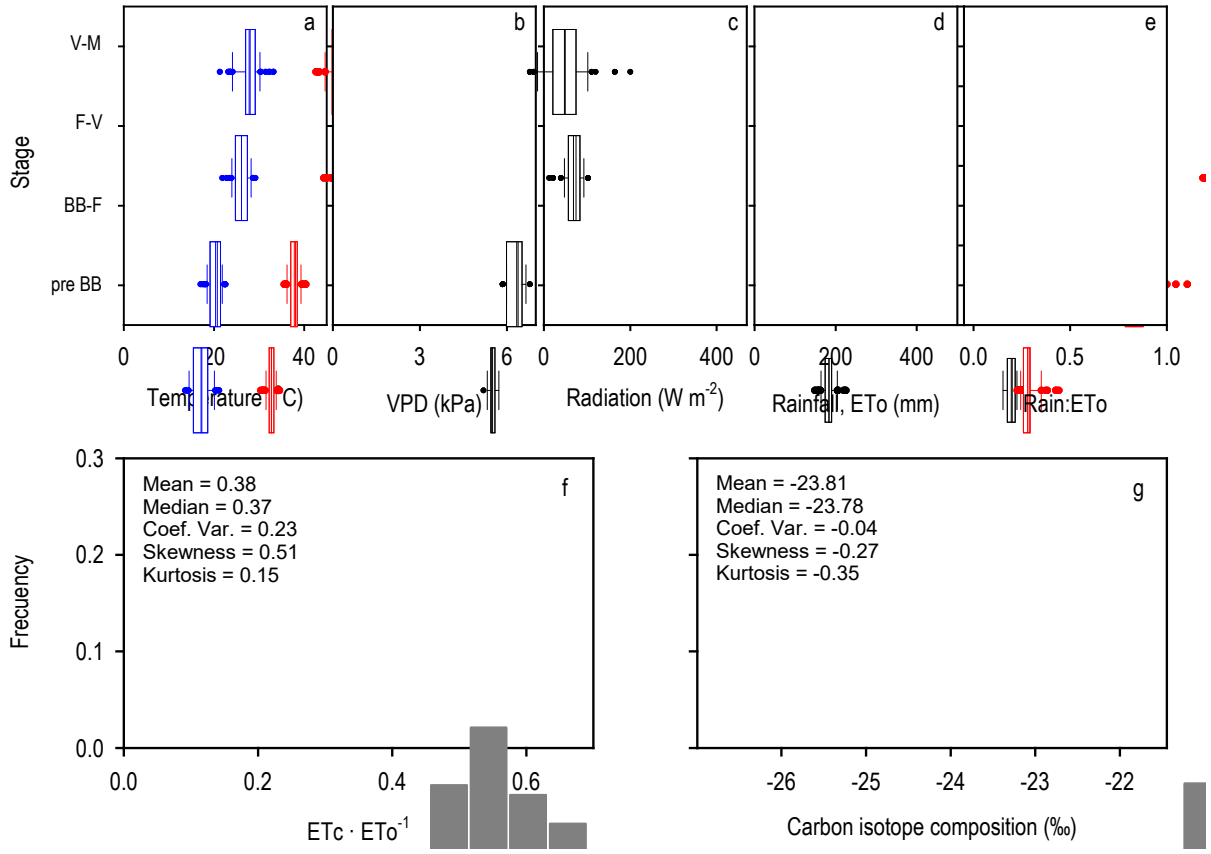

a
b
c
d
e
V-M
F-V
BB-F
pre BB
Stage
0
20
40
0
3
6
0
200
400
0
200
400
0.0
0.5
1.0
Temperature (°C)
VPD (kPa)
Radiation (W m-2)
Rainfall, ETo (mm)
Rain:ETo
0.3
0.2
0.1
0.0
Frecuency
Mean = 0.38
Median = 0.37
Coef. Var. = 0.23
Skewness = 0.51
Kurtosis = 0.15
f
0.0
0.2
0.4
0.6
ETc · ETo-1
Mean = -23.81
Median = -23.78
Coef. Var. = -0.04
Skewness = -0.27
Kurtosis = -0.35
g
-26
-25
-24
-23
-22
Carbon isotope composition (‰)

Figure2:

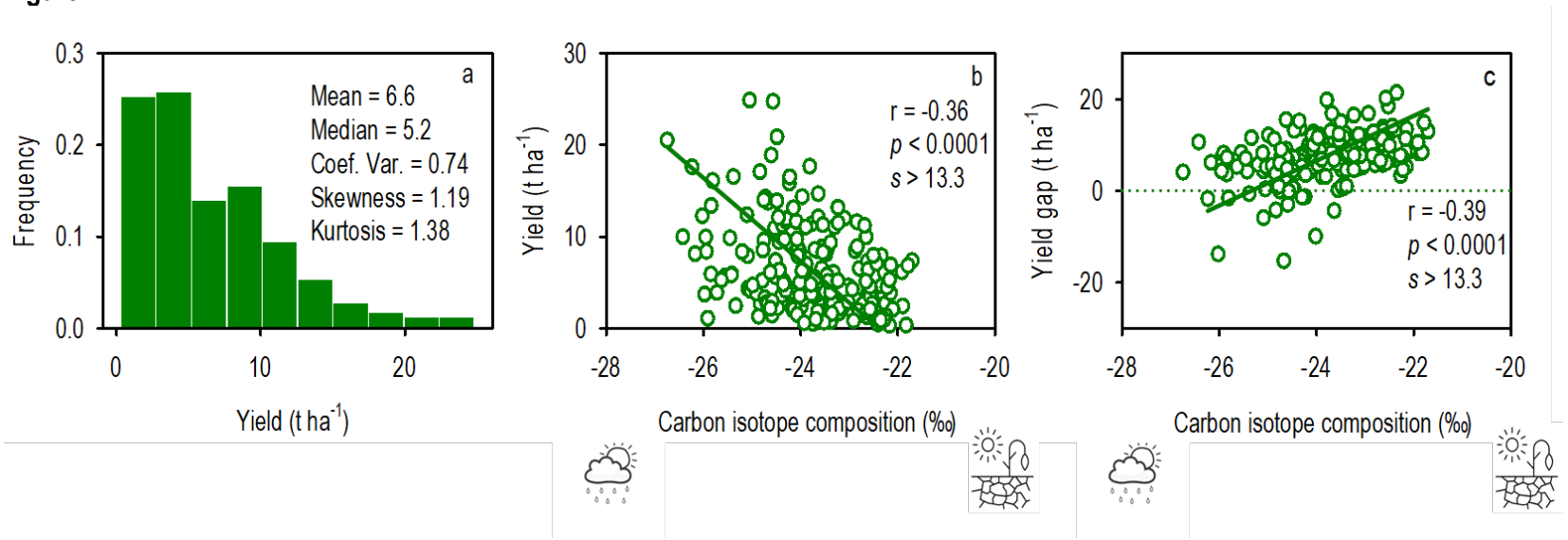

a
Mean = 6.6
Median = 5.2
Coef. Var. = 0.74
Skewness = 1.19
Kurtosis = 1.38
Frequency
Yield (t ha-1)
b
r = -0.36
p < 0.0001
s > 13.3
Yield (t ha-1)
Carbon isotope composition (‰)
c
r = -0.39
p < 0.0001
s > 13.3
Yield gap (t ha-1)
Carbon isotope composition (‰)

Figure 3:

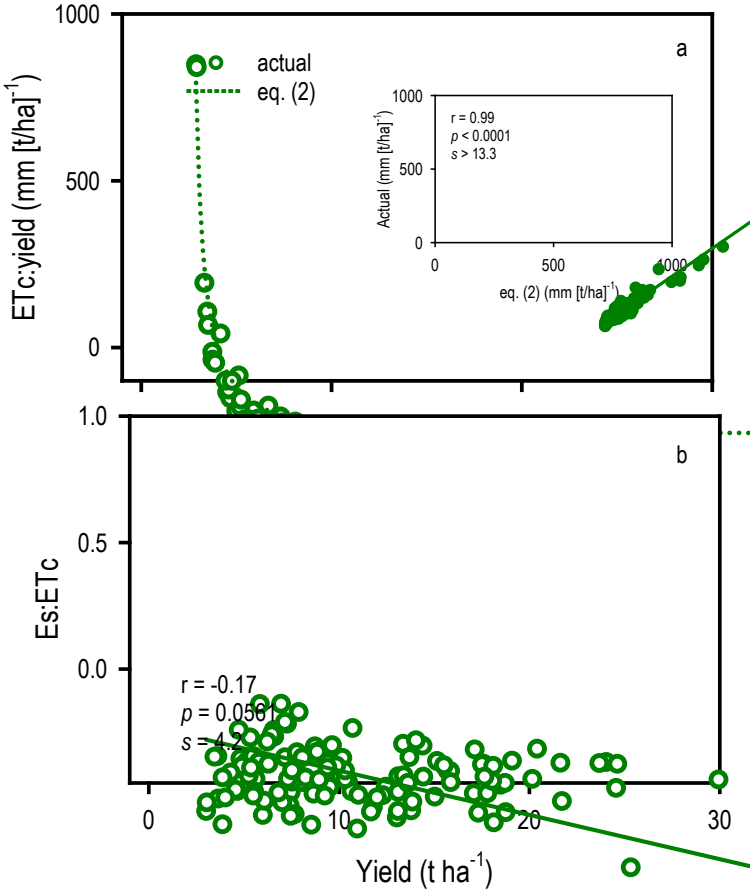

1000
500
0
ETc:yield (mm [t/ha]-1)
actual
eq. (2)
a
1000
500
0
Actual (mm [t/ha]-1)
r = 0.99
p < 0.0001
s > 13.3
0
500
1000
eq. (2) (mm [t/ha]-1)
1.0
0.5
0.0
Es:ETc
b
r = -0.17
p = 0.0561
s = 4.2
0
10
20
30
Yield (t ha-1)

Figure 4

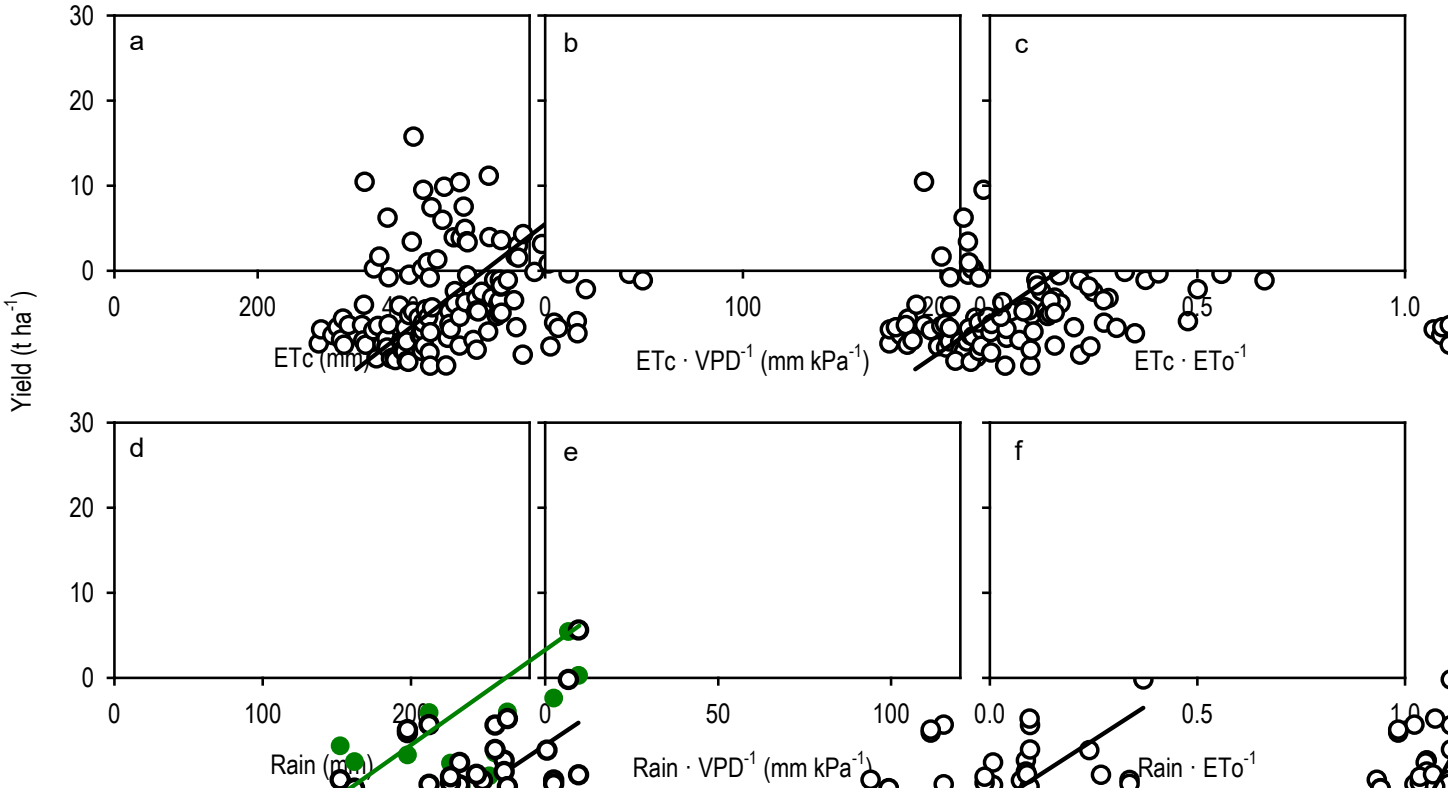

a
b
c
d
e
f
Yield (t ha-1)
ETc (mm)
ETc · VPD-1 (mm kPa-1)
ETc · ETo-1
Rain (mm)
Rain · VPD-1 (mm kPa-1)
Rain · ETo-1

Figure 5:

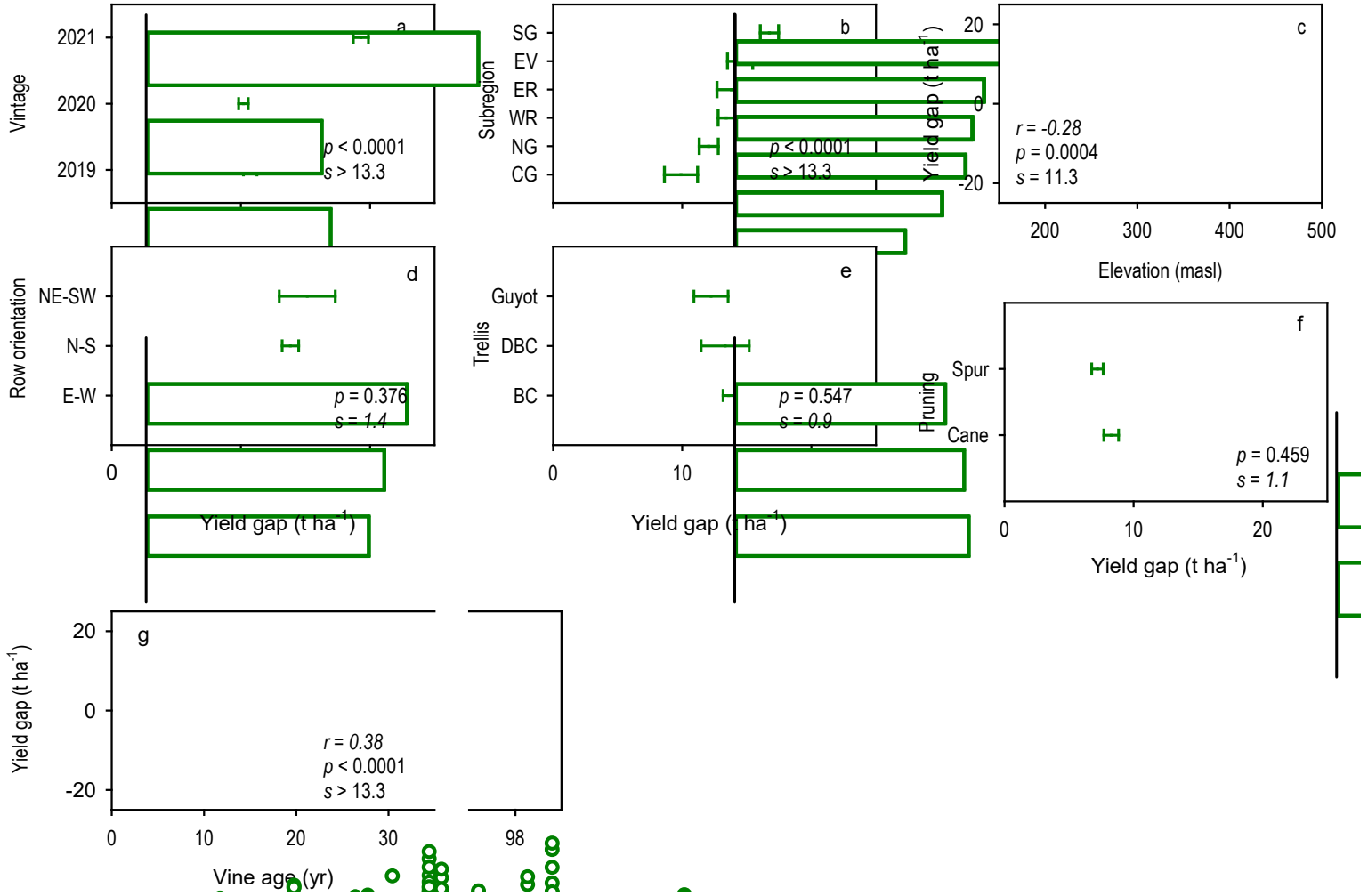

a
Vintage
2021
2020
2019
p < 0.0001
s > 13.3
b
Subregion
SG
EV
ER
WR
NG
CG
p < 0.0001
s > 13.3
c
Yield gap (t ha-1)
20
0
-20
r = -0.28
p = 0.0004
s = 11.3
200
300
400
500
Elevation (masl)
d
Row orientation
NE-SW
N-S
E-W
p = 0.376
s = 1.4
0
Yield gap (t ha-1)
e
Trellis
Guyot
DBC
BC
p = 0.547
s = 0.9
0
10
Yield gap (t ha-1)
f
Pruning
Spur
Cane
p = 0.459
s = 1.1
0
10
20
Yield gap (t ha-1)
g
Yield gap (t ha-1)
20
0
-20
r = 0.38
p < 0.0001
s > 13.3
0
10
20
30
98
Vine age (yr)

Figure 6:

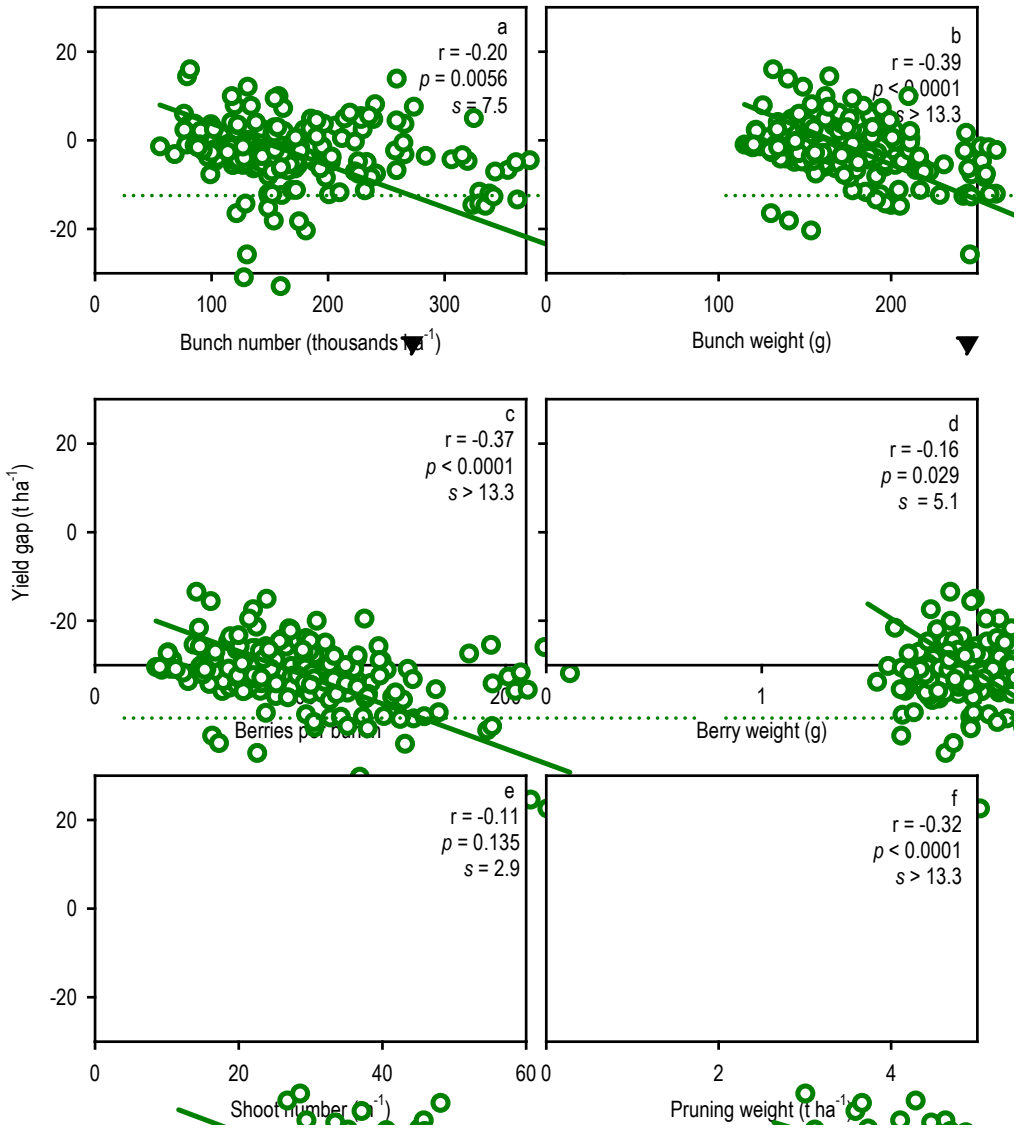
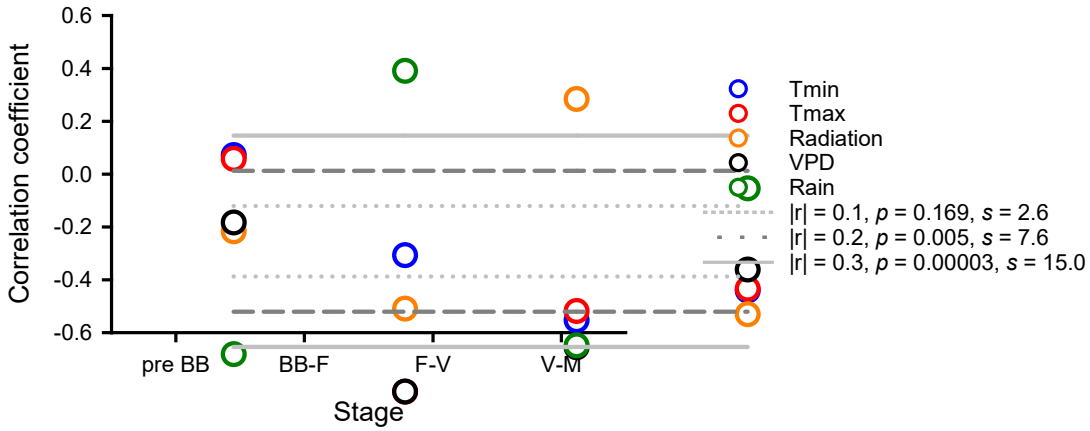

a
r = -0.20
p = 0.0056
s = 7.5
b
r = -0.39
p < 0.0001
s > 13.3
c
r = -0.37
p < 0.0001
s > 13.3
d
r = -0.16
p = 0.029
s = 5.1
e
r = -0.11
p = 0.135
s = 2.9
f
r = -0.32
p < 0.0001
s > 13.3
Yield gap (t ha-1)
Bunch number (thousands t ha-1)
Bunch weight (g)
Berries per bunch
Berry weight (g)
Shoot number (t ha-1)
Pruning weight (t ha-1)

Figure 7:


0.6
0.4
0.2
0.0
-0.2
-0.4
-0.6
Correlation coefficient
pre BB
BB-F
F-V
V-M
Stage
Tmin
Tmax
Radiation
VPD
Rain
|r| = 0.1, p = 0.169, s = 2.6
|r| = 0.2, p = 0.005, s = 7.6
|r| = 0.3, p = 0.00003, s = 15.0

References

Bonada, M., A.A. Catania, J.M. Gambetta, and P.R. Petrie (2021) Soil water availability during spring modulates canopy growth and impacts the chemical and sensory composition of Shiraz fruit and wine. Australian Journal of Grape and Wine Research 27, 491-507. doi: 10.1111/ajgw.12506.

Bonada, M., E.J. Edwards, M.G. McCarthy, G.C. Sepúlveda, and P.R. Petrie (2020) Impact of low rainfall during dormancy on vine productivity and development. Australian Journal of Grape and Wine Research 26, 325-342. doi: 10.1111/ajgw.12445.

Bradley, J.V. (1982) The insidious L-shaped distribution. Bulletin of the Psychonomic Society 20, 85-88.

Bramley, R.G.V. and J. Ouzman (2021) Underpinning terroir with data: on what grounds might subregionalisation of the Barossa Zone geographical indication be justified? Australian Journal of Grape and Wine Research. doi: 10.1111/ajgw.12513.

Brett, M.T. (2004) When is a correlation between non-independent variables "spurious"? Oikos 105, 647-656. doi: 10.1111/j.0030-1299.2004.12777.x.

Buesa, I., J.M. Mirás-Avalos, and D.S. Intrigliolo (2020) Row orientation effects on potted-vines performance and water-use efficiency. Agricultural and Forest Meteorology 294, 108148. doi: https://doi.org/10.1016/j.agrformet.2020.108148.

Cai, W. and T. Cowan (2013) Southeast Australia Autumn Rainfall Reduction: A Climate-Change-Induced Poleward Shift of Ocean–Atmosphere Circulation. Journal of Climate 26, 189-205. doi: 10.1175/jcli-d-12-00035.1.

Coipel, J., B. Rodriguez Lovelle, C. Sipp, and C. Van Leeuwen (2006) "Terroir" effect, as a result of enviromental stess, depends more on soil depth than on soil type (Vitis vinifera L. cv. Grenache Noir, Côtes du Rhône, France, 2000). OENO One 40, 177. doi: 10.20870/oeno-one.2006.40.4.867.

Condon, A.G., R.A. Richards, G.J. Rebetzke, and G.D. Farquhar (2002) Improving Intrinsic Water-Use Efficiency and Crop Yield. Crop Science 42, 122. doi: 10.2135/cropsci2002.0122.

di Castri, F. and H.A. Mooney, "Mediterranean type ecosystems", (Springer-Verlag, Heildeberg, 1973), pp. 405.

Dry, P., D.J. Maschmedt, C.J. Anderson, E. Riley, S.-J. Bell, and W.S. Goodchild (2005) The grapegrowing regions of Australia. In: Viticulture. Volume 1 - resources, Eds. P. Dry and B. Coombe (Winetitles: Adelaide) pp. 17-55.

Du, T., S. Kang, J. Zhang, F. Li, and B. Yan (2008) Water use efficiency and fruit quality of table grape under alternate partial root-zone drip irrigation. Agricultural Water Management 95, 659-668.

Dunn, G.M., S.R. Martin, and P.R. Petrie Managing yield variation in vineyards. Proceedings of the 12th Australian Industry Technical Conference, Melbourne 51-56.

Evans, R.G., S.E. Spayd, R.L. Wample, M.W. Kroeger, and M.O. Mahan (1993) Water-use of *Vitis vinifera* grapes in Washington. Agricultural Water Management 23, 109-124.

French, R.J. and J.E. Schultz (1984) Water use efficiency of wheat in a Mediterranean type environment. I. The relation between yield, water use and climate. Australian Journal of Agricultural Research 35, 743-764.

Friend, A., M. Trought, and G. Creasy (2009) The influence of seed weight on the development and growth of berries and live green ovaries in Vitis vinifera L. cvs. Pinot Noir and Cabernet Sauvignon. Australian Journal of Grape and Wine Research 15, 166-174. doi: 10.1111/j.1755-0238.2009.00050.x.

Fuller, P. and B. Walsh (1999) Barossa Vintage Classification 1947-1998. (Barossa Wine and Turism Association: Nuriootpa).

González-Fernández, E., A. Piña-Rey, M. Fernández-González, M.J. Aira, and F.J. Rodríguez-Rajo (2020) Prediction of Grapevine Yield Based on Reproductive Variables and the Influence of Meteorological Conditions. Agronomy 10, 714.

Henderson, B., M.R. Sosnowski, M.G. McCarthy, and E.S. Scott (2021) Incidence and severity of Eutypa dieback in grapevines are related to total surface area of pruning wounds. Australian Journal of Grape and Wine Research 27, 87-93. doi: 10.1111/ajgw.12465.

Iland, P., P. Dry, T. Proffit, and S. Tyerman (2011) The grapevine. From the science to the practice of growing vines for wine. (Patrick Iland Wine Promotions Adelaide).

Intrigliolo, D.S. and J.R. Castel (2008) Effects of irrigation on the performance of grapevine cv. Tempranillo in Requena, Spain. American Journal of Enology and Viticulture 59, 30-38.

Jackson, D. (2001) Pruning and Training: Monographs in Cool Climate Viticulture -1. (Daphne Brasell Associates Ltd.: New Zealand).

Jackson, J.E. and J.W. Palmer (1972) Interception of light by model hedgerow orchards in relation to latitude, time of year and hedgerow configuration and orientation. Journal of Applied Ecology 9, 341-&. doi: 10.2307/2402436.

Jiao, L.J., R.S. Ding, S.Z. Kang, T.S. Du, L. Tong, and S.E. Li (2018) A comparison of energy partitioning and evapotranspiration over closed maize and sparse grapevine canopies in northwest China. Agricultural Water Management 203, 251-260. doi: 10.1016/j.agwat.2018.03.019.

Jones, H. (1992) Energy balance and evaporation. In: Plants and microclimate: a quantitative approach to environmental plant physiology, Ed. C.U. Press pp. 106-130.

Kliewer, W.M. (1977) Effect of high temperatures during the bloom-set period on fruit-set, ovule fertility, and berry growth of several grape cultivars. American Journal of Enology and Viticulture 28, 215-222.

Koussa, T., L.A. Rifai, B. Dubos, and M. Broquedis (2006) Variations of abscisic acid contents in various organs of grapevine infected by the eutypa dieback fungus, Eutypa Lata. OENO One 40, 187. doi: 10.20870/oeno-one.2006.40.4.863.

Ludbrook, J. (2012) A primer for biomedical scientists on how to execute Model II linear regression analysis. Clinical and Experimental Pharmacology and Physiology 39, 329-335. doi: 10.1111/j.1440-1681.2011.05643.x.

Moran, M., P. Petrie, and V. Sadras (2019) Effects of Late Pruning and Elevated Temperature on Phenology, Yield Components, and Berry Traits in Shiraz. American Journal of Enology and Viticulture 70, 9-18. doi: 10.5344/ajev.2018.18031.

Moran, M.A., S.E. Bastian, P.R. Petrie, and V.O. Sadras (2018) Late pruning impacts on chemical and sensory attributes of Shiraz wine. Australian Journal of Grape and Wine Research 24, 469-477. doi: 10.1111/ajgw.12350.

Moran, M.A., S.E. Bastian, P.R. Petrie, and V.O. Sadras (2021) Impact of late pruning and elevated ambient temperature on Shiraz wine chemical and sensory attributes. Australian Journal of Grape and Wine Research 27, 42-51. doi: 10.1111/ajgw.12470.

Morgani, M.B., J.E.P. Peña, M. Fanzone, and J.A. Prieto (2022) Pruning after budburst delays phenology and affects yield components, crop coefficient and total evapotranspiration in Vitis vinífera L. cv. 'Malbec' in Mendoza, Argentina. Scientia Horticulturae 296, 110886. doi: https://doi.org/10.1016/j.scienta.2022.110886.

Munkvold, G.P., J.A. Duthie, and J.J. Marois (1994) REDUCTIONS IN YIELD AND VEGETATIVE GROWTH OF GRAPEVINES DUE TO EUTYPA DIEBACK. Phytopathology 84, 186-192. doi: 10.1094/Phyto-84-186.

Niklas, K.J. (1994) Plant allometry: the scaling of form and process. (University of Chicago Press: Chicago).

O'Brien, P., R. De Bei, M. Sosnowski, and C. Collins (2021) A Review of Factors to Consider for Permanent Cordon Establishment and Maintenance. Agronomy-Basel 11. doi: 10.3390/agronomy11091811.

Ollat, N., P. Diakou-Verdin, J.P. Carde, F. Barrieu, J.P. Gaudillere, and A. Moing (2002) Grape berry development: A review. Journal International Des Sciences De La Vigne Et Du Vin 36, 109-131.

Palmer, J.W. (1989) The effects of row orientation, tree height, time of year and latitude on light interception and distribution in model apple hedgerow canopies. Journal of Horticultural Science & Biotechnology 64, 137-145. doi: 10.1080/14620316.1989.11515937.

Petrie, P.R., S.J. Brooke, M.A. Moran, and V.O. Sadras (2017) Pruning after budburst to delay and spread grape maturity. Australian Journal of Grape and Wine Research 23, 378-389. doi: 10.1111/ajgw.12303.

Petrie, P.R. and P.R. Clingeleffer (2005) Effects of temperature and light (before and after budburst) on inflorescence morphology and flower number of Chardonnay grapevines (*Vitis vinifera* L.). Australian Journal of Grape and Wine Research 11, 59-65.

Pouzoulet, J., A.L. Pivovaroff, L.S. Santiago, and P.E. Rolshausen (2014) Can vessel dimension explain tolerance toward fungal vascular wilt diseases in woody plants? Lessons from Dutch elm disease and esca disease in grapevine. Frontiers in Plant Science 5. doi: 10.3389/fpls.2014.00253.

Ristic, R. and P.G. Iland (2005) Relationships between seed and berry development of Vitis Vinifera L. cv Shiraz: Developmental changes in seed morphology and phenolic composition. Australian Journal of Grape and Wine Research 11, 43-58. doi: doi:10.1111/j.1755-0238.2005.tb00278.x.

Robinson, S. and N. Sandercock (2014) An analysis of climate, soil and topographic information to aid the understanding of Barossa terroir – a Barossa Grounds project (PIRSA Spatial Information Services, SA, Australia).

Rockström, J. (2003) Water for food and nature in drought–prone tropics: vapour shift in rain–fed agriculture. Philosophical Transactions of the Royal Society of London. Series B: Biological Sciences 358, 1997-2009. doi: 10.1098/rstb.2003.1400.

Sadras, V.O. (2020) On water-use efficiency, boundary functions and yield gaps: French and Schultz insight and legacy. Crop Science. doi: 10.1002/csc2.20188.

Sadras, V.O., K.G. Cassman, P. Grassini, A.J. Hall, W.G.M. Bastiaanssen, A.G. Laborte, A.E. Milne, G. Sileshi, and P. Steduto (2015) Yield gap analysis of rainfed and irrigated crops: Methods and Case Studies. (FAO: Rome).

Sadras, V.O. and H.R. Schultz (2012) Grapevine. In: Crop yield response to water. FAO Irrigation and Drainage Paper 66, Ed. P. Steduto (FAO: Roma) pp. 324-349.

Sosnowski, M.R., M.R. Ayres, R. Baaijens, S. Savocchia, T.J. Wicks, and E.S. Scott Innovations in the management of grapevine trunk diseases Proceedings of the 16th Australian Wine Industry Technical Conference Adelaide 91-95.

Sosnowski, M.R., M.R. Ayres, and E.S. Scott (2021) The Influence of Water Deficit Stress on the Grapevine Trunk Disease Pathogens Eutypa lata and Diplodia seriata. Plant Disease 105, 2217-2221. doi: 10.1094/pdis-07-20-1538-re.

Sosnowski, M.R., M.L. Creaser, T.J. Wicks, R. Lardner, and E.S. Scott (2008) Protection of grapevine pruning wounds from infection by Eutypa lata. Australian Journal of Grape and Wine Research 14, 134-142. doi: 10.1111/j.1755-0238.2008.00015.x.

Staudt, G. (1982) Pollen germination and pollen-tube growth-invivo with vitis and the dependence on temperature. Vitis 21, 205-216.

Steduto, P., T.C. Hsiao, E. Fereres, and D. Raes (2012) Crop yield response to water. (FAO: Rome).

van Ittersum, M.K., K.G. Cassman, P. Grassini, J. Wolf, P. Tittonell, and Z. Hochman (2013) Yield gap analysis with local to global relevance—A review. Field Crops Research 143, 4-17. doi: http://dx.doi.org/10.1016/j.fcr.2012.09.009.

Vasconcelos, M.C., M. Greven, C.S. Winefield, M.C.T. Trought, and V. Raw (2009) The Flowering Process of Vitis vinifera: A Review. American Journal of Enology and Viticulture 60, 411-434.

Water, D.o.E.a. (2022) Draft guide to the Barossa water security strategy. Department of Environment and Water, SA Government.

Webb, L., J. Whiting, A. Watt, T. Hill, F. Wigg, G. Dunn, S. Needs, and E.W.R. Barlow (2010) Managing Grapevines through Severe Heat: A Survey of Growers after the 2009 Summer Heatwave in South-eastern Australia. Journal of Wine Research 21, 147-165. doi: 10.1080/09571264.2010.530106.

Williams, L.E. (2010) Interaction of rootstock and applied water amounts at various fractions of estimated evapotranspiration (ETc) on productivity of Cabernet Sauvignon. Australian Journal of Grape and Wine Research 16, 434-444. doi: 10.1111/j.1755-0238.2010.00104.x.

Yang, C., C. Menz, H. Fraga, S. Costafreda-Aumedes, L. Leolini, M.C. Ramos, D. Molitor, C. van Leeuwen, and J.A. Santos (2022) Assessing the grapevine crop water stress indicator over the flowering-veraison phase and the potential yield lose rate in important European wine regions. Agricultural Water Management 261, 107349. doi: https://doi.org/10.1016/j.agwat.2021.107349.

Yunusa, I.A.M., R.R. Walker, and D.H. Blackmore (1997) Characterisation of water use by Sultana grapevines (Vitis vinifera L.) on their own roots or on Ramsey rootstock drip-irrigated with water of different salinities. Irrigation Science 17, 77-86.

Yunusa, I.A.M., R.R. Walker, and J.R. Guy (1997) Partitioning of seasonal evapotranspiration from a commercial furrow-irrigated Sultana vineyard. Irrigation Science 18, 45-54.

Yunusa, I.A.M., R.R. Walker, and P. Lu (2004) Evapotranspiration components from energy balance, sapflow and microlysimetry techniques for an irrigated vineyard in inland Australia. Agricultural and Forest Meteorology 127, 93-107. doi: 10.1016/j.agrformet.2004.07.001.

Zhang, B., S. Kang, F. Li, L. Tong, and T. Du (2010) Variation in vineyard evapotranspiration in an arid region of northwest China. Agricultural Water Management 97, 1898-1904. doi: https://doi.org/10.1016/j.agwat.2010.06.010.

5.3 The relationship between terroir and the phenology of Barossa Shiraz

THE RELATIONSHIP BETWEEN TERROIR AND THE PHENOLOGY OF BAROSSA SHIRAZ

MARCOS BONADA[1,2], VICTOR SADRAS[1,3], DANE THOMAS[1], CASSANDRA COLLINS[3,4], LEIGH SCHMIDTKE[5], VINOD PHOGAT[1,3] AND PAUL PETRIE[1,2,3,6]

[1]South Australia Research and Development Institute, Waite Campus, Adelaide, Australia

[2]College of Science and Engineering, Flinders University, Adelaide, Australia

[3]The University of Adelaide, Waite Research Institute, School of Agriculture, Food and Wine, Adelaide, Australia

[4]ARC Industrial Transformation Training Centre for Innovative Wine Production, Adelaide, Australia

[5]Gulbali Institute, Charles Sturt University, Wagga Wagga, NSW, Australia

[6]Faculty of Engineering, University of New South Wales, Sydney, Australia

***Keywords**: berry, development, flowering, maturity, sugar, yield, vintage*

Abstract

Background and Aims: Vine phenology results from the interaction between the genotype, environment and management, with implications for fruit, and wine composition. The impact of weather, site and management practices, underlying elements of terroir, impacting the timing of key phenological stages were explored across the Barossa Zone (GI).

Methods and Results: Vine phenology was assessed in three zones of 24 vineyards over three vintages using the E-L scale before veraison, and total soluble sugars (TSS) in berries during ripening. We explored the associations between weather, plant traits and viticultural variables, and development in four periods: pre-budburst, budburst-flowering, flowering-veraison and veraison-maturity. The spatial structure of the timing of phenological events suggested three main groups of vineyards. This structure followed gradients in topography and soils across the landscape, and were maintained despite the effect of the season (vintage). On average, differences between early and late groups of vineyards were 13 days at budburst, 20 days at flowering and 24 days at TSS = 24 ^{o}Brix. Phenology responded mainly to temperature until flowering, and to temperature and canopy size from flowering to maturity. The strength of the relationship between the duration of the period and temperature ranked pre-budburst (r^2 = 0.94) > budburst-flowering (r^2 = 0.40) > veraison-maturity (r^2 = 0.17). Duration of pre-budburst and budburst-flowering periods was shortened at 6 d $^{o}C^{-1}$, compared to 2 d $^{o}C^{-1}$ for veraison-maturity. The duration from veraison to maturity increased with yield (r^2 = 0.29, P_a < 0.0001).

Conclusions

The spatial variation in development was maintained despite vintage effects and management practices. Variation in temperature due to topography and elevation were the major drivers of vine phenological development until flowering. During ripening, development was driven by temperature and carbon capture and partitioning.

Significance of the Study

This is the first attempt to show spatial variability on phenology across the Barossa Valley GI. The observed switch on drivers on phenology during development from temperature-driven processed before flowering to resource-dominated processes during ripening have implications for modelling and vineyard management.

Introduction

Terroir refers to the multiple physical and biological elements that interact with the management practices in the vineyard, and in the winery providing distinctive characteristics to the wine produced from the site (Castellucci 2010). As a concept, terroir has multiple definitions that depend on the level of observation (Spielmann and Gélinas-Chebat 2012). Conceptual models desegregate terroir in geography, topography, soil, climate, and plant material (van Leeuwen, et al. 2004). These dimensions can be seen in a hierarchical context, where a given level of study (N) gives explanation to a higher level (N+1), or adds context to a lower level (N-1) (Passioura 1979). Understanding the functioning of the system at a particular layer may be fragmented and lacking context unless it can be related to adjacent levels. For example, the relationship between temperature and anthocyanin concentrations (N-1) (Mori, et al. 2007) may provide an explanation to the spatial variation in wine composition (Barnuud, et al. 2013) in zoning of terroir (N). This relationship between temperature and fruit composition, however, lacks significance if we do not explore how other elements of terroir such as vineyard and winemaking practices interact with weather elements to define a "landscape" of wine styles (N+1).

Against this multi-level framework, we focus on vine phenological development in the context of terroir. The fruit phenotype results from the interaction between the genotype, environment and management, with implications for wine attributes (Pearson, et al. 2021,Sadras, et al. 2015). Growing conditions after fruit set that influence berry phenotype (N) are largely defined by the timing of the phenostage (N-1). This accounts, for example, for management practices to displace ripening to cooler conditions to maintain fruit composition in warm environments and seasons (Böttcher, et al. 2021,Moran, et al. 2018,Moran, et al. 2019,Parker, et al. 2014). To understand how fruit composition varies with space and vintage, we need first to explore the elements of terroir that affect vine phenological development and define the timing between key phenological stages and growing conditions.

Plant phenology is critical to plant adaptation determining the timing of vegetative and reproductive development and acquisition of resources (Forrest and Miller-Rushing 2010,Nord and Lynch 2009). Environment-driven processes dominate the initial stages of development, and phenology is a sound indicator of climate signals. Soil moisture at the end of winter (Bonada, et al. 2020) and ambient and soil temperature during spring (Clarke, et al. 2015,Moncur, et al. 1989) are the first environmental drivers triggering plant activation and the cascade of biological processes after chilling requirements for budburst have been met (Dokoozlian 1999). From fruit set, however, development transits to resource-driven and phenological development during berry growth and ripening results from the combination of both climate and available resources (Sadras, et al. 2008). Conditions that modulate phenology vary in time and space. Beyond the seasonal variation in temperature that advance or delay development year-to-year, time series studies have shown that warming associated with climate change has advanced plant development during the growing season (Cameron, et al. 2022). Spatially, at a regional level (meso-climate), variation in latitude, continentality, aspect and altitude drive variation in temperature with implications for vine phenology (de Rességuier, et al. 2020,Falcao, et al. 2010,Ramos, et al. 2015). At a vineyard level (micro-climate), variations in phenology are mainly given by the interaction between aspects of the site (soil x climate x cultivar/rootstock) and management practices (Verdugo-Vásquez, et al. 2022). For example, dry soil in spring delays budburst (Bonada, et al. 2020), and late winter pruning (Moran, et al. 2019) and auxin application (Böttcher, et al. 2011) shift vine development later in the season. Similarly, other practices that affect the source:sink ratio such as double-pruning (Palliotti, et al. 2017) and shoot, leave or bunch thinning may impact on the length of

the ripening period (Parker, et al. 2014,Poni, et al. 2013). These aspects, which underpin the concept of terroir, define the daily and seasonal dynamics of fruit sunlight exposure and temperature, leaving a unique "fingerprint" in the composition of the fruit and the wine.

With a focus on Shiraz, the flagship cultivar grown in the Barossa Zone, this paper explores phenological variation in a context of terroir. We assess the impact of weather, site and management practices on the timing and duration of key phenostages, and the inter-annual variation on vine development across sites of the Barossa Zone Geographical Indication (GI).

Materials and Methods

Study area and experimental design

The study was conducted in the Barossa Zone GI that comprises 13,989 ha under vines, and includes the Barossa Valley and Eden Valley regions, and the High Eden sub-region (Wine Australia). The Barossa Valley runs from the N-E to the S-W with a minimum elevation of 112 meters above sea level (m.a.s.l.), more than half of the vineyards under 280 m.a.s.l, and is bounded by small hills and gentle slopes in the west and steeper hills in the east, peaking at 597 m.a.s.l. (Wine Australia). The Eden Valley runs parallel to the Barossa Valley, and elevation ranges from 217 to 630 m.a.s.l., with almost all the vineyards over the 280 m.a.s.l. Soil, climate and vineyard practices of these regions have been described elsewhere (Dry, et al. 2004).

Twenty-four sites were established during the 2017/18 and 2018/19 seasons in Shiraz vineyards (Figure 1 and Table 1), four from each of the six sub-regions previously identified by the Barossa Grape and Wine Association (www.barossawine.com/vineyards/barossa-grounds/): Northern Grounds (NG), Central Grounds (CG), Eastern Edge (EE), Southern Grounds (SG), Western Ridge (WR) and Eden Valley (EV). Average age of the vineyards at the end of the experiment was 24 years, with one vineyard older than 33 years and two yonger than 10 years. Three quarters of the vineyards were grown on their own roots and the most common clone (62%) was 1654. The most widely used training system was the bilateral cordon (87%) in one (19 sites) or two levels (2 sites). The remaining 3 sites were trained on bilateral Guyot. Vineyards were planted mostly in E-W orientation (13 sites) or N-S orientation (10 sites), with only one vineyard planted in NE-SW orientation. Elevation across experimental sites ranged from 187 m.a.s.l (site 7) to 435 m.a.s.l (site 21). Median elevation was 286 m.a.s.l, with 75% of the sites below 303 m.a.s.l. All the Eden Valley sites (sites 21 to 24) were over 300 m.a.s.l, together with some sites from Eastern Edge (site 11) and Western Ridge (site 19). Most of the Northern Grounds sites (sites 1, 3 and 4) ranged from 292 to 300 m.a.s.l. All the sites in Central Grounds (5 to 8) and Southern Grounds (13 to 16) were under 286 m.a.s.l, at the floor of the valley. On the slopier Western Ridge and Eastern Edge, there was a high variation in elevation.

Three sampling zones were identified at each site to capture the variation within the block. Zones were selected based on *k*-means cluster analysis; two data layers were used; an electromagnetic (EM38) soil survey (completed on every row) and vine canopy size maps (supplementary figure 1). Remotely sensed Plant Cell Density (PCD) imagery at 40 cm resolution at veraison were acquired from a commercial provider (SpecTerra, Churchlands, WA). The PCD is the ratio of infrared:reflectance and closely relates to vine canopy size (Dobrowski, et al. 2003). All methods of spatial analysis used for this work have been described by Bramley et al. (2011) and references therein.

Table 1: Detail of 24 Shiraz vineyards (sites) selected from the existing sub-regionalization of the Barossa Zone GI (www.barossawine.com/vineyards/barossa-grounds/). Aspect (as degree from north)

and slope are from a digital elevation model calculated in Bramley and Ouzman (2020). Elevation obtained as described in Bramley and Ouzman (2020). Coordinates are defined according to the GDA94 system.

Site	Location	Vineyard age	Clone	Rootstock	Pruning method	Trellising system	Density (vines ha^{-1})	Row orientation	Elevation (m.a.s.l.)	Longitude (m)	Slope (%)	Aspect (°)
1	Northern Grounds_NG	16	1654	Own root	Spur	Bilateral cordon	1515	E-W	295	319708.40	1.7	125.7
2	Northern Grounds_NG	26	Unknown	Own root	Spur	Bilateral cordon	1010	N-S	282	316561.61	1.1	86.5
3	Northern Grounds_NG	12	R6WV28	Own root	Spur	Bilateral cordon	1852	E-W	292	316124.42	0.8	77.8
4	Northern Grounds_NG	23	1654	Own root	Spur	Bilateral cordon	1852	E-W	300	320307.03	1.9	108.3
5	Central Grounds_CG	13	1654	Own root	Cane	Guyot	1515	N-S	264	313845.37	2.9	163.9
6	Central Grounds_CG	17	1654	Own root	Spur	Bilateral cordon	1667	N-S	187	305168.20	8.4	84.2
7	Central Grounds_CG	20	1654	Unknown	Spur	Bilateral cordon	1443	E-W	286	311546.54	2.0	86.8
8	Central Grounds_CG	Unknown	Unknown	Unknown	Spur	Double bilateral cordon	1852	N-S	261	312556.58	2.8	138.9
9	Eastern Edge_EE	23	1654	Own root	Spur	Bilateral cordon	1515	N-S	259	312119.36	3.8	67.4
10	Eastern Edge_EE	7	BVOVS10	Paulsen	Spur	Bilateral cordon	1429	E-W	285	315393.98	4.4	71.2
11	Eastern Edge_EE	6	R6WV28	Ruggeri 140	Spur	Bilateral cordon	2058	E-W	326	319812.37	4.7	72.4
12	Eastern Edge_EE	31	1654	Own root	Spur	Bilateral cordon	2304	E-W	301	314973.78	13.9	20.8
13	Southern Grounds_SG	98	Unknown	Own root	Cane	Guyot	1351	E-W	229	311179.18	1.8	0.1
14	Southern Grounds_SG	23	1654	Own root	Spur	Bilateral cordon	1196	N-S	198	306618.47	1.0	17.5
15	Southern Grounds_SG	24	1654	Unknown	Spur	Double bilateral cordon	1852	N-S	250	308809.91	19.2	57.1
16	Southern Grounds_SG	33	1654	Own root	Spur	Bilateral cordon	1389	N-S	193	306989.39	2.7	69.0
17	Western Ridge_WR	18	1654	Own root	Spur	Bilateral cordon	1792	E-W	248	308984.62	5.6	163.8
18	Western Ridge_WR	20	1654	Own root	Spur	Bilateral cordon	1515	N-S	287	309275.81	4.3	98.9
19	Western Ridge_WR	17	1654	Own root	Spur	Bilateral cordon	1389	E-W	312	310252.57	4.5	139.9
20	Western Ridge_WR	22	1654	Own root	Spur	Bilateral cordon	1786	N-S	231	307930.94	8.3	123.1
21	Eden Valley_EV	27	BVRC30	Own root	Cane	Guyot	1667	NE-SW	435	326454.21	3.6	12.9
22	Eden Valley_EV	24	BVRC12	Own root	Spur	Bilateral cordon	1563	E-W	396	327278.26	5.9	70.5
23	Eden Valley_EV	Unknown	Unknown	Unknown	Spur	Bilateral cordon	1667	E-W	383	325233.53	3.2	89.7
24	Eden Valley_EV	23	1654	Own root	Spur	Bilateral cordon	1563	E-W	405	322585.64	5.9	129.6

Weather data and soil moisture

A network of 24 weather stations (MEA Junior WS, Magill, South Australia), one at each site, was installed at the beginning of the experiment. Weather stations logged temperature, relative humidity (RH), wind speed and direction, solar radiation, and rainfall at 15-minutes intervals. The weather station calculated daily reference evapotranspiration (ET_o) using the method of Penman–Monteith (Allen, et al. 1998).

Soil moisture was continually monitored at each site sub-zone during the experiment at four depths using capacitance probes (EnviroSCAN system, Sentek, Magill, South Australia). For consistency, the sensors were installed at the same depths across the three sampling zones at each site. The PVC access tubes were installed directly below the irrigation lateral and between drippers. Data were logged every 15 minutes and retrieved from the logger at least monthly for processing using the IrriMax10 software (Sentek). Processing consisted of the calibration of the volumetric water content by texture using response curves provided by the manufacturer and re-analysis of the data. Textural analyses were conducted at each horizon to match the corresponding calibration curve with the texture at the depth of the capacitance probe. The soil horizons were determined visually from intact 0.9 m cores collected approximately one meter apart from each capacitance probe access tube using a Geoprobe Macro-Core® soil sampling system (Earthtech Drilling Products Pty. Ltd., Victoria, Australia). Plant available water content (PAWC) for the soil profile was estimated for each horizon at the two most contrasting sampling zones (A and C) of the 24 sites as determined from the PCD analysis (see above). Particle size analysis was completed using an existing MIR model (APAL Agricultural Laboratoty, Hindmarsh, SA) and including the analysis of 23 samples (10%) by dispersion to confirm the model validity. Existing information of soil crop lower limit (CLL) and drained upper limit (DUL) for the most typical Barossa soils (Dr Mike McCarthy, South Australian Research and Development Institute, pers.

comm., 2018). Daily plant available water (PAW) was estimated as the difference between the CLL and the volumetric soil water content from the soil as measured by the capacitance probes.

Phenological development

Phenological development was assessed on the same vines each season. For this purpose, at each of the sampling zones, a ~ 0.03 ha section of the vineyard was marked the first year. This section included approximately 48 vines distributed across four rows (12 vines per row, 3 vines per panel). For consistency, one representative vine of the section was visually identified and marked at the time of the first visual assessment each year and used for the successive phenological observations. Vine development was assessed visually using the E-L scale (Coombe 1995) from budburst to veraison, and as total soluble sugars (TSS) in berries from veraison to commercial maturity (E-L38), defined as 24 ^{o}Brix. Visual assessments were conducted weekly from budburst (E-L4) to berry pea size (E-L31), and during the period of veraison from incipient to total colouring of the bunches (E-L35). Fortnightly assessments were conducted between berry pea size (E-L31) and the beginning of berry colouring. The date of key phenological stages (budburst, E-L4; shoots 10 cm, E-L12; flowering, E-L23; veraison, E-L35) was estimated by interpolation of weekly observations when necessary and expressed as days after day one of the vintage, from July 1st. For missing observations of budburst, i.e., when the phenological stage had occurred prior to the time of the first vineyard visit, timing of E-L4 was modelled using local weather data and a model based on GDD, base temperature of 10 ^{o}C. This model using n = 126 observations, had a Pearson correlation coefficient of 0.68 ($P < 0.01$) and a RMSE of 4 days. TSS was measured weekly from veraison in a sample of at least eight bunches within each zone. In the laboratory, berries from each bunch were manually destemmed and mixed to create a homogeneous sample. Sub-samples of 100 berries were manually crushed for determination TSS with a digital bench refractometer (ATAGO PR-101, Tokyo, Japan). Timing of 24 ^{o}Brix was calculated from linear interpolations from the samples of TSS immediately less than and greater than 24 °Brix.

Yield, pruning mass and vine water stress

We sampled three one-meter sections of cordon to measure yield, pruning mass and yield:pruning mass per meter of canopy. Water stress during the season was quantified with carbon isotope composition ($\delta^{13}C$) analysis conducted on juice from berry samples collected at the time of harvest, and processed and analysed as described in Bonada et al. (unpublished).

Statistical analysis

We explored the associations between timing of each phenostage and the duration of the interval between stages, and weather, plant traits and viticultural variables. Weather elements included maximum (T_{max}), minimum (T_{min}) and mean temperature (T_{mean}), relative humidity (RH), solar radiation, vapour pressure deficit (VPD), rainfall and ET_o. Means for each period were calculated for each variable, except for rainfall and ET_o that were aggregated and expressed as rain:ET_o. Plant traits and viticultural variables include vineyard age, yield, pruning mass, yield:pruning mass, $\delta^{13}C$ and PAW.

Agglomerative hierarchical clustering (AHC, Ward's method) was conducted using XLSTAT (version 2020.3.1, Addinsoft, New York, NY, USA) on the loading scores for each site and vintage on PC1 and 2 from the principal components analysis (PCA). For the PCA, timing and the duration between key phenostages were used as explanatory variables and the sites as the observations. Loading scores were rotated on the second principal component during vintage 2021 to coincide with the classification

of factors in vintages 2019 and 2021. Partial least-squares regression (PLS-2) was completed with the timing of key phenostages (E-L4, 12, 23, 35 and 38) and the duration between phenostages [day 60 of the vintage (from August 29th) to budburst, pre-BB; budburst to flowering, BB-F; flowering to veraison, F-V; and veraison to maturity, V-M] as x-data and growing conditions resulting from the combination of weather, plant traits and viticultural variables as y-data, using XLSTAT. Before the PLS regression analysis, each dataset was divided into a calibration block composed of 70% of the data (51 observations) and a validation block made of 30% of the data (21 observations). Predictive models were cross- validated using 5 equal subsets of random samples removed from the calibration sample block for each iteration. The number of latent variables was determined based on the balance between "fit" (Q^2) and "predictability" (R^2Y) of the model during the cross-validation (Eriksson 2001).

Results

Variation in the timing of phenological stages across sites and vintages

Figure 2 and Table S1 show the variation of phenological stages across 24 sites and three vintages. Median day of budburst (E-L4) was 75, with 80% of the sites reaching this stage between day 69 (10th percentile) and 88 (90th percentile). Median day of E-L12, i.e. shoot length ~ 10 cm with separated leaves and visible inflorescences, was 97, with 80% of the observations between day 85 and 109. Median flowering day, i.e., 50% of the bunches in a vine with 50% cap fall (E-L23), was on day 136, and ranged between day 130 and 147. Median day for veraison (E-L35) was 207, ranging from day 199 and 217. Median day for 24 °Brix was 235, and ranged between day 225 and 245. Variance ranged from 41 to 88 days between budburst and fruit setting (E-L27; average 54 days) but the range spread significantly from 56 to 120 days between berry pea size (E-L31) to 24 °Brix (average 89 days).

Phenological variation among sub-regions of the Barossa Zone GI

We used two complementary approaches to analyse differences in phenology between sites. The first supervised analysis consisted of sites aggregated by location based on the existing sub-regions of the Barossa Zone (Figure 3a and b). Sites were classified in each of the six sub-regions and the timing of phenological stages averaged between sites. The second approach consisted of an unsupervised clustering (Figure 3c and d) where timing of phenological stages were averaged within clusters after the number of clusters have been defined by AHC (see statistical analysis for more details and Figure 4 for the description of the clusters). We then compared differences between sub-regions and clusters on chronological (Figures 3a and c) and thermal time (Figure 3b and d) scales.

On a chronological scale (Figure 3b and c), vine development was slower in the Eden Valley compared to the other environments, with the timing of key phenostages diverging by six to 11 days for budburst, seven to 14 days for flowering and veraison, and 13 to 19 days for 24 °Brix. Vine development in the Northern Grounds was faster than in Eden Valley, and slower than in the other sub-regions, with a difference from one to seven days between budburst and 24 °Brix. There were minor differences between the other subregions.

On a thermal time scale (Figure 3b), the timing of key phenological stages was similar between sub-regions in early stages of development, from budburst to 10 cm shoot, and sub-regions diverged from flowering to 24 °Brix, suggesting than factors other than temperature influenced vine development later in the season.

The unsupervised clustering analysis of phenological development returned three main clusters within the Barossa Zone (Figure 4). Central objects were defined by site 1 for cluster one, site 9 for cluster two and site 21 in cluster three. Distances between central objects were 2.37 between groups one and two, 4.9 between groups one and three, and 7.01 between groups two and three; indicating that the timing of development on sites in cluster one and two were closer than between sites of group three. Fourteen sites consistently clustered within the same group regardless of the vintage, whereas clustering of 10 sites varied between vintages. None of the sites had a vintage in more than two groups.

The chronological timing of phenological stages between these clusters (Figure 3c and d) showed some similarities with the six sub-regions from the supervised analysis (Figure 3a and b). Vine development was slowest in cluster three (C3), which included only Eden Valley sites (21, 23 and 24), followed by cluster one (C1), which included all the Northern Ground sites (1 to 4), and some other sites from Eden Valley (22), Central Grounds (5 and 8), Eastern Edge (11), Southern Grounds (13 and 14), and Western Ridge (18 and 20). Development was fastest in cluster two (C2), which included sites from Central Grounds (6 and 7), Eastern Edge (9 and 12), Southern Grounds (15 and 16), and Western Ridge (17 and 19). On a thermal time scale (Figure 3d) and in comparison with the supervised analysis (Figure 3b), differences between clusters were negligible from budburst to flowering, but clusters separated as development progressed from veraison to 24 ^{o}Brix.

Drivers of development across the Barossa GI

Relationship between the duration of phenostages with weather, plant traits and viticultural variables

We analysed the associations between phenological development and components of terroir across the 24 sites and three vintages with PLS-R analyses (Figure 5). Four periods were analysed: pre-budburst, budburst-flowering, flowering-veraison and veraison-maturity. Models were generated including all the variables, and the variable importance in projection (VIP) scores were used to identify the variables that best explained variance in the duration of the intervals (Farrés, et al. 2015). Global goodness of fit of the models by period returned "fit", Q^2 from 0.13 to 0.72 and "predictability", R^2Y between 0.41 to 0.90. The first two dimensions of the model consistently gave the best balance between Q^2 and R^2Y during the cross-validation. (Table S2 shows statistics of the model by period).

The PLS-R analyses highlight the preponderant effect of weather over plant and vineyard variables driving the duration of pre-budburst and budburst-flowering periods (Figure 5 a-f). Correlation loadings indicate a strong association between radiation and temperatures (T_{mean}, T_{min}, and T_{max}) with the duration of the pre-budburst period, and between RH, rain:ET_o ratio, VPD and temperature (T_{mean} and T_{max}) with the duration of the budburst-flowering period. In both these periods, high temperature shortened the intervals, but high radiation (mainly in the pre-budburst period), and high RH, rain:ET_o ratio, and low VPD extended their duration. Neither plant traits nor viticulture practices included in the analysis (green bars in Figures 5c and f) had a substantial affect on the duration of these intervals (VIP < 1).

Correlation loadings of the variables on the biplot and VIP suggest that weather, plant and vineyard variables influenced on the duration of flowering-veraison and veraison-maturity phases (Figure 5 g-l). Correlation loadings indicate that the duration of the flowering-veraison phase was positively associated with VPD and temperature (T_{mean} and T_{max}), and negatively related to pruning mass and yield in the current season. On the contrary, duration of the veraison-maturity phase was negatively associated to

VPD, radiation and temperature (T_{mean}, T_{max} and T_{min}), and positively correlated with pruning weight and yield. The low Q^2 and R^2Y of the PLS-R model indicate a poor fit and predictability during the period flowering-veraison (Table S2).

Relationship between the duration of phenological period with mean temperature and VIPs identified as part of the PLS-R analyses

Figure 6 shows the relationship between the duration of each of the four periods and the mean temperature during the period. Period duration declined with increasing temperature in three out the four periods; these relationships were described by either an exponential (pre-budburst and veraison-maturity) or linear equation (budburst-flowering). The strength of the relationship ranked pre-budburst (r^2 = 0.94) > budburst-flowering (r^2 = 0.40) > veraison-maturity (r^2 = 0.17). Duration of pre-budburst and budburst-flowering periods was shortened at 6 d $^oC^{-1}$, compared to 2 d $^oC^{-1}$ for veraison-maturity. The duration of flowering-veraison was unrelated to mean temperature (r^2 = 0.03, P_a = 0.24).

We then analysed the relationship between the duration of each period and the variables with the highest or the second highest VIP score (if T_{mean} had the highest score, refer to Figure 5). In the periods pre-budburst and veraison-maturity the duration was related to T_{min}, with a stronger relationship in the period pre-budburst (r^2 = 0.81) than in veraison-maturity (r^2 = 0.12). The time from veraison to maturity increased with yield (inset Figure 6h; r^2 = 0.29, a = 2.64, P_a < 0.0001). The time from budburst to flowering increased linearly with relative humidity (r^2 = 0.45); while the time from flowering to veraison was unrelated to temperature (r^2 = 0.02, P_a = 0.29), or any other weather parameter (data not shown).

Growing condition between phenological periods

We compared growing conditions during each phenological period after pooling weather data between sites corresponding to the clusters identified using the unsupervised clustering analysis (see Figure 4). Temperature (T_{Min}, T_{mean} and T_{Max}) peaked from flowering to veraison and plateaued between veraison and maturity in sites of C1, slightly increased in C2 or decreased in C3 (Figure 7). T_{min} was slightly higher at each of the four periods in C2 sites, and consistently lower in C3 sites during veraison-maturity. Relative humidity correlated negatively with temperature; it reached a minimum in flowering-veraison and slightly increased in veraison-maturity. Relative humidity from budburst until harvest was higher in sites comprising C3. Sites in C2 had lower relative humidity at all four periods. Radiation and VPD followed a trend similar to temperature; both peaked at flowering-veraison and decreased in veraison-maturity. VPD in flowering-veraison, however, plateaued in sites for C2 and decreased in sites in C1 and C3. The ratio rain:ET_o decreased markedly, from approx. 0.3 during pre-budburst and budburst-flowering, to approx. 0.1 from flowering to maturity. This indicates that in early stages of development when there is more rainfall and lower atmospheric evaporative demand, around 30% of the ET_o was covered with winter and spring rainfall, which contrast with the approx. 10% contribution that rainfall had on ET_o later during flowering-veraison and veraison-maturity. The biggest difference between clusters on rain:ET_o were for veraison-maturity, where C3 sites had lower ratios. Soil profile PAW captured the changes on water inputs, rainfall and irrigation, and outputs during the season; and decreased during the growing season for all three clusters, ranking C2 > C1 > C3.

Contribution of phenological stages to the duration of the budburst to maturity period

The time from budburst to maturity was positively associated with the time between budburst and flowering (r^2 = 0.36, a = 0.94, P_a < 0.0001) and veraison to maturity (r^2 = 0.64, a = 1.06, P_a < 0.0001), and was unrelated to the time between flowering and veraison (a = 0, P_a = 0.95) (Figure 8).

Discussion

Is the effect of terroir on development stable from vintage-to-vintage?

Terroir encompasses geography, topography, soil, climate, plant material, and human interventions defining fruit and wine composition. van Leeuwen et al. (2004) ranked elements of terroir modulating fruit composition as climate (measured as "vintage effect") > soil > cultivar. Wine composition integrates these elements and consistency over vintages allows to track its origin (Roullier-Gall, et al. 2014). However, the hierarchy of the elements of terroir vary with temporal and spatial scale (van Leeuwen 2022); for example, the vintage effect may override the effect of other elements of terroir on wine composition at a sub-regional scale (Danner, et al. 2020,Roullier-Gall, et al. 2014), but may not be strong enough to remove differences in wine composition between distant regions (Urvieta, et al. 2021). Similarly, the response to the environment varies with the trait; for example, a highly plastic trait, such as rotundone concentration in the skin of Shiraz berries, is more likely to be more responsive to the vintage effect (Scarlett, et al. 2014,Zhang, et al. 2015) than $\delta^{13}C$ or yeast assimilable nitrogen concentration, which are more stable over time and within a region (Brillante, et al. 2020,van Leeuwen, et al. 2018). Phenological development has a large impact in fruit traits, directly as the progression of sugar accumulation in berries interacts with other traits including pH, acidity, flavonoids, and flavour precursors, and indirectly as the timing of critical stages determine the background growing condition; for example, concentration of anthocyanins in Shiraz relate to temperature two weeks after veraison (Moran, et al. 2018). Here we explored the interaction between vine phenological development and selected elements of terroir at a sub-regional scale.

Our unsupervised clustering analysis of phenology revealed some consistencies on the timing of phenostages at a sub-regional scale that were stable despite the vintage effect and aspects of the site, including vineyard management (Figure 4). Notwithstanding the limitations of our approach relaying on 72 observational points to infer zoning, the progression of development across the Barossa Zone showed a marked spatial structure following the gradients of topography and soil across the landscape, and the associated variations in temperature and resources, i.e. water and nutrients (Bramley and Ouzman 2021). We found that within the Barossa region, vines developed faster on the south and south-west than on the centre and north; vine development was slowest at the Eden Valley region (Figure 3). On average, differences between sites with faster and slower vine development within the Barossa region ranged between 2 days at budburst, 6 days at flowering and 8 days at harvest. Differences were 13 days at budburst, 20 days at flowering, and up to 24 days at harvest, between the Barossa and Eden Valley regions. This spatial variation of phenology overlaps partially with the spatial variation in bioclimatic and topographic indices, along with soil properties in the region (Bramley and Ouzman (2021).

Along with the variation on soil properties, the north-west to south-east decrease in both annual and seasonal temperature and the increase in elevation and rainfall across the Barossa Zone drive four clusters of vineyards [Figure 8c in the study of Bramley and Ouzman (2021)]. In agreement with the delay in development observed here in Eden Valley, Bramley and Ouzman (2021) found that the coolest and wettest vineyards in the Eden Valley regions separated from the rest of the vineyards from the Barossa Zone. Similarly, the central band of flat vineyards running north-east to south-west on the

floor of the valley within the Barossa region in Bramley and Ouzman, coincides with vineyards on cluster 2 in our analysis that ranked second in development after vineyards on the west region. The analysis of Bramley and Ouzman (2021) identified two more clusters running south-north on the warmest and driest western side of valley; sharing similarities on temperatures and soil available water and fertility, but differing mainly on the aspect and slope. We found a single cluster that agglomerates these western sites where phenological development was fastest.

The Barossa Valley Grape & Wine Association (BGWA) proposed a sub-regionalization of the Barossa using wine sensory analysis that returned three distinctive "Grounds": Northern, Central, and Southern Grounds, with two smaller grounds, Eastern Edge and Western Ridge. Both our phenological analysis and Bramley and Ouzman (2021) agree with the BGWA's clear separation of the Eden Valley from the rest of the Barossa, and partially with the distinction between sub-regions. However, both of these studies also caution about the proposed BGWA's demarcation and the number of Grounds. Against the multi-level nature of terroir, existing efforts on zoning of the Barossa Zone, including this current study, are fragmented and inclusive, as they only partially captured elements of terroir. Nevertheless, given the clear pattern on the progression of phenology across the Barossa Zone that withstand variation in factors changing across the landscape and between vintages, further analysis may justify the use of phenology maps in integrated terroir zoning.

Drivers of phenology: viticultural and modelling implications

The strength of the association between vine development and temperature varied with phenophase, and different phenophases contributed differentially to the time from budburst to maturity. Flowering-veraison did not associate with temperature and did not contribute to the variation in budburst-maturity, which related to the duration of both budburst-flowering and veraison-maturity (Figure 8). This reinforces previous findings showing that variation on development rate during the post-veraison period was the main driver of the timing of maturity, with a negligible contribution of the flowering to veraison period (Sadras, et al. 2008). With a focus on development during ripening, they found an inverse relationship between the rate of accumulation of sugars and the timing of maturity, revealing the resource-driven nature of the duration of this period. In agreement with this, we found that yield was positively associated with the duration of the veraison-maturity period (inset Figures 6h), (Cameron, et al. 2021). This does not completely override the effect of temperature affecting veraison-maturity (Figure 6d and h), but stresses the resource-dominated nature of processes, seemingly reduced carbon, from veraison to harvest, which are normally overlooked in phenological models based on temperature (Parker, et al. 2020). The length of the veraison-maturity period was also negatively associated with high temperature, high radiation, and high vapour pressure deficit (Figure 5j and l); all these factors modulate the assimilation and transport of sugars to the berries (Matthews, et al. 2009,Rebucci, et al. 1997). The duration of the periods pre-budburst and budburst-flowering was primarily a function of the mean temperature during the period (Figures 5a,d and 6a,b); however, minimum temperature had a higher impact pre-budburst (Figure 5c) than in budburst-flowering (Figure 5f), where the duration of the interval was strongly associated to the maximum temperature (Cameron, et al. 2022). These relationships reflect the interdependence between the rates of development at each phenological stage and the cardinal temperatures (minimum, optimal and maximum) which explains the better predictability of phenology on temperature-capped models (Wang and Engel 1998). The dominant force of temperature driving development prior to flowering is extensively documented but only recently explored in the context of advancement development with warming. Cameron et al. (2022) reported a higher sensitivity to temperature between budburst to flowering than in the subsequent

stages, and a curvilinear response to the duration of this interval with maximum temperature. Consistent with this, we found a higher sensitivity of development to temperature before flowering (Figure 6). The duration of the period budburst-flowering was also positively correlated to RH and rain:ET_o ratio, but negatively associated to VPD and radiation (Figure 5d). These factors are highly correlated as a rainy site or season is typically cooler, with lower radiation and lower VPD. The length of the interval flowering-veraison was unrelated to temperature (Figure 6c and g), and poorly predicted for the PLS-R analysis (Figure 5g and supplementary Table 2). This highlights the complex nature of the processes driving the onset berry colouring (Delfino, et al. 2019,Matthews, et al. 2009) and, therefore, the duration of this period, and explains why temperature-based models predict veraison poorly (Parker, et al. 2011,Zapata, et al. 2017). Indeed, veraison is a transition from purely developmental to more closely connected developmental and growth processes, where both resource and non-resource factors drive the processes.

Acknowledgements

We thank Mr Gaston Sepulveda, Mrs Annette James, and Mr Han Chow for assistance with vineyard data collection and site establishment. Wine Australia for funding project UA1602, and our project partners. Wine Australia invests in and manages research, development and extension on behalf of Australia's grapegrowers and winemakers and the Australian Government. The South Australian Research and Development Institute and the University of Adelaide are members of the Wine Innovation Cluster in Adelaide.

Captions to figures:

Figure 1: Location of the 24 sites sampled across the Barossa GI. Sites are identified by small points colour coded according to the sub-regions: Northern Grounds (yellow), Central Grounds (black), Eastern Edge (red), Southern Grounds (blue), Western Ridge (purple) and Eden Valley (green). Pie chart next to each point indicates grouping of the sites across the three vintages (2019, 2020 and 2021) for the three clusters defined as part of the unsupervised AHC analysis: cluster 1 (orange), cluster 2 (blue) and cluster 3 (purple). See materials and methods and Figure 4 for more details. Coloured areas indicate boundaries for the Barossa Zone GI (orange), and the Barossa (blue) and Eden Valley (gray) regions. Source: Google Earth V 7.3.3.7721 (June 17, 2021).

Figure 2: Timing of phenological E-L stages and sugar concentration across 24 vineyards and three vintages (2019, 2020 and 2021) in the Barossa Zone GI. Timing of phenological stages is expressed as day of vintage from 1st July for the southern hemisphere. Each box plot corresponds to observations pooled across sites and vintages. The boundary of the box closest to zero indicates the 25th percentile, the pink line indicates the mean, the black line the median and the boundary farthest from zero indicates the 75th percentile. Whiskers left and right of the box indicate the 5th and 95th percentiles and points beyond the whiskers indicate outliers.

Figure 3: Progression of phenological stages across 24 vineyards and three vintages (2019, 2020 and 2021) in the Barossa Zone GI in (a and c) chronological and (b and d) thermal time scales. Thermal time was calculated as GDD base 10 °C commencing on vintageday-60 (29th August in the southern hemisphere). In a and b, sites have been pooled together based in the existing sub-regionalization proposed by the Barossa Grape and Wine Association (www.barossawine.com/vineyards/barossa-grounds/): Northern Grounds (NG), Central Grounds (CG), Eastern Edge (EE), Southern Grounds (SG), Western Ridge (WR) and Eden Valley (EV). In c and d, sites were grouped using an unsupervise clustering analysis (Agglomerative hierarchical clustering). Each box plot corresponds to observations pooled across sites and vintages. The boundary of the box closest to zero indicates the 25th percentile, the pink line indicates the mean, the black line the median and the boundary farthest from zero indicates the 75th percentile. Whiskers left and right of the box indicate the 5th and 95th percentiles and points beyond the whiskers indicate outliers. Letter indicates differences at $P < 0.05$ by Fishers's LSD test.

Figure 4: Agglomerative hierarchical clustering (AHC) for the combination of sites (1 to 24) and vintages (2019 to 2021) based in the timing of budburst (E-L4), 10 cm shoot (E-L12), flowering (E-L23), veraison (E-L35) and maturity (E-L38), and the duration between phenological stages (vintageday-60 to budburst, budburst to flowering, flowering to veraison, and veraison to maturity.

Figure 5: Partial last squares regression analysis of (centre panels) sites and (left panels) correlation loadings of the relationship between the duration of the periods: (a-c) vintageday-60 to budburst (pre-BB), (d-f) budburst to flowering (BB-F), (g-i) flowering to veraison (F-V), and (j-l) veraison to maturity (V-M) with vineyard, climate and soil parameters measured during vintages 2019 to 2021. (right panels) variable influence on the projection scores (VIP) for weather (blue) and vineyard x management (green) parameters.

Figure 6: Relationship between duration of the period (pre-BB, Bb-F, F-V and V-M) and (a-d) mean temperature (T_{mean}), or (e-h) variables with the highest VIP scores (variable influence on the projection) on the PLS-R analysis on Figure 5. During the periods when T_{mean} had the highest VIP score, i.e. pre-

BB and V-M, the regression was built with the variable with the second highest score. Lines represent the best fit regression for the data set.

Figure 7: Growing conditions during phenological periods (vintageday-60 to budburst, pre-BB; budburst to flowering, BB-F; flowering to veraison, F-V; and veraison to maturity, V-M) between clusters identified as part of the AHC on Figure 4. Each point is the mean from data collected across vineyards within the same cluster during vintages 2019 to 2021.

Figure 8: Relationships between de duration of the budburst to maturity (24 ^{o}Brix) period with the duration of the intervals a) BB-F, budburst to flowering; b) F-V, flowering to veraison; and, V-M, veraison to maturity, V-M). Data are mean from three vineyard observations and for 24 sites and three vintages (2019 to 2021).

Figure 1:

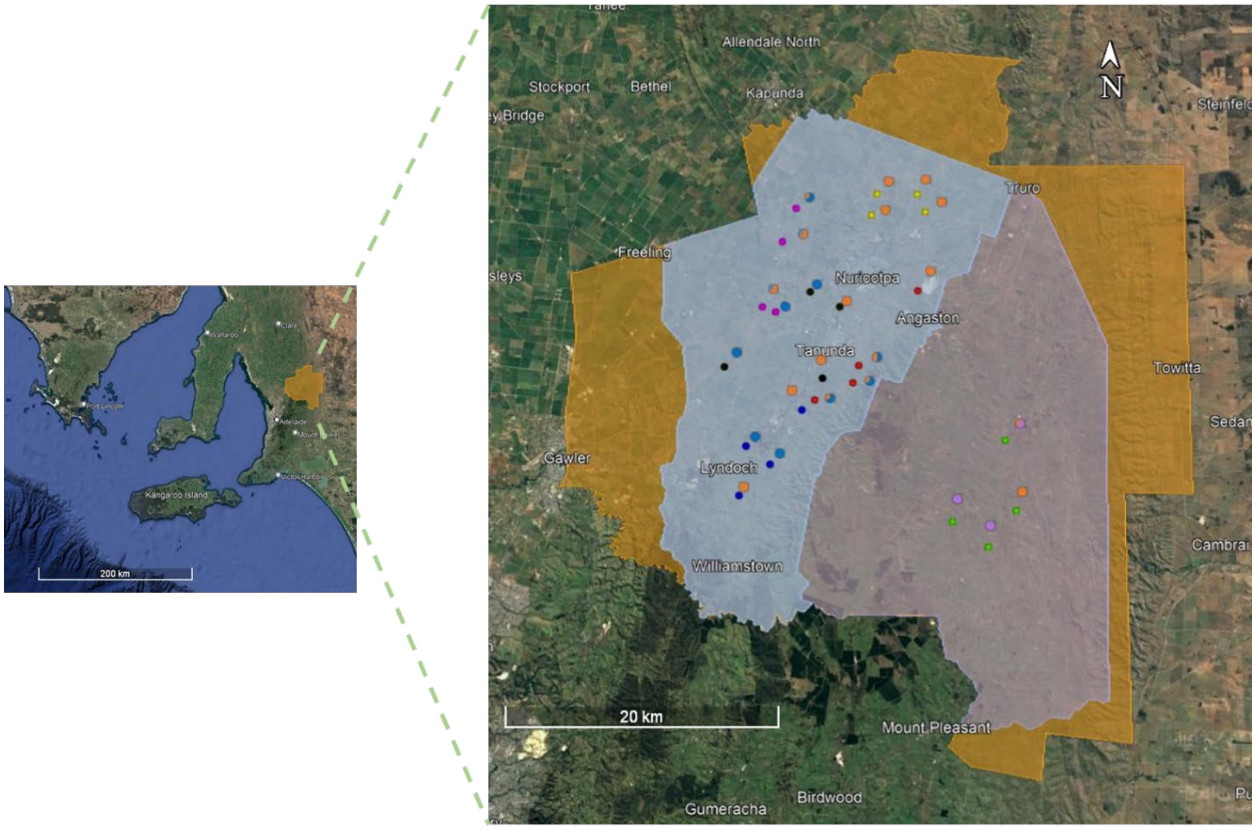

Allendale North
Stockport
Bethel
Kapunda
Truro
Freeling
Nuriootpa
Angaston
Tanunda
Towitta
Gawler
Lyndoch
Williamstown
Mount Pleasant
Gumeracha
Birdwood
N
20 km
Kangaroo Island
200 km

Figure 2:

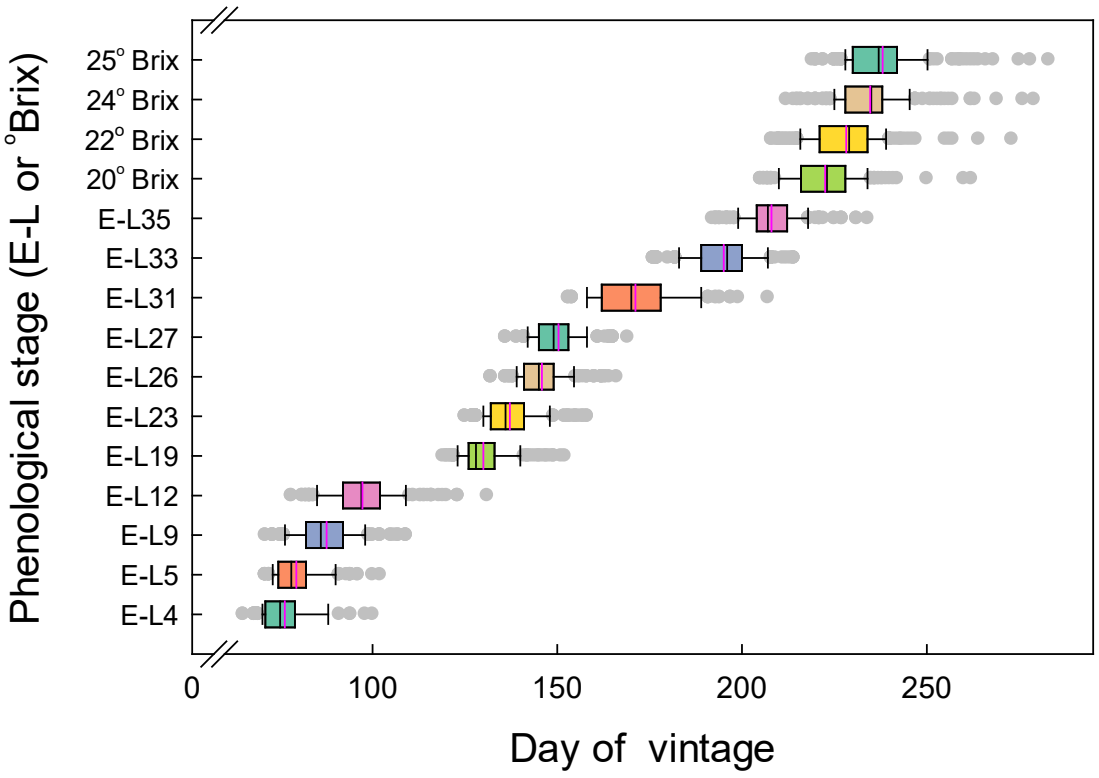

Phenological stage (E-L or °Brix)
25° Brix
24° Brix
22° Brix
20° Brix
E-L35
E-L33
E-L31
E-L27
E-L26
E-L23
E-L19
E-L12
E-L9
E-L5
E-L4
0
100
150
200
250
Day of vintage

Figure 3:

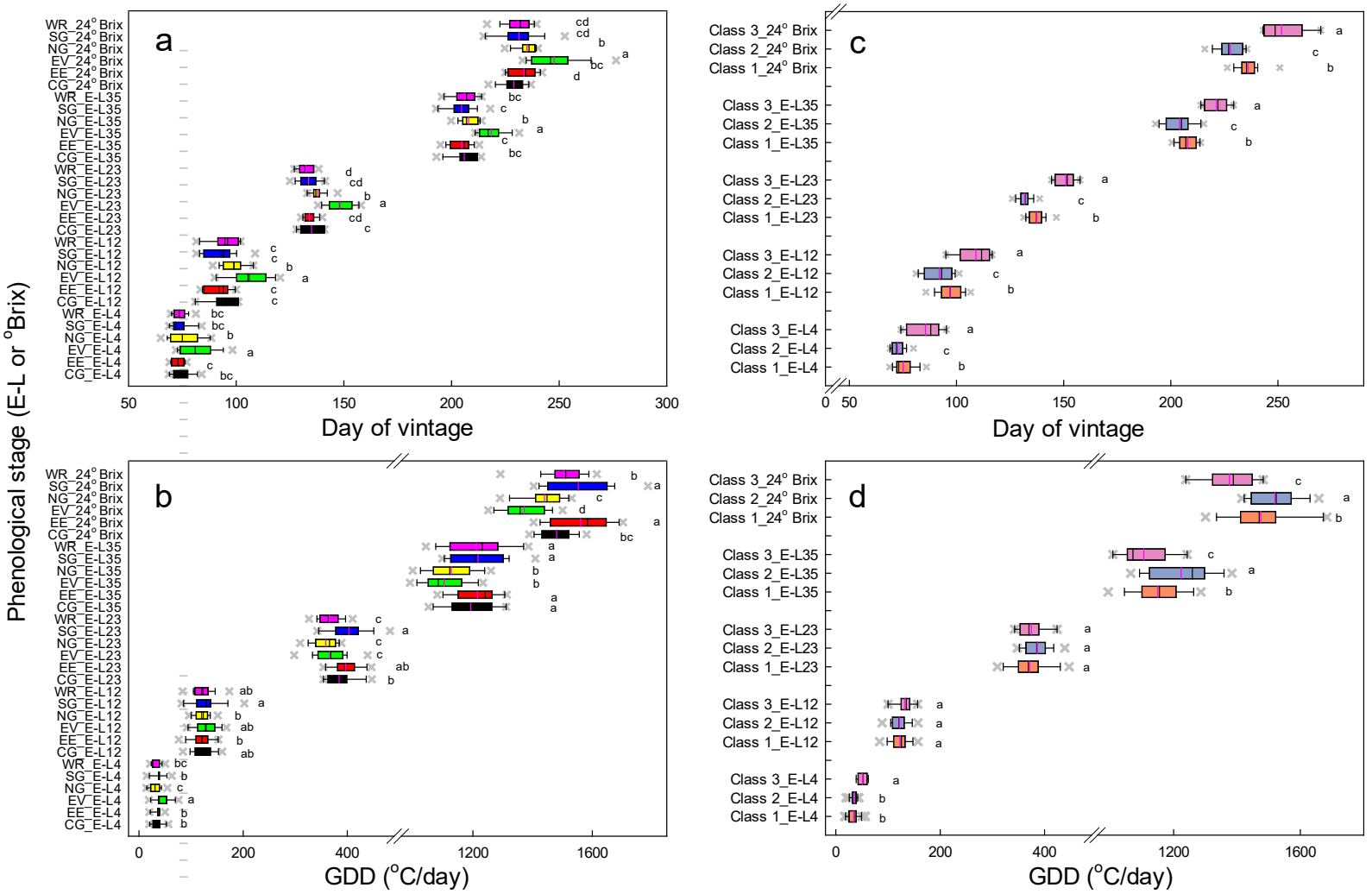

a
b
c
d
Phenological stage (E-L or °Brix)
Day of vintage
GDD (°C/day)
WR_24° Brix
SG_24° Brix
NG_24° Brix
EV_24° Brix
EE_24° Brix
CG_24° Brix
WR_E-L35
SG_E-L35
NG_E-L35
EV_E-L35
EE_E-L35
CG_E-L35
WR_E-L23
SG_E-L23
NG_E-L23
EV_E-L23
EE_E-L23
CG_E-L23
WR_E-L12
SG_E-L12
NG_E-L12
EV_E-L12
EE_E-L12
CG_E-L12
WR_E-L4
SG_E-L4
NG_E-L4
EV_E-L4
EE_E-L4
CG_E-L4
Class 3_24° Brix
Class 2_24° Brix
Class 1_24° Brix
Class 3_E-L35
Class 2_E-L35
Class 1_E-L35
Class 3_E-L23
Class 2_E-L23
Class 1_E-L23
Class 3_E-L12
Class 2_E-L12
Class 1_E-L12
Class 3_E-L4
Class 2_E-L4
Class 1_E-L4

Figure 4:

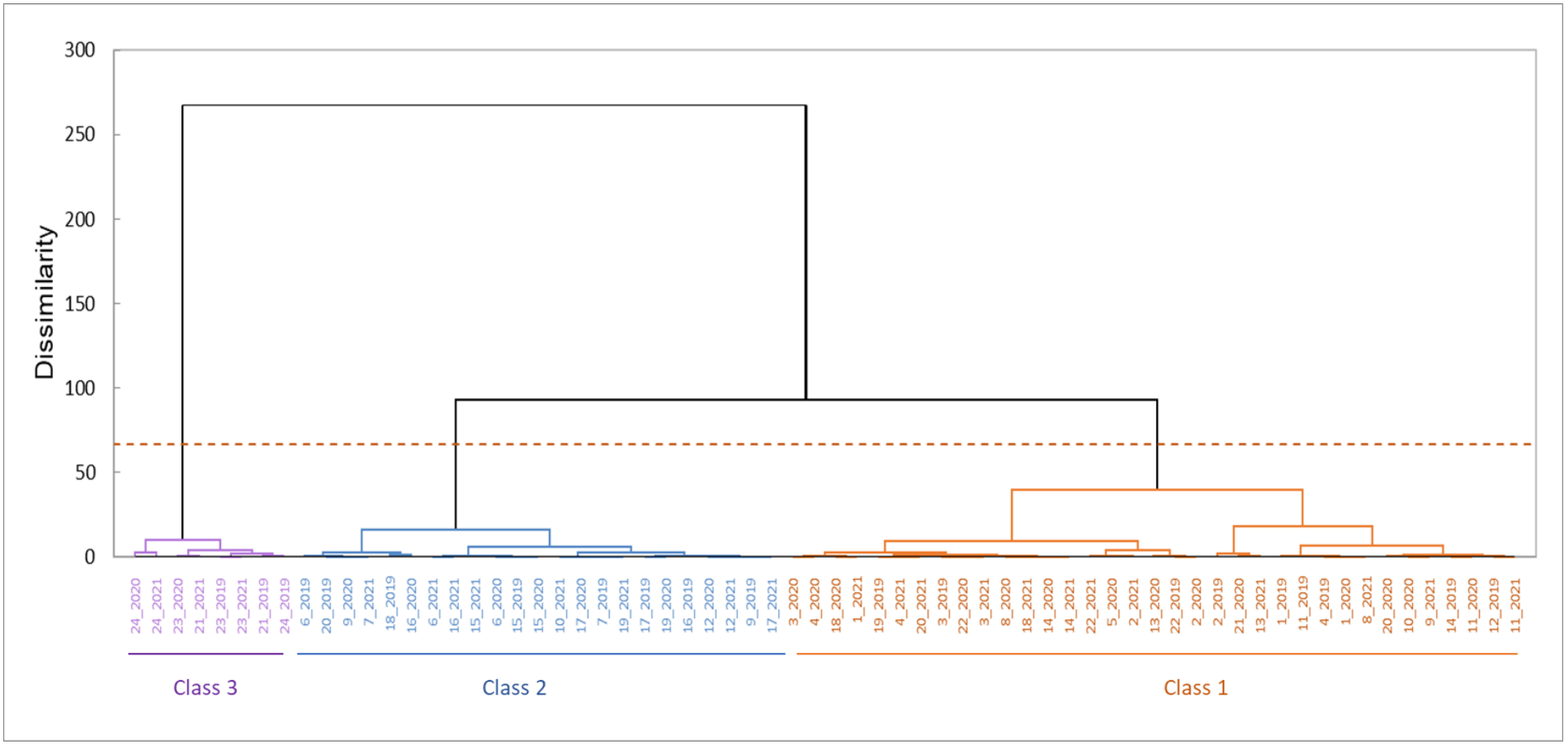

Dissimilarity
300
250
200
150
100
50
0
24_2020 24_2021 23_2020 21_2021 23_2019 23_2021 21_2019 24_2019
6_2019 20_2019 9_2020 7_2021 18_2019 16_2020 6_2021 16_2021 15_2021 6_2020 15_2019 15_2020 10_2021 17_2020 7_2019 19_2021 17_2019 19_2020 16_2019 12_2020 12_2021 9_2019 17_2021
3_2020 4_2020 18_2020 1_2021 19_2019 4_2021 20_2021 3_2019 22_2020 3_2021 8_2020 18_2021 14_2020 14_2021 22_2021 5_2020 2_2021 13_2020 22_2019 2_2020 2_2019 21_2020 13_2021 1_2019 11_2019 4_2019 1_2020 8_2021 20_2020 10_2020 9_2021 14_2019 11_2020 12_2019 11_2021
Class 3
Class 2
Class 1

Figure 5:

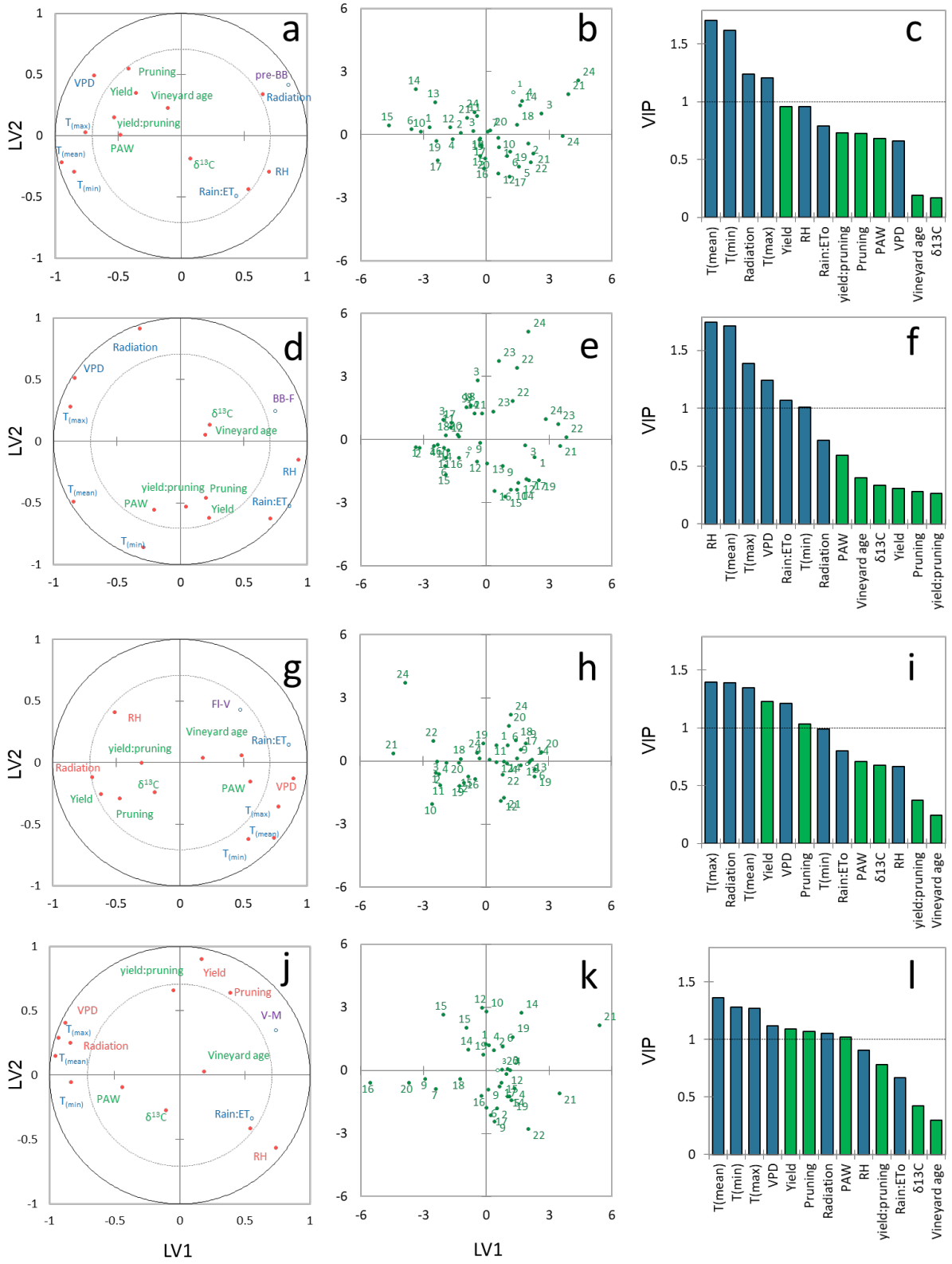

a
b
c
d
e
f
g
h
i
j
k
l
LV2
LV1
VIP
VPD
Pruning
pre-BB
Radiation
Yield
Vineyard age
yield:pruning
PAW
δ13C
RH
Rain:ETo
T(max)
T(mean)
T(min)
BB-F
Fl-V
V-M
T(mean) T(min) Radiation T(max) Yield RH Rain:ETo yield:pruning Pruning PAW VPD Vineyard age δ13C
RH T(mean) T(max) VPD Rain:ETo T(min) Radiation PAW Vineyard age δ13C Yield Pruning yield:pruning
T(max) Radiation T(mean) Yield VPD Pruning T(min) Rain:ETo PAW δ13C RH yield:pruning Vineyard age
T(mean) T(min) T(max) VPD Yield Pruning Radiation PAW RH yield:pruning Rain:ETo δ13C Vineyard age

Figure 6

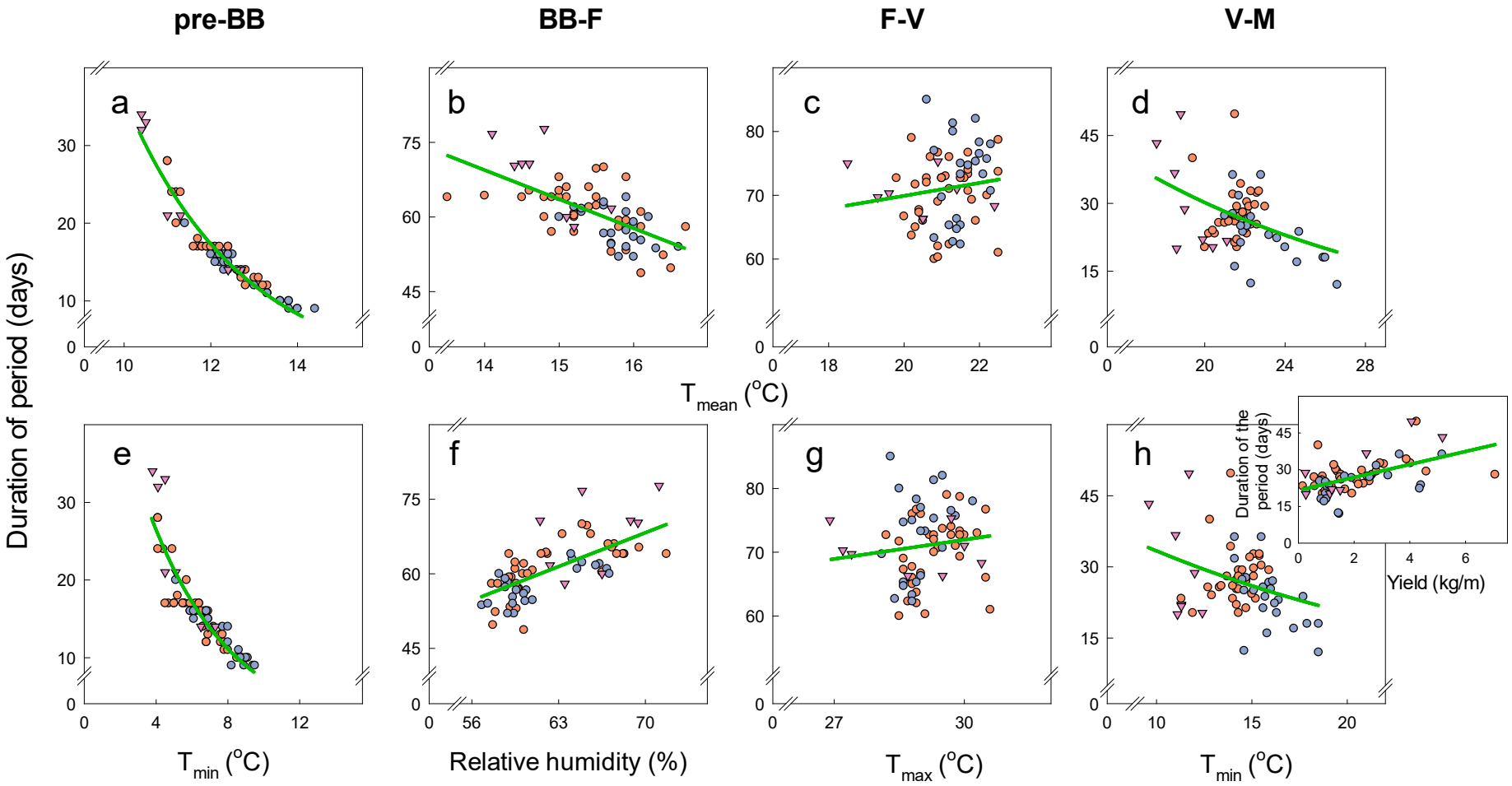

pre-BB
BB-F
F-V
V-M
a
b
c
d
e
f
g
h
Duration of period (days)
T mean (°C)
T min (°C)
Relative humidity (%)
T max (°C)
T min (°C)
Duration of the period (days)
Yield (kg/m)

Figure 7

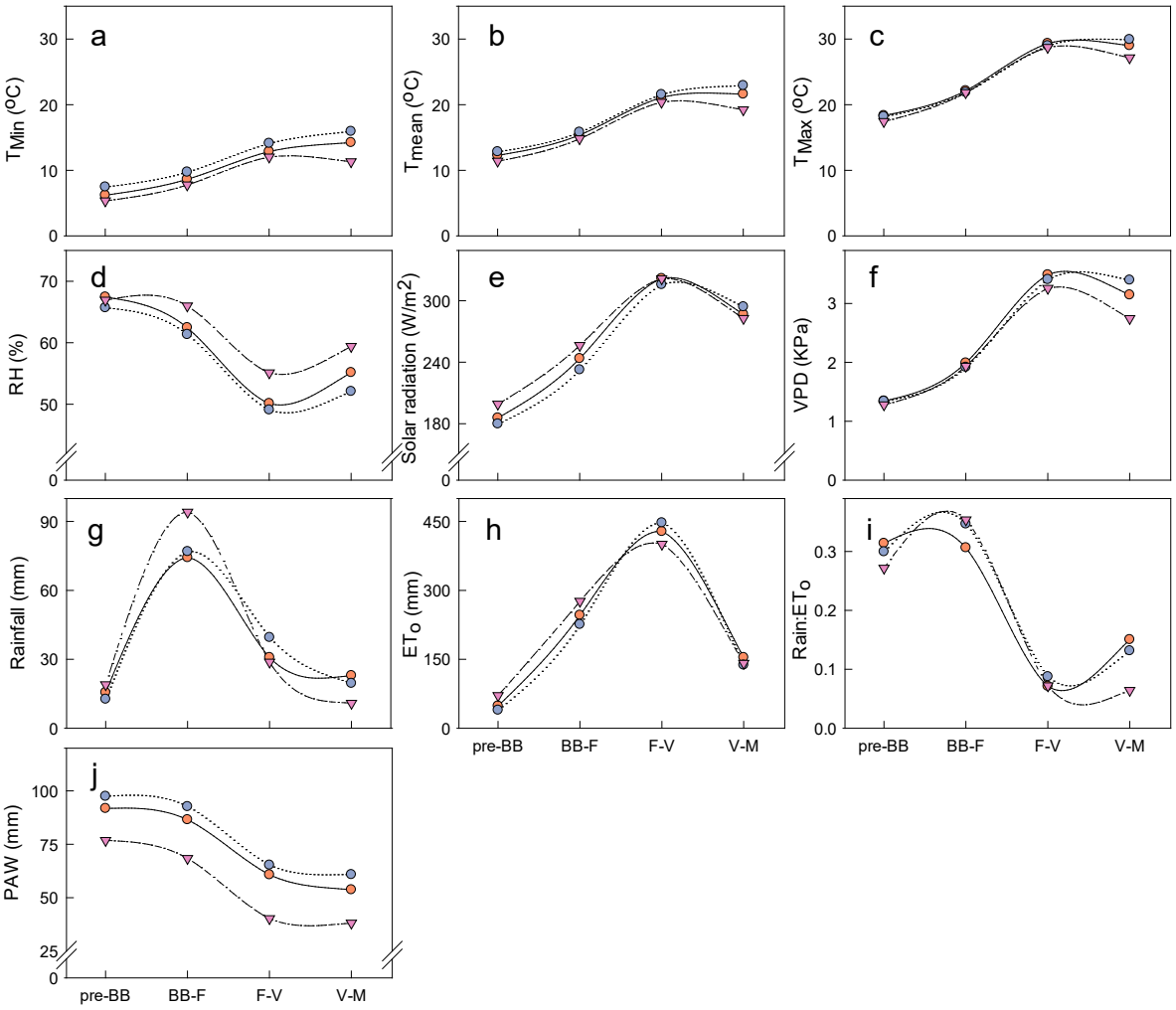

a
b
c
d
e
f
g
h
i
j
T_{Min} (°C)
T_{mean} (°C)
T_{Max} (°C)
RH (%)
Solar radiation (W/m^2)
VPD (KPa)
Rainfall (mm)
ET_o (mm)
Rain:ET_o
PAW (mm)
pre-BB
BB-F
F-V
V-M

Figure 8

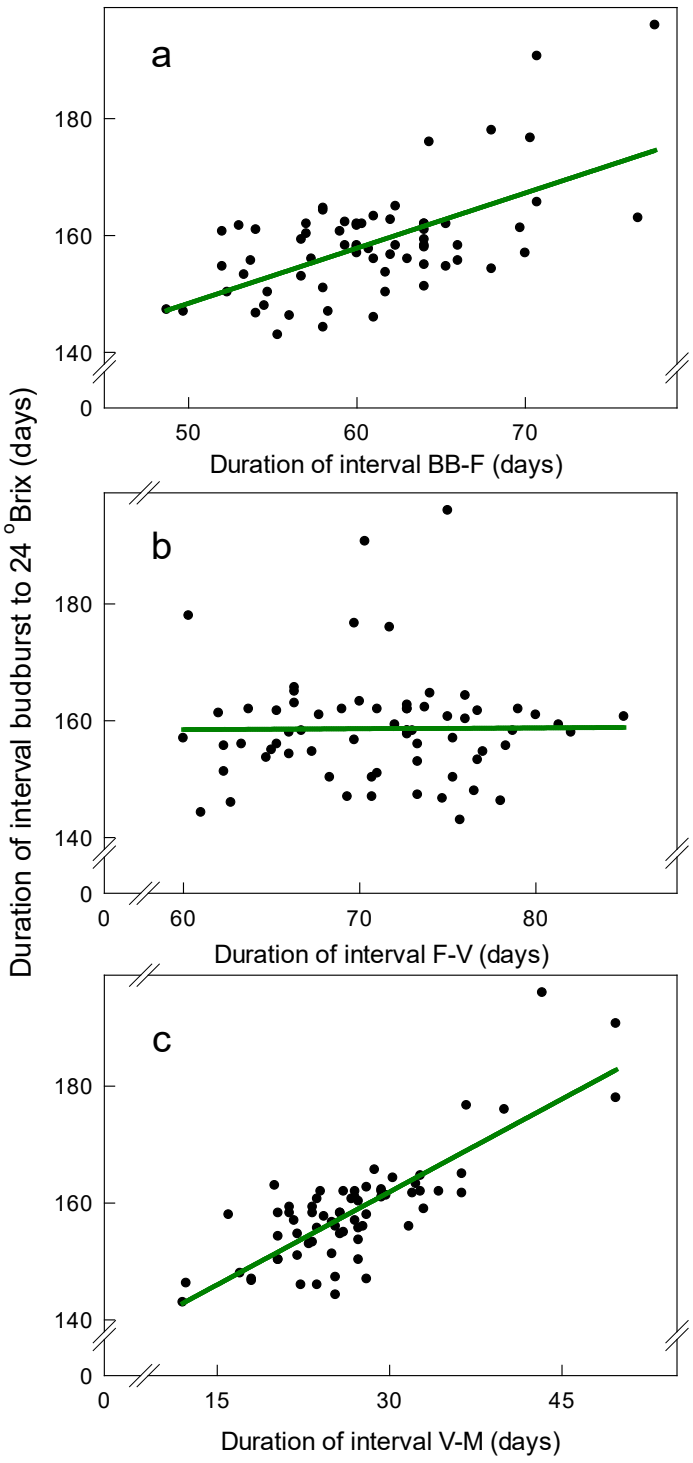
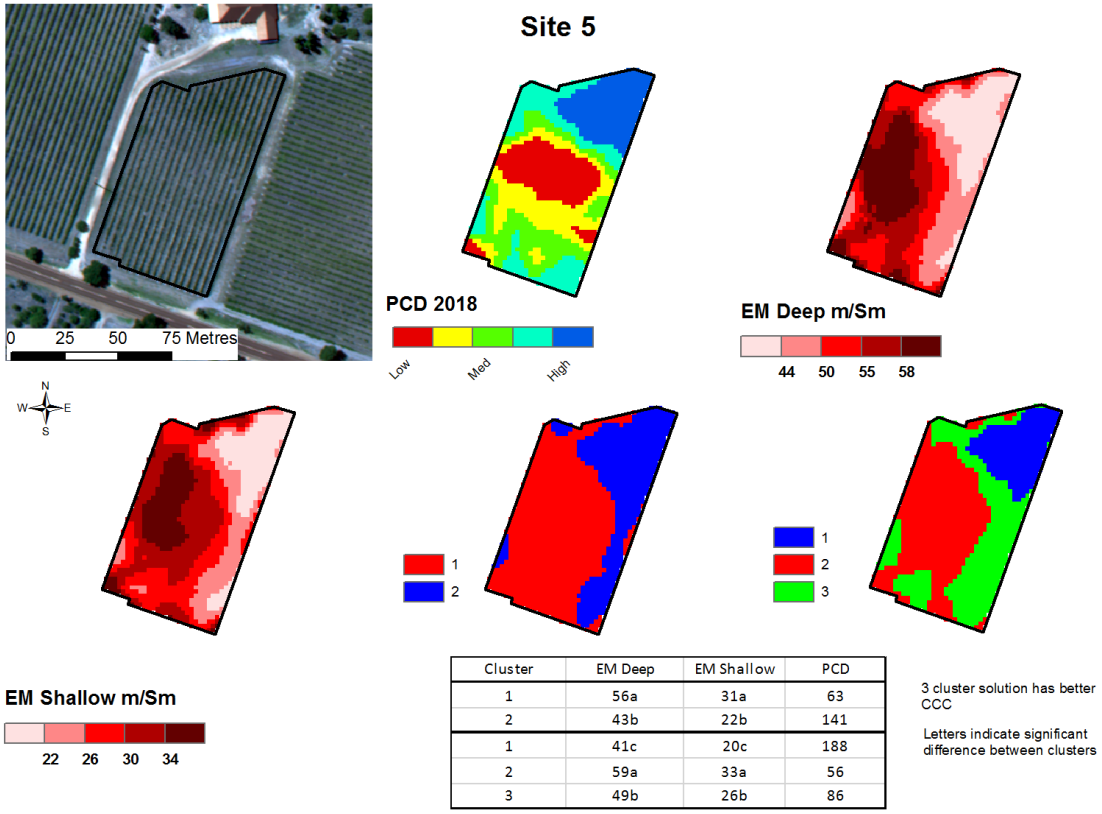

a
b
c
180
160
140
0
50
60
70
80
15
30
45
Duration of interval BB-F (days)
Duration of interval F-V (days)
Duration of interval V-M (days)
Duration of interval budburst to 24 °Brix (days)

Figure S1 Example of clustering using *k*-means to identify vineyard zones based on the EM38 and PCD data.



Cluster	EM Deep	EM Shallow	PCD
1	56a	31a	63
2	43b	22b	141
1	41c	20c	188
2	59a	33a	56
3	49b	26b	86

3 cluster solution has better CCC

Letters indicate significant difference between clusters

Table S1. Statistics of the timing of phenological stages across 24 sites and three consecutive seasons since 2018/19. Time is day of vintage where vintage day commences on July 1st).

Statistic	E-L4	E-L5	E-L9	E-L12	E-L19	E-L23	E-L26	E-L27	E-L31	E-L33	E-L35	20 °Brix	22 °Brix	24 °Brix
Mean	76	79	88	97	130	137	146	150	171	195	208	223	228	235
Median	75	78	86	97	128	136	145	149	170	196	207	223	229	235
Standard deviation	6.8	6.6	8.7	9.4	6.4	7.0	6.5	6.6	11.0	8.6	7.5	9.4	9.8	9.9
Variance	45.9	44.0	76.1	87.9	41.3	48.6	42.8	43.5	120.0	73.2	55.9	89.3	95.9	98.1
Minimum	65	71	71	78	119	125	132	136	153	176	192	205	208	212
Maximum	100	102	131	131	152	158	166	169	207	214	234	262	273	279
Range	35	31	60	53	33	33	34	33	54	38	42	57	65	67
10th percentile	69	73	76	85	123	130	139	142	158	183	199	210	215	225
90th percentile	88	90	98	109	140	147	154	158	189	207	217	234	239	245
Skewness	1.2	1.1	0.8	0.6	1.2	1.0	0.8	0.5	0.7	-0.2	0.5	0.6	0.7	1.2
Kurtosis	1.2	0.8	2.3	0.7	1.3	0.9	0.5	-0.1	-0.1	-0.3	0.9	1.5	2.3	3.5

Table S2: Model performance data by phenological period: BB-F, budburst to flowering; F-V, flowering to veraison; and V-M, veraison to maturity, V-M.

Period	pre-BB	BB-F	F-V	V-M
Number of components	2	2	2	2
Q^2 cumulative	0.72	0.28	0.13	0.26
R^2Y cumulative	0.90	0.62	0.41	0.67
R^2X cumulative	0.46	0.60	0.43	0.60
R^2	0.92	0.77	0.52	0.71
SDP	1.86	3.71	4.05	4.44
MSEP	2.81	11.45	13.97	16.05
RMSEP	1.68	3.38	3.74	4.01

References:

Allen, R.G., L.S. Pereira, D. Raes, and M. Smith, "Crop evapotranspiration. Guidelines for computing crop water requirements. FAO Irrigation and Drainage paper No. 56", (FAO, Rome, Italy, 1998), Vol. 300, pp. 6541.

Barnuud, N.N., A. Zerihun, M. Gibberd, and B. Bates (2013) Berry composition and climate: responses and empirical models. International Journal of Biometeorology, doi: 10.1007/s00484-00013-00715-00482.

Bonada, M., E. Edwards, M. McCarthy, G. Sepulveda, and P.R. Petrie (2020) Impact of low rainfall during dormancy on vine productivity and development. Australian Journal of Grape and Wine Research 26, 325-342.

Böttcher, C., K. Harvey, C.G. Forde, P.K. Boss, and C. Davies (2011) Auxin treatment of pre-veraison grape (*Vitis vinifera* L.) berries both delays ripening and increases the synchronicity of sugar accumulation. Australian Journal of Grape and Wine Research 17, 1–8.

Böttcher, C., T.E. Johnson, C.A. Burbidge, E.L. Nicholson, P.K. Boss, S.M. Maffei, S.E.P. Bastian, and C. Davies (2021) Use of auxin to delay ripening: sensory and biochemical evaluation of Cabernet Sauvignon and Shiraz. Australian Journal of Grape and Wine Research.

Bramley, R.G.V. and J. Ouzman (2021) Underpinning terroir with data: on what grounds might subregionalisation of the Barossa Zone geographical indication be justified? Australian Journal of Grape and Wine Research 28, 196-207.

Bramley, R.G.V., J. Ouzman, and P.K. Boss (2011) Variation in vine vigour, grape yield and vineyard soils and topography as indicators of variation in the chemical composition of grapes, wine and wine sensory attributes. Australian Journal of Grape and Wine Research 17, 217–229.

Bramley, R.G.V., J. Ouzman, and M.C.T. Trought (2020) Making sense of a sense of place: precision viticulture approaches to the analysis of terroir at different scales.

Brillante, L., Martínez-L., R. Yu, and S.K. Kurtural (2020) Carbon isotope discrimination ($\delta^{13}C$) of grape musts is a reliable tool for zoning and the physiological ground-truthing of sensor maps in precision viticulture. Frontiers in Environmental Science.

Cameron, W., P.R. Petrie, and E.W.R. Barlow (2022) The effect of temperature on grapevine phenological intervals: Sensitivity of budburst to flowering. Agricultural and Forest Meteorology 315, 108841.

Cameron, W., P.R. Petrie, E.W.R. Barlow, C.J. Patrick, K. Howell, and S. Fuentes (2021) Is advancement of grapevine maturity explained by an increase in the rate of ripening or advancement of veraison? Australian Journal of Grape and Wine Research 27, 334-347.

Castellucci, F., "Resolution OIV/VITI 333/2010", edited by I.O.o.V.a. Wine (OIV, 2010).

Clarke, S.J., K.J. Lamont, H.Y. Pan, L.A. Barry, A. Hall, and S.Y. Rogiers (2015) Spring root-zone temperature regulates root growth, nutrient uptake and shoot growth dynamics in grapevines. Australian Journal of Grape and Wine Research 21, 479-489.

Coombe, B.G. (1995) Growth stages of the grapevine: adoption of a system for identifying grapevine growth stages. Australian Journal of Grape and Wine Research 1, 104–110.

Danner, L., C. Collins, A. James, M. Bonada, J. Gledhill, P.R. Petrie, and S. Bastian Sensory profiles of Shiraz wine from six Barossa sub-regions: a comparison between industry scale and standardised small lot research wine making. Proceedings of the XIIIth International Terroir Congress, Adelaide, Australia.

de Rességuier, L., S. Mary, R. Le Roux, T. Petitjean, H. Quénol, and C. van Leeuwen (2020) Temperature variability at local scale in the Bordeaux area. Relations with environmental factors and impact on vine phenology. Frontiers in plant science 11.

Delfino, P., S. Zenoni, Z. Imanifard, G.B. Tornielli, and D. Bellin (2019) Selection of candidate genes controlling veraison time in grapevine through integration of meta-QTL and transcriptomic data. BMC Genomics 20.

Dobrowski, S.Z., S.L. Ustin, and J.A. Wolpert (2003) Grapevine dormant pruning weight prediction using remotely sensed data. Australian Journal of Grape and Wine Research 9, 177-182.

Dokoozlian, N.K. (1999) Chilling temperature and duration interact on the budbreak of `Perlette' grapevine cuttings. HortScience 34, 1-3.

Dry, P.R., D.J. Maschmedt, C.J. Anderson, E. Riley, S.-J. Bell, and W.S. Goodchild (2004) The grapegrowing regions of Australia. In: Viticulture. Volume 1 – Resources, Eds. P.R. Dry and B.G. Coombe (Winetitles: Adelaide, SA, Australia) pp. 17–55.

Eriksson, L. (2001) Multi- and megavariate data analysis : principles and applications. (Umea, Sweden : Umetrics Academy: Umea, Sweden).

Falcao, L.D., V.M. Burin, E. Sidinei Chaves, H.J. Vieira, E. Brighenti, J.P. Rosier, and M.T. Bordignon-Luiz (2010) Vineyard altitude and mesoclimate influenced on the phenology and maturation of Carbernet Sauvignon grapes from Santa Catarina State. Journal International des Sciences de la Vigne et du Vin 44, 135–150.

Farrés, M., S. Platikanov, S. Tsakovski, and R. Tauler (2015) Comparison of the variable importance in projection (VIP) and of the selectivity ratio (SR) methods for variable selection and interpretation. Journal of Chemometrics 29, 528-536.

Forrest, J. and A.J. Miller-Rushing (2010) Toward a synthetic understanding of the role of phenology in ecology and evolution. Philosophical Transactions of the Royal Society B: Biological Sciences 365, 3101-3112.

Matthews, M.A., T.R. Thomas, and K.A. Shackel (2009) Fruit ripening in *Vitis vinifera* L.: possible relation of veraison to turgor and berry softening. Australian Journal of Grape and Wine Research 15, 278–283.

Moncur, M.W., K. Rattigan, D.H. Mackenzie, and G.N. Mc Intyre (1989) Base temperatures for budbreak and leaf appearance of grapevines. American Journal of Enology and Viticulture 40, 21-26.

Moran, M.A., S.E. Bastian, P.R. Petrie, and V.O. Sadras (2018) Late pruning impacts on chemical and sensory attributes of Shiraz wine. 24, 469-477.

Moran, M.A., P.R. Petrie, and V.O. Sadras (2019) Effects of late pruning and elevated temperature on phenology, yield components, and berry traits in Shiraz. American Journal of Enology and Viticulture 70, 9-18.

Mori, K., N. Goto-Yamamoto, M. Kitayama, and K. Hashizume (2007) Loss of anthocyanins in red-wine grape under high temperature. Journal of Experimental Botany 58, 1935–1945.

Nord, E.A. and J.P. Lynch (2009) Plant phenology: a critical controller of soil resource acquisition. Journal of Experimental Botany 60, 1927-1937.

Palliotti, A., T. Frioni, S. Tombesi, P. Sabbatini, J.G. Cruz-Castillo, V. Lanari, O. Silvestroni, M. Gatti, and S. Poni (2017) Double-pruning grapevines as a management tool to delay berry ripening and control yield. American Journal of Enology and Viticulture 68, 412-421.

Parker, A.K., I.G. de Cortazar-Atauri, C. van Leeuwen, and I. Chuine (2011) General phenological model to characterise the timing of flowering and veraison of *Vitis vinifera* L. Australian Journal of Grape and Wine Research 17, 206-216.

Parker, A.K., I. García De Cortázar-Atauri, M.C.T. Trought, A. Destrac, R. Agnew, A. Sturman, and C. Van Leeuwen (2020) Adaptation to climate change by determining grapevine cultivar differences using temperature-based phenology models. OENO One 54, 955-974.

Parker, A.K., R.W. Hofmann, C. van Leeuwen, A.R.G. McLachlan, and M.C.T. Trought (2014) Leaf area to fruit mass ratio determines the time of veraison in Sauvignon Blanc and Pinot Noir grapevines. Australian Journal of Grape and Wine Research 20, 422-431.

Passioura, J.B. (1979) Accountability, philosophy and plant physiology. Search 10, 347-350.

Pearson, W., L.M. Schmidtke, I.L. Francis, S. Li, A. Hall, and J.W. Blackman (2021) Regionality in Australian Shiraz: compositional and climate measures that relate to key sensory attributes. Australian Journal of Grape and Wine Research 27, 458-471.

Poni, S., M. Gatti, F. Bernizzoni, S. Civardi, N. Bobeica, E. Magnanini, and A. Palliotti (2013) Late leaf removal aimed at delaying ripening in cv. Sangiovese: physiological assessment and vine performance. Australian Journal of Grape and Wine Research 19, 378-387.

Ramos, M.C., G.V. Jones, and J. Yuste (2015) Spatial and temporal variability of cv. Tempranillo phenology and grape quality within the Ribera del Duero DO (Spain) and relationships with climate. International Journal of Biometeorology 59, 1849-1860.

Rebucci, B., S. Poni, C. Intrieri, E. Magnanini, and A.N. Lakso (1997) Effects of manipulated grape berry transpiration on post-veraison sugar accumulation. Australian Journal of Grape and Wine Research 3, 57-65.

Roullier-Gall, C., L. Boutegrabet, R.D. Gougeon, and P. Schmitt-Kopplin (2014) A grape and wine chemodiversity comparison of different appellations in Burgundy: vintage vs terroir effects. Food Chemistry 152, 100-107.

Roullier-Gall, C., M. Lucio, L. Noret, P. Schmitt-Kopplin, and R.D. Gougeon (2014) How subtle is the "terroir" effect? Chemistry-related signatures of two "climats de Bourgogne". PloS one 9, e97615.

Sadras, V.O., M. Collins, and C.J. Soar (2008) Modelling variety-dependent dynamics of soluble solids and water in berries of *Vitis vinifera*. Australian Journal of Grape and Wine Research 14, 250–259.

Sadras, V.O., M.A. Moran, and P.R. Petrie Wine as G x E: effect of temperature on vine and fruit phenotype. Proceedings of the GiESCO 19th International Meeting, Pech Rouge, Montpellier.

Scarlett, N.J., R.G.V. Bramley, and T.E. Siebert (2014) Within-vineyard variation in the 'pepper' compound rotundone is spatially structured and related to variation in the land underlying the vineyard. Australian Journal of Grape and Wine Research 20, 214-222.

Spielmann, N. and C. Gélinas-Chebat (2012) Terroir? That's not how I would describe it. International Journal of Wine Business Research 24, 254-270.

Urvieta, R., G. Jones, F. Buscema, R. Bottini, and A. Fontana (2021) Terroir and vintage discrimination of Malbec wines based on phenolic composition across multiple sites in Mendoza, Argentina. Scientific Reports 11, 2863.

van Leeuwen, C. (2022) 9 - Terroir: the effect of the physical environment on vine growth, grape ripening, and wine sensory attributes. In: In: Managing Wine Quality (Second Edition), Ed. A.G. Reynolds (Woodhead Publishing) pp. 341-393.

van Leeuwen, C., P. Friant, X. Chone, O. Tregoat, S. Koundouras, and D. Dubourdieu (2004) Influence of climate, soil, and cultivar on terroir. American Journal of Enology and Viticulture 55, 207-217.

van Leeuwen, C., J.-P. Roby, and L. de Rességuier (2018) Soil-related terroir factors: a review. OENO One 52, 173-188.

Verdugo-Vásquez, N., C. Acevedo-Opazo, H. Valdés-Gómez, C. Pañitrur-De La Fuente, B. Ingram, I. García De Cortázar-Atauri, and B. Tisseyre (2022) Identification of main factors affecting the within-field spatial variability of grapevine phenology and total soluble solids accumulation: towards the vineyard zoning using auxiliary information. Precision Agriculture 23, 253-277.

Wang, E. and T. Engel (1998) Simulation of phenological development of wheat crops. Agricultural Systems 58, 1-24.

Wine Australia, "Geographical indications", Vol. 2022.

Zapata, D., M. Salazar-Gutierrez, B. Chaves, M. Keller, and G. Hoogenboom (2017) Predicting key phenological stages for 17 grapevine cultivars (*Vitis vinifera* L.). American Journal of Enology and Viticulture 68, 60-72.

Zhang, P., S. Barlow, M.P. Krstic, M. Herderich, S. Fuentes, and K. Howell (2015) Within-vineyard, within-vine, and within-bunch variability of the rotundone concentration in berries of *Vitis vinifera* L. cv. Shiraz. Journal of Agricultural and Food Chemistry 63, 4276-4283.

14. Appendix 6: Models between sub-regions

For each binary model, biplots were plotted to show predictors that drove separation of regions. The misclassified samples were labelled on the biplots. All predictors included in the model were also tabulated. As expected for models including only two regions, the first dimension accounted for most of variance within the dataset. Thus, loading value on the first dimension of each predictor was used to indicate which sub-region the predictor is positively associated with.

6.1.1 Model between Central Grounds and Eastern Edge

A model with 9 predictors achieved the lowest classification error of 4.3%. Three samples were misclassified, all of which are from site 9. Site 9 was also consistently misclassified in the global model (Table 6.1). Since the first dimension in multidimensional scaling accounted for 73.1% total variance, predictors that positively associated with the first dimension are considered to be associated with Eastern Edge, while the predictors negatively associated with the first dimension are considered to be associated with Central Grounds (Figure 6.1).

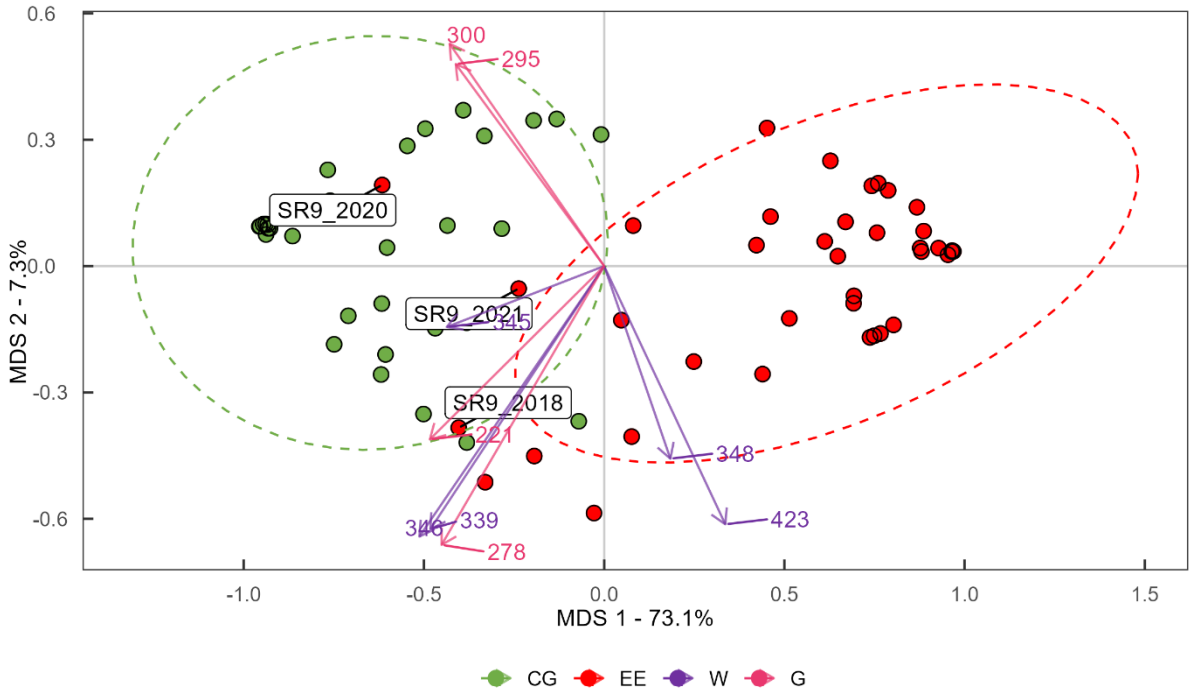


Figure 6.1 Biplot of the best RF model between Central Grounds and Eastern Edge. The misclassified samples (site_vintage) were labelled on the plot. The selected predictors were labelled with their sequential number in Table 6.1, and coloured based on the measurement type: grape measurements (magenta) and wine measurements (purple).

Table 6.1 Selected predictors for the RF model between Central Grounds and Eastern Edge.

Sequential no.	Predictor	Type of measurement	Data block	Predictor associated with	
				CG	EE
339	Cobalt	Wine	11		
345	Manganese	Wine	11		
346	Nickel	Wine	11		
348	Sodium	Wine	11		
423	Ethyl propanoate	Wine	14		
221	Methyl hexanoate	Grape	7		
278	Diethyl succinate	Grape	7		
295	Peonidin-3-O-glucoside	Grape	8		
300	Peonidin-3-acetyl-glucoside	Grape	8		

6.1.2 Model between Central Grounds and Eden Valley

The best RF model between Central Grounds and Eden Valley achieved a classification error of 0%, albeit with a relatively high number of predictors.

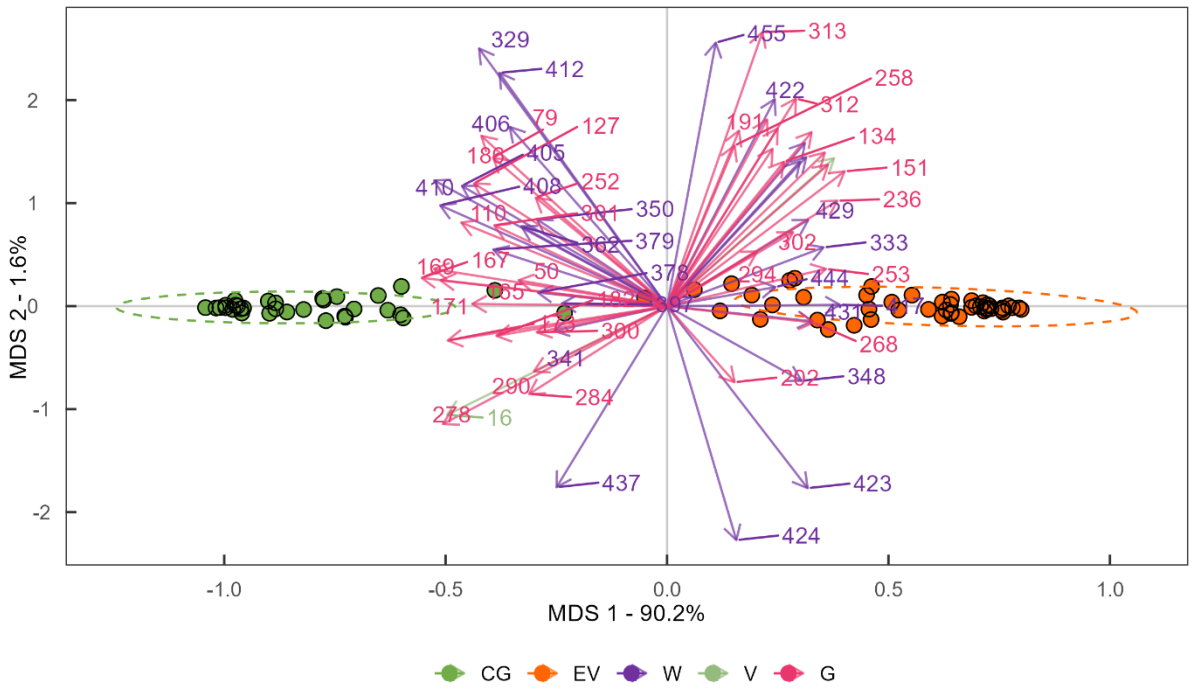


Figure 6.2 Biplot of the best RF model between Central Grounds and Eden Valley. The selected predictors were labelled with their sequential number in Table 6.2, and coloured based on the type of measurement: Vineyard measurements (green), grape measurements (magenta) and wine measurements (purple).

Table 6.2 Selected predictors for the RF model between Central Grounds and Eden Valley.

Sequential no.	Predictor	Type of measurement	Data block	Predictor associated with	
				CG	EV
329	Specific gravity	Wine	10		
333	Free sulphur	Wine	10		
341	Iron	Wine	11		
348	Sodium	Wine	11		
350	Zinc	Wine	11		
362	Malvidin-3-glucoside	Wine	12		
378	Chemical age 1	Wine	12		
379	Chemical age 2	Wine	12		
397	% Epicatechin extension	Wine	12		
405	Glucuronic acid	Wine	13		
406	Galacturonic acid	Wine	13		
408	Galactose	Wine	13		
410	Arabinose	Wine	13		
412	Total polysaccharide	Wine	13		
415	2-Methyl butyl acetate	Wine	14		
416	3-Methyl butyl acetate	Wine	14		
417	Hexyl acetate	Wine	14		
422	Ethyl acetate	Wine	14		
423	Ethyl propanoate	Wine	14		
424	Ethyl-2-methyl propanoate	Wine	14		
425	Ethyl butanoate	Wine	14		
429	Ethyl octanoate	Wine	14		
431	Phenylethyl acetate	Wine	14		
437	3-methylbutanoic acid	Wine	14		
444	Cineole	Wine	14		
455	Dimethyl sulfide	Wine	14		
16	pH	Vineyard	2		
17	Titratable Acidity	Vineyard	2		
41	Phenylalanine	Grape	3		
50	3-hexanol	Grape	4		
79	1,1,4,6,7-Pentamethyl-2,3-dihydroindene	Grape	4		
110	2-Methylenebornane	Grape	4		
127	2,3-Dihydro-3,3,4,5-tetramethyl-1H-Inden-1-one	Grape	4		
134	4-Vinylphenol	Grape	4		
148	Neoxanthin	Grape	5		
151	Chlorophyll B	Grape	5		
152	Chlorophyll A	Grape	5		
153	Beta-Carotene	Grape	5		
155	Unknown 2	Grape	5		
159	Glutathione	Grape	5		
165	Methyl pentadecanoate	Grape	6		

Sequential no.	Predictor	Type of measurement	Data block	Predictor associated with	
				CG	EV
167	Methyl heptadecanoate	Grape	6		
169	Methyl nonadecanoate	Grape	6		
171	Methyl eicosanoate	Grape	6		
173	Methyl heneicosanoate	Grape	6		
182	Methyl octacosanoate	Grape	6		
186	Methyl octadecanoate	Grape	6		
191	Ethyl acetate	Grape	7		
202	Methyl glycolate	Grape	7		
236	2,2,6-Trimethyl-cyclohexanone	Grape	7		
252	Ethyl octanoate	Grape	7		
253	(E)-Linalool oxide	Grape	7		
258	Acetic acid	Grape	7		
268	1-Octanol	Grape	7		
278	Diethyl succinate	Grape	7		
284	5-Ethyl-2(5H)-furanone	Grape	7		
290	Methyl 2-oxo-hexanoate	Grape	7		
294	Petunidin-3-glucoside	Grape	8		
300	Peonidin-3-acetyl-glucoside	Grape	8		
301	Malvidin-3-acetyl-glucoside	Grape	8		
302	Delphinidin-3-coumaroyl-glucoside	Grape	8		
312	% catechin extension	Grape	9		
313	% epicatechin extension	Grape	9		

6.1.3 Model between Central Grounds and Northern Grounds

The best RF model between Central Grounds and Northern Grounds achieved a classification error of 0%, with 26 predictors. Notably, first dimension in multidimensional scaling only accounted for 48.8% of total variance.

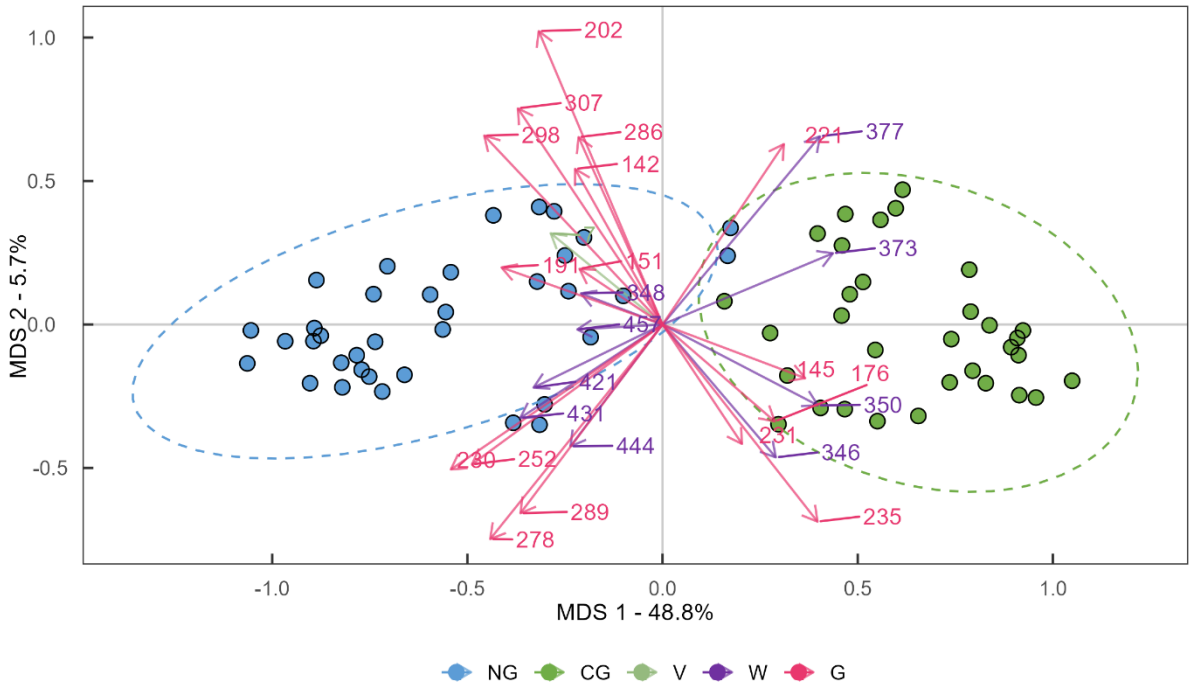


Figure 6.3 Biplot of the best RF model between Central Grounds and Northern Grounds. The selected predictors were labelled with their sequential number in Table 6.3, and coloured based on the type of measurements: vineyard measurements (green), grape measurements (magenta) and wine measurements (purple).

Table 6.3 Selected predictors for the RF model between Northern Grounds and Central Grounds.

Sequential no.	Predictor	Type of measurement	Data block	Predictor associated with	
				NG	CG
7	Plant area index	Vineyard	1		
346	Nickel	Wine	11		
348	Sodium	Wine	11		
350	Zinc	Wine	11		
373	Myricetin	Wine	12		
377	Isorhamnetin	Wine	12		
421	3-methyl butanol	Wine	14		
431	Phenylethyl acetate	Wine	14		
444	Cineole	Wine	14		
457	Methanethiol	Wine	14		
142	3-Oxo-alpha-ionol	Grape	4		
145	Methyl 2-hydroxy-4-methylbenzoate	Grape	4		
151	Chlorophyll B	Grape	5		
176	Methyl (Z)-13-docosenoate	Grape	6		
191	Ethyl acetate	Grape	7		
202	Methyl glycolate	Grape	7		
221	Methyl hexanoate	Grape	7		
230	Styrene	Grape	7		
231	Hexyl acetate	Grape	7		
235	1-Octen-3-one	Grape	7		
252	Ethyl octanoate	Grape	7		
278	Diethyl succinate	Grape	7		
286	beta-Damascenone	Grape	7		
289	Phenylethyl alcohol	Grape	7		
298	Cyanidin-3-acetyl-glucoside	Grape	8		
307	Malvidin-3-coumaroyl-glucoside	Grape	8		

6.1.4 Model between Central Grounds and Southern Grounds

Central Grounds and Southern Grounds were two regions with lower classification accuracies in the global model. However, the best binary RF model them achieved a classification error of 0%, with only 19 predictors. The two regions separate well on the first dimension which accounted for 69% of total variance. Some predictors selected by the binary model were not included in the global model.

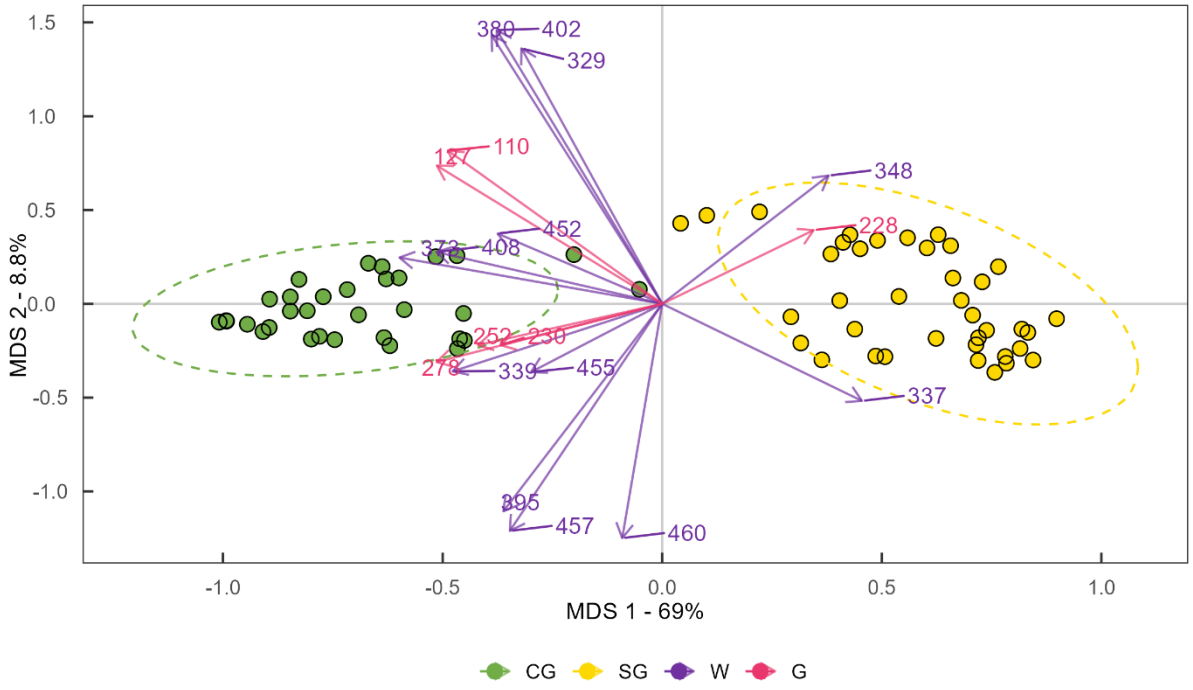


Figure 6.4 Biplot of the best RF model between Central Grounds and Southern Grounds. The selected predictors were labelled with their sequential number in Table 6.4, and coloured based on the measurement type: grape measurements (magenta) and wine measurements (purple).

Table 6.4 Selected predictors for the RF model between Central Grounds and Southern Grounds.

sequential no.	Predictor	Type of measurement	Data block	Predictor associated with	
				CG	SG
329	Specific gravity	Wine	10		
337	calcium	Wine	11		
339	cobalt	Wine	11		
348	Sodium	Wine	11		
373	Myricetin	Wine	12		
380	WDC	Wine	12		
395	CIELab-c*	Wine	12		
402	CIELab-b*	Wine	12		
408	Galactose	Wine	13		
452	β-Damascenone	Wine	14		
455	Dimethyl sulfide	Wine	14		
457	Methanethiol	Wine	14		
460	3-Mercaptohexanol	Wine	14		
110	2-Methylenebornane	Grape	4		
127	2,3-Dihydro-3,3,4,5-tetramethyl-1H-Inden-1-one	Grape	4		
228	1-Pentanol	Grape	7		
230	Styrene	Grape	7		
252	Ethyl octanoate	Grape	7		
278	Diethyl succinate	Grape	7		

6.1.5 Model between Central Grounds and Western Ridge

The best binary RF model between Central Grounds and Western Ridge achieved a classification error of 0%, with 8 predictors. The two regions separated well on the first dimension which accounted for 79.5% of total variance.

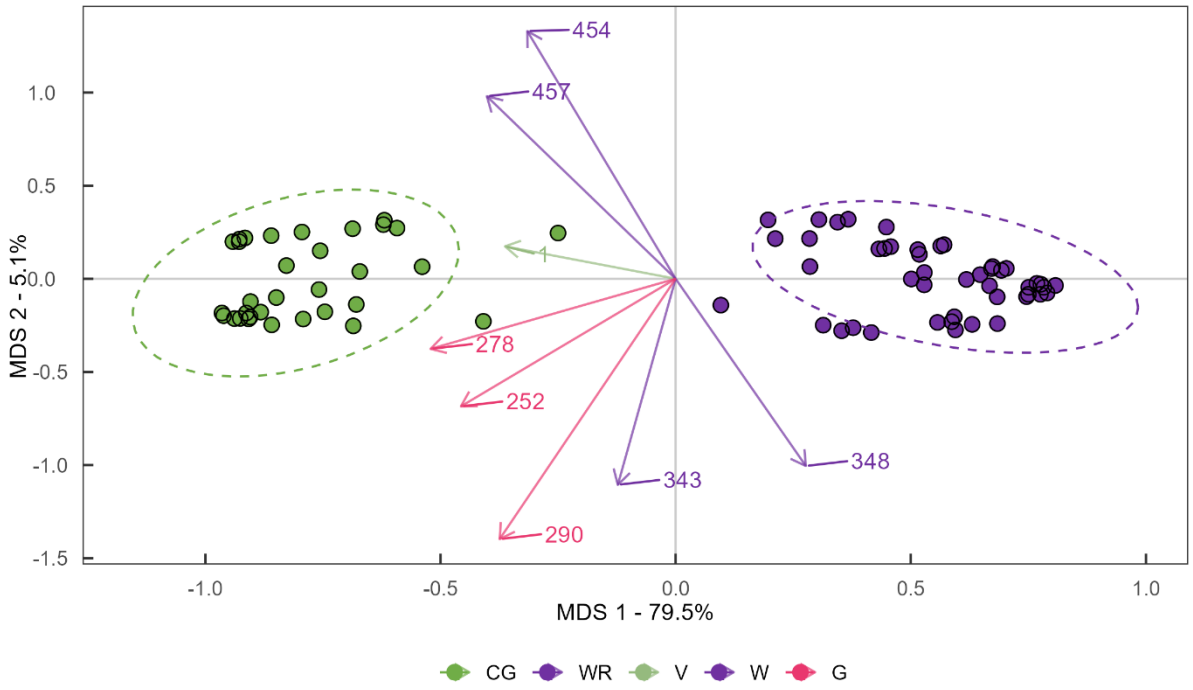


Figure 6.5 Biplot of the best RF model between Central Grounds and Western Ridge. The selected predictors were labelled with their sequential number in Table 6.5, and coloured based on the measurement type: vineyard measurements(green), grape measurements (magenta) and wine measurements (purple).

Table 6.5 Selected predictors for the RF model between Central Grounds and Western Ridge.

Sequential no.	Predictor	Type of measurement	Data block	Predictor associated with	
				CG	WR
1	Pruning shoot number	Vineyard	1		
343	Lithium	Wine	11		
348	Sodium	Wine	11		
454	Carbon disulfide	Wine	14		
457	Methanethiol	Wine	14		
252	Ethyl octanoate	Grape	7		
278	Diethyl succinate	Grape	7		
290	Methyl 2-oxo-hexanoate	Grape	7		

6.1.6 Model between Eastern Edge and Eden Valley

The best binary RF model between Eastern Edge and Eden Valley achieved a classification error of 0%, with 24 predictors. The two regions separated well on the first dimension which accounted for 75% of total variance.

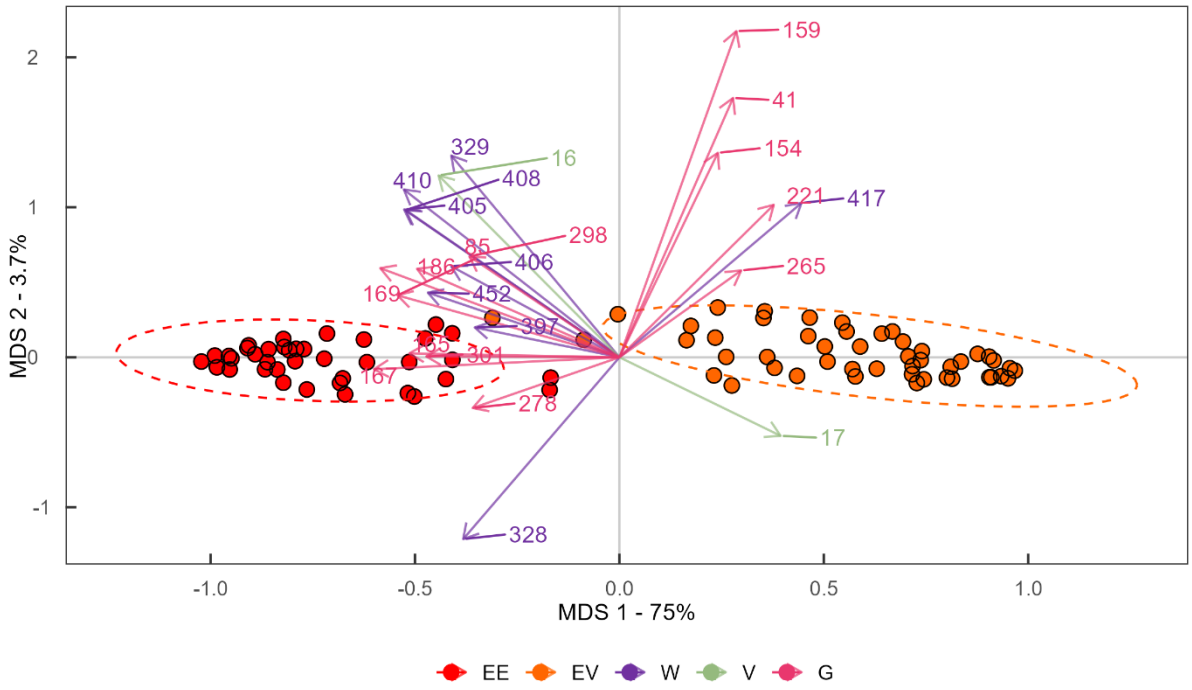


Figure 6.6 Biplot of the best RF model between Eastern Edge and Eden Valley. The selected predictors were labelled with their sequential number in Table 6.6, and coloured based on the measurement type: vineyard measurements (green), grape measurements (magenta) and wine measurements (purple).

Table 6.6 Selected predictors for the RF model between Eastern Edge and Eden Valley.

sequential no.	Predictor	Type of measurement	Data block	Predictor associated with	
				EE	EV
328	Glucose + fructose	Wine	10		
329	Specific gravity	Wine	10		
397	% Epicatechin extension	Wine	12		
405	Glucuronic acid	Wine	13		
406	Galacturonic acid	Wine	13		
408	Galactose	Wine	13		
410	Arabinose	Wine	13		
417	Hexyl acetate	Wine	14		
452	β-Damascenone	Wine	14		
16	pH	Vine	2		
17	Titratable Acidity	Vine	2		
41	Phenylalanine	Grape	3		
85	beta-damascenone	Grape	4		
154	unknown 1	Grape	5		
159	Glutathione	Grape	5		
165	Methyl pentadecanoate	Grape	6		
167	Methyl heptadecanoate	Grape	6		
169	Methyl nonadecanoate	Grape	6		
186	Methyl octadecanoate	Grape	6		
221	Methyl hexanoate	Grape	7		
265	Theaspirane B	Grape	7		
278	Diethyl succinate	Grape	7		
298	Cyanidin-3-acetyl-glucoside	Grape	8		
301	Malvidin-3-acetyl-glucoside	Grape	8		

6.1.7 Model between Eastern Edge and Northern Grounds

The best binary RF model between Eastern Edge and Eden Valley achieved a classification error of 2.7%, with only 8 predictors. One replicate of Site 3 and one replicate of Site 4 in 2018 were classified wrongly. The first dimension accounted for 76.7% of total variance.

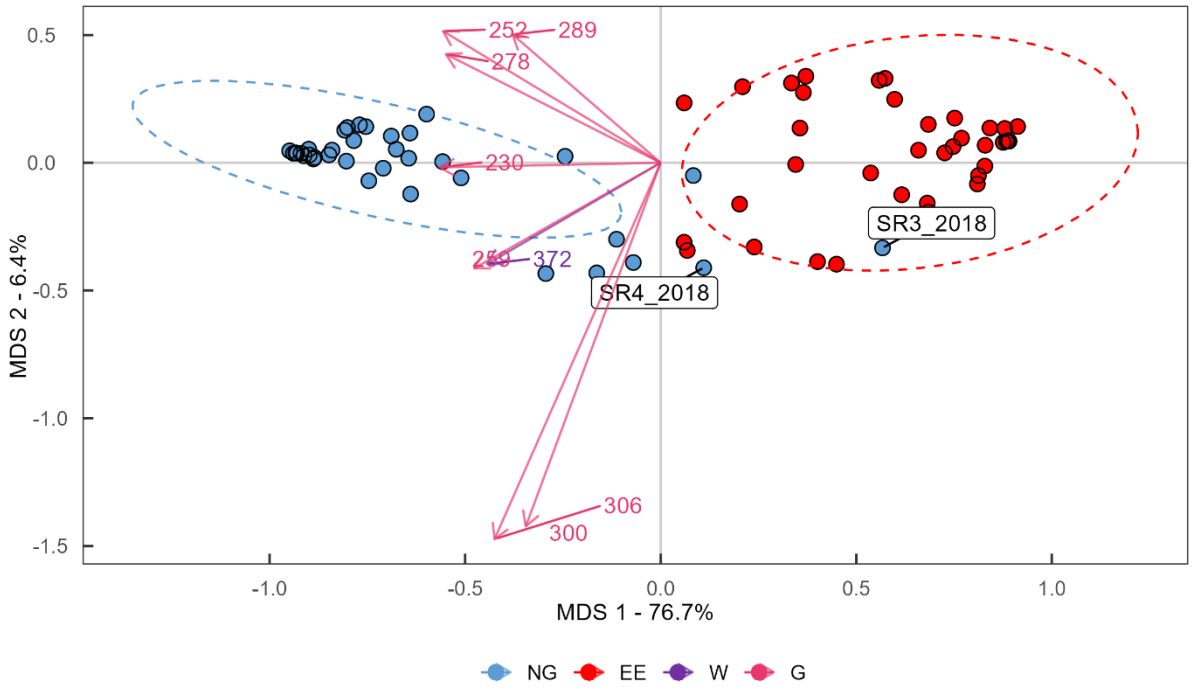


Figure 6.7 Biplot of the best RF model between Eastern Edge and Northern Grounds. The selected predictors were labelled with their sequential number in Table 6.7, and coloured based on the measurement type: grape measurements (magenta) and wine measurements (purple).

Table 6.7 Selected predictors for the RF model between Eastern Edge and Northern Grounds.

Sequential no.	Predictor	Type of measurement	Data block	Predictor associated with	
				NG	EE
372	Syringetin-3-*o*-glucoside	Wine	12		
230	Styrene	Grape	7		
252	Ethyl octanoate	Grape	7		
259	2-Ethyl-1-hexanol	Grape	7		
278	Diethyl succinate	Grape	7		
289	Phenylethyl alcohol	Grape	7		
300	Peonidin-3-acetyl-glucoside	Grape	8		
306	Peonidin-3-coumaroyl-glucoside	Grape	8		

6.1.8 Model between Eastern Edge and Southern Grounds

The best binary RF model between Eastern Edge and Southern Grounds achieved a classification error of 3.9%, with 36 predictors. Eastern Edge and Southern Grounds had relatively low classification accuracy in the global model. Three samples from Site 12, one each in vintage 2018, 2019 and 2020, were misclassified. Site 12 was consistently misclassified in the global model, where, however, they were mostly misclassified as Western Ridge. It is possible that Site 12 showed substantial variation compared to other sites in Eastern Edge, which may cause the RF algorithm to struggle to find similarities between Site 12 and other sites within Eastern Edge. The first dimension accounted for only 42.6% of total variance, and the second dimension accounted for 9.2%. This indicate that the relationship between Eastern Edge and Southern Grounds was more complex than that between regions with good separation in the binary model.

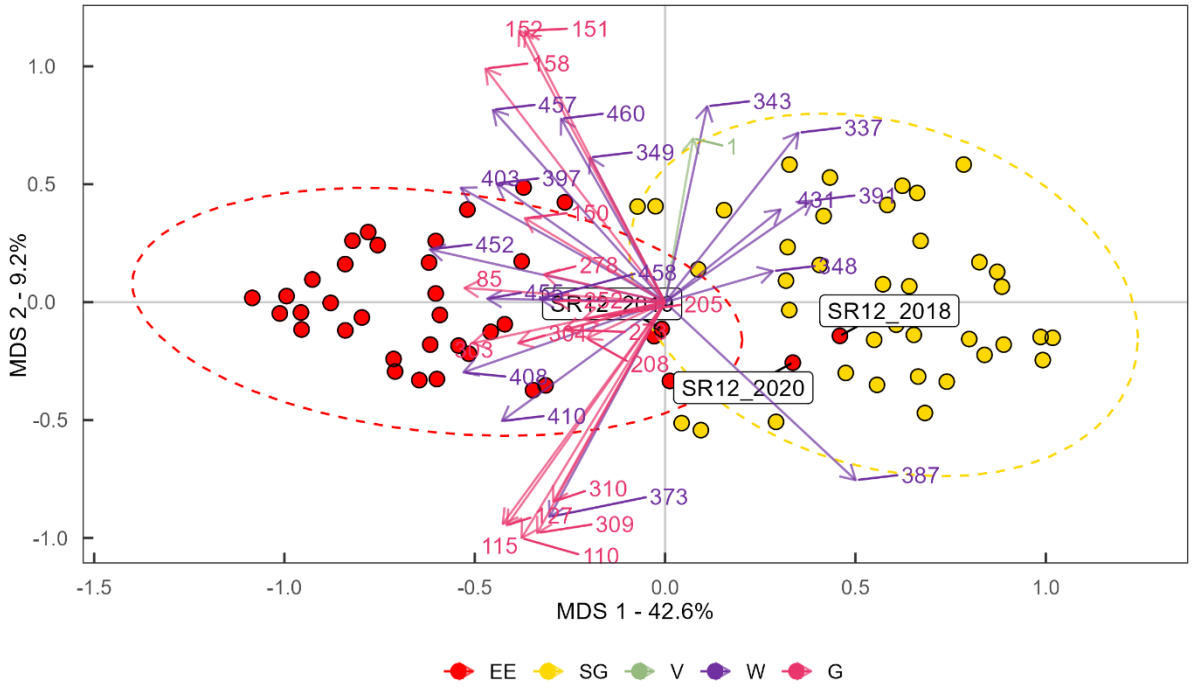


Figure 6.8 Biplot of the best RF model between Eastern Edge and Southern Grounds. The selected predictors were labelled with their sequential number in Table 6.8, and coloured based on the measurement type: grape measurements (magenta) and wine measurements (purple).

Table 6.8 Selected predictors for the RF model between Eastern Edge and Southern Grounds.

Sequential no.	Predictor	Type of measurement	Data block	Predictor associated with	
				EE	SG
1	Pruning shoot number	Vine	1		
337	Calcium	Wine	11		
343	Lithium	Wine	11		
348	Sodium	Wine	11		
349	Strontium	Wine	11		
373	Myricetin	Wine	12		
387	Tannin molecular mass	Wine	12		
391	Mass conversion %	Wine	12		
397	Epicatechin %	Wine	12		
403	Mannose	Wine	13		
408	Galactose	Wine	13		
410	Arabinose	Wine	13		
431	Phenylethyl acetate	Wine	14		
452	β-Damascenone	Wine	14		
455	Dimethyl sulfide	Wine	14		
457	Methanethiol	Wine	14		
458	Methyl thioacetate	Wine	14		
460	3-Mercaptohexanol	Wine	14		
85	beta-damascenone	Grape	4		
110	2-Methylenebornane	Grape	4		
115	1-(2,3,6-Trimethylphenyl)-3-buten-2-one	Grape	4		
127	2,3-Dihydro-3,3,4,5-tetramethyl-1H-Inden-1-one	Grape	4		
150	Zeaxanthin	Grape	5		
151	Chlorophyll B	Grape	5		
152	Chlorophyll A	Grape	5		
158	Total Carotenoids	Grape	5		
205	alpha-Pinene	Grape	7		
208	Methylbenzene	Grape	7		
252	Ethyl octanoate	Grape	7		
273	gamma-Butyrolactone	Grape	7		
278	Diethyl succinate	Grape	7		
303	Peounidin-3-caffeoyl-glucoside	Grape	8		
304	Cyanidin-3-coumaroyl-glucoside + malvidin-3-caffeoyl-glucoside	Grape	8		
309	Extractable tannin (as mg/g berry weight)	Grape	8		
310	Extractable anthocyanin (as mg/g berry weight)	Grape	8		

6.1.9 Model between Eastern Edge and Western Ridge

The best binary RF model between Eastern Edge and Western Ridge achieved a classification error of 2.4%, with 7 predictors. One sample from Western Ridge in 2018 and one sample from Eastern Edge in 2021 were misclassified. Interestingly, for these two regions, three parameters from the vineyard measurements were chosen as the most important predictor.

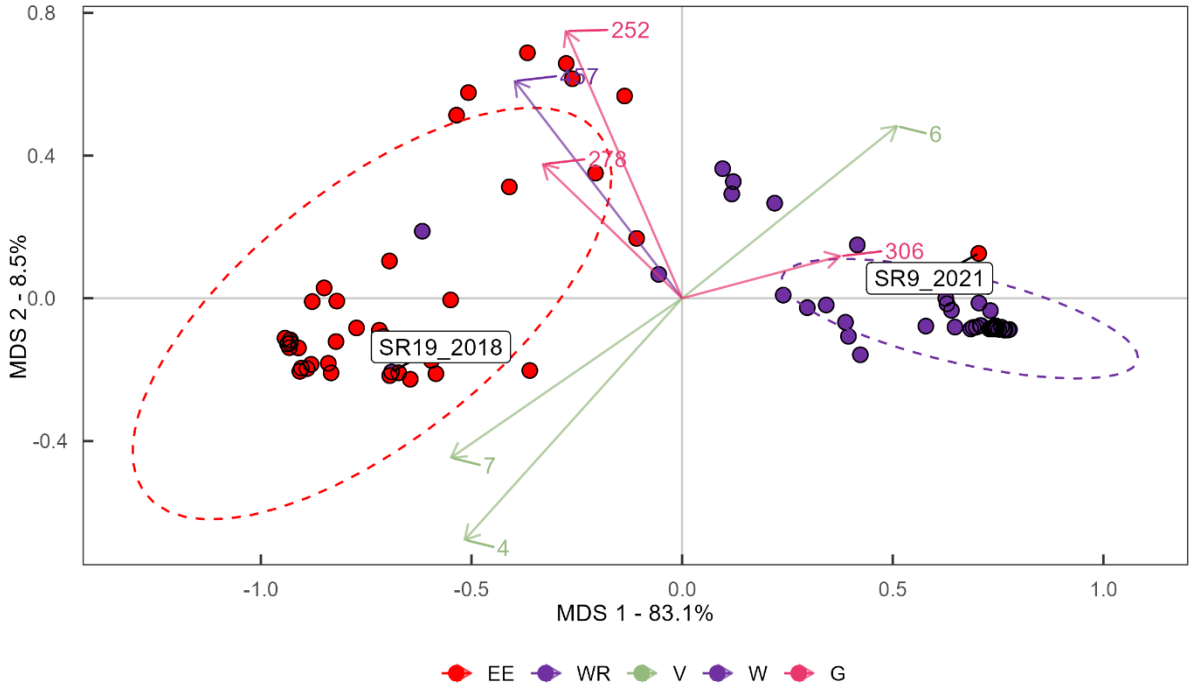


Figure 6.9 Biplot of the best RF model between Eastern Edge and Western Ridge. The selected predictors were labelled with their sequential number in Table 6.9, and coloured based on the measurement type: vineyard measurements (green), grape measurements (magenta) and wine measurements (purple).

Table 6.9 Selected predictors for the RF model between Eastern Edge and Western Ridge.

Sequential no.	Predictor	Type of measurement	Data block	Predictor associated with	
				EE	WR
4	Bunch number	Vine	1		
6	Porosity	Vine	1		
7	Plant area index	Vine	1		
457	Methanethiol	Wine	14		
252	Ethyl octanoate	Grape	7		
278	Diethyl succinate	Grape	7		
306	Peonidin-3-coumaroyl-glucoside	Grape	8		

6.1.10 Model between Northern Grounds and Eden Valley

The best binary RF model achieved a classification error of 1.2%, with 6 predictors. The first dimension accounted for 88.6% of total variance. Both Northern Grounds and Eden Valley had relatively high classification accuracy in the global model. It is not surprising that a relatively simple combination of predictors achieved good separation between these two regions.

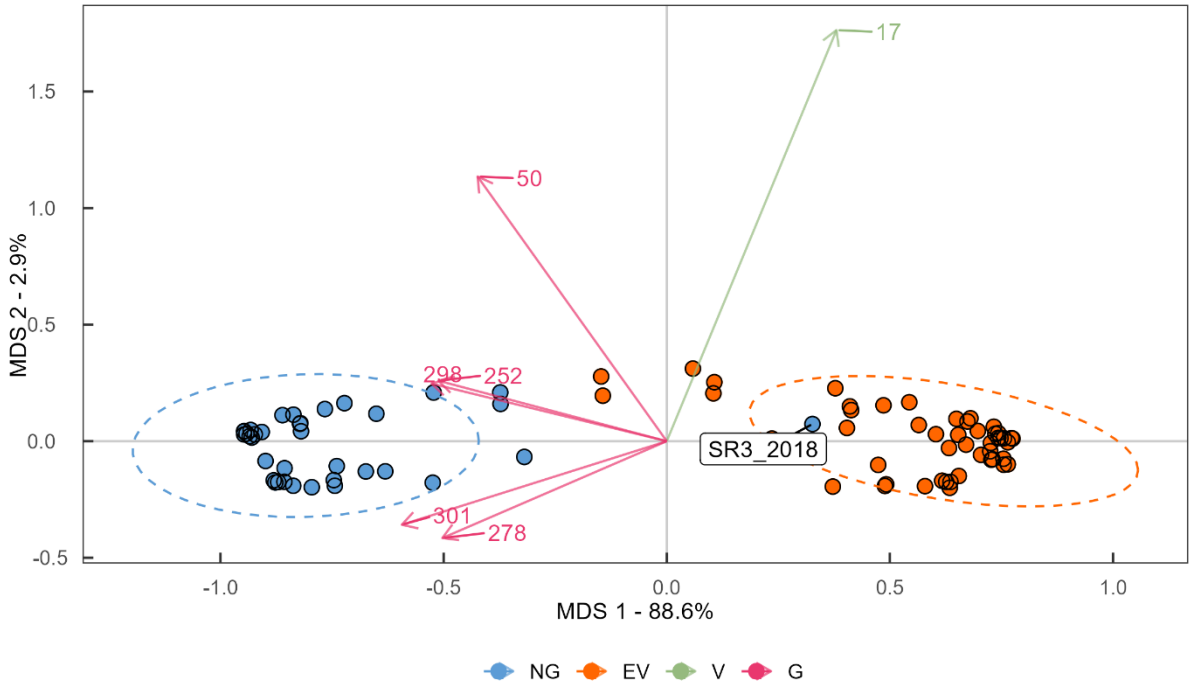


Figure 6.10 Biplot of the best RF model between Northern Grounds and Eden Valley. The selected predictors were labelled with their sequential number in Table 6.10, and coloured based on the measurement type: vineyard measurements (green), grape measurements (magenta) and wine measurements (purple).

Table 6.10 Selected predictors for the RF model between Northern Grounds and Eden Valley.

				Predictor associated with	
Sequential no.	Predictor	Type of measurement	Data block	NG	EV
17	Titratable Acidity	Vine	2		
50	3-hexanol	Grape	4		
252	Ethyl octanoate	Grape	7		
278	Diethyl succinate	Grape	7		
298	Cyanidin-3-acetyl-glucoside	Grape	8		
301	Malvidin-3-acetyl-glucoside	Grape	8		

6.1.11 Model between Southern Grounds and Eden Valley

The best binary RF model achieved a classification error of 1.2%, with 6 predictors.

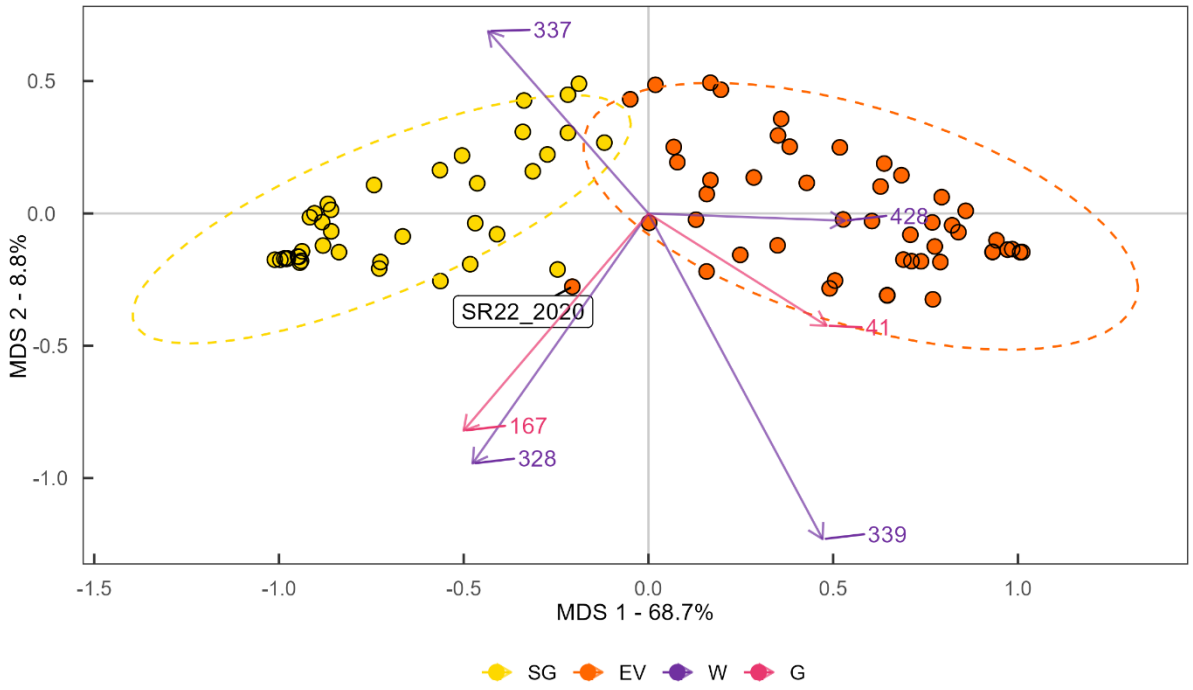


Figure 6.11 Biplot of the best RF model between Southern Grounds and Eden Valley. The selected predictors were labelled with their sequential number in Table 6.11, and coloured based on the measurement type: grape measurements (magenta) and wine measurements (purple).

Table 6.11 Selected predictors for the RF model between Southern Grounds and Eden Valley.

Sequential no.	Predictor	Type of measurement	Data block	Predictor associated with	
				SG	EV
328	Glucose + fructose	Wine	10		
337	Calcium	Wine	11		
339	Cobalt	Wine	11		
428	Ethyl hexanoate	Wine	14		
41	Phenylalanine	Grape	3		
167	Methyl heptadecanoate	Grape	6		

6.1.12 Model between Western Ridge and Eden Valley

The best binary RF model achieved a classification error of 1.2%, with 28 predictors. One sample from Eden Valley (Site 22) and two samples from Western Ridge (Site 18 and Site 20) were misclassified. The first dimension accounted for 69.2% total variance, which is lower than many other binary models. This result is somewhat surprising as both Western Ridge and Eden Valley had high classification accuracy in the overall model. It was expected that samples from these two regions could be discriminated with relative ease.

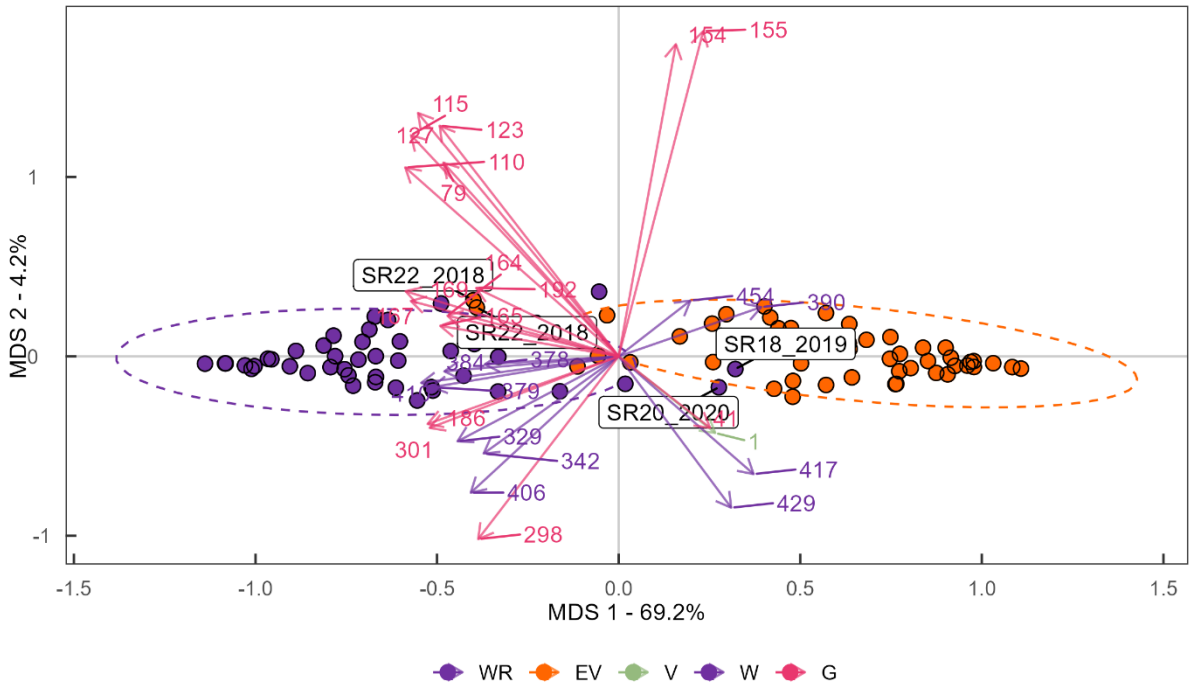


Figure 6.12 Biplot of the best RF model between Western Ridge and Eden Valley. The selected predictors were labelled with their sequential number in Table 6.12, and coloured based on the measurement type: vineyard measurements (green), grape measurements (magenta) and wine measurements (purple).

Table 6.12 Selected predictors for the RF model between Western Ridge and Eden Valley.

Sequential no.	Predictor	Type of measurement	Data block	Predictor associated with	
				WR	EV
1	Pruning shoot number	Vine	1		
329	Specific Gravity	Wine	10		
342	Lead	Wine	11		
378	Chemical age 1	Wine	12		
379	Chemical age 2	Wine	12		
384	Total phenolics	Wine	12		
390	% Epicatechin gallate (terminal and extension)	Wine	12		
406	Galacturonic acid	Wine	13		
410	Arabinose	Wine	13		
417	Hexyl acetate	Wine	14		
429	Ethyl octanoate	Wine	14		
454	Carbon disulfide	Wine	14		
41	Phenylalanine	Grape	3		
79	1,1,4,6,7-Pentamethyl-2,3-dihydroindene	Grape	4		
110	2-Methylenebornane	Grape	4		
115	1-(2,3,6-Trimethylphenyl)-3-buten-2-one	Grape	4		
123	1-(2,3,6-Trimethylphenyl)-2--butanone	Grape	4		
127	2,3-Dihydro-3,3,4,5-tetramethyl-1H-Inden-1-one	Grape	4		
154	Unknown 1	Grape	5		
155	Unknown 2	Grape	5		
164	Methyl tetradecanoate	Grape	6		
165	Methyl pentadecanoate	Grape	6		
167	Methyl heptadecanoate	Grape	6		
169	Methyl nonadecanoate	Grape	6		
186	Methyl octadecanoate	Grape	6		
192	2-Butanone	Grape	7		
298	Cyanidin-3-acetyl-glucoside	Grape	8		
301	Malvidin-3-acetyl-glucoside	Grape	8		

6.1.13 Model between Northern Grounds and Southern Grounds

The best binary RF model achieved a classification error of 0%, with 28 predictors. The two regions separated well on the first dimension, which accounted for 70% of variance.

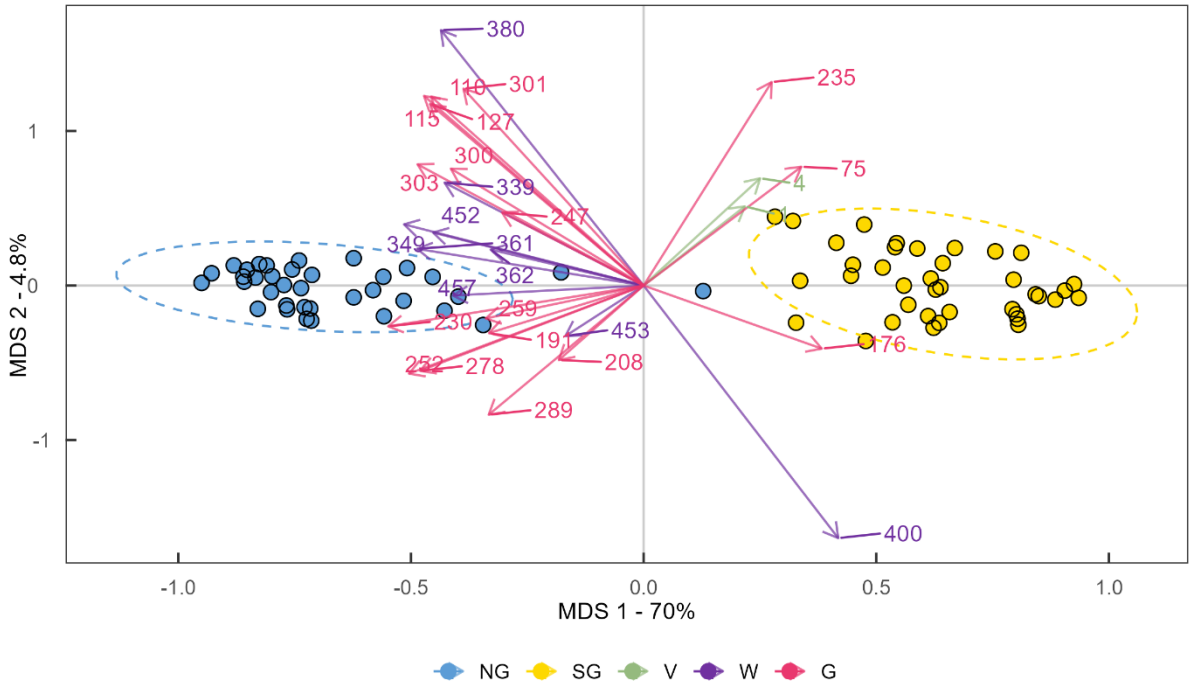


Figure 6.13 Biplot of the best RF model between Northern Grounds and Southern Grounds. The selected predictors were labelled with their sequential number in Table 6.13, and coloured based on the measurement type: grape measurements (magenta) and wine measurements (purple).

Table 6.13 Selected predictors for the RF model between Northern Grounds and Southern Grounds.

Sequential no.	Predictor	Type of measurement	block	Predictor associated with	
				NG	SG
1	Pruning shoot number	Vine	1		
4	Bunch number	Vine	1		
339	Cobalt	Wine	11		
349	Strontium	Wine	11		
361	peonidin-3-acetyl-glucoside	Wine	12		
362	malvidin-3-acetyl-glucoside	Wine	12		
380	Wine Colour Density	Wine	12		
400	CIELab-L*	Wine	12		
452	β-Damascenone	Wine	14		
453	β-Ionone	Wine	14		
457	Methanethiol	Wine	14		
75	alpha-Fenchene	Grape	4		
110	2-Methylenebornane	Grape	4		
115	1-(2,3,6-Trimethylphenyl)-3-buten-2-one	Grape	4		
127	2,3-Dihydro-3,3,4,5-tetramethyl-1H-Inden-1-one	Grape	4		
176	Methyl (Z)-13-docosenoate	Grape	6		
191	Ethyl acetate	Grape	7		
208	Methylbenzene	Grape	7		
230	Styrene	Grape	7		
235	1-Octen-3-one	Grape	7		
247	2,4-Hexadienal	Grape	7		
252	Ethyl octanoate	Grape	7		
259	2-Ethyl-1-hexanol	Grape	7		
278	Diethyl succinate	Grape	7		
289	Phenylethyl alcohol	Grape	7		
300	Peonidin-3-acetyl-glucoside	Grape	8		
301	Malvidin-3-acetyl-glucoside	Grape	8		
303	Peounidin-3-caffeoyl-glucoside	Grape	8		

6.1.14 Model between Northern Grounds and Western Ridge

The best binary RF model achieved a classification error of 0%, with 15 predictors. The two regions separated well on the first dimension which accounted for 85.3% of total variance.

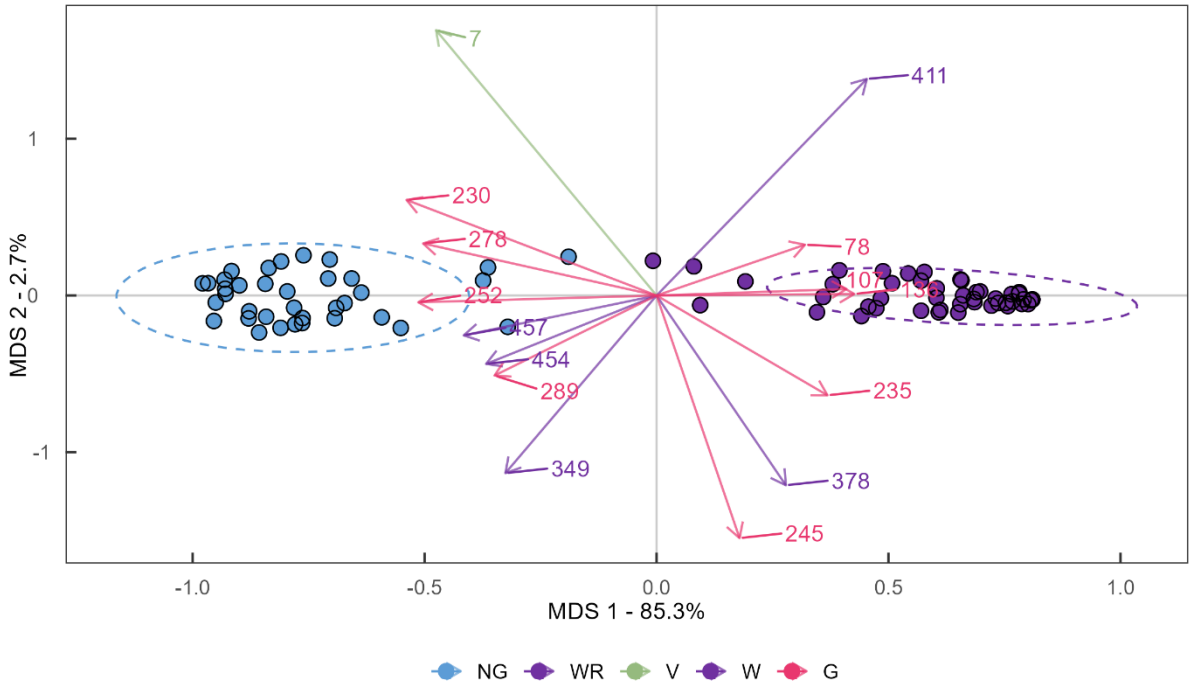


Figure 6.14 Biplot of the best RF model between Northern Grounds and Western Ridge. The selected predictors were labelled with their sequential number in Table 6.14, and coloured based on the measurement type: vineyard measurements (green), grape measurements (magenta) and wine measurements (purple).

Table 6.14 Selected predictors for the RF model between Northern Grounds and Western Ridge.

Sequential no.	Predictor	Type of Measurement	Data block	Predictor associated with	
				NG	WR
7	Plant area index	Vine	1		
349	Strontium	Wine	11		
378	Chemical age 1	Wine	12		
411	Fucose	Wine	13		
454	Carbon disulfide	Wine	14		
457	Methanethiol	Wine	14		
78	Alpha-terpineol	Grape	4		
107	4-(2,6,6-Trimethylcyclohexa-1,3-dienyl)but-3-en-2-one	Grape	4		
136	(Z)-5-Methyl-4-phenyl-3-hexen-2-ol	Grape	4		
230	Styrene	Grape	7		
235	1-Octen-3-one	Grape	7		
245	(Z)-3-Hexen-1-ol	Grape	7		
252	Ethyl octanoate	Grape	7		
278	Diethyl succinate	Grape	7		
289	Phenylethyl alcohol	Grape	7		

6.1.15 Model between Southern Grounds and Western Ridge

Compared to all other binary models, this model had the highest misclassification rate at 8.3%. Five samples from Southern Grounds were misclassified, of which four were from Site 16. Site 16 samples were also consistently misclassified as Western Ridge sample in the global model. It is possible that Site 16 shared similarities with characteristics of Western Ridge. Interestingly, it seems that vineyard measurements were relatively important in discriminating Southern Grounds and Western Ridge samples.

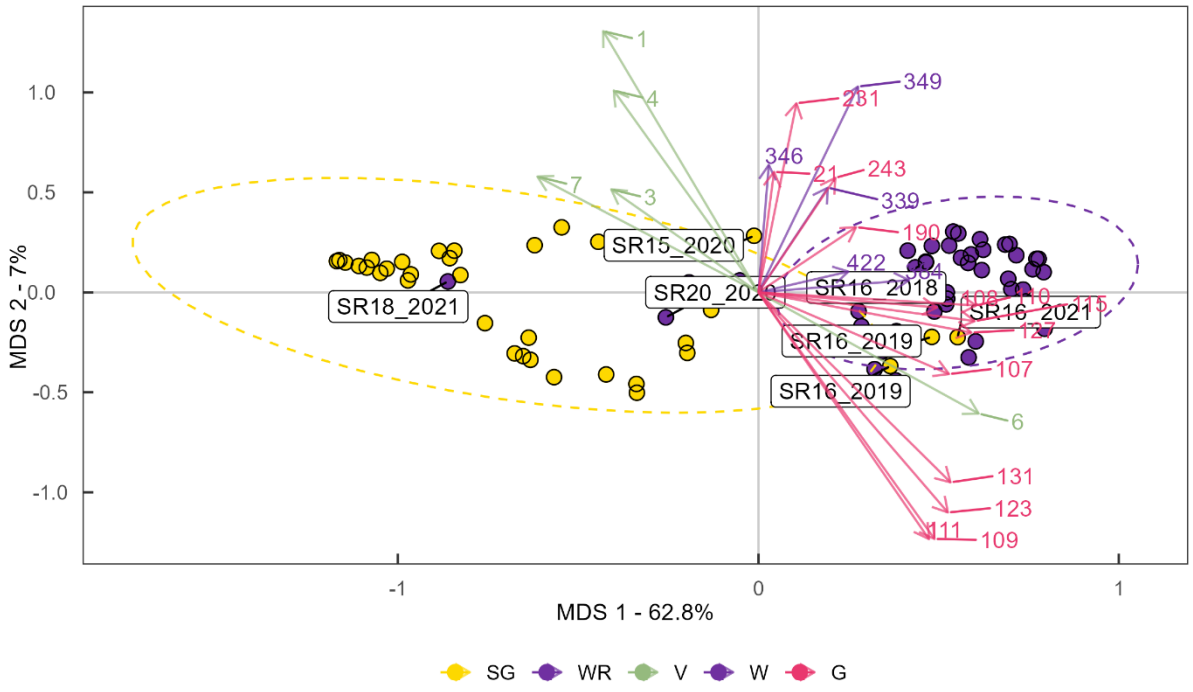


Figure 6.15 Biplot of the best RF model between Southern Grounds and Western Ridge. The selected predictors were labelled with their sequential number in Table 6.15, and coloured based on the measurement type: vineyard measurements (green), grape measurements (magenta) and wine measurements (purple).

Table 6.15 Selected predictors for the RF model between Southern Grounds and Western Ridge.

Sequential no.	Predictor	Type of measurement	Data block	Predictor associated with	
				SG	WR
1	Pruning shoot number	Vine	1		
3	Yield	Vine	1		
4	Bunch number	Vine	1		
6	Porosity	Vine	1		
7	Plant area index	Vine	1		
339	Cobalt	Wine	11		
346	Nickel	Wine	11		
349	Strontium	Wine	11		
384	Total phenolics	Wine	12		
422	Ethyl acetate	Wine	14		
21	Aspartic acid	Grape	3		
107	4-(2,6,6-Trimethylcyclohexa-1,3-dienyl)but-3-en-2-one	Grape	4		
108	Unknown 1	Grape	4		
109	1,2-Dihydro-1,4,6-trimethyl-naphthalene,	Grape	4		
110	2-Methylenebornane	Grape	4		
111	1,2-Dihydro-3,5,8-trimethyl-naphthalene,	Grape	4		
115	1-(2,3,6-Trimethylphenyl)-3-buten-2-one	Grape	4		
123	1-(2,3,6-Trimethylphenyl)-2--butanone	Grape	4		
127	2,3-Dihydro-3,3,4,5-tetramethyl-1H-Inden-1-one	Grape	4		
131	4-(2,4,6-Trimethylphenyl)-butan-2-ol	Grape	4		
190	Methyl (Z,Z,Z)-9,12,15-octadecenoate	Grape	6		
231	Hexyl acetate	Grape	7		
243	1-Hexanol	Grape	7		